UNIVERSIDAD COMPLUTENSE DE MADRID
FACULTAD DE CIENCIAS FÍSICAS

TESIS DOCTORAL

A far-infrared study of low and intermediate mass evolved stars using "Herschel" PACS and SPIRE Spectroscopy

Estudio en el infrarrojo lejano de estrellas evolucionadas de masa baja e intermedia usando datos espectroscópicos de los instrumentos de Herschel PACS y SPIRE

MEMORIA PARA OPTAR AL GRADO DE DOCTOR

PRESENTADA POR

Jesús Ramos Medina

Supervisors

Carmen Sánchez Contreras
Pedro García Lario

Madrid

Universidad Complutense de Madrid
Facultad de Ciencias Físicas

Centro de Astrobiología (CAB, INTA-CSIC)
European Space Astronomy Center (ESAC-ESA)

Doctoral Thesis

A Far-Infrared Study of Low and Intermediate Mass Evolved Stars using *Herschel* PACS and SPIRE Spectroscopy

Estudio en el infrarrojo lejano de estrellas evolucionadas de masa baja e intermedia usando datos espectroscópicos de los instrumentos de *Herschel* PACS y SPIRE

Author:
Jesús Ramos Medina

Supervisors:
Dra. Carmen Sánchez Contreras
(CAB-CSIC)
Dr. Pedro García Lario
(ESAC-ESA)

UNIVERSIDAD COMPLUTENSE MADRID

DECLARACIÓN DE AUTORÍA Y ORIGINALIDAD DE LA TESIS PRESENTADA PARA OBTENER EL TÍTULO DE DOCTOR

D./Dña. JESÚS RAMOS MEDINA,
estudiante en el Programa de Doctorado ASTROFÍSICA,
de la Facultad de FÍSICAS de la Universidad Complutense de Madrid, como autor/a de la tesis presentada para la obtención del título de Doctor y titulada: A FAR-INFRARED STUDY OF LOW AND INTERMEDIATE MASS EVOLVED STARS USING HERSCHEL PACS AND SPIRE SPECTROSCOPY

ESTUDIO EN EL INFRARROJO LEJANO DE ESTRELLAS EVOLUCIONADAS DE MASA BAJA E INTERMEDIA USANDO DATOS ESPECTROSCÓPICOS DE LOS INSTRUMENTOS DE HERSCHEL, PACS Y SPIRE

y dirigida por: DRA. CARMEN SÁNCHEZ CONTRERAS
DR. PEDRO GARCÍA LARIO

DECLARO QUE:

La tesis es una obra original que no infringe los derechos de propiedad intelectual ni los derechos de propiedad industrial u otros, de acuerdo con el ordenamiento jurídico vigente, en particular, la Ley de Propiedad Intelectual (R.D. legislativo 1/1996, de 12 de abril, por el que se aprueba el texto refundido de la Ley de Propiedad Intelectual, modificado por la Ley 2/2019, de 1 de marzo, regularizando, aclarando y armonizando las disposiciones legales vigentes sobre la materia), en particular, las disposiciones referidas al derecho de cita.

Del mismo modo, asumo frente a la Universidad cualquier responsabilidad que pudiera derivarse de la autoría o falta de originalidad del contenido de la tesis presentada de conformidad con el ordenamiento jurídico vigente.

En Madrid, a 25 de SEPTIEMBRE de 2019

Fdo.: _____

Esta DECLARACIÓN DE AUTORÍA Y ORIGINALIDAD debe ser insertada en la primera página de la tesis presentada para la obtención del título de Doctor.

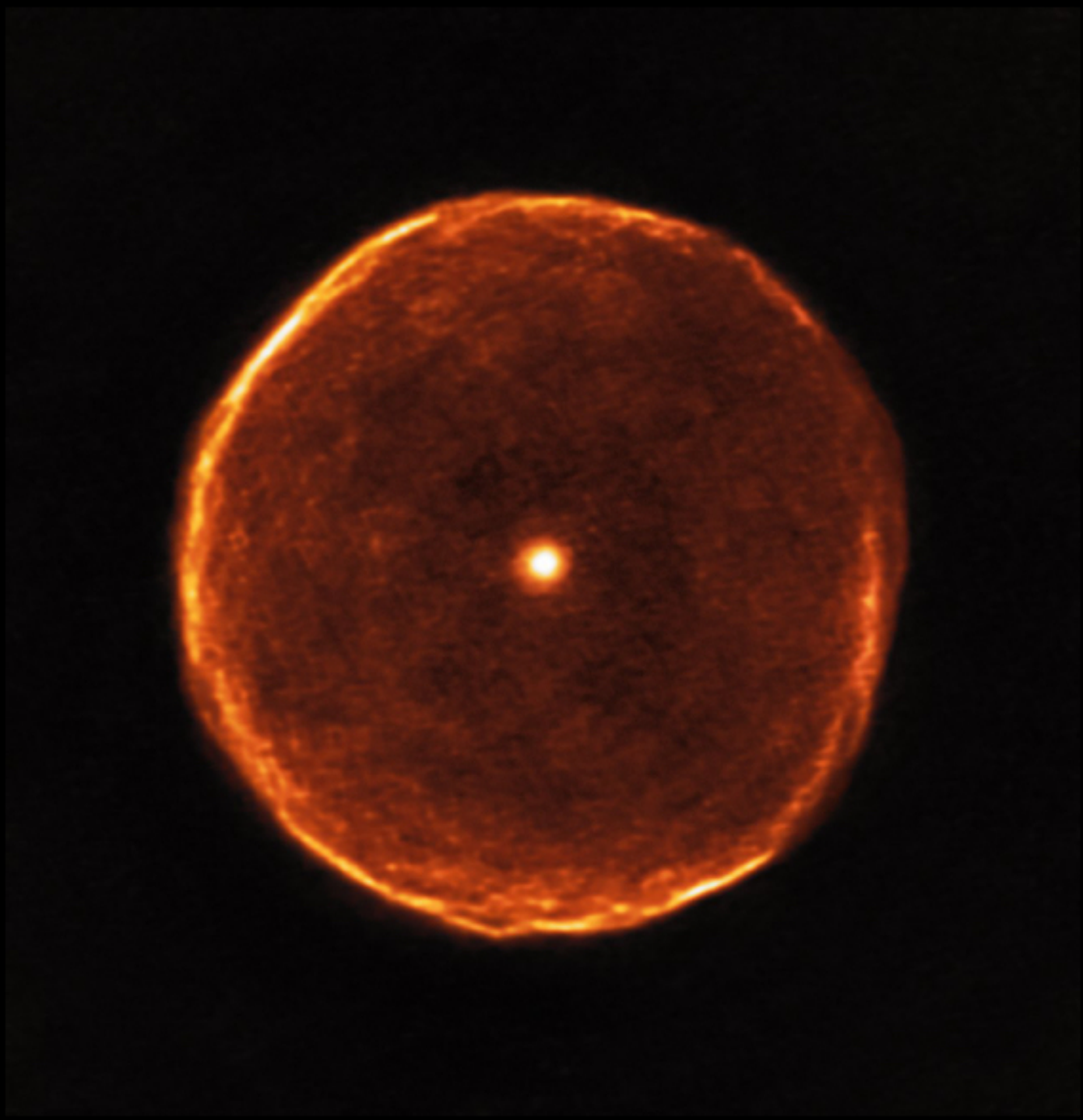

UNIVERSIDAD COMPLUTENSE MADRID

DECLARACIÓN DE AUTORÍA Y ORIGINALIDAD DE LA TESIS PRESENTADA PARA OBTENER EL TÍTULO DE DOCTOR

D./Dña._____,
estudiante en el Programa de Doctorado _____,
de la Facultad de _____ de la Universidad Complutense de Madrid, como autor/a de la tesis presentada para la obtención del título de Doctor y titulada:

_____

_____

y dirigida por: _____

_____

_____

DECLARO QUE:

La tesis es una obra original que no infringe los derechos de propiedad intelectual ni los derechos de propiedad industrial u otros, de acuerdo con el ordenamiento jurídico vigente, en particular, la Ley de Propiedad Intelectual (R.D. legislativo 1/1996, de 12 de abril, por el que se aprueba el texto refundido de la Ley de Propiedad Intelectual, modificado por la Ley 2/2019, de 1 de marzo, regularizando, aclarando y armonizando las disposiciones legales vigentes sobre la materia), en particular, las disposiciones referidas al derecho de cita.

Del mismo modo, asumo frente a la Universidad cualquier responsabilidad que pudiera derivarse de la autoría o falta de originalidad del contenido de la tesis presentada de conformidad con el ordenamiento jurídico vigente.

En Madrid, a ____ de _____ de 20___

Fdo.: _____

Esta DECLARACIÓN DE AUTORÍA Y ORIGINALIDAD debe ser insertada en la primera página de la tesis presentada para la obtención del título de Doctor.

"*Caminante, son tus huellas el camino y nada más. Caminante, no hay camino, se hace camino al andar.*"

Antonio Machado

Agradecimientos

Según el diccionario de la Real Academia Española la definición de *tesis* es: *"Disertación escrita que presenta a la universidad el aspirante al título de doctor en una facultad"*. Siendo esencialmente cierta, todas aquellas personas que han desarrollado una tesis doctoral o que lo han vivido de forma cercana, saben que esta definición es bastante incompleta. Una tesis va mucho más allá de los estudios y las investigaciones, en mi opinión, una tesis es un viaje académico, profesional y, principalmente, **personal**. Por ello, ha llegado el momento de hacer justicia y agradecer y reconocer la labor de todas aquellas personas que, de una forma u otra, han formado parte de esta aventura.

En primer lugar me gustaría dar las gracias a mis directores de tesis: Carmen y Pedro que sin duda han sido una pieza fundamental e imprescindible para que este proyecto haya podido llegar a término. Gracias por vuestra confianza, vuestros consejos y vuestra dedicación durante estos años en los que me habéis transmitido numerosas enseñanzas que han permitido que me desarrolle como profesional a diario. Gracias también a Joao por sus aportaciones a lo largo de este proyecto.

También quiero agradecer a Miguel Sánchez Portal, a Isaac Domínguez y a Ricardo Pérez por permitirme formar parte de ISDEFE y apoyarme en todo lo necesario durante este periodo. Gracias también a Elena Puga, Ivan Valtchanov y Katrina Exter, miembros del equipo de *Herschel*, por sus consejos y ayuda en la fase inicial de la tesis.

Siempre he creído que la grandeza de una organización depende de la calidad humana de las personas que la componen, por este motivo, me gustaría destacar a aquellas personas que se esconden detrás de las siglas, aunque son muchos los nombres y es difícil destacarlos a todos, vamos a intentarlo:

Gracias a los compañeros del CAB: a Miguel, David, Margie, María, Giovanni, Jorge Sanz, Fran, Miriam, Jesús Maíz, Almudena, Julia, Jose Manuel, Antonio, Sergio, Mauro y Ángel Luis. Gracias a Carlos Rodrigo y a Enrique Solano por el soporte y ayuda durante el desarrollo de los catálogos.

Gracias a Miguel y a Alice por convertirse en mis compañeros de despacho durante mis últimos meses en ESAC y por hacer del día a día un verdadero disfrute.

Gracias a Jose Antonio Caballero, por nuestra pasión compartida por la música, desde el flamenco hasta el *Requiem* de Mozart, gracias también por su vitalidad y su pasión en todo lo que hace. Gracias a Nuria por su empatía y su afecto.

Gràcies a l´Albert per la seva simpatia, la seva temprança i per fer de la prudència virtut.

Gracias a Bea por su sonrisa constante y su buen humor. Por convertir un simple "Buenos días" en un pequeño ritual.

Gracias a Pablo Riviere, por nuestras múltiples y variadas conversaciones: científicas, futbolísticas y, las más importantes, políticas. Porque siempre es reconfortante encontrar espacios y momentos para pensar y dialogar.

Gracias a Benja, por ser una persona tremendamente especial. Gracias por los consejos y el apoyo en los malos momentos y gracias por estar ahí para disfrutar de los buenos. Espero que en el futuro podamos seguir compartiendo juntos las evoluciones de nuestro amigo de la infancia, ese de colores blaugranas.

Si lo bueno de permanecer muchos años en un lugar es que puedes establecer contacto con un gran número de personas, lo malo es que debes aprender a despedirte de algunas de ellas. En mi caso quiero destacar a aquellos que me acompañaron en mis primeros años:

Gracias a Lillo, Alba, Bea, Nacho, Mario y Aguado porque todos sabemos lo importante (y lo difícil) que es hacer reír en según qué momentos y con vosotros siempre se conseguía.

Gracias también a Irene y Álvaro, mis primeros compañeros de despacho. Gracias por todas esas conversaciones hablando de lo divino y de lo humano, gracias por todo lo compartido porque, pase lo que pase, nunca se nos puede olvidar el RES-PE-TO.

Gracias a Paco, básica y principalmente, por ser una gran persona, por su sentido del humor, su ironía, su filosofía de vida. Por todo lo reído, lo sufrido y lo disfrutado. Porque nadie mejor que tú sabe que cuando la carretera se empina es el momento de lanzar el ataque.

La tesis, como metáfora de la vida que puede llegar a ser, crece y evoluciona contigo acompañándote en tus diferentes caminos. Uno de esos caminos me ha llevado a terminar este proyecto lejos de donde lo empecé. Sin embargo, en mi nuevo destino, he encontrado unos compañeros que han vivido con verdadera pasión este proyecto haciéndolo, prácticamente, un proyecto común. Por ello es de justicia dar las gracias también a Marcos, Diego, Luis, Pablo y Pedro por su afecto, sus ánimos y su apoyo durante este último año. Gracias a Jáuregui, Dani, Mario, Rubén, Edu, Fer, Leticia, Ángel, Vicente, Juan y Diana por su interés en esta tesis. Gracias, finalmente, a Carlos y Álvaro por su comprensión, su curiosidad y su disponibilidad para ayudarme en todo lo necesario. Gracias, en definitiva, a todos ellos por ser un ejemplo perfecto de compañerismo, ilusión y talento.

Como comentaba al principio, la tesis es también un viaje personal. Un viaje que obliga en muchas ocasiones a alejarse de aquellas personas que más nos quieren y a las que de forma continuada se les pide comprensión, paciencia y sacrificio, sin ofrecerles nada a cambio. Ellos son pilares fundamentales de este proyecto y a ellos debo darles las gracias de una forma especial.

Gracias a Willie y Gonzalo, porque a pesar de la distancia siempre nos tenemos presentes para compartir los momentos especiales que vamos viviendo.

Gracias a los físicos, Bea, Inés, Cristina, Bae, Jesús, Bolu, Manu y Guille porque como hemos reiterado en muchas ocasiones, la carrera y todo lo que hemos vivido con posterioridad, se habría hecho mucho más difícil sin vosotros. De verdad, gracias por las risas.

Gracias a Nebreda, Fer, Chiwi, Iglesias, Jaime, Ramón, Sergio, Chuso, Arturo, Luis, Richi, Borja y Pitu, porque a pesar de las ausencias sabemos que nos tenemos los unos a los otros. Porque nos quedan muchos años por delante para seguir disfrutando. Es un inmenso placer teneros en mi vida.

Gracias a los de siempre: Ángel, Gonzalo, Jimmy y Sergio, porque sobran las palabras entre nosotros, porque es un gusto mirar a los lados y veros en el mismo lugar desde hace ya tantos años, porque todo lo vivido no es nada comparado con lo que nos queda por vivir, por ser tan distintos y a la vez tan iguales. Gracias porque nos hemos visto crecer, porque nuestros sueños de pequeños se van haciendo realidad, porque todavía quedan muchos por cumplir. Gracias.

Gracias a Mari, por tu afecto y tu cariño, por tu sacrificio y tu comprensión, gracias por querer compartir todo conmigo, gracias por estar a mi lado, gracias por tu confianza, gracias por todos estos años, gracias por todos los que están por venir. Gracias, simplemente, por ser como eres. Gracias por ser **tú**.

Gracias, de corazón, a mis hermanas, Itzíar y Rocío, por ser el mejor espejo en el que mirarme, gracias por vuestra generosidad y cariño desinteresados, gracias por vuestras atenciones, vuestros consejos y vuestros ánimos. Por vuestro coraje, por vuestra valentía y vuestra capacidad de superación, por ser el mejor ejemplo de talento y constancia que haya conocido nunca. Gracias por apoyarme en cada momento, gracias por ser únicas y especiales. Gracias por hacer de este mundo un lugar mejor.

Finalmente, un sencillo y contundente GRACIAS a mis padres. Mamá, papá, no tengo palabras para agradeceros todo lo que habéis hecho por mí durante toda mi vida. Gracias por todo el amor que me habéis dado. Gracias por la educación y los valores que me habéis transmitido, gracias por dejar siempre bien claro que el fin nunca justifica los medios, gracias por demostrar a diario que lo primero son las personas. Gracias por vuestra valentía, vuestro sosiego, vuestra **sabiduria**, vuestros desvelos. Gracias por toda la confianza que habéis depositado siempre en mí, gracias por disfrutar de este camino juntos, gracias por todas las horas que hemos pasado juntos, gracias por ser los mejores padres que podría desear, gracias por ser mis referentes, gracias por enseñarme a vivir la vida con pasión. Gracias porque sois el motor de mi vida, gracias porque sin vosotros, nada de esto hubiera sido posible.

Contents

List of Figures

List of Tables

A mi familia, por brillar siempre con luz propia.

Summary

In this thesis, a far-infrared (FIR) study of evolved low and intermediate mass stars is presented. The characterization of these evolved stars is particularly interesting when we analyse their properties in the FIR and the sub-millimeter wavelength regions. Due to the very promising spectroscopic data of *Herschel*, PACS (50-220 μm) and SPIRE (200-600 μm) observations have been included in this thesis to carry out a systematic an homogeneous study of a relatively big sample of evolved stars which cover different evolutionary stages (AGBs, post-AGBs and PNe) and chemical types.

The first main step of this work was the systematic and homogeneous data reduction process developed for two different sample of sources observed with PACS and (or) SPIRE in spectroscopic mode. The stars included in the reprocessed sample were taken from the *Herschel* Science Archive, as they have been previously observed with these instruments as part of numerous observing programs. As a result two different web-based catalogues (*https://throes.cab.inta-csic.es* and *https://throes-spire.cab.inta-csic.es*) were created to offer, to the whole scientific community, 220 science-ready spectroscopic data corresponding to 114 different evolved stars observed with PACS and, also, 109 fully-reduced SPIRE spectra associated to 68 individual targets.

Once the spectroscopic data were completely reduced, the next step consisted on the study and characterization of the Circumstellar Envelopes (CSEs), generated around these evolved stars. To do that, CO rotational emitting lines were detected and measured from both PACS and SPIRE spectra, covering a complete ladder of rotational levels from J=4-3 up to J=42-41. From these fluxes, basic physical magnitudes such as: total emitting masses, rotational temperatures of the gas and mass-loss rates were estimated by using basic Rotational Diagram (RD) analysis. The samples included in the different studies were separately studied attending to the chemical types of the stars (O-rich or C-rich).

Due to the different wavelength regions covered by PACS and SPIRE, we were able to observe a wide sample of CO emission lines which probe different regions of the CSEs at typical distances of $\sim10^{15}$-$\sim10^{16}$ cm, with $E_{\rm u}$ from ~55 to ~5500 K. As expected, the rotational temperatures derived from SPIRE RDs are lower than those found for PACS ones (~80 K and ~500 K, respectively). Regarding total mass, the values derived from SPIRE analysis were approximately an order of magnitude larger than that from PACS. Meanwhile, the mass-loss rates estimated were reasonably similar ($\sim10^{-7}$ to $\sim10^{-4}$ $M_{\odot}$ yr^{-1}).

The complementary analysis developed joining PACS and SPIRE data, has allowed to understand in a better way the global picture of the physical properties of the gas at different regions of the CSEs. Apart from estimated magnitudes mentioned above, we have also studied how the temperature profile varies across the CSE. Certainly, some interesting (anti-)correlations have been found between fundamental parameters such as: the total emitting mass versus the rotational temperature (negative).

From all these analysis we conclude that multi-wavelength studies are essential to properly

understand the physical phenomena that take place in the inner-to-intermediate envelope layers of the CSEs. Furthermore, PACS Spectroscopy has generated really unique observations that have allowed us to study, for the first time, in a systematically and homogeneous way, the innermost regions of CSEs. The comparison of our results with previous works found in bibliography based of rotational CO lines has shown a good agreement which reinforces the RD technique as a good method to obtain first order estimates of fundamental magnitudes such as: mass and temperature. Finally, this thesis can be taken as good starting point of future analysis where new data and more amount of objects will be included. In this way, all the trends and interpretations derived from these results, could be statistically confirmed.

Part of the work presented in this thesis is included in the following scientific papers: Ramos-Medina et al., 2018a, Ramos-Medina et al., 2018b, Ramos-Medina et al., 2018c and da Silva Santos et al., 2019. Since its publication, the THROES-PACS catalogue has received more than 1700 visits while 4500 observations have been downloaded.

Resumen

En esta tesis se ha llevado a cabo un estudio homogéneo y sistemático de una amplia muestra de estrellas evolucionadas con masas menores a 8 masas solares observadas en el infrarrojo lejano y en el sub-milimétrico haciendo uso de los espectros generados con los instrumentos PACS (50-220 μm) y SPIRE (200-600 μm) del telescopio espacial *Herschel*. La muestra incorporada en este estudio presenta una gran variedad de tipos químicos, así como diferentes estados evolutivos.

Como primer paso, fue necesario realizar una recopilación de todas las observaciones espectroscópicas realizadas con PACS y SPIRE relacionadas con estrellas evolucionadas no masivas disponibles en el Archivo Científico de *Herschel*. Cada una de estos espectros formaban parte de diferentes programas de observación que se han ido llevando a cabo durante el tiempo de vida del telescopio espacial *Herschel*. Una vez identificadas las observaciones que queríamos incluir en nuestra tesis desarrollamos uno de las fases más importantes de este proyecto, la reducción sistemática de los datos. Esta reducción permitió generar observaciones completamente explotables desde un punto de vista científico, a partir de los datos "crudos" descargados del Archivo. Como resultado 220 espectros de PACS asociados a 114 objetos distintos y 109 espectros de SPIRE asociados a 68 estrellas, fueron incorporadas en sendos catálogos (uno para los datos de PACS y otro para los de SPIRE) para ser accesibles vía web, de forma pública, por toda la comunidad científica.

Tras la reducción de los espectros, se inició la fase de estudio y caracterización de las envolturas circumestelares. Para ello se decidió hacer uso de las líneas rotacionales de emisión de CO dado que son fácilmente identificables y medibles tanto en los espectros de PACS como los de SPIRE. Además, el uso conjunto de ambos tipos de datos nos ha dotado de una valiosa información al cubrir un amplio rango de líneas rotacionales desde la J=4-3 hasta la J=42-41. Los flujos estimados para todas estas líneas fueron la pieza fundamental para poder derivar, posteriormente, magnitudes físicas básicas de las envolutras como, por ejemplo: su masa total en emisión, la temperatura rotacional del gas o la tasa de pérdida de masa de la estrella, haciendo uso del método de diagramas rotacionales. En los estudios realizados separamos las muestras en función de su tipo químico (ricas en oxígeno, ricas en carbono o estrellas de tipo S).

De los análisis rotacionales obtuvimos los siguientes resultados: las temperaturas rotacionales estimadas para ambas muestras de estrellas oxigenadas y carbonadas, con datos de PACS cubren un rango similar entre los ∼200 y los ∼700 K, por su parte las masas totales derivadas varían entre las $\sim 10^{-6}$ and $\sim 10^{-2}$ masas solares que dan lugar a unas tasas de pérdida de masas entre las $\sim 10^{-7}$ to $\sim 10^{-4}$ $M_{\odot}$ yr^{-1}. Por otro lado, analizando los resultados de SPIRE obtuvimos menores temperaturas rotacionales (∼40-∼90 K) y valores de masas algo mayores que varían entre los $\sim 10^{-5}$ and $\sim 10^{-1}$ $M_{\odot}$, esto es esperado al trazar SPIRE regiones más externas dentro de las envolturas estelares que PACS. Finalmente, los valores de tasas de pérdida de masa son muy similares a los ya encontrados en PACS entre los $\sim 10^{-7}$ to $\sim 10^{-4}$ $M_{\odot}$ yr^{-1}.

El estudio conjunto de los datos de PACS y SPIRE incorporado en esta tesis es de gran

interés ya que nos ha permitido obtener un visión global de las propiedades físicas del gas presente en las envolturas estelares en diferentes regiones de las mismas. En este sentido, hemos sido capaces de obtener una estimación aproximada de cómo varía el perfil de temperaturas a lo largo de la envoltura. Por último, diferentes correlaciones, positivas y negativas, se han extraído al comparar diferentes parámetros fundamentales de las estrellas como por ejemplo: la anticorrelación identificada entre la masa total y la temperatura rotacional.

Tras el análisis de los datos realizado, podemos concluir que los estudios observacionales que abarcan diferentes rangos de longitudes de onda (sub-mm e infrarrojo lejano en nuestro caso) son fundamentales para conocer de forma adecuada los diferentes fenómenos físicos que tienen lugar en el interior de las envolturas estelares. Además, los espectros obtenidos con el instrumento PACS han demostrado poseer un valor único a la hora de estudiar por primera vez de forma sistemática las regiones más internas de las envolturas de un amplio número de fuentes. La buena congruencia encontrada entre nuestros resultados y aquellos obtenidos en trabajos anteriores, encontrados en la literatura, permiten confirmar que la técnica de los diagramas rotacionales es un método suficientemente bueno para obtener estimaciones razonables de magnitudes fundamentales, tales como la masa y la temperatura promedio en las regiones de emisión. Finalmente, esta tesis, junto con los datos proporcionados en el catálogo, puede ser tomada como un buen punto de inicio para ampliar los estudios aquí presentados con nuevas observaciones y una muestra de objetos más amplia que permita confirmar de una forma estadísticamente significativa, las tendencias e interpretaciones derivadas actualmente.

Parte del análisis desarrollado en esta tesis ha quedado plasmado en diferentes artículos científicos: Ramos-Medina et al., 2018a, Ramos-Medina et al., 2018b, Ramos-Medina et al., 2018c and da Silva Santos et al., 2019. Por otro lado, el catálogo de THROES-PACS ha recibido más de 1700 visitas y más de 4500 observationes han sido descargadas desde su publicación.

Chapter 1

Introduction

Aire

José Mercé

In this chapter we present a description of the physical properties of the CSEs of Asymptotic giant Branch stars (AGBs), post-AGBs and (Planetary Nebulae) PNe, based on the current knowledge of this topic. Furthermore, different mass-loss rates estimators are described analysing the favourable and unfavourable factors of each one. Finally, a detailed description of *Herschel* and its instrument is included.

1.1 A few notes on stellar evolution

The fate of stars in the Universe is, mainly, determined by its birth mass. This magnitude will define the evolutionary track that stars will follow as it determines the physical processes that take place in their inner regions. The Hertzsprung-Russell (HR) diagram is one of the most useful tools to study and understand stellar evolution. In this diagram stars are located attending to their luminosities (L) and their effective temperatures ($T_{\rm eff}$) and the changes in the L and $T_{\rm eff}$ magnitudes along the life of the stars, as a result of their evolution, determine the path followed in the HR diagram, see Fig. 1.1. The following section is mainly based on *Asymptotic giant branch stars* 2003, van Winckel, 2003.

The Main Sequence (MS) is defined as that stage in the evolution of the stars characterized by the presence of fusion reactions of Hydrogen in their cores. Stars spend most of their lifetime in the MS stage, keeping their luminosities and effective temperatures roughly constant while the Hydrogen is converted in a very efficient way into heavier elements such as: Helium, Carbon or Oxygen, producing, also, an enormous amount of energy. There are two main mechanisms that drive the fusion reactions: the proton-proton chain, for stars with masses $< 2\ M_{\odot}$, and the CNO cycle, that is dominant in stars with M$>2\ M_{\odot}$.

Stars in the MS are located in the HR diagram along the diagonal strip, from top left to bottom right, where the more massive stars, at the top left, are characterized by high luminosities and effective temperatures, while the less massive ones are located in the bottom right region of the diagram due to their low luminosities and effective temperatures.

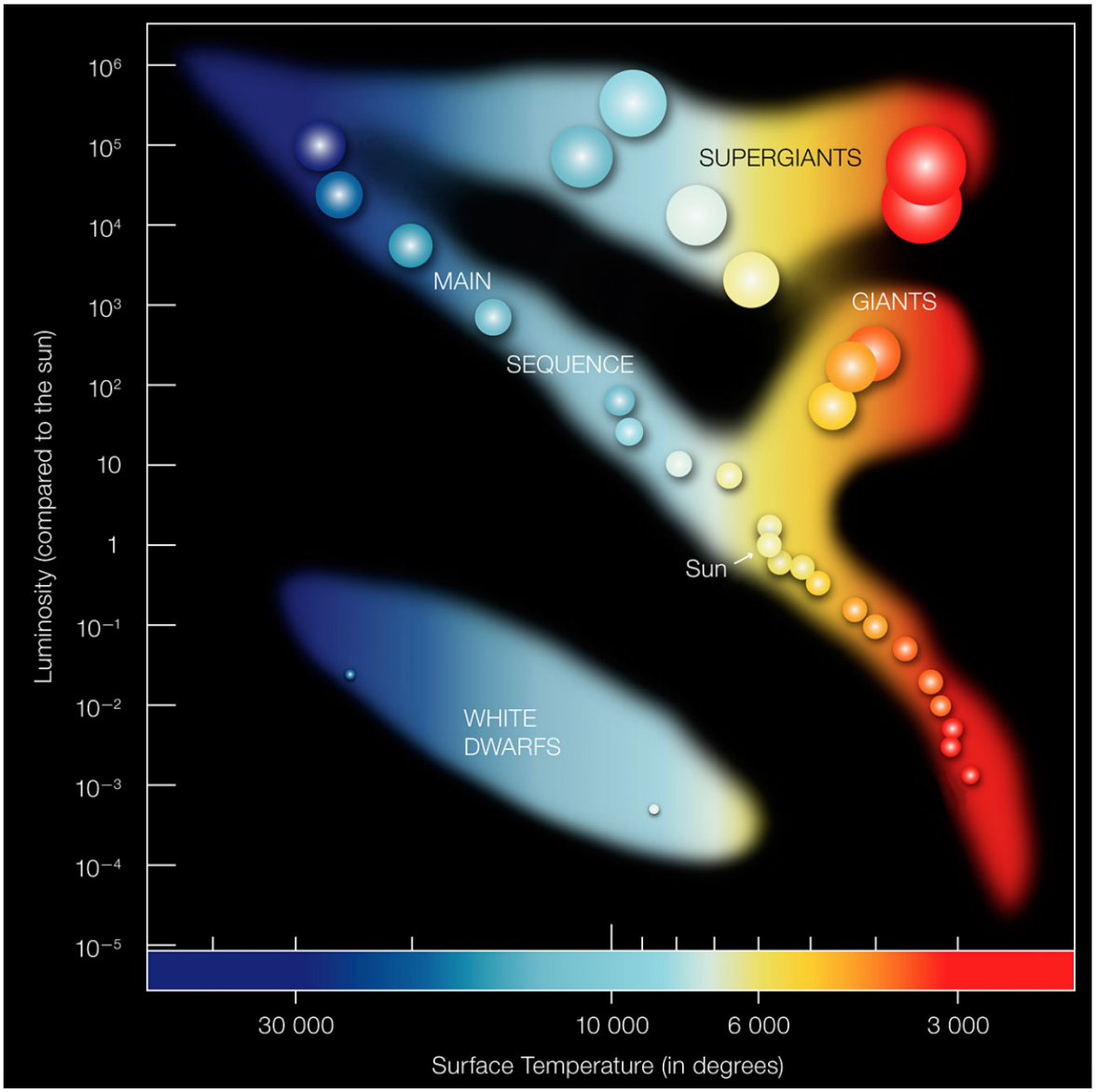

FIGURE 1.1: Hertzsprung-Russell diagram where the luminosities of the stars are represented against their effective temperature. The diagram is dominated by a diagonal strip, from top left to bottom right, where all the stars at the Main Sequence (MS) stage are located. Above this strip, more evolved stars that have already left the MS are found. Depending on their initial masses these evolved stars can be classified as giants or super giants. Finally, the white dwarfs appear below the MS strip. *Credit: ESO.*

As mentioned before, the birth mass of a star is a key parameter to understand its evolution. On important aspect is that the mass-luminosity relation ($L \propto M^{3.5}$), derived for the first time by Arthur Eddington in 1924, is useful to estimate the time stars spend in the MS phase based on their initial mass. In that way, stars up to tens of solar masses ($M_\odot$) takes only 10^6 years to leave this stage while those with the lowest masses (~0.1 $M_\odot$) are expected to spend almost 10^{12} years in the MS, more than the current age of the Universe.

After enough H in the core has been converted to He, the H burning starts in a shell around the inert He core. At this point the star arrives at the Red Giant Branch (RGB) in the HR diagram. The core suffers a gravitational contraction while the envelope of the giant star expands becoming more luminous leading to a cool star with a big, unstable convective envelope.

1.1.1 AGB stage

The late stages of evolution of low and intermediate-mass stars ($M \sim 0.6 - 8 M_\odot$) is the main topic of this thesis. Assuming a standard Salpeter initial mass function (IMF) 97% of all stars in the Universe are born with masses in this range and are expected to go through the so-called Asymptotic Giant Branch (AGB) phase. Mass loss is the dominant factor in the stellar evolution of AGB stars reaching values from 10^{-7} to 10^{-4} $M_\odot$ yr^{-1}, and almost half of the heavy elements which are originated in the stellar interiors of these stars are returned to the ISM via this mass loss mechanism. AGB stars present typical luminosities of 10^4 $L_\odot$, and effective temperatures that range from 2000 to 4000 K.

The ignition of the He burning in the core depends on the initial mass of the star. For stars with masses below 2 $M_\odot$, the He core is electron-degenerate and they experience a He flash which is the starting point of the He-core burning phase on the zero-age horizontal branch (ZAHB). For more massive stars (M>2$M_\odot$) the ignition of the He core occurs in a non-violent way. The He-core burning phase leaves an inert C/O core and it is 10 times faster than the H-core burning stage. Once finished, the stars go up through the RGB phase in the HR diagram, increasing their luminosities and decreasing their effective temperatures, until they arrive to the AGB phase, see Fig. 1.2.

The inner configuration of AGB stars is composed of a C/O core surrounded by two thin shells of He and H. The H-shell burning dominates the energy production at this phase. This energy production is interrupted, periodically, by intense He-shell flash phenomena, which last ~ 10^4 years. He-shell burning does not only extinguish, momentaneously, the H-shell burning, but it also activates the nucleosynthesis in the intershell region. The products of this nucleosynthesis will reach the outer regions of the envelopes via several dredge-ups. In Fig. 1.3 a representation of this inner structure is shown.

Dredge-ups

The dredge-ups are convective processes that take place in AGB stars when the envelope expands and cools while, at the same time, the core reduces its size after the end of a dominant

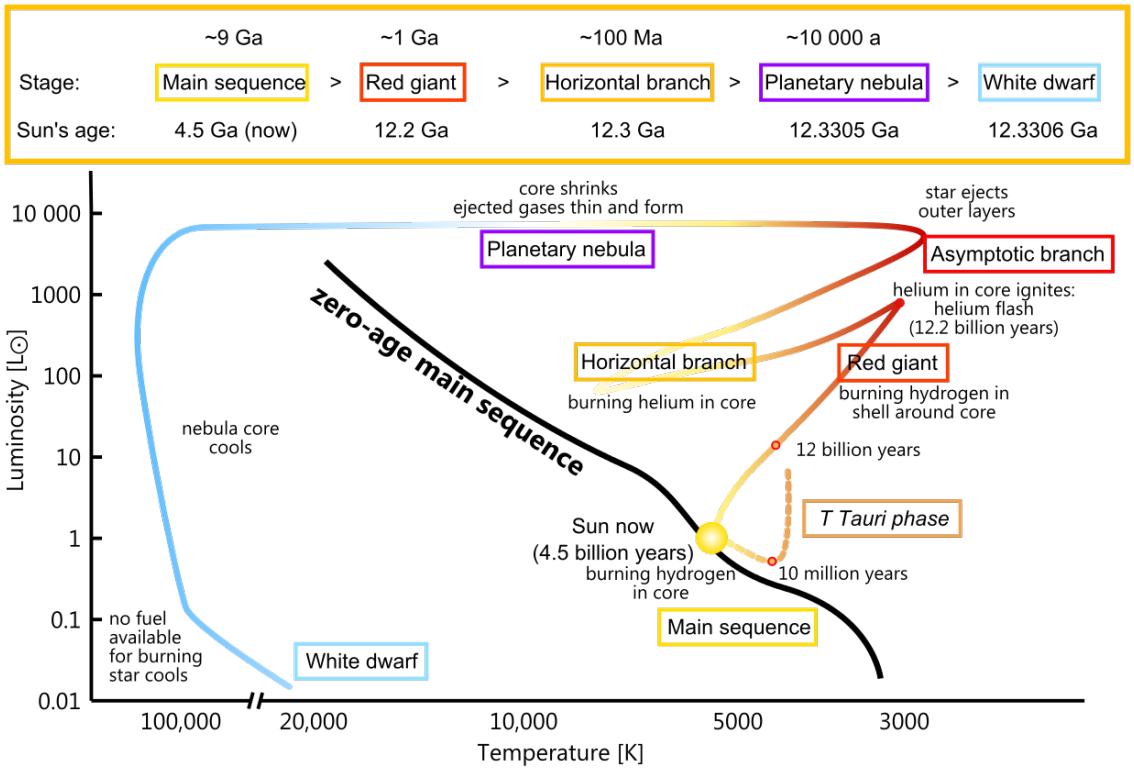

FIGURE 1.2: Evolutionary track of a sun-like star of from the end of the Main Sequence stage until the White Dwarf stage. The duration of each phase is indicated at the top.*Credit: Creative Commons.*

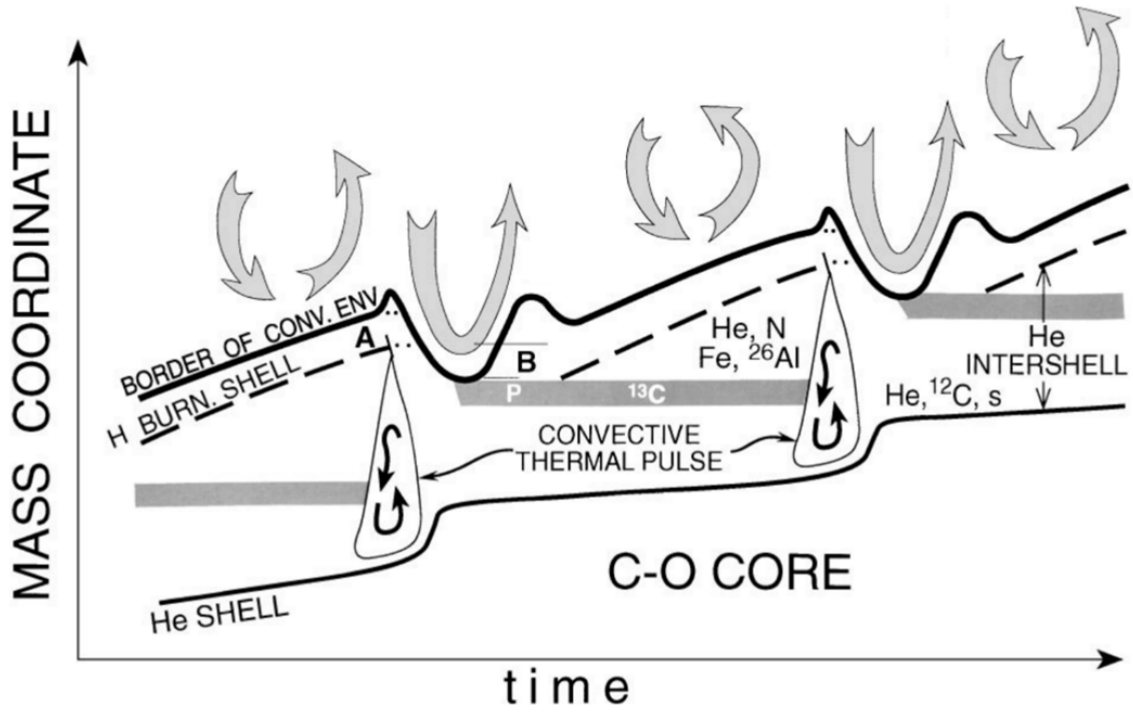

FIGURE 1.3: Evolution of the internal structure of an AGB star after several, consecutive thermal pulses, which implies convection and mixing process. For more details see *Busso, Gallino, and Wasserburg, 1999*.

nuclear burning event (Lambert, 1992). The first dredge up takes place when the H-core burning ceases at the time when a MS star enters the red-giant branch. The second one takes place as a consequence of the convective instability that occurs when the He-core burning comes to an end at the core, then, convection mixes the products of the CNO cycle. This second dredge-up, which only takes place in high-mass stars, results in an increase in the surface abundance of ^{4}He and 14N, whereas the amount of ^{12}C and ^{16}O decreases.

Massive stars can undergo He-shell flashes (also called thermal pulses) and after each thermal pulse new convective mixing processes are expected to occur (third dredge up). Third dredge-up causes helium, carbon and the s-process products to be brought to the surface. Dredge-ups are a key mechanism to transport nucleosynthesis products from the intershell region to the surface of the stars, besides, they have a great influence in the chemical evolution of the AGB stars. (Kwok, 2000a; *Asymptotic giant branch stars* 2003).

Originally the stars are all born as oxygen rich sources, that is, with a larger number of O atoms than C atoms, and therefore a ratio C/O < 1. However, for those more massive stars (>2 $M_{\odot}$), huge amount of ^{12}C atoms are generated as a consequence of the nucleosynthesis reactions taking place in the He-shell burning and, thanks to successive third dredge-ups, they are injected in the convective envelope (see Fig. 1.3), turning the carbon over oxygen ratio into C/O >1, and therefore to a C-rich composition. This chemical evolution is favoured as the production of oxygen is expected to be negligible being carbon 5 to 10 times more abundant than oxygen in this intershell region. When the C/O ratio becomes larger than 1, a carbon star has formed. The stars with C/O ratio ∼1 are known as S-type stars.

The efficiency of the third dredge-up mechanism is fundamental to convert an O-rich object into a C-rich one and, again, the initial mass is the critical parameter. At solar metallicity, masses larger than 2 $M_{\odot}$ are necessary to develop efficient enough dredge-ups to change the chemical composition of the surface of the stars.

Hot-bottom burning

High-mass stars ($M > 4M_{\odot}$), unlike low-mass stars, which are characterized by the presence of a thin radiative layer, does not have any layer separating the convective envelope and the H burning shell. As a consequence of that, the base of the convective envelope can reach high temperatures up to 8×10^{7} K and, under these conditions, ^{4}He atoms start to form via the CNO-cycle and the process known as “hot-bottom burning” (HBB) is triggered (Sackmann and Boothroyd, 1992).

A consequence of the CNO-cycle is the conversion of ^{12}C into ^{14}N, this reduction of ^{12}C atoms mitigates the effects of chemical mixing carried out by the third dredge up and, due to that, stars with masses larger than 4 $M_{\odot}$, remain as O-rich sources until the end of their lives. (See Karakas and Lattanzio, 2014 for a more detailed overview of nucleosynthesis on AGBs).

1.1.2 Post-AGB and Planetary Nebula phases

The end of the AGB stage, previously described, is characterized by an intense period of very strong mass-loss rates (10^7–10^4 $M_\odot$ yr^{-1}). At the end of this intense mas-loss period, the CSE is detached and the star has reached the post-AGB phase. In parallel, the central star increases its effective temperature and the ionization of the surrounding material of the envelope starts while the total luminosity of the object remains almost constant (with typical values of $\sim 10^4$ $L_\odot$) as the star evolves rapidly in the HR diagramme from the top right corner to the top left one. The post-AGB phase has been reached (see Kwok, 1993, van Winckel, 2003 and Zijlstra, 2015 for extent and complete review.)

The post-AGB phase is a very short-lived stage in the final evolution of low to intermediate mass stars lasting only from a few hundred to several thousands of years and, for that reason, is still one of the most unknown periods of the stellar evolution. A wide range of temperatures is found in these objects as they evolve from ~5000 to ~35000 K, when the temperature of the central star reaches ~20000 K the ionization of the surrounding CSE material expelled during the AGB phase, starts. This stage is also identified in the literature as the pre-Planetary Nebula (pPN) phase. However, not all the post-AGB stars end up this phase as PNe because, for some post-AGB stars, the time scale required to increase the effective temperature until a value high enough to ionize the material is larger than the dilution time of the CSE in the interstellar medium (ISM), so the PN stage is never reached. For that reason, the term 'post-AGB' is more accurate to describe these objects and is the one used in this thesis.

Regarding the circumstellar envelopes, morphological changes take place in the post-AGB phase. As it was described in section 1.2, the usually round shapes of the CSEs around AGB stars turn into complex morphologies in the post-AGB. These morphological changes are, mainly, thought to be a consequence of the onset of fast collimated winds (*jets*). These winds, originated close to the central star, interact wit the slow layers of the CSE leading to a new morphological configuration (Arrieta et al., 2003).

In terms of the chemistry, the central stars of post-AGB objects are heavily obscured due to the huge amounts of dust found around them so they are hard to observe. However, the envelopes around the central stars are one of the most luminous objects in the sky in the optical and in the (far)-infrared regime. The analysis of spectra (covering from UV to FIR wavelength regions) corresponding to these envelopes reinforces the idea of post-AGBs to be transition objects between AGB stars and PNe. Analysing the spectral features observed, a lower number of molecular species compared to AGBs, while some features corresponding to atomic elements are present. Finally, dust features are also found to be representative of these kind of objects. The dust species typically found in the O-rich envelopes are: water ice, forsterite, enstanite and other olivines (Waters, 1996; Molster et al., 2002); while the Polycyclic Aromatic Hydrocarbons (PAHs) are commonly reported in C-rich post-AGB objects (Geballe et al., 1989).

The central star keeps increasing its effective temperature until it reaches values up to ~250000 K. Under these conditions the UV photons generated by the star continues the ionization of the surrounding material until most of it is ionized, at this point a PN is born. The luminosities found in PNe are similar to those of post-AGBs ($\sim 10^4$ $L_\odot$) and they have

also a complex morphological structure: bipolar, multipolar, elliptical, spherical or even irregular are common shapes found in PNe (Huarte Espinosa et al., 2010; Shaw, 2012). Their spectra are characterised by atomic elements such as: OI, OIII, NII and CII, but also molecular species as complex as fullerenes have been reported (García-Hernández et al., 2010). Objects in the PN stage spend $\sim 10^5$ years of their final life until the surrounded, ionized, material completely vanish into the ISM leaving a single, compact C/O core as a remnant, which is commonly known as *white dwarf* (WD). A complete review of PNe can be found in Zijlstra, 2015 and Kwok, 2000b.

1.2 Circumstellar envelope (AGB CSEs)

The circumstellar envelope is a component of gas and dust that surrounds the stars. This structure is, typically, the dominant source of the emission of the AGB stars in the far infrared domain (FIR). The study of CSEs provides useful information about basic physical parameters such as: mass, temperature, the chemical composition and its evolution, as well as, the mass-loss history of this kind of objects. This section describes the physical and chemical properties of the CSEs of AGB stars, as well as, the mass-loss mechanisms, for a more detailed review see Höfner and Olofsson, 2018.

1.2.1 Physical and chemical properties

This thesis is mainly based on the study and characterization of the inner regions CSEs surrounding the evolved stars included in our analysis. So it is necessary to describe the current knowledge about the AGB CSEs to put in context our work.

The physical structure of a standard AGB CSE

In this subsection we are going to describe, in a simplified way, the three main regions that are found in the CSEs of AGB stars, each of them being characterized by specific chemical processes and temperatures. In Fig. 1.4, a schematic view of a typical CSE is shown.

The closest region to the star is that known as that of the **inner wind** that is characterized by a fast temperature decrease from ~3000 K, close to the stellar atmosphere, to ~1000 K at a distance of only ~5 $R_\star$. The stellar wind is activated in this region due to the action of stellar pulsations which result in shock waves that pass through the material starting an incipient mass-loss phenomenon. From a chemical point of view, the inner region is characterized by non-equilibrium processes which are favoured because of the, previously mentioned, shocks that are formed close to the stellar atmosphere.

The inner wind region ends at the condensation zone which, together with the acceleration zone, defines that corresponding to the **intermediate wind** which extends up to a distance of ~30 to 100 ~ $R_\star$. At these distances from the stellar atmosphere the temperature

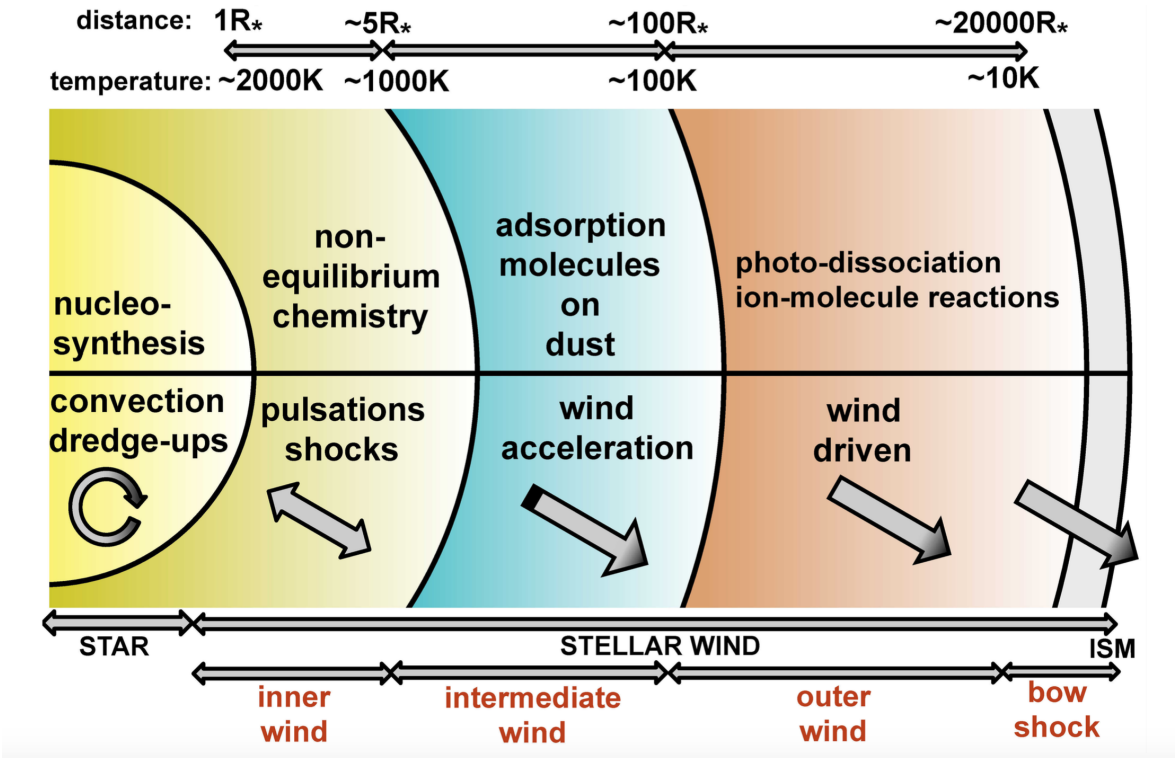

FIGURE 1.4: Inner structure of the CSE of an AGB star. The different regimes are shown, not to scale, as well as the physical and chemical processes which take place across the envelope. At the top of the figure the characteristic values of temperature are shown. *Credit: L. Decin.*

drops down to typical values from several hundreds to ~100 K, what allows the formation of dust grains. Thanks to the condensation of dust grains, the material is accelerated by the radiation pressure and terminal velocities of 5 to 20 km/s are reached. This region has not been extensively observed in the past as it requires FIR observatories to characterize it, properly. *In this thesis we present an homogeneous and systematic study of this intermediate region for a big sample of sources.*

Finally the **outer wind** is found in that region containing the material which expands at constant velocity covering an extension of up to thousands of stellar radii. Assuming a constant mass loss rate the density of this wind follows a r^{-2} distribution and the temperature decreases down to ~10 K in the outer regions of the envelope. This region is observable using radio, mm and sub-mm wavelength ranges detectors and has been deeply studied in numerous works found in bibliography.

The chemistry of the CSE

The different physical properties found across the CSE of AGBs lead to the formation of a wide variety of molecular species. Under local thermodynamic equilibrium (LTE) conditions the most stable molecules are formed first, for example molecular hydrogen (H_2) and carbon monoxide (CO). It has a critical influence in the subsequent species that will be formed. For O-rich sources (C/O<1) most of C is locked into the CO molecule facilitating the formation

of oxygen based products like: H_2O, SiO or OH while, in the case of C-rich stars (C/O>1) an excess of atoms of C are available to produce carbon based species, such as: HCN, CS or CN. Nevertheless, the detection of oxygen bearing molecules in C stars has been reported in previous works (e.g. Lombaert et al., 2016a and Bujarrabal and Cernicharo, 1994), this fact has been interpreted as a consequence of the shocks that could, eventually, break the CO molecules allowing the O and C atoms react with other elements to form new species. Interpreting properly the chemistry found in the CSEs of the AGBs requires a deep knowledge of the different chemical processes that take place along the different regions described above, the main three being:

- **Shock-induced chemistry:** The shocks associated to the periodic pulsations are expected to have an important effect in the chemistry found in the **inner region** of the CSE. The pass of these shocks through the material in the envelope introduces enough energy to destroy the existing molecules of CO providing, in this way, free atoms of C and O that can react with other atoms or molecules to generate new species. Some theoretical models found in Cherchneff, 2006; Cherchneff, 2011; Cherchneff, 2012, indicate that there is a set of molecules that are expected to be created under these circumstances in both O-rich and C-rich sources, like: CO, C_2H_2, N_2, SiS, CS, HCN, H_2O and SiO.
- **Gas-dust interaction:** The molecules produced in the inner region of AGB stars are dragged to the **intermediate region** where they can react with the grains that are formed in the dust-condensation zone. These reactions are favoured due to the high densities that enhance the collisions between the molecules and the dust components. As a consequence of that, new molecules like water or hydrocarbons can be formed on the surface of dust grains that sometimes act as catalysts of further more complex reactions. (e.g. Latter and Charnley, 1996; Kress, 1997.
- **UV photodissociation:** Finally, high energetic UV photons from the ISM are able to break the molecules in the **outer region** facilitating the formation of additional complex chemical species. The efficiency of the UV photodisscociation process depends on several factors such as the potential presence of dust that can block the penetration of UV photons as well as the homogeneity and distribution of the material found in the CSE.

The standard CSE model

The **standard CSE model** is a simplified scenario that assumes that the CSE is a spherical shell of gas and dust particles, formed at a constant mass-loss rate and expanding at constant velocities outside a limited inner acceleration region. Other considerations like heating and cooling processes as well as chemical reactions or photodissociation have to be taken also into account in the CSE description. In the following, the three main elements of the standard CSE model are described.

The determination of the **velocity profiles** is fundamental to accomplish a proper study of the CSE. It is widely accepted that radiation pressure plays an essential role in the acceleration of dust grains in the inner wind region. These grains move through the gas found in

the envelope and, if the material is dense enough, they will collide against the gas particles transmitting them a drag force. The denser the material is the more similar the velocities of gas and dust are, although the velocity of the dust will always be higher than that of the gas, as shown in Eq. 1.1.

$$v_d(r) = v_g(r) + v_{dr}(r), \tag{1.1}$$

where $v_g(r)$ is the gas velocity profile and v_{dr} is the drift velocity between dust and gas. The simplest approach to reproduce the profile of the velocity of the gas is the kinematic one, where the radial profile is assumed to follow a parametrized shape shown in Eq. 1.2.

$$v_g(r) = v_{g,i} + (v_{g,\infty} - v_{g,i}) \times \left(1 - \frac{R_i}{r}\right)^{\beta}, \tag{1.2}$$

where $v_{g,i}$ is the gas velocity at the inner radius, $v_{g,\infty}$ the terminal velocity of the gas, R_i represents the inner radius and β describes how fast the gas accelerate. This kinematic approach is commonly used when modelling molecular line profiles as gas velocity information can, eventually, be extracted from them, allowing to constrain the free parameters introduced in the radial profiles.

At long distances from the central star both gas and dust velocities reach their terminal velocities that are connected through the drift terminal velocity given by equation 1.3. In low-density regions, like the outer ones of the CSE, the terminal values of the drift velocities are non-negligible.

$$v_{dr,\infty} = \sqrt{\frac{L v_{g,\infty} Q}{\dot{M} c}}, \tag{1.3}$$

where L is the stellar luminosity, Q is the scattering efficiency, $\dot{M}$ is the mass-loss rate and c is the speed of light.

The gas and dust **density profiles** are also related to the mass-loss rates and velocities corresponding to both components by the continuity equation. Particularly, for a steady wind, the mass-loss rate can be expressed as $\dot{M} = 4\pi r^2 v(r)\rho(r)$. This equation can be simplified assuming a constant expansion velocity (v_∞). Under these conditions the density profile follows a r^{-2} distribution, meanwhile the acceleration zone, where the velocity flow increases with r, the resulting velocity profile is steeper $\rho(r) \propto v(r)^{-1} r^{-2}$.

The density distributions of particular molecular species could differ from the total gas density distribution shown above as those depend on photodissocitation and chemical processes that occur in the CSE. However, assuming a constant velocity flow and under a CSE standard scenario, the density profile of the most abundant molecule, H_2, keeps the r^{-2} trend. The density distributions of other molecules are expressed in terms of their fractional abundance with respect to H_2, $n_X(r) = f_X(r) n_{H_2}$.

Finally, the kinetic energy in the CSE is determined by all the heating and cooling processes involved in the energy-balance equation (see Decin et al., 2006). The dominant heating process is the friction and collisions of dust grains with the gas particles; while on the cooling side, the principal one is the adiabatic expansion of the gas as well as the line cooling. The molecules that contribute most to line cooling are CO (for sources of all chemical types), H_2O (for O-rich objects) and HCN (in C-rich CSEs). The solution of this energy-balance drives a **temperature profile** of the form:

$$T_g(r) = T_\star \left(\frac{r}{R_\star} \right)^{-\epsilon}, \tag{1.4}$$

where $T_\star$ represents the temperature of the stellar atmosphere. Studies like Teyssier et al., 2006a, De Beck et al., 2010a and Maercker et al., 2016b have derived values of ϵ between 0.6 and 1.2, although Lombaert et al., 2016a suggests that in the inner regions of the CSE the temperature profile may be shallower ($\epsilon \approx 0.4$).

As a word of caution, it is always important to keep in mind that all the mass-loss rate estimations made under the standard CSE scenario are dependent on the extent to which the above assumptions are valid.

1.2.2 The mass-loss mechanisms

It is generally accepted that dust grains, which condensate at typical distances of 10^{14} cm, play a very important role in the wind acceleration process, as dust grains absorb and scatter the stellar photons emitted by the central star, transferring their acquired momentum to the surrounding gas via collisions. In order for dust grains to form in the envelopes, an initial nucleation process has to occur, and, once the new grains are created, they must be able to grow and survive to intercept enough starlight to be accelerated. These processes of growing and survival requires the following conditions: 1) The radiative equilibrium temperature (T_{RE}) of the grains must remain low enough; 2) gas kinetic temperature must not be too high for too long; 3) the relative motion of the grains through the gas cannot be too fast, to avoid the erosion of the dust grains.

In a stationary wind, dust forms in those regions where T_{RE} is lower than the condensation temperature, which depends on the density of the molecules, but it takes typical values of ~1350 K. For an AGB with $T_{\rm eff} \approx$ 2500-3000 K, it requires distances $r/R_\star > 2$ for the temperature to reach values low enough below the $T_{condensation}$. Nevertheless, in these regions the density is expected to be also so low that it is impossible that dust grains can be created. All this indicates that is very difficult to start driving a dusty wind in a static atmosphere.

For that reason, pulsations in the stellar atmosphere have to be taken into account as they may drive and enhance the stellar wind. Primarily, they contribute to the heating of the atmosphere thanks to their associated mechanical energy. A second effect is the levitation of the atmosphere after each pulsation, which partially overcomes the gravitational potential allowing higher density material to become part of the outflow. Finally, departures from

the radiative equilibrium lead to a decrease of the temperature enabling the formation of molecules and dust in regions closer to the star than those regions where molecules form in the case of stationary wind model.

1.3 Observational characterization of AGB and post-AGB CSEs

The formation of the CSEs described in the previous section is the primary consequence of the mass-loss processes that, mainly, take place during the AGB phase. Mass loss is usually represented in a first approach by a continuous and mainly steady outflow of gas and dust. The mass-loss rate is defined as the total mass that escapes from the stellar atmosphere, in all directions, per unit of time. The typical values found in AGBs range from $\sim 10^{-8}$ to $\sim 10^{-4}$ $M_{\odot}$ yr^{-1}.

1.3.1 Mass-loss rate estimators

Mass-loss rates are closely linked to the densities and velocities found in the CSEs. A total estimation of the mass-loss rate is usually not possible as the dominant mass component, the H_2, is difficult to observe given the symmetry of this molecule. For that reason, other indirect estimators have to be used. There are two main options in order to derive the mass-loss rates of these objects: the first one is to derive the value associated to the gas component while the second one is based on the study of the dust. It is important to remark that the mass-loss rates corresponding to the dust and gas components may not be the same as they are usually decoupled and move at the different expansion velocities.

A good estimator of the mass-loss rate should fulfil the following criteria: 1) it has to be applicable to objects of all kind of chemistries (O-rich, C-rich and S-type), 2) the estimator has to work properly when applied to a wide range of mass-loss rates and evolutionary stages; 3) the emission should be strong enough to allow the study of distant objects; 4) the properties of the gas and dust have to be well known to ease the radiative transfer analysis; 5) finally, the fractional abundance of lines should be easily estimated. The best mass-loss rate estimators, according to the above conditions, are described in the following subsections.

Rotational line emission of CO

The CO rotational lines are one of the most reliable and widely used mass-loss rate estimators due to the following reasons: CO is one of the most abundant species in CSEs of all chemical types; the saturation of these lines is unlikely except for the objects with extremely high mass-loss rates; CO rotational transitions are one of the strongest lines in AGB stars because the molecule is so abundant that many energy levels are easily excited due to collisions; the energy level structure of the rotational lines cover a wide range of energies; the abundance is easily estimated as CO is very stable against dissociation and then, the C or O abundances

can be used to determine the CO abundance in the O-rich and C-rich CSEs, respectively. Furthermore, the line shape carries information about the expansion velocity of the gas, which is very useful to study the kinematic properties of the CSEs.

The analysis of CO rotational line emission has also some sources of uncertainty which have to be discussed. The first one is common to all the estimators, the distance to the object represents one of the major sources of uncertainties in the analysis involving the rotational line emission of CO as it is fundamental to derive the absolute line intensities. The fractional abundance of CO ($f_{\rm CO}$) necessary to convert the mass-loss rates estimated with the CO lines to total gas mass-loss rate, is a source of uncertainty too. As mentioned previously, the CO abundance is linked to the C or O abundance depending on the chemistry of the studied CSE. No proper observational constraint of the CO abundance has been made to date, and for that reason some values are generally accepted and used by the scientific community, based on the solar abundances for C and O, leading to $f_{\rm CO}$ $\sim 6 \times 10^{-4}$ and 10^{-3} for O-rich and C-rich CSEs, respectively. The extent of the CO emitting region ($r_{\rm CO}$) in the CSEs is also an important source of uncertainty in the determination of the mass-loss rates. This emitting region has an upper limit in the photodissociation radius of CO ($R_{\rm CO}$) which is typically traced by CO emission lines associated to low J-values, however the study of high rotational J lines of CO, as it is the case of this thesis, requires a deep discussion to determine, properly, the linear extension of the emitting region of CO ($r_{\rm CO}$).

Numerous studies such as: Groenewegen, 1994; Teyssier et al., 2006a; Ramstedt et al., 2008a; De Beck et al., 2010a; Danilovich et al., 2014; Danilovich et al., 2015; Maercker et al., 2016b have developed radiative transfer models, under non-LTE conditions, to determine the mass-loss rates of a wide range of low to intermediate mass evolved stars of different chemical types. Despite the complexity of the models created, some errors related to distance or fractional abundance of CO can be introduced leading to estimations of mass-loss rates with typical uncertainties of a factor of three (Ramstedt et al., 2008a; Maercker et al., 2016b).

Finally, one of the most fundamental points derived from the analysis of the rotational lines of the CO, is the study of the temporal variation of the mass-loss rates. Since the kinetic temperature varies with radius, it is expected that CO lines with different excitation-energy levels trace different regions of the CSE. In that way, the study of low-J CO lines like those corresponding to the transitions $J = 1 - 0$ or $J = 2 - 1$ which probe the external layers (r ≈ 2 $\times 10^{17}$ cm) of the CSE, give us information about the mass-loss rate of past epochs, while the study of high-J lines up to $J = 42 - 41$ as those described and analysed in this manuscript, has allowed us to derive what could be interpreted as *current* mass-loss rate found in the different CSEs, as we are probing very close and warm layers ($\sim 10^{15}$ cm).

It is very important to realize that lines coming from different transitions probe the mass loss rate at different epochs and average the mass-loss rate over different time scales. For that reason, developing projects, as the one presented in this thesis, where a wide range of rotational CO lines are covered (from J= 4-3 to J= 42-41) is crucial to properly understand the global picture of the mass loss rate history in evolved stars.

Circumstellar OH maser emission

The use of OH maser emission, detected at radio-wavelengths (1612 and 1667 MHz), as a mass-loss estimator has also extensively been used along last decades (Engels, 1997; Goldman et al., 2017). There is a well known connection between the mass-loss rate and the extent of the emitting region of OH which is at the same time linked to the luminosity of a saturated maser of OH. This estimator has an evident limitation as it can only be applied to O-rich CSEs. Nevertheless, it has successfully served as a good estimator because the strong maser emission can be detected in very distant objects, although the maser effect difficult the conversion of the line brightness into quantitative estimation of mass-loss rates. A relation between the luminosity of the OH maser and the mass-loss rate was presented by Baud and Habing, 1983, this relation provides order of magnitude estimates, being less accurate than estimations derived from the analysis of the CO rotational lines mentioned before. In addition, the double-peak profile of the circumstellar 1612 MHz OH emission can be used to measure the expansion velocity of the gas with high precision.

Dust features and dust continuum emission

The strong dust emission coming from the circumstellar envelopes of evolved stars can also be used to obtain rough estimates of the dust mass-loss rates.

From the dust continuum we can estimate the optical depth of the CSE, which combined with the dust expansion velocity, can be used to derive a dust mass-loss rate estimation. However, it does not provide information about the composition of the dust, some important properties of the dust grains like their shape, size and structure which are fundamental in the dust modelling and analysis are unknown. It introduces some considerable uncertainties that cannot be ignored.

Dust features provide such information, however, they are less useful to estimate mass-loss rates for several reasons. They are more difficult to identify and the absolute (inherent) strength of the feature is not properly known. Furthermore we do not know the fraction of the dust that contributes to a particular feature and it can not be estimated a priori. Only a fit of the global SED with all the features of dust included could help us to determine it (de Vries et al., 2010). Finally, it is not easy to directly connect the strength of the dust features to the mass-loss rates as for low mass-loss rates the strength of the features increases proportionally to the mass-loss rate until the feature saturates and it starts to weaken until an absorption dust profile is generated which increases its strength with the mass-loss rate.

1.3.2 Far-infrared properties of evolved stars

The cool layers of gas and dust found in the ABG, post-AGB and PN CSEs, make these low to intermediate mass evolved stars very bright sources in the far-infrared, sub-mm, mm and radio domains. For that reason, these kind of observations are fundamental to properly characterize the physical and chemical properties of the CSEs surrounding the central stars.

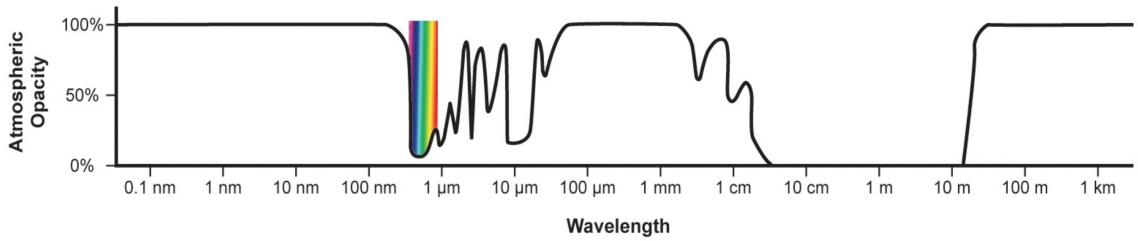

FIGURE 1.5: Profile of the atmospheric opacity in the electromagnetic spectrum ranging from short-wavelength γ-rays to long-wavelength radio waves. *Image from NASA.*

Due to the presence of our Earth atmosphere, however, only the radio emission can be detected from ground based observatories (see Fig. 1.5) therefore, space telescopes, like *IRAS*, *AKARI*, *ISO* and *Herschel* in recent past years are very important to study their infrared and sub-mm properties. In fact, the advent of infrared observations led in the decades of 1960 and 1970 to considerable progress in the mass-loss rate characterization.

Complementing radio and mm observations, FIR data allow us to study the physical and chemical properties of the inner layers of the CSEs at typical distances of 10^{15} to $\sim 10^{17}$ cm (e.g. Danilovich et al., 2015; De Beck et al., 2010a; Teyssier et al., 2006a)where the gas and dust at warmer temperatures from 100 to $\sim$1000 K. This region was first accessed via spectroscopic data thanks to *ISO* but *Herschel* has meant a big step in terms of resolution and sensitivity of data.

At these FIR wavelengths high-J rotational emission lines of CO (up to J =45-44) may, eventually, be detected and a proper analysis of the CO emission could report important information about different physical parameters such as: total mass, temperature of the gas and mass-loss rate. Combining multi-wavelength observations the temperature profile ($T(r) \sim r^{\alpha}$) can be properly described across the whole envelope from the innermost regions to the most external layers. The same happens when focussing on total emission masses. Regarding the mass-loss rate ($\dot{M}$) it is very interesting to analyse and compare the values derived from the *low*− and *high*−J CO lines because they probe different regions of the envelope, and could give us information about the mass-loss history.

Finally, it is also expected to derive information about the dust properties as some of these dust features such as forsterite can be easily detected and identified in the far infrared. For all these reasons, *Herschel* Space Observatory was tremendously useful and it has provided an unprecedented amount of high quality data that is boosting the analysis of the physical and chemical properties of evolved low to intermediate mass stars.

1.4 *Herschel* observations of evolved stars

1.4.1 *Herschel*

Herschel (Pilbratt et al., 2010) was launched, together with the *Planck* satellite, on 14th May 2009 from Europe's spaceport in Kourou, French Guyana, in South America. *Herschel*was

a Far Infrared (FIR) telescope covering a spectral range from 55 to 672 μm, (530-5000 GHz), a region completely inaccessible from ground based telescopes. On board *Herschel*, three instruments with great photometric and spectroscopic capabilities were the responsible of carrying out the scientific observations. They were: the Photodetector Array Camera and Spectroscopy (PACS) (Poglitsch et al., 2010), the Spectral and Photometer Imaging REceiver (SPIRE) (Griffin et al., 2010) and the Heterodyne Instrument of the Far Infrared (HIFI) (de Graauw et al., 2010).

Unlike Planck, whose goal was to carry out an all-sky survey at submilimeter wavelengths, *Herschel*was an observatory-like mission and, as such, its observing time was made available to the scientific community. As every cryogenic mission, the operational lifetime of *Herschel*was limited by the lifetime of the helium in the dewar that was used to cool down the temperature of the instruments until close to absolute zero. After 1447 operational days, the helium was exhausted and the mission came to an end, two weeks before completing 4 years in space.

From a technical point of view, *Herschel*represented a complete revolution as a space telescope. With its 3.5 meters diameter primary mirror, it was the space telescope with the largest mirror ever launched. This fact, added to the design and unique capabilities of the instruments onboard, resulted in the generation of science data with a spatial resolution and sensitivity never reached before at these spectral wavelengths. Thanks to that, *Herschel*observations have had and will still have for many years to come, an enormous impact on all the astronomy fields and, particularly, in the study of evolved stars.

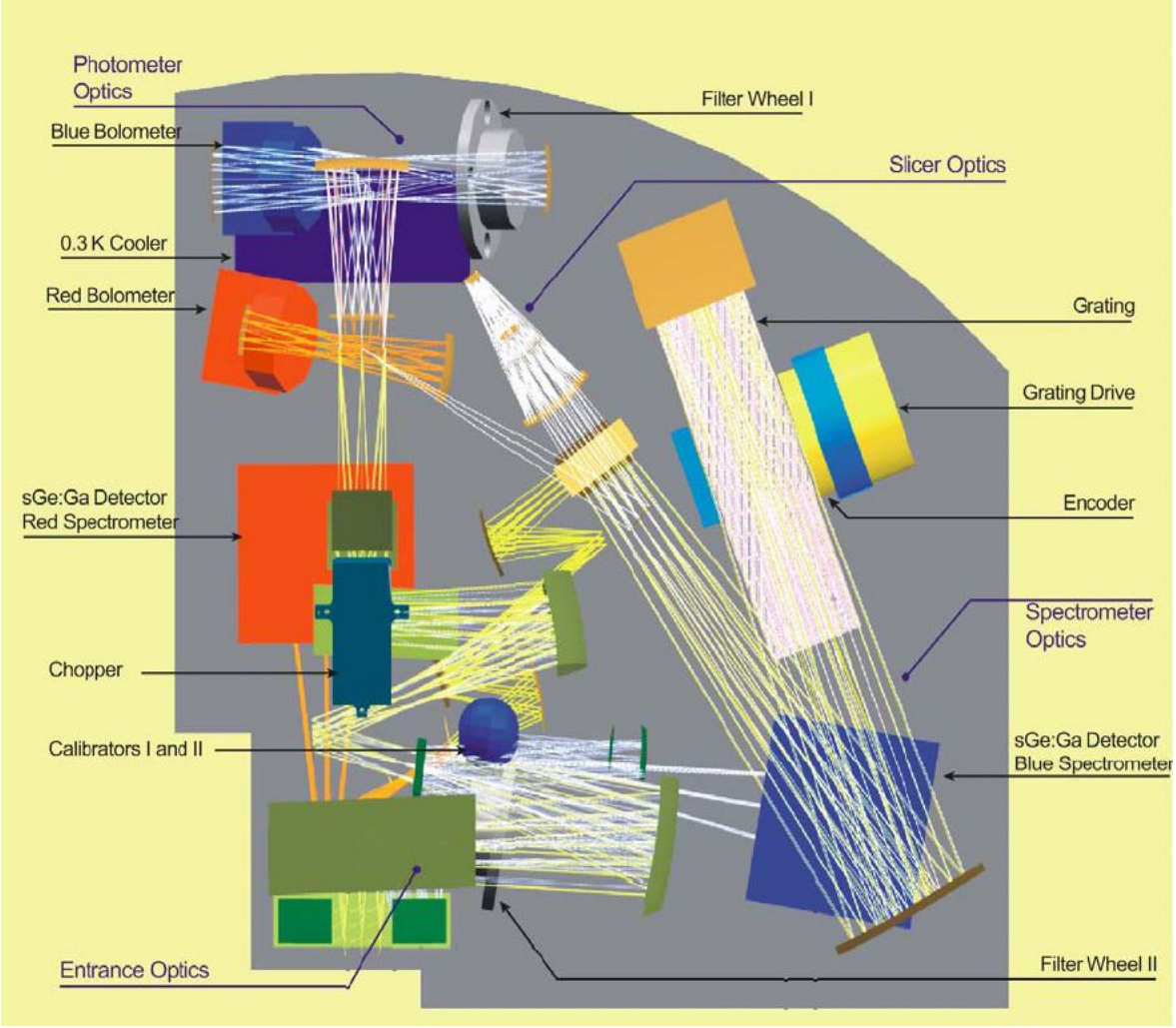

FIGURE 1.6: PACS optical layout. After the common entrance optics, light is split into the spectrometer train and the photometer train. (Figure collected from the *PACS Observer's Manual*).

1.4.2 PACS

The PACS instrument is composed of two different sub-instruments:

PACS Photometer: offers two different channels, blue and red. On the one hand, the blue channel has 32×64 pixel arrays and offers two different photometric filters, one covering from 60 to 85 μm, centered at 70 μm, and another one covering from 85 to 125 μm, and centred at 100 μm. On the other hand, the red channel has a 16×32 pixels array and only offers one filter covering from 125 to 210 μm, centered at 160 μm. The two short wavelength bands associated to the blue channel can be selected via a filter wheel but only one can be used at a time. Each observation consists, always, of two images corresponding to the blue and red channels, respectively. The field of view (FoV) covered by both channels are the same 1.75'×3.5'.

PACS Spectrometer: is an integral field spectrograph. This type of spectrographs are characterized because they combine spectrographic and imaging capabilities, with a simultaneous coverage in spectral and spatial dimensions. The final structure of data is a three

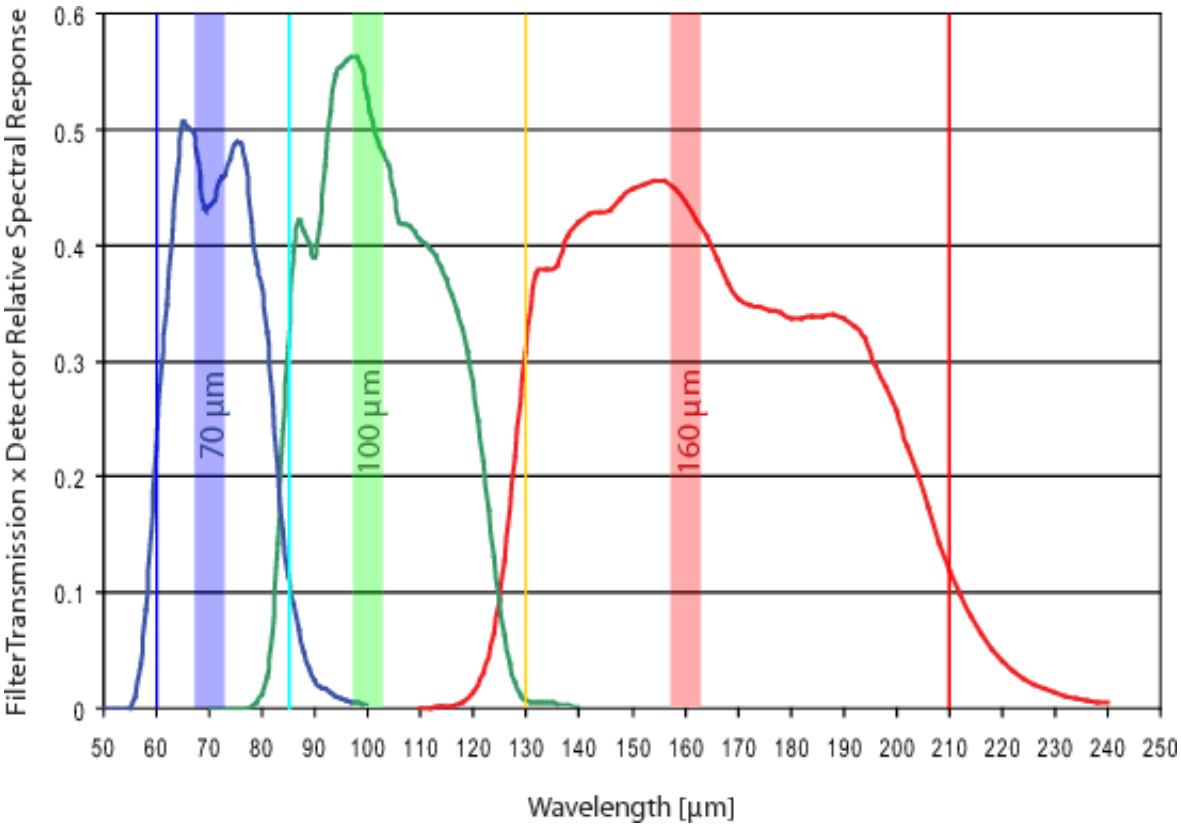

FIGURE 1.7: PACS Photometer filters transmission multiplied by the detector relative spectral response. (Poglitsch et al., 2010)

dimensional cube. The field of view covered by the PACS Spectrometer is 47"×47" making use of a 5×5 pixels structure. The dimension of each pixel is 9.4"×9.4". An image slicer is used to re-arrange the 2 dimensional FoV along a 1×25 pixels entrance slit for the grating.

The wavelength region covered by this sub-instrument ranges from 51 to 220 μm, in two channels that operate at the same time in the blue (51-105 μm) and in the red (102-220 μm) band. The resolving power $\lambda/\Delta\lambda$ varies from 1000 to 4000 which means a spectral resolution of ~75-300 km/s depending on wavelength. The instantaneous coverage is ~1500 km/s.

The grating is Littrow-mounted, that is, the entrance and exit optical paths are the same. To cover the full wavelength range, the grating is operated in three different orders. The first order covers the range from 102 to 210 μm, the second one ranges from 71 to 105 μm, and, finally, the third order covers the 51-73 μm, subrange. Due to the relatively short instantaneous coverage, the grating is rotated from 25 to 70 degrees to access the full wavelength range of each order.

The light coming from the diffraction orders is guided to feed the two detector arrays: blue (51-105 μm) and red (102-220 μm). Thanks to a dichroic beamsplitter, the light from the first order is separated from the light coming from the other two. In the short-wavelength optical path, there is a filter wheels that selects the second or third grating orders. It is possible to operate both detector arrays simultaneously.

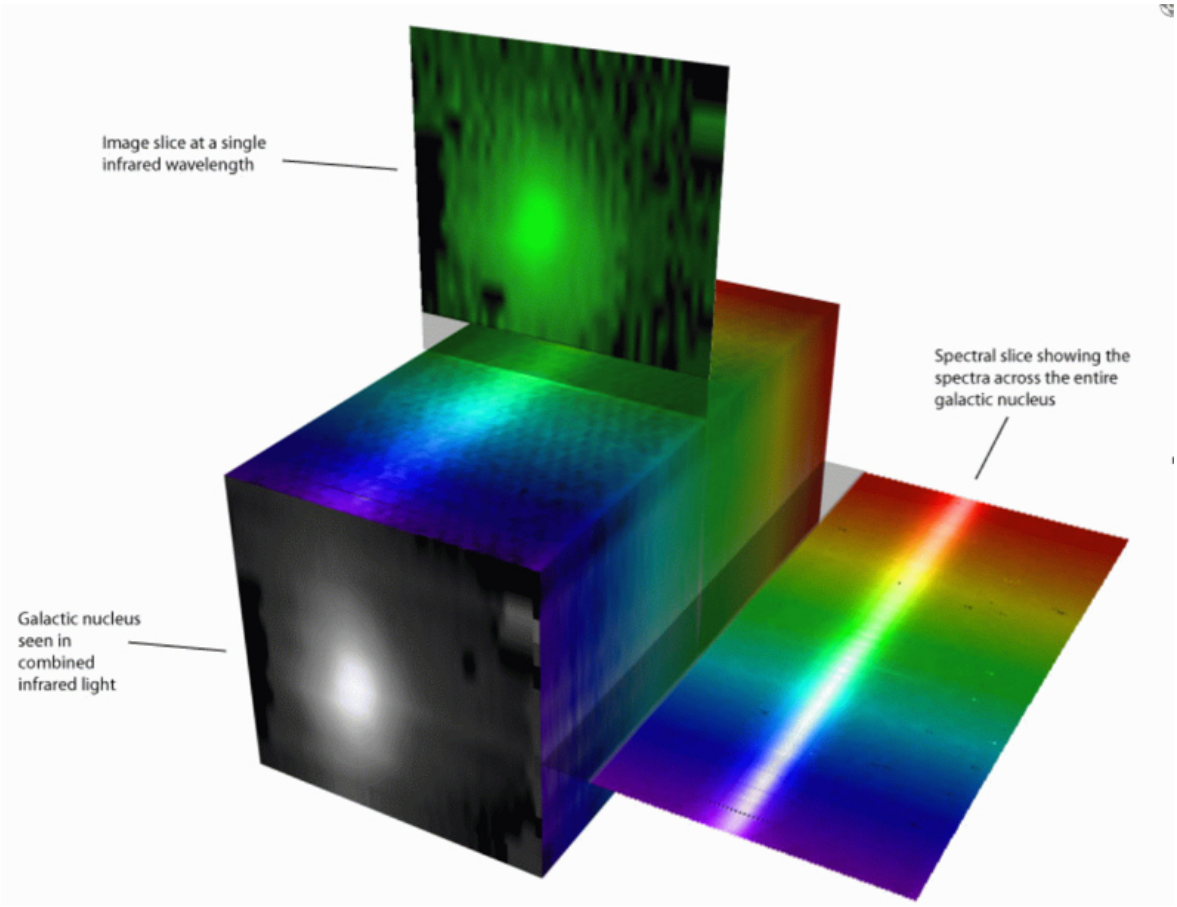

FIGURE 1.8: Integral Field Spectrograph scheme. (Image taken from http://ifs.wikidot.com/what-is-ifs).

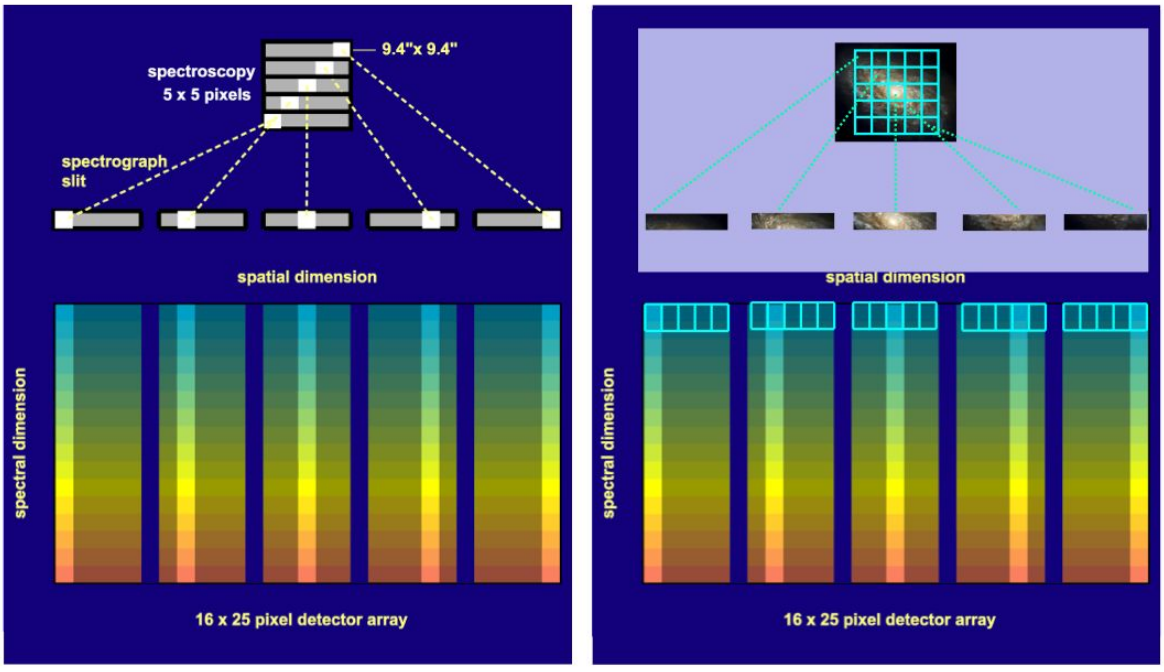

FIGURE 1.9: PACS Spectrometer slicer concept. Image collected from *PACS Observer's Manual*.

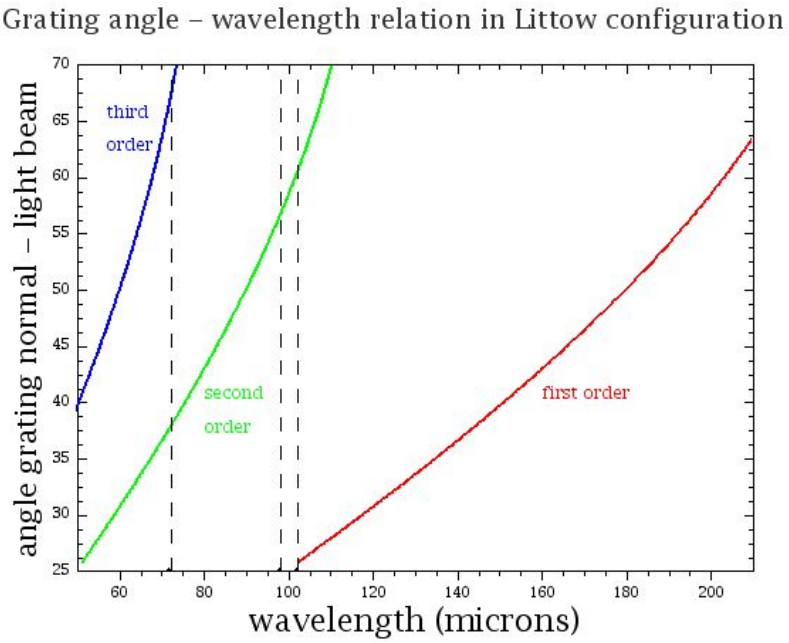

FIGURE 1.10: Relation between grating angle and wavelength range covered by the PACS Spectrometer. Image collected from the *PACS Observer's Manual*.

Observing with the PACS Spectrometer

To observe with the PACS Spectrometer sub-instrument, the user had to select one of the two Astronomical Observing Templates (AOTs) offered: Line Spectroscopy or Range Spectroscopy:

- **Line Spectroscopy:** A limited number of relatively narrow emission or absorption lines could be observed for a fixed diffraction order. The fixed angular range scanned by the grating mechanism was optimized for a given diffraction order to fully cover the profile of the unresolved line, ensuring the detection of enough continuum at both sides of the line to facilitate a reliable profile fitting. The grating covered several times a resolution element providing information on a small but highly redundant wavelength range.
- **Range Spectroscopy:** In this mode, the user could define a wider wavelength coverage than the one offered by the 'Line Spectroscopy' mode by stepping through the relevant angles of the preferred grating and selecting the grating sampling density (Nyquist sampling mode or high sampling mode). This AOT was used for for long-range spectroscopy and also for full coverage of broad lines.

Once the AOT has been selected, the PACS Spectrometer offered two different observing modes: 'Standard chopping-nodding mode' and 'Unchopped grating scan mode'.

- **Standard chopping-nodding mode:** This mode, also known as 'Chopping/Nodding' or 'Chop/Nod', was the standard technique to observe with the PACS Spectrometer,

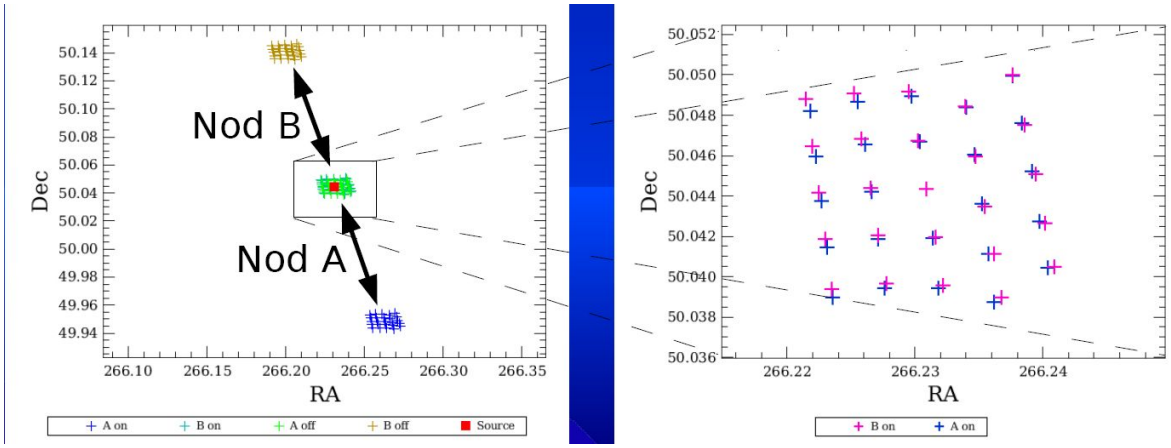

FIGURE 1.11: Spatial footprint of the chop/nod observing mode: two chopper positions are shown for both nods A and B. Figure collected from the *PACS Observer's Manual*.

and it was recommended for faint lines (below 4-5 Jy peak-to-continuum) combined with faint or bright continuum. The results obtained from this mode were only reliable if there were clean off-fields within a radius of 6' from the coordinates of the target.

At each nod position, the 'chopper' took, alternatively, information from the on-source position and from the off-source position. At every grating position, the detector signal was modulated between on and off source via an [on-off-off-on]-[on-off-off-on] chopping pattern. The observer could select a chopper throw "Small", "Medium" and "Large", which referred to 1.5', 3' and 6', respectively. The chopper throw selection depended on the level of isolation of the source as the off position had to be a clean, nearby region in the sky.

The optical paths followed by the light coming from the On-source and Off-source positions were different so the telescope background for both pointings was not the same. For that reason, the sequence of scanning was repeated at two nod (A and B) positions of the telescope.

In the second nod position (B), the source was located on the off chopping position of the first nod (nod A). With this technique the telescope background could be eliminated:

$$F_{Observed} = \frac{[NodA(on-off)] + [NodB(on-off)]}{2} = \\ = \frac{[T2 + F_{Source} - T1] + [T1 + F_{Source} - T2]}{2} = F_{Source} \tag{1.5}$$

being T1 and T2 the telescope backgrounds at chopper positions On and Off. The sky background was assumed to be negligible compared to the telescope background. Nod cycles were repeated in a way that A to B slew time was minimized, this is, in case of two repetitions the pattern of the nod cycle was [A-B-B-A].

In the standard chopping-nodding mode the On and Off observations were included in the same ObsID.

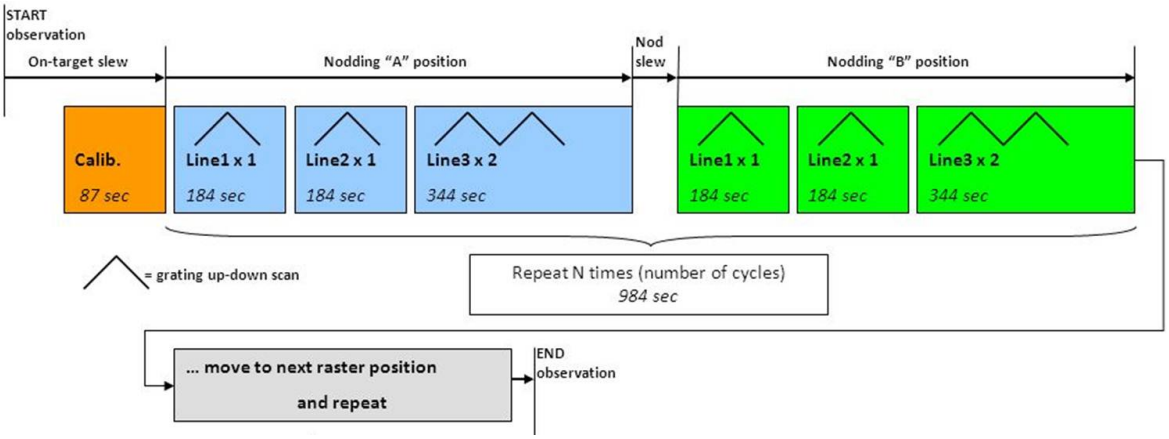

FIGURE 1.12: Instrument observing blocks are shown for a typical chop/nod observation. Line repetitions adjust the relative depth required for spectral lines, while the number of observing cycles is used to repeat the entire nodding cycle. Figure collected from the *PACS Observer's Manual*.

- **Unchopped grating scan mode:** This mode was a necessary alternative to the chopping/nodding mode for those sources without an emission free region within a 6' region around them. The "Unchopped" mode was useful, for example, for targets embedded in crowded fields or for very extended objects. In this case, the off position was set within two degrees radius with respect to the target coordinates.

  This mode was not recommended for very faint lines, the peak-to-continuum had to be above 1 Jy. Furthermore, the continuum level could be recovered in a reliable way only for bright sources, that is, with a minimum continuum level of 20-30 Jy.

  Due to its configuration, this unchopped technique had to be robust against instantaneous responsivity changes caused by, for example, cosmic ray hits. For this purpose, the grating scan was made much faster than in the chopped mode, and every line repetition requested by the user is doubled. The on-source integration time in this mode was half the time PACS spends on-source in the chopped mode, for that reason, although the number of repetitions in unchopped mode was doubled, the overall effective observed times in both modes were comparable.

  In pointed mode, after the on-source block is completed, the spacecraft slewed to the off-position. This position had to be selected carefully to an efficient subtraction of the telescope background. Under ideal conditions, the sky background towards the on and off-position was at the same level respectively and the 5×5 spaxels of the FoV were free of structures, it means, all of them detected the same sky emission.

  On the other hand, for raster observations, PACS executed always an obligatory Off observation before moving to the On position to carry out all the raster observations defined by the observer. After these raster observations, the spacecraft slewed, again, to the Off position and took one more observation. To clarify, in case of a 2×2 raster, with a single cycle and with an off position request after two raster positions, the spatial pattern followed would be: [OFF-ON-ON-OFF-ON-ON-OFF].

  In both, pointed and raster modes, the off-observation was always executed with a single repetition, irrespective to what the user had defined as line repetition factor. If line repetition factor had been set larger than one, the duration and signal-to-noise ratio in the off-position blocks would be lower than the on-target block.

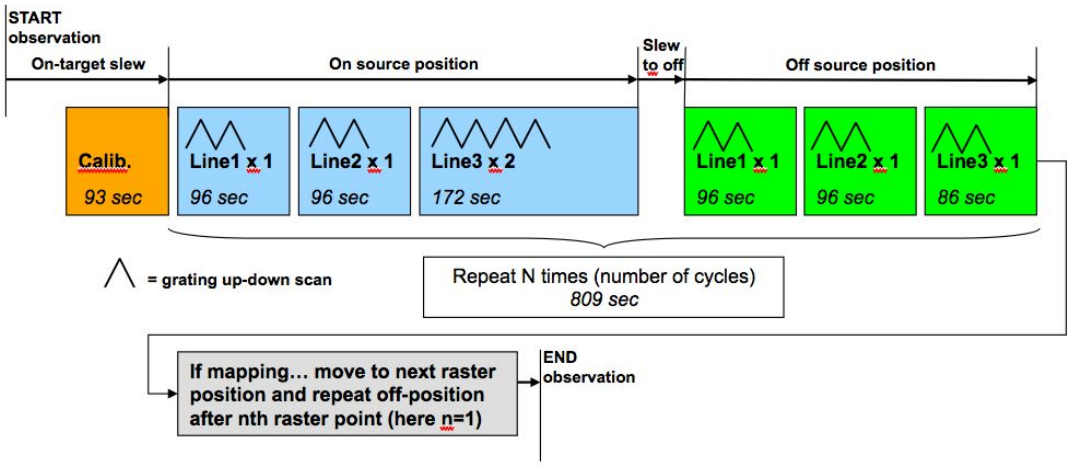

FIGURE 1.13: Instrument observing blocks are shown for a typical unchopped observation. Similarly to Chop/Nod cases, line repetitions adjust the relative depth required for spectral lines, while the number of observing cycles is used to repeat the entire on-off cycle. Figure taken from the *PACS Observer's Manual*.

Finally, the PACS Spectrometer offered two different modes regarding pointing: 'Pointed mode' and 'Mapping mode'.

- **Pointed mode:** It was the default mode for point-source spectroscopy, a single pointing centred on the source. The line flux from a point source or semiextended object would always be collected at least by the 5×5 spatial pixels that covered a 47"×47" FoV, so for a plain detection of a line source emitted by this kind of sources, one pointing would be enough.

  As it will be explained below, the observer could set up a pointed observation in combination with chopping/nodding or unchopped grating scan techniques.

- **Mapping mode:** This mode allowed the observer to set up a raster map observation in combination, also, with chopping/nodding or unchopped grating scan techniques.

  In chop/nod mode, the map could only be defined in instrument coordinates, and the map size was restricted to 6'×6' to obtain clean offset positions with the large chopper throw for each raster position. Furthermore, the observer had to define a map with the same number of raster points and step sizes on the raster X and Y axis.

  In unchopped mode the map could be defined in instrument, as well as, sky coordinates, with a maximum size of 2 degrees.

1.4.3 SPIRE

The SPIRE instrument (Griffin et al., 2010) consisted also of two sub-instruments: a three-band imaging photometer and an imaging Fourier Transform Spectrometer (FTS), both of them covering the sub-millimetre region of the wavelength range. The photometer carried out broad-band photometry in three spectral bands centered at 250, 350 and 500 μm, while the FTS used two overlapping bands to cover 194-671 μm.

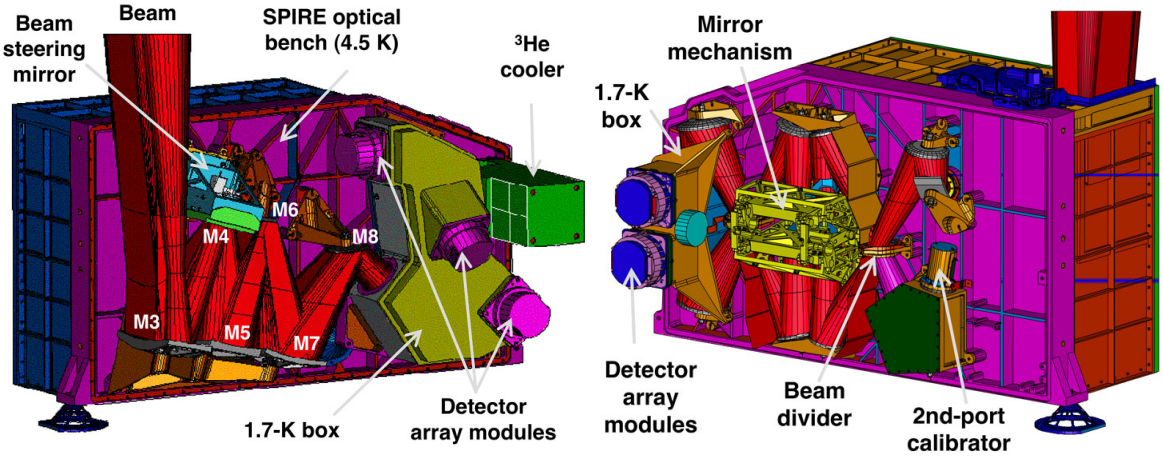

FIGURE 1.14: Left) SPIRE photometer layout. Right) SPIRE spectrometer layout. Figures selected from the *SPIRE Handbook*.

The **SPIRE Photometer** optics layout is shown in Fig. 1.14. The main elements found in this subinstrument were: the reflective mirrors, the dichroics, used to direct the light onto the bolometer arrays, and the filters used to define the passbands. The presence of the two dichroic beam splitter allowed to observe the same field of view (4'×8') simultaneously in the three bands. The number of detectors associated to each array were: 139 (250 μm), 88 (350 μm) and 43 (500 μm). In Fig. 1.14 a schematic view of the photometer bolometer arrays is shown.

The **SPIRE Fourier Transform Spectrometer** (FTS) was based on the principle of interferometry: the incident radiation was separated by a beam splitter in two beams that travelled different optical paths before recombining. With a moving mirror the Optical Path Difference (OPD) of both paths was changed and then an interferogram of signal versus OPD, was created. This interferogram was the Fourier transform of the incident radiation, that is, the signal registered by the Spectrometer detectors was not a measurement of the integrated flux density within the passband, like in the case of the Photometer, but rather the Fourier component of the full spectral content (telescope+instrument+source). The inverse Fourier transform produced a spectrum as a function of the frequency.

For an FTS, the spectral resolution is given by: $\delta f = c\delta\sigma$, being c the speed of light and $\delta\sigma = 1/(2 \times OPD_{max}$, where OPD_{max} is the maximum optical path difference of the scan mirror. Particularly, in SPIRE, OPD_{max} was 14 cm, which resulted in a $\delta f = 1.2GHz$. Unlike the PACS Spectrometer, the spectral resolution in the case of SPIRE Spectrometer kept constant along the whole wavelength range, from 194 to 671 μm.

In Fig. 1.14 an schematic view of the optical layout of the SPIRE Spectrometer is displayed. The main elements of this structure were: the beam splitter, the moving mirror mechanism that fed both arms of the interferometer and the two detector array modules where the final interferogram pattern was collected.

There were two overlapping spectral bands of 194-313 μm, (SSW) and 303-671 μm, (SLW). The transmission of the spectrometer filters were shown in Figure 1.15. There were also two spectrometer detector arrays with 19 and 36 hexagonally packed detectors for SLW

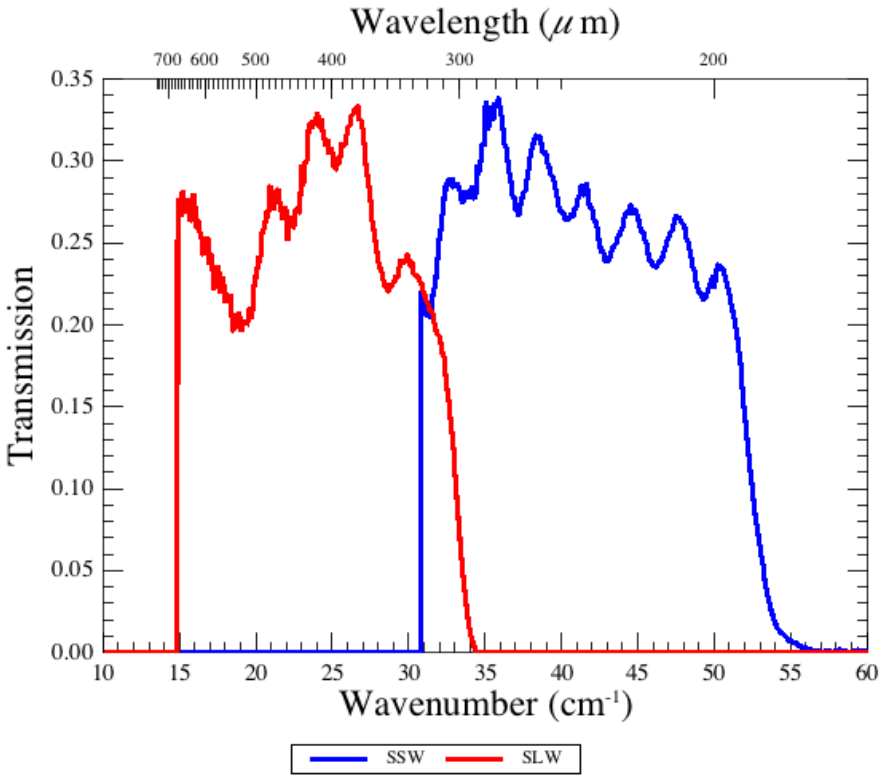

FIGURE 1.15: SPIRE Spectrometer filter transmission curves for the central detectors. Figure taken from the *SPIRE Handbook*.

and SSW, respectively. Each detector array had its own individual feedhorn, a schematic view of the bolometer arrays is presented in Fig. 1.16. The spectrometer field of view was a 2.6' diameter circular area.

Observing with SPIRE Spectrometer

To observe with the SPIRE Fourier Transform Spectrometer, it was necessary to define the observations according to the preferred spectral resolution, pointing modes and image sampling mode.

The Spectrometer Mirror Mechanism (SMEC) was scanned continuous at constant velocity over different distances to provide different spectral resolutions. For every repetition, two scans of the SMEC were done: one in the forward direction and one in the backward direction. In this way, the wavelength range was covered twice.

The movement of SMEC in terms of the optical path difference resulted in three types of spectral resolutions. See Fig. 1.17:

- **Low resolution (LR):** This mode was used to make continuum measurements at the resolution of δf=25 GHz ($\lambda/\delta\lambda$= 48 at λ=250 μm). SMEC took only 6.4 seconds in scanning, symmetrically around the Zero Path Distance (ZPD), a short distance in one

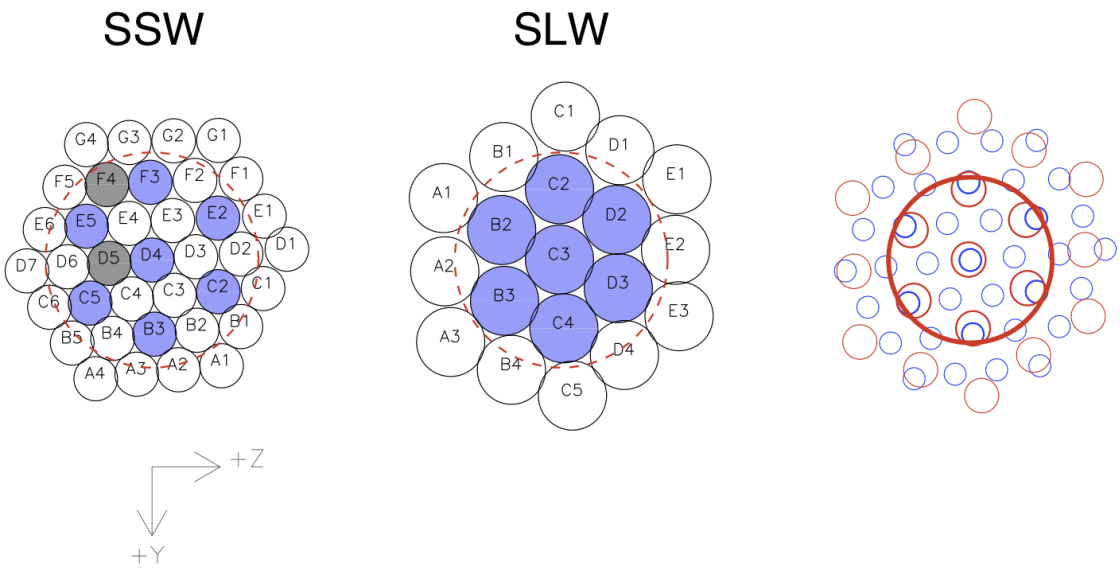

FIGURE 1.16: Schematic view of the bolometers array. The circles shaded in blue represent those detectors centered on the same sky position. On the other hand the grey circles are dead bolometers. The red dashed circle represents the 2.6' unvignetted field of view of each array. The overlapping of both arrays on the sky is shown in the rightmost figure where SLW bolometers are the red circles and the SSW bolometers are blue circles, the sizes of the circles correspond to the FWHM of the beam. The bold red circle shows the 2' unvignetted field of view for FTS observations. At the bottom, the spacecraft coordinate system (Y,Z) is shown. Figure taken from the *SPIRE Handbook*.

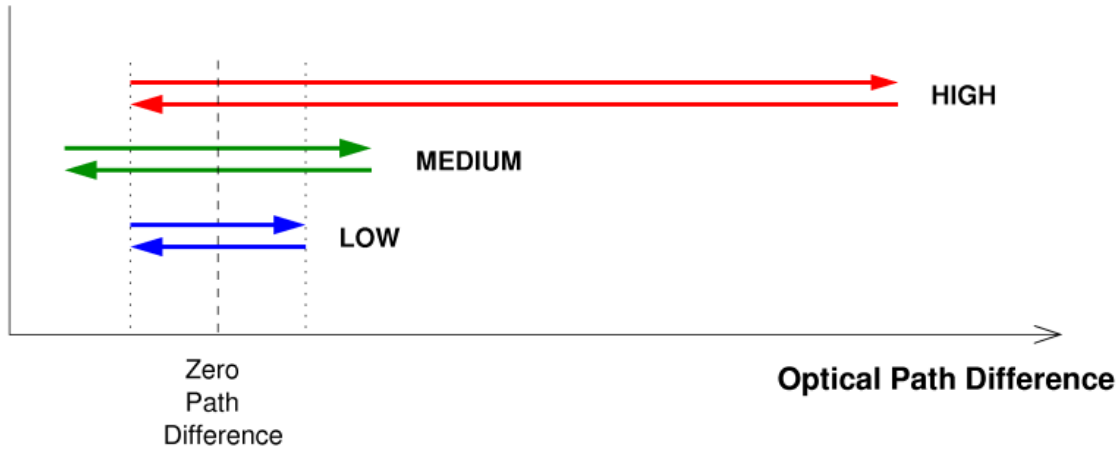

FIGURE 1.17: This figure shows how the SMEC moves, in terms of optical paths difference, during one repetition for High, Medium and Low spectral resolution. Figure taken from the *SPIRE Handbook*.

direction. This mode was intended to survey sources with an absence of spectral lines or very faint sources where only a SED was required.

- **Medium resolution (MR):** This medium resolution mode offered spectra with an spectral resolution of δf=7.2 GHz ($\lambda/\delta\lambda$=160 at λ=250 μm). However, this mode was never used for scientific purposes.

- **High resolution (HR):** This mode gave spectra at the highest resolution available with the SPIRE spectrometer, δf=1.2 GHz, and corresponded to $\lambda/\delta\lambda$=1000 at λ=250 μm. This resolution was reached by scanning the SMEC to the maximum possible distance from the ZPD.

  It took 66.6 seconds to perform one scan in one direction at high resolution. This mode was recommended for discovery spectral surveys where the whole range from 194 to 671 μm, could be explored to find new lines. It was also useful to observe and study sequence of spectral lines across the band (e.g. the CO rotational ladder).

  It was possible to extract low resolution spectra from high resolution observations.

- **High and Low Resolution (H+LR):** This mode was very useful to observe a high resolution spectrum as well as using additional integration time to increase the SNR of the low resolution continuum to a higher value than would be available from using a high resolution observation on its own. This mode was faster in terms of time spent than doing two separates observations.

To get the required sky coverage, the pointing mode and the image sampling needed to be set and combined. Attending to the pointing modes we have two options to select: Single Pointing Mode and Raster Pointing Mode.

- **Single Pointing Mode:** With this mode the astronomer only took the spectra associated to the region covered by the instrument field of view (2' diameter circle, unvignetted).

- **Raster Pointing Mode:** This mode was necessary to take spectra from a region larger than the field of view of the instrument (2' diameter circle). The telescope was pointed at several positions creating a hexagonally packed map See Fig. 1.18. At each position the image was taken at one or more Beam Steering Mirror (BSM) positions depending on the image sampling chosen, this will be explained in detail in the next paragraph.

Finally the image sampling had to be configured, in this case SPIRE FTS offered three different options: Sparse Image Sampling, Intermediate Image Sampling and Full Image Sampling. See Fig. 1.19

- **Sparse Image Sampling:** In conjunction with a single pointing, this option was used to measure the spectrum of a point or compact source well centred on the central detectors of the Spectrometer. For a point source this required accurate pointing and good knowledge of the source position to ensure that the object was well centered in the central detector beam.

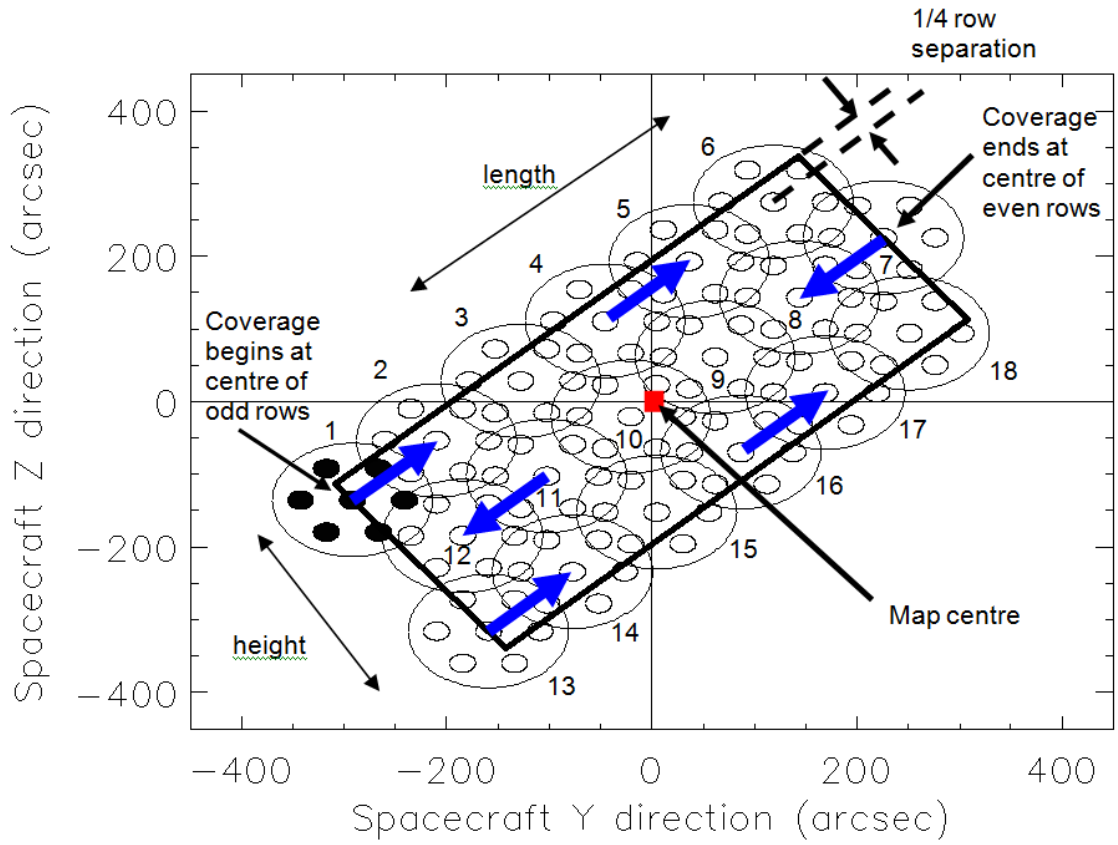

FIGURE 1.18: This figure shows, schematically, the pattern followed by the telescope to cover an extended area. This figure was selected from the *SPIRE Handbook*.

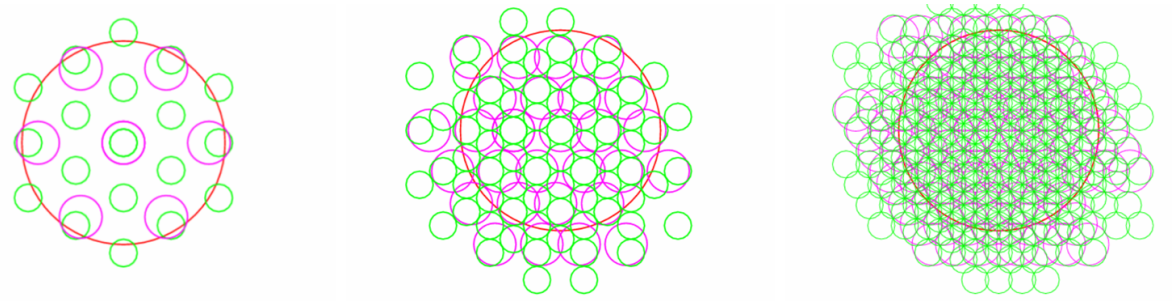

FIGURE 1.19: Left) SPIRE Spectrometer sparse spatial sampling. Center) Intermediate spatial sampling. Right) Full spatial sampling. The green (SSW) and magenta (SLW) circles indicate the regions where spectra will be observed for different spatial samplings. The large red circle represent the unvignetted 2' diameter field of view. Figure collected from the *SPIRE Handbook*.

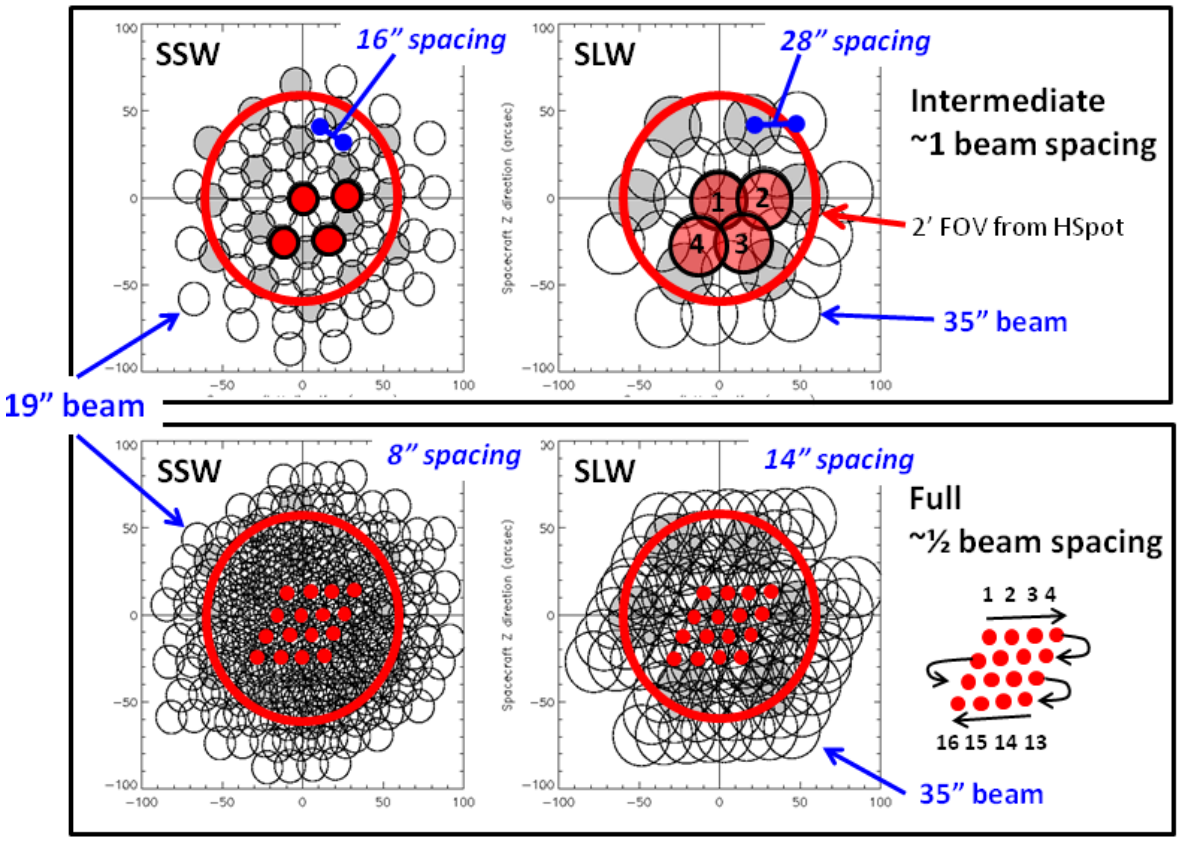

FIGURE 1.20: Top) Mapping pattern of the FTS with intermediate spatial sampling for both bolometer detector arrays (4-point jiggle. Bottom) The same for full spatial sampling (16-point jiggle). The red circle shows the 2' unvignetted field of view of the FTS. The spacing of the beams is shown for each of the detector arrays and the two image sampling modes. The red dots indicate the position of the central detector of each array at each of the 4 jiggle position (top) and 16 jiggle position (bottom). Figure collected from the *SPIRE Handbook*.

The result of this sampling was an observation of the selected source position plus a hexagonal-pattern sparse map of the surrounding region with beam centre spacing of 32.5" and 50.5" in the SSW and SLW bands, respectively. See Fig. 1.19

- **Intermediate Image Sampling:** This gave intermediate spatial sampling (~ 1 beam spacing). To obtain this level of sampling, the BSM was moved in a 4-point low frequency jiggle, giving a beam spacing of 16.3" and 25.3" for SSW and SLW, respectively. The input number of repetitions was performed at each of the 4 positions to produce the spectra. The final coverage was shown in Fig. 1.19 and Fig. 1.20.

- **Full Image Sampling:** This was achieved by moving the BSM in a 16-point jiggle to provide complete Nyquist sampling (1/2 beam spacing) of the required area. The beam spacing in the final map was 8.1" and 12.7" for SSW and SLW, respectively. As happened with the Intermediate Image Sampling, the input number of repetitions was performed at each one of the 16 positions to produce the spectra. The coverage maps are shown in Fig. 1.19 and Fig. 1.20.

1.5 Motivation and structure of this thesis. THROES: a caTalogue of HeRschel Observations of Evolved Stars.

During its operational time *Herschel*, performed an outstanding number of observations of sources classified as evolved low to intermediate mass stars. All these observation were collected in the *Herschel*Science Archive (HSA) but most of them had not been scientifically exploited. The THROES (A caTalogue of HeRschel Observations of Evolved Stars) project was born to increase the analysis of these objects and intended to provide a comprehensive overview of the spectroscopic results obtained in the far-infrared and sub-mm wavelength regions (55-670 μm).

The initial major goal of the THROES project was the development of two catalogues of interactively reprocessed PACS and SPIRE spectra covering the 55-200μm, and the 500-1500 GHz, respectively. Both catalogues include objects spanning a range of evolutionary stages, from the asymptotic giant branch to the planetary nebula phase, displaying a wide variety of chemical and physical properties. To allow the access to these catalogues, we created two different web-based interfaces (https://throes.cab.inta-csic.es/ and https://throes-spire.cab.inta-csic.es/) corresponding to the THROES/PACS and the THROES/SPIRE catalogues, respectively. We have created a legacy-value *Herschel*PACS and SPIRE dataset that can be used by the scientific community in the future to deepen our knowledge and understanding of these latest stages of the evolution of low-to-intermediate mass stars.

The main steps taken to develop both catalogues were:

- **1)** Exploration of the HSA and generation of an initial inventory of observations made by Herschel of evolved stars.
- **2)** Interactive and detailed data reduction of the selected sample to generate a comprehensive set of homogeneously reduced, absolute calibrated spectra.
- **3)** Creation of a web-based catalogue where all the reduced data are made available to the whole scientific community.

The main scientific goal of THROES was:

- The determination and characterization of fundamental physical magnitudes such as: the nebular mass, the gas rotational temperature as well as the mass loss rate of the objects of the sample making use of the CO rotational emission lines. Thanks to the combination of PACS and SPIRE spectra collected the ladder of CO emission lines from low J levels (4-3) to high J levels (42-41) can be studied.

  Although previous spectra taken with ISO-LWS instrument covered a wavelength range similar to PACS, the higher sensitivity of PACS spectra eases the characterization of the hot gas located close to the central star.

This manuscript is organised as follows: In Chapter. 2 we extensively described the data reduction process developed separately for PACS and SPIRE spectra. In Chapter. 3 all the

information regarding the THROES-PACS and the THROES-SPIRE catalogues, regarding the sample of sources included and the web-based interface, is included. The analysis of the PACS and SPIRE data for O-rich and C-rich sources is presented in Chapters. 4, 5 and 6, respectively. Finally, the main conclusions derived from this thesis are collected in Chapter. 7, together with a brief list of possible future projects that could follow the studies presented in this thesis.

Chapter 2

Data Reduction

Nessum Dorma (Turandot)

Giacomo Puccini

The first step of this thesis was focussed on the identification, recompilation and reduction of the PACS and SPIRE spectra associated to different evolved low to intermediate mass stars available in the HSA. This reduction process allowed us to obtain fully-reduced, science-ready, high quality data from the "raw" observations taken from the Archive.

2.1 The *Herschel* Interactive Processing Environment

To perform the reduction process of *Herschel*data and to interact with the whole *Herschel*environment, the *Herschel*Science Center (HSC) developed a specific software known as HIPE (*Herschel* Interactive Processing Environment) that was the tool used to carry out the data reduction of the PACS and SPIRE spectra presented in this thesis. HIPE enables the user to:

- Access data from the Herschel Science Archive (HSA).
- Perform interactive data reduction from raw data to publishable products, using Herschel-provided and user-developed routines, both in GUI form or in console-batch mode.
- Visualise and manipulate data.
- Perform science analysis.
- Get access to context-sensitive documentation and help.

HIPE also has the great advantage that the same framework can be used to download, reprocess, analyse and compare data from all three instruments in *Herschel* simultaneously. The scripting language is Jython.

This software offers a wide variety of official pipelines to carry out the standard processing of observations. These pipelines are a combination of tasks that, applied properly, take the data from the raw level to a science ready context.

Each pipeline is adapted to the different kind of observations taking into account the instrument and the AOTs. Nevertheless, users can edit and configure the official pipelines as well as create new scripts to adapt the processing of data to their needs.

With each new version of HIPE, all data taken by *Herschel* were processed by the Herschel Science Center using the Standard Product Generator. Once processed, the new set of processed data is ingested to the HSA, where data is fully available for the whole scientific community.

Along the reduction process data go through different levels:

- **Level 0:** Raw data, formatted from the raw telemetry by an external pre-processing stage.
- **Level 0.5:** Products have been partially reduced, corrected for instrument effects generally by tasks for which no interaction is required by the user.
- **Level 1:** Products have been more fully reduced, some pipeline tasks requiring inspection and maybe interaction on the part of the user.
- **Level 2:** Products are fully reduced, including tasks that require the highest level of inspection and interaction on the part of the user.

For some observations of PACS and SPIRE **level 2.5** and **level 3** data are achieved. The data at these levels do not include new processing or reduction tasks respect to level 2 data, they are new products generated through the combination of level 2 ones.

2.2 PACS Spectroscopy data reduction

As mentioned in Section. 2.1, there is an specific pipeline adapted to the characteristics of each observation. Particularly, for PACS Spectroscopy, there are 4 major routines that could be applied:

- Chop/Nod line and short range observations.
- Chop/Nod range and SEDs observations.
- Unchopped line observations.
- Unchopped range, for single or combined observations.

Typically, "range" observations were designed to cover a wide wavelength region, meanwhile the "line" ones were useful to observe short wavelength regions. In this project we have focussed our efforts on Chop/Nod range and SEDs observations and in Unchopped range ones. The reduction process can be split in two main parts: the, so-called, processing,

that includes all the tasks applied to data from level 0 to level 2, and the post-processing, that includes a number of tasks applied to the level 2 data. See Sect. 2.2.1 for more details.

Along the reduction process followed in this thesis there are some improvements with respect to what the standard pipeline does. These improvements are:

- **Processing improvements (from level 0 to level 2):**

  - *Spectral FlatFielding:* This task fits a function to the continuum of the spectrum to improve its shape, obtain, in some cases, a better signal to noise ratio and remove those regions of spectrum affected by *leakage*[1]. At the moment of starting the reduction process of data, the *Spectral Flatfielding* task was not applied in the SPG pipeline as it requires user inspection. In this thesis, the *Spectral Flatfielding* task was applied to all spectra. In following versions of SPG data products the *Spectral Flatfielding* correction was applied, although the HSC highly recommend a visual inspection of the data to ensure that the task is working properly.

  - *Telescope Background Normalization:* This task uses the telescope background temperature to flux calibrate spectra instead of using the theoretical Relative Spectra Response Function (RSRF) to do this calibration. The last version of SPG data introduces this task in the reduction process.

- **Post-processing tasks (from level 2):**

  - *Point Source Correction (PSC):* Once the level 2 cubes are generated, this task is applied to take into account the flux losses derived from the fraction of the Point Spread Function (PSF) that falls out of the spaxel where the source is located (commonly, the central one). The output is a 1D spectrum.

  - Correction for slightly mispointed observations and semiextended sources (3×3): Once applied the PSC, this task recovers the total flux level of the spectrum attending to the emission that falls into the adjacent 3×3 spaxels around the central one.

  - Correction for semiextended, fully mispointed sources (3×3): Once applied the PSC, this task recovers the total flux level of the spectrum attending to the emission that falls into the adjacent 3×3 spaxels around the spaxel where the source is located, which is not the central one. This correction is not available in HIPE so we created it to deal with the mispointed sources.

  - Correction for extended sources (5×5): Once applied the PSC, this task recovers the total flux level of the spectrum attending to the emission that falls into the whole 5×5 spaxels FoV. This task is not available in HIPE, so we developed it to deal with those very extended sources that occupy the whole FoV.

[1]The PACS spectra near the band borders of bands R1, B3A and B2B are affected by higher or lower order wavelengths leaking into the spectra.

2.2.1 From level 0 to post-processing

To reduce data we have used the pipelines and scripts provided by HIPE v.13 (user release) and calibration files 65. These pipelines guided us to take data from level 0 (raw data) along the next levels until we achieve the level 2. In the following we describe in detail the data reduction process for Chop/Nod and Unchopped observations. (See more details in "PACS Data Reduction GUide: Spectroscopy").

Chop/Nod

Chop/Nod observations have been reduced using the "ChopNodBackgroundNormalization-Range" pipeline. The main steps are:

- **Level 0 to 0.5:**

  This first part is the same for all pipelines and does not require the interaction from the user. At this stage data is structured in **frames** following a 25×16 pixels array. The 25 pixels corresponds to the spatial dimension of the PACS Integrated Field of View (IFU) while the 16 ones are spectral pixels. At this part the the instrument signature is removed and the data are sliced according to an astronomical logic (wavelength and pointing). The detailed steps are:

  1) Retrieve the observation using *getObservation*. To take data from the HSA the option *useHsa* has to be set to 1.

  2) Extract raw, level 0, data from the *ObservationContext*.

  3) Identify saturated pixels creating the masks SATURATION and RAWSATURATION using *specFlagSaturationFrames*.

  4) Convert units to V/s with *specConvDigit2VoltsPerSecFrames*.

  5) Add to the Status table the location of the calibration block in the data timeline to separate the non-science data from the science data (*detectCalibrationBlock*)

  6) Convert from spacecraft time to UTC via *addUtc*.

  7) Assign the pointing and position angle, that is, the coordinates (RA, Dec), to the central detector pixel. (*specAddinstantPointing*).

  8) If object is a Solar System Object, *correctRaDec4Sso* moves it to a fixed position in the sky.

  9) Include in the Status table the information about the grating, chopping and nodding position of each point at each moment along the observation. (*specExtendStatus*).

10) The chopper position is converted to sky position using *convertChopper2Angle*.

11) Calculate the coordinates (RA, Dec) for every pixel, it depends on the position of the central pixel and the chopper position seen by each pixel. (*specAssignRaDec*).

12) Introduce wavelength array and identify those points that fall outside of the filter bands to create the OUTOFBANDS mask. This mask will be activated when level 2 cubes are created. (*waveCalc*).

13) Wavelengths have to be corrected for Herschel's velocity. (*specCorrectHerschelVelocity*).

14) Figure out the organisation of the data blocks. (*findBlocks*).

15) Flag for bad and noisy pixels creating the masks BADPIXELS and NOISYPIXELS. Noisy pixels are those that have been determined, from instrument tests, to be noisier than the rest. (*specFlagBadPixelsFrames*).

16) Data is sliced according to an astronomical and observational logic. *pacsSliceCOntext* slices on wavelength range, pointing and repetition (NodCycleNum).

17) Using *flagGratMoveFrames* and *flagChopMoveFrames*, the pipeline flags those datapoints taken while parts of the instruments are moving.

18) For **Unchopped** observations, *specAddGratingCycleStatus* adds to the Status table the necessary information to distinguish on- from off-chop data.
The first part of the pipeline ends here. The Level 0.5 has been reached.

- **Level 0.5 to 1.0:**

From this point the tasks described are specific of the 'ChopNodBackgroundNormalizationRange' pipeline.
19) The data contained in the sliced Frames, generated previously, is flagged for glitches (e.g. cosmic rays) using the Q statistical test and generating the mask GLITCH. (*specFagGlitchFramesQTest*).

20) To develop the calibration tasks is necessary to covert the signal as it would have been taken at the lowest detector capacitance setting. This is done using *convertSignal2StandardCap*.

21) Now, using *specDiffChop*, the pipeline computes the pairwise difference-ratio 2*(A-B)(A+B), rather than the pairwise differences (A-B: on-off). After this, the flux density can be considered to be in units of 'telescope background', it is not converted to Jy until a little later. Besides, apart of the removing of the telescope + sky background and dark current, this computation allow a better elimination of detector drifts

since any drift will be almost the same for the on-source data and the off-source data.

The next tasks are involved in the flatfielding process. This flatfielding computes a reference spectrum created from all the non-masked datapoints for each spaxel; then, it computes the continuum fit to this reference spectrum and to that for each individual population in each spaxel; finally, it shifts the individual fits to that to the reference spectrum.

22) *specFlatFieldRange* applies the flat fielding task that normalises the response of all pixels within each module to the same level. It fits a polynomial function over the available wavelength range as it computes the scaling factor. For SEDs and long wavelength ranges the PACS Data Reduction Guide (PDRG) [2] suggests that a polynomial of order 5 should be appropriate. The experience earned in this project indicates that a polynomial of order 4 generates better results. This order should be lower for shorter wavelength regions. *specFlatFieldRange* allows to remove the regions of the spectra affected by leakage. The effects of this task are shown in Fig. 2.1.

23) Finally, *specFrames2PacsCube*, rearranges the data turning the SlicedFrames to SlicedPacsCubes. These cubes have a spatial arrangement of 5×5 spaxels (created from the 25 modules) and, along the wavelength dimension, they contain the spectra from the 16 pixels all packed together.

After this rearrangement data have achieved the end of the Level 1.

- **Level 1.0 to 2.0:**

  Here starts the process of turning the PacsCubes into PacsRebinnedCubes. The following task will also combine all the individual spectra held in each spaxel (for each wavelength range and raster position separately) into 25 single spectra.

  24) *wavelengthGrid* creates the wavelength grids, one per wavelength range that is in the SlicedPacsCubes, that will be used to rebin on them. As each of the 16 pixels that feed each spaxel have a wavelength sampling that is slightly offset from the previous one, all together cover the entire wavelength range requested. It is necessary to create the wavelength grid so all rebinned cubes created, and all spaxels in each cube, will have the same range. A mask named OUTOFBAND is created by this task to flag those spectral regions that have fallen out of the applicable band.

  The sampling of the wavelength grid is set using the parameters 'oversample' and 'upsample'. 'Oversample' sets how many bins we want the grid to have per resolution element, while 'upsample' sets by how many bins we want to shift forward when calculating the new grid. Along our the data reduction process both parameters were set to 2.

[2] http://herschel.esac.esa.int/twiki/pub/Public/PacsCalibrationWeb/pacs$_spec_Hipe12.pdf$

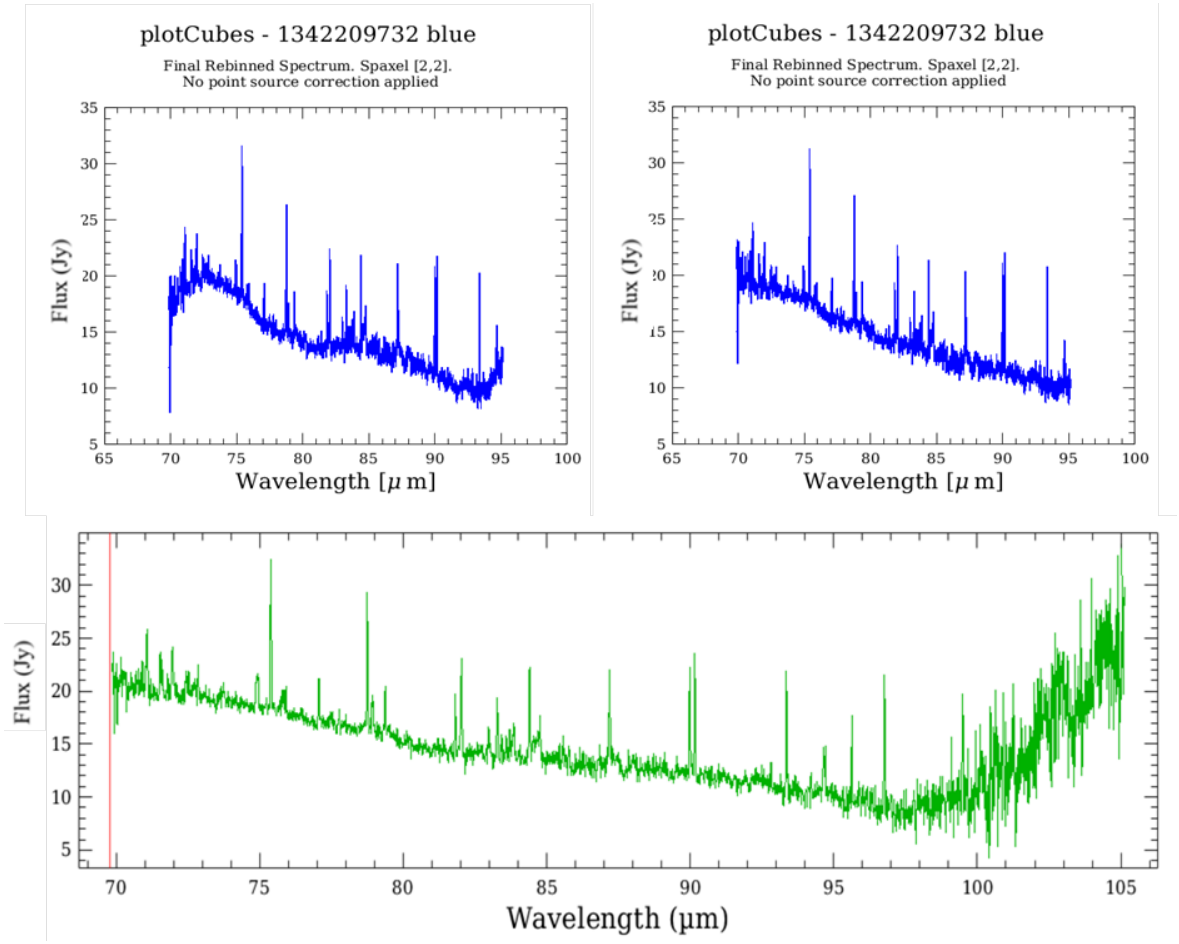

FIGURE 2.1: **Top left)** Spectral region from 70 to 95 microns corresponding to W Aql after *FlatFielding* with *polyOrder* = 5 and *excludeLeaks* = "True". Note the ondulations found in the spectrum. **Top right)** Same spectral region corresponding, also, to W Aql after *FlatFielding* with *polyOrder* = 4 and *excludeLeaks* = "True" was applied. Note that the ondulations found in the "top left" spectrum have disappeared. This is final spectrum incorporated to THROES Catalogue. **Bottom)** Spectral region from 70 to 105 microns corresponding to W Aql retrieved directly from HSA (no *FlatFielding* has been applied). Note the region affected by leakage (from 95 to 105 μm).

25) Now a second level glitch-detection task is created by *specFlagOutliers* generating a mask named OUTLIERS.

26) At this point the spectral rebinning takes place. *specWaveRebin* takes the input wavelength grid and running over it, bin by bin, mean-combines the data from the input cubes into the output cubes with the new grid. The differences between the cubes (raster pointing, wavelength range, nods (A and B) and nod cycle) are maintained. The output is a set of `PacsRebinnedCubes` held in a `SlicedPacsRebinnedCube`.

27) PacsRebinnedCubes are now combined on nod. All the nod A and B are average-combined by *specAddNodCubes*.

28) Finally, *specRespCalToTelescope* is the task that computes the telescope background spectrum for your observations. Basically, it takes the telescope background that has been created from numerous calibration observations, scales it by the temperature that had the telescope while the observations were taken and uses it to perform the flux conversion from 'telescope backgrounds' to Jy.

At this point, level 2 data has been achieved, so it is possible to apply some, new, tasks (post-processing) to obtain final, science products. The steps followed along the post-processing of 'Pointed' and 'Mapping' observations are different so, in the following, both cases are described independently.

- **Post-processing. Pointed observations**

For pointed observations the post-processing tasks applied depend on: The pointing of the observation (well pointed or mispointed) and the extension of the sources (point, semiextended or extended).

- Good pointing, point or semiextended sources: To extract the spectrum of the source recovering the whole emitting flux it is necessary to apply the task *extractCentralSpectrum*. This task, available in HIPE, applies two different corrections to the level 2 rebinned cubes to generate, as output, 3 different 1D spectra:
1) The first 1D spectrum returned is the spectrum taken from the central spaxel corrected for point source flux losses. This correction is needed to take into account that, even for point-like sources, the whole emitting flux is not recovered by the central spaxel because the spaxel size (9.4"×9.4") is lower than the size of the PSF. A theoretical model of the PSF is used to know the fraction of PSF that falls out of the central spaxel and has to be recovered. 2) The second 1D spectrum generated contains the integrated flux of the 3×3 central spaxels with the point source correction applied to the central spaxel. 3) Finally, the third 1D spectrum created is that corresponding to the central spaxel (with the point source correction applied) scaled to the flux level of the spectrum extracted from the 3×3 central spaxels.

Using this third spectrum the whole flux from sources that are semiextended or slightly mispointed is recovered. In Fig. 2.2 the difference between the 1D spectrum generated

after applying all the corrections described above and the spectrum taken, directly, from the level 2 cube, before post-processing, is shown (top and middle panels). The vast majority of the sources in the sample has been reduced following this procedure.

- Good pointing, extended sources: There are some sources in the sample larger than the central 3×3 spaxels. (IRAS 16122-5122, NGC 3242, NGC 40, NGC 6445, NGC 6543, NGC 6781, NGC 6826, NGC 7009, NGC 7026 and PN Mz3). For these cases the 3×3 correction described above would not be enough and the flux level of the 1D spectrum obtained would be a lower limit of the real one. For that reason we have applied a new correction, not available in HIPE, that works in a similar way to *extractCentralSpectrum* but scaling, in this case, the 1D spectrum extracted from the central spaxel, with the point source correction applied, to the 1D spectrum obtained integrating the 5×5 spaxels that conform the PACS FoV. The improvement obtained with this correction is shown in Fig. 2.2 (bottom panel).

- Mispointed observations, semiextended sources: Unfortunately, not all the observations in the sample are well centered in the PACS 5×5 spaxels array. In the sample we have found 7 mispointed objects (IRAS 17347-3139, NGC 6302, IRC -10529, OH 21.5+0.5, IRAS 16279-4757, IRAS 13428-6232 and AFGL 5379) For these cases the *extractCentralSpectrum* task is not applicable as the object is not located at the central spaxel. To deal with them we are going to make use of two other tasks available in HIPE: *extractSpaxelSpectrum* and *pointSourceLossCorrection*.

With *extractSpaxelSpectrum* it is possible to extract the 1D spectrum contained in any of the 5×5 spaxels. However, this task does not apply, automatically, the point source loss correction to take into account the PSF losses. That is why, after extracting the 1D spectrum, it is necessary to apply the second task *pointSourceLossCorrection*.

After using these two tasks, our product is similar to the first spectrum returned by the task *extractCentralSpectrum*. However, this spectrum does not recover the flux losses due to the extension of the sources so, to correct it, this 1D spectrum has been scaled to the flux level of the 1D spectrum extracted from the 3×3 spaxels reconstructed around the spaxel where the source is located. The extraction of the spectrum associated to the corresponding 3×3 spaxels around the source and the subsequent scaling have been done manually as HIPE does not have any task to deal with semiextended sources that are mispointed. In Fig. 2.2 the comparison between our final 1D spectrum and the one obtained from the central spaxel before post-processing is displayed.

- Sources only corrected of Point Source Correction Losses: There are three sources in our sample that have been only corrected by PSF losses. They are: OH 32.8-0.3, AFGL 5379 and IRAS 16279-4757. The first one is a well pointed, semiextended source that presents bad quality data in the spaxels around the central one, what derives in a bad result after scaling the 1D spectrum of the central spaxel with the analogue corresponding to the 3×3 central spaxels.

The other two cases are very mispointed cases, that is, the source is located in one of the outermost spaxel of the 5×5 PACS FoV, so it was impossible to reconstruct a 3×3 'superspaxel' around the source.

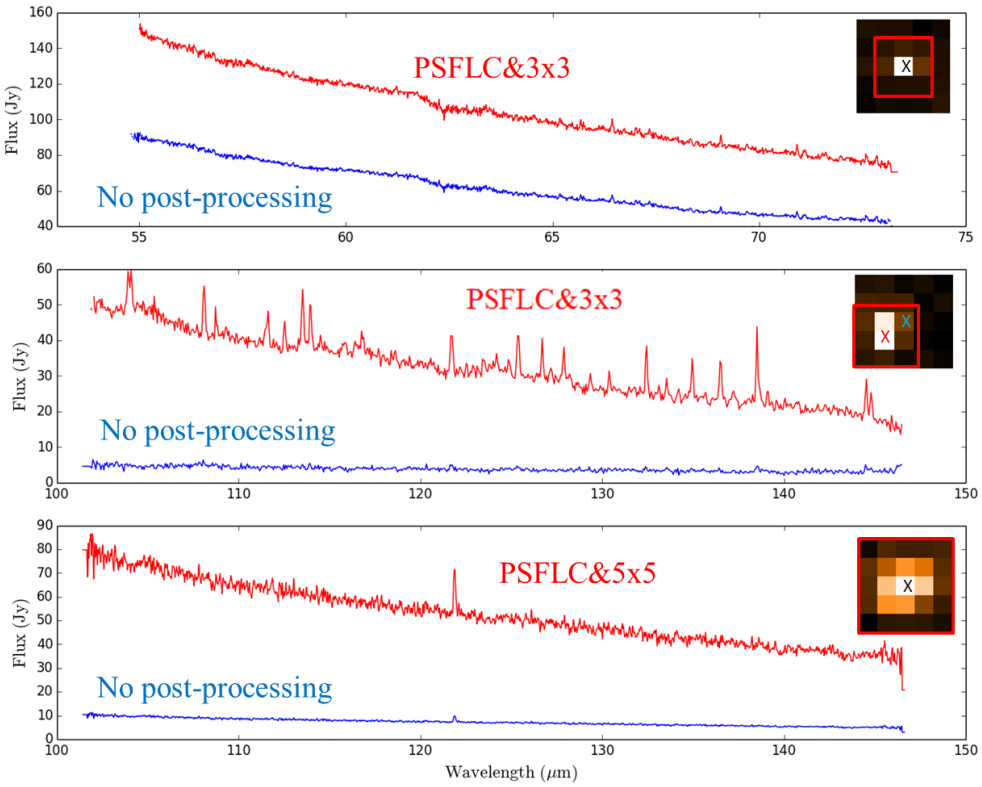

FIGURE 2.2: Example of one-dimensional spectra extracted for three different targets in the THROES catalogue (red) following the processing and post-processing steps explained in Sect. 2.2.1. For comparison, we show the same spectra from the central spaxel without post-processing (blue). **Top)** AFGL 3116, blue camera of PACS (ObsID: 1342212512). Well pointed and semiextended source, PSFLC-3x3 correction. **Center)** Same as above but for IRC-10529, red camera of PACS (ObsID: 1342208931). This is a mispointed case being the blue spectrum that extracted from the central spaxel without post-processing while the red one is the spectrum taken from the brightest spaxel and with the post-processing applied (PSFLC-3x3). **Bottom)** Same as the first two panels but for NGC 6543, red camera (ObsID: 1342238389). This an extended source, PSFLC-5x5 correction. At the top right corner of each box we show a layer of the FinalCube. The black cross (top and bottom) indicates that both spectra were taken from the central spaxel. For the mispointing case of the central box, the two crosses (red and blue) indicate the spaxels from which each spectrum was taken. In all three layers of the FinalCube, the red square limits the spaxels used to apply the *Semiextended3x3* or *Extended5x5* corrections.

- **Post-processing. Mapping observations**

  For spatially oversampled observations the pipeline does not end with the creation of the SlicedFinalCubes, as it is possible to perform a final step to combine the separate pointings into a single cube. At the same time the size of the spaxel of the new cube can be changed and set to adopt a smaller value.

  specProject is the task used for large wavelength range observations and SEDs. In this task the parameter 'outputPixelSize' is set to 3 arcsecs by default. This task will do a 'spectral projection' to generate a spectrum associated to each output spaxel based on a weighted combination of the spectra of the input spaxels. It creates a new, regular spatial grid that covers the field of view of the raster sequence and combines all the input cubes into a single one.

Unchopped

The reduction process applied to unchopped observations is analogue to the one described before. However, there are some differences due to the way the observations were taken. As for Unchopped PacsRange observations the On and Off data are in different ObsIDs we first reduce, independently, both on and off observations using *UnchoppedRangeScan* and, finally, we subtract the Off to the On observation using *UnchoppedRangeMultiObs*.

- **Level 0 to 0.5**

  This first part is the same for all pipelines, as described in section 2.2.1, in this stage the instrument signature is removed and the data are sliced according o an astronomical logic. Steps (1) to (18).

- **Level 0.5 to 1**

  19) Using *specFlagGlitchFramesQTest*, the pixels affected by, for example, cosmic rays are flagged and a mask named GLITCH is created.

  20) As happened in the Chop/Nod data reduction process, the signal is converted to a value that would be if the observation had been done at the lowest detector capacitance setting as it is necessary for the calibration tasks. It is done with the *convertSignal2StandardCap* task.

  21) Using *specDiffCs*, the response and the dark current of the observation are calculated.

  22) Now the dark current is subtracted as a single value held in the calibration file thanks to the *specSubtractDark*.

  At this point the pipeline performs the calibration of the flux.

  23) The task *rsrfCal* is necessary to apply the relative spectral response function. The

RSRF is taken from the calibration tree.

24) *specRespCal* Uses the absolute response correction calculated from the calibration block to convert the units of the flux to Jy. (Note that in the Chop/Nod case the flux units are not converted to Jy until the end of the level 2).

After the flux calibration, the next step in the pipeline is to perform the flatfielding.

25) *specFlatFieldRange* is the task in charge of applying the FlatField correction. The process is similar to the one described in the Chop/Nod reprocessing.

26) Once the flatfiending has been applied, the SlicedFrames are turned to a SlicedPacsCube that contains the PacsCubes with the task *specFrames2PacsCube*.

After these tasks and corrections, the level 1 data have been generated. The next goal of the pipeline is to turn the PacsCubes into PacsRebinnedCubes. This process is the same followed in the Chop/Nod reprocessing.

27) *wavelengthGrid* is the task responsible of creating the wavelength grids to rebin on, one per wavelength range that is in the slicedCubes. More details about this task can be found in the Chop/Nod data reduction description.

28) A second level glitch-detection task is applied, using *specFlagOutliers* to flag the outliers and to create a mask named OUTLIERS.

29) *specWaveRebin* this task takes the input wavelength grid and, running over it, bin by bin, mean-combines the data from the input cubes into the output cubes with the new grid. The output is a set of PacsRebinnedCubes held in a SlicedPacsRebinneCube. This task operates in the same way as described in the Chop/Nod part.

At this point the processing of the On-source data and Off-source data are reprocessed until the last level that can be achieved. Now, for our range scan AOTs, both observations have to be subtracted to get a final On-Off product. This subtraction is done using a script named 'Combine on-off obs'. The main steps of this script are described below.

30) Once both on and off-data have been reprocessed, *concatenateSliced* take the individual cubes of input On and Off cubes and concatenate them to create the allAverageCubes product where all the previous PacsRebinnedCubes are contained.

31) Finally, *specSubtractOffPosition*, subtracts the off from the on, generating the final, science-ready, product.

Post-processing. Pointed observations

To extract the 1D spectrum from the final On-Off products the tasks applied in the

Chop/Nod post-processing are also available and useful here. However, the *extractCentralSpectrum* task is not recommended as, unfortunately, for unchopped observations the accuracy and reliability of the continuum level of the source can not be guaranteed. This problem is present in our final On-Off products as we found continuum levels below zero. For that reason, in case to want to extract the 1D spectrum from a spaxel, it is recommended to use *extractSpaxelSpectrum* followed by *pointSourceLossCorrection*.

Post-processing. Mapping observations

In this case the task applied, *specProject*, works identically as described in the Chop/Nod post-processing part. See Sect. 2.2.1 for more details.

2.3 SPIRE Spectrometer data reduction

As happened with PACS Spectroscopy the pipelines available in HIPE to process the spectroscopic data of SPIRE must be adapted to the way the observations were taken in terms of spatial sampling or pointing. The two pipelines are:

- **Spectrometer Point Pipeline (SOF1):** This pipeline is adapted to reduce observations with 'sparse' image sampling with both 'raster' and 'point' pointings.
- **Spectrometer Mapping Pipeline (SOF2):** This pipeline is used to reprocess observations with 'intermediate' and 'full' image sampling for, again, both 'raster' and 'point' pointings. Note that 'intermediate' image sampling was never used for scientific purposes.

To process the SPIRE Spectrometer data, HIPE 13, user release version, was used with SPIRE calibration files version 13.1. Opposite to PACS Spectroscopy data reduction, the steps followed to process the SPIRE Spectrometer data from level 0 to level 2, do not differ from the steps applied by the SPG. However, all the SPIRE data of the sample was reduced, again, to ensure that all products were homogeneously processed.

Once level 2 data was achieved, a post-processing task was applied to correct the spectra of semiextended sources. This task was not applied by the SPG.

Now, a detailed description of all the task applied along the data reduction for SOF1 and SOF2 pipelines are described.

- **Spectrometer Point Pipeline (SOF1)**

  First it is necessary to configure the pipeline, as well as, extracting the necessary products to perform the processing of the data.

1) Using *getObservation* the data is retrieved. If parameter useHsa is set to 1. Data is retrieved from the HSA.

2) With *processOnlyCenterDetectors* is possible to decide if the processing is going to be applied for all the detectors (0) or only for the central ones (1).

3) User has to decide, also, if the apodized spectra will be saved as FITS files or not, by setting *apodize* to 1 or 0.

4) Define the central detectors of each spectral range (SLWC3 and SSWD4).

5) Create the calibration tree by *spireCal*.

6) Retrieve all the necessary calibration and auxiliary products from the Observation Context.

7) Get the level 0.5 data directly from observation.

In contrast to PACS Spectroscopy data reduction, the starting point of the reprocessing is the level 0.5. Data at this stage, consists of blocks of time-dependant signal converted into physical units (e.g. voltages).

8) If *processOnlyCenterDetectors* is set to 1, at this stage, the task *filterChannels* removes all the unnecessary channels. This was not the case in the reduction process of carried out in this thesis.

9) Using *waveletDeglitcher* the effects of the cosmic ray hits can be removed (first-level deglitching). The elimination of the glitches is very important as an unremoved deglitch could generated a sinusoidal artefact in the spectral domain of the final spectrum. The values of the parameters used in this task are conservative to avoid affecting the interference patterns from the detectors, particularly, from the SSW.

10) *specNonLinearityCorrection* is used to correct from the non-linearities generated because the RMS voltage measured by the SPIRE bolometers only responds linearly to incoming radiation within a limited range of power.

11) As the detectors have a limited dynamic range, for bright sources they can saturate deriving in a 'clipping' of the extrema of the interference pattern. This is necessary to be corrected before the Fourier transform.

12) With the task *timeDomainPhaseCorrection* it is possible to correct the effects of time delay shown in the recorded signals because the thermal response of the detectors and the read-out electronics are not instantaneous.

13) At this stage the pipeline creates the SPIRE pointing product that collects information from four inputs to calculate the absolute pointing of the detectors during the observation. These inputs are:

a) The absolute pointing of the *Herschel* telescope.

b) The offset of the detector arrays from the boresight of the *Herschel* telescope.

c) The relative offset of the detectors in each array from the central detectors.

d) The angle of the SPIRE Beam Steering Mirror.

The task used is *createSpirePointing*.

14) Now it is the moment to produce a level-1 interferogram, that is, the signal is displayed as a function of the optical path difference. To do that, *createIfgm* combines the position timeline of the FTS mirror with the timeline of the detector signals.

15) After generating the interferogram the baseline is subtracted. This subtraction allows the interferometers to be easily zero-padded when calculating the Fourier transform, without creating spectral artefacts. The baseline correction module can either fit the baseline with a polynomial function or use Fourier components up to a certain frequency threshold. The Fourier configuration is the most robust and the one used in the SPG. However, for faint to medium strength and for extended sources it may therefore be preferable to use polynomial baseline fitting. For that reason, in our processing of data both, Fourier and polynomial, options were used to subtract the baseline. The order of the polynomial fit was 4. The task used is *baselineCorrection*.

16) Once the baseline has been subtracted, a second level deglitching is applied. This correction worked under the assumption that, at the same sky position, two repeated observations of the same source yield identical results, within the associated random noise. In this way, comparing the observations in an OPD per OPD basis it is possible to identify and remove outliers. There are two statistical algorithms available to set the thresholds beyond which data are considered to be outliers. They are the standard deviation (STD) and the Median Absolute Deviation (MAD), this is the one used in the SPG and in the data reduction of this thesis as it is more robust. The task in charge of this deglitching is *deglitchIfgm*.

17) *phaseCorrection* is the task responsible of correcting the asymmetries in the interferogram phase before the Fourier transform occurs. These asymmetries appeared due to several reasons, such as: photon noise, differences between the optical path lengths for different frequencies, maximum signal may not occur at ZPD.

18) At this point, the Fourier transform can be applied to produce a spectrum that contains the signal along the frequency axis. The task used is *fourierTransform*.

19) *removeOutOfBand* truncates the spectral data to the scientifically useful range to save processing time and memory.

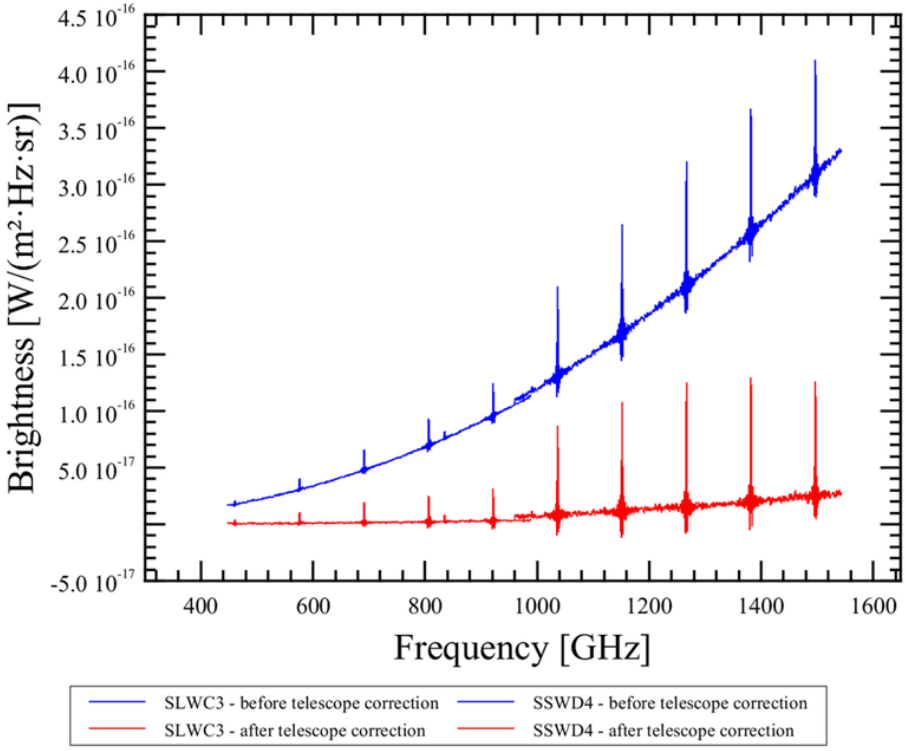

FIGURE 2.3: Spectra for the central detectors (SSWD4 and SLWC3) before (blue) and after (red) telescope correction.

20) For sources observed with bright source settings it is necessary to use *specApplyBrightGain* to apply an additional gain factor.

21) As the SPIRE instrument acts as a source if radiation that is measured by the SPIRE spectrometer, it is necessary to correct this emission using the temperature of the instrument measured during the observations and assuming that SPIRE emits as a black body. SLW detectors are more sensible to this emission compared to the SSW detectors.

22) Now the Relative Spectral Response Function (RSRF) is used to calibrate the actual signal from V/GHz to brightness. This calibration is valid for uniformly extended emission across the beam. The resulting spectrum has units of W/m^2/Hz/sr. The task that occupies of this conversion is *specExtendedFluxConversion*.

23) As happened with the SPIRE instrument the primary and secondary mirrors of *Herschel* telescope also emit at temperatures around 80 and 90 K that generate a significant contribution to the flux measured by the SPIRE-FTS. Again, the temperature of the mirrors are derived from the satellite housekeeping product and are used to model the contribution of the mirrors as black bodies. With *telescopeCorrection* this contribution is removed from the spectra. In Fig. 2.3 we show the high contribution of the telescope emission.

24) The scans of each detector are averaged to obtain a single spectrum per detector using *averageSpectra*.

25) At this stage the point source flux calibration is applied using *specPointFluxConversion*. This calibration is valid when the source extent is much smaller than the area of the beams. Furthermore this correction translates the units of the spectra from W/m^2/Hz/sr to Jy (10^{-26} W/m^2/Hz). Now we have two independent products: the one with the extended source flux conversion ('ExtendedConversion') and the one with the point source flux calibration ('PointCalibration').

26) The next correction applied is the apodization. This task is applied for both 'ExtendedConversion' and 'PointCalibration' products and generate two new independent products 'ExtendedConversionApod' and 'PointCalibrationApod'. *apodizeSpectra* applies this correction by convolving the apodization function with the spectrum. In the new apodized spectra the sinc profile has been removed but the spectral resolution is lower. Furthermore if the apodized lines are fitted using a Gaussian function the resulting flux could be overestimated.

27) Finally, the frequency scale of the spectrum is corrected from the satellite from to the Local Standard of Rest (LSR). This correction is applied to the 4 final products (spectral cubes= generated in this pipeline: 'ExtendedConversion', 'ExtendedConversionApod', 'PointCalibration' and 'PointCalibrationApod', making use of the task *applyRadialVelocity*.

- **Post-processing**

  The pipeline processing for sparse observations, described above, assumes that the source is either uniformly extended across the beam or it is point-like and centered on the optical axis. However, not all the sources of the sample satisfy one of this two assumptions so we can consider them as semiextended sources.

  Semiextended sources can be identified as those sources for which the overlap between the two bands SLW and SSW differs for both 'ExtendedConversion' and 'PointCalibration' spectra. See Fig. 2.4.

  For these cases *semiExtendedCorrector* task, based on the Semi-Extended Correction Tool (SECT), can be used to generate a new set of spectral cubes ('SemiExtended' and 'SemiExtendedApod') for which SSW and SLW bands overlap perfectly after an automated and iterating process carried out by SECT. In Fig. 2.5 the effects of this correction are shown.

  At this point is important to be aware that the slightly extension of the source is not the unique reason that could lead to a bad overlapping between both spectral bands. Other reasons like background (foreground) extended emission or a pointing offset can also produce the same effect so it is recommended to study each object case by case.

  The final product generated by SOF1 are:

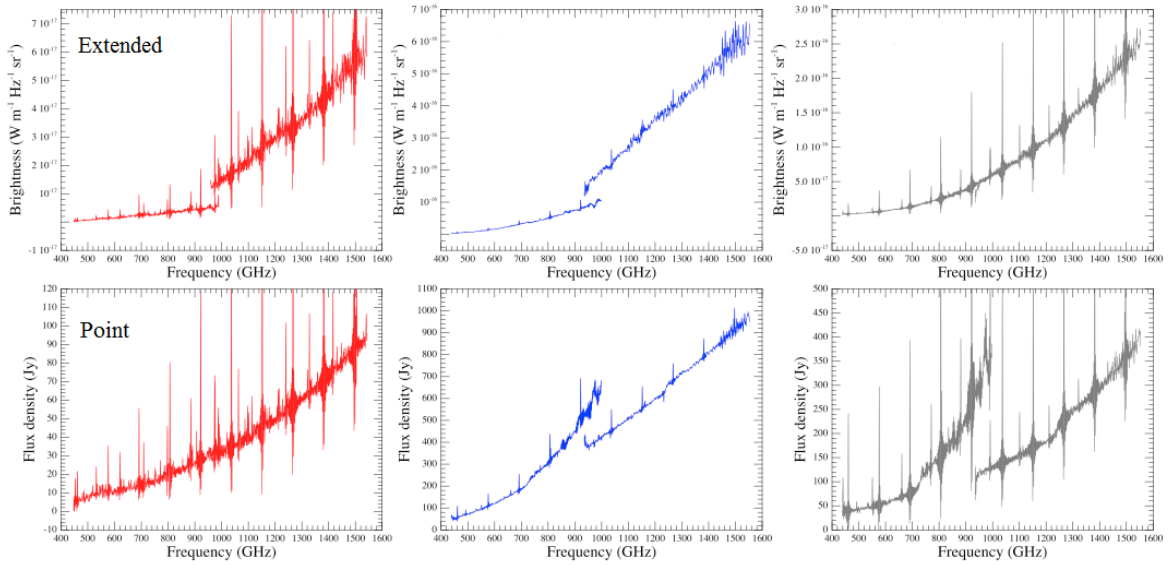

FIGURE 2.4: Three spectra of sources with different angular size, which increases from left to right, processed with extended calibration (top row) and point source calibration (bottom row). The object on the left is a point source (red), the one at the center is a semiextended object (blue) and the source on the right an extended one (grey). When the appropriate correction is applied (top right and bottom left) good results are achieved. For the source in the middle the semiextended correction is needed. The observations used correspond to AGL 618 (left), M 83 (center) and the Orion Bar (right). This figure is taken from the *SPIRE Spectroscopy Mode Cookbook*.

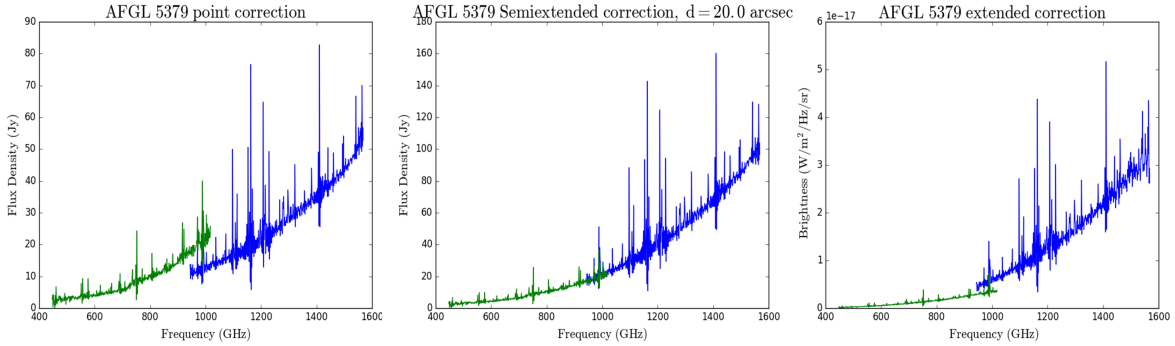

FIGURE 2.5: Left) Spectra associated to the source AFGL 5379, taken from the central detectors SLWC3 and SSWD4 after the point source calibration was applied. Note the shift between both subspectra in the overlapping region. Center) The same but applying the *semiExtendedCorrector* task. In this case the overlapping is perfect for both subranges. Right) In this box the extended calibration was applied and, as happened with the point source correction, there is not a good overlapping between SLWC3 and SSWD4 spectra.

- Extended calibrated spectra of SLW and SSW detector arrays. (FITS format).

- Apodized, extended calibrated spectra of SLW and SSW detector arrays. (FITS format).

- Point-source calibrated spectra of SLW and SSW detector arrays. (FITS format).

- Apodized, Point-source calibrated spectra of SLW and SSW detector arrays. (FITS format).

- If necessary, semiextended calibrated spectra of SLW and SSW detector arrays. (FITS format).

- If necessary, apodized, semiextended calibrated spectra of SLW and SSW detector arrays. (FITS format).

Both apodized and un-apodized spectra are included in THROES-SPIRE catalogue.

- **Spectrometer Mapping Pipeline (SOF2)**

  The steps followed along the processing of full image sampling data is very similar to those described for the SOF1 pipeline. For this reason only the differences between both pipelines are going to be described here:

  1) For mapping observations, in the preliminary configuration stage (between steps 4 and 5), the spatial grid that is going to be used to create the spectral cubes for the SSW and SLW arrays must be specified.

  2) The point source flux calibration, applied in SOF1 using *specPointFluxConversion*, is not taken into account in SOF2.

  3) After correcting the frequency scale to be in the Local Standard of Rest, SOF2 pipeline performs an additional processing step creating spectral maps. At this stage the individual spectra (per detector array) are projected onto a spatial grid that is equidistant in both spatial dimensions. This grid is the one mentioned in 1).

  The final product generated by SOF2 are:

  - Spectral cubes after spatial regriding for SLW and SSW. (FITS format).

  - Apodized, spectral cubes after spatial regriding for SLW and SSW. (FITS format).

  - 2D list of concatenated spectra of SLW and SSW detectors before regriding. (FITS format).

  - Apodized, 2D list of concatenated spectra of SLW and SSW detectors before regriding. (FITS format).

No post-processing is applied to these products.

Chapter 3

THROES Catalogues

Thunderbird

Bruce Springsteen

One of the main output products of this thesis have been the THROES, web based, catalogues, one for PACS and the other one for SPIRE spectra. They they represent the basis to all the scientific analysis that have been, and will be, performed. Both catalogues have been created in parallel and present the same structure. In this chapter a detailed description of each one is shown.

3.1 THROES. PACS Spectroscopy

3.1.1 Building the THROES-PACS Spectroscopy sample

During its operational lifetime *Herschel* successfully performed more than 37,000 science observations. The full list can be found in the Herschel Observing Log, available at *http://herschel.esac.esa.int/obslog/*. The Herschel Observing Log contains a total of 530 PACS spectroscopy observations executed successfully, associated to science proposals that were submitted under the 'Evolved Stars/Planetary Nebulae/Supernova Remnants' category by the original proposers. As a first main step, we read the bibliography associated to the objects included in these original 530 observations and we were able to identify 347 of them as corresponding to low- or intermediate-mass stars, besides, 258 out of these 347 observations were taken in PACS RangeScan mode.

All these observations were originally included in the THROES-PACS Spectroscopy sample. We carried out a deep examination of the original data to check their quality. After this test, we discarded 7 observations taken in PACS 'mapping' pointing mode, as the final pipeline products, the projected spectral cubes, showed 'holes' along different positions of the spectral axis, see Fig. 3.1 (left panel). This issue was reported to the HSC but no solution was offered.

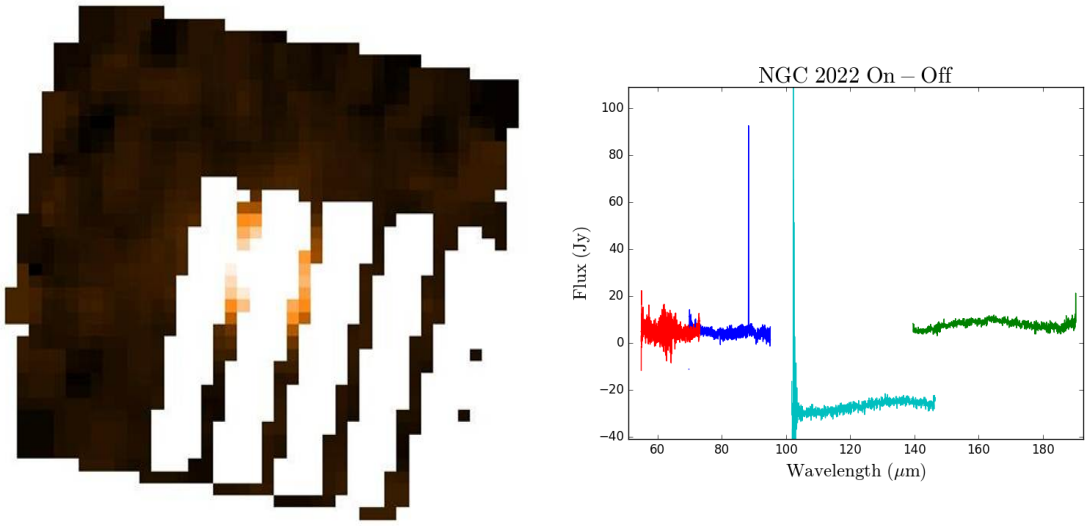

FIGURE 3.1: Left) Layer of the projected spectral cube generated for NGC 6543 (ObsID: 1342212264, camera: blue) extracted at 69.5 μm. Note the absence of data in the some regions of the map. Right) NGC 2022 (Obs Ids, On: 1342250909, 1342250911. Obs Ids, Off: 1342250910, 1342250912) 1D spectrum extracted from the central spaxels after the On,Off subtraction. The continuum level of the 100-145 μm subrange is clearly below zero.

As we described in Chapter 2, for 'Unchopped' observations, the accuracy and the reliability of the continuum level of the source can not be guaranteed. For that reason we paid particularly attention to the final spectra of these observations. Analysing them, we saw how our final 1D On-Off spectra presented continuum levels below zero for some wavelength subranges, see Fig. 3.1 (right panel). After the interaction with HSC a solution for this technical issue could not be fixed. As a consequence of that the 20 'Unchopped' observations of our sample have not been included in this version of the THROES-PACS Spectroscopy catalogue.

Finally, eleven observations were also discarded as several problems were found during the data reduction. In particular, one observation of the planetary nebula NGC 6153 (ObsID 1342249998) and another one of NGC 7662 (ObsID 1342246642) failed because of the too narrow spectral range covered, centred at the forbidden [O III] emission line at 52 μm, at the edge of the spectral coverage of the PACS blue detector where the spectral response function is not well characterized; six observations (ObsIDs: 1342230895 and 1342230905 to 1342230909) associated to the Red Rectangle failed because they cover very narrow spectral regions affected by leakage; one observation of the post-AGB star HR 4049 (ObsID 1342247550), covering a very short wavelength region between 103 and 116 μm, was extremely noisy in the red channel and failed reprocessing in the blue channel; and finally, we could not reprocess two very long exposure SED mode observations of the proto-planetary nebula IRAS 01005+7910 (ObsIDs 1342247005 and 1342247006) as they demanded too much memory, exceeding the capacity of our local hardware environment.

In summary, a total of 220 Herschel observations (ObsIDs) of good quality were finally considered for interactive data reduction, corresponding to 114 individual targets (see full list in Table B.1), comprising a total of 440 individual spectral ranges.

3.1.2 Characteristics of the THROES-PACS Spectroscopy sample

Evolutionary stage and IRAS colours

Information on the evolutionary stage of each object in the THROES sample was extracted from the SIMBAD (Set of Indications, Measurements, and Bibliography for Astronomical Data) database and from the literature. Accordingly, we have classified our objects into four main groups: AGB stars, OH/IR stars (extreme O-rich AGB stars with high mass-loss rates and long variability periods), post-AGB stars (or pre-PNe), and PNe. In its current version, the catalogue contains PACS range spectra for 43 (38 %) AGB stars, 17 (15 %) OH/IR stars, 29 (25 %) post-AGB stars, and 25 (22 %) PNe (see Fig. 3.2).

Figure 3.2 shows the distribution of our targets in the IRAS two-colour diagram which is defined as: [12]-[25]=2.5log$_{10}$ $\frac{IRAS_{25}}{IRAS_{12}}$ and [25]-[60]=2.5log$_{10}$ $\frac{IRAS_{60}}{IRAS_{25}}$, where the location of various types of sources is indicated, following the original description presented by van der Veen and Habing, 1988. This diagram illustrates the variety of evolutionary stages covered by the THROES sample. The AGB stars are distributed along a sequence of increasing infrared excess, which represents the evolution expected during the AGB as a result of the formation of thick and dense shells of dust and gas around these mass-losing stars, with the reddest IRAS colours corresponding to the most extreme OH/IR stars. Once the mass-loss phase ends, objects evolve towards the right in the two-colour diagram (region IV, V, and VIII in the plot), which are the areas populated by most of the sources in our sample classified as post-AGB stars and PNe, surrounded by detached cool dust shells.

Galactic distribution

The galactic distribution of the THROES sample is shown in Fig. 3.3. Our sources are strongly concentrated at relatively low galactic latitudes, as expected from a distant population of luminous sources concentrated in the galactic disk, although a significant number of them are also observed at high galactic latitudes, corresponding to the small fraction of bright, nearby sources. Interestingly, most of the OH/IR stars are found at very low galactic latitudes, as they correspond to a population of stars that are proposed to represent the most massive precursors of PNe (García-Hernández et al., 2007).

Dominant chemistry

The sample contained in THROES-PACS catalogue cover a wide range of chemical types, and the sources are distributed as follows: 55% of O-rich, 29% C-rich, 3% S-type stars, objects with mixed chemistry, which contain O-rich and C-rich species, simultaneously, and, finally, 7% sources with an unknown chemistry, see Fig. 3.2 for a visual representation. The C/O ratio in the mixed chemistry objects may be different depending on the region of the source considered. Some of them are known to be objects in transition between O-rich and C-rich objects (Herwig, 2005); others display a strong bipolar morphology, and may be surrounded by disks that could explain the mixed chemistry observed.

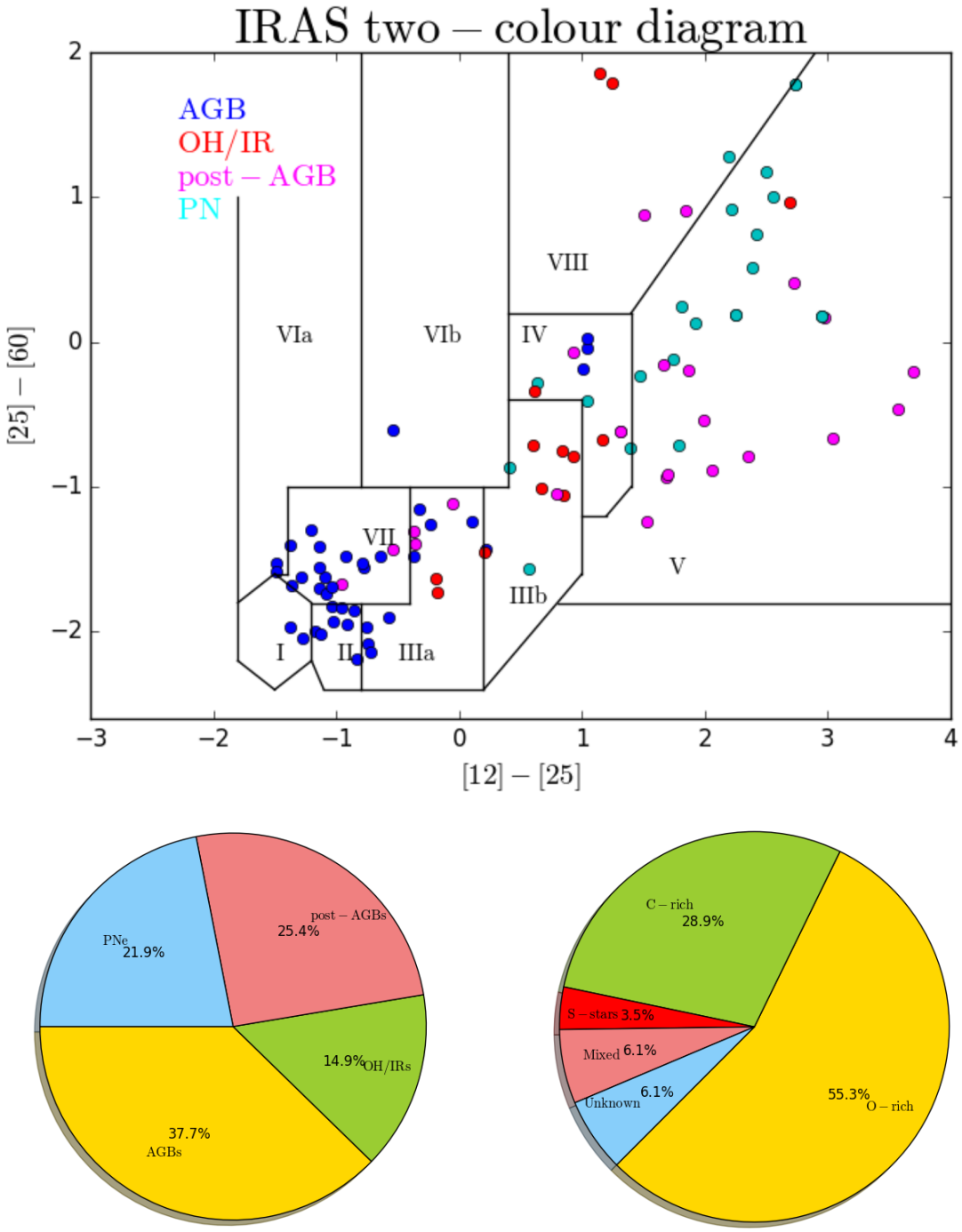

FIGURE 3.2: Top) IRAS colour-colour diagram of the THROES sample with good quality IRAS data (Quality Flag=3) in the 12, 25, and 60 μm bands. The diagram is divided into different boxes where sources with different characteristics and evolutionary stage are contained (see van der Veen and Habing, 1988, for a detailed description). Bottom left) Pie chart illustrating the distribution of stars in the THROES sample according to their evolutionary stage. Bottom right) Pie chart illustrating the distribution of stars in the THROES sample according to their dominant chemistry.

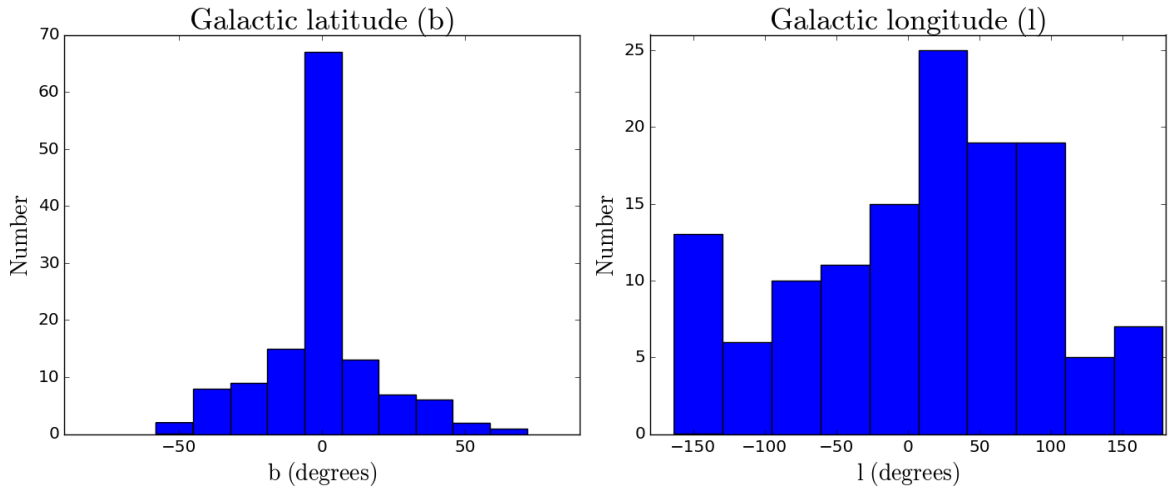

FIGURE 3.3: Galactic distribution of the THROES targets.

3.1.3 THROES PACS Spectroscopy. Web interface

All the processed THROES-PACS data are publicly available for the whole scientific community thanks to a specific catalogue, developed by us, which is accessible via webpage through the next link *https://throes.cab.inta-csic.es/*. At this webpage apart from PACS spectra, we included, also, information about the object and the observations as well as a plot with the reduced PACS Spectroscopy data and complementary spectroscopic and photometric observations from other observatories (*IRAS*, *AKARI* and *ISO*).

SVOCat

The tool used to create the web-based catalogue is SVOCat. This application, developed by the Spanish Virtual Observatory (SVO) is designed to make easier the publication of an astronomical catalogue, both as a webpage and a a Virtual Observatory *Cone Search* service.

Using SVOCat to create the catalogue ensures that the archive system has been designed following the IVOA [1] standards and requirements. In particular, it implements the previously mentioned *Cone Search* protocol, a standard defined by the IVOA for retrieving records from a catalogue of astronomical sources. Queries made through the *Cone Search* service are based on the description of a sky position and an angular distance, defining a cone on the sky. The response returns a list of astronomical sources from the catalogue whose positions in the sky lie within the pre-defined cone, formatted as a VOTable. The system as a whole is included in the IVOA Registry and can therefore be discovered by any VO-tool.

The intention of the developers is to offer an easy to use tool that guides the astronomer along the installation and configuration process while, at the same time, let the user to change the application to adapt it to each specific case.

[1] International Virtual Observatory Alliance; http://www.ivoa.net

SVOCat requires a web server (Apache) and a MySQL database, although the configuration of the catalogue in carried on using an user friendly web interface, some PHP scripting knowledge is useful to refine and adapt the application to the needs of each project.

SVOCat assumes that the catalogue can be seen as a single table with several columns (one for each property provided by the catalogue) and several lines (one for each catalogue entry, typically, for each object observed). Two of the columns have to be RA and Dec in decimal degrees format.

The single table that contains all the information of the catalogue must be a CSV file or a a table in a MySQL database. If the table is a CSV file, as it is in our project, the SVOCat tool allows the astronomer to generate a table in MySQL format, as it is the specific structure needed to show the information in the webpage.

Following the next url *http://svo2.cab.inta-csic.es/vocats/SVOCat-doc/*, more information about the downloading and installation of SVOCat or concerning to the configuration of the database and the web design can be found.

Web description

The catalogue is accessible through the following the url *https://throes.cab.inta-csic.es/*. The first interface ('Home') shows the information about the current version of the THROES-PACS catalogue and allow the access to the rest of the interfaces available in the webpage. They are:

- **Data retrieval:** This interface presents the catalogue itself, including the 'Search fields'. By default, Only the reprocessed observations are shown. The description of the catalogue and the 'Search fields' will be explained below.
- **Change log:** Here, a description of the updates associated to each new version of the catalogue is shown, such us, number of objects reprocessed or information about the version of HIPE used to carry on the data reduction.
- **Documentation:** At this interface an explanation about how to filter the results of the catalogue and a description of the columns associated to each entry are shown.
- **Contact:** Through this option, any user can contact via e-mail with the administrator of the catalogue.

To structure our catalogue in a homogeneous and logical way, all the observations with the same pointing have been grouped into an unique entry in the archive. So, at the end, there is a single line per region in the sky observed, in Fig. 3.4 a screenshot of the 'Data Retrieval' interface of the catalogue is shown. For each entry, there are 13 columns, providing, each of them, information about to the object or the observation, as well as, plots and the processed data. All the 13 columns are:

- **Columns 1 to 4**: The equatorial coordinates (right ascension and declination) of the observation in different units: decimal degrees in columns 1 and 2, and hh:mm:ss and dd:mm:ss in columns 3 and 4.
- **Column 5**: Name of the object in the THROES catalogue.
- **Column 6**: The astronomical observation template (AOT). This could be PacsRange or PacsLine. For some objects there are spectra taken in both modes. These cases appear in the catalogue as PacsLine/PacsRange. Only the PacsRange spectra have been reprocessed in the current version of the THROES catalogue.
- **Column 7**: The number of observations taken in that position of the sky. By clicking on the number shown in this column, a new table is deployed with detailed information for each observation, such as: target name, equatorial coordinates (RA and Dec), proposal name, AOT, observation ID, observing date and time, and original AOR (Astronomical Observation Request) label.
- **Column 8**: Object classification based on the progenitor mass (low-to-intermediate., massive, unknown) as deduced from the bibliography and the SIMBAD[2] database.
- **Column 9**: Object classification including the evolutionary stage and its dominant chemistry (based on the bibliography and SIMBAD), the options are: O-rich AGBs, C-rich AGBs, S stars, OH/IR stars, O-rich post-AGBs, C-rich post-AGBs, mixed chemistry post-AGBs, O-rich PNe, C-rich PNe, mixed chemistry PNe, or Unknown.
- **Column 10**: This column indicates if the observations have been reprocessed under the THROES project or not. This is because THROES may be expanded in the future to other observing modes of PACS and/or massive evolved stars.
- **Column 11**: By double clicking on 'SED', a pop-up window is displayed showing the 1D PACS spectra generated after the interactive data reduction and subsequent post-processing, together with complementary photometric (IRAS and AKARI) and spectroscopic (Infrared Space Observatory-Long-Wave Spectrometer (ISO-LWS)) data, when available.
- **Column 12**: By double clicking on 'CSV' (Comma-Separated Values), a compressed folder with the name of the target is downloaded containing a gzipped tar file with the 1D PACS spectra, in CSV format.
- **Column 13**: Similarly, by double clicking on 'FITS' (Flexible Image Transport System), a compressed gzipped tar file is downloaded containing a folder named "FinalCube" which has the THROES reprocessed final spectral cubes (level2) in FITS format and another folder named "Final1D" which contains the 1D PACS spectra, also in FITS format, derived from these final spectral cubes after post-processing.

The results of the catalogue can be filtered making use of the search fields available in the catalogue. These search fields are:

[2]http://simbad.u-strasbg.fr/simbad/.

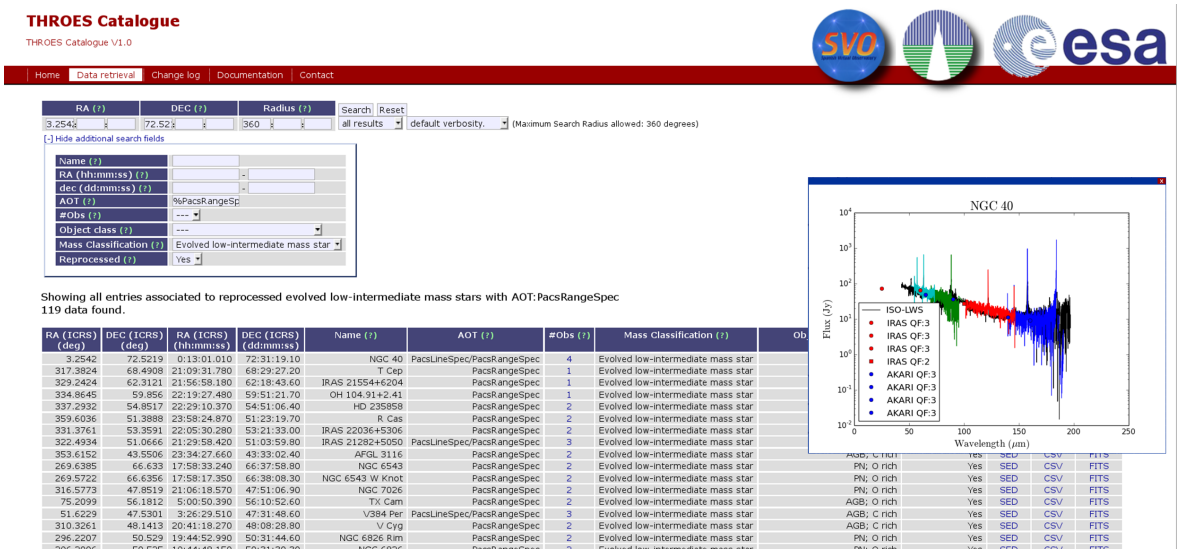

FIGURE 3.4: Screenshot of the THROES-PACS catalogue webpage. All the columns and search fields described in text are visible here, as well as, a complete SED with IRAS, AKARI and ISO data, overplotted.

- **Target Name:** Allow the user to search for an specific source introducing the name of the object. It is possible, also, to search those sources that has parts of their name in common. For these cases it is necessary to use '%' to indicate partial matching. For example, introducing 'IRAS%' in the Target Name box all the sources whose name start with 'IRAS' will be shown.

- **RA, Dec:** To search sources using the coordinates it is possible to use the 'RA', 'Dec' and 'Radius' boxes at the top of the webpage or the 'RA' and 'Dec' boxes that appear listed below. In this second boxes a range of coordinates can be set instead of using the 'Radius' option.

- **AOT:** This field filter all the sources that share a common AOT. Introducing, in the AOT box, the specific AOT that the user is looking for (PacsRange, PacsLine or PacsLine/PacsRange) all the observations labelled with that AOT will be retrieved. In this case, '%' can be used, again, for partial matching. For example, using '%PacsRange' the catalogue will filter all the sources whose AOT is PacsRange or PacsLine/PacsRange.

- **Number of Observations:** This option allow the user to select all the sources that have been observed the same number of times. The desired number of observations is selected from a list.

- **Object Class:** In this case, as happens with AOT, instead of looking for a single object user can filter all the objects that are of the same class. The object class is chosen from a deployable list.

- **Mass Classification:** It is similar to the Object Class case. User selects from a list all the evolved low-int mass stars, all the evolved massive stars or those objects labelled as 'Unknown'.

- **Reprocessed:** From a list it is possible to select the sources that have been reprocessed in THROES project or not.

3.1.4 Multi-mission comparisson

To complete the vision about the THROES-PACS sample and to put the data into context, the final 1D post-processed spectra have been compared to photometric (IRAS and AKARI) and spectroscopic (ISO-LWS) data for each source, when available. The plots that include PACS and IRAS, AKARI or ISO, when available, for each source are shown in Figs. C.1-C.4 (Appendix. C).

IRAS and AKARI Photometry

On the photometric side, all the objects of THROES sample have complementary IRAS photometric information while, attending to AKARI data, the proportion of common objects decreases to 89%.

The *Infrared Astronomical Satellite* (IRAS) (http://irsa.ipac.caltech.edu/IRASdocs/iras.html) Point Source Catalogue presents photometric data in four bands that are centered at 12, 25, 60 and 100 μm. The beam size of IRAS observations is much larger than that of PACS (47"×47"). The IRAS beam varies from 2' at 12 μm, to 5' at 100 μm, (Neugebauer et al., 1984).

AKARI (http://www.ir.isas.jaxa.jp/AKARI/index.html) covers longer wavelengths: 65, 90, 140 and 160 μm with a beam size that varies from 0.5' to 0.9' (Jeong et al., 2007). Although the AKARI beam is significantly smaller than that of IRAS, it is still significantly larger than the beam of PACS.

The different beam sizes of the instruments is a key point that has to be kept in mind when comparing PACS Spectroscopy to IRAS and AKARI photometric data.

In order to check the quality of the final processed PACS Spectroscopy data and to obtain information about the effect of the post-processing tasks applied to generated the final 1D spectra, we have done a comparison between the synthetic photometry derived from the PACS spectroscopic data and the IRAS and AKARI photometric data at 100 and 160 μm, respectively.

Synthetic photometry is generated by convolving the transmission curve of the photometric filters, $IRAS_{100}$ and $AKARI_{160}$, with the PACS spectroscopy data. The transmission curve of $IRAS_{100}$ has been obtained from the IRSA-IPAC webpage:
`http://irsa.ipac.caltech.edu/IRASdocs/exp.sup/ch2/tabC5.html` and the transmission curve of $AKARI_{160}$ has been estimated from the relative response function available in:
`http://svo2.cab.inta-csic.es/theory/fps3/?id=AKARI/FIS.N160`. Both curves are shown in Fig. 3.5.

To properly estimate the synthetic photometry, it is necessary that the spectral coverage of the PACS spectrum extends, at least, along the whole wavelength subrange covered by the

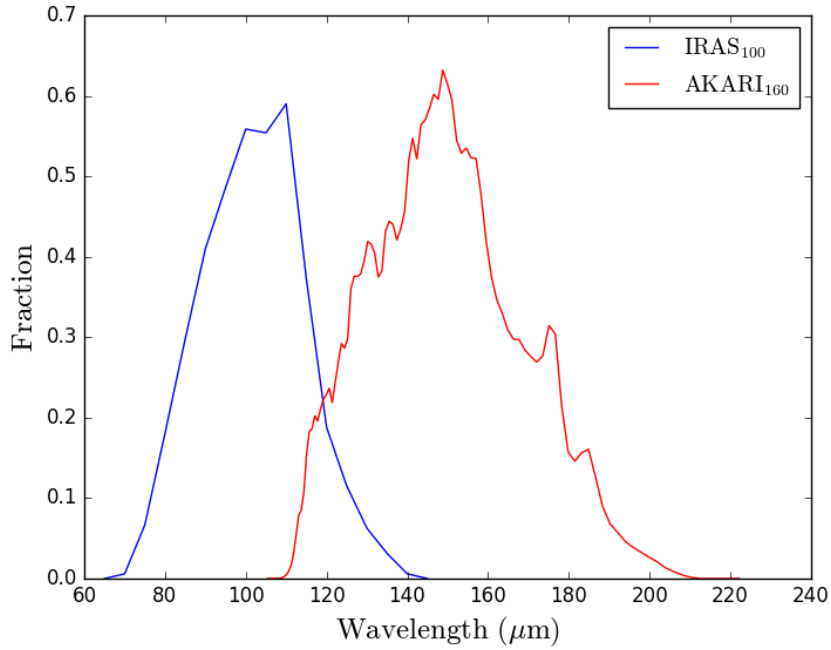

FIGURE 3.5: The photometric curves of the $IRAS_{100}$ and $AKARI_{160}$ bands are displayed in blue and red colors, respectively. These curves are necessary to derive the synthetic photometry from the PACS spectroscopic data. *Data taken from the Spanish Virtual Observatory.*

photometric curves. For this reason, the synthetic photometry has been estimated for those, 71, sources that present a complete coverage of the PACS spectral wavelength range.

As mentioned in Chapter 2, due to the instrument configuration and the exclusion of those regions affected by leakage, all the 1D PACS spectra show a small gap (less than 10 μm) around 100 μm, even for these sources which present a complete spectral coverage.

As the photometric curve of IRAS 100 μm is centered at this region, it is important to find a solution. To manage with that in the synthetic photometry estimation, a linear interpolation was done to approximate the continuum flux level in this region. This assumption is good enough as intense emission lines are not expected in this small spectral region.

On the AKARI 160 μm side, due to the exclusion of the wavelength regions affected by leakage, there are no PACS data to cover the wavelength range from 190 to 220 μm. To solve that, a power law (λ^{α}) was fitted to the red bands of the PACS SED and, after that, we have extrapolated the flux values to the 190-220 μm region. At these wavelengths, we are mainly tracing the Rayleigh-Jeans approximation, so this extrapolation is reasonably good.

To show the effect of the post-processing tasks applied in the THROES-PACS Spectroscopy reduction process, the synthetic photometry has been estimated for 1D PACS spectra before and after applying the post-processing tasks. In Fig. 3.6 the comparison between $IRAS_{100}$ and $AKARI_{160}$ and their synthetic counterparts using (PACS) data with and without postprocessing is plotted. It is clearly seen, that a good agreement between the photometric and the synthetic photometric data is obtained for most of the sources. This confirms that the postprocessing tasks applied in our reduction process are necessary to recover the total flux

emitted by the source. The few points that fall out of the *Photo = PhotoSynthetic* relation, are points which have bad photometric data, QF≠3, (red triangles) or are associated to extended objects (blue crosses). The extension of the sources can be a a cause of disagreement between the synthetic photometry obtained from PACS and the real IRAS or AKARI photometry as for very extended objects, they may not be fully covered by PACS while IRAS and AKARI may due to its larger beam size.

ISO-LWS Spectroscopy

On the spectroscopic side, it is interesting to compare our PACS spectroscopic data to ISO-LWS spectra, as this ISO instrument covers a wavelength range from 43 to 197 μm that largely overlaps with PACS. However, it is important to keep in mind that ISO-LWS presents a lower spectral resolution: R=200 (medium resolution) and R=1000 (high resolution) and a larger beam size (80"×100") than PACS.

In Figs. C.1, C.2, C.3 and C.4, the PACS data of the 114 targets included in THROES are shown, complemented with IRAS, AKARI and ISO data, when available. After a visual inspection of those objects which present both, PACS and ISO data, objects can be grouped in 5 main families:

1. Good agreement between PACS and ISO: For most of the sources,a good agreement between PACS and ISO-LWS spectroscopic data is found. For example, HD 161796, CIT 6, AFGL 618 or CPD -568032 (see Fig. C.1 and C.3).

2. Very extended sources: Extended sources in THROES sample have been corrected using the extended 5x5 correction to recover the whole flux taken by PACS spectroscopy. However, there are some objects, such as NGC 6781, that are even larger than the PACS FoV and, therefore, PACS spectroscopic data do not measure all the flux emission from the source in contrast to ISO-LWS, which has a larger beam. For that reason, for these very extended sources, the continuum flux level of the ISO-LWS spectra is higher than that of PACS (see Fig. C.2).

3. Mispointed PACS observations without 3x3 correction: Due to its location close to the edge of the PACS 5×5 array, it was not possible to apply the semi-extended 3x3 correction to one source, AFGL 5379. This could explain why the continuum flux level of the ISO-LWS is higher than that of the PACS spectrum (see Fig. C.4).

4. Background ISO contamination: One of the most remarkable facts found with this comparison is that, for some sources, the ISO-LWS spectra show a continuum level higher than PACS. This effect seems to be more evident at longer wavelengths (> 100 μm). Besides, for all these spectra we find an emission line at 158 μm associated to [C II] due to interstellar emission, so the origin of this extra contribution is more likely to contamination by the interstellar medium. There are 11 sources that have been classified in this group: AFGL6815, IRAS 16342-3814, IRAS 16594-4656, IRAS 22036+5306, IRAS 21282+5050, MWC 922, NGC 6537, NML Cyg, OH 26.5+0.6, OH 32.8-0.3, and V Cyg. The reason why ISO-LWS spectra show this contamination is the larger FoV of ISO-LWS with respect to PACS (see Figs. C.1 to C.4).

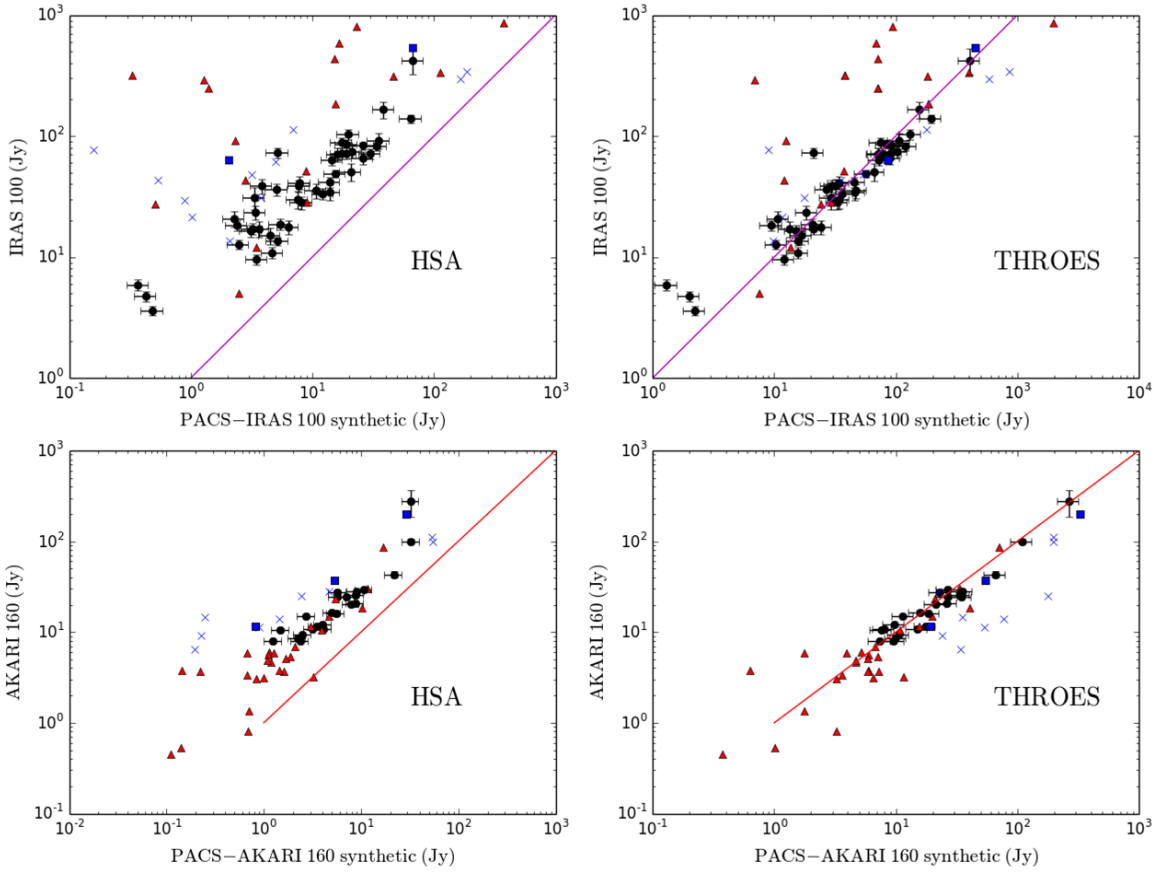

FIGURE 3.6: **Top left panel)** In this plot we compare the synthetic photometry extracted from PACS spectroscopy data before post-processing to the photometric data of $IRAS_{100}$. The objects plotted here are those which present the four bands of the PACS Spectroscopy SED complete. From these objects we have established a code to distinguish the extended objects (blue crosses), the mispointed ones (blue squares), the objects with $IRAS_{100}$ QF≠3 (red triangles) and objects with $IRAS_{100}$ QF=3 (black circles with error bars). The blue line represents PACS-$IRAS_{Synthetic100}$=$IRAS_{100}$. **Top right panel)** This plot is similar to the previous one but comparing the synthetic photometry extracted from PACS spectroscopy data after post-processing (PSFLC and Semiextended 3x3 correction or Extended 5x5 correction applied) to the photometric data of $IRAS_{100}$. **Bottom left panel)** In this plot we compare the synthetic photometry extracted from PACS spectroscopy data before post-processing to the photometric data of AKARI160. The colour code is analogue to the described above but changing $IRAS_{100}$ for $AKARI_{160}$. **Bottom right panel)** This plot is similar to the one presented in the bottom left panel but comparing the synthetic photometry extracted from PACS spectroscopy data after post-processing to the photometric data of $AKARI_{160}$.

5. Bad ISO data: Finally, for some sources like IRAS 07027-7934 or HD 56126, ISO-LWS data present evident artefacts that make the ISO spectroscopic data unreliable (see Fig. C.1).

3.2 THROES. SPIRE Spectrometer

3.2.1 Sample of evolved low to intermediate mass stars

As mentioned in Section 3.1.1, *Herschel* successfully performed more than 37,000 science observations. The Herschel Observing Log contains a total of 148 SPIRE Spectrometer observations executed, successfully, associated to 44 scientific proposals that were submitted under the 'Evolved Stars/Planetary Nebulae/Supernova Remnants' category by the original proposers. As did for PACS observations, we read the bibliography associated to the objects included in these observations to identify 109 sources as low- or intermediate-mass stars, according to the information available in the bibliography.

From these 109 observations, 104 of them were taken using SPIRE Point pointing mode, while the other 5 correspond to SPIRE Mapping observing mode. The Obs Ids associated to these 5 mapping observations are: 1342221681 (NGC 7009), 1342221698 (NGC 7027), 1342221687 (NGC 6826 Mid), 1342227789 (NGC 6543) and 1342227787 (NGC 6543 WKnot).

We consider a total of 109 Herschel observations (ObsIDs) for interactive data reduction, corresponding to 68 individual targets, comprising a total of 218 individual spectral ranges. The SEDs corresponding to the objects in the THROES-SPIRE sample are found in Figs. C.5, C.6 and C.7.

3.2.2 The sample

The objects contained in THROES-SPIRE Spectrometer sample are grouped attending, as we did for PACS Spectroscopy, to their evolutionary stage, the galactic distribution of the sources in the sky, the location at the IRAS 2 colour diagram and the chemical type.

Information on the evolutionary stage of each object in the THROES-SPIRE Spectrometer sample was extracted from the SIMBAD database and from the literature. The sample is distributed as follows: 20 (29 %) AGB stars, 6 (9 %) OH/IR stars, 20 (29 %) post-AGB stars and 22 (33 %) PNe. See Fig 3.7.

In our sample we have 25% of C-rich stars, 63% of O-rich stars, 6% of sources with mixed chemistry and a 6% of sources with unknown chemistry. No S-stars are present in our THROES-SPIRE sample. See Fig. 3.7.

The galactic distribution of the THROES-SPIRE sample is shown in Fig. 3.8. Our sources are mainly located at relatively low galactic latitudes, as expected from a distant

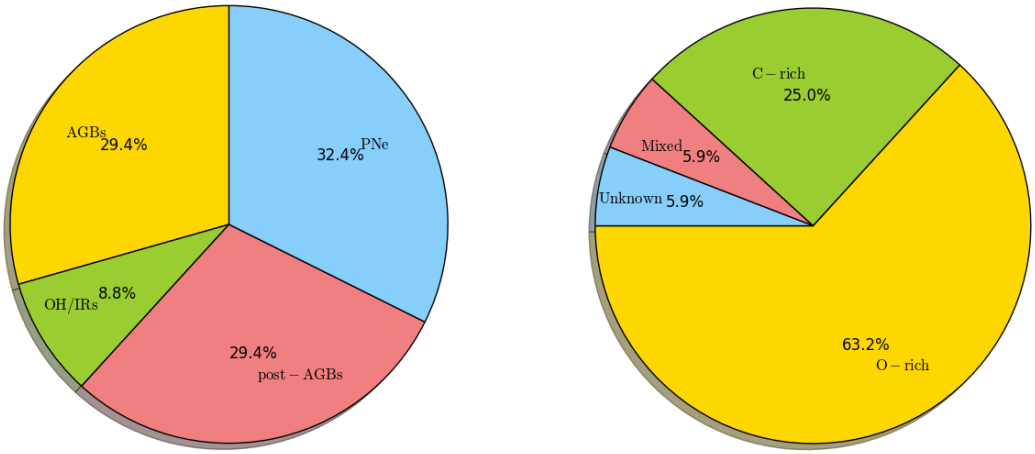

FIGURE 3.7: Left) Distribution of sources in the THROES-SPIRE catalogue, attending to its evolutionary stage. All the evolutionary stages are roughly equally well represented. Right) Distribution of sources in the THROES-SPIRE catalogue, attending to its chemistry classification. O-rich objects represent more than a half of the total number of sources.

population of luminous sources concentrated in the galactic disk, although some of them are also observed at high galactic latitudes, corresponding to the bright, nearby sources.

Finally, Fig. 3.8 shows the distribution of the targets, contained in the THROES-SPIRE catalogue, along the *IRAS* two-colour diagramme, the location of various types of sources is indicated following the original description presented by van der Veen and Habing, 1988.

3.2.3 THROES SPIRE Spectrometer. Web interface

The catalogue developed for THROES-SPIRE is accessible via webpage in the next url *https://throes-spire.cab.inta-csic.es/*. At this webpage all the processed data are publicly available for the whole scientific community including, also, information about the object and the observations, as well as, a plot with the reduced SPIRE Spectrometer data.

The tool used to create the web-based catalogue is, again, SVOCat. This application, developed by the Spanish Virtual Observatory (SVO) is designed to make easier the publication of an astronomical catalogue, both as a webpage and a a Virtual Observatory *Cone Search* service. More information about SVOCat can be found in Section. 3.1.3.

Web description

The SPIRE catalogue is accessible through the following link *https://throes-spire.cab.inta-csic.es/*. The catalogue created for SPIRE spectra (see Fig. 3.9) is completely analogue to that for PACS data described below so we refer to Sect. 3.1.3 for details. Here we only present its particularities:

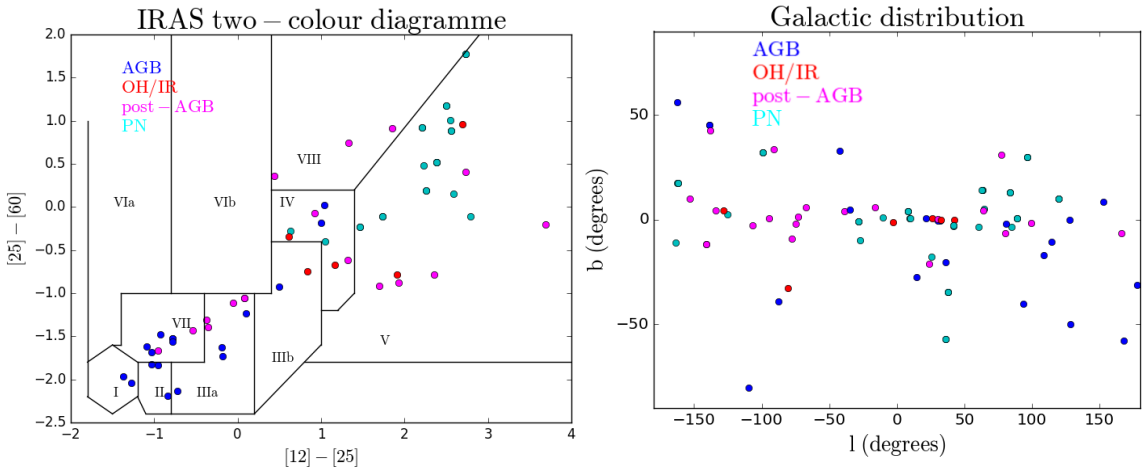

FIGURE 3.8: Left) *IRAS* colour-colour diagramme of the sources contained in the THROES-SPIRE sample with *IRAS* data (QF=3) in the 12, 25 and 60 μm bands. Right) Galactic distribution of the sources included in the THROES-SPIRE sample.

- **Column 6**: The Astronomy Observing Template (AOT). For all the observations of the THROES-SPIRE sample it is *SPIRESpectrometer*.
- **Column 10**: This column indicates if the observations have been reprocessed in THROES-SPIRE project or not.
- **Column 11**: By double clicking on SED, a figure is plotted displaying the 1D spectra generated after the interactively reduction and post-processing of SPIRE Spectrometer data. Except for those SPIRE Mapping observations for which no 1D spectra were extracted.
- **Column 12**: By clicking on this column a compress folder (.tar.gz) is downloaded with the 1D, post-processed, spectra, in CSV format. Both, apodized and non-apodized, 1D spectra are available in these folders. Except for those SPIRE Mapping observations for which no 1D spectra were extracted.
- **Column 13**: Similarly, clicking on this column, a compressed tar file (.tar.gz) is downloaded including the THROES-SPIRE reprocessed Final Spectral Cubes (level2) in FITS format and the 1D spectra, also in FITS format, obtained from these Final Spectral Cubes after applying the post-processing tasks. Except for those SPIRE Mapping observations for which no 1D spectra were extracted. In these cases, apart from the Final Spectral Cubes, a concatenation of all the spectra, of each raster position, in FITS format is included.

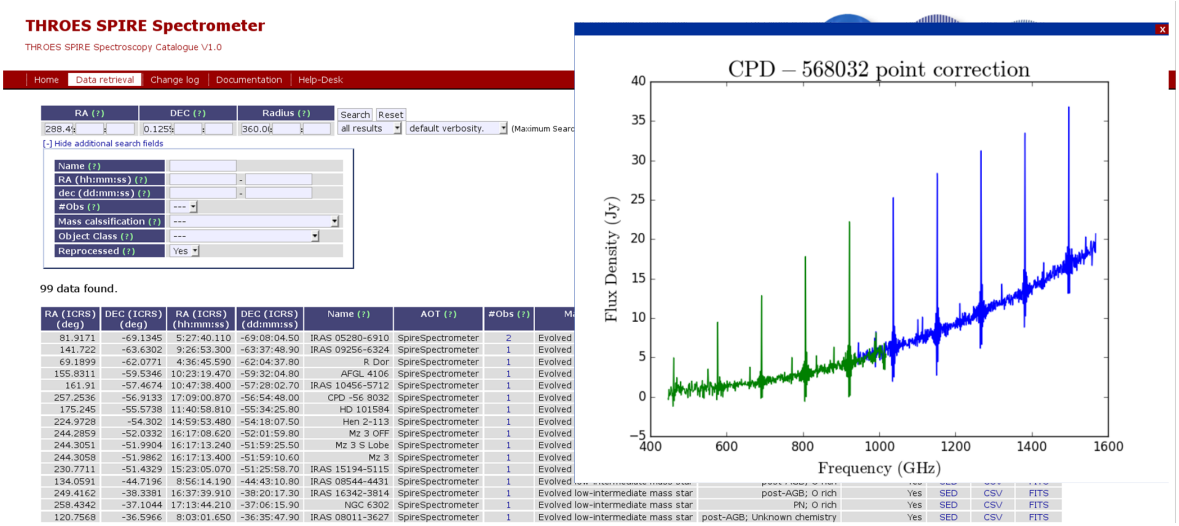

FIGURE 3.9: Screenshot of the THROES-SPIRE catalogue webpage. Some columns and search fields described in Sect. 3.2.3 are shown, as well as, a complete SED with SPIRE spectroscopic data.

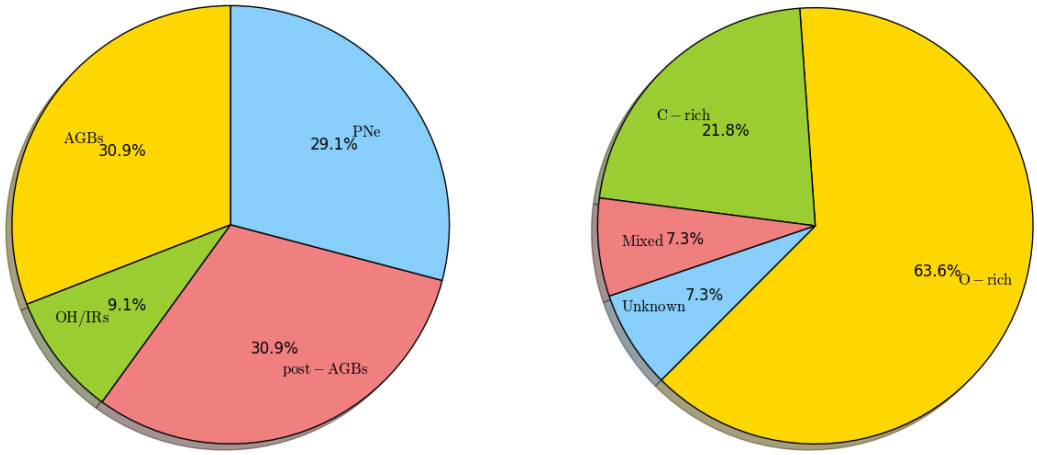

FIGURE 3.10: Left) In this pie chart the distribution of common sources, contained in THROES-PACS and THROES-SPIRE, attending to its evolutionary stage, is shown. Right) Distribution of common sources attending to its chemistry classification.

3.3 Common objects in THROES-PACS and THROES-SPIRE samples

There are 55 objects in common among the THROES-PACS and THROES-SPIRE samples, which represent a 48% and a 80% of the total number of objects contained in the PACS Spectroscopy and SPIRE Spectrometer samples, respectively. The distribution of this sample in terms of the evolutionary stage and the chemistry type is shown in Fig. 3.10. From these percentages, it is easy to see how the subsample of common objects between THROES-PACS and THROES-SPIRE is clearly dominated by oxygen-rich sources, while the distribution along the different evolutionary stages is homogeneously sampled.

We have checked the good agreement between PACS and SPIRE spectra for those sources

in common in both catalogues analysing the overlap of both spectral regions around 200 μm, this comparison is found in Fig. C.8 in Appendix. C. It is important to highlight that the good agreement found between both kind of spectra attending to the continuity of the continuum level, means that the data reduction processes carried out for both PACS and SPIRE spectra were completely satisfactory.

Chapter 4

Warm CO in evolved stars from the THROES catalogue. PACS spectroscopy of O-rich envelopes

My way

Frank Sinatra

4.1 Introduction

In this chapter, we analyse, in an uniform and systematic way, PACS spectroscopy data of a sample of O-rich (and a few S-type) evolved stars from the THROES catalogue (Chapter. 3). PACS spectra enable the analysis of high-excitation rotational emission lines of CO that allow us to characterize the inner regions of the CSEs, poorly studied to date, by deriving fundamental magnitudes such as: $T_{\rm rot}$, $M_{\rm tot}$, and $\dot{M}$. This chapter is organized as follows, in section 4.2 we describe the sample information; the spectral features identified in them are presented in section 4.3; then, in sections 4.4 and 4.5 we present the RD method and the derived results which are discussed in 4.6. Finally, main conclusions are included in Sect. 4.7.

4.2 Sample information

In this work we have studied 26 evolved stars at different evolutionary stages, from the AGB to PN phase, taken from the THROES catalogue (Ramos-Medina et al., 2018a). In its current version, the THROES catalogue contains PACS spectroscopic cubes for a total of 114 low-to-intermediate mass evolved stars. In this study, we focus on non C-rich targets, with most of our sources being O-rich objects but also including a few S-type AGB stars (Table 4.9). Sources with a dominant C-rich chemistry are studied separately in Chapter 5. Our sources are grouped in five main categories as originally defined in the THROES catalogue: classical O-rich and S-type AGB stars, OH/IR stars (strong far-IR emitters with intense OH

maser lines, typically late-AGB or early post-AGB stars heavily obscured by dust at optical wavelengths), post-AGB objects, and PNe. For this study, we have selected objects with a minimum of three CO transitions detected with a signal-to-noise ratio of S/N>3, a total of 26 out of 66 non C-rich targets in the THROES catalogue.

In Fig. 4.1 we present IRAS fluxes and colours of the sources of our sample in comparison with the rest of objects (C-rich or CO non-detections of any chemical type) contained in the THROES catalogue. In the colour-colour diagram, the sources included in the THROES catalogue follow a well-known evolutionary sequence, with the AGBs located at the bottom left region (boxes: I, II, IIIa and VII) and the post-AGBs and PNe occupying the upper right area (boxes: V and VIII); more details can be found in van der Veen and Habing, 1988. Note that the only OH/IR star located close to other PNe in region V is OH 231.8+4.2, which is a peculiar AGB star with a massive outflow with physical and chemical particularities uncommon for the AGB stage but approaching those of post-AGB objects (e.g. Alcolea et al., 2001; Sánchez Contreras et al., 2015).

The objects included in this study are, typically, well known stars which have been extensively studied in bibliography making use of a great variety of observations (see, Teyssier et al., 2006a, De Beck et al., 2010a, Danilovich et al., 2014; Khouri et al., 2014; Danilovich et al., 2015 or Maercker et al., 2016b among others). All the objects of our sample except two, IRAS 17347-3139 and NGC 6537, have previous estimations of the mass loss rate using low-J CO lines detected in the sub-millimetre and millimetre ranges (see Table 4.3). Only for five objects namely, NML Tau, TX Cam, R Dor, R Cas and W Aql, the mass loss rates provided come from recent works (Danilovich et al., 2014; Khouri et al., 2014; Maercker et al., 2016b) based on detailed non-LTE radiative transfer models which make use of a combination of different sets of CO lines taken from several telescopes and including HIFI and PACS observations that cover CO rotational lines up to J=24-23. We have paid particular attention to the mass loss rates estimations derived in these works in order to test the results obtained with the rotational diagram method used in this thesis.

4.3 Observational results

In Figs. 4.2 and 4.3 we display the continuum subtracted PACS spectra of the sources studied in this chapter from 55 to 95 μm and from 110 to 190 μm, respectively. The continuum, for each target, was fitted using a non-parametric method after identifying the line-free regions of the spectrum for each target.

The sources are sorted in Figs. 4.2 and 4.3 attending to their classification with the O-rich AGBs at the top, followed by S-type stars, OH/IR stars, post-AGB stars and PNe. Inside each group, the objects are sorted attending to the effective temperature of the central star, with the coolest object at the top and the hottest one at the bottom. The way the objects have been sorted is useful to illustrate the spectral changes along the different evolutionary stages from AGB phase to the PN stage. While the spectra of the envelopes around AGB stars show hundreds of molecular emission lines, the density of emission lines in post-AGB objects is clearly lower. Finally, the most evolved objects (PNe), with highest temperatures of central

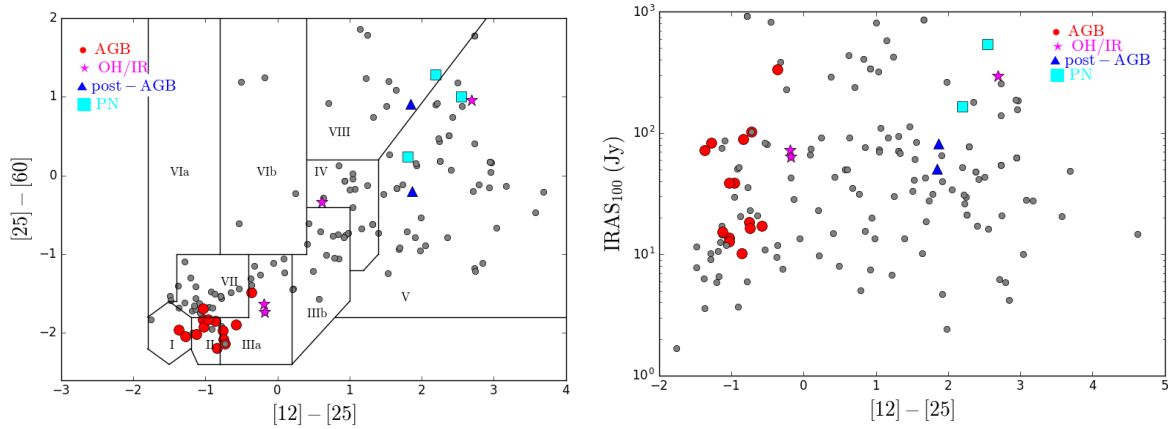

FIGURE 4.1: *IRAS* colour-colour diagram (left) and 100μm flux vs. [12]−[25] IRAS colour (right) of the THROES targets with good quality *IRAS* data (Quality Flag=3) in the 12, 25, 60 and 100 μm bands. The colour-colour diagram is divided in different boxes where sources with common characteristics and evolutionary stages are located (see van der Veen and Habing, 1988, for details). Objects with CO line detections, studied in this work, are highlighted using the symbol and colour code shown in the figure. In the rest of the plots presented throughout this chapter, AGBs, OH/IRs, post-AGBs and PNe are coloured and symbol-coded as indicated in this figure. The grey circles represent the rest of objects contained in the THROES-PACS Catalogue which are not included in this CO analysis.

stars, show intense atomic emission lines in their envelopes and a lack of molecular features compared to the AGBs.

Rotational CO transitions in the ground vibrational state (v=0) are the most prominent molecular lines found in all the spectra. We have detected rotational lines with high-J levels, up to J=42 (E_u~4700 K). The lack of data between 95 and 101 μmmeans we cannot detect the transitions J=26-25 and J=27-26 in any source.

The integrated fluxes of the CO rotational emission lines detected in our sample are shown in Table B.2, in Appendix B. As expected, the resolving power of PACS (of a few 100 km s^{-1}) does not allow us to spectrally resolve the line profiles, which are expected to have full widths at half intensity similar to the terminal expansion velocity of the envelopes, FWHM~20-40 km s^{-1} in the majority of our sample. The PACS CO line profiles are also unresolved for the few post-AGB objects and PNe in our sample, although some of them are known to have fast outflows sampled by low-J transitions, e.g. OH 231.8+4.2 (Alcolea et al., 2001). For this reason we measured ^{12}CO fluxes by simply fitting a standard Gaussian function. The uncertainties in the flux measurements correspond to the propagated statistical errors and do not contain absolute flux calibration errors.

Certain CO rotational lines are known to be blended with transitions by other abundant species that lie within the same PACS spectral resolution element. We have identified, for example, the blend of CO (J=23-22) with o-H_2O (414-303), and that of CO(J=22-21) with the ^{13}CO(J=23-22) and HNC (J=28-27) transitions. Line blends were excluded in our RD analysis, but they are listed, and integrated fluxes are reported, in Table B.2 for completeness. In this table, we also list the lines that present a poor estimation of the underlying continuum level, although they have not been used for the rotational diagram analysis given their flux

uncertainties.

Apart from CO, we have also detected molecular emission lines from several other species, including H_2O, in its orto- and para- configurations, OH, HCN or SiO amongst others. Some of these lines have been reported for certain objects of our sample in e.g. Danilovich et al., 2014; Maercker et al., 2016b. Atomic lines such as OI (63 μm), OIII (88 μm), NII (122 μm) and CII (158 μm) are also identified in post-AGBs and PNe, but not in AGBs. Finally, broad dust emission features associated to forsterite (Mg_2SiO_4) at 69 μm are also found in 4 objects: NGC 6537, NGC 6302, OH 231.8+4.2 and OH 26.5+0.6. Previous detections of forsterite in evolved stars with *Herschel* are shown, e.g., in de Vries et al., 2015.

In Fig. 4.4 we compare the integrated flux of the CO (J=15-14) transition at 173.6 μm ($F_{\rm CO\,15-14}$) with other observational parameters, in particular, with the IRAS 100 μm flux ($\rm IRAS_{100}$), the PACS continuum at 170 μm ($\rm PACS_{170}$), i.e. near the CO (J=15-14) line, and the [12]-[25] IRAS colour. As expected, there is a correlation between the CO line strength and the $\rm IRAS_{100}$ and $\rm PACS_{170}$ continuum fluxes, which confirms that objects with stronger molecular emission show, typically, stronger continuum emission from dust as well. Of course, in addition to an intrinsic relation between these two observational parameters, there is also a dependence with the distance to the sources, which is partially responsible of the observed relation. The scatter of the points is significantly larger in the $F_{\rm CO\,15-14}$ vs. $\rm IRAS_{100}$ distribution, which partially reflects the variability of the majority of the targets (pulsating AGB stars) given that PACS and IRAS observations were obtained at different epochs, as well as different instrument calibration uncertainties, background contamination sources, beam size, pointing, etc. These effects are discussed for the whole sample of THROES catalogue in Chapter 3. We find an anti-correlation between the line-to-continuum ($F_{\rm CO\ 15-14}$/$\rm PACS_{170}$) ratio and the IRAS [12]-[25] colour, which are both distant-independent parameters. In general, we find that the ratio between the molecular emission and the dust emission is higher in AGBs and OH/IRs than in post-AGBs and PNe.

4.4 CO emission analysis: Rotational diagram (RD)

The CO rotational lines provide a fundamental diagnostic of the physical conditions of the molecular gas. As a first approximation, we calculated the rotational population diagrams of the CO ($J_{\rm u}$-$J_{\rm l}$) v=0 transitions observed with PACS assuming optically thin emission under Local Thermal Equilibrium (LTE) conditions. We have used the approach presented by Justtanont et al., 2000, where the total flux observed is used to derive the total mass of the CO-emitting volume adopting the distance to the source indicated in Table 4.3.

The concept of the RD analysis is very simple, see Goldsmith and Langer, 1999. Assuming LTE, the population of each level $N_{\rm u}$ can be described by a single rotation temperature $T_{\rm rot}$, which is expected to be the same as the kinetic temperature, and given by the Boltzmann distribution:

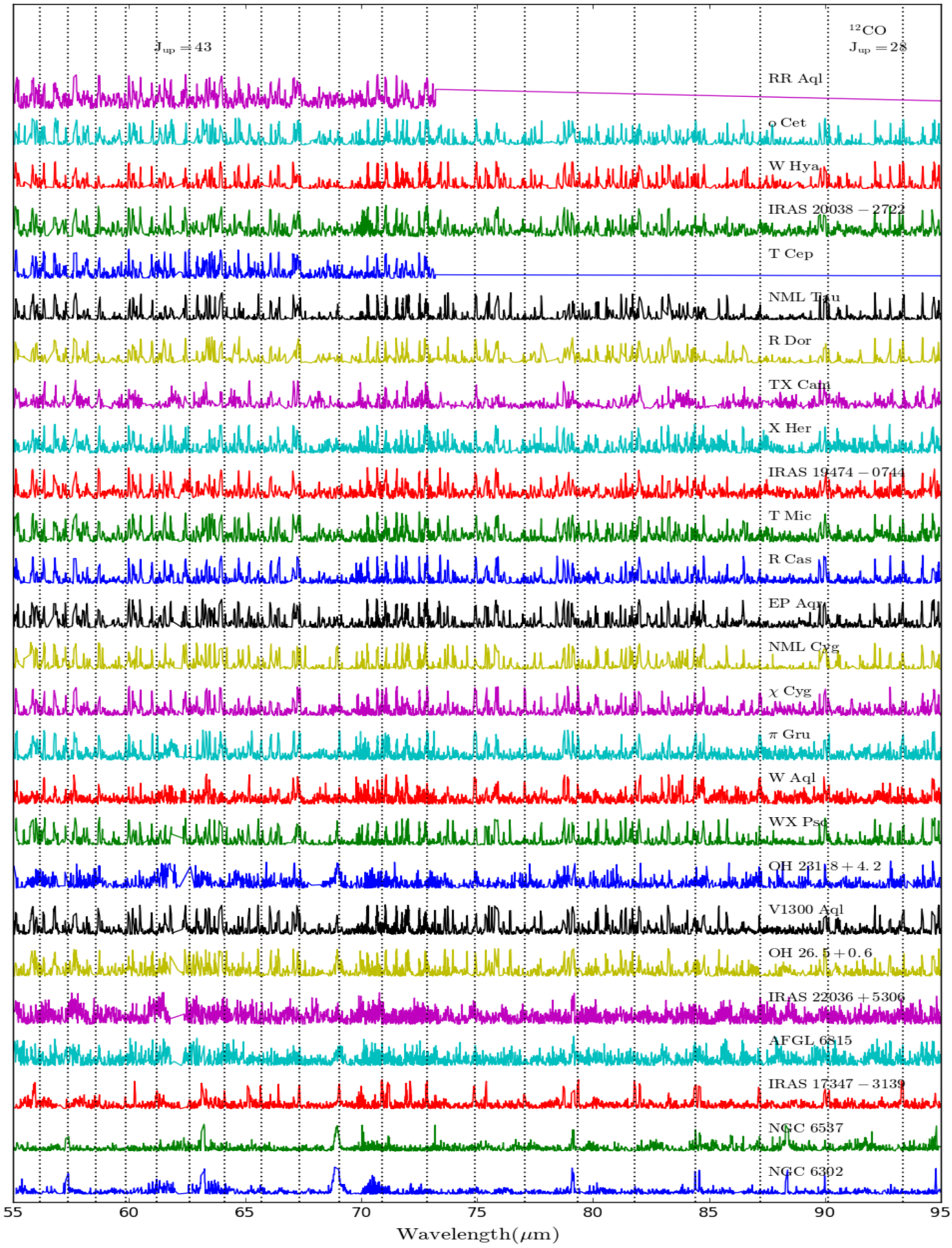

FIGURE 4.2: PACS, continuum subtracted, spectra of our sample in the 55 to 75 μm range. The ^{12}CO rotational lines are indicated by vertical dotted lines. The upper-level rotational quantum number J_u of a few selected CO transitions are shown as a reference. The sources are sorted from top to bottom in these five groups: AGBs, S-type stars, extreme OH/IR stars, post-AGBs, and PNe. Within each category, targets are ordered based on the stellar effective temperature from the coolest source to the hottest one.

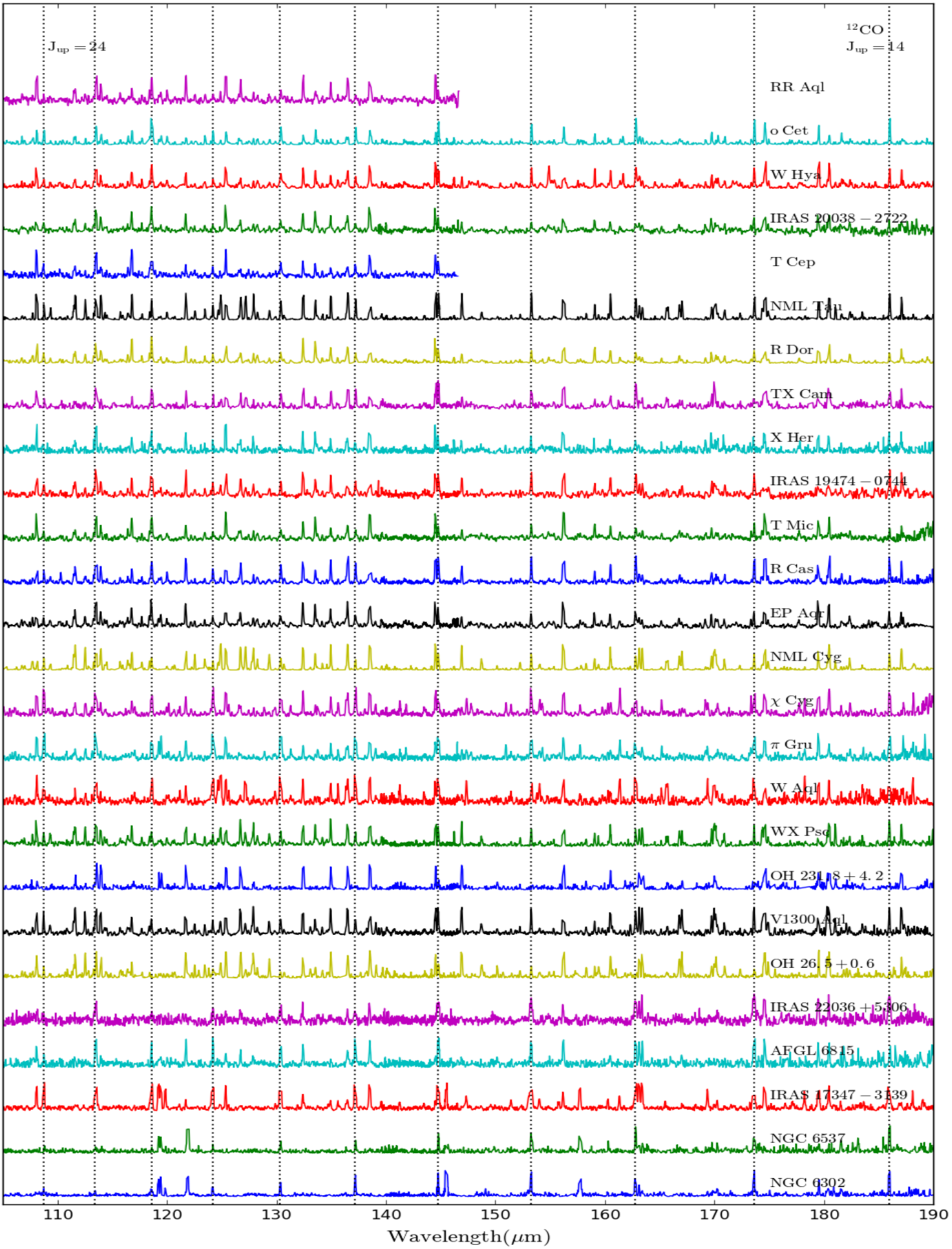

FIGURE 4.3: The same as in Fig. 4.2 but covering the spectral range from 110 to 190 μm.

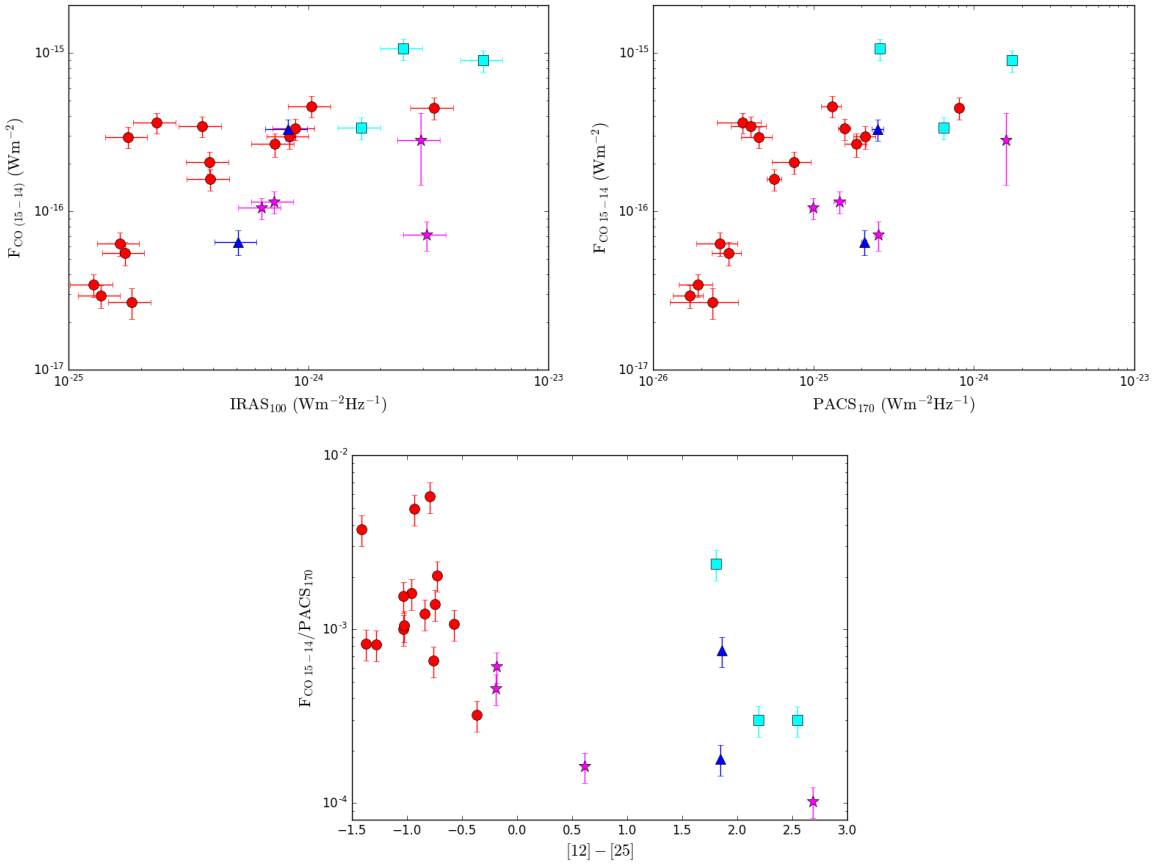

FIGURE 4.4: Top left) Integrated flux of the CO J=15-14 transition at 173.6 μm ($F_{CO\ 15-14}$) against the IRAS 100 μm flux. Targets with no PACS data beyond ~145 μm (i.e. not covering this CO transition; RR Aql and T Cep – see Fig. 4.3) or with bad quality (Quality Flag≠3) IRAS$_{100}$ data (OH 26.5+0.6) are excluded. Top right) Fluxes of the CO J=15-14 transition and the adjacent continuum (PACS$_{170}$). In this diagram, OH 26.5+0.6 is included. Bottom) Line-to-continuum ($F_{CO\ 15-14}$-to-PACS$_{170}$) flux ratio against the IRAS colour [12]−[25].

$$N_u = \frac{N_{CO}}{Q(T_{rot})} g_u e^{-E_u/(\kappa T_{rot})}, \tag{4.1}$$

where N_{CO} is the total number of CO molecules in the emitting volume, $Q(T_{rot})$ is the rotational partition function and g_u are the statistical weights for each upper level. The Eq. 4.1 can be rewritten in the following form:

$$\ln\left(\frac{N_u}{g_u}\right) = \ln\left(\frac{N_{CO}}{Q(T_{rot})}\right) - \frac{E_u}{\kappa T_{rot}} - \ln C_\tau, \tag{4.2}$$

where $\ln C_\tau$ is the opacity correction term defined as $C_\tau = \frac{\tau_\lambda}{1-e^{-\tau_\lambda}}$ by, e.g, Goldsmith and Langer, 1999. The left hand side of Eq. 4.2 can be estimated using the relation between the observed flux of a single line and the number of molecules at the upper level (N_u):

$$N_{\rm u} = \frac{4\pi F \lambda_{\rm ul} d^2}{A_{\rm ul} hc}, \tag{4.3}$$

where F is the integrated line flux, λ is the rest wavelength of the transition, d is the distance to the source, A_{ul} is the Einstein's spontaneous emission coefficient associated to the transition, h is the Planck's constant and c represents the speed of light.

In our RDs we represent $\ln\left(\frac{N_{\rm u}}{g_{\rm u}}\right)$ against $\frac{E_{\rm u}}{\kappa}$ and we apply a linear regression that allow us to obtain $T_{\rm rot}$ (derived from the slope) and $N_{\rm CO}$ (estimated from the intercept in the y-axis) following Eq. 4.2.

With the values of $N_{\rm u}$ and $T_{\rm rot}$ derived from this first fitting we estimate τ and C_τ from Eq. 4.4 in Sect. 4.4.1. This initial estimation can be used to obtain new values of $\ln\left(\frac{N_{\rm u}}{g_{\rm u}}\right)$ applying the correction shown in Eq. 4.2. Then we can apply a new linear fitting to this new set of values to obtain the so-called opacity corrected values for $T_{\rm rot}$ and $N_{\rm CO}$ that are the ones adopted for the rest of the analysis. We want to highlight that the opacity correction derived from this method is moderate being the τ values estimated for each object close to 1. Very high values of τ would lead to unreliable rotational diagrams, see Goldsmith and Langer, 1999 for details.

4.4.1 Opacity Correction

The optical depth (τ) of a CO line is given by:

$$\tau_\lambda = \frac{A_{\rm ul} \lambda_{\rm ul}^3 N_{\rm u}^{\rm col}}{8\pi V_{\rm exp} \sqrt{\pi}/(2\sqrt{\log 2})} \times (e^{(hc/(\lambda \kappa T_{\rm rot}))} - 1), \tag{4.4}$$

where $\rm N_u^{col}$ is the column density of the gas in the upper level of the transition.

We need an estimation of $T_{\rm rot}$ and $\rm N_u^{col}$ to calculate τ. $T_{\rm rot}$ is directly extracted from the RDs and $\rm N_u^{col}$ is derived from the total number of CO molecules, $N_{\rm CO}$, through the following, simplified, equation: $N_{\rm u}^{\rm col} = \frac{N_{\rm CO}}{\pi {r_{\rm CO}}^2}$. Where $r_{\rm CO}$ represents the characteristic radius of the region where the bulk of the CO emission is produced.

The value of $r_{\rm CO}$ is one of the main sources of uncertainty to compute the optical depth and the subsequent opacity correction term. Unfortunately, as mentioned in Sect. 2, the inner envelope layers where the CO PACS lines are produced are unresolved or barely resolved in the PACS spectroscopy cubes for most of the sources given the large PSF (~9"-13") and pixel size (9."4) of the instrument (see Sect. 2). Therefore, the value of $r_{\rm CO}$ needs to be adopted based on several criteria. These criteria are described in detail in Appendix 4.8.1, and a summary is offered in the following paragraphs.

For AGB stars, an estimate of $r_{\rm CO}$ is obtained by comparing the values of $T_{\rm rot}$ deduced

from our analysis, ~200-700 K, with the radial temperature distribution ($T(r)$) in the envelopes of a number of AGB stars with detailed nonLTE excitation and radiative transfer studies of the CO emission. The gas temperature is ≈1000-2000 K close to the dust condensation radius (~5-15 $R_\star$), and decreases gradually towards the outermost layers following, approximately, a power-law of the type ~1/r$^\alpha$, with α ~0.5-1.0 (see e.g. (Van de Sande et al., 2018; Maercker et al., 2016b; Danilovich et al., 2014; Khouri et al., 2014). For our sample, we deduce a range of values of $r_{\rm CO}$ from about 2×10^{14} cm to [2-4]$\times10^{15}$ cm, with the highest mass-loss rate objects requiring the largest values of $r_{\rm CO}$. The values of $r_{\rm CO}$ adopted for our targets are given in Table 4.1.

The CO column densities derived from our RD analysis adopting a range of $r_{\rm CO}$ from ~10^{14} to ~10^{15} cm are moderate, N_{CO}^{col}<10^{19} cm^{-2}, resulting in line optical depths of the order of ~0.9, and even lower in some cases, for the CO J=14→ 13 transition, which is the line with the largest opacity in our study. For AGBs, we have tuned $r_{\rm CO}$ to a value slightly larger than the radius of the wind layer where $\tau_{J=14\rightarrow13}$ ~ 1; the latter is indeed the deepest region of the envelope observationally accessible, because of the almost null escape probability ($1/C_\tau=\frac{(1-e^{-\tau})}{\tau}$ →0) from much deeper, optically thicker (τ >>1) layers of the wind.

Not only for the AGB stars but also for the OH/IR stars, we find that values of the radius around $r_{\rm CO}$~[2-4]$\times10^{15}$ cm result in line optical depths close to, but smaller than, unity (typically $\tau_{J=14\rightarrow13}$ ~0.5-0.7) that result in moderate C_τ opacity correction factors. For all the objects studied in this work, the opacity correction is typically negligible for lines higher than J = 19 − 18.

Unlike for AGBs and OH/IR stars, for post-AGBs/PNe there are no theoretical or observationally constrained temperature profiles of the molecular gas component available in the literature. For these targets, we find that $\tau_{J=14\rightarrow13}$ approaches a value of ~1 at distances of $r_{\rm CO}$~1×10^{16} cm, which therefore have been taken as a lower limit to the radius of the CO emitting volume detected with PACS. The PACS spectroscopy cubes indeed show extended, partially resolved nebulae consistent with a linear diameter of ≲[1-2]$\times10^{17}$ cm (da Silva Santos, 2016), in some of these cases. Using additional information on the molecular envelope extent from the literature and aiming to treat the sources as homogeneously as possible, we have adopted a common value of $r_{\rm CO}$=6×10^{16}cm for the 5 post-AGBs/PNe in our sample, resulting in column densities of $N_{\rm CO}$≲1-5$\times10^{17}$ cm^{-2} and small line optical depths of $\tau_{J=14\rightarrow13}$ ~0.02-0.07.

It must be noted that, in addition, we have completed our analysis by systematically exploring a range of radii around the value of $r_{\rm CO}$ adopted in each case to investigate the impact of this uncertain parameter in our results (see Fig. C.9 in Appendix C.4.1). As expected, the smaller the $r_{\rm CO}$, the larger the opacity correction, which results in lower values of $T_{\rm rot}$ and larger values of $N_{\rm CO}$. For example, in AGBs and OH/IR stars, values of $r_{\rm CO}$≳5×10^{15} cm always result in negligible opacity corrections, whereas for values of $r_{\rm CO}$≲8×10^{14} cm the opacity becomes larger than one for most targets, except for the sources with the lowest mass-loss rates ($\dot{M}$≈$10^{-8}M_\odot$ yr^{-1}, see Table. 4.3) where the CO lines remain optically thin at these radii. Note that after applying the C$_\tau$ correction, the slope of the RD increases, as a direct result of the frequency-dependence of C$_\tau$ and the typical values of $T_{\rm rot}$ that we measure decrease, see Appendix 4.8.1.

4.5 Results

4.5.1 Rotational temperatures and total emitting mass of H_2

The CO RDs of our targets, from which we derive the rotational temperature ($T_{\rm rot}$) and the total number of CO molecules ($N_{\rm CO}$) in the emitting volume, are shown in Fig. 4.5a-4.5d. For most objects, the RDs include CO transitions with upper-level energies that range from $E_{\rm u}$~580 K to $E_{\rm u}\lesssim$2500 K and are well fitted using a single temperature component. The single-fit rotational temperatures obtained range from ~200 K (NGC 6537) to ~700 K (π Gru), with an average value of $T_{\rm rot}$~450 K.

For a number of strong CO emitters (NML Tau, χ Cyg, W Aql, NML Cyg and IRAS 17347-3139) transitions with upper-level energies of up to $E_{\rm u}$~5000 K are also detected. In these cases, the data points in the RD over the full $E_{\rm u}$ covered are not well reproduced by a single straight-line fit. A double-slope in the RD is expected if a range of temperatures occur along the line of sight. We have formally tested that a double-slope fit is indeed most appropriate in these cases using statistical tools for model selection (F statistics and Bayesian Information Criterion (BIC)), implemented in R programming language in the *strucchange*[1] package (see appendix A and figure A.1 for more details). We refer to the CO emitting regions with the lowest and highest $T_{\rm rot}$ values derived from the double-fit as the "warm" and "hot" CO components, respectively (Fig. 4.5a-4.5d). The rotational temperatures of the warm and hot components are in the range ~370-480 K and ~570-900 K, respectively. As expected, the values of $T_{\rm rot}$ obtained from a single-fit to the RDs are intermediate to those of the warm and hot components.

The total number of CO molecules in the emitting volume, $N_{\rm CO}$, derived from the RDs has been converted to total mass of molecular hydrogen using:

$$M_{\rm H_2} = \frac{N_{\rm CO}}{\chi_{\rm CO}} m_{\rm H_2}, \tag{4.5}$$

where m_{H_2} is the mass of a molecule of hydrogen (m_{H_2}= 2.0159 a.u.= 3.3475×10^{-24} g) and $\chi_{\rm CO}$ is the CO-to-H_2 fractional abundance, assumed to be 2×10^{-4} for O-rich objects (Ramstedt and Olofsson, 2014a) and 6×10^{-4} for S-type stars (Ramstedt and Olofsson, 2014a; Danilovich et al., 2014).

The resulting values of M and $T_{\rm rot}$ are listed for each target in Table 4.1, together with a few other relevant parameters (such as the adopted $r_{\rm CO}$ for the moderate opacity correction applied, § 4.4.1). In Fig. 4.6 we show the M and $T_{\rm rot}$ values for each target, with and without the opacity correction, and the final histogram distributions.

The single-fit values of the total mass of the CO-emitting volume range between M~3×10^{-6} $M_\odot$ (X Her) and ~5×10^{-2} $M_\odot$ (IRAS 17347-3139), with an average/mean value of M~4×10^{-3} $M_\odot$.

[1] https://cran.r-project.org/web/packages/strucchange/index.html

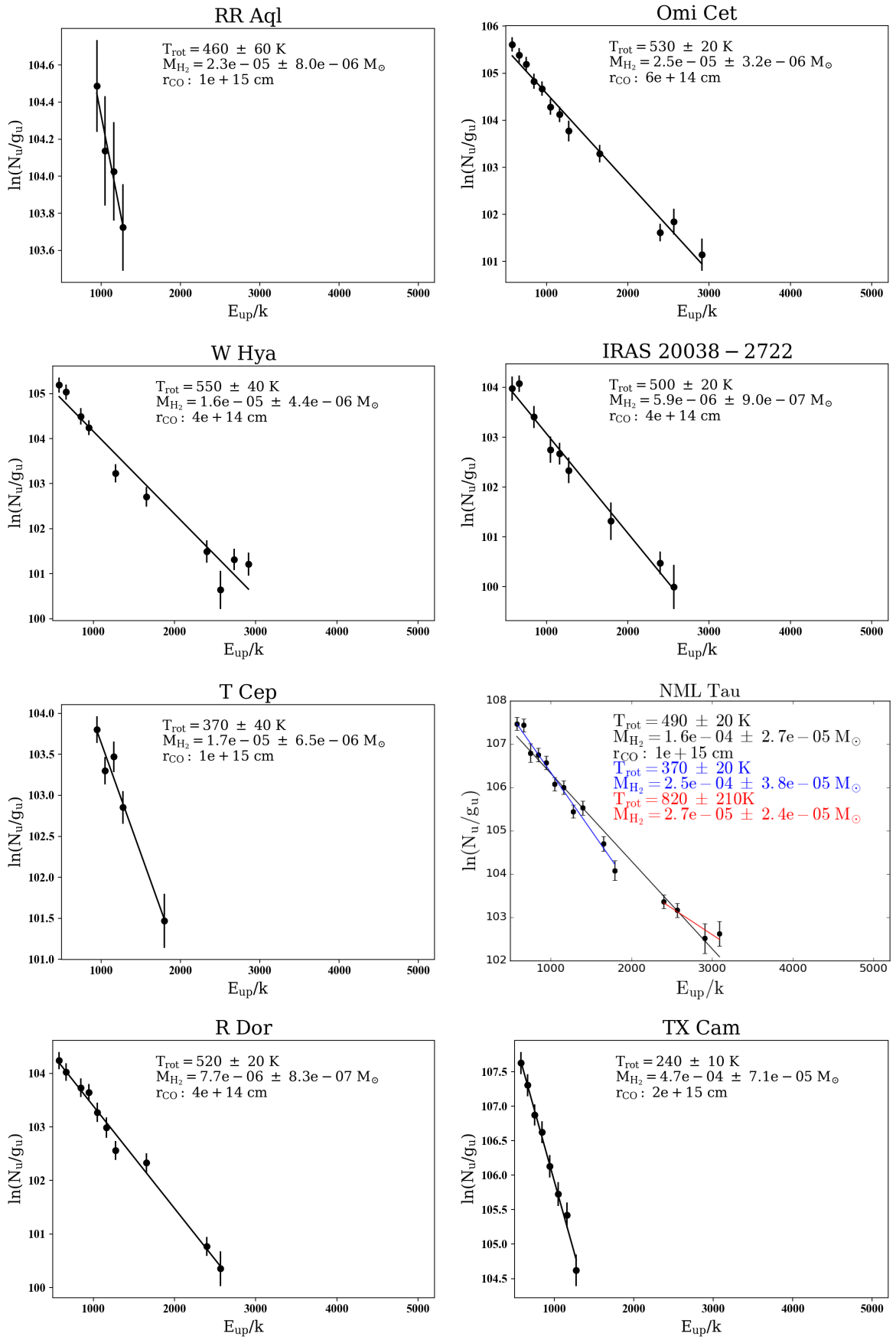

FIGURE 4.5A: RDs of CO for our targets. For each source, the values of $T_{\rm rot}$ and $M_{\rm tot}$ derived from the fits (solid lines) as well as the characteristic radius of the emitting layers adopted ($r_{\rm CO}$) are shown (Sect. 4.4). For a few sources, a double component fit was necessary. For these cases, the values of $T_{\rm rot}$ and $M_{\rm tot}$ for the so-called "warm" (blue) and "hot" (red) components are also indicated.

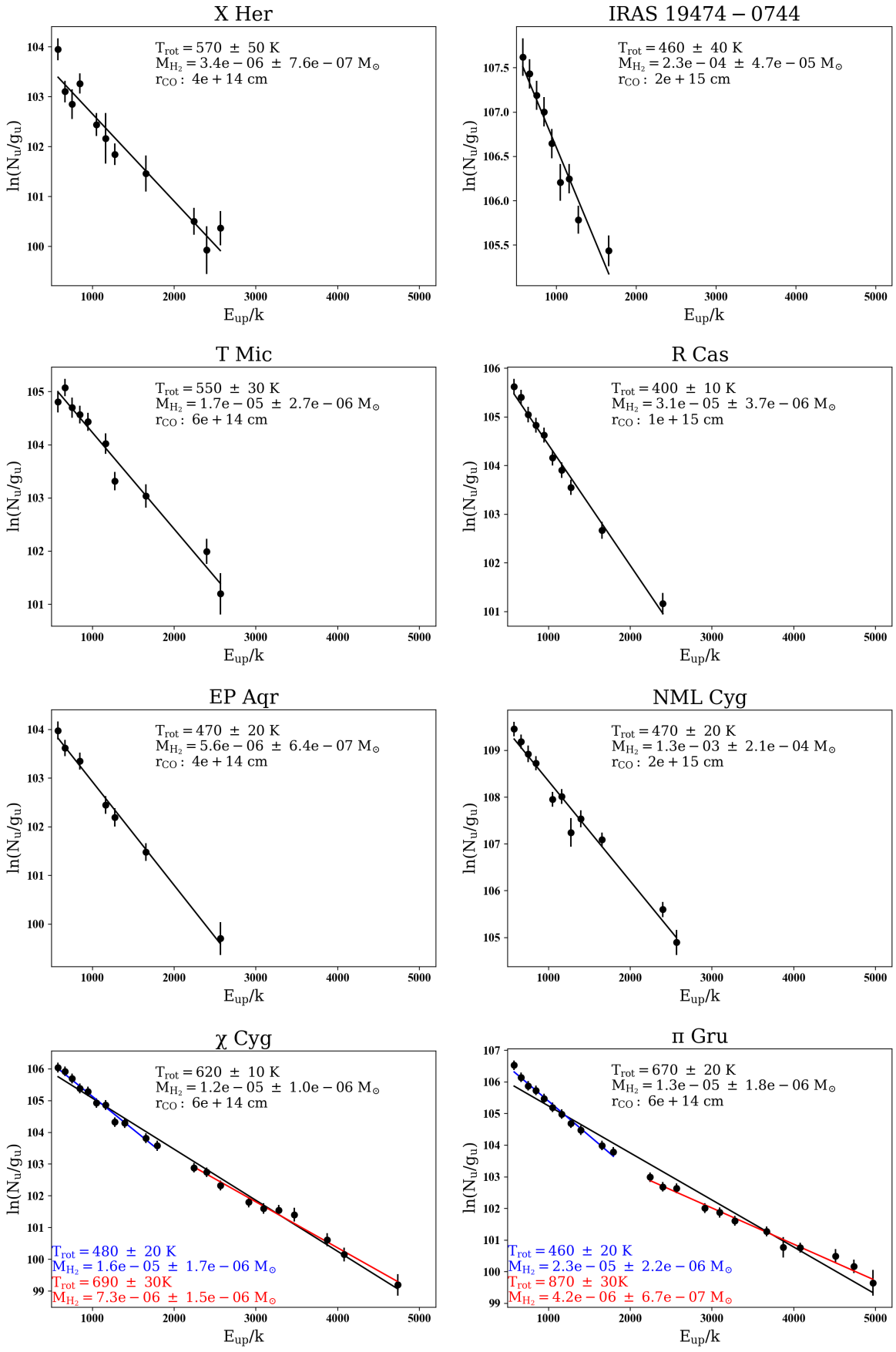

FIGURE 4.5B: Continued

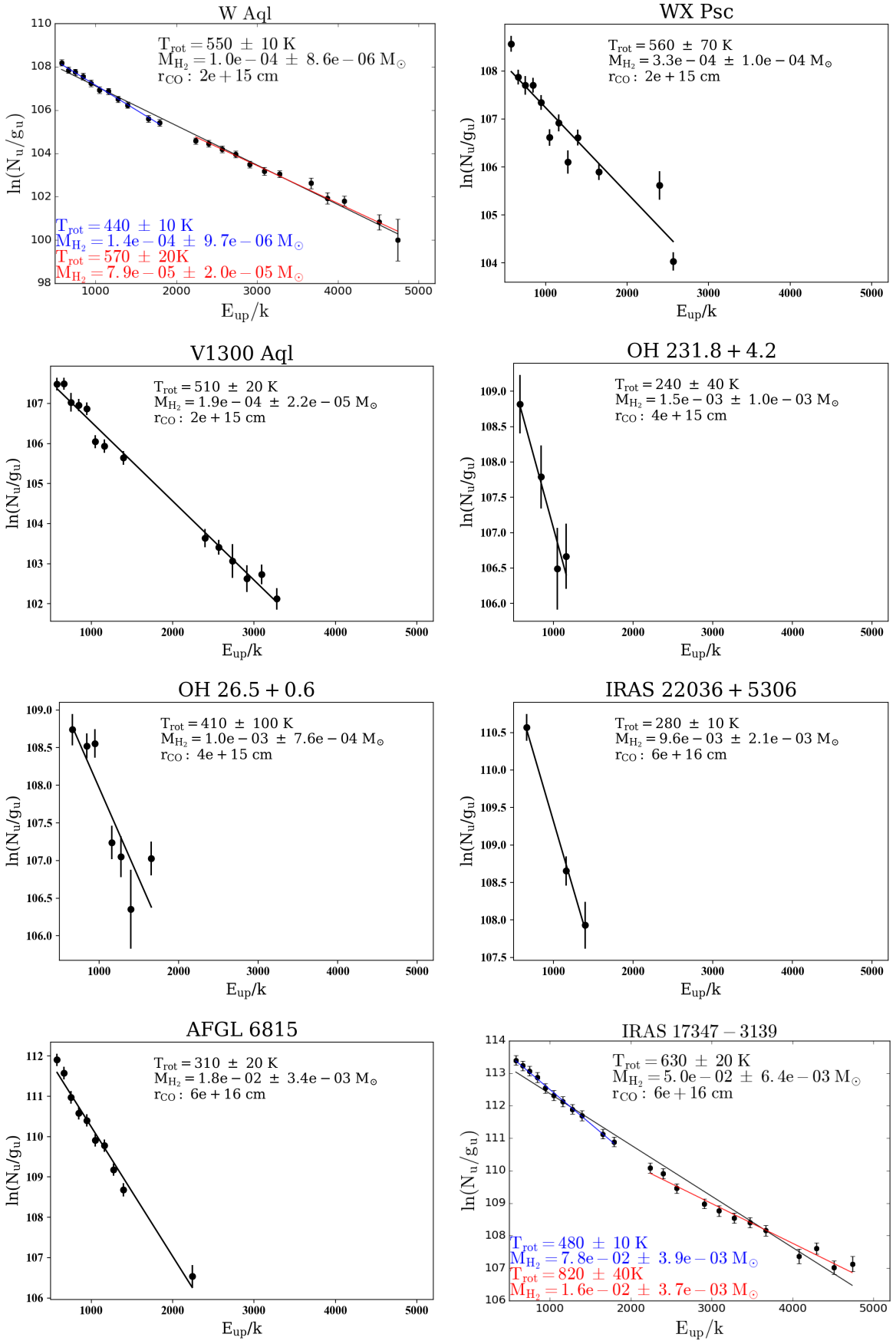

FIGURE 4.5c: Continued.

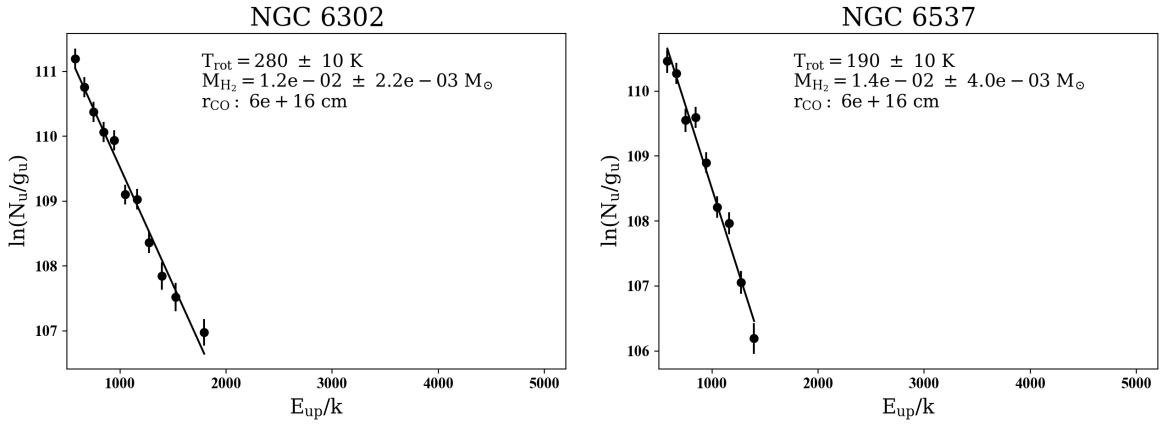

FIGURE 4.5D: Continued.

The opacity correction applied in all cases is small-to-moderate, which results in a mass-correction factor less than 20% in most sources. The source with the largest opacity correction (of a factor ~1.5) is NML Cyg, a red supergiant based on Teyssier et al., 2012, and the AGB star with the largest M, and highest mass-loss rate in our sample (Table 4.1).

The mass of the warm CO component is always larger than the mass of the hot component. For the warm component, these values vary from M~1.3×10^{-5} to $7.8\times10^{-2} M_{\odot}$, and for the hot between 3.7×10^{-6} and $1.6\times10^{-2} M_{\odot}$. The warm-to-hot M and $T_{\rm rot}$ ratio, and their relation, is further examined in Sect. 4.6.

We have investigated if there are any trends between $T_{\rm rot}$ and M, derived for our RD analysis, and other observational parameters, such as the terminal expansion velocity of the envelope ($V_{\rm exp}$) and the strength of the CO (J=15-14) transition (Fig.4.7). First, we notice that objects in the most advances stages of the evolution, namely, post-AGBs and PNe, systematically have the lowest temperatures, $T_{\rm rot}$~200-300 K, and the highest masses, M>0.01 $M_{\odot}$ (see also Fig. 4.6). IRAS 17347-3139 is the only object with an exceptionally large $T_{\rm rot}$ for its class. The distribution of $T_{\rm rot}$ and M for post-AGB and PNe is also much narrower than for AGBs and OH/IR. The latter show a broad range of $T_{\rm rot}$~200-700 K and M≈10^{-6}-10^{-3} $M_{\odot}$. This segregation of the sources exists before and after the opacity correction has been applied; the opacity correction is indeed marginal for post-AGBs and PNe (grey symbols in Fig. 4.6). The observed bias in favour of massive post-AGB/PNe could reflect that, in our sample, post-AGB/PNe are on average more distant (d >1 kpc) than AGBs and OH/IRs stars, which hampers CO line detections in the less massive post-AGB/PNe.

We observe an anticorrelation between M and $T_{\rm rot}$ (Fig. 4.7, top-left panel). This is most clearly noticed amongst AGB and OH/IRs, which are more numerous and cover a broader range of $T_{\rm rot}$ and M values, but it is also followed by post-AGB/PNe. Note that for objects for which a double-$T_{\rm rot}$ component has been identified (NML Tau, χ Cyg, W Aql, NML Cyg and IRAS 17347-3139), both the double- and the single-fit values (connected with dashed lines in Fig. 4.7, top-left panel) follow the trend. The object IRAS 17347-3139 is an outlier, since it has a much larger $T_{\rm rot}$ than anticipated based on the overall properties of the rest of our sample. This object is known to be at the earliest stages of the post-AGB evolution and making a fast transition to the PN phase at present (Table 2, see Gómez et al., 2005; Tafoya

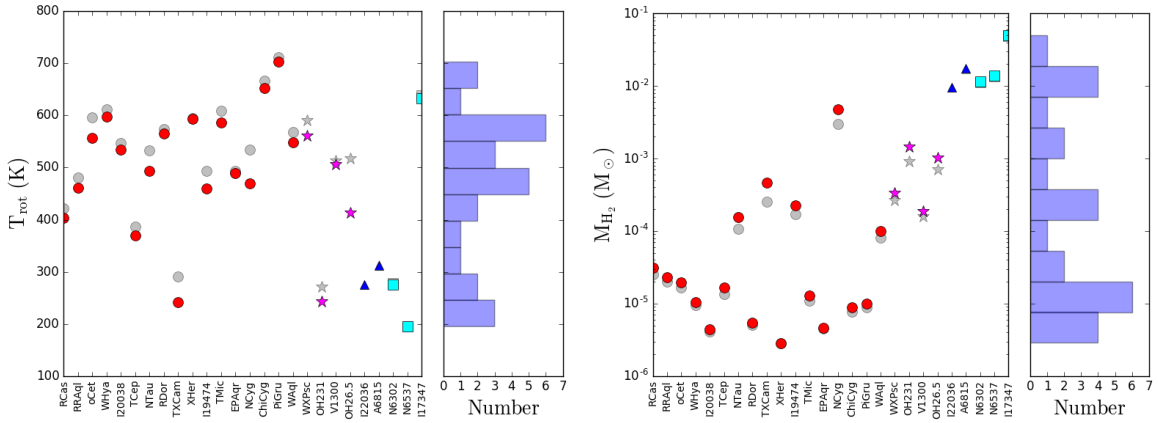

FIGURE 4.6: Values of $T_{\rm rot}$ and $M_{\rm tot}$ from our CO rotational diagram analysis (single fit; Sect. 4.5) before and after applying the opacity correction (grey and coloured symbols, respectively).

et al., 2009).

For AGBs and OH/IRs stars, there is also an evident linear correlation between M and the terminal expansion velocity of the envelope (from the literature – Table 4.1). As we will see in Sect. 4.6.4, this is linked to an analogue $\dot{M}$-to-$V_{\rm exp}$ relation, which is known to exist based on previous low-J CO studies of AGB CSEs (e.g. Danilovich et al., 2015) and that we corroborate in this work using higher-J CO lines. The post-AGB objects and PNe in our sample, however, show very similar values of the mass over a the full range of velocities.

As expected, the integrated flux of the CO lines correlate with the total mass of the CO-emitting volume and, as we will see later, with the average mass-loss rate of the envelopes. As an example we show this relation for the CO J=15-14 transition ($E_{\rm u}$~660 K) in Fig. 4.7 (bottom-left). There is a significant scatter in the line flux vs. M relation since the latter also depends on the excitation temperature ($T_{\rm rot}$), the velocity field in the envelope, the optical depth, etc (§ 4.4).

Finally, we investigated if a correlation exist between the CO J=15-14 line integrated flux normalized to the underlying ~170μm-continuum observed with PACS ($F_{\rm CO\,15-14}$/$PACS_{170}$) and the parameters derived from the RD analysis. The strongest correlation is found with $T_{\rm rot}$ (Fig. 4.7, bottom-right), which is somewhat expected since the mass and the distance dependence is removed in the line-to-continuum flux ratio. The relation between $F_{\rm CO\,15-14}$/$PACS_{170}$ with M (not shown) has a much larger scatter and suggests a certain anticorrelation (given that $T_{\rm rot}$ anticorrelates with M in our sample).

In Sect. 4.6 we further discuss the observed trends.

4.5.2 Mass-loss rate

Using the values of the total emitting mass, we calculate the mass-loss rates ($\dot{M}$) for each source in a simplified manner dividing the total mass by the crossing time of the CO-emitting layers, that is:

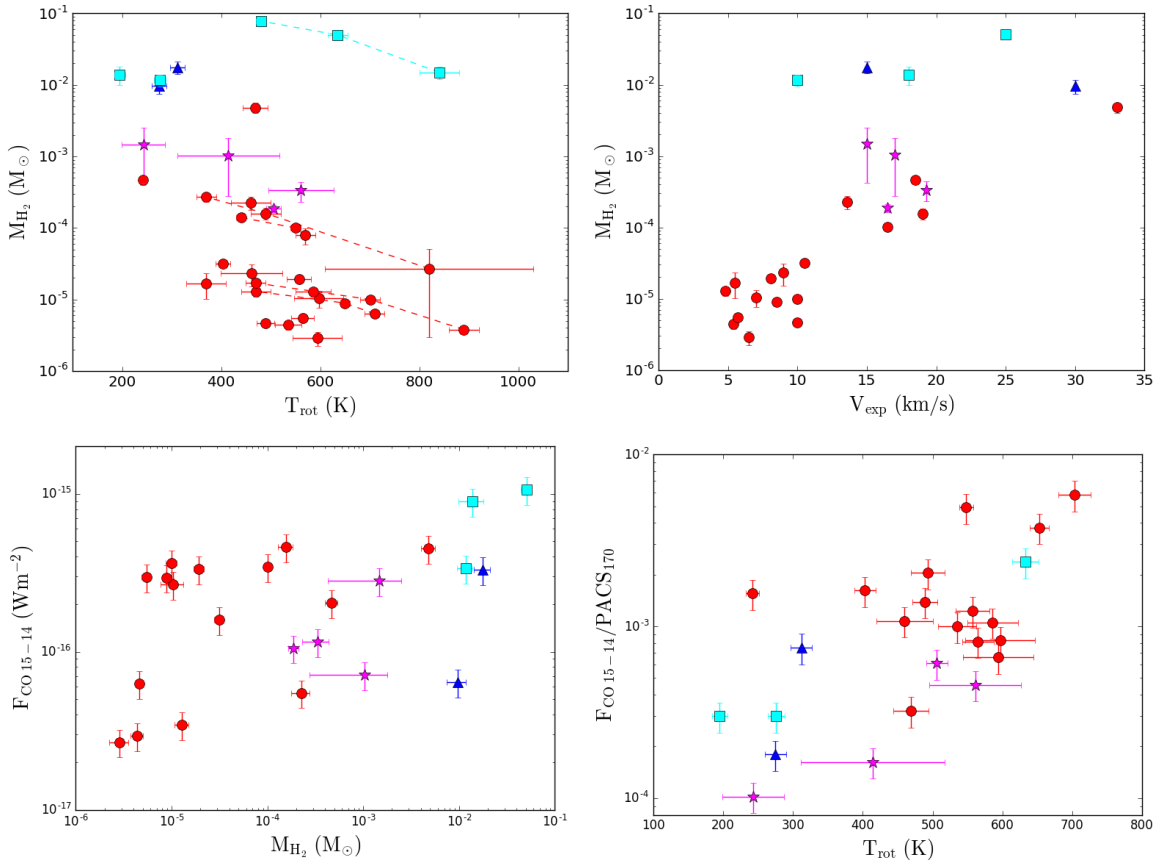

FIGURE 4.7: Relation between M_{H_2} and T_{rot} derived from our CO RD analysis and other magnitudes. Top-left) M_{H_2} vs T_{rot}. For objects (a total of five) with a double-T_{rot} component, both the single-fit and double-fit values are connected with dashed lines for an easier identification. Top-right) Values of M_{H_2} (single-fit) vs. V_{exp} taken from literature. Bottom panels) Integrated fluxes of CO (J=15-14) line vs M_{H_2} (left) and the same line normalised to its adjacent continuum versus T_{rot} (right).

$$\dot{M} = \frac{M_{\rm tot}\, V_{\rm exp}}{r_{\rm CO}} \tag{4.6}$$

Apart from $M_{\rm tot}$, derived from the RDs, we need to adopt a value for the expansion velocity ($V_{\rm exp}$), which has been taken from literature, as well as for the characteristic radius of the CO emitting region, for which we use the same value used for the estimation of the opacity correction, $r_{\rm CO}$. The values of $\dot{M}$ are given in Table 4.3.

In Sect. 4.4, we already mentioned the uncertainties associated to the adoption of a particular linear radius for the emitting region of each source and the importance of exploring a wide range of values to determine a reasonable estimation of the opacity correction and, thus, of M. The same kind of analysis is even more important now, as the impact of $r_{\rm CO}$ in the mass-loss rate estimation is larger than in the calculation of the opacity correction (it affects $M_{\rm tot}$ but also directly $\dot{M}$ as $\sim 1/r_{\rm CO}$). Another uncertainty arises in $V_{\rm exp}$, however, this parameter is rather well known (from previous works), to an accuracy of ~10-20% typically.

In Fig. C.11 (Appendix C.4.1), we show, for every object, the different values of $\dot{M}$ and $T_{\rm rot}$ that correspond to three different values of the radius around the adopted value. For each source, we have also plotted a grey region that represents the broad interval of mass-loss rates found in the literature. The latter are usually derived from the analysis of low-J CO lines and, therefore, they represent the average mass-loss rate in the outer envelope layers. These values of $\dot{M}$ from the literature have been re-scaled after matching the expansion velocity ($V_{\rm exp}$), the distance (d) and the relative abundance of CO ($\chi_{\rm CO}$) to the values adopted here, which is needed for a proper comparison with our estimates of $\dot{M}$. The values of the mass-loss rates reported in the bibliography for each object are displayed in Table 4.3 together with the associated interval range of mass-loss rates after scaling and relevant references. To our knowledge, for IRAS 17347-3139 and NGC 6537 there are no previous estimates of the gas mass-loss rate in the literature.

Our estimates of the mass-loss rates are shown in Fig. 4.8 plotted against the rotational temperature, the expansion velocity, and the CO (J=15-14) line strength to explore any trends that may be present. In the $\dot{M}$ versus $T_{\rm rot}$ diagram we also include the mass-loss rates associated to the warm and hot component for objects with a double-slope in their RDs. There is an anti-correlation between $\dot{M}$ and $T_{\rm rot}$, which was expected based on a similar trend observed directly between $M_{\rm tot}$ and $T_{\rm rot}$ (Fig. 4.7). This trend together with the clear correlation between $\dot{M}$ and $V_{\rm exp}$ and, more scattered, trend with $F_{\rm CO\,15-14}$ are briefly discussed in Sect. 4.6.

4.6 Analysis and interpretation of the results

In this section, we analyse and discuss the results obtained from the rotational diagrams as well as the correlations found between different magnitudes.

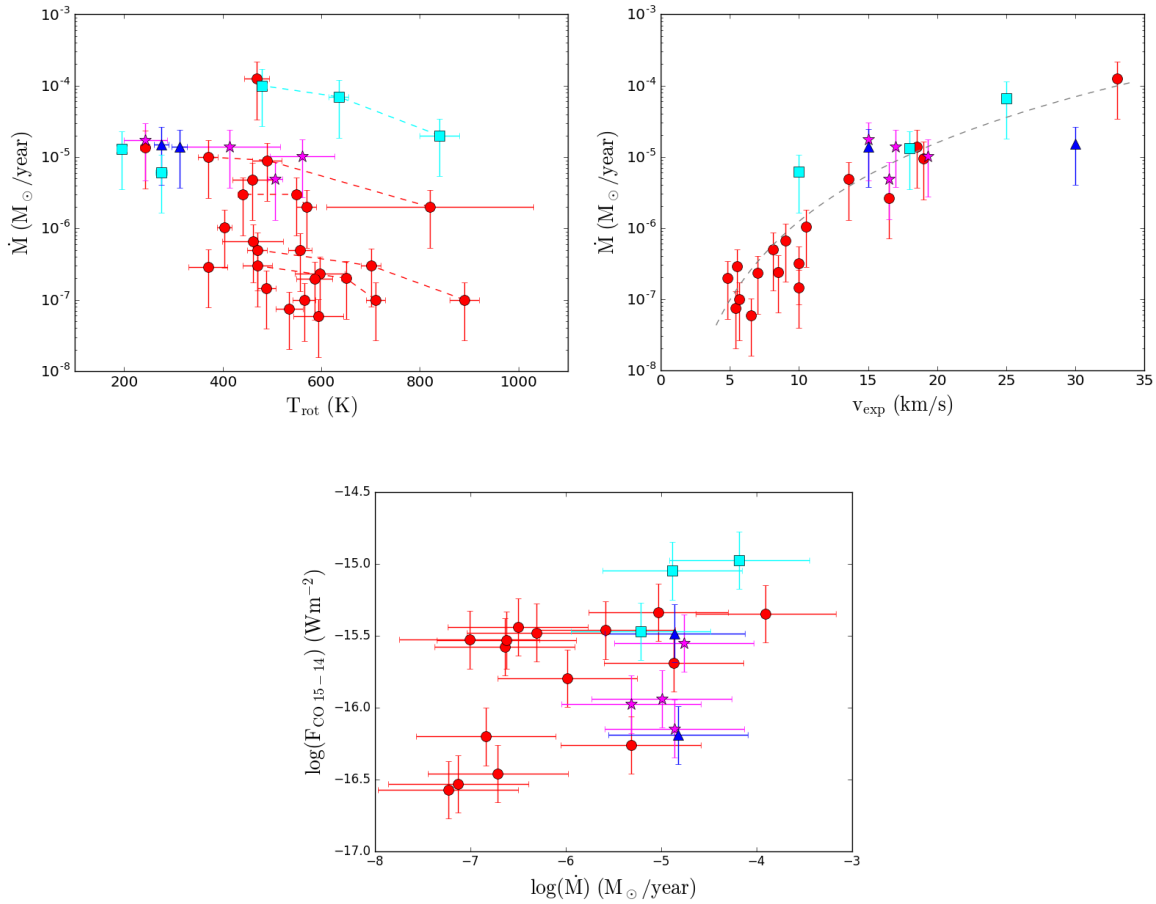

FIGURE 4.8: Top) Relation between $\dot{M}$ and $T_{\rm rot}$. Single- and double-fit (warm and hot) values, whenever these exist, are connected using dashed lines. Middle) Relation between $\dot{M}$ and $V_{\rm exp}$. The distribution approaches a power-law of the type $\dot{M} \propto V_{\rm exp}{}^{2.5}$ (dashed line). Bottom) Integrated flux of the CO J=15-14 line versus $\dot{M}$ in a logarithmic scale.

4.6.1 Rotational temperature and total mass

For most of our sources, a single-$T_{\rm rot}$ component was sufficient to obtain a good fit of the CO RD, leading to single-fit rotational temperatures and total (H_2) masses of the CO-emitting region of $T_{\rm rot}$ ~200-700 K and M~3×10^{-6}-5×10^{-2} $M_{\odot}$, respectively (Sect. 4.5).

The rotational temperatures of a few 100 K derived in this work using CO-PACS data ($J_{\rm u}$~14-27, and up to $J_{\rm u}$=40 lines in some cases) are clearly larger than the typical values of $T_{\rm rot}$≈10-100 K found from CO low-J line studies (most commonly using $J_{\rm u}$<4 lines at mm and sub-mm wavelengths) in the external layers of the CSE around evolved stars, at ≈10^{16}-10^{17} cm from the center (e.g. Teyssier et al., 2006a, and references therein). This corroborates that, as anticipated, the CO-PACS lines sample the warm, presumably inner, regions of the CSEs, probably at a typical/average distance from the central star of about ≈10^{15} cm for AGB stars (e.g. Danilovich et al., 2014).

We find that the total mass of the warm inner layers where the PACS CO ($J_{\rm u}$>14) lines mainly arise is typically a factor ~100-1000 lower than the masses deduced from low-J CO line studies in the literature, reinforcing the idea that CO PACS lines sample mainly the inner part of the envelopes, which contains a small fraction of the total envelope mass.

For a total of five targets in our sample (NML Tau, π Gru, W Aql, χ Cyg and IRAS 17347-3139), the RD diagram shows a double slope and, thus, a double-$T_{\rm rot}$ fit is most appropriate. Deviations from a single straight line fit of the RDs, most likely denoting a temperature stratification along the line of sight (see below), are not uncommon and have been previously found in a number of AGB and post-AGB CSEs using, e.g., ISO and/or SPIRE CO spectra (e.g. Justtanont et al., 2000; Wesson et al., 2010a; Matsuura et al., 2014; Cernicharo et al., 2015a; Cordiner et al., 2016).

The rotational temperatures and masses of the hot and warm components of these five objects are displayed in Fig. 4.7 (together with the single-fit $T_{\rm rot}$ and M values derived for the whole sample). The mass of the warm component is always larger (by a factor 2-10) than that of the hot component. Adopting a constant mass-loss rate and a gas temperature that decreases with the distance, the difference between the mass of the warm and hot component suggests a CO-emitting volume smaller for the hot component than for the warm one.

We compare in detail the hot-to-warm M and $T_{\rm rot}$ ratios in Fig. 4.9. We find that the mass and temperature ratios are well correlated and follow approximately a power-law function. For AGB CSE with a inverse-square density profile, the latter is indeed expected if the temperature stratification within the emitting layers is described by a power-law function, $T(r) \sim 1/r^{\alpha}$. This is because, in this case, the total mass within a given CO-emitting volume is roughly proportional to its radius (M∝r) and, therefore, it is easy to derive that:

$$\frac{T_{\rm rot}^{\rm hot}}{T_{\rm rot}^{\rm warm}} \sim \left(\frac{M_{\rm H_2}^{\rm hot}}{M_{\rm H_2}^{\rm warm}} \right)^{-\frac{1}{\alpha}} \tag{4.7}$$

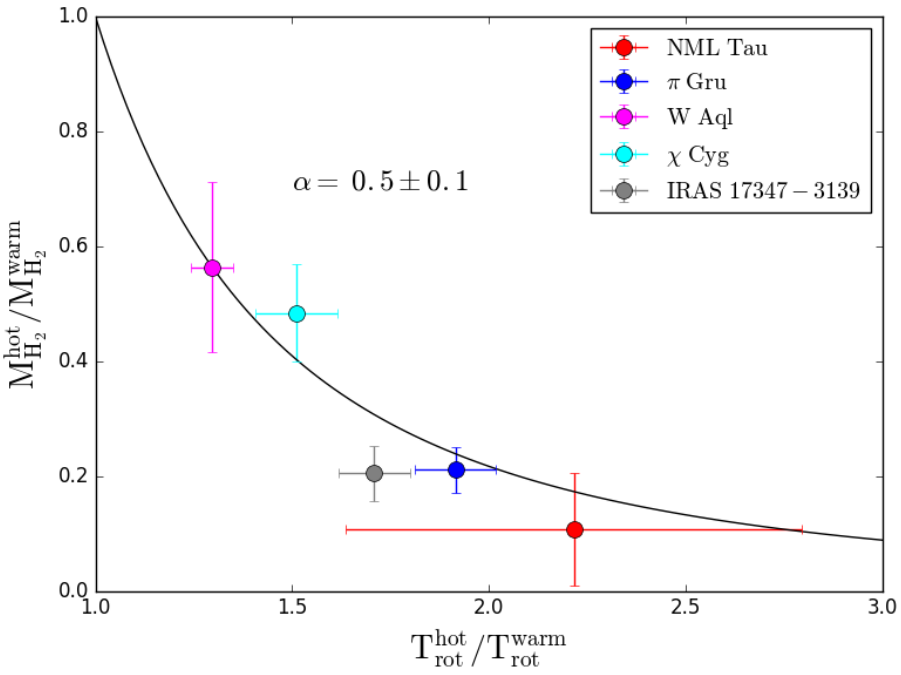

FIGURE 4.9: Ratio of the mass and rotational temperatures for the hot and warm components, $M_{H_2}^{hot}/M_{H_2}^{warm}$ vs $T_{rot}{}^{hot}/T_{rot}{}^{warm}$, for sources with a double-T_{rot} component, namely, the AGB stars NML Tau, π Gru, W Aql, and χ Cyg and the yPN IRAS 17347-3139. The solid line is a fit by a power-law function ($y \sim x^{-1/\alpha}$) to the AGB stars' data (see text in Sect. 4.6.1, for more details). A similar trend is found in our analogue study of the THROES C-rich sample reported in Chapter 5.

Fitting a power-law function to the set of points corresponding to our AGB stars[2], we obtain α=0.5±0.1. This value is at the low end of the range of exponents found in the literature (from a combination of theoretical/modelling and observational works) for AGB CSEs, typically α ~0.5-1 (e.g. De Beck et al., 2010a; Maercker et al., 2016b; Danilovich et al., 2015, and references therein). There is some indication from recent works that the kinetic temperature distribution is shallower, with values of α down to ~0.4, for the inner CSE layers (~5×10^{14}-3×10^{15} cm; De Beck et al., 2012a; Lombaert et al., 2016a) than for the outer regions, where the steepest temperature variations (α ~1-1.2) are found ($\gtrsim$10^{16} cm; Teyssier et al., 2006a). This is indeed in very good agreement with the relatively small value of α found in the inner envelope layers from our analysis. (The hot-to-warm mass vs. T_{rot} trend with a similar value of α is also deduced in our sample of C-rich targets studied in Chapter 5). We believe that the empirical relation between the hot-to-warm ratio of M and T_{rot} therefore supports that the double-T_{rot} component identified in some of our objects (and possibly also present in more targets for which CO J_u>27 transitions remain undetected), is a natural consequence of the temperature stratification across the inner envelope layers. Detailed non-LTE excitation and radiative transfer of the CO emission including high-J transitions, J_u~14-40, are needed for a proper characterization of the temperature structure in the warm inner-wind regions of AGB stars. See Appendix 4.8.2 for a discussion of non-LTE effects on the RD analysis.

[2]Although IRAS 17347-3139 does not deviate significantly from the observed hot-to-warm M_{tot} vs. T_{rot} trend, we excluded this object from the fit because, being a young PNe, it does not necessarily follows the same density and temperature profiles of the AGB CSEs.

4.6.2 Comparison with other works: $\dot{M}_{\rm THROES}$ vs. $\dot{M}_{\rm Bibliography}$

In Fig. 4.10 we show, for each source, the mass-loss rate estimated in this work for the adopted radius ($r_{\rm CO}$) against a mean value of gas mass-loss rates found in the bibliography ($\dot{M}_{\rm Bibliography}$). We assign error bars of a factor 3 to our estimates of the mass-loss rate; this is a common uncertainty value adopted in most molecular line-emission studies (e.g. Maercker et al., 2016b). The error bars of $\dot{M}_{\rm Bibliography}$ represent the low and high ends of the broad range of values found in bibliography after scaling to our d, $V_{\rm exp}$ and χ_{CO} values, and is always ~3 or more. For objects with only one value of $\dot{M}$ from the literature, an uncertainty factor of 3 has also been assumed after scaling.

The comparison between our mass-loss rates and those found in the bibliography is in good agreement for all the objects, see also Appendix C.4.1 (Fig. C.11). As already mentioned, we are particularly interested in the comparison of our $\dot{M}$ rates with those obtained from comprehensive non-LTE excitation and radiative transfer models that make use of some CO rotational lines (normally, J<20) measured with PACS, which exist for a small sample of objects: for R Cas, NML Tau, TX Cam, R Dor, W Hya and W Aql (Van de Sande et al., 2018; Maercker et al., 2016b; Khouri et al., 2014; Danilovich et al., 2014). We find that, also in these cases, discrepancies with our values are always within 50% for all except W Hya, demonstrating that the simple and approximate RD approach and the assumptions (e.g. the adopted size of the emitting layers) used in this work yield reasonable first estimates results.

Considering again our sample as a whole, our mass-loss rate estimations of post-AGBs and PNe seem to be systematically lower than those in the literature by a ~20%. In principle, this small difference could suggest that the radius of the CO-emitting region is slightly smaller than the value of $r_{\rm CO}$ adopted by us (at least in some objects). As it is shown in Appendix C.4.1, Fig. C.11, a fine tuning of $r_{\rm CO}$ can be performed to obtain a perfect match between $\dot{M}_{\rm Bibliography}$ and our estimates for each individual object. However, we prefer to treat the sources as homogeneously as possible and to be conservative avoiding the use of very small values of $r_{\rm CO}$, which would result in large opacities ($\tau >>1$) and would consequently lead to unreliable opacity corrections.

A similar discrepancy is reported by Danilovich et al., 2015 from a CO-line study (including non-LTE radiative transfer modelling) of AGB CSEs in the SUCCESS program including CO transitions from J=1-0 to J=9-8, as well as J=14-13 in some targets. Their models give mass-loss rates that are on average 40% lower than from past studies (see their Fig. 7). Danilovich et al., 2015 note that, as already mentioned here, most past studies are based on observations of a small number of low-J CO transitions (with similar excitation requirements, i.e., $E_{\rm u}$), and conclude that taking a large sample of CO transitions, including high-J lines, properly into account when modelling mass-loss rates, results in lower derived values.

It is important to stress that the mass-loss rates derived in this work represent average values during the period of time when the warm, inner envelope layers were ejected, that is, during the last <50-100 years, for AGBs, and the last ~600-2000 years, for PNe (considering the values of $r_{\rm CO}$ and $V_{\rm exp}$ given in Table 4.1). Since the low-J lines commonly used in the previous studies to derive $\dot{M}_{\rm Bibliography}$ mainly trace the outer envelope layers, the discrepancies observed with respect to past studies could reflect a real time variation of the mass-loss

rate in some cases. This is indeed the case, e.g., of OH 231.8+4.2, where mass-loss rate when the bulk of the nebula was ejected during the last ≈1000 yr years (~2×10^{-4} $M_{\odot}$, Alcolea et al., 2001) is much larger than the present-day mass-loss rate (<2×10^{-5} $M_{\odot}$), Sánchez Contreras et al., 2002). The upper limit to the present-day mass-loss rate of OH 231.8+4.2 is indeed in very good agreement with our estimate using high-J CO transitions.

Finally, as a word of caution we note that the mass-loss rates estimated for post-AGB objects and PNs are particularly uncertain as it is not easy to define essential parameters like $r_{\rm CO}$ or $V_{\rm exp}$ for these spatio-kinematically and morphologically complex objects. This makes the comparison with values from past studies subject to larger uncertainties. In spite of this, the agreement is reasonably good for the two post-AGBs in our sample with values of $\dot{M}$ reported in the literature.

4.6.3 Mass/mass-loss rate vs T$_{rot}$

As shown in Fig. 4.7, we find a statistically significant anticorrelation between the total mass of the PACS-CO emitting region, M, and the rotational temperature, $T_{\rm rot}$, derived from our RD analysis. As expected, a similar trend is present between the mass-loss rate, $\dot{M}$, and $T_{\rm rot}$ (Fig. 4.8).

Prior to this work, Teyssier et al., 2006a and Danilovich et al., 2015 noticed a weak/tentative $\dot{M}$ vs. $T_{\rm rot}$ anticorrelation based on their studies of the intermediate-to-outer regions of the envelopes of AGB and post-AGB stars using submm/mm-wavelength CO transitions. Particularly, Danilovich et al., 2015 reported $\dot{M}$ and $T_{\rm kin}$ at a representative distance of $\approx10^{16}$ cm (i.e. ~100 times the dust condensation radius) for a sample of 53 AGB stars. Form their analysis, using self-consistent non-LTE radiative transfer models of the dust continuum emission and the CO emission transitions over a range of excitations (from J =1-0 to J =9-8, and in a few cases, up to J =14-13), Danilovich et al., 2015 found that in general high mass-loss rate objects show relatively low temperatures (see their Fig. 6).

The temperatures of the regions studied by Danilovich et al., 2015, at distances ~[1-2]$\times10^{16}$ cm, range between ~10-80 K to be compared with the larger temperatures, ~200-600 K, found by us at distances typically a factor ~10 smaller in our AGB+OH/IR targets. This indicates that this trend is preserved from the inner envelope layers, traced by $J_{\rm u}\geq14$ CO lines, through the outer parts of the CSE, sampled by lower-J transitions.

As discussed by Danilovich et al., 2015, a possible reason for the anticorrelation observed is the more efficient line cooling expected for high mass-loss rate objects (see also Groenewegen, 1994, and references therein). Another factor to explain the trend found is presented in Olofsson, 1996. As the velocity by which the grains stream through the gas is considered an important source of heating, the CSEs are expected to be cooler the more massive and dense they are, due to the low velocity the grains moving through the gas can reach. In addition to this, we believe that optical depth effects can partially contribute to, and reinforce, the observed anticorrelation. This is because for high mass-loss rate objects, the $\tau_{\rm CO}$ ~1 surface layer, which is the deepest region that can be observationally sampled by a

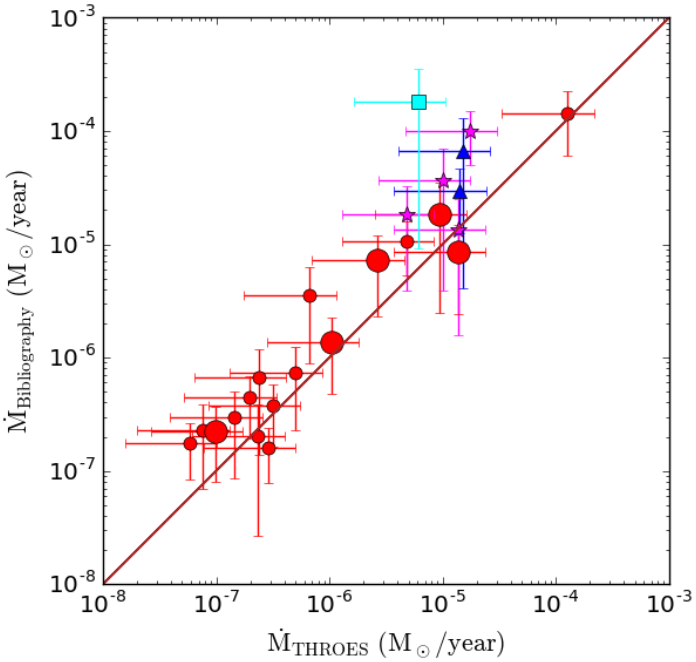

FIGURE 4.10: Comparison of the mass-loss rates from this work and from the literature (Tables 4.3 and 4.1). The solid line represents a 1:1 ratio. Target colour and symbol code as in Fig. 4.1. The big circles are used to locate a few targets with previous $\dot{M}_{\rm Bibliography}$ estimates obtained from non-LTE excitation and radiative transfer analysis of CO lines, including some of the PACS transitions.

given CO line, is located at larger distances from the star where the gas kinetic temperature is lower.

4.6.4 Mass/mass-loss vs expansion velocities

In Sect. 4.5 we already mentioned the presence of evident correlations between $M_{\rm tot}$ and $V_{\rm exp}$ and between $\dot{M}$ and $V_{\rm exp}$ (Figs. 4.7 and 4.8, respectively).

The correlation found between $M_{\rm tot}$ and $V_{\rm exp}$ is stronger if we consider only the AGB and OH/IR stars in our sample. In AGB and OH/IRs stars, the observed correlation could be telling us about the processes which are responsible for the acceleration stellar wind. Since AGB winds are primarily driven by radiation pressure on dust, the most luminous objects (which are also the most massive) will exhibit the largest expansion velocities.

The fact that post-AGB and PNs deviate from the observed trend is probably related with the different mass-loss mechanism (not driven by radiation pressure on dust) in these latest stages (Bujarrabal et al., 2001). Indeed, the expansion velocities of post-AGBs and PNe do not represent the terminal velocity of the present-day stellar wind but the result from the complex hydrodynamical interaction between the stellar high-velocity winds, that appear beyond the AGB phase, and the slow ambient circumstellar material (expelled in the previous AGB stage).

Based on the above conclusion that, in AGB stars, V_{exp} correlates with M_{tot} via the stellar luminosity, the trend found between V_{exp} and $\dot{M}$ is not surprising (Fig. 4.8). In this case, however, the post-AGBs and PNs in our sample do not deviate significantly from the general trend, although, as we mentioned above, the values and interpretation of V_{exp} as well as the $\dot{M}$ derived (under simplifying assumptions) have to be regarded with caution.

The $\dot{M}$-to-V_{exp} relation has been observed before in other CO line studies in AGB CSEs. For example, Danilovich et al., 2015 report a correlation between $\dot{M}$ and V_{exp} including stars of different chemical types (O-rich, C-rich and S-stars), which is in very good agreement with our data-points (in spite of the lower-J transitions, J <14, used by these authors). We have fitted a power-law function to the observed distribution (dashed line in Fig. 4.8-middle panel), the best fit gives an index of about 3 (i.e., $\dot{M} \propto V_{exp}{}^{2.5}$) although the uncertainties associated to the fitting are important (±1).

4.6.5 Other trends

As shown in Sect. 4.5, we find a clear and expected correlation between the strength of the CO line emission, in particular, of the J=15-14 line ($F_{CO\ 15-14}$), with M_{tot} and $\dot{M}$ (Fig.4.7 and 4.8, respectively). The correlation found by us is in very good agreement with that reported recently by Lombaert et al., 2016a using a number of CO transitions observed with PACS to model the envelopes of sample of C-rich AGB CSEs with H_2O emission. The dependence with the distance to the sources of $F_{CO\ 15-14}$ and $M_{tot}/\dot{M}$ partially explain the observed trend; additionally, the line flux is proportional to the amount of mass in the emitting volume (eq. 3), although other factors, such as the opacity and the excitation temperature, have an important influence.

The influence of the excitation temperature in the resulting strength of the CO lines relative to the continuum becomes evident in Fig. 4.8-bottom panel, where we see a clear correlation between $F_{CO\,15-14}/PACS_{170}$ and T_{rot}, which are both distance independent parameters. We find that objects with the lowest values of T_{rot} show small line-to-continuum ($F_{CO\ 15-14}/PACS_{170}$) ratios. We have found from this work that post-AGBs and PNs have the most massive envelopes in our sample (>0.01-0.1 $M_{\odot}$), but in spite of this, they are relatively weak high-J CO emitters as a consequence of the relatively low excitation conditions prevailing in their envelopes (T_{rot}~200-300 K). Other factors, such as a different gas-to-dust mass fraction at different evolutionary stages, may also lie behind the observed trend.

TABLE 4.1: Results from our CO RD analysis (Sect.4.5), including double-fit (hot and warm) components for NML Tau, χ Cyg, π Gru, W Aql, and IRAS 17347-3139. Col. 1: Target name; col. 2: distance to the source (d); col. 3: expansion velocity of the gas (V_{exp}); col. 4: characteristic radius of the CO-emitting region adopted (r_{CO}); col. 5: rotational temperature (T_{rot}); col. 6: column density of CO (N_{col}); col. 7: total mass of H_2 within the CO-emitting volume (M_{tot}); col. 8: mass-loss rate ($\dot{M}$=M_{tot}×V_{exp}/r_{CO}); and col. 9: ratio between M_{tot} after and before the opacity correction was applied.

Target Name	d (pc)	V_{exp} (km/s)	r_{CO} (cm)	T_{rot} (K)	N_{col} (cm^{-2})	M_{tot} ($M_\odot$)	$\dot{M}$ ($M_\odot$ yr^{-1})	Correction$_{M_{H_2}}$
RR Aql	530	9.0	1×10^{15}	460±60	$(8.8 \pm 3.0)\times10^{17}$	$(2.3 \pm 0.8)\times10^{-5}$	7×10^{-7}	1.2
o Cet	110	8.1	6×10^{14}	530±20	$(2.6 \pm 0.3)\times10^{18}$	$(2.5 \pm 0.3)\times10^{-5}$	10^{-6}	1.6
W Hya	98	7.5	4×10^{14}	550±40	$(3.8 \pm 1.0)\times10^{18}$	$(1.6 \pm 0.4)\times10^{-5}$	9×10^{-7}	1.6
IRAS 20038-2722	197	5.4	4×10^{14}	500±20	$(1.4 \pm 0.2)\times10^{18}$	$(5.9 \pm 0.9)\times10^{-6}$	3×10^{-7}	1.4
T Cep	190	5.5	1×10^{15}	370±40	$(6.3 \pm 2.5)\times10^{17}$	$(1.7 \pm 0.7)\times10^{-5}$	3×10^{-7}	1.2
NML Tau	260	18.0	1×10^{15}	490±20	$(5.9 \pm 1.0)\times10^{18}$	$(1.6 \pm 0.3)\times10^{-4}$	9×10^{-6}	1.5
NML Tau	260	18.0	1×10^{15}	370±20	$(9.5\pm1.4)\times10^{18}$	$(2.5\pm0.4)\times10^{-4}$	1×10^{-5}	-
NML Tau	260	18.0	1×10^{15}	820±210	$(1.0\pm0.9)\times10^{18}$	$(2.7\pm2.4)\times10^{-5}$	2×10^{-6}	-
R Dor	59	5.5	4×10^{14}	520±20	$(1.8 \pm 0.2)\times10^{18}$	$(7.7 \pm 0.8)\times10^{-6}$	3×10^{-7}	1.5
TX Cam	380	18.5	2×10^{15}	240±10	$(4.4 \pm 0.7)\times10^{18}$	$(4.7 \pm 0.7)\times10^{-4}$	10^{-5}	1.5
X Her	137	6.5	4×10^{14}	570±50	$(8.0 \pm 1.8)\times10^{17}$	$(3.4 \pm 0.8)\times10^{-6}$	2×10^{-7}	1.2
IRAS 19474-0744	810	13.6	2×10^{15}	460±40	$(2.1 \pm 0.5)\times10^{18}$	$(2.3 \pm 0.5)\times10^{-4}$	5×10^{-6}	1.3
T Mic	290	4.8	6×10^{14}	550±30	$(1.8 \pm 0.3)\times10^{18}$	$(1.7 \pm 0.3)\times10^{-5}$	4×10^{-7}	1.6
R Cas	176	10.5	1×10^{15}	400±20	$(1.2 \pm 0.1)\times10^{18}$	$(3.1 \pm 0.4)\times10^{-5}$	10^{-6}	1.2
EP Aqr	114	10.0	4×10^{14}	470±20	$(1.3 \pm 0.2)\times10^{18}$	$(5.6 \pm 0.6)\times10^{-6}$	4×10^{-7}	1.2
NML Cyg	620	33.0	2×10^{15}	470±20	$(1.2 \pm 0.2)\times10^{19}$	$(1.3 \pm 0.2)\times10^{-3}$	7×10^{-5}	1.6
χ Cyg	149	8.5	6×10^{14}	620±10	$(3.7 \pm 0.3)\times10^{18}$	$(1.2 \pm 0.1)\times10^{-5}$	5×10^{-7}	1.6
χ Cyg	149	8.5	6×10^{14}	480±20	$(4.9 \pm 0.4)\times10^{18}$	$(1.6 \pm 0.2)\times10^{-5}$	7×10^{-7}	-
χ Cyg	149	8.5	6×10^{14}	690±30	$(2.3 \pm 0.2)\times10^{18}$	$(7.3 \pm 1.5)\times10^{-6}$	3×10^{-7}	-
π Gru	152	10.0	6×10^{14}	670±20	$(4.0 \pm 0.6)\times10^{18}$	$(1.3 \pm 0.2)\times10^{-5}$	7×10^{-7}	1.4
π Gru	152	10.0	6×10^{14}	460±20	$(7.1 \pm 1.1)\times10^{18}$	$(2.3 \pm 0.2)\times10^{-5}$	10^{-6}	-
π Gru	152	10.0	6×10^{14}	870±30	$(1.3 \pm 0.2)\times10^{18}$	$(4.2 \pm 0.7)\times10^{-6}$	2×10^{-7}	-

W Aql	395	16.5	2×10^{15}	550±10	$(2.9 \pm 0.2)\times10^{18}$	$(1.0 \pm 0.1)\times10^{-4}$	3×10^{-6}	1.2
W Aql	395	16.5	2×10^{15}	440±10	$(3.9\pm0.3)\times10^{18}$	$(1.4\pm0.1)\times10^{-4}$	3×10^{-6}	-
W Aql	395	16.5	2×10^{15}	570±20	$(2.3\pm0.6)\times10^{18}$	$(7.9\pm2.0)\times10^{-5}$	2×10^{-6}	-
WX Psc	700	19.3	2×10^{15}	560±70	$(3.2 \pm 1.0)\times10^{18}$	$(3.3 \pm 1.0)\times10^{-4}$	10^{-5}	1.0
V1300 Aql	620	16.5	2×10^{15}	510±20	$(1.8 \pm 0.2)\times10^{18}$	$(1.9 \pm 0.2)\times10^{-4}$	5×10^{-6}	1.0
OH 231.8+4.2	1500	15.0	4×10^{15}	240±40	$(3.5 \pm 2.5)\times10^{18}$	$(1.5 \pm 1.0)\times10^{-3}$	2×10^{-5}	1.0
OH 26.5+0.6	1370	17.0	4×10^{15}	410±100	$(2.4 \pm 1.8)\times10^{18}$	$(1.0 \pm 0.8)\times10^{-3}$	10^{-5}	1.0
IRAS 22036+5306	4000	30.0	6×10^{16}	280±20	$(1.0 \pm 0.2)\times10^{17}$	$(9.6 \pm 2.1)\times10^{-3}$	2×10^{-5}	1.1
AFGL 6815	2900	15.0	6×10^{16}	310±20	$(1.9 \pm 0.4)\times10^{17}$	$(1.8 \pm 0.3)\times10^{-2}$	10^{-5}	1.1
IRAS 17347-3139	3680	25.0	6×10^{16}	630±20	$(5.3 \pm 0.7)\times10^{17}$	$(5.0 \pm 0.6)\times10^{-2}$	7×10^{-5}	1.0
IRAS 17347-3139	3680	25.0	6×10^{16}	480±10	$(8.2\pm0.4)\times10^{17}$	$(7.8\pm0.4)\times10^{-2}$	10^{-4}	-
IRAS 17347-3139	3680	25.0	6×10^{16}	820±40	$(1.7\pm0.4)\times10^{17}$	$(1.6\pm0.4)\times10^{-2}$	2×10^{-5}	-
NGC 6302	1170	10.0	6×10^{16}	280±10	$(1.2 \pm 0.2)\times10^{17}$	$(1.2 \pm 0.2)\times10^{-2}$	6×10^{-6}	1.1
NGC 6537	1500	18.0	6×10^{16}	200±10	$(1.5 \pm 0.4)\times10^{17}$	$(1.4 \pm 0.4)\times10^{-2}$	10^{-5}	1.0

4.7 Conclusions

In this chapter we have analysed *Herschel*-PACS 1D spectra of 26 non C-rich evolved low-to-intermediate mass stars, in different evolutionary stages from the AGB to the PN phase, contained in the THROES catalogue (`https://throes.cab.inta-csic.es`). Our sample includes 23 O-rich and 3 S-type objects.

RDs using high-excitation CO v=0 rotational emission lines, with upper-level energies $E_{\rm u}$~580 to 5000 K, have been created to study the warm inner layers of the CSEs of these objects. We derive fundamental physical parameters such as: rotational temperatures ($T_{\rm rot}$), total molecular mass in the CO-emitting layers ($M_{\rm tot}$) and average mass-loss rates during the ejection of these layers ($\dot{M}$).

The rotational temperatures are found to vary from ~200 K to ~700 K. For AGB and OH/IR stars, which represent ~80% of our sample, the rotational temperatures are around $T_{\rm rot}$~500 K and systematically larger than for the most evolved objects, post-AGBs and PNs ($T_{\rm rot}$~200 K). These temperatures are one order of magnitude higher than estimated from past low-J CO line studies of the outer envelope. This is expected as, in the PACS far-infrared range, we are tracing gas that is closer to the central star ($\approx 10^{15}$ cm for AGBs and $\approx 10^{16}$ cm for post-AGBs and PNs).

The total mass of the inner CSE regions where the PACS CO lines arise ranges from $M_{\rm tot} \approx 10^{-6}$ to 10^{-2} $M_{\odot}$ in our sample, with the most evolved objects being the most massive. The values of $M_{\rm tot}$ found in this work are typically 100 to 1000 times lower than the total envelope mass obtained from previous low-J CO line studies.

The mass-loss rates estimated are in the range $\dot{M} \approx 10^{-7}$-$10^{-4} M_{\odot}$ yr^{-1}, in agreement (within uncertainties) with values found in the literature. Essentially, the data in this study do not show evidence of time-variation in the mass-loss rate over the probed time span of the envelope formation. To properly study the mass-loss history of evolved stars, a more detailed radiative transfer analysis is needed.

For some strong CO emitters in our sample (NML Tau, χ Cyg, W Aql, NML Cyg and IRAS 17347−3139) a double temperature (hot and warm) component is inferred. The temperatures of the warm and hot components are ~400-500 K and ~600-900 K, respectively. The mass of the warm component (~10^{-5}-$8\times10^{-2} M_{\odot}$) is always larger than that of the hot component, by a factor ~2-10.

The warm-to-hot M and $T_{\rm rot}$ ratios in our sample of AGBs are correlated and are consistent with an average temperature radial profile of $\propto r^{-0.5\pm0.1}$, that is, slightly shallower than in the outer envelope layers, in agreement with recent studies.

We have explored the distributions of the different magnitudes and physical parameters of these objects and if any trends exist. We find that $M_{\rm tot}$, and $\dot{M}$ are both anticorrelated with $T_{\rm rot}$. This is interpreted as a combination of two different processes: CO line cooling, heating due to the friction between dust and gas and opacity effects. Previous works have also reported similar trends based on low-J CO line observations.

A strong correlation has been found, also, between $M_{\rm tot}$ and $V_{\rm exp}$, particularly for AGB stars. This correlation is also present in the $\dot{M}$ vs. $V_{\rm exp}$ distribution, as expected. This trend, which is observed in past studies using low-J CO transitions, is consistent with the wind acceleration mechanism, found in AGBs, being more efficient in the more luminous and massive stars.

4.8 Extra content. Determination of $r_{\rm CO}$, and Non-LTE discussion

4.8.1 The characteristic radius of the CO-emitting volume.

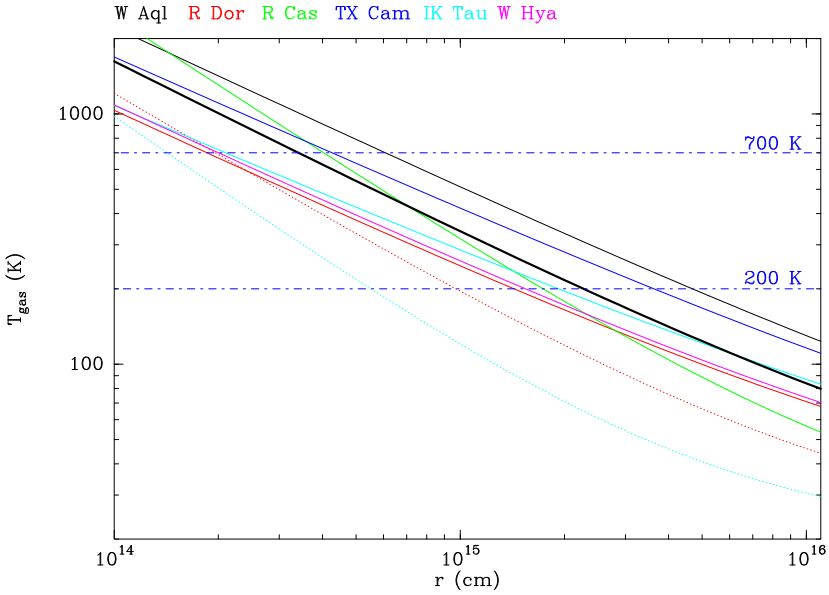

FIGURE 4.11: Power-law radial distribution of the gas kinetic temperature estimated from non-LTE excitation and radiative transfer models of the CO emission in a number of AGB envelopes (indicated at the top of the box using the same colour for the temperature laws) from the literature. References: Van de Sande et al., 2018; Maercker et al., 2016b; Khouri et al., 2014; Decin et al., 2010. The solid and dotted lines of R Dor and IK Tau are different temperature profiles derived by different authors (solid from Maercker et al., 2016b, and dotted from Van de Sande et al., 2018 (R Dor) and Decin et al., 2010 (IK Tau)). The thick black line is an average temperature law.

In this appendix, we provide a more detailed description of the procedure that we have followed to decide on a 'characteristic' radius of the CO-emitting volume ($r_{\rm CO}$) to be used to compute, and correct for, the CO line opacities (§ 4.4.1) and to obtain an estimate of the mean mass-loss rate of our targets (§ 4.5.2).

For AGB CSEs (also including OH/IRs), a first estimate of the size of the CO-emitting volume is derived using the envelope temperature structure estimated from detailed non-LTE excitation and radiative transfer calculations in the literature. These exist for many AGB CSEs using low-J CO transitions (typically $J_{\rm u}\lesssim$6), and, for more reduced samples, also using certain CO transitions from higher J levels.

In Fig. 4.11 we show temperature power-law radial profiles in the form

$T(r)=T_i\times(\frac{r}{R_i})^{\alpha}$

that have been deduced in a number of previous works (references are given in the figure caption) for the *few* targets in our sample that include at least one high-J CO line observed with any of the three *Herschel* instruments (HIFI, SPIRE, or PACS). As we see in this figure, the full range of rotation temperatures deduced from our RD analysis, T_{rot}~200-700 K (§ 4.5), is consistent with the bulk of the PACS CO emission studied here arising from layers between ~2×10^{14} and ~5×10^{15} cm, if we take together all the $T(r)$ distributions in Fig. 4.11 (coloured lines), or between ~3×10^{14} and *sim*3×10^{15} cm, if we use an average $T(r)$ power-law (thick black line, in Fig. 4.11). The quadratic mean of these two ranges is r_{CO}~10^{15} cm, which we uniformly use as the reference value in most AGB stars to compute M_{tot}, T_{rot}, and $\dot{M}$ (but see more details below). Since the radius is, in any case, uncertain, we offer additional estimates of these parameters for a larger range of radius around the default r_{CO} (Appendix C). As we will see next, for the lowest (larger) mass-loss rate AGB stars in our sample, the characteristic CO-radius could be a factor of ~2-4 smaller (larger) than the r_{CO}~10^{15} cm reference value.

In the following, we perform a case-by-case RD analysis of three targets (R Dor, W Aql, and TX Cam) that are representative of three main mass-loss regimes in our sample: low, medium and high ($\dot{M}\approx10^{-7}$ $M_\odot$ yr^{-1}, $\approx10^{-6}$ $M_\odot$ yr^{-1}, and $\gtrsim10^{-5}$ $M_\odot$ yr^{-1}, respectively) and for which detailed non-LTE excitation and radiative transfer studies of the CO emission including some mid-to-high J_u-CO transitions exist in the literature. The purpose is twofold: 1) to better illustrate our method to constrain r_{CO} in our sample (needed to decide on a plausible reference value for a uniform analysis), and 2) to compare the mass-loss rates from our approximate RD analysis with those computed using more sophisticated modelling tools.

R Dor: Precise CO-modelling studies of the molecular envelope of this object, including CO transitions up to J_u=16 (E_u=750 K), have been carried out by Maercker et al., 2016b and Van de Sande et al., 2018. (References to other molecular line studies using lower-J_u transitions are given in Table 2). The gas temperature structure deduced from these works, which use the same set of CO lines, are not fully coincident (dotted and solid red lines in Fig. 4.11). Van de Sande et al., 2018 claim that their model achieves a better fit to more lines, and therefore, we adopt the $T(r)$ power-law determined by these authors, with an exponent α=0.65.

Our general procedure to determine an optimal/acceptable value of r_{CO} is as follows. From a linear fit to the CO datapoints in the RD diagram (dotted line and black dots, respectively, in the top panel of Fig. 4.12) we find a first or iteration-zero estimate of $T_{rot}(i=0)$ before any opacity correction is applied. Assuming that $T_{rot}(i=0)$~570 K represents (or is close to) the average gas temperature within the CO-emitting volume and using the $T(r)$ function depicted in Fig. 4.11, we derive an initial value of $r_{CO}(i=0)$~2.5×10^{14} cm. We use this radius to compute the opacity of the different transitions. In this case, we obtain $\tau_{14\rightarrow13}$ ~1.8 for the CO J=14-13 line, and smaller for higher-J lines (see Eq. 4). After applying the opacity correction, through the frequency-dependent factor $C_\tau=\tau/(1-e^{-\tau})$, a second linear fit to the opacity-corrected datapoints is performed (pink line and dots, respectively, in top panel of Fig. 4.12), resulting in a new estimate of $T_{rot}(i=1)$. The latter always is smaller than the

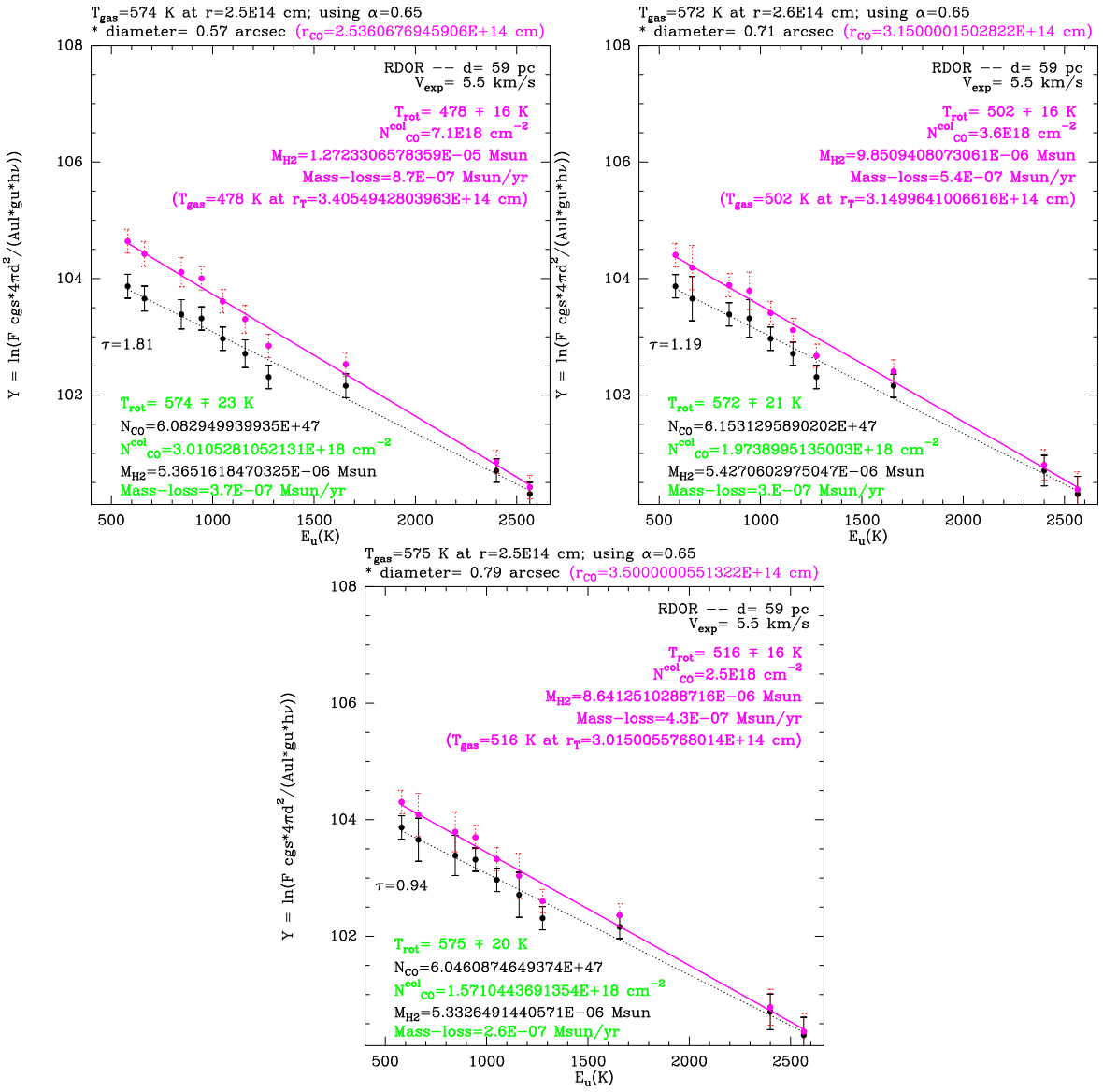

FIGURE 4.12: Rotational diagrams of the low mass-loss rate O-rich AGB star R Dor to illustrate the different steps that we have routinely followed to constrain r_{CO} in our sample. The bottom panel shows an optimal value of r_{CO} according to our temperature-opacity combined criteria (full details are given in the text, § 4.8.1).

iteration-zero value because after applying the C_τ correction, the slope of the RD increases, as a direct result of the frequency-dependence of C_τ and the typical values of T_{rot} that we measure in our sample. Comparing again the value of T_{rot}(i=1)~480 K with the $T(r)$ law, we deduce a *new* value of $r_{CO}(i=1)$~3.4×10^{14} cm, where the gas would have such a temperature.

This exercise indicates that an intermediate value between r_{CO}(i=0) and r_{CO}(i=1) is needed to reach full consistency between the r_{CO} value used for the opacity correction and the one that reproduces the opacity-corrected T_{rot} derived (according to the $T(r)$ adopted). In the particular case of R Dor, we find a *perfect* match between r_{CO}(i=0) and r_{CO}(i=1) for r_{CO}~3.15×10^{14} cm (leading to T_{rot}(i=1)~500 K at this radius – Fig. 4.11, middle panel).

An additional constrain to the radius is obtained from the fact that, as already explained in § 4.4, the deepest layer traced by the observed CO emission must be such that τ <1. In order to satisfy this moderate-opacity condition, a value of r_{CO} slightly larger than the 'perfect-match' r_{CO} above is preferred. For R Dor, a value of r_{CO}~3.5×10^{14} cm satisfies the opacity criteria ($\tau_{14\rightarrow13}$ <1) and is, within uncertainties, still fully consistent with the radius where the final value of T_{rot} is attained, adopting the $T(r)$ law from previous works – Fig. 4.12, bottom panel). The mass-loss rate that results adopting this value of the radius r_{CO}~3.5×10^{14} cm, which guarantees line opacities lower than 1, is $\dot{M}$~4×10^{-7} $M_\odot$ yr^{-1}.

In this and in most targets, in principle we cannot rule out a larger radius (leading to even lower line opacities), even if T_{rot} deviates from the gas temperature predicted at that radius based on the $T(r)$ law adopted. This is because there is no guarantee that the adopted $T(r)$ is a 100% accurate representation of the real temperature structure in these inner-wind regions and because T_{rot} may not be either a 100% accurate representation of the temperature of the gas (especially for low mass-loss rate objects). For R Dor, if we adopt the default radius of r_{CO}~1×10^{15} cm previously established as a reasonable characteristic radius for the overall AGB class, we deduce a temperature of T_{rot}~570 K and a mass-loss rate of $\dot{M}$~1×10^{-7} $M_\odot$ yr^{-1}.

For R Dor, the mass-loss rates derived from Van de Sande et al., 2018 and Maercker et al., 2016b from their non-LTE CO excitation and radiative transfer analysis are very similar in both cases (~2×10^{-7} $M_\odot$ yr^{-1}) and lie within the range of values estimated by us from our simple RD approach and the *plausible* range of r_{CO} explored, $\dot{M}$~[1-4]$\times10^{-7}$ $M_\odot$ yr^{-1}.

W Aql: Non-LTE excitation and radiative transfer of the CO emission, including CO transitions up to J_u=25 (E_u=1796 K), have been carried out for this S-type AGB star by Danilovich et al., 2014. The mass-loss rate obtained in this work is $\dot{M}$~4×10^{-6} $M_\odot$ yr^{-1} (as quoted in Table 2, where we provide additional references to other molecular line studies using lower-J_u transitions). Danilovich et al., 2014 derive the gas and dust temperature profile in the 2×10^{14}-10^{17} cm envelope layers (see their Fig. 3). Both the gas and dust temperatures are quite similar throughout the whole envelope, with the dust being slightly cooler than the gas below 2×10^{15} cm (i.e. the region sampled by the PACS CO data). In this region, the gas and dust temperatures do not differ by more than 50% (in particular, at ~10^{15} cm, values of T_{dust}~400 K and T_{kin}~500 K are expected).

In Fig. 4.11 we reproduce the gas temperature structure deduced by Danilovich et al.,

2014; the exponent of this power-law function is α=0.65. We have used this profile to constrain r_{CO} following the same procedure explained in the previous paragraphs for R Dor. As we can see in the left panel of Fig. 4.13, a radius of r_{CO}~1×10^{15} cm produces a perfect match between the final (opacity-corrected) temperature derived (T_{rot}~ 500 K) and the radius where this temperature is expected (r_T) according to Danilovich et al., 2014. This value of the radius, however, results in line opacities larger than desirable and a mass-loss rate of $\dot{M}$~9×10^{-6} $M_\odot$ yr^{-1}. In this case, the radius that produces $\tau_{14\rightarrow13}$ <1 and simultaneously satisfies (within uncertainties) the temperature criteria is r_{CO}~1.4×10^{15} cm (right panel of Fig. 4.13. This results in a somewhat smaller mass-loss rate of $\dot{M}$~5×10^{-6} $M_\odot$ yr^{-1}, which is in excellent agreement with previous estimates.

IK Tau: The physical properties of the circumstellar gas, including the temperature, velocity and density structure, have been determined from the radiative transfer modelling of the multi-transitional (sub)millimetre CO line observations by Decin et al., 2010 and Maercker et al., 2016b. The temperature distributions from these two works differ substantially (as for R Dor) and are shown in Fig. 4.11 (solid and dotted cyan lines).

Adopting the α=0.6 distribution derived by Decin et al., 2010, we find that a radius of r_{CO}~5×10^{14} cm produces a perfect match between the final (opacity-corrected) value of the temperature (T_{rot}=420 K) and the radius r_T where this temperature is expected, however, it results in opaque lines (Fig. 4.13, bottom-left). For IK Tau, a radius of r_{CO}~9×10^{14} cm or larger is needed to meet the $\tau_{14\rightarrow13}$ <1 criteria (Fig. 4.13, bottom-rigth). This results in a somewhat smaller mass-loss rate of $\dot{M}$~1×10^{-5} $M_\odot$ yr^{-1}, also in agreement with the range of values from previous estimates ($\dot{M}$~[0.2-3.5]×10^{-5} $M_\odot$ yr^{-1}, Table 2).

Rest of the targets: We have followed this procedure to constrain the range of r_{CO} values that are plausible (based on our opacity- and temperature- combined criteria) for each target individually. Whenever a $T(r)$ distribution was available in the literature (this happened for a few targets, see Fig. 4.11) we used that specific law, and for the rest we used a mean $T(r)$ distribution represented by the thick black line in Fig. 4.11 as a guide.

Remarks on the temperature profiles: The $T(r)$ profiles used and represented in Fig. 4.11, although obtained from detailed non-LTE excitation and radiative transfer models of the CO emission, are not free from large uncertainties. This is denoted by the discrepancies between the temperature structure derived for the same targets when computed by different teams (notable cases are R Dor and IK Tau, in spite of these being among the most studied and best characterized AGB envelopes). Moreover, the power-law distribution is only an approximation to the real temperature structure. Indeed, the latter can deviate significantly from a simple power-law in some regions, in particular, $T(r)$ can have multiple-slopes as well as local minima and maxima as shown in De Beck et al., 2010a (see their Fig. 9) and Maercker et al., 2016b (see their Fig. 5).

Additionally, given the moderate range of J_u in the CO transitions predominantly modelled and published to date, the curves represented in Fig. 4.11 are expected to be most reliable in the intermediate-to-outer envelope layers, beyond ~10^{15} cm. Recently, Lombaert et al., 2016a performed non-LTE excitation and radiative transfer models of a sample of C-rich AGB CSEs using a selection of seven high-J CO transitions observed with PACS and SPIRE covering levels from J_u=15 to 38, that is, higher than in the studies represented in Fig. 4.11.

One interesting result from this study is that the temperature of the gas falls off less steeply, with a power-law exponent close to α ~0.4-0.5, in the inner-warm envelope regions sampled by these high-J CO transitions. This is indeed consistent with the crude estimate of α deduced in this work by comparing the hot and warm envelope components for a few targets in our sample (see Sect. 4.6). More dedicated non-LTE excitation and radiative transfer models of the high-J CO emission in larger samples is needed to confirm this result and to obtain a more precise description of the temperature distribution in these inner and warm regions of the envelopes of AGB stars.

Final remark on the reference values of r_{CO}: It is evident that the value of r_{CO} derived using a temperature criteria is very model-dependent since it fully relies on $T(r)$ and on T_{rot} being a perfect representation of T_{kin}. For this reason, we prefer to be cautious and, after having explored carefully the range of plausible r_{CO} values based on a temperature-opacity combined criteria for all targets, to use a set of (order-of-magnitude) estimates of r_{CO} for the whole sample, rather than using the best-match radius individually found for each target. As shown in Table 2, we chose a reference radius: r_{CO}=1×10^{15}cm for most AGB CSEs, r_{CO}=[2-4]×10^{15} cm for high-$\dot{M}$ AGB CSEs (>1×10^{-5} $M_{\odot}$ yr^{-1}) and r_{CO}=[4-6]×10^{14} cm for low-$\dot{M}$ AGB CSEs (<1×10^{-6} $M_{\odot}$ yr^{-1}).

As discussed in Sect. 4.4, the temperature profile in the molecular envelopes of post-AGB objects and PN is extremely poorly characterized due to a much more limited number of CO emission cartography and, most importantly, modelling studies (especially using high-J CO transitions). Based on the systematically low values of T_{rot} in post-AGB objects and PNs found in this work (~200 K) as well as their generally larger dimensions, we chose a reference value of the radius of r_{CO}=6×10^{16} cm in these cases (Table 3), although we explored a larger range of r_{CO} (examples are given in Figs. C.1 and C.2). This range of r_{CO} resulted in negligible RD opacity corrections in all these sources.

4.8.2 Non-LTE effects

The rotational diagram (RD) method is a classical and widely used line-emission analysis technique useful to obtain a first estimate of the excitation temperature and mass of the gas in the line emitting region (Goldsmith and Langer, 1999; Justtanont et al., 2000). As explained in Section 4.4, it is based on two major assumptions: optically thin emission and excitation under LTE conditions. A canonical opacity correction factor, C_{τ}, has been included to take into account moderate optical depth effects (§ 4.4). Here, we examine whether non-LTE excitation effects are expected to be significant in our sample and, if this is the case, what is the impact on the values of M and T_{rot} inferred from our RD analysis. We present several arguments that suggest that although small LTE deviations cannot be ruled out (particularly, in the lowest mass-loss rate objects), we expect a negligible impact on the derived values of M. Additionally, the double slope in the RD observed for some targets predominantly reflects the temperature stratification in the emitting layers.

A first simple evaluation of LTE deviations is obtained from the comparison of the critical densities of the CO transitions studied here and the densities expected in the CO-emitting regions in our sample. For most (80%) of our targets, the far-IR CO transitions detected and

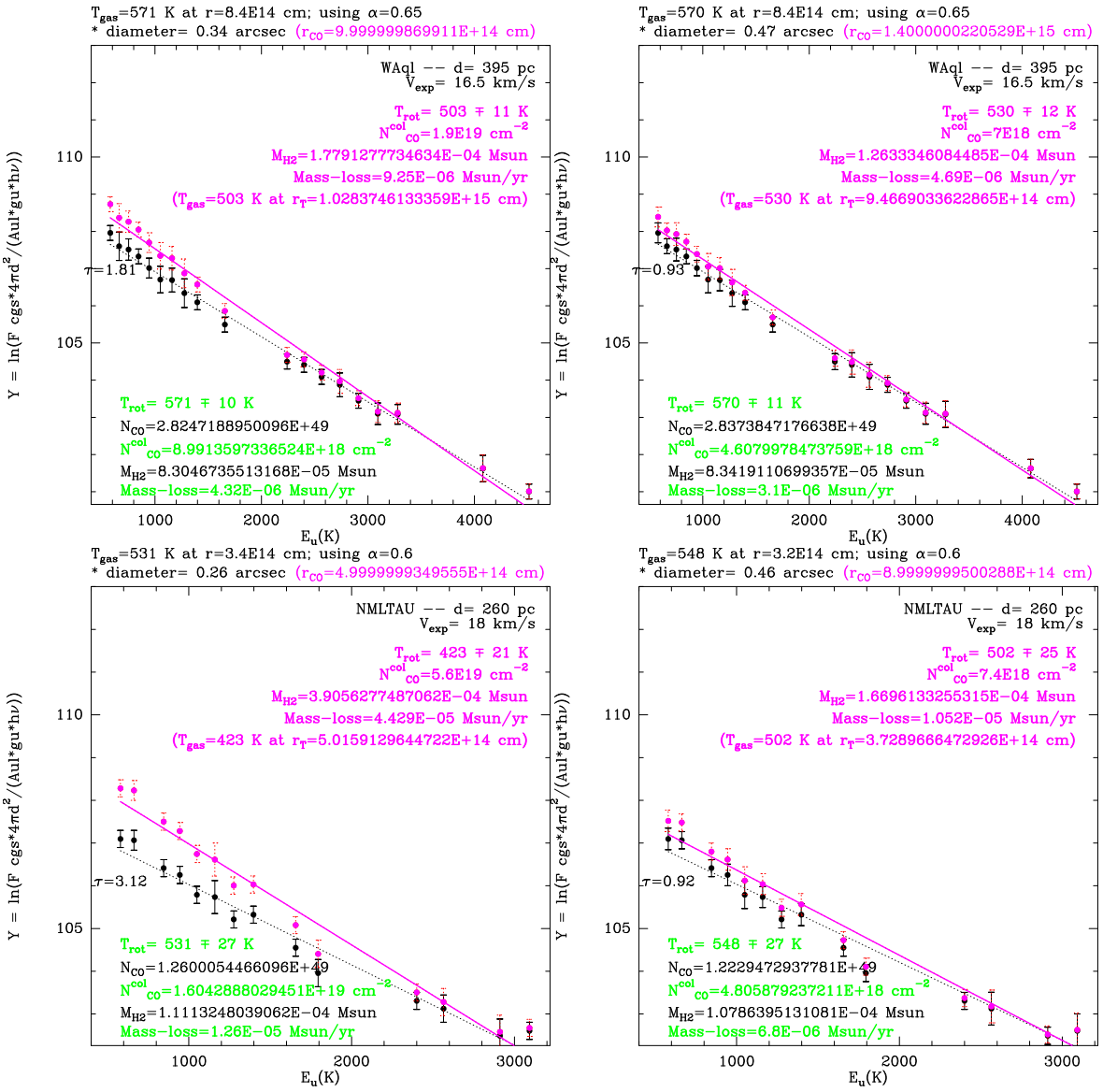

FIGURE 4.13: Rotational diagram of W Aql and NML Tau (bottom). **Left)** Results of the RD for r_{CO}=1×10^{15} cm, which results in a perfect match between the opacity- and temperature-radius (labelled as r_{CO} and r_T, respectively, in the plot) but results in an undesired large opacity correction, $\tau_{14\rightarrow13}$ >1. **Right)** Results of the RD for r_{CO}=1.4×10^{15} cm, which satisfies our $\tau_{14\rightarrow13}$ <1 criteria.

used in our RD analysis arise from states ~500-2000 K above the ground, i.e. with upper-level rotational quantum numbers J_u~14-27. According to most recent collisional rate coefficients computed by Yang et al., 2010[3], these transitions have critical densities of n_{crit}~5×10^5 and 3×10^6 cm^{-3}, for J_u=14 and J_u=27, respectively, for a range of temperatures consistent with our estimates, ~200 and 700 K, see Fig. 10 in Yang et al., 2010.

From the lowest to the highest mass-loss rate objects in our sample ($\dot{M}$~2×10^{-7}-1×10^{-4} $M_\odot$ yr^{-1}, Fig. 4.8), densities of $n_{H_2}\gtrsim10^6$-10^8 cm^{-3} are expected at the typical radius adopted (from r_{CO}~4×10^{14} to r_{CO}~[1-4]$\times10^{15}$ cm, respectively – see Table 2, Appendix B) consistent with CO population levels predominantly thermalized in most cases.

As already pointed out in pioneering studies of ISO-LWS observations of high-J CO lines using the RD approach, see Justtanont et al. 2000, the mere fact that we detect CO J_u~14 to 27 transitions together with a roughly linear distribution in the RD is a hint of high-density gas and level populations in this range of J_u close to thermal equilibrium.

For a few targets, we also detect CO lines with upper-levels above J_u>27, which have critical densities of $n_{crit}\approx10^6$-10^7 cm^{-3} and, therefore, some LTE deviations cannot be rule out (but we note that these transitions presumably arise from regions closer to the center, within the dust formation layers).

The simple calculations above are indeed corroborated by non-LTE excitation and radiative transfer analysis computations of a selection of high-J CO transitions observed with PACS (from J_u=14 to 38) on a sample of C-rich AGB CSEs by Lombaert et al., 2016a. These authors conclude that over the broad range of mass-loss rates studied in their work, $\dot{M}$~10^{-7}-2×10^{-5} $M_\odot$ yr^{-1}, which is comparable to the range in our sample, the CO molecule is predominantly excited through collisions with H_2, with a minor effect of far-IR radiative pumping due to the dust radiation field.

We stress that even under non-LTE conditions, for a simple diatomic molecule like CO, the RD method provides a reliable measure of the total mass within the emitting volume. This is because, although T_{rot} may deviate from the kinetic temperature, T_{kin}, in regions where the local density is lower than the critical densities of the transitions considered, it does describe quite precisely the molecular excitation (i.e. the real level population). To test this idea and to check the reliability of our analysis, we have compared our values of M and $\dot{M}$ with those obtained from state-of-the-art line excitation and radiative transfer models of high-J CO transitions, sometimes including PACS data, performed by other authors in objects of our sample. To our knowledge, these have been published for a total of 6 sources: R Cas, R Dor, TX Cam, NML Tau, W Hya and W Aql (see Van de Sande et al., 2018; Maercker et al., 2016b; Danilovich et al., 2014; Khouri et al., 2014 and references therein). For these objects, the CO emission over a broad range of E_u has been modelled to derive the temperature, density and velocity profile across their ~10^{14}-10^{17} cm CSE layers, as well as the mass-loss rate of the stellar wind. As shown in Sect. 4.5, discrepancies between our values of $\dot{M}$ and those obtained from comprehensive non-LTE radiative transfer analysis are very small, always within 50%, demonstrating that the simple and approximate RD approach and the assumptions (e.g. the adopted size of the emitting layers) used in this work yield reasonable results.

[3]Also available from the Leiden Lambda Database web page.

An additional test of the reliability and uncertainties of the RD method is presented in Chapter 5, where we perform our RD analysis using multi-epoch CO-PACS spectra for the C-rich AGB star IRC+10216. This object shows prominent line variability (mainly of high-excitation transitions of CO and other molecules) denoting radiative farIR (ro-vibrational) pumping via the dust radiation field modulated by the stellar pulsation (Cernicharo et al., 2014; Teyssier et al., 2015a; He, Dinh-V-Trung, and Hasegawa, 2017a). This object, thus, serves as a benchmark for testing the effect of radiative versus collisional excitation and its impact of the values of M and $T_{\rm rot}$ derived from our RD analysis. We corroborate that, in spite of strong CO line flux variations and confirmed changes in the relative level population, the total number of emitting molecules (adding up all levels) from the RD analysis remains constant (within uncertainties, <15%) at multiple epochs. This is true for both the warm and hot components (both identified in IRC+10216) and, thus, for the single-fit value of M.

We also find that line variability has also a small impact on the value of $T_{\rm rot}$ derived at multiple epochs in IRC+10216. The values of $T_{\rm rot}$ from the single-fit and warm component (using $J_{\rm u}$<27 transitions) remain essentially constant within uncertainties, consistent with negligible impact of non-LTE effects (if any). The highest-excitation CO lines ($J_{\rm u}$>27) show stronger variations and, as a consequence, the variations of $T_{\rm rot}$ for the hot component are larger, of $\lesssim \pm 15\%$ about the average, maybe denoting some repercussion of LTE deviations on $T_{\rm rot}$ in this case.

Although it is improbable given our previous discussion, let us now consider whether the double slope in the RD diagram found for a few objects in our sample could predominantly result from non-LTE effects, with $T_{\rm rot}$ deviating most significantly from $T_{\rm kin}$ for the highest-J CO transitions, and what would be the implications in this case.

Among our targets (O-rich and S-type), we find a double-$T_{\rm rot}$ component in a total of five sources, covering a broad range of mass-loss rates, from $\dot{M}\sim2\times10^{-7}$ to 8×10^{-5} $M_{\odot}$ yr^{-1}. The mass-loss rate distribution of these sources is the same as the sources for which only one $T_{\rm rot}$ component is found. Moreover, we do not find any correlation between $\dot{M}$ and the properties of the hot and warm components (also including C-rich targets, see e.g. Fig. 4.14), which makes improbable the double $T_{\rm rot}$ component being predominantly a non-LTE effect (expected to be most remarkable in low mass-loss rate objects).

Moreover, to explain the observed double slope as a purely non-LTE effect, two conditions need to be simultaneously met in all double-$T_{\rm rot}$ targets. First, a very specific value of the number density, in a narrow range around $\sim10^{7}$ cm^{-3}, is needed to have $J_{\rm u}$<27 levels close to thermal equilibrium but $J_{\rm u}$>27 levels deviating perceivably from LTE (this would generate the double slope in the RD diagram). Second, a strong background radiation source $T_{\rm bg}$>$T_{\rm kin}$ is required to reproduce a $T_{\rm rot}$ that is higher for $J_{\rm u}$>27 transitions than for $J_{\rm u}$<27 lines. Dust mixed with the gas in the CO-emitting volume and heated by the stellar radiation to 800 K could produce the required $T_{\rm bg}$. If this is the case, then it would also imply similarly high gas temperatures in the emitting region since the difference between the gas and dust temperature across these inner wind layers is expected to be moderate (of <100 K) and to follow a similar radial dependence based on detailed dust-continuum and non-LTE radiative transfer CO emission models (e.g. for W Aql, $T_{\rm kin}\sim T_{\rm dust}\sim$ 300 K at $r_{\rm CO}=2\times10^{15}$ cm Danilovich et al., 2014). In the extreme case (e.g. maybe for very low mass-loss rate objects with densities <10^{6} cm^{-3}) that $T_{\rm rot}$ is totally decoupled from $T_{\rm kin}$ but very close to $T_{\rm bg}$ for all

transitions from J_u=14 to 40, then the double-slope of the RDs would most likely reflect the stratification of the *dust* temperature (rather than the gas) across the envelopes.

Summarizing, a minor impact of small LTE deviations on the values of M and $\dot{M}$ is expected, even for the targets with the lowest mass-loss rates, $\dot{M}\approx10^{-7}\ M_\odot\ \mathrm{yr}^{-1}$. The double slope of the RD is unlikely to be primarily due to large LTE deviations and points to a temperature stratification in the warm inner layers of the envelopes probed by PACS CO line emission. The temperature profile deduced is further discussed in Sect.4.6.1.

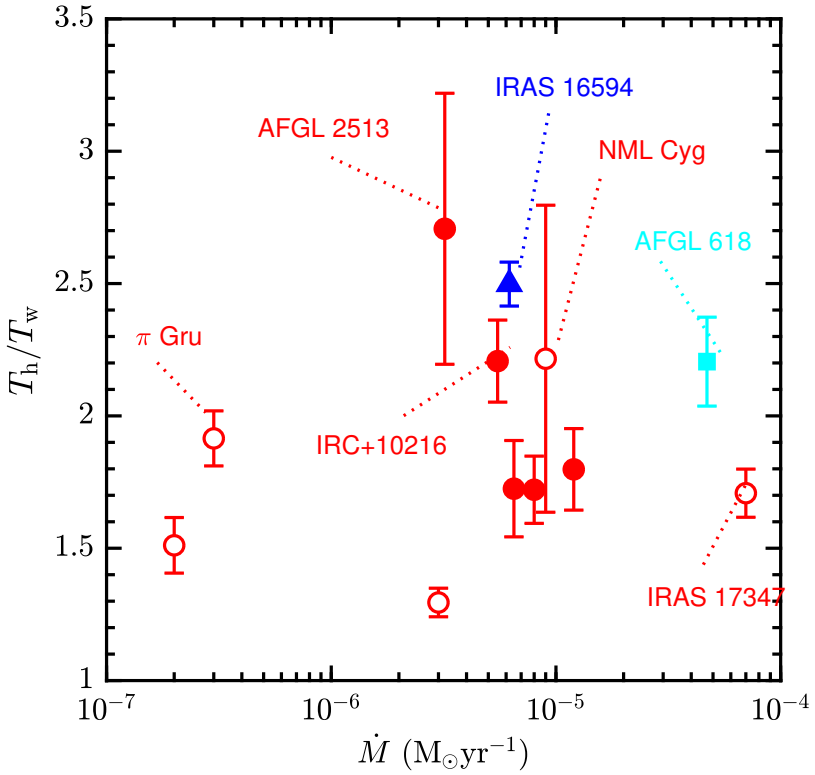

FIGURE 4.14: Ratio of the hot-to-warm rotational temperature versus the mass-loss rates for objects with a double-T_{rot}, component: targets from Chapter 4 are represented by open symbols, C-rich objects (from Chapter 5) are plotted using filled symbols.

4.9 Extra content. Tables

In this appendix we include those tables with relevant information about those objects studied in Chapter 4.

TABLE 4.2: Observations log

Target Name	Alternative Name	Class	RA (J2000) (hh:mm:ss.s)	Dec (J2000) (dd:mm:ss.s)	Obs IDs	Observing Date (yyyy-mm-dd)
RR Aql	-	O-rich AGB	19:57:36.1	-1:53:11.3	1342269414	2013-04-05
Omi Cet	Mira	O-rich AGB	2:19:20.8	-2:58:39.5	1342213286	2011-01-25
					1342213286	2011-01-25
W Hya	-	O-rich AGB	13:49:02.0	-28:22:03.5	1342212604	2011-01-14
					1342223808	2011-07-09
IRAS 20038-2722	V1943 Sgr	O-rich AGB	20:06:55.2	-27:13:29.8	1342268730	2013-03-29
					1342268569	2013-03-27
T Cep	-	O-rich AGB	21:09:31.8	68:29:27.2	1342246557	2012-06-01
NML Tau	IK Tau	O-rich AGB	3:53:28.8	11:24:22.6	1342203679	2010-08-28
					1342203680	2010-08-28
					1342203681	2010-08-28
R Dor	-	O-rich AGB	4:36:45.6	-62:04:37.8	1342197794	2010-06-05
					1342197794	2010-06-05
TX Cam	-	O-rich AGB	5:00:50.4	56:10:52.6	1342225855	2011-08-08
					1342225856	2011-08-08
X Her	-	O-rich AGB	16:02:39.2	47:14:25.3	1342197802	2010-06-05
					1342202120	2010-07-28
IRAS 19474-0744	GY Aql	O-rich AGB	19:50:06.3	-7:36:52.5	1342268638	2013-03-25
					1342268449	2013-03-26
T Mic	-	O-rich AGB	20:27:55.2	-28:15:39.8	1342268729	2013-03-29
					1342268788	2013-03-29
					1342269458	2013-04-06
R Cas	-	O-rich AGB	23:58:24.9	51:23:19.7	1342212576	2011-01-12
					1342212577	2011-01-12
EP Aqr	-	O-rich AGB	21:46:31.9	-2:12:45.9	1342270639	2013-04-20
					1342270684	2013-04-21

TABLE 4.2: Continued.

Target Name	Alternative Name	Class	RA (J2000) (hh:mm:ss.s)	Dec (J2000) (dd:mm:ss.s)	Obs IDs	Observing Date (yyyy-mm-dd)
NML Cyg	-	O-rich AGB	20:46:25.5	40:06:59.6	1342198174	2010-06-02
					1342198174	2010-06-02
χ Cyg	-	S-type	19:50:33.9	32:54:50.6	1342198176	2010-06-02
					1342198177	2010-06-02
π Gru	-	S-type	22:22:44.2	-45:56:52.6	1342210397	2010-11-28
					1342210398	2010-11-28
W Aql	-	S-type	19:15:23.4	-7:02:49.9	1342209731	2010-11-06
					1342209732	2010-11-07
WX Psc	IRC +10011	OH/IR star	1:06:26.0	12:35:53.0	1342202121	2010-07-28
					1342202122	2010-07-28
V1300 Aql	IRC -10529	OH/IR star	20:10:27.9	-6:16:13.6	1342269516	2013-04-07
					1342269910	2013-04-11
OH 231.8+4.2	-	OH/IR star	7:42:16.8	-14:42:52.1	1342196694	2010-05-19
					1342196695	2010-05-19
OH 26.5+0.6	V437 Sct	OH/IR star	18:37:32.5	-5:23:59.4	1342207776	2010-10-31
					1342207777	2010-10-31
IRAS 22036+5306	-	O-rich p-AGB	22:05:30.3	53:21:33.0	1342221882	2011-05-29
					1342221883	2011-05-29
AFGL 6815	Cotton Candy Nebula	O-rich p-AGB	17:18:19.9	-32:27:20.2	1342216629	2011-03-22
					1342216630	2011-03-22
IRAS 17347-3139	-	O-rich PN	17:38:01.3	-31:40:58.0	1342229696	2011-09-24
					1342229697	2011-09-24
NGC 6537	Red Spider Nebula	O-rich PN	18:05:13.1	-19:50:34.9	1342231322	2011-10-22
					1342231323	2011-10-22

TABLE 4.2: Continued.

Target Name	Alternative Name	Class	RA (J2000) (hh:mm:ss.s)	Dec (J2000) (dd:mm:ss.s)	Obs IDs	Observing Date (yyyy-mm-dd)
NGC 6302	Butterfly Nebula	O-rich PN	17:13:44.2	-37:06:15.9	1342230150	2011-10-05
					1342230151	2011-10-05

TABLE 4.3: Stellar and circumstellar, bibliographic, information for the objects of the sample.

Target Name	Variability	$T_{\rm eff}$ (K)	d (pc)	$v_{\rm exp}$ (km/s)	$\dot{M}_{\rm Bibliography}$ ($M_\odot$ yr^{-1})		References
RR Aql	Mira	2000	530	9.0	2.4×10^{-6} 9.1×10^{-7}	$(0.9,6.2)\times10^{-6}$	7, 34
Omi Cet	Mira	2200	110	8.1	2.5×10^{-7} 5×10^{-7}	$(0.2,1.2)\times10^{-6}$	18, 29, 34
W Hya	SRa	2200	98	7.0	1.5×10^{-7} 7.8×10^{-8} 10^{-7} 7×10^{-8} 8.1×10^{-8}	$(0.3,3.8)\times10^{-7}$	10, 12, 18, 23, 32, 34
IRAS 20038-2722	SRb	2200	197	5.4	9.9×10^{-8} 1.3×10^{-7}	$(0.7,3.9)\times10^{-7}$	7, 14, 32
T Cep	Mira	2400	190	5.5	9.1×10^{-8}	$(0.8,2.4)\times10^{-7}$	7
NML Tau	Mira	2700	260	19.0	5×10^{-6} 8×10^{-6} 2×10^{-5} 4.5×10^{-6} 10^{-5} 4.7×10^{-6} 4.4×10^{-6}	$(0.2,3.5)\times10^{-5}$	3, 10, 18, 19, 23, 27, 34
R Dor	SRb	2800	59	5.7	1.6×10^{-7} 2×10^{-7} 1.3×10^{-7} 6.9×10^{-8}	$(0.9,4.2)\times10^{-7}$	1, 3, 10, 23, 32, 34
TX Cam	Mira	2800	380	18.5	4×10^{-6} 5.5×10^{-6} 7×10^{-6} 6.5×10^{-6}	$(0.2,1.5)\times10^{-5}$	3, 10, 18, 23, 24
X Her	SRV	2800	137	6.5	1.5×10^{-7} 10^{-6}	$(0.8,2.6)\times10^{-7}$	14, 32, 34

TABLE 4.3: Continued.

Target Name	Variability	$T_{\rm eff}$ (K)	d (pc)	$v_{\rm exp}$ (km/s)	$\dot{M}_{\rm Bibliography}$ ($M_\odot$ yr^{-1})		References
IRAS 19474-0744	SR	2800	810 [4]†	13.6	4.1×10^{-6}	$(0.5,1.6)\times10^{-5}$	34, 35
T Mic	SRb	2800	290	4.8	8×10^{-8} 2.7×10^{-7}	$(1.9,6.9)\times10^{-7}$	29, 32, 34
R Cas	Mira	3100	176	10.5	8×10^{-7} 9×10^{-7} 4×10^{-7}	$(0.5,2.2)\times10^{-6}$	3, 10, 18, 23
EP Aqr	SRb	3200	114	10.0	3.1×10^{-7} 1.2×10^{-7}	$(0.9,5.0)\times10^{-7}$	8, 18
NML Cyg	SRc	3800	620	33	8.7×10^{-5} 1.8×10^{-6}	$(0.6,2.3)\times10^{-4}$	18, 35
χ Cyg	Mira	2000	149	8.5	7×10^{-7} 4×10^{-7} 2.4×10^{-7}	$(0.1,1.2)\times10^{-6}$	10, 17, 18, 20, 27
π Gru	SRb	2300	152	10.0	8.5×10^{-7} 7.7×10^{-7}	$(1.6,4.9)\times10^{-7}$	2, 7, 18
W Aql	Mira	2800	395	16.5	2.7×10^{-6} 1.3×10^{-5} 2.2×10^{-6} 2.5×10^{-6} 4×10^{-6}	$(0.2,1.2)\times10^{-5}$	10, 11, 18, 21, 28
WX Psc	Mira	2000	700	19.3	1.7×10^{-5} 4×10^{-5} 1.9×10^{-5} 6×10^{-6} 8.5×10^{-6}	$(0.4,6.9)\times10^{-5}$	10, 13, 18, 26, 35

TABLE 4.3: Continued.

Target Name	Variability	$T_{\rm eff}$ (K)	d (pc)	$v_{\rm exp}$ (km/s)	$\dot{M}_{\rm Bibliography}$ ($M_\odot$ yr^{-1})		References
V1300 Aql	Mira	2000	620	16.5	10^{-5} 4.5×10^{-6} 1.6×10^{-5}	$(0.4,3.3)\times10^{-5}$	7, 10, 18, 24
OH 231.8+4.2	Mira	2500	1500	15.0	1.6×10^{-4}	$(0.9,2.8)\times10^{-4}$	15, 33
OH 26.5+0.6	Mira	2750	1370	17.0	1.0×10^{-4} 9.7×10^{-6}	$(3,0.8)\times10^{-4}$	13, 18
IRAS 22036+5306	No	6900	4000	30.0	7.5×10^{-5} 7×10^{-6}	$(0.04,1.3)\times10^{-4}$	16
AFGL 6815	No	7000	2900	15.0	2.1×10^{-5} 3×10^{-5}	$(1.3,4.7)\times10^{-5}$	5, 9, 18, 31
IRAS 17347-3139	No	30000 [5]†	3680 [6]†	25.0	-	-	5, 30
NGC 6537	No	200000	1500	18.0	-	-	31
NGC 6302	No	250000	1170	10.0	1.5×10^{-4} 2.7×10^{-5}	$(0.09,3.6)\times10^{-4}$	4, 6, 22, 25

7

[7]Column 1: Target name; Column 2: Variability of the central star; Column 3: Effective temperature of the star; Column 4: Adopted distance to the object; Column 5: Expansion velocity of the circumstellar envelope; Column 6: *Left)* Mass loss rate taken from literature. *Right)* Range of mass loss rates shown at left after being scaled to the values of d, $v_{\rm exp}$ and χ_{CO} used in this work. For those with only one previous estimation, the range cover a factor of 3 around that value after scaling. Column 7: References. Uncertain.

1) Van de Sande et al., 2018 2) Doan et al., 2017 3) Maercker et al., 2016b, 4) Santander-García et al., 2015, 5) Vickers et al., 2015, 6) Santander-García et al., 2015, 7) Danilovich et al., 2015, 8) Nhung et al., 2015, 9) He et al., 2014, 10) Ramstedt and Olofsson, 2014a, 11) Danilovich et al., 2014, 12) Khouri et al., 2014, 13) Justtanont et al., 2013, 14) Cox et al., 2012, 15) Choi et al., 2012, 16) Sánchez Contreras and Sahai, 2012a, 17) Schöier et al., 2011, 18) De Beck et al., 2010a, 19) Decin et al., 2010, 20) Justtanont et al., 2010, 21) Ramstedt, Schöier, and Olofsson, 2009, 22) Meaburn et al., 2008, 23) Maercker et al., 2008, 24) Ramstedt et al., 2008a, 25) Dinh-V-Trung et al., 2008a, 26) Decin et al., 2007, 27) Teyssier et al., 2006a, 28) Ramstedt et al., 2006, 29) Heras and Hony, 2005, 30) Matsuura et al., 2005, 31) Woods and Nyman, 2005, 32) Olofsson et al., 2002, 33) Alcolea et al., 2001, 34) Loup et al., 1993 and 35) Knapp et al., 1982

Chapter 5

Warm CO in evolved stars from the THROES catalogue. PACS spectroscopy of C-rich envelopes.

Canto a la libertad

José Antonio Labordeta

5.1 Introduction

In this chapter we present an analogue analysis to that explained in Chapter 4 but focussed on a sample of C-rich evolved stars taken from the THROES-PACS catalogue. We divide our study in O-rich and C-rich targets since these two major chemistry classes correspond to progenitor stars with different masses, which follow somewhat different evolutionary paths, and also have a dissimilar dust composition, both facts potentially affecting the mass-loss process. Furthermore, we use multi-epoch spectra for the well studied C-rich envelope IRC+10216 to investigate the impact of CO flux variability on the values of $T_{\rm rot}$, and M.

This chapter is organized as follows, in section 5.2 we describe the sample information; the spectral features identified in them are presented in section 5.3; then, in sections 5.4 and 5.5 we present the RD method and the derived results which are discussed in 5.6. Finally, main conclusions are included in Sect. 5.7.

5.2 Sample information

From the whole sample of C-rich sources contained in THROES-PACS catalogue we found 15 evolved stars spanning the three main evolutionary classes with at least three CO emission lines above S/N=3. In Table 5.1 a description of the observations associated to each source is included.

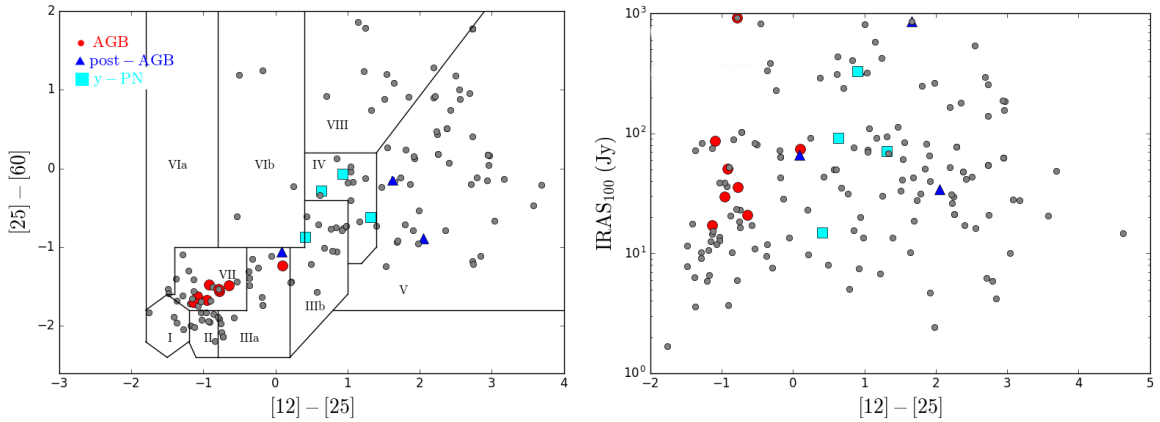

FIGURE 5.1: The same as Fig. 4.1 but highlighting the C-rich sources studied in this chapter.

This sub-sample contains bright infrared targets with distinct morphological properties, but sharing similar carbon chemistry with strong CO emission at high excitation temperatures (up to $E_u/k \approx 5688$ K). We provide a summary table 5.2 with some relevant properties such as period, distance, luminosity, effective temperature and gas mass-loss rate, along with additional references.

Figure 5.1 displays the classic IRAS color diagram (van der Veen and Habing, 1988) featuring the colors [25]−[60] and [12]−[25] of all the stars in THROES. The stars studied in this chapter are highlighted with appropriate symbols which are consistent with those used in Chapter. 4. Note how C-rich AGBs clearly constellate in a different box compared to the O-rich stars in previous chapter which has been interpreted as a consequence of different grains' emissivities (Zuckerman and Dyck, 1986). The AGB star that falls outside the expected box with a clear 25 μm excess is AFGL 3068 (LL Peg) which is an "extreme carbon star": very dust-obscured by optically thick shells due to high mass-loss rate (Volk, Kwok, and Langill, 1992; Winters et al., 1997). The Red Rectangle is also outlying in this same box typically associated to O-rich stars.

5.3 Observational results

5.3.1 Features in PACS spectra

The PACS continuum-subtracted spectra are plotted in Fig. 5.2 sorted in terms of effective temperature and scaled for better comparison of the CO spectra. We identified some of the strongest line carriers by coloured lines at the top. A summary of the identified spectral lines is given in the table B.3 in Appendix B. The broad emission feature at 62 μm visible in some of the spectra is an instrumental artefact. The spectra of IRC+10216 corresponding to different epochs are separately shown in the top panel of Fig. 5.3. For all targets we only analysed the spectra between [55-95] and [101-190] μm because the flux densities are unreliable above 190 μm, below 55 μm and between 95-101 μm due to spectral leakage.

TABLE 5.1: Observation log.

Target name	Alt. name	Class	R.A. (J2000)	DEC (J2000)	OBSID	Obs. date
AFGL 3068	LL Peg	C-rich AGB	$23^h19^m12^s.39$	$1711'35''.4$	1342199417 1342199418	2010-06-30
AFGL 3116	LP And	C-rich AGB	$23^h34^m27^s.67$	$4333'2''.52$	1342212512 1342212513	2011-01-11
IRC+10216	CW Leo	C-rich AGB	$9^h47^m57^s.41$	$1316'43''.60$	1342221889 1342241328 1342245395 1342246381 1342253754 1342255741 1342256262	2011-05-29 2011-10-25 2012-05-05 2012-05-30 2012-10-21 2012-11-21 2012-11-30
IRAS 15194-5115	II Lup	C-rich AGB	$15^h23^m4^s.91$	$-5125'59''.0$	1342215685 1342215686	2010-03-10
CIT 6	RW Lmi	C-rich AGB	$10^h16^m2^s.28$	$3034'18''.48$	1342197799 1342197800	2010-06-05
AFGL 2513	V1969 Cyg	C-rich AGB	$20^h09^m14^s.25$	$3125'44''.9$	1342270010 1342269936	2013-04-14 2013-04-12 [1]
V Cyg		C-rich AGB	$20^h41^m18^s.27$	$4808'28''.8$	1342208939 1342208940	2010-11-15
V Hya		C-rich AGB	$10^h51^m37^s.25$	$2115'00''.3$	1342197790 1342197791	2010-06-05
AFGL 2688	Egg Nebula	C-rich pAGB	$21^h2^m18^s.74$	$3641'37''.68$	1342199233 1342199234	2010-06-26
HD 44179	Red Rectangle	C-rich pAGB	$6^h19^m58^s.22$	$-1038'14''.7$	1342220928 1342220929	2011-04-30
IRAS 16594-4656	Water Lily Nebula	C-rich pAGB	$17^h03^m10^s.03$	$-4700'27''.7$	1342228414 1342228415	2011-09-10
AFGL 618	CRL 618	C-rich yPN	$4^h42^m53^s.66$	$366'53''.28$	1342225838 1342225839	2011-08-07
IRAS 21282+5050		C-rich yPN	$21^h29^m58^s.42$	$513'59''.76$	1342220741 1342223375	2011-05-12 2011-06-30
CPD-568032	Hen 3-1333	mixed yPN	$17^h7^m0^s.87$	$-5654'48''.0$	1342228201 1342228202	2011-09-06
Hen 2-113		mixed yPN	$14^h59^m53^s.52$	$-5418'07''.20$	1342225142 1342225143	2011-08-02

[1] The spectra correspond to bands B2B and R1 in IRC+10216 and B2A, B2B and R1 for the remaining targets.

TABLE 5.2: Properties of stars with carbon CSEs in the sample: type of variability, period (P), distance (d), luminosity (L), effective temperature ($T_{\rm eff}$) and gas mass-loss rate ($\dot{M}$).

Target name	Var.	P (days)	d (kpc)	L ($L_\odot$)	$T_{\rm eff}$ (K)	$\dot{M}$ ($M_\odot$ yr^{-1})	ref.
AFGL 3068	Mira	696	1.1	10887	2000	$(0.9-6)\times10^{-5}$	2, 10, 23, 29
AFGL 3116	Mira	614	0.63	9561	2000	$(4.6-12)\times10^{-6}$	2, 10, 23
IRC+10216	Mira	630	0.15	11300	2330	$(1-4)\times10^{-5}$	2, 10, 12, 23, 24
IRAS 15194-5115	Mira	575	0.5	8933	2400	$(0.4-1.5)\times10^{-5}$	2, 10, 13
CIT 6	SRa	640	0.44	8165	2445	$(5-6)\times10^{-6}$	2, 10, 23
AFGL 2513	Mira	550	1.76	8470	2500	2×10^{-5}	6, 14
V Cyg	Mira	421	0.271	6000	2581	$(0.4-6.3)\times10^{-6}$	2, 10, 15
V Hya	SR/Mira	530	0.38	7850	2650	$(0.25-6)\times10^{-5}$	1, 10, 17, 25
AFGL 2688			0.34	5500	7250	$(0.7-2)\times10^{-4}$	3, 8, 19, 27
HD 44179			0.71	6050	7750	$10^{-7}-10^{-4}$	7, 10
IRAS 16594-4656			1.8	4900	10000	1×10^{-5}	9, 18
AFGL 618			0.9	10000	33000	$(0.3-2)\times10^{-4}$	4, 16, 26, 27, 30
IRAS 21282+5050			2	2400	30000	$(6\pm4)\times10^{-5}$	5, 11, 21, 26
CPD-568032			1.53	5250	30000	$(1.2-4)\times10^{-6}$	20, 28
Hen 2-113			1.23	5250	30900	$(6.3-8)\times10^{-7}$	20, 28

[(1)]Bergeat and Chevallier, 2005, [(2)]Ramstedt and Olofsson, 2014b, [(3)]Balick et al., 2012, [(4)]Sánchez Contreras et al., 2004, [(5)]Castro-Carrizo et al., 2010 [(6)]Guandalini et al., 2006, [(7)]Men'shchikov et al., 2002, [(8)]Ishigaki et al., 2012, [(9)]Mishra, Li, and Jiang, 2015 [(10)]De Beck et al., 2010b, [(11)]Hasegawa and Kwok, 2003, [(12)]Cernicharo et al., 2015b, [(13)]Ryde, Schöier, and Olofsson, 1999a, [(14)]Groenewegen et al., 2002, [(15)]Neufeld et al., 2010, [(16)]Huang et al., 2016a, [(17)]Knapp, Jorissen, and Young, 1997, [(18)]Woods et al., 2005, [(19)]Milam, Woolf, and Ziurys, 2009, [(20)]De Marco and Crowther, 1998, [(21)]Likkel et al., 1988, [(22)]Bujarrabal et al., 2016, [(23)]Teyssier et al., 2006b, [(24)]De Beck et al., 2012b, [(25)]Knapp et al., 1999, [(26)]Meixner et al., 1998, [(27)]Fong et al., 2001, [(28)]Leuenhagen, Hamann, and Jeffery, 1996, [(29)]Sánchez Contreras and Sahai, 2012b, [(30)]Wesson et al., 2010b

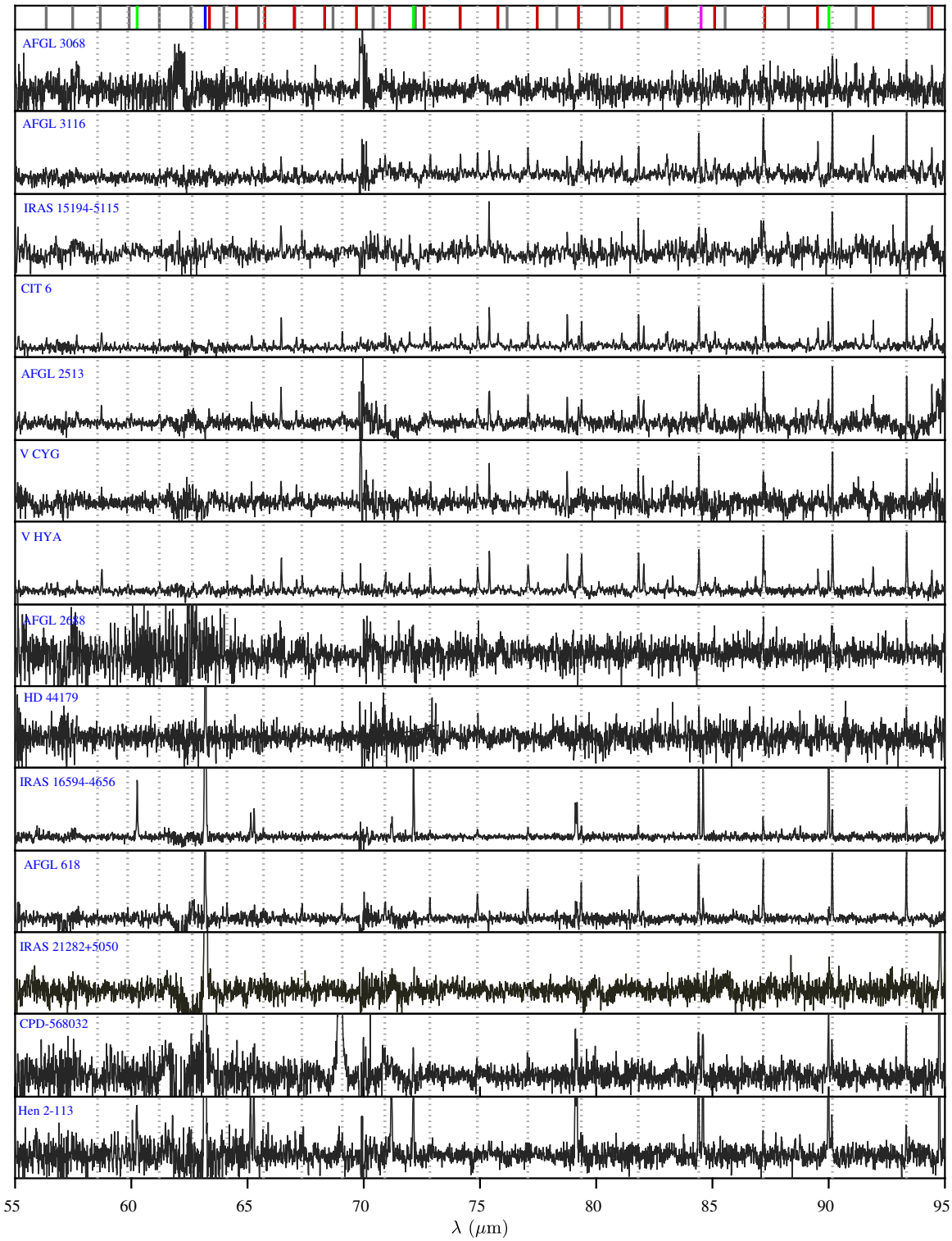

FIGURE 5.2: Continuum-subtracted PACS spectra of evolved stars scaled for comparison. The top panel indicates the rest frame wavelength of ^{12}CO (light gray, dotted lines), ^{13}CO (dark gray), HCN (red), CS (yellow), OH (magenta), CH^+ (green) and forbidden lines (blue) of [C II] 157.7 μm, [O I] 63.2, 145.5 μm, [N II] 121.9 μm.

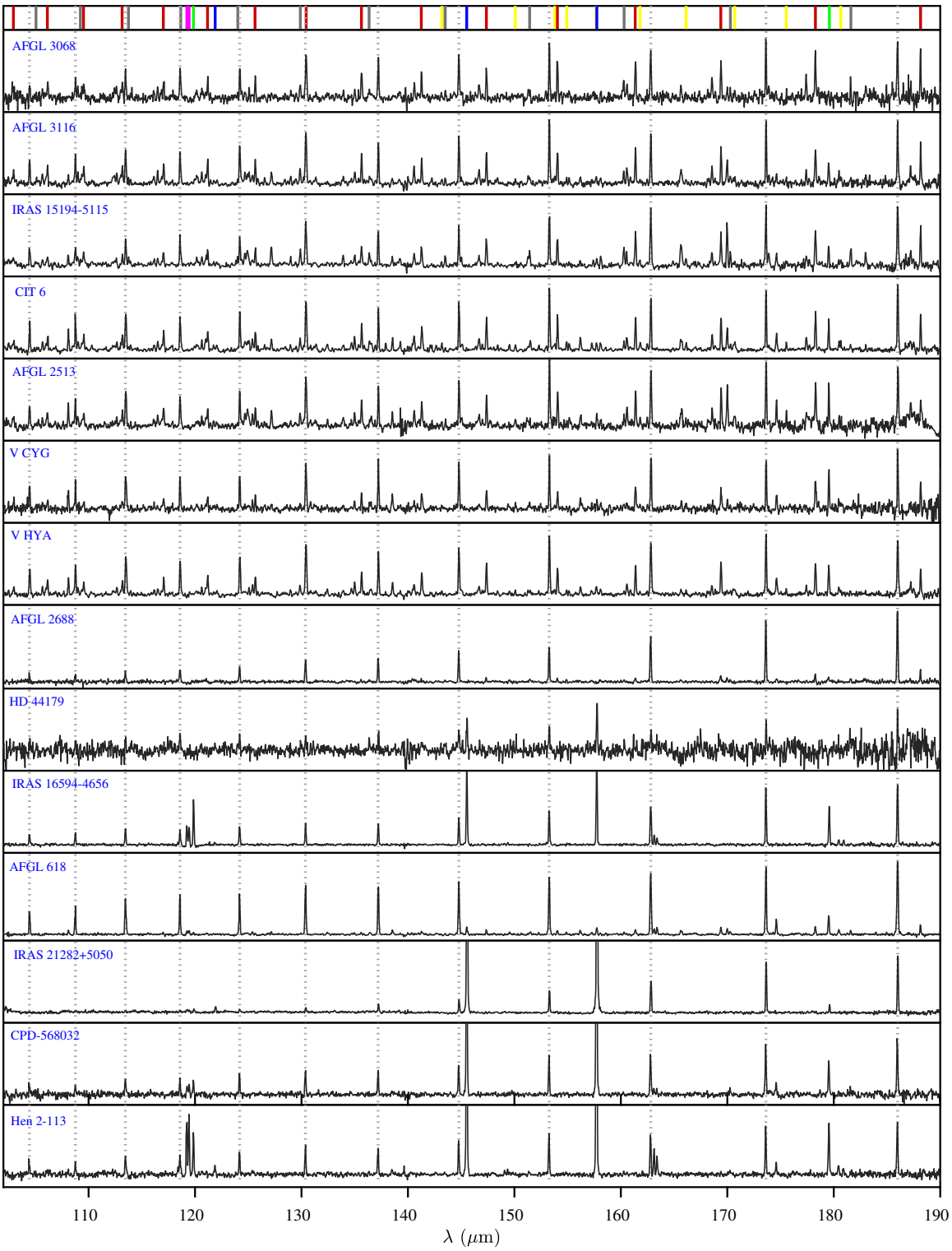

FIGURE 5.2A: Continued.

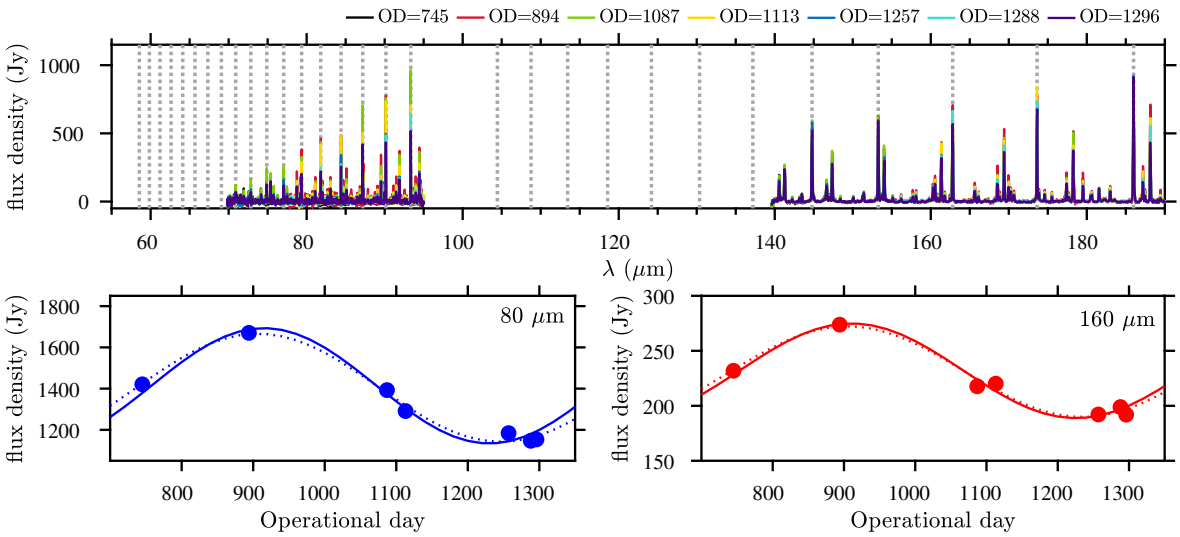

FIGURE 5.3: Variability of the FIR spectrum of IRC+10216. Top: Continuum subtracted spectra at different epochs; the dotted lines sign the ^{12}CO lines. Bottom: Sine-wave fit to the continuum variability at two selected wavelengths for a fixed period of 630 days (solid lines) and free-period fit corresponding to 680 days and 660 days for the blue and red dashed curves, respectively.

Straightaway we see, in Fig. 5.2, significant differences between the emission line spectra of these targets such as the richer molecular content in the less evolved stars compared to post-AGBs and young PNe as expected. The strongest spectral lines in this sample are due to CO emission in AGBs and post-AGBs, while the four young PNe also show prominent forbidden lines. Additional molecular features are attributed to rotational transitions of common carbon-bearing chemical species such as ^{13}CO, HCN and CS. Not so common in C-rich stars is the presence of the OH doublet at [119.23, 119.44] μm, and at 84.51 μm, in some of the most evolved targets, namely AFGL 618, IRAS 16594-4656, Hen2-113 and CPD-56°8032 where the UV-ionization is stronger. In addition, we also identified five pure rotational CH^+ transitions at 179.61, 119.86, 90.02, 72.15 and 60.26 μm, in the targets that show the strongest fine structure lines of this sample, which definitely establishes its presence there. Interestingly we do not see it in the spectrum of the Red Rectangle where it was observed before (Balm and Jura, 1992), neither in the spectrum of AFGL 618 for which weak emission is detected in *Herschel*/SPIRE data (Wesson et al., 2010b). However, the features at 179.61 μm and 90.02 μm could be blended with water vapour lines as in the case of NGC 7027 (Cernicharo et al., 1997).

In all AGBs and in AFGL 618 and AFGL 2688 we identify lines probably due to H_2O (orto- and para-) transitions. The study of water lines in the AGB stars of our sample (except AFGL 2513) was already conducted by Lombaert et al., 2016b who suggested that both shocks and UV photodissociation may play a role in warm H_2O formation. Water lines had also been previously identified in the spectrum of AFGL 618 and AFGL 2688 in SPIRE data by Wesson et al., 2010b.

Atomic transitions corresponding to the fine structure lines of [O I] at 63.18 μm, and 145.53 μm, and [C II] at 157.74 μm, , are very prominent in the spectra of all of post-AGBs and young PNe in this sample with the exception of AFGL 2688. IRAS 16594-4656 demonstrates clear signs of ionization, contrary to what is mentioned in Woods et al., 2005,

since it shows a [C II] line even stronger than in AFGL 618.

The broad emission line at 69 μm, in the spectrum of CPD-56°8032 is probably dust emission by forsterite according to Cohen et al., 2002 and Blommaert et al., 2014b.

5.3.2 Line flux variability in IRC+10216

In this chapter we also present PACS spectra at multiple epochs of the well known IRC+10216 displaying periodic variations both in the continuum and in the lines 5.3. Variability in visible and IR wavelength magnitudes is one of the characteristics of many AGB stars, and in particular of all Mira-like stars such as the prototypical IRC+10216.

Cernicharo et al., 2014 discovered flux changes in spectral lines of different molecular species in IRC+10216 using Herschel/HIFI and IRAM 30m data. Intensity variations were attributed to oeriodic changes in the infrared pumping rates. Teyssier et al., 2015b also reported continuum variability and CO flux variability using several Herschel/PACS, Herschel/SPIRE and Herschel/HIFI observations. The conclusions were that the amplitude of the continuum variability increases with decreasing wavelengths, and that IR pumping has an important contribution for raising the populations of the higher J rotational levels of CO and other molecules. More recently, He, Dinh-V-Trung, and Hasegawa, 2017b reported 5-30% intensity variability of mm lines with periodicities between approximately 450-1180 days, strengthening the idea that non-collisional processes in the inner CSE are important to explain variations in line emission. How that reflects on the physical parameters of the CSE is to be assessed.

Since we dispose of several observations spanning an extended period of time we can study in greater detail non-LTE effects on the CO emission spectra, and consequently on the estimates of temperature and mass. We devote section 5.5.3 to this topic.

5.3.3 CO line fluxes

We now focus on the purely rotational spectrum of CO in the ground vibrational state (v=0), which we use to study the physical properties of the warm regions of the molecular CSEs of our targets. In the PACS range one can potentially find very high CO rotational transitions, from J = 14-13 (E_u=581 K) to J = 45-44 (E_u=5688 K). The lack of data between 95 and 101 μmmeans we cannot detect the transitions J=26-25 and J=27-26. In the case of IRC +10216, the much larger gap in the PACS coverage (95-140 μm) prevents detection of CO transitions with upper-level rotational number between J_u=19 and J_u=27. The line fluxes are given in Table B.3. The quoted uncertainties correspond to the propagated statistical errors and do not contain absolute flux calibration errors (typically of 15%-20%) or underlying continuum subtraction uncertainties. As expected, the resolving power of PACS (80-300 km s^{-1}) does not allow to spectrally resolve the CO profiles. This is true not only for AGB CSEs with FWHM similar to or smaller than the terminal expansion velocity of the envelopes (FWHM 10-25 km s^{-1}), but also for post-AGB objects and yPNe, even in targets that are known to

have fast (100 km s^{-1}) molecular outflows like AFGL 618 (Bujarrabal et al., 2010). For this reason we measured CO fluxes by simply fitting a Gaussian function to the PACS lines.

Due to insufficient spectral resolution some reported line fluxes are affected by line blend. These are identified with asterisks in the tables and figures. Some of the well-known line blends are CO J=30-29 with HCN J=39-38 and CO J=20-19 with HCN J=26-25 at 87.2 and 130.4 μm, respectively. Also, the CO transitions J=21-20 and J=22-21 are blended with ^{13}CO J=22-21 and J=23-22 at 124.2 μmand 118.6 μm, respectively.

Figure 5.4 compares the integrated flux of the CO(J=15-14) line (F_{CO}(15-14)) with the IRAS 100 μm, flux ($IRAS_{100}$), the PACS continuum at 170 μm, ($PACS_{170}$), i.e. near the CO(J=15-14) line, and the [12]-[25] IRAS color. The J=15-14 transition is a strong, non-blended line, detected towards all of our targets, and it was also used by Lombaert et al., 2016a who analysed PACS data of most of the AGBs here studied, which facilitates comparison.

As for the O-rich sample (Chapter 4), there is a positive correlation between the CO line strength and the $IRAS_{100}$ and $PACS_{170}$ continuum fluxes. The correlation between the CO J=1-0 line and the IRAS fluxes of evolved stars of various chemical types had been previously reported (Olofsson, Eriksson, and Gustafsson, 1987, Olofsson, Eriksson, and Gustafsson, 1988, Bujarrabal, Alcolea, and Planesas, 1992).We also confirm the anticorrelation between the line-to-continuum (F_{CO} 15-14/$PACS_{170}$) ratio and the IRAS [12]-[25] color (both distance-independent) for the AGB stars, which was noted in Chapter 4. For the more evolved targets the trend is not so obvious, but the sample size is small. We also see that, in general, the ratio between the molecular emission and the dust emission is higher in less evolved objects than in the most evolved ones, which could be partially attributed to more prominent CO photodissociation as the objects evolves along the AGB-to-PNe track. AFGL 618 and IRAS 16594-4656 are two clear outliers in this relation since they show a line-to-continuum emission ratio as large as that of the AGB class. The Red Rectangle (HD 44179) is well isolated in all the panels due to its comparatively weak CO emission and low CO-to-dust ratio. This surely reflects the different nature of this object with respect to the rest of post-AGB and yPNe in our sample, which is well known from previous works. The Red Rectangle belongs to a special class of post-AGB objects with relatively weak CO emission coming from large (~1000-2000 AU) circumbinary rotating disks, with very prominent IR emission by warm/hot dust in the disk, but lacking massive molecular outflows found in many other evolved stars (e.g., Bujarrabal, 2016, and references therein).

5.4 Rotational diagram analysis

As we did in the Chapter 4, we have analysed the CO emission found in the sources of our C-rich sub-sample using the RD method after applying a slight opacity correction.

To compute column densities (N^{col}) we divided the total number of molecules (N_{tot}) by the projected area on the sky. For that we need the radius (r_{CO}) of the emitting region which as we discussed in the Chapter 4 is a major source of uncertainty that also affects the computation of line opacities.

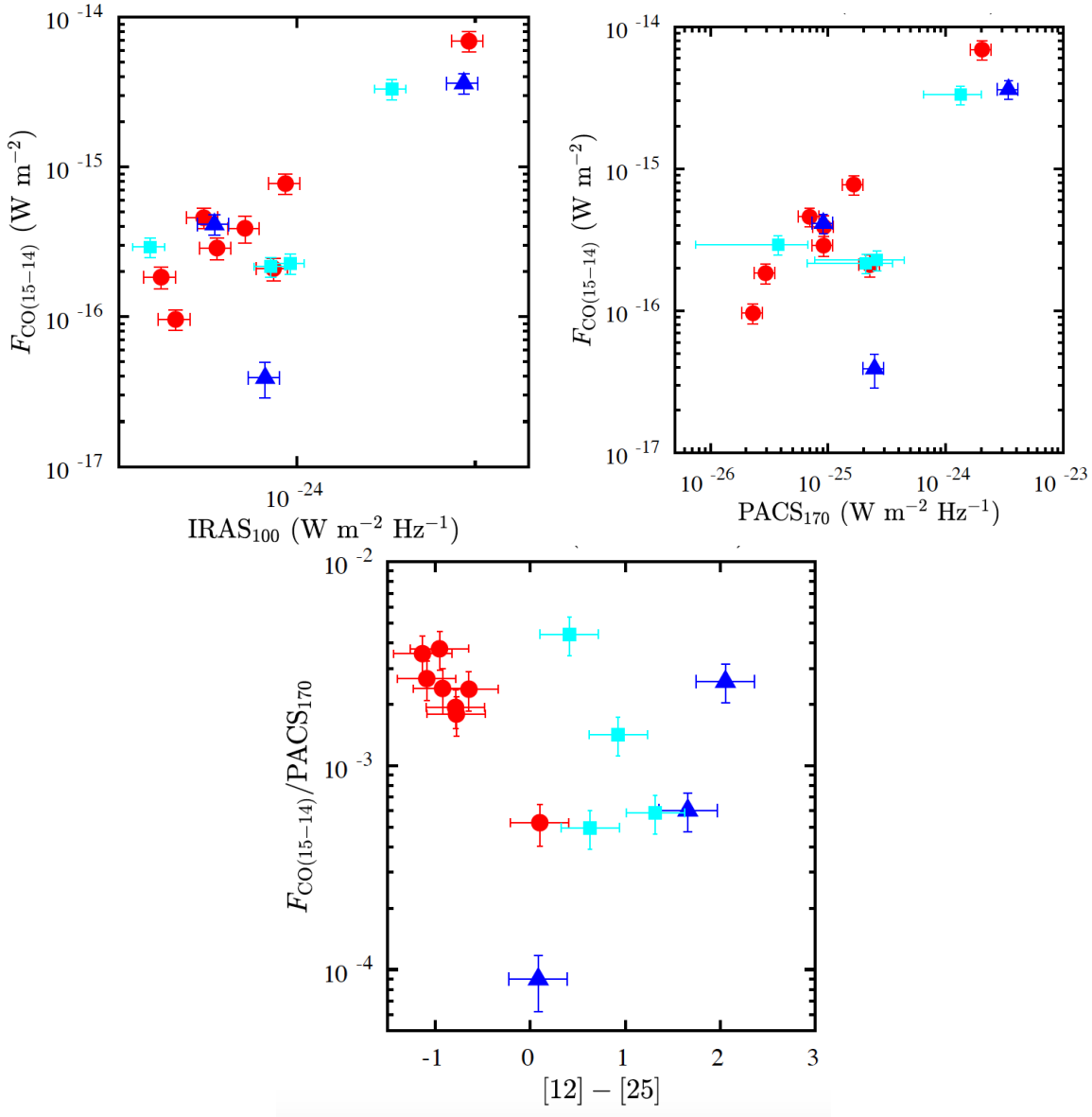

FIGURE 5.4: Correlation between ^{12}CO line flux and continuum intensities. Top left: CO $J = 15 - 14$ vs IRAS 100 μm flux. Top right: CO $J = 15 - 14$ vs PACS 170 μm continuum flux. Bottom: continuum normalized CO $J = 15 - 14$ flux vs IRAS [12]-[25] color. The symbols and colors are the same as in Fig. 5.1.

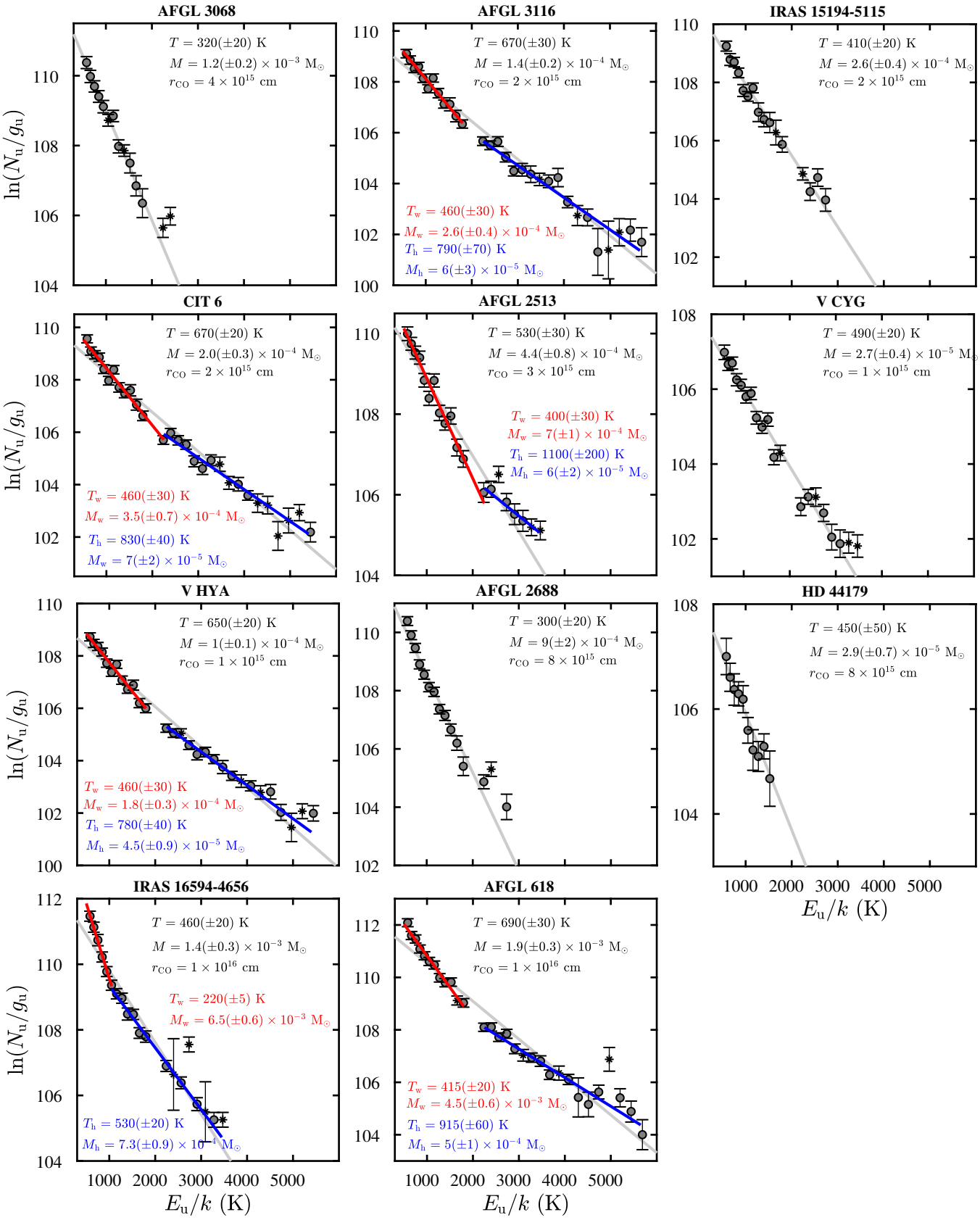

FIGURE 5.5: Rotational diagrams of the ^{12}CO molecule. The gray line correspond to a single least-squares fit to the full range of transitions from where a rotational temperature, T, and total gas mass, M, is computed. r_{CO} is the optimal radius. The red and blue lines correspond to a two-component model consisting of a "warm" and "hot" region, respectively. Asterisks mark line blends.

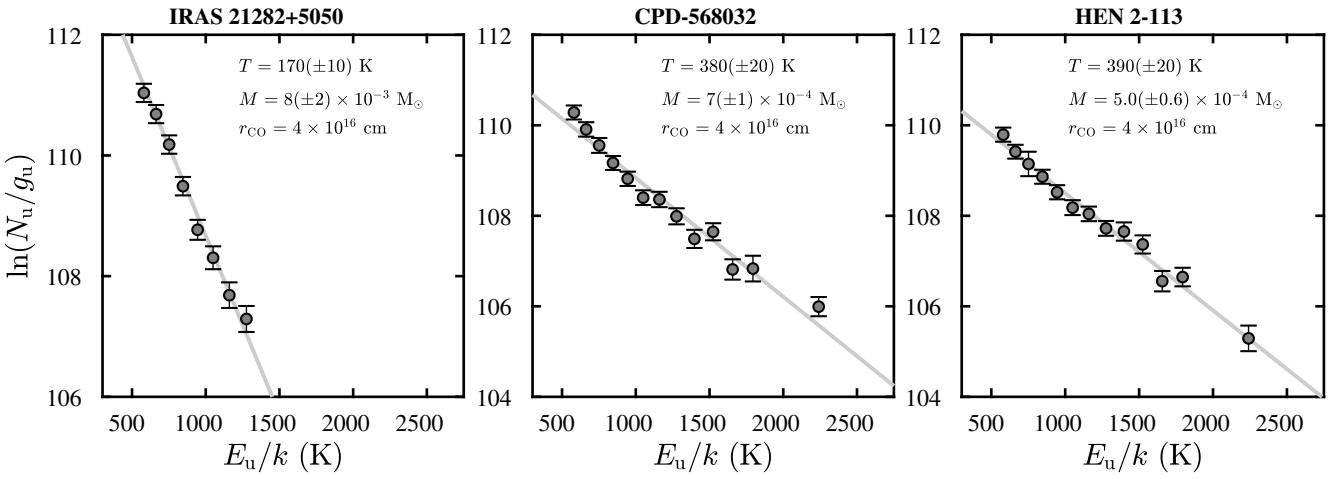

FIGURE 5.5A: Continued.

The method used to estimate the characteristic radius (r_{CO}) of the emitting regions is completely analogue to that which was extensively explained in the Chapter. 4. To confirm the reliability of the estimated r_{CO}, ($\sim 1-4\times10^{15}$ cm) we have compared these values with the upper limits to the size of their envelopes deduced from the PACS spectral cubes and/or spectroscopic maps by Teyssier et al., 2006b and with any other information on the molecular envelope extent from the literature. IRC+10216 was found to be an obvious exception because it looks slightly extended with a FWHM 4σ above the FWHM of the PSF in both bands. For example, in the blue band this implies a deconvolved Gaussian size of about $\sqrt{6.8^2-5.5^2} \approx 4$". At a distance of 150 pc this corresponds to approximately 4×10^{15} cm. This value is in good agreement with the lower limit to r_{CO}, needed to satisfy the τ_J=14-13 <1 criteria in this target, r_{CO}=2×10^{15} cm. In this case, we then rather confidently use an intermediate value of r_{CO}=3×10^{15} cm. The r_{CO}, values derived for C-rich AGB sample are in completely agreement with those derived for the O-rich AGBs.

Contrary to AGBs, for post-AGBs and yPNe there are no model temperature profiles in the literature of the molecular gas in the CSEs. The range of representative radius adopted for post-AGBs and yPNe is r_{CO}=[0.4-4]×10^{16} cm based on the moderate opacity criteria, the extent of the emission in the PACS cubes and photometric maps, and on additional information on the extent of the intermediate-to-outer molecular envelope from the literature. Again the r_{CO}, values derived for the most evolved objects of the C-rich sub-sample are in agreement with those derived for the O-rich ones.

For the post-AGBs we chose a slightly larger radius. In AFGL 2688 a deconvolved size of ~4" in the blue band suggests that r_{CO} is unlikely larger than 1×10^{16} cm, whereas previous CO $J = 2-1$ mapping observations have identified a compact shell ~2" (5×10^{15} cm for a distance of 340 pc) around the center of the nebula (Cox et al., 2000), meaning that higher J transitions could come from an even more inner layer of the CSE. However, for such radius $\tau_{J14\rightarrow13}$ goes well above unity and the opacity correction is not reliable. Therefore we only explored a radii range between $6-10\times10^{15}$ cm. HD 44179 is a point-source in PACS photometry, therefore for a distance of 710 pc r_{CO} should be of the same order as AFGL 2688 which is roughly consistent with observations (e.g. Bujarrabal et al., 2016). For IRAS 16594-4656 the range $r_{CO} \sim 0.8-2\times10^{16}$ seems to be the best fit.

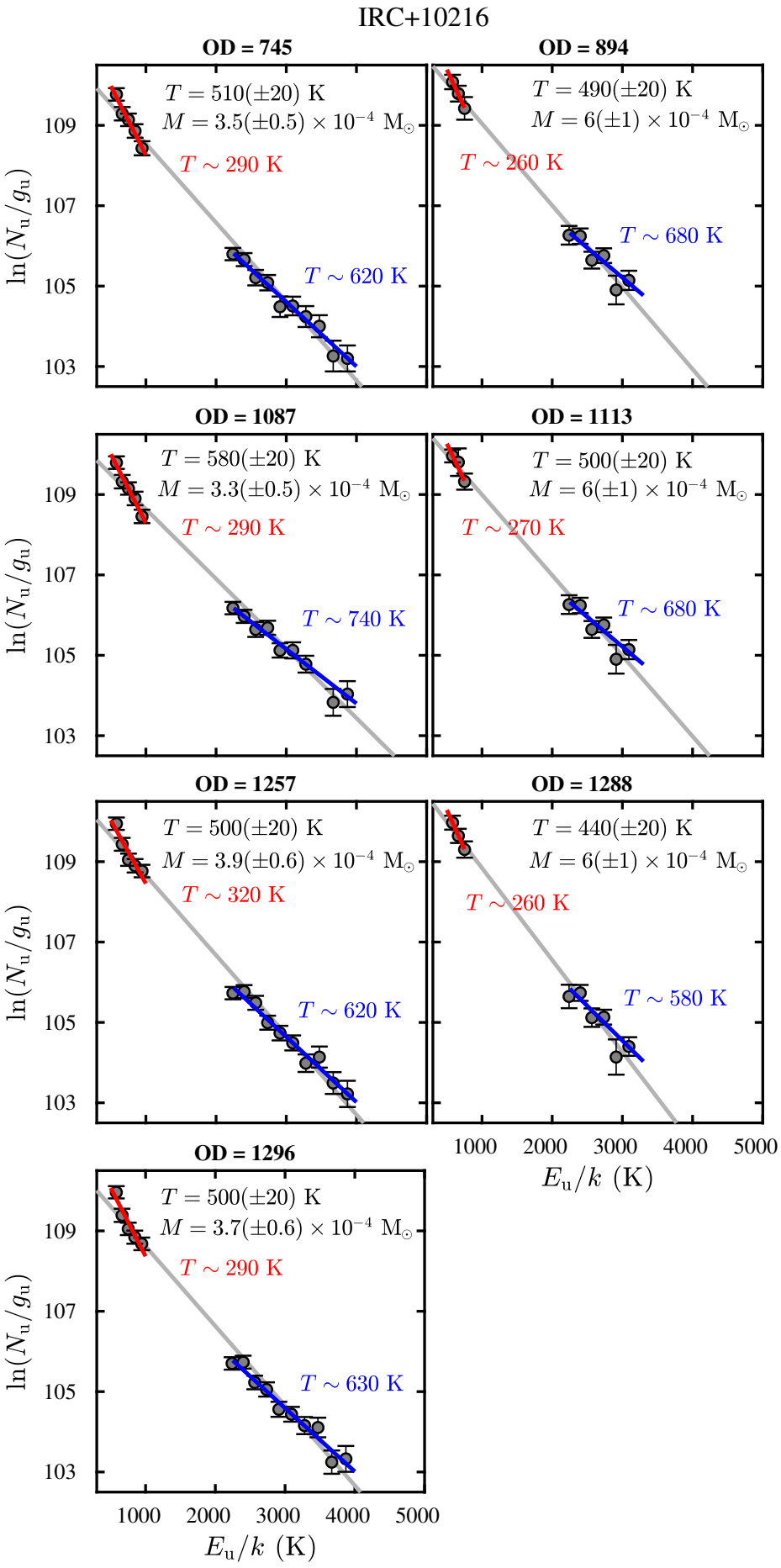

FIGURE 5.6: Rotational diagram of the ^{12}CO molecule in IRC+10216 at different epochs. Analogous to Fig. 5.5.

The young PNe do not have available PACS photometry data (with the exception of AFGL 618) but we have indications that they are point-sources from visual inspection of the spectral cubes. We found an upper limit of approximately 1×10^{17} cm above which the sources would appear as extended targets compared to the size of the PACS spectrometer spaxel (9.4") for the assumed distances. On the other hand, because the CO envelope is expected to surround the ionized nebula, then the minimum radius should be around ≈1-2" according to H_α observations by Danehkar and Parker, 2015 of Hen 2-113 and CPD-56°8032. Regarding IRAS 21282+5050, an elongated hole with 4"×2" in CO $J = 1 - 0$ and $J = 2 - 1$ maps sets the lower limit for the radius Castro-Carrizo et al., 2010. This being said, the plausible radii range to explore for these 3 young PNe should be approximately within $r_{CO} \sim 2 - 6 \times 10^{16}$ cm. Finally, in the case of AFGL 618 a reasonable estimate for r_{CO} lies between 0.8-2×10^{16} cm based on previous observations of the central H II region (~0.5") and $J = 3 - 2$ CO emission (~2") (Sanchez Contreras et al., 2017; Lee et al., 2013), so we set a representative radius to $r_{CO} \sim 1 \times 10^{16}$ cm.

Given the uncertainty in r_{CO}, we have have proceeded in the same way as for O-rich sources, systematically exploring a range of radii around optimal/plausible values of r_{CO}, to asses the impact of this parameter in our results (Fig. C.10).

5.5 Results

5.5.1 Gas temperatures and masses

The opacity corrected rotational diagrams RDs of the CO molecule are plotted in Fig. 5.5 and Fig. 5.6, together with the best-fit parameters. Table 5.3 summarizes the fitting results.

We found rotational temperatures in the range $T \approx$ 300-700 K with some of the post-AGBs and young PNe being the targets with the coolest gas to no surprise. However, IRAS 16594-4656 and AFGL 618 have a rotational temperature that is more similar to that of the AGB class. Overall, these values are larger than the typical temperatures determined from radio observations ($T \lesssim 100$ K), and even *Herschel*/SPIRE observations by Wesson et al., 2010b, corroborating that PACS CO lines arise in warmer layers of CSEs.

There are seven cases where it is clear by the analysis of residuals that a single straight line does not fit the entire range of excitation energies. That is the case of AFGL 2513, IRC +10216, V Hya, IRAS 16594-4656, AFGL 3116, CIT 6 and AFGL 618. For example, in the latter a single linear fit corresponding to a rotational temperature of $T \approx 690$ K, clearly does not explain the variance of the lowest and the highest J transitions simultaneously.

To know whether the slope changes and at which point it occurs, we used the already mentioned, Bayesian information criterion (BIC) to help us deciding where to split the diagram and to quantify significance. This is explained in the appendix A and illustrated in the supplementary figure A.1.

We provide the fitting parameters corresponding to a single fit and a double-component

fit in targets where a single line does not equally fit all data points. As in Chapter 4, we call these two components "warm" and "hot" with $T_{\rm w} < T_{\rm single} < T_{\rm h}$. Their typical temperatures are $T_{\rm w} \sim 450$ K and $T_{\rm h} \sim 800$ K respectively. The corresponding masses are $M_{\rm w}$ and $M_{\rm h}$ with the former being 4-10 times larger than the latter.

The total number of CO molecules ranges between $N_{\rm tot} \sim 10^{49} - 10^{51}$, while column masses lie between $N^{\rm col} \sim 10^{16} - 10^{19}$ cm^{-2}. To estimate the total gas mass from CO, we assumed the same fractional abundance $X_{\rm CO} = 8 \times 10^{-4}$ (e.g. Teyssier et al., 2006b) with respect to H_2 for all targets. Consequently, we found total gas masses approximately between $M \sim 10^{-5} - 10^{-3}$ $M_\odot$.

Figure 5.7 shows the single-fit temperature versus mass for the opacity corrected diagram (coloured symbols) and uncorrected (gray symbols). The opacity-correction results in changes in $T_{\rm rot}$, of 10-15% in AGBs, and lower than 5% in post-AGBs and yPNe. In mass this typically corresponds to 60% in AGBs and lower in the post-AGBs and AFGL 618 (< 10% in M), and negligible in the other three yPNes.

As in Chapter 4 we found an anti-correlation between mass and temperature with $r = -0.65$, i.e., this anti-correlation is reinforced if we consider only the group of AGBs. In general, post-AGBs and yPNe have the highest masses. One clear exception to trend is The Red Rectangle, which is one of the least massive targets ($\sim 10^{-5}$ $M_\odot$ yr^{-1}) in contrast to the rest of the of post-AGBs and yPNe. This is not surprising given the nature of this object, which is the prototype of a special class of post-AGB objects with hot rotating disks and tenuous winds very different from the massive and fast (high-momentum) outflows of standard pre-PNe (see, Bujarrabal, 2016 and references therein).

We also investigated the correlation between the CO J=15-14 flux and the gas mass and find that the strongest CO emitters have tendentiously more massive envelopes, although there is a significant scatter (Fig. 5.13) Also, the targets with the highest temperatures have the highest line-to-continuum ($F_{\rm CO15-14}$/PACS$_{170}$) ratios. IRAS 21282+5050, which has the most massive warm envelope in our sample, defies this trend since it shows relatively strong CO J = 15-14 emission, although its $T_{\rm rot}$, 170 K is the lowest in the sample. The Red Rectangle appears isolated in a region of rather weak CO emission in spite of relatively high temperatures (400-500 K). We compare these results to those in Chapter 4 in Section. 5.6.

5.5.2 Mass-loss rates

The mass-loss rates are also listed in table 5.3. We found a range of values between $\dot{M} \sim 10^{-7} - 10^{-5}$ $M_\odot$ yr^{-1}. The median value in the AGB class is $\sim 7 \times 10^{-6}$ $M_\odot$ yr^{-1}. This is larger than the typical values in C-rich stars (1.5×10^{-7} $M_\odot$ yr^{-1}; Olofsson et al., 1993), meaning that our sample is biased towards stars with very high mass-loss rates. In fact, the AGB stars in our sample are known in literature for their high-mass loss-rates (Schöier and Olofsson, 2001a; Ramstedt et al., 2008b). The post-AGBs and young PNe in our sample have equally high $\dot{M}$.

As in Chapter 4, we investigated a possible correlation between $\dot{M}$, and $T_{\rm rot}$, $V_{\rm exp}$. We see

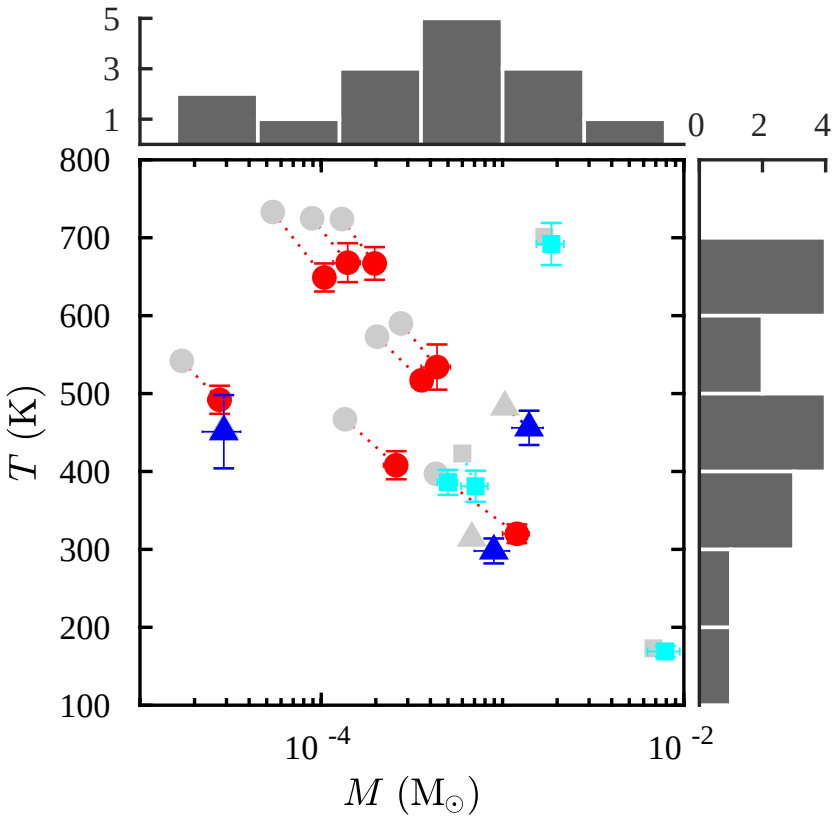

FIGURE 5.7: Summary of the RD results. The colored symbols correspond to the opacity corrected results which are connected by dotted lines to the corresponding uncorrected values in gray. On the sides we show the histograms of temperature and mass of the single fits. In the case of IRC+10216 we show weighted averages of four observations.

little evidence of an anti-correlation between $\dot{M}$, and $T_{\rm rot}$, although the relation is strongly influenced by AFGL 618, which is a strong outlier in this parameter space (Fig. 5.10). In this, and maybe other objects (mainly post-AGB/yPNe), we expect departures from the simple (constant mass-loss rate, spherically symmetric) model adopted to estimate the "equivalent" $\dot{M}$. We compare the results obtained here and in Chapter 4 in Section 5.6.

Figure 5.8 shows the logarithm of the integrated flux of the CO J = 15-14 line versus the logarithm of the mass-loss rate of the single component fit. We find a positive trend which is consistent with a power-law relation similar to that found by Lombaert et al., 2016a in their sample of C-rich AGB CSEs with H_2O FIR emission lines.

Separate values of $\dot{M}$, for the hot and warm components are computed for completeness, but the difference found ($M_{hot} < M_{warm}$) should not be overinterpreted as a recent decrease of the mass-loss rate. The hot and warm components most likely trace adjacent layers of the inner-winds of our targets, with the hot component presumably best sampling regions closer to the center. However, for simplicity and since we ignore the true CO excitation structure, we use the same radius to formally compute $\dot{M}$, for both components.We note that due to the $1/r_{\rm CO}$, dependence, the values of M_{hot} and M_{warm} can be brought closer to the single fit

value if the warm and hot correspond to different r_{CO}. We refrain from discussing M_{hot} and M_{warm} separately since a more sophisticated analysis is needed in order to assess mass-loss time variability. For this reason we only compare our single-component mass-loss rates to the literature.

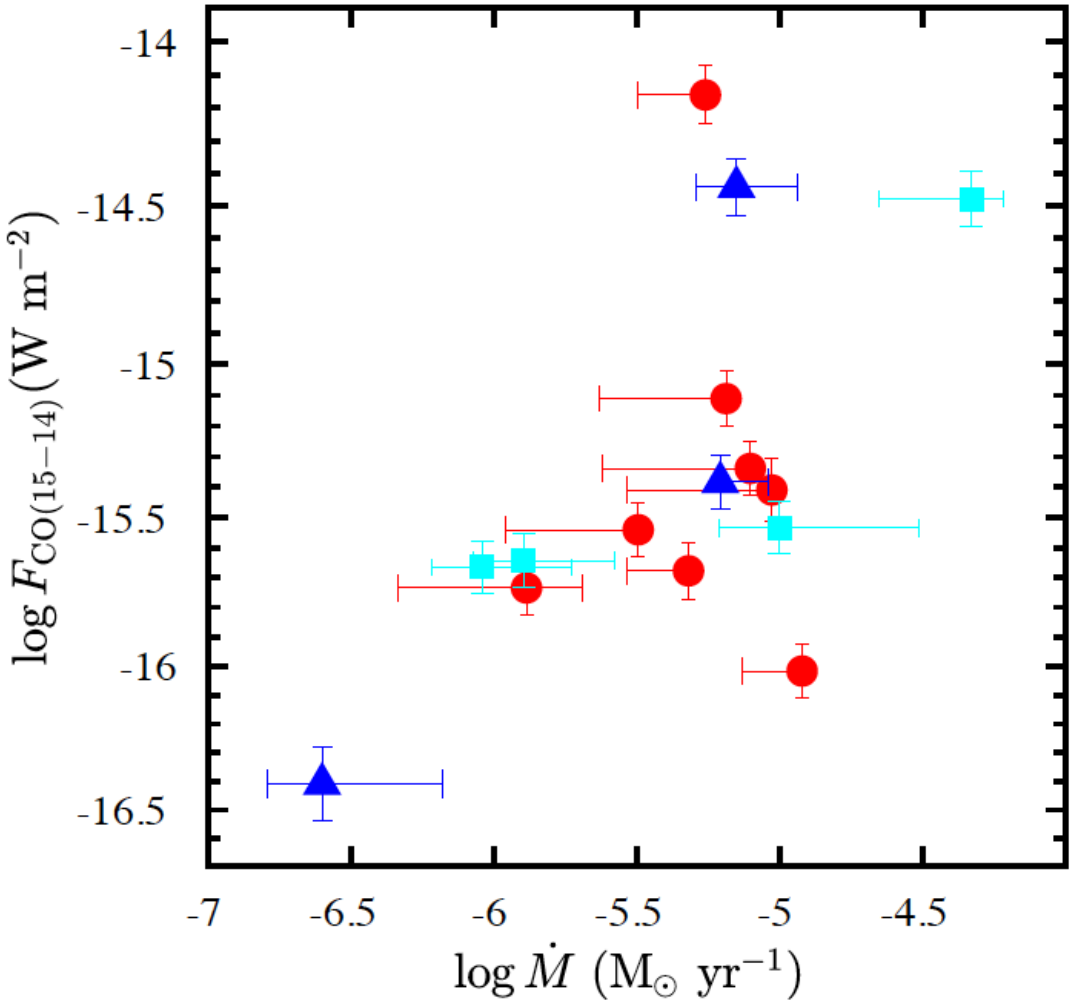

FIGURE 5.8: Logarithm of the mass-loss rate versus total CO J =15-14 flux.

5.5.3 The influence of line variability on T_{rot} and M

We have shown in Fig. 5.3 the temporal variability of the continuum and line fluxes in the case of the Mira-type variable AGB star IRC+10216. The higher-J CO lines (E_u>2000 K) are the ones that show the strongest variations with time. Here, we are interested in studying how CO line variability affects the values of M, and T_{rot}, derived using the RD method but using data acquired at different epochs.

The RDs of IRC+10216 for these seven different observing epochs are shown in Fig. 5.6, and the results of the RD analysis are tabulated in Table 5.3, together with the remaining

targets. Since three of the OBSIDs corresponding to the ODs 894, 1133 and 1288 have a more restricted wavelength coverage, the fits to the RDs have an inherently larger uncertainty because the fit is more sensitive to the low number statistics. The error-weighted mean (single-fit) rotational temperature and mass are $T_{\rm rot}$=520 K and M~4×10^{-4} $M_{\odot}$, respectively.

In Fig. 5.9, we plot the temperature and the mass, for single and double-temperature components, versus the operational day of the observations. The bottom panel shows that the total gas mass deduced from the single-fit of the RD or for the warm and hot components does not reflect the line flux variability since it stays essentially constant with time about the average value (dotted lines), well within the estimated uncertainties.

In a similar manner, the temperature of the warm component does not clearly reflect the CO line flux variations, since all multi-epoch values are in good agreement within uncertainties. The hot component is the one that shows the largest variations (perhaps periodic) of the temperature, with T$_{hot}$ going ~100 K (~16%) above the average (~640 K) at OD 1087, and then relaxing back to normal values in the remaining epochs. This variation is echoed in the single-fit value of $T_{\rm rot}$, (~12%).

Temperature variations are not necessarily expected to be periodic, but if we assume that to be true by fitting a sinusoidal function with the known pulsation period P = 630 days to the RD parameters, we find that such model accommodates reasonably well the data points corresponding to T$_{hot}$ (and also the single-fit $T_{\rm rot}$). It is also possible that IRC+10216 underwent an abrupt change of the physical conditions in its inner wind layers at epoch OD 1087, since the remaining data points by themselves will not justify/indicate periodic variability.

In summary, probably due to a compensation between the changes in the y-intercept and the slope of the RD due to CO line flux variations, which are largest for transitions with the highest J, the total gas mass M, appears to be quite robust to FIR pumping (non-LTE) effects. These, however, could have a measurable, yet moderate impact on the rotational temperatures.

5.6 Discussion

5.6.1 Gas temperatures and masses

The detection of high-J CO rotational lines is an indication of a significant amount of molecular gas under relatively high temperature conditions. From our simple RD analysis we inferred that the average gas temperatures of the layers sampled by FIR CO lines are much larger ($T_{\rm rot}$~200-900 K) than those typically derived from mm/sub-mm observations, which are sensitive to < 100 K gas from the intermediate-to-outer layers of the envelopes of evolved stars (at ~10^{16}-10^{17} cm, see e.g. De Beck et al., 2010a; Schöier et al., 2011) and completely compatible with those temperatures estimated in Chapter. 4.

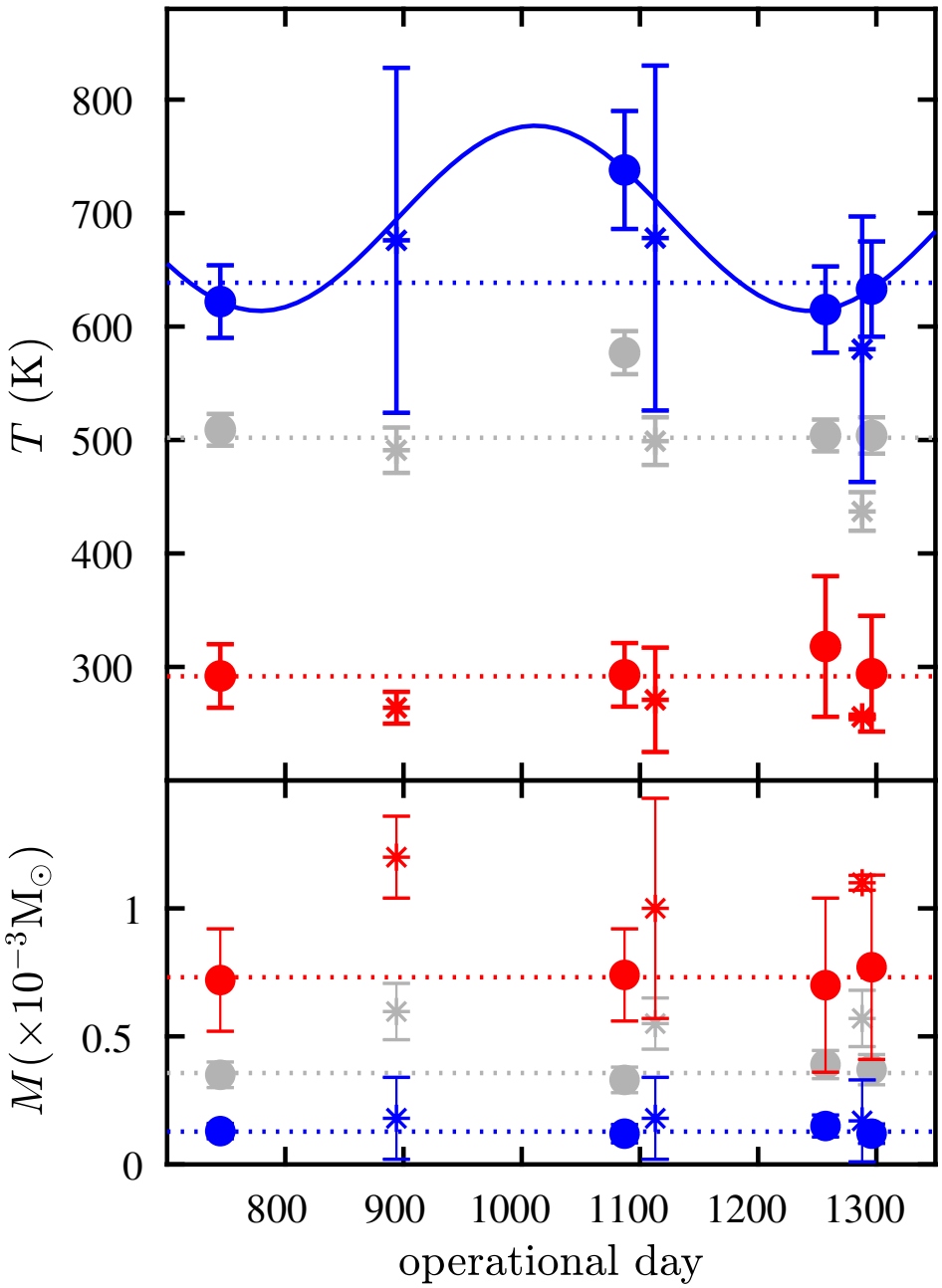

FIGURE 5.9: Rotational temperature and mass versus operational day in IRC+10216. Top: sinusoidal fit to the T variation with fixed period of 630 days (solid line). Bottom: total gas mass as a function of time. In each panel, the dotted lines are the average of each component and the asterisks mark unused data points in the fitting (see text). The color code is the same as in Fig. 5.6.

TABLE 5.3: Rotational diagram results for the ^{12}CO molecule with opacity correction. The assumed expansion velocity (v_{exp}) and radius (r_{CO}), derived rotational temperature (T), total number of ^{12}CO molecules (N_{tot}), CO column density (N^{col}), total molecular gas mass (M), mass-loss rate ($\dot{M}$), and in the rightmost column the ratio between opacity corrected and uncorrected masses. In some targets only a single temperature was fitted, while in others we split the diagram in two regions.

Target	v_{exp} (km s^{-1})	r_{CO} (cm)	T (K)	N^{col} (cm^{-2})	M ($M_\odot$)	$\dot{M}$ ($M_\odot$ yr^{-1})	Correction $_M$
AFGL 3068	13	4×10^{15}	320±20	1.1×10^{19}	$1.2(\pm0.2)\times10^{-3}$	1×10^{-5}	2.78
AFGL 3116	14	2×10^{15}	670±30	5.4×10^{18}	$1.4(\pm0.2)\times10^{-4}$	3×10^{-6}	1.6
			460±30	9.8×10^{18}	$2.6(\pm0.4)\times10^{-4}$	6×10^{-6}	1.75
			790±70	2.4×10^{18}	$6(\pm3)\times10^{-5}$	1×10^{-6}	1.29
IRAS 15194-5115	23	2×10^{15}	410±20	9.8×10^{18}	$2.6(\pm0.4)\times10^{-4}$	9×10^{-6}	1.92
CIT 6	21	2×10^{15}	670±20	7.4×10^{18}	$2(\pm0.3)\times10^{-4}$	7×10^{-6}	1.57
			460±30	1.3×10^{19}	$3.5(\pm0.7)\times10^{-4}$	1×10^{-5}	1.7
			830±40	2.8×10^{18}	$7(\pm2)\times10^{-5}$	2×10^{-6}	1.27
AFGL 2513	26	3×10^{15}	530±30	7.3×10^{18}	$4.4(\pm0.8)\times10^{-4}$	1×10^{-5}	1.58
			400±30	1.1×10^{19}	$7(\pm1)\times10^{-4}$	2×10^{-5}	1.66
			1100±200	9.5×10^{17}	$6(\pm2)\times10^{-5}$	2×10^{-6}	1.27
V CYG	15	1×10^{15}	490±20	4.2×10^{18}	$2.7(\pm0.4)\times10^{-5}$	1×10^{-6}	1.59
V HYA	24	1×10^{15}	650±20	1.6×10^{19}	$1.0(\pm0.1)\times10^{-4}$	8×10^{-6}	1.94
			460±30	2.7×10^{19}	$1.8(\pm0.3)\times10^{-4}$	1×10^{-5}	2.11
			780±40	6.7×10^{18}	$4.5(\pm0.9)\times10^{-5}$	3×10^{-6}	1.45
AFGL 2688	20	8×10^{15}	300±20	2×10^{18}	$9(\pm2)\times10^{-4}$	7×10^{-6}	1.2
HD 44179	8.3	8×10^{15}	450±50	7.6×10^{16}	$2.9(\pm0.7)\times10^{-5}$	1×10^{-7}	1.02
IRAS 16594-4656	14	1×10^{16}	460±20	2×10^{18}	$1.4(\pm0.3)\times10^{-3}$	6×10^{-6}	1.36
			220±5	1×10^{19}	$6.5(\pm0.6)\times10^{-3}$	3×10^{-5}	1.49
			530±20	1×10^{18}	$7.3(\pm0.9)\times10^{-4}$	3×10^{-6}	1.27
AFGL 618	80	1×10^{16}	2.8×10^{18}	$1.9(\pm0.3)\times10^{-3}$	5×10^{-5}	1.07	
			415±20	6.8×10^{18}	$4.5(\pm0.6)\times10^{-3}$	1×10^{-4}	1.09
			915±60	7.9×10^{17}	$5(\pm1)\times10^{-4}$	1×10^{-5}	1.03
IRAS 21282+5050	14	4×10^{16}	170±10	7.5×10^{17}	$8(\pm2)\times10^{-3}$	1×10^{-5}	1.17
CPD-568032	22.6	4×10^{16}	380±20	6.8×10^{16}	$7(\pm1)\times10^{-4}$	1×10^{-6}	1
Hen 2-113	23	4×10^{16}	390±20	4.7×10^{16}	$5.0(\pm0.6)\times10^{-4}$	9×10^{-7}	1

TABLE 5.3A: Continued.

Target	v_{exp} (km s^{-1})	r_{CO} (cm)	T (K)	N^{col} (cm^{-2})	M ($M_\odot$)	$\dot{M}$ ($M_\odot$ yr^{-1})	Correction $_M$
IRC+10216 (OD 745)	14.5	3×10^{15}	510±20	5.8×10^{18}	$3.5(\pm0.5) \times 10^{-4}$	5×10^{-6}	1.76
			290±30	1.2×10^{19}	$7(\pm2) \times 10^{-4}$	1×10^{-5}	1.86
			620±30	2.3×10^{18}	$1.3(\pm0.3) \times 10^{-4}$	2×10^{-6}	1.27
(OD 894)*	14.5	3×10^{15}	490±20	1×10^{19}	$6(\pm1) \times 10^{-4}$	9×10^{-6}	2.19
			260±20	2×10^{19}	$1.2(\pm0.2) \times 10^{-3}$	2×10^{-5}	2.15
			680±150	3×10^{18}	$2(\pm2) \times 10^{-4}$	3×10^{-6}	1.5
(OD 1087)	14.5	3×10^{15}	580±20	5.5×10^{18}	$3.3(\pm0.5) \times 10^{-4}$	5×10^{-6}	1.69
			290±30	1.2×10^{19}	$7(\pm2) \times 10^{-4}$	1×10^{-5}	1.71
			740±50	2.1×10^{18}	$1.2(\pm0.4) \times 10^{-4}$	2×10^{-6}	1.34
(OD 1113)*	14.5	3×10^{15}	500±20	9×10^{18}	$6(\pm1) \times 10^{-4}$	8×10^{-6}	2.12 [2]
			270±50	1.7×10^{19}	$1.0(\pm0.4) \times 10^{-3}$	2×10^{-5}	2.01
			680±150	3×10^{18}	$2(\pm2) \times 10^{-4}$	3×10^{-6}	1.5
(OD 1257)	14.5	3×10^{15}	500±20	6.6×10^{18}	$3.9(\pm0.6) \times 10^{-4}$	6×10^{-6}	1.84
			320±60	1.2×10^{19}	$7(\pm3) \times 10^{-4}$	1×10^{-5}	1.95
			620±40	2.5×10^{18}	$1.5(\pm0.4) \times 10^{-4}$	2×10^{-6}	1.29
(OD 1288)*	14.5	3×10^{15}	440±20	1×10^{19}	$6(\pm1) \times 10^{-4}$	9×10^{-6}	2.23
			260±5	1.9×10^{19}	$1.1(\pm0.3) \times 10^{-3}$	2×10^{-5}	2.11
			580±120	2.9×10^{18}	$2(\pm2) \times 10^{-4}$	3×10^{-6}	1.51
(OD 1296)	14.5	3×10^{15}	500±20	6.3×10^{18}	$3.7(\pm0.6) \times 10^{-4}$	6×10^{-6}	1.81
			290±50	1.3×10^{19}	$8(\pm4) \times 10^{-4}$	1×10^{-5}	1.93
			630±40	2.1×10^{18}	$1.2(\pm0.4) \times 10^{-4}$	2×10^{-6}	1.28

[2] For OBSIDS marked with an asterisk (OD 894, 1113, 1296) the fitting was performed using 9 lines. 15 lines were used for the rest of OBSIDS.

In a number of targets we identified a double-temperature ("warm" and "hot") component. These deviations from a single straight line fit are in line with those found in some of the O-rich objects in Chapter. 4 and in other previous works (e.g. Justtanont et al., 2000; Wesson et al., 2010a; Matsuura et al., 2014; Cernicharo et al., 2015a; Cordiner et al., 2016). AFGL 618 and IRAS 16594-4656 are the targets whose RDs show the most obvious departure from linearity. IRAS 16594-4656 is particularly interesting since we found a much cooler warm-component of just T_{warm} ~220 K, and a breakpoint at lower energies (E_u/k = 1049.9 K) compared to other targets typically with T_{warm} ~ 450 K up to E_u/k=1794.3 K.

As in Chapter 4, in order to investigate if the double temperature component is consistent with resulting from the temperature stratification within the inner layers of the CSEs, we compared the hot-to-warm M, and T_{rot}, ratios (Fig. 5.11), and find that they are correlated. If the temperature profiles in the envelope follow a power-law of the type $T(r) \propto r^{-\alpha}$, with α being a constant, then the trend in Fig. 5.11 should also follow approximately a power-law function. We find $\alpha \sim 0.4$, which is similar to the value found for the O-rich targets studied in Chapter 4. The value of α is in agreement with past works that suggested that the kinetic temperature distribution is shallower, with values of α down to ~ 0.4-0.5, for the inner (~5×10^{14}-3×10^{15} cm) CSE layers (De Beck et al., 2012a; Lombaert et al., 2016a; Matsuura et al., 2014) than for the outer regions, where the steepest temperature variations (α ~1-1.2) are found (>10^{16} cm; Teyssier et al., 2006a).

We have also estimated α for IRC +10216 obtaining a value ($\alpha = 0.45 \pm 0.06$) in good agreement with the power-law exponent in the inner CSE (up to ~3×10^{15} cm) deduced from detailed non-LTE excitation and radiative transfer models (De Beck et al., 2012a).

Therefore, the empirical relation found between the hot-to-warm ratio of M, and T_{rot}, is consistent with the double-T_{rot}, component in some of our targets stemming (at least partially) from the temperature stratification across the inner envelope layers. The two components in the RD do not necessarily imply two distinct/detached shells of gas at different temperatures, but they most likely reflect the temperature decay laws. As explained in Chapter 4, in case of LTE deviations (not impossible in the lowest mass-loss rate objects), the value of α obtained from this simple approach would more closely represent the dust (rather than the gas) temperature distribution. This needs confirmation by detailed non-LTE models to the individual targets.

Individual targets: comparison with previous works

It is not possible to directly compare most of our results with literature because past studies have been focusing on the cold, outer components of CSEs. Prior to Herschel there was a study based on ISO LWS data in roughly the same wavelength range by Justtanont et al., 2000 who also performed RD analysis (without opacity correction). They found T_{rot}, ~700(±90) K and T_{rot}, ~380(±30) K for AFGL 618 and AFGL 2688 respectively. We obtained similar results without opacity correction, but introducing this effect lowered these values to T_{rot},~690(±30)K and T_{rot}, ~300(±20) K. In AFGL 618 the central star is hot enough (T_{eff}~ 33000 K) to produce FUV photons that heat the gas. In AGFL 2688 this is probably

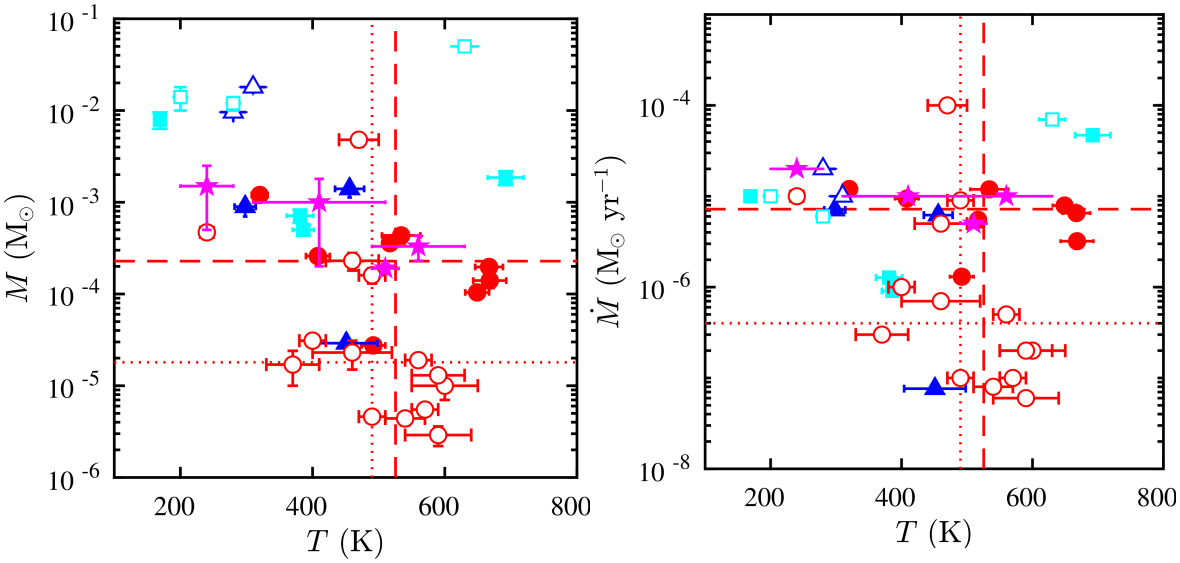

FIGURE 5.10: Temperature, mass and mass-loss rate of C-rich stars and O-rich stars. The filled symbols correspond to the C-rich sample in this chapter while the open symbols are the O-rich targets in Chapter 4; The magenta star markers are OH/IR stars from their sample. In every panel we show the median of each quantity using dashed lines for the C-rich AGBs and dotted lines for the O-rich AGBs.

not the case since the central star is much cooler ($T_{\rm eff}$~7250 K), so low-velocity shocks are the most likely heating mechanism.

Also partially based on ISO data, Ryde, Schöier, and Olofsson, 1999b used a number of spectral lines of CO between J = 1-0 and J =21-20 to infer the kinetic temperature profile across the CSE of IRAS 15194-5115. According to their model, $T_{\rm kin}$~400 K at $r_{\rm CO}$(1-2)× 10^{15} cm, which is in excellent agreement with our opacity-corrected single component $T_{\rm rot}$~410 K for $r_{\rm CO}$= 2×10^{15} cm. This is because, as already pointed out by Ryde, Schöier, and Olofsson, 1999b, these high-J levels are mainly populated by collisions, therefore they are proxies for the kinetic temperature, at least out to a few ~10^{15} cm. Also using ISO data, Schöier, Ryde, and Olofsson, 2002 presented a kinetic temperature model for CIT 6 that shows that $T_{\rm kin}$~400-500 K at approximately $r_{\rm CO}$~ (1-2)×10^{15} cm, which is consistent with the warm component (T_{warm} 460 K) that we infer and the representative radius $r_{\rm CO}$= 2×10^{15} cm adopted. The hot component (T_{hot} ~830 K) found by us would imply that regions closer to the star have an important contribution to the emission of the highest-J lines.

The only star whose inner/warmer (gaseous) CSE had been studied in detail before using Herschel/PACS data is IRC+10216. This was done by Decin et al., 2010 using high-J CO spectral lines to infer the kinetic temperature profile as a function of radial distance. They find $T_{\rm kin}$~500-600 K at $r_{\rm CO}$~(1-2)×10^{15} cm. Here we applied the opacity correction for $r_{\rm CO}$=~3×10^{15} cm which seems to be the layer at which $T_{\rm kin}$~300 K in their model. This is also the average value of T_{warm} that we found by fitting only the lowest J transitions, which does not change appreciably with time despite strong line flux variability (Fig. 5.9). The hot component (~600-700 K) may correspond to $r_{\rm CO}$~1×10^{15} cm according to their model.

Using *Herschel*/SPIRE data,Wesson et al., 2010a also performed RD analysis of CO spectra and derived $T_{\rm rot}$~70-230 K and $T_{\rm rot}$~100-200 K for AFGL 618 and AFGL 2688,

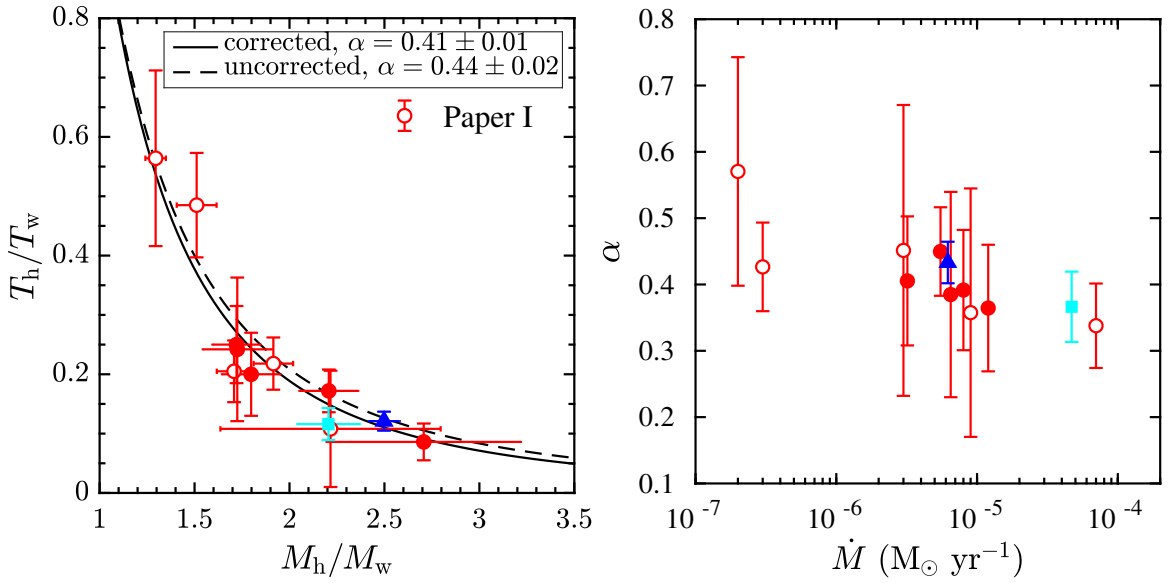

FIGURE 5.11: Hot/warm temperature ratio versus hot/warm mass ratio for AGBs and post-AGBs. The lines correspond to power-law fits with index α = 0.4 for the opacity corrected RDs (solid) and α = 0.44 for the uncorrected RDs (dashed). Blanked symbols (Paper I) correspond to Chapter. 4.

respectively. The rotational temperatures we find are thus higher than the ones obtained in Wesson et al., 2010a as expected. Further Large-velocity gradient (LVG) calculations by those authors suggested that hot material at approximately 1000 K might exist at the high-velocity wind region of AFGL 618, which could be the one traced by PACS since we found T_{hot} ~900 K.

For HD44179 (the Red Rectangle) we obtained $T_{\rm rot}$, ~440 K, which is about 2-3 times larger than the range of values inferred by Bujarrabal and Alcolea, 2013 from *Herschel*/HIFI lower-J CO observations. It is not surprising that we find a larger value since the higher J lines probed by PACS are probably formed deeper inside the rotating circum-binary disk at the core of this object. Meanwhile follow up analysis has shown more clearly an outflow with ~500K (Bujarrabal, 2016), but also seems that such temperature conditions could exist in a region of the inner disk with a radius of about $r_{\rm CO}$, ~2×10^{15} cm, unresolved by PACS. The opacity correction would still be moderate for this value ($\tau_{J=14-13}$ ~ 0.67), and it lowers the rotational temperature to $T_{\rm rot}$, 410 K which is still within the uncertainties. For the remaining yPNe (IRAS 21282+5050, CPD- 568032, Hen 2-113) there are no kinetic temperature models in the literature that we could compare our results to.

5.6.2 Mass-loss rate

As in Chapter 4, we have compared the values of the mass-loss rates derived from our simple RD analysis with other values found in the literature mostly from low-J observations, paying special attention to a few targets with detailed non-LTE excitation and radiative transfer analysis of CO data including at least some high-J transitions observed with *Herschel*. This is also a way of ascertaining the robustness of the RD method.

Figure 5.12 shows our estimate of the mass-loss rate versus that found in the literature. For each target the markers correspond to the single temperature component for the radius mentioned in Table 5.3, and the error bars represent the uncertainty in the radius for the adopted $V_{\rm exp}$. The range of values found in literature are shown by the gray shaded area whose bounds are set by the maximum and minimum $\dot{M}$, plus uncertainties when reported (factor of ~3 in AGBs, Ramstedt et al., 2008a, De Beck et al., 2010a. Those values have been rescaled to the same distance, $V_{\rm exp}$, and $\chi_{\rm CO}$, here adopted.

Similarly to the non C-rich THROES targets in Chapter 4, our mass-loss rates are in good agreement with values in the literature within the large uncertainties. In our case, these are dominated by the uncertainty in $r_{\rm CO}$. We see that the range of radii we explored yields a $\dot{M}$, that fits within the shaded area. In many cases, the error bars are truncated at the upper limit above which the line opacities would be too large to allow reliable estimates of the masses and mass-loss rates (see Fig. C.10). For example, in the case of AFGL 3068 this seems to imply smaller radius than what we have adopted to better match the values in literature.

In the case of IRC+10216, the opacity correction for $r_{\rm CO}$= ~2×10^{15} cm (instead of $r_{\rm CO}$= 3×10^{15} cm) would result in $\dot{M}\approx$ 1.4×10^{-5} $M_\odot$ yr^{-1}, (not displayed) that would best match the estimate from mm observations. However in these circumstances the expected opacities in the lowest J lines would be too large (τ »1). Nonetheless, the derived T$_{warm}$ and T$_{hot}$ are consistent with kinetic temperature profile models as explained in Section 5.6.1. We find an average value of four OBSIDs of $\dot{M}$~5×10^{-6} $M_\odot$ yr^{-1}, which is lower than the range $\dot{M}$, (1-3)×10^{-5} $M_\odot$ yr^{-1}, scaled from Teyssier et al., 2006a; De Beck et al., 2010a, De Beck et al., 2012a. However the value obtained for the warm component agrees with the lower limit of this range (because of the larger M). We obtain T$_{warm}$ ~300 K and $\dot{M}_{warm}$ ~1×10^{-5} $M_\odot$ yr^{-1}, for a radius of $r_{\rm CO}$= 3×10^{15} cm, in good agreement with the results of radiative transfer modelling of the same high-J CO lines by Decin et al., 2010. Scaling their $\dot{M}$, to the same distance and $\chi_{\rm CO}$, gives $\dot{M}$~1.2×10^{-5} $M_\odot$ yr^{-1}, with an uncertainty of a factor 2.

For V Hya we obtained $\dot{M}$~8×10^{-6} $M_\odot$ yr^{-1}, which is lower than $\dot{M}$~3×10^{-5} $M_\odot$ yr^{-1}, from Camps, 2011 who performed radiative transfer calculations using the same PACS spectrum. In this case, however, the spatio-kinematic structure of the molecular outflow is more complex than assumed here. In particular, multiple kinematic (fast and slow) components seem to be present Hirano et al., 2004; Sahai, Sugerman, and Hinkle, 2009, which not only translates into a larger uncertainty in the characteristic value of $V_{\rm exp}$, in the PACS CO-emitting layers, but also implies that the "equivalent" mass-loss rate is particularly questionable.

For V Hya, for pPNe and yPNe, the assumption of constant-velocity spherically- symmetric mass loss may also not hold so their $\dot{M}$, estimations are supposed to present larger uncertainties and have to be interpreted with caution. in spite of this, we have checked that, even in these cases, our values are in good agreement with previous estimates (making similar simplifying assumptions) in the literature. For example, for the Red Rectangle, we obtained $\dot{M}$~2×10^{-7} $M_\odot$ yr^{-1}, which is within the (scaled) range of $\dot{M}$~(0.2-1.4)×10^{-7} $M_\odot$ yr^{-1}, reported by De Beck et al., 2010a.

In summary, our results are consistent with the literature within the typical uncertainties, but it is hard to tell what is the exact cause of the slight discrepancies from case to case. One

obvious reason is that the simple RD method and our assumption of a characteristic value of r_{CO}, (unknown, but crudely constrained from first principles and observations) only provides a rough estimate of the mass-loss. We also note, that the bulk of the CO emission under study is produced in the warm inner layers of the CSEs of our targets down to a location where $\tau \sim 1$. For very optically thick CSEs, there may be an additional amount of gas that is not fully recovered after the moderate opacity correction applied. Another reason for $\dot{M}$, discrepancies is the different number of transitions and range of E_u covered by different studies. Non-LTE excitation and radiative transfer models of the CO emission including a wide range of J- transitions is needed to obtain accurate estimates of the mass-loss rates and, in particular, to address $\dot{M}$, time modulations.

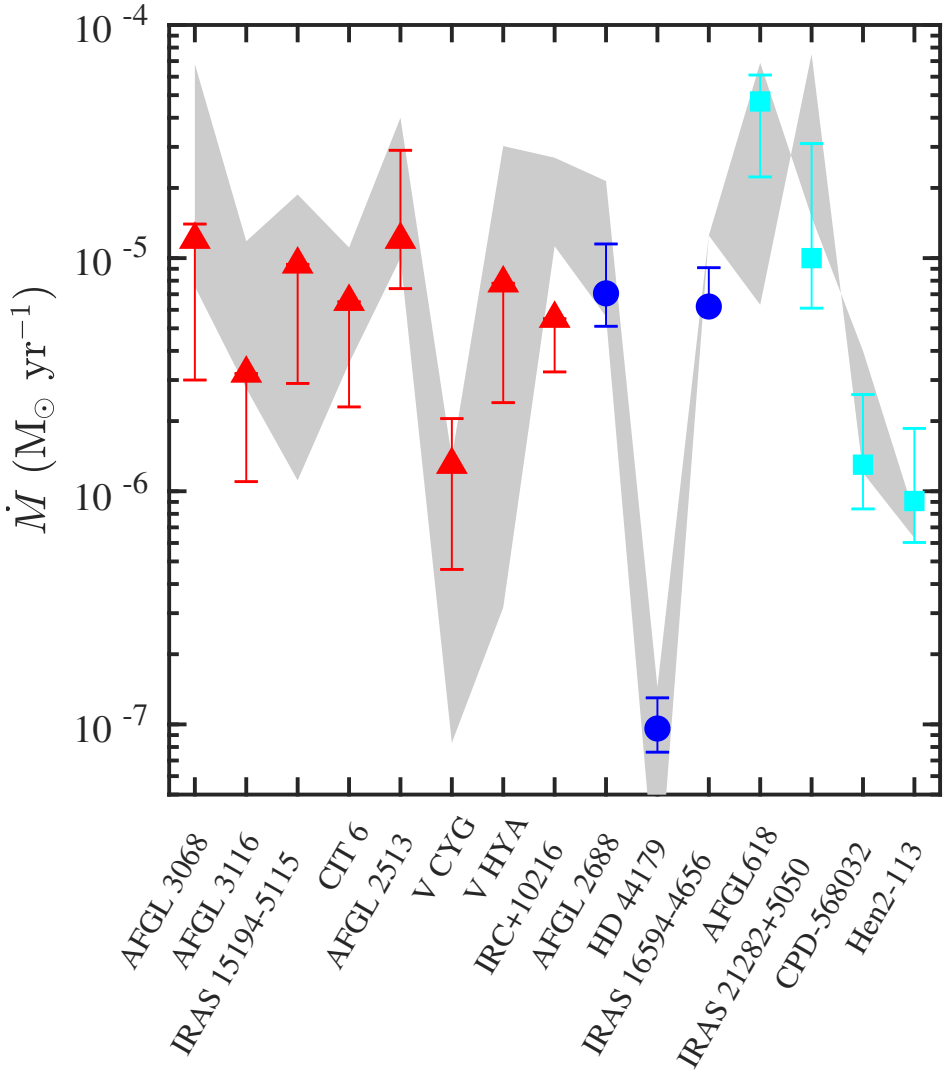

FIGURE 5.12: Comparison between the mass-loss rate in this work and the literature. The markers correspond to the radius listed in table 5.3 for each target and the error bars are mass-loss rates for a given range of radii. The shaded area are the results from literature scaled to the same parameters here assumed (see text).

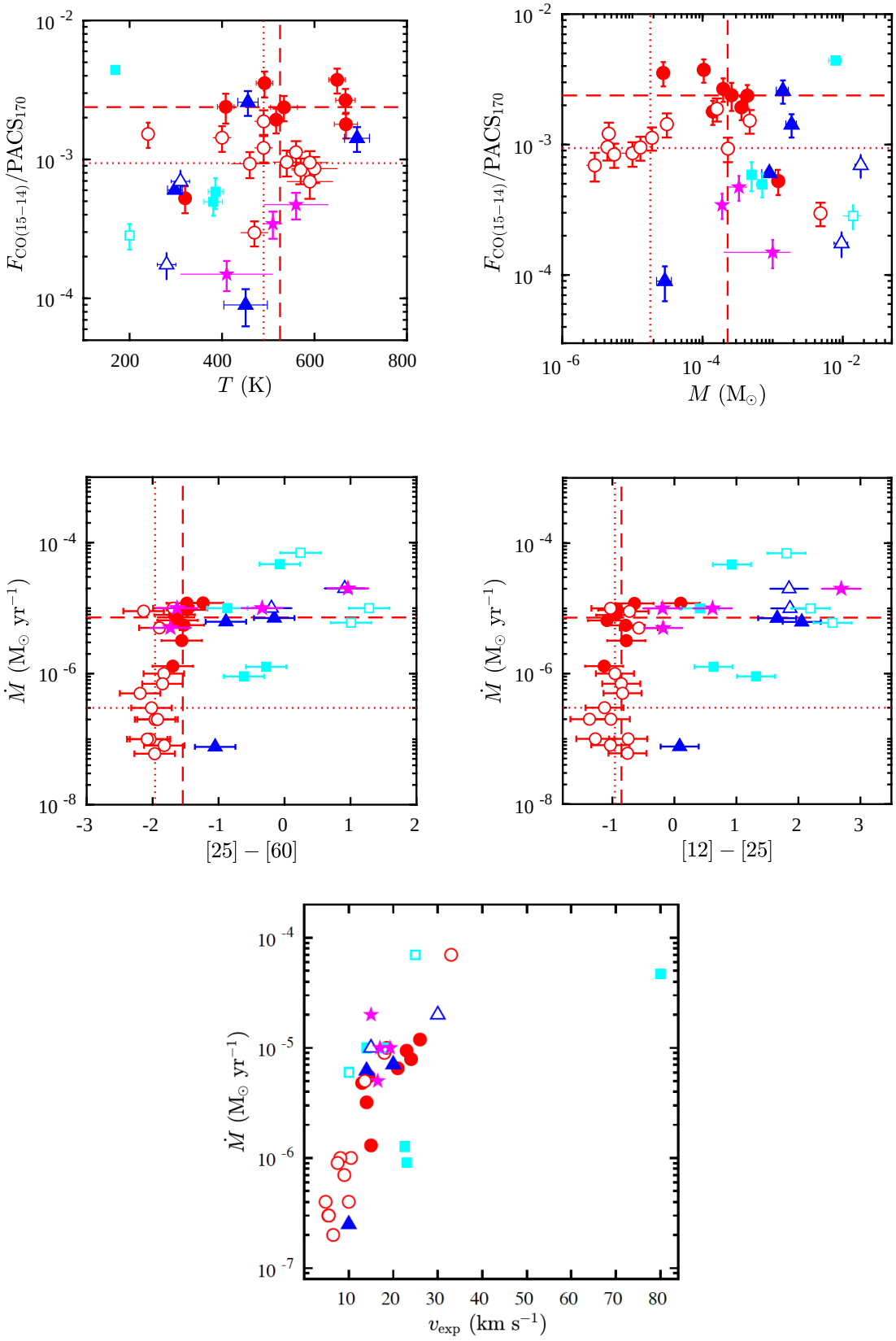

FIGURE 5.13: Line to continuum ratio, temperature, mass, mass-loss-rate, expansion velocity and IRAS colors of the sample of C-rich and O-rich stars. Same color coding and symbols as in Fig. 5.10.

5.6.3 Comparison between the sample of O-rich and C-rich stars

In Figs. 5.10, 5.11 and 5.13 we plot together the results presented here to the ones obtained for the sample of O-rich and S-type stars in Chapter 4.

We find that the range of $T_{\rm rot}$, is approximately the same among C-rich and O-rich stars, but the O-rich AGBs have less massive CSEs by typically one order of magnitude, and lower expansion velocities. This in turn reflects on lower mass-loss rates on average. The scenario is reversed in the groups of PNe with the few O-rich PNe having more warm gas than the carbon counterparts. Probably the O-rich AGB stars studied in Chapter 4 are typically low massive stars with very large evolution times, while the O-rich post-AGBs and PNe are very massive objects that have undergone through the Hot Bottom Burning stage.

We stress that despite these trends being indicative of clear differences in the properties of the CSEs of the targets in the THROES catalogue, they may not be a general property of C-rich versus non C-rich targets, since our samples are not necessarily unbiased and they are definitely not statistically significant.

5.7 Conclusions

In this chapter, we use Herschel/PACS FIR spectra of a sample of 15 C-rich evolved stars, including AGBs, post-AGBs and PNe. Our findings can be summarized as follows:

The range of temperatures found in our sample, $T_{\rm rot}$=200-700 K, is larger than what had been deduced from mm/sub-mm observations, confirming that PACS CO lines probe deeper layers traditionally poorly studied (typically, $\sim10^{15}$ cm for AGBs and $\sim10^{16}$ cm for post-AGBs and PNes). The total gas mass of the warm envelope layers sampled by PACS data are between $M_{\rm tot}$=10^{-5}-10^{-3} $M_{\odot}$, with post-AGBs and yPNe being overall more massive.

We find clearly different temperature distributions for the different classes with AGBs having typically hotter gas (up to $T_{\rm rot}$= 1000 K) than post-AGBs ($T_{\rm rot}$< 500 K) and yPNe ($T_{\rm rot}$<400 K). The yPN AFGL 618 is a clear outlier with a very high amount ($M_{\rm tot}\sim10^{-3}$ $M_{\odot}$) of rather hot (up to $T_{\rm rot}\sim$900 K) gas, similar to the most massive AGBs in the sample.

For AFGL 3116, CIT 6, AFGL 2513, VHya, IRAS 16594-4656 and AFGL 618 a double temperature (hot and warm) component is inferred from the RDs. The mean temperatures of the warm and hot components are 400 K and 820 K, respectively. The mass of the warm component (10^{-5}-8×10^{-3}) $M_{\odot}$, is always larger than that of the hot component, by a factor 4-10.

The warm-to-hot $M_{\rm tot}$, and $T_{\rm rot}$, ratios in our sample are correlated and are consistent with an average temperature radial profile of $T \propto r^{-0.4}$, that is, slightly shallower than in the outer envelope layers, in agreement with recent studies.

The mass-loss rates estimated are in the range $\dot{M}$, $\sim10^{-7}$-10^{-4} $M_{\odot}$ yr^{-1}, in agreement (within the uncertainties) with values found in the literature for our targets.

We investigated the impact of CO line flux variability on the values of $M_{\rm tot}$, and $T_{\rm rot}$, derived from the simple RD analysis. We studied in detail the case of the Mira-variable AGB star IRC+10216, for which multi-epoch PACS data exist. In spite of strong line flux variability we find that the total gas mass and the average temperature derived from the RDs at different epochs are minimally affected. Only the hot component does show the sign of line variability ($\delta, T/T = 16\%$), roughly in-phase with the continuum periodicity.

Similarly to previous chapter we find an anti-correlation between $T_{\rm rot}$, and $M_{\rm tot}$, which may result from a combination of CO line cooling and opacity effects, and we find a correlation between $\dot{M}$, and $V_{\rm exp}$, which is consistent with the wind acceleration mechanism being more efficient the more luminous/massive the star is. These trends had been reported in previous studies using low-J CO transitions. We show that high-J CO emission lines probed by *Herschel*/PACS are good tracers of the warm gas ($T_{\rm rot}$, =200-900 K) surrounding evolved carbon stars. Using the simple RD technique, we have provided systematic and homogeneous insight into the deepest layers of these CSEs, though it relies on several approximations. Detailed non-LTE excitation and radiative transfer calculations are needed to determine the temperature stratification of the CSEs, to infer mass-loss rates and to address their time-variability.

Chapter 6

Study of the CO emission from the THROES sample with SPIRE

Amante Bandido

Miguel Bosé

6.1 Introduction

To complete our knowledge about the physical properties of the CSEs, we have carried out an analogue study to those presented in Chapters. 4 and 5 based on SPIRE spectroscopy data of a sample of O-rich and C-rich evolved stars from the THROES-SPIRE catalogue (Ramos-Medina in prep.). As we know, SPIRE covers a wide range of frequencies from 500 to 1500 GHz which enables the detection of CO rotational lines from J=4-3 (E_u=55 K) to J=13-12 (E_u=500 K) bridging the inner regions studied with PACS ($\sim 10^{15}$-10^{16} cm) and the outermost layers (up to $\sim 10^{18}$ cm) traditionally studied in the sub-mm and mm wavelength range observed from the ground.

The structure of the chapter is as follows. In Sect. 6.2, a general description of the sample is provided. In Sect. 6.3 the main observational results and the measurements of the CO line fluxes, are presented. These CO fluxes are used to create the rotational diagrams that are shown in Sect. 6.4. The physical results and their consequent analysis are found in Sect. 6.5 and Sect. 6.6, respectively. Finally, some conclusions are highlighted in Sect. 6.8.

6.2 Sample information

In its current version, the THROES-SPIRE catalogue contains spectroscopic data for a total of 68 low-to-intermediate mass evolved stars. Apodized spectra have been used in order to improve the line detection and fitting. We have selected objects with a minimum of three CO transitions detected with a signal-to-noise ratio of S/N>3, leading to a total of 34 out of 68 targets in the THROES-SPIRE catalogue.

These 34 evolved stars, 20 O-rich and 14 C-rich, cover different evolutionary stages, from the AGB to PN phase being the distribution as follows: For the O-rich sample we have 35% of AGBs, 25% of OH/IR stars, 20% of post-AGBs and 20% of PNe, regarding the C-rich sources we find 43% of AGBs, 43% of post-AGBs and 14% of PNe. A 70% of the O-rich sample and a 53% of the C-rich sources have, also, complementary high-J CO data studied in Chapters 4 and 5, respectively.

In Fig. 6.1 we present IRAS colours of the sources of our sample in comparison with the rest of CO non-detections objects of any chemical type contained in the THROES-SPIRE catalogue. The objects follow the evolutionary sequence described in previous chapters. As expected, the sources included in this study are intense FIR emitters with the $IRAS_{100}$ fluxes ranging from 10 to 1000 Jy and most of them presenting values around 100 Jy.

All the objects studied in this chapter except three, IRAS 19411-1416, NGC2440 and NGC 6720, have previous estimations of mass-loss rates in bibliography, mainly based on low-J CO lines, (see Table 6.3). The study presented here is the first one that makes use of the CO lines covered by SPIRE spectral range (from J =4-3 to J =13-12) in a systematic and homogeneous way.

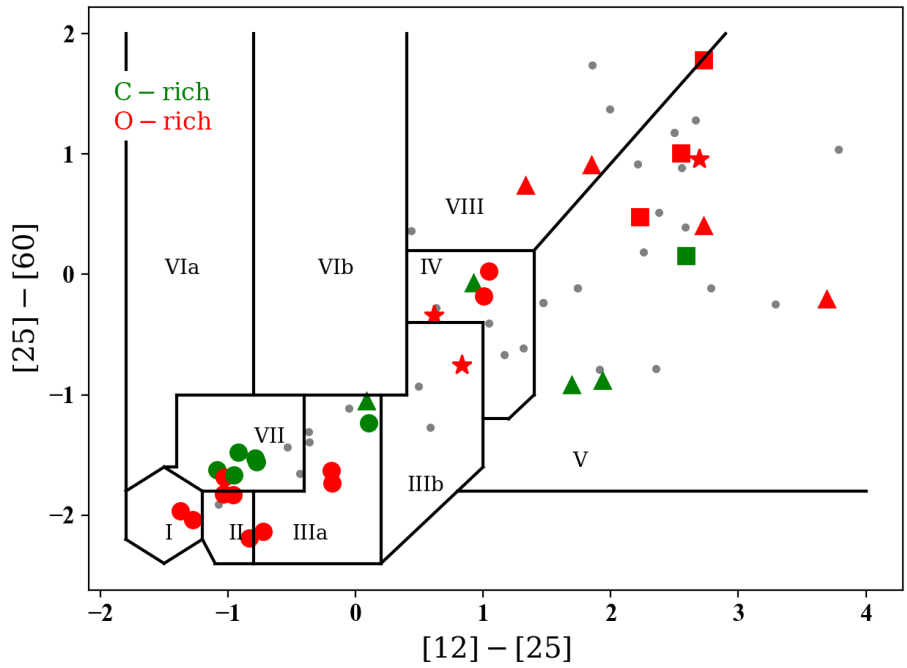

FIGURE 6.1: IRAS colour-colour diagram for SPIRE targets. In this figure O-rich (red) and C-rich (green) sources are plotted together. Symbols code is similar to that used in previous chapters: circles (AGBs), stars (OH/IR stars), triangles (post-AGBs) and squares (PNe).

6.3 Observational results

In Figs. 6.2 and 6.3 we display the continuum subtracted SPIRE spectra of the O-rich and C-rich sources (respectively) studied in this chapter. The continuum was subtracted following

the same method as for PACS data.

The way the objects have been sorted in these figures facilitates the comparison and identification of differences along the main evolutionary stages. For example, the molecular rich spectra of AGB stars are dissimilar to those coresponding to PNe which are characterized by intense atomic features. Some differences are also found between the O-rich and C-rich spectra due to the amount (O-rich spectra appears to be more populated) and kind of features found in them. For example: the HCN J_u=6-5 emission (531 GHz) present in less-evolved C-rich sources or the o-H_2O and p-H_2O (at 1096 GHz and 1114 GHz, respectively) identified in most of the O-rich objects. Other studies such as: Matsuura et al., 2016 and Van de Sande et al., 2018 have identified emission lines from abundant and common species in this frequency ranges like HCN, SiO, H_2O, SO_2, NH_3 and CN amongst others. Atomic lines such as CH+ (~820 GHz) and OH+ (~970 and 1030 GHz) are also identified in some post-AGBs and PNe of our study but not in AGBs.

The rotational CO transitions in the ground vibrational state (v=0) are very prominent, however as happened with PACS, the resolving power of SPIRE (from 300 up to few thousands of km s^{-1}) does not allow us to spectrally resolve any of the line profiles, even sources with fast and collimated winds in our sample (e.g. OH 231.8+4.2 Alcolea et al., 2001 or M1-92 Arrieta et al., 2003).

In this work we have measured the integrated flux of CO v=0 rotational lines with high-J levels, up to J=13 (E_u~500 K). These values are shown in Tables B.5-B.6, in Appendix B.

Certain CO rotational lines are known to be blended with transitions by other abundant species that lie within the same SPIRE spectral resolution element. We have identified, for example, the blend of CO (J=10-9) with H_2O (312-221) transition. Line blends have been excluded from our RD analysis, although they are also listed in Tables B.5-B.6 for completeness. In this table, we also list the lines that present a poor estimation of the underlying continuum level, although they have not been used for the rotational diagram analysis. As mentioned in previous chapters, the errors shown correspond to the mere propagation of the statistical errors.

In Fig. 6.4 we compare the integrated flux of the CO (J=7-6) transition at 806.7 GHz ($F_{CO\,7-6}$) with the IRAS 100 μm flux ($IRAS_{100}$) and the SPIRE continuum at 800 GHz ($SPIRE_{800}$), i.e. near the CO (J=7-6) line. As expected, there is a correlation between the CO line strength and the $IRAS_{100}$ and $SPIRE_{800}$ continuum fluxes, which confirms that objects with stronger molecular emission show, typically, stronger continuum emission from dust as well. As $F_{CO\,7-6}$ and $SPIRE_{800}$ were taken at the same time and using a similar configuration their correlation is stronger.

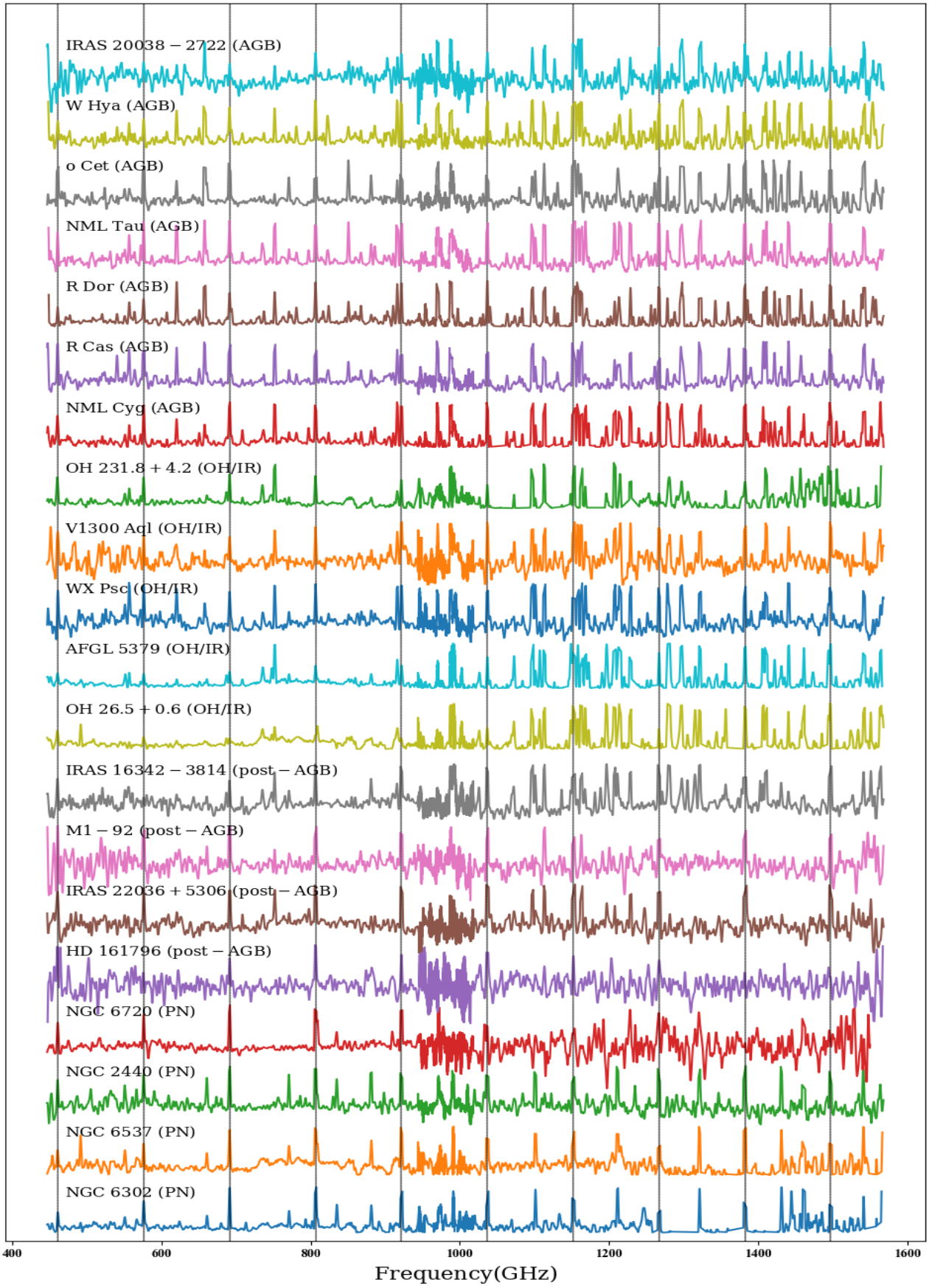

FIGURE 6.2: SPIRE, continuum subtracted, spectra of our O-rich sample. The ^{12}CO rotational lines are indicated by vertical dotted lines (see B.2). The upper-level rotational quantum number J_u of a few selected CO transitions are shown as a reference. The sources are sorted from top to bottom in these four groups: AGBs, extreme OH/IR stars, post-AGBs, and PNe. Within each category, targets are ordered based on the stellar effective temperature from the coolest source to the hottest one.

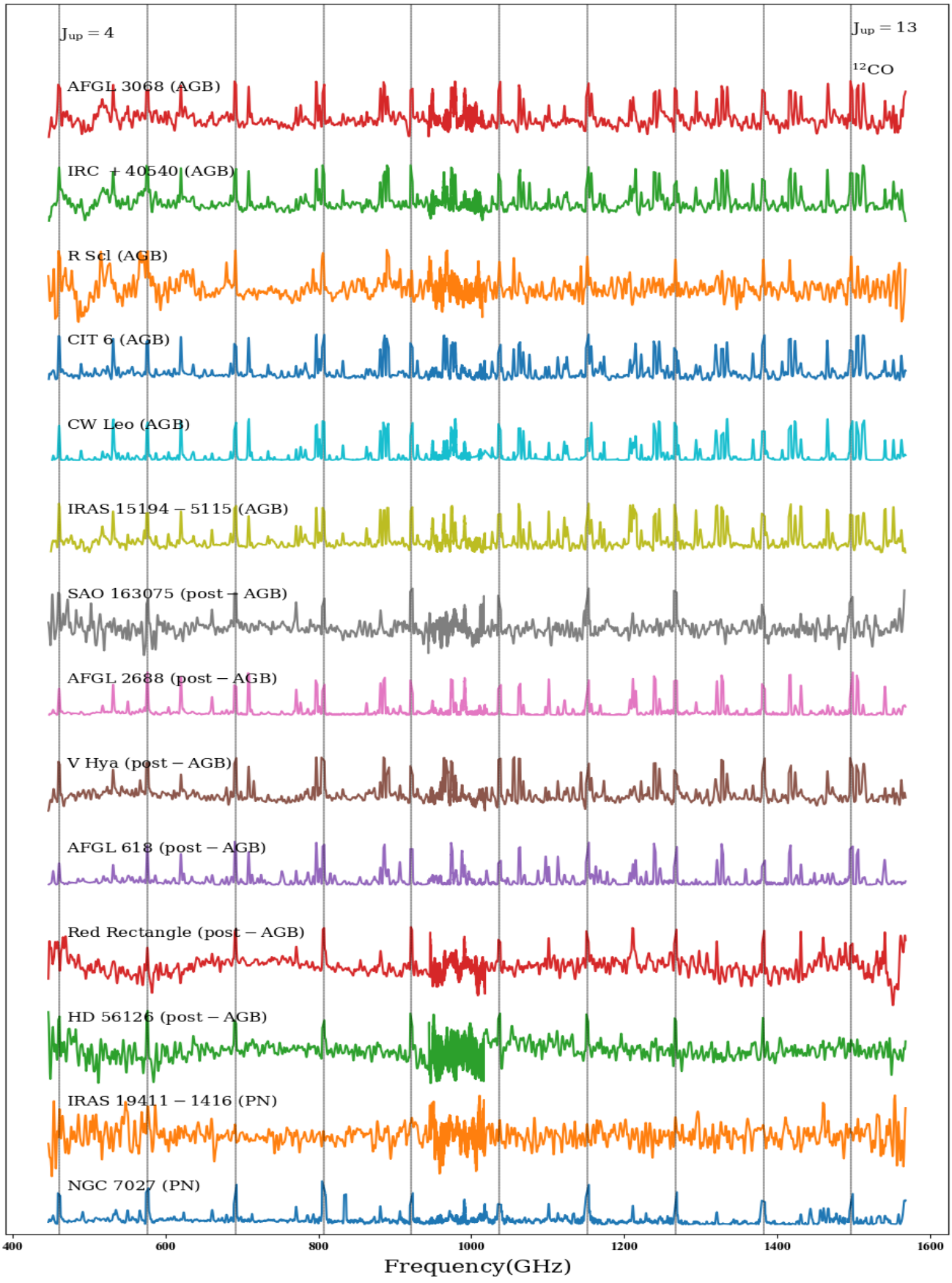

FIGURE 6.3: The same as in 6.2 but corresponding to the C-rich sample.

TABLE 6.1: Observations log. O-rich sources.

Target Name	Alternative Name	Class	RA (J2000)	Dec (J2000)	ObsIDs	Observing Date
IRAS 20038-2722	V1943 Sgr	AGB star	20:06:55.2	-27:13:29.8	1342268314	2013-03-24
W Hya	-	AGB star	13:49:02.0	-28:22:03.5	1342189116	2010-01-09
o Cet	Mira	AGB star	2:19:20.8	-2:58:39.5	1342189546	2010-01-19
NML Tau	IK Tau	AGB star	3:53:28.8	11:24:22.6	1342192176	2010-03-12
R Dor	-	AGB star	4:36:45.6	-62:04:37.8	1342245114	2012-04-27
R Cas	-	AGB star	23:58:24.870	51:23:19.70	1342246981	2012-06-12
NML Cyg	-	AGB star	20:46:25.5	40:06:59.4	1342243592	2012-04-01
OH 231.8+4.2	-	OH/IR star	7:42:16.8	-14:42:52.1	1342193665	2010-04-06
V1300 Aql	IRC -10529	OH/IR star	20:10:27.9	-6:16:13.6	1342216902	2011-03-27
WX Psc	IRC +10011	OH/IR star	1:06:26.0	12:35:53.0	1342246973	2012-06-11
AFGL 5379	IRAS 17411-3154	OH/IR star	17:44:24.0	-31:55:35.0	1342268287	2013-03-23
OH 26.5+0.6	V437 Sct	OH/IR star	18:37:32.5	-5:23:59.2	1342243624	2012-04-02
IRAS 16342-3814	-	post-AGB	16:37:39.9	-38:20:17.3	1342251319	2012-09-24
M1-92	Minkowski´s Footprint	post-AGB	19:36:18.9	29:32:50.0	1342243606	2012-04-01
IRAS 22036+5306	-	post-AGB	22:05:30.3	53:21:32.8	1342257338	2012-12-17
HD 161796	-	post-AGB	17:44:55.5	50:02:39.5	1342189117	2010-01-09
NGC 6720	M 57	PN	18:53:35.1	33:01:45.0	1342243616	2012-04-01
NGC 2440	-	PN	7:41:54.9	-18:12:29.7	1342221712	2011-05-26
NGC 6537	Red Spider Nebula	PN	18:05:13.1	-19:50:34.9	1342243627	2012-04-02
NGC 6302	Butterfly Nebula	PN	17:13:44.2	-37:06:15.9	1342191224	2010-02-26

TABLE 6.2: Observations log. C-rich sources.

Target Name	Alternative Name	Class	RA (J2000)	Dec (J2000)	ObsIDs	Observing Date
AFGL 3068	LL Peg	AGB star	23:19:12.4	17:11:35.4	1342189126	2010-01-09
IRC +40540	LP And	AGB star	23:34:27.5	43:33:01.2	1342246288	2012-05-30
R Scl	-	AGB star	1:26:58.1	-32:32:35.5	1342189545	2010-01-19
CIT 6	RW Lmi	AGB star	10:16:02.3	30:34:18.6	1342198264	2010-06-13
CW Leo	IRC +10216	AGB star	9:47:57.4	13:16:43.7	1342197466	2010-05-31
IRAS 15194-5115	II Lup	AGB star	15:23:05.1	-51:25:58.7	1342251281	2012-09-22
SAO 163075	HD 187885	post-AGB	19:52:52.7	-17:01:50.3	1342216903	2011-03-27
AFGL 2688	Egg Nebula	post-AGB	21:02:18.8	36:41:37.8	1342189123	2010-01-09
V Hya	-	post-AGB	10:51:37.3	-21:15:00.3	1342247570	2012-07-01
AFGL 618	CRL 618	post-AGB	4:42:53.7	36:06:53.2	1342191214	2010-02-26
					1342192835	2010-03-27
Red Rectangle	HD 44179	post-AGB	6:19:58.2	-10:38:14.5	1342227779	2011-08-28
					1342227781	2011-08-28
HD 56126	post-AGB	7:16:10.3 9:59:48.0	1342193664	2010-04-06		
IRAS 19411-1416	NGC 6818	PN	19:43:57.8	-14:09:11.9	1342268315	2013-03-24
					1342189124	2010-01-09
NGC 7027	-	PN	21:07:01.590	42:14:10.20	1342189125	2010-01-09
					1342221698	2011-05-26

TABLE 6.3: Stellar and circumstellar, bibliographic, information for the objects of the sample.

Target Name	Variability	$T_{\rm eff}$ (K)	d (pc)	$v_{\rm exp}$ (km/s)	$\dot{M}_{\rm Bibliography}$ ($M_\odot$ yr^{-1})		References
IRAS 20038-2722	SRb	2200	197	5.4	(0.2,1.3)$\times10^{-7}$	(0.1,4.0)$\times10^{-7}$	1,6,22
W Hya	SRa	2200	98	7.0	(0.5,1.5)$\times10^{-7}$	(0.3,4.0)$\times10^{-7}$	1,8,9,12,14,22,26
o Cet	Mira	2200	110	8.1	(2.2,5)$\times10^{-7}$	(0.1,1.0)$\times10^{-6}$	1,12,26
IK Tau	Mira	2700	260	19.0	(0.1,2)$\times10^{-5}$	(0.5,30)$\times10^{-6}$	1,3,9,12,13,14,18,26
R Dor	SRb	2800	59	5.7	(0.3,2.0)$\times10^{-7}$	(0.2,4.0)$\times10^{-7}$	1,3,9,14,22,26
R Cas	Mira	3100	176	10.5	(2.1,9.0)$\times10^{-7}$	(0.1,2.0)$\times10^{-6}$	1,3,9,12,14
NML Cyg	SRc	3800	1220	33.0	(0.2,8.7)$\times10^{-5}$	(0.2,20)$\times10^{-5}$	1,12,27
OH 231.8+4.2	Mira	2500	1500	15.0	(0.1,8.0)$\times10^{-5}$	(0.6,30)$\times10^{-6}$	1,12
V1300 Aql	Mira	2000	620	16.5	(0.1,1.0)$\times10^{-5}$	(0.7,30)$\times10^{-6}$	1,6,9,12,15
WX Psc	Mira	2000	700	19.3	(0.2,4.0)$\times10^{-5}$	(0.1,7.0)$\times10^{-5}$	1,9,10,12,15,16,26
AFGL 5379	Mira	2750	1190	22.0	(0.3,2.8)$\times10^{-5}$	(0.5,3.0)$\times10^{-4}$	12,26
OH 26.5+0.6	Mira	2750	1370	17.0	(1.6,9.7)$\times10^{-6}$	(0.1,2.0)$\times10^{-5}$	1,10,12
IRAS 16342-3814	No	3000[1]†	2000	23.0	3.5$\times10^{-4}$	(2.0,6.0)$\times10^{-4}$	2
M1-92	No	20000	2500	8.0	2.2$\times10^{-4}$	(1.0,4.0)$\times10^{-4}$	23
IRAS 22036+5306	No	40000	4000	30.0	(0.7,7.5)$\times10^{-5}$	(0.4,10)$\times10^{-5}$	1,11
HD 161796	No	40000	4000	10.0	(1.0,4.0)$\times10^{-5}$	(0.2,2.0)$\times10^{-5}$	20,23
NGC6720	No	120000	450	50.0	-	-	-
NGC2440	No	200000	1500	18.0	-	-	-
NGC6537	No	200000	1500	18.0	2$\times10^{-5}$	(1.0,3.0)$\times10^{-5}$	1
NGC6302	No	250000	1170	10.0	(0.1,1.5)$\times10^{-4}$	(0.6,30)$\times10^{-5}$	1,7,17
AFGL 3068	Mira	2000	1100	16.0	(2.0,6.0)$\times10^{-5}$	(0.2,2.0)$\times10^{-4}$	9,12,15,18
IRC +40540	Mira	2040	630	14.0	(0.7,1.2)$\times10^{-5}$	(0.3,2.0)$\times10^{-5}$	9,12,15,18

TABLE 6.3: Continued.

Target Name	Variability	$T_{\rm eff}$ (K)	d (pc)	$v_{\rm exp}$ (km/s)	$\dot{M}_{\rm Bibliography}$ ($M_\odot$ yr^{-1})		References
R Scl	Mira	2300	290	16.5	(1.6,3.5)×10^{-6}	(0.3,5.0)×10^{-5}	3b,12
CIT 6	SRa	2450	400	17.0	6×10^{-6}	(0.2,1.0)×10^{-5}	9,12,18,19
CW Leo	Mira	2200	120	14.5	(0.2,2.0)×10^{-5}	(0.1,5.0)×10^{-5}	12,15,18,24,25
IRAS 15194-5115	Mira	2400	500	21.5	(0.4,1.7)×10^{-5}	(0.2,4.0)×10^{-4}	6,9,12
SAO 163075	No	7000	2400	11.3	3.5×10^{-6}	(2.0,7.0)×10^{-5}	20
AFGL 2688	No	7000	7250	17.6	3×10^{-5}	(0.3,1.0)×10^{-4}	28
V Hya	SR/Mira	2650	2160	30.0	6.1×10^{-5}	(0.4,1.0)×10^{-4}	12
AFGL 618	No	33000	1000	12.0	5.5×10^{-5}	(0.8,2.0)×10^{-5}	4
Red Rectangle	No	7750	710	15.0	1×10^{-6}	(0.9,2.0)×10^{-6}	5
HD 56126	No	6500	2400	10.0	(0.5,2.3)×10^{-5}	(0.3,4.0)×10^{-5}	20,21
IRAS 19411-1416	No	160000	2000	15.0	-	-	-
NGC 7027	No	190000	1000	10.0	2×10^{-4}	(0.5,2.0)×10^{-4}	19

2

[2]Column 1: Target name; Column 2: Variability of the central star; Column 3: Effective temperature of the star; Column 4: Adopted distance to the object; Column 5: Expansion velocity of the circumstellar envelope; Column 6: *Left)* Mass loss rate taken from literature. *Right)* Range of mass loss rates shown at left after being scaled to the values of d, $v_{\rm exp}$ and χ_{CO} used in this work. For those with only one previous estimation, the range cover a factor of 3 around that value after scaling. Column 7: References. [3]†Uncertain.

1) Ramos-Medina et al., 2018a 2) Sahai et al., 2017 3) Maercker et al., 2016b, 3b) Maercker et al., 2016a 4) Huang et al., 2016b, 5) Bujarrabal, 2016, 6) Danilovich et al., 2015, 7) Santander-García et al., 2015, 8) Khouri et al., 2014, 9) Ramstedt and Olofsson, 2014a, 10) Justtanont et al., 2013, 11) Sánchez Contreras and Sahai, 2012a, 12) De Beck et al., 2010a, 13) Decin et al., 2010, 14) Maercker et al., 2008, 15) Ramstedt et al., 2008a, 16) Decin et al., 2007, 17) Dinh-V-Trung et al., 2008b, 18) Teyssier et al., 2006a, 19) Fong et al., 2006, 20) Hrivnak and Bieging, 2005, 21) Meixner and Fong, 2004, 22) Olofsson et al., 2002, 23) Bujarrabal et al., 2001, 24) Schöier and Olofsson, 2001b, 25) Groenewegen et al., 1998, 26) Loup et al., 1993, 27) Knapp et al., 1982, 28) Bechis, 1976

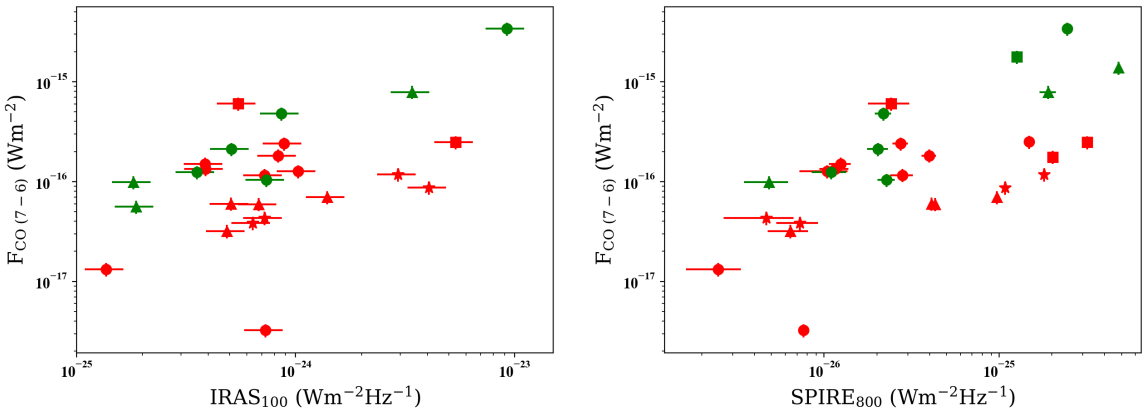

FIGURE 6.4: Left) Integrated flux of the CO J=7-6 transition against the IRAS 100 μm flux. Targets with bad quality (Quality Flag≠3) IRAS$_{100}$ data are excluded. Right) Fluxes of the CO J=7-6 transition and the adjacent continuum (SPIRE$_{800}$).

6.4 CO: Rotational Diagrams

To study the intermediate region of the CSEs probed by the rotational CO lines detected in SPIRE we have made used of the RD method described in Chapters 4 and 5, the lines were fitted using gaussian functions in an interactively mode. The adopted distance to the sources used to determine the total mass of the CO-emitting volume are indicated in Table 6.3.

To derive the extent of the emitting region (r_{CO}) for AGBs, we have taken the same representative temperature distribution in the circumstellar envelope ($T(r)$ ~1/r$^{\alpha}$; α ~0.5-1.0) used for PACS analysis. Assuming the typical values of rotational temperatures found for these objects, which are found to range between 60 and 190 K (See Sect. 6.5.1), we infer values of r_{CO} between ~ 4×10^{15} cm and 4×10^{16} cm.

Once estimated these r_{CO} values fro AGB stars, we introduced a second, opacity-based, criterion to estimate r_{CO}, for post-AGBs and PNe and, also, constrain the one previously derived for AGBs. The CO column densities derived from our RD analysis, assuming typical values of ~10^{16} cm, are moderate, N_{CO}^{col}<2×10^{18} cm^{-2} for most of the sources, resulting in line optical depths of the order of ~0.9, and even lower in some cases, for the CO J=6→5 transition, which is the line with the largest opacity among the CO lines detected with SPIRE. However, for some objects of our SPIRE sample, the r_{CO} adopted had to be adapted to a value slightly larger than the radius of the wind layer where $\tau_{J=6\rightarrow5}$ ~ 1 to satisfy the "opacity criterion". For most of the objects of both O-rich and C-rich samples, the opacity correction is negligible for CO lines higher than J=11→ 10. The final r_{CO} adopted for each source can be found in Table. 6.4. At the same time, the opacity curves applied are displayed in Figs. C.12-C.13a.

6.5 Results

The CO RDs of our targets, from which we derive the rotational temperature ($T_{\rm rot}$), the total emitting mass ($M_{\rm tot}$), as well as, the mass-loss rates ($\dot{M}$) for their adopted $r_{\rm CO}$, are shown in Fig. 6.5a-6.6a.

6.5.1 Rotational temperatures and total emitting mass of H_2

The values of M and $T_{\rm rot}$ deduced from the CO-SPIRE RDs are listed for each target in Table 6.4, together with a few other relevant parameters such as the adopted $r_{\rm CO}$, the distance to the object and the expansion velocity of the circumstellar envelope. In Fig. 4.6 we show the M and $T_{\rm rot}$ values for each target, with and without the opacity correction, and the final histogram distributions.

For most objects, the RDs include CO transitions with upper-level energies that range from $E_{\rm u}$~50 K to $E_{\rm u}$~500 K and are well fitted using a single temperature component. The single-fit rotational temperatures obtained range from ~40 K (OH 231.8+4.2) to ~190 K (IRAS 16342-2814), with an average value of $T_{\rm rot}$~100 K. If we determine the mean value of $T_{\rm rot}$ for O-rich and C-rch sources, independently, we find no significant difference.

For 12 sources (seven O-rich and five C-rich) in the sample, it was necessary to use a double-slope component to properly fit to all the data points. We refer to the CO emitting regions with the lowest and highest $T_{\rm rot}$ values derived from the double-fit as the "cold" and "mild" CO components, respectively (Fig. 6.5a-6.6a). The rotational temperatures of the cold and mild components are in the range ~40-70 K and ~140-300 K, respectively. As expected, the values of $T_{\rm rot}$ obtained from a single-fit to the RDs are intermediate to those of the cold and mild components. At this point it is important to highlight that the temperatures of the "mild" component derived from SPIRE are similar to that "warm" one derived from PACS data (see Table. 4.1), indicating that they are mapping adjacent regions.

The single-fit values of the total mass of the CO-emitting volume range between M~8×10^{-5} $M_{\odot}$ (IRAS 20038-2722) and ~9×10^{-2} $M_{\odot}$ (AFGL 5379), with a mean value of M~2×10^{-2} $M_{\odot}$. Studying the C-rich and O-rich sources separately we derive very similar average values of 10^{-2} and 2.4×10^{-2} $M_{\odot}$, respectively.

The small to moderate opacity correction applied to the SPIRE RDs leads to also moderate mass-correction factors around 20-30% with three extreme cases from 60% to 80% corresponding to (HD 161796, NGC 6720, SAO 163075). No evident difference has been found between the mass-correction factors estimated for the O-rich and C-rich samples.

The mass of the cold CO component is always larger than the mass of the mild component, for both O-rich and C-rich samples. For the cold component, these values vary from M=7.4×10^{-5} (R Dor) to ~1.9×10^{-1} $M_{\odot}$ (V Hya), and for the mild one between 1.2×10^{-5} (R Dor) and $4.0\times10^{-2}M_{\odot}$ (V Hya). These values are compatible to those derived for the "warm" component of CO-PACS analysis (see Table. 4.1). The cold-to-mild M and $T_{\rm rot}$ ratio, and their relation, is further examined in Sect. 6.6.

Following a similar schema to that used in Chapters 4 and 5, we have investigated if there are any trends between $T_{\rm rot}$ and M, derived for our SPIRE-RD analysis, and other observational parameters, such as the terminal expansion velocity of the envelope ($V_{\rm exp}$) and the strength of the CO (J=7-6) transition (Figs.6.7 and 6.8).

First, in Fig. 6.7, we notice that C-rich and O-rich objects cover similar ranges of $T_{\rm rot}$ and $M_{\rm tot}$ values, from ∼50-180 K and from $\sim10^{-4}$ to 10^{-1} $M_{\odot}$ respectively. In terms of $T_{\rm rot}$ the less evolved objects (that is, AGB stars) of both C-rich and O-rich samples cover a narrower interval, from ∼60 to 100 K, while the most evolved ones (post-AGBs and PNe) are spread along a wider range (∼50-180 K). Regarding $M_{\rm tot}$ both O-rich and C-rich subsamples follow a common trend where, typically, the most evolved objects present the highest values. This is particularly evident in the O-rich subsample where post-AGBs, PNe and even OH/IR stars are located around the 10^{-3} to 10^{-1} $M_{\odot}$ range. In contrast, O-rich AGB stars present $M_{\rm tot}$ values from $\sim10^{-5}$ to 10^{-3} $M_{\odot}$ with the only exception of NML Cyg a well know very massive AGB star that present a $M_{\rm tot}$ value of 4×10^{-2} $M_{\odot}$. This distribution of masses could reflect an observational bias in favour of massive post-AGBs and PNe stars, the same effect was described in Chapter 4. The described distributions of both $T_{\rm rot}$ and $M_{\rm tot}$ magnitudes are the same before and after the opacity correction is applied.

In Fig. 6.8 (top-left panel) we identify two different groups of sources when representing the $M_{\rm tot}$, versus the $T_{\rm rot}$. The first one, mainly populated by AGB stars, cover a wide range of $M_{\rm tot}$ (from $\sim10^{-4}$ to $\sim10^{-2}$ $M_{\odot}$) and a narrower one in terms of $T_{\rm rot}$ (80-100 K). The second group, where the most evolved stars are located, has typically higher $M_{\rm tot}$, values (from $\sim10^{-2}$ to $\sim10^{-1}$ $M_{\odot}$) and present hotter temperatures (from 100 to 200 K). The anti-correlation found in Chapters 4 and 5 is evident when focussing only in AGB stars.

In Fig. 6.8 (top-right), C-rich and O-rich sources do not follow the same distribution. C-rich objects present an incipient positive correlation between the integrated flux of CO J=7-6 (∼150 K) line and $M_{\rm tot}$, ranging between 10^{-17}-10^{-15} (W m^{-2}) and 10^{-4}-10^{-1} $M_{\odot}$, respectively. This correlation was not found in O-rich objects as they populate an horizontal area which covers the whole range of $M_{\rm tot}$, (10^{-4}-10^{-1} $M_{\odot}$) and is around 10^{-16} W m^{-2}.

Finally, we investigated if a correlation exist between the CO J=7-6 line integrated flux normalized to the underlying ∼800 GHz-continuum observed with SPIRE ($F_{CO\,7-6}$/$SPIRE_{800}$) and the $T_{\rm rot}$ derived from the RD analysis of SPIRE data. No reliable correlation was found (Fig. 6.8, bottom), which is in contrast to the correlations found in Chapters 4 and 5. What we have found is that the C-rich sources typically present higher ratios than O-rich ones. The rotational line of CO ($J_{\rm u}$=7-6) presents a low $E_{\rm u}$∼150 K so all the sources studied have rotational temperatures high enough to populate this level, this fact leads us to think about the presence of opacity effects that may be playing a role in the observed distribution.

In Sect. 6.6 we further discuss the observed trends.

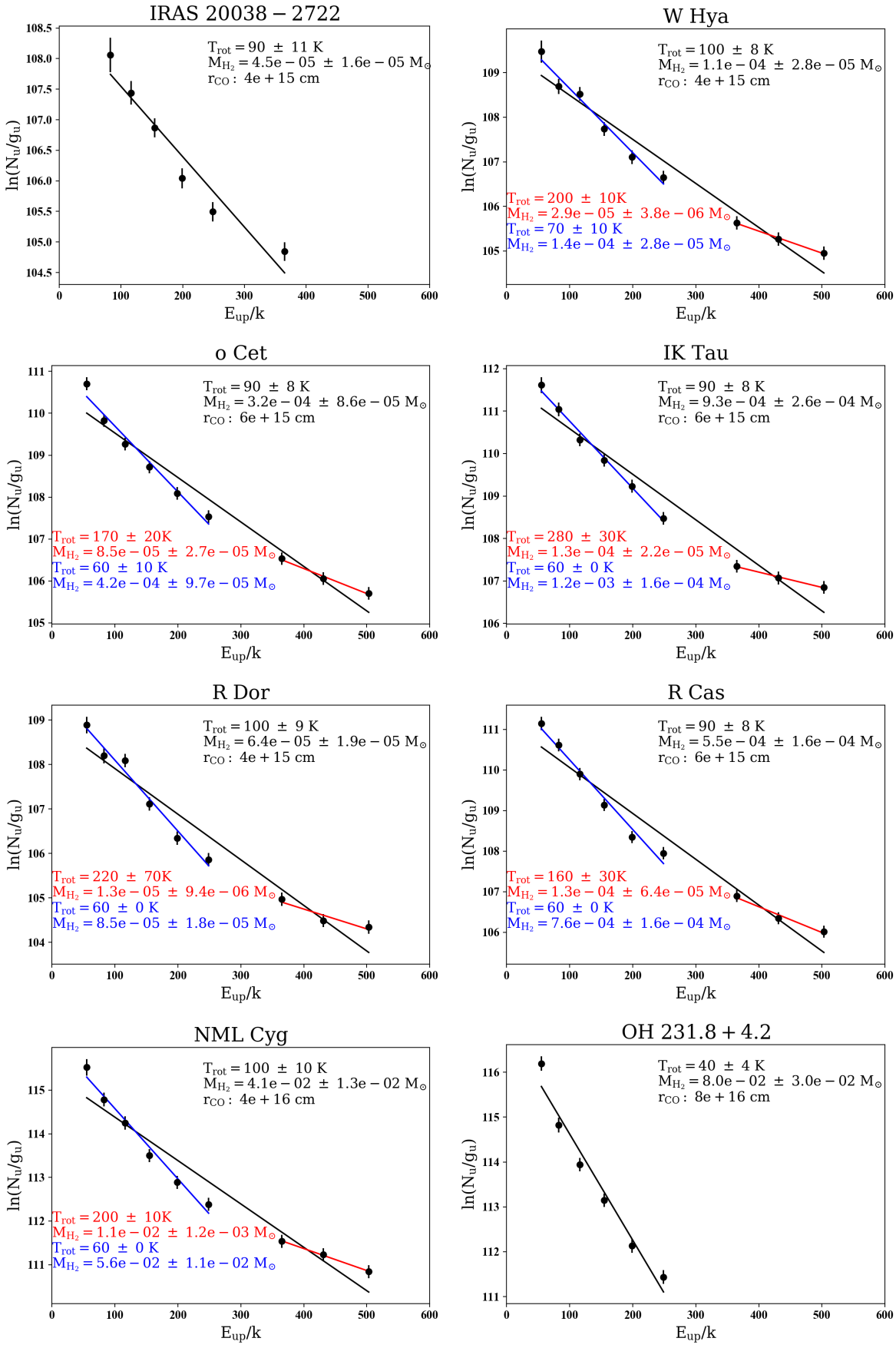

FIGURE 6.5A: Rotational diagrams of CO for our O-rich targets. For each source, the values of $T_{\rm rot}$ and $M_{\rm tot}$ derived from the fits (solid lines) are shown. Opacity correction has been applied.

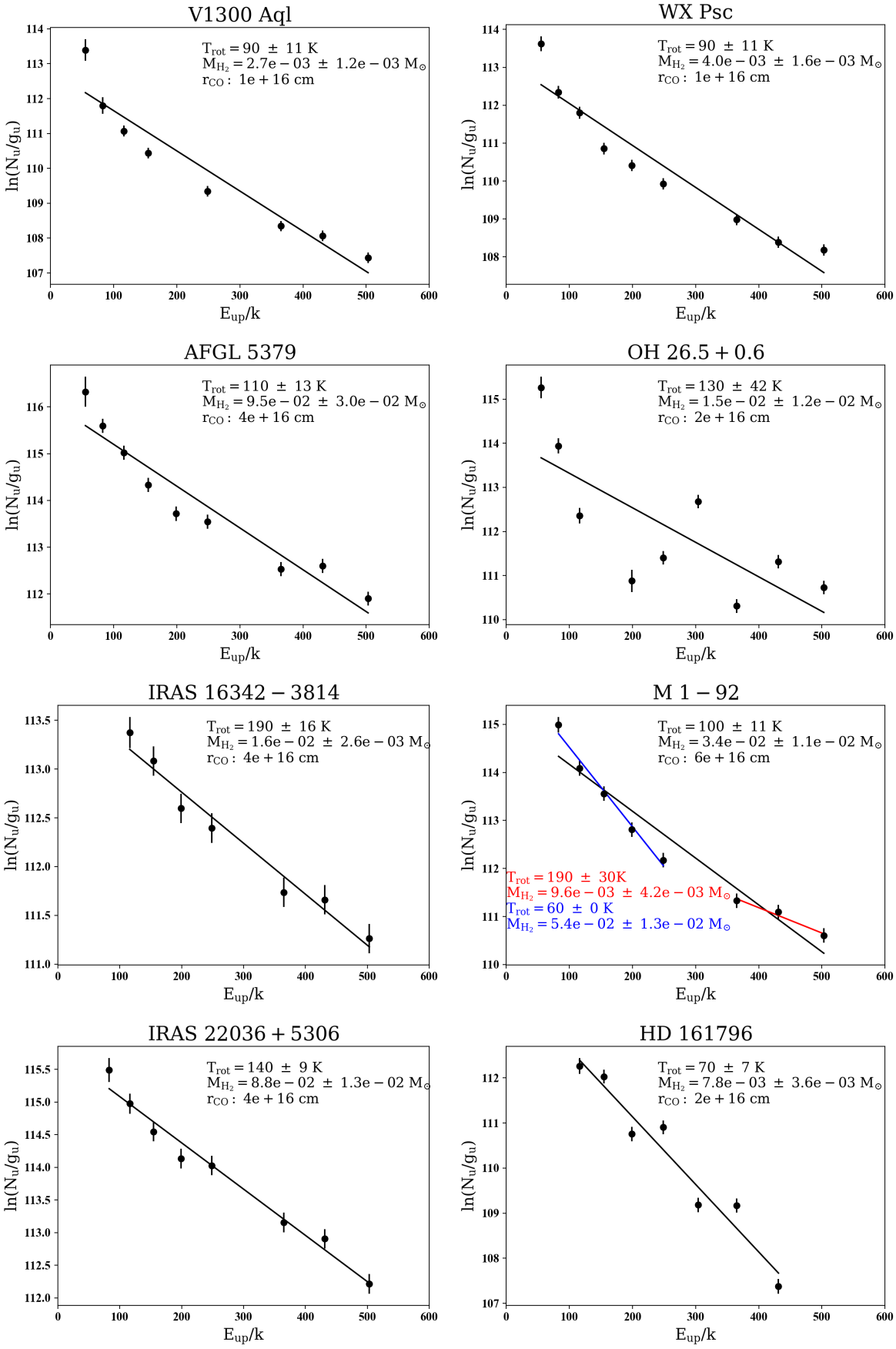

FIGURE 6.5A: Continued O-rich sources.

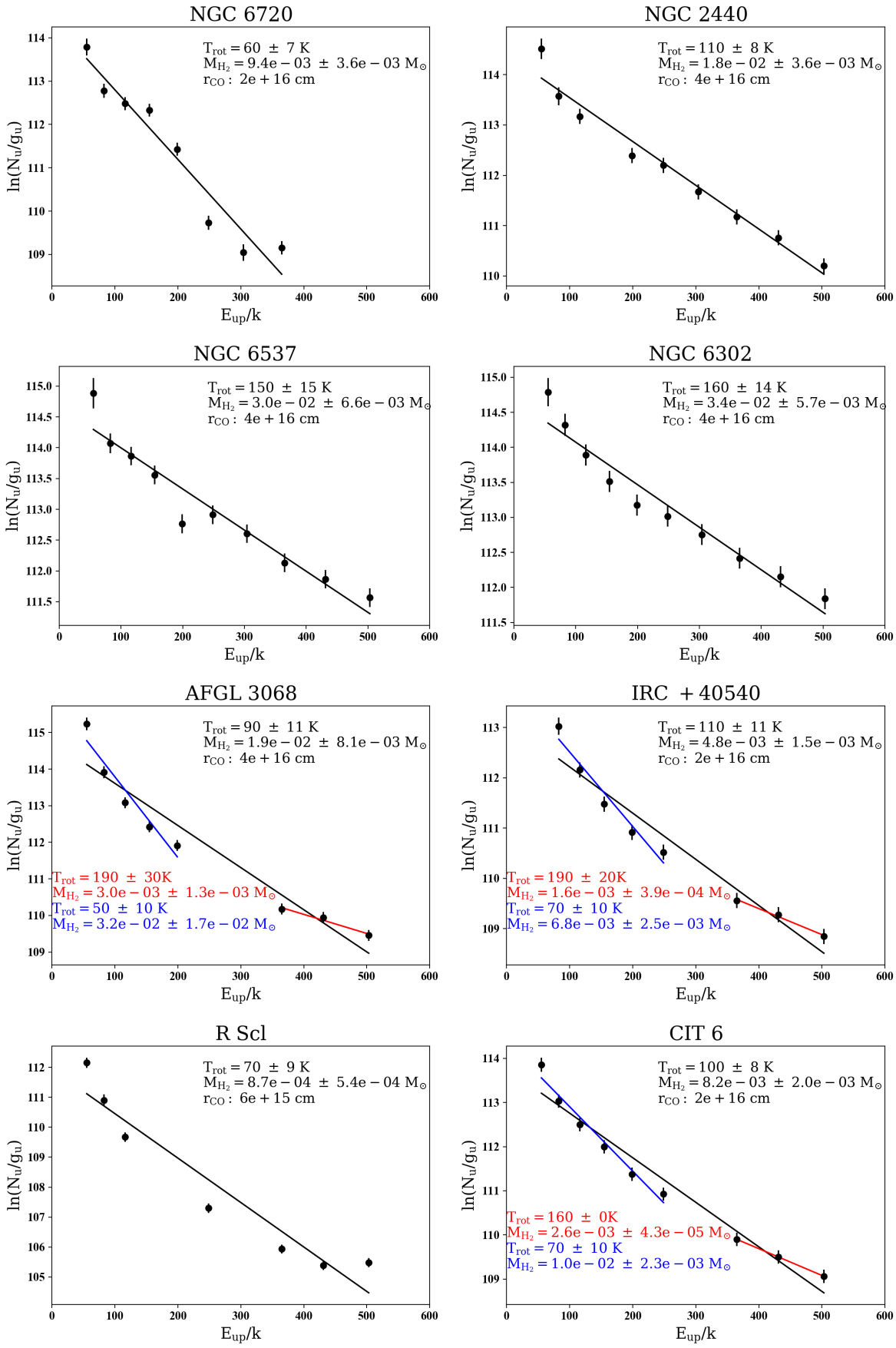

FIGURE 6.6A: C-rich sources.

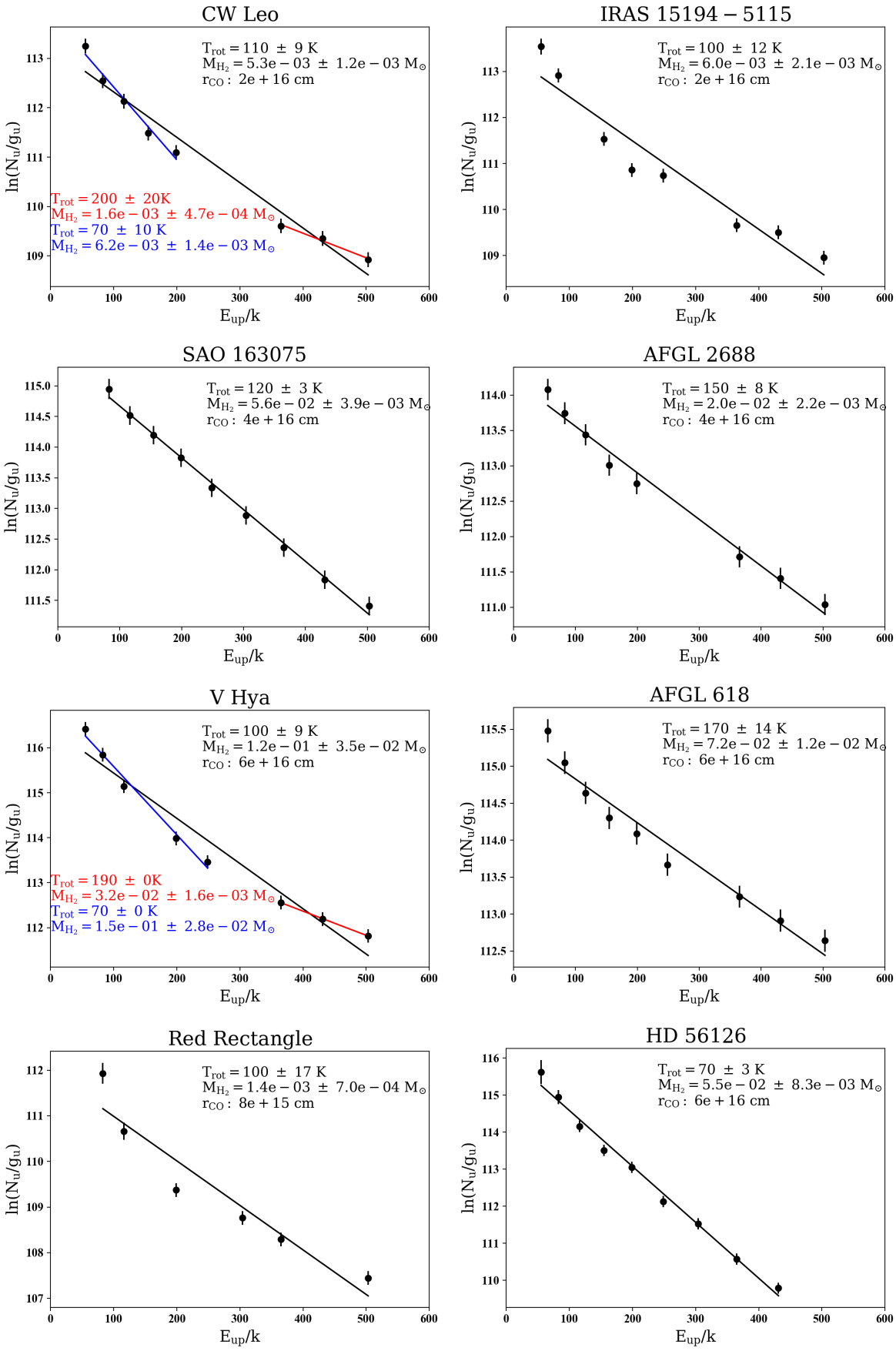

FIGURE 6.6A: Continued C-rich sources.

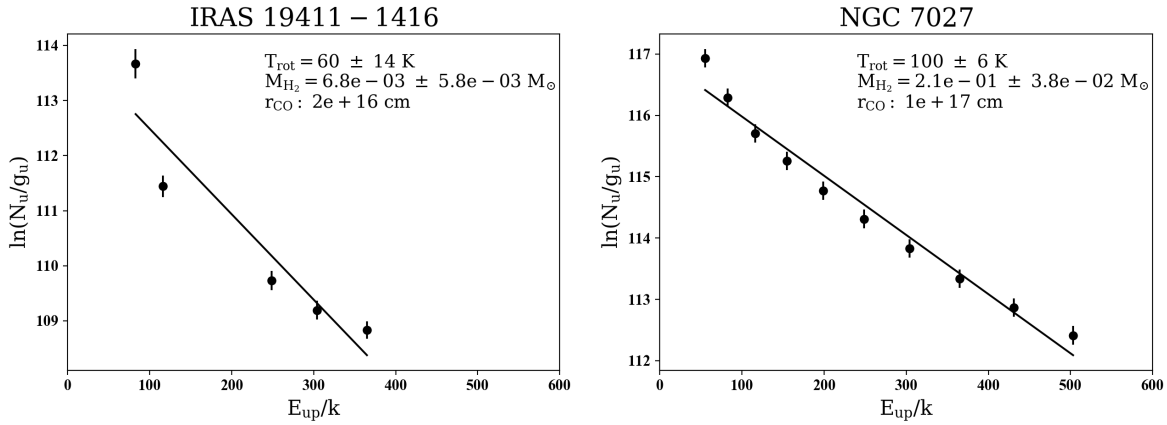

FIGURE 6.6A: Continued C-rich sources.

6.5.2 Mass-loss rate

The values of $\dot{M}$ deduced from the CO-SPIRE data are given in Table 6.4 and have been computed as explained in Sect. 4.5.2. In this table the $V_{\rm exp}$, taken from bibliography, as well as, the $r_{\rm CO}$, determined for each source are included.

In Figs. C.14a-C.15a (Appendix C.4.1), we show, for every object, the different values of $\dot{M}$ and $T_{\rm rot}$ that correspond to three different values of the radius around the adopted value ($r_{\rm CO}$). For each source, we have also plotted a grey region that represents the broad interval of mass-loss rates found in the literature. These values of $\dot{M}$ from the literature have been re-scaled after matching the expansion velocity ($V_{\rm exp}$), the distance (d) and the relative abundance of CO ($\chi_{\rm CO}$) to the values adopted here, which is needed for a proper comparison with our estimates of $\dot{M}$. The values of the mass-loss rates reported in the bibliography for each object are displayed in Table 6.3 together with the associated interval range of mass-loss rates after scaling and relevant references. To our knowledge, for NGC 6720, NGC 2440 (both O-rich) and IRAS 19411-1416 (C-rich) there are no previous characterization of their molecular envelopes in terms of mass and temperature.

Our estimates of the mass-loss rates are shown in Fig. 6.9 plotted against the rotational temperature, the expansion velocity, and the CO (J=7-6) line strength. In the $\dot{M}$ versus $T_{\rm rot}$ diagram there is a correlation as it is expected based on the similar trend observed directly between $M_{\rm tot}$ and $T_{\rm rot}$ (Fig. 6.8). This trend together with the clear correlation between $\dot{M}$ and $V_{\rm exp}$ and, the more scattered trend with $F_{\rm CO\,7-6}$ are briefly discussed in Sect. 6.6.

To validate our results we have compared our mass-loss rates estimations using SPIRE with those derived using PACS data, for common sources, and with $\dot{M}$, values found in bibliography.

In Fig. 6.10 (left-panel) we show, for each source, the mass-loss rate estimated in this chapter for the adopted SPIRE-radius ($r_{\rm CO}$) against a mean value of gas mass-loss rates found in the bibliography ($\dot{M}_{\rm Bibliography}$). We assign error bars of a factor 3 to our estimates of the mass-loss rate similar to what we did in Chapters 4 and 5.

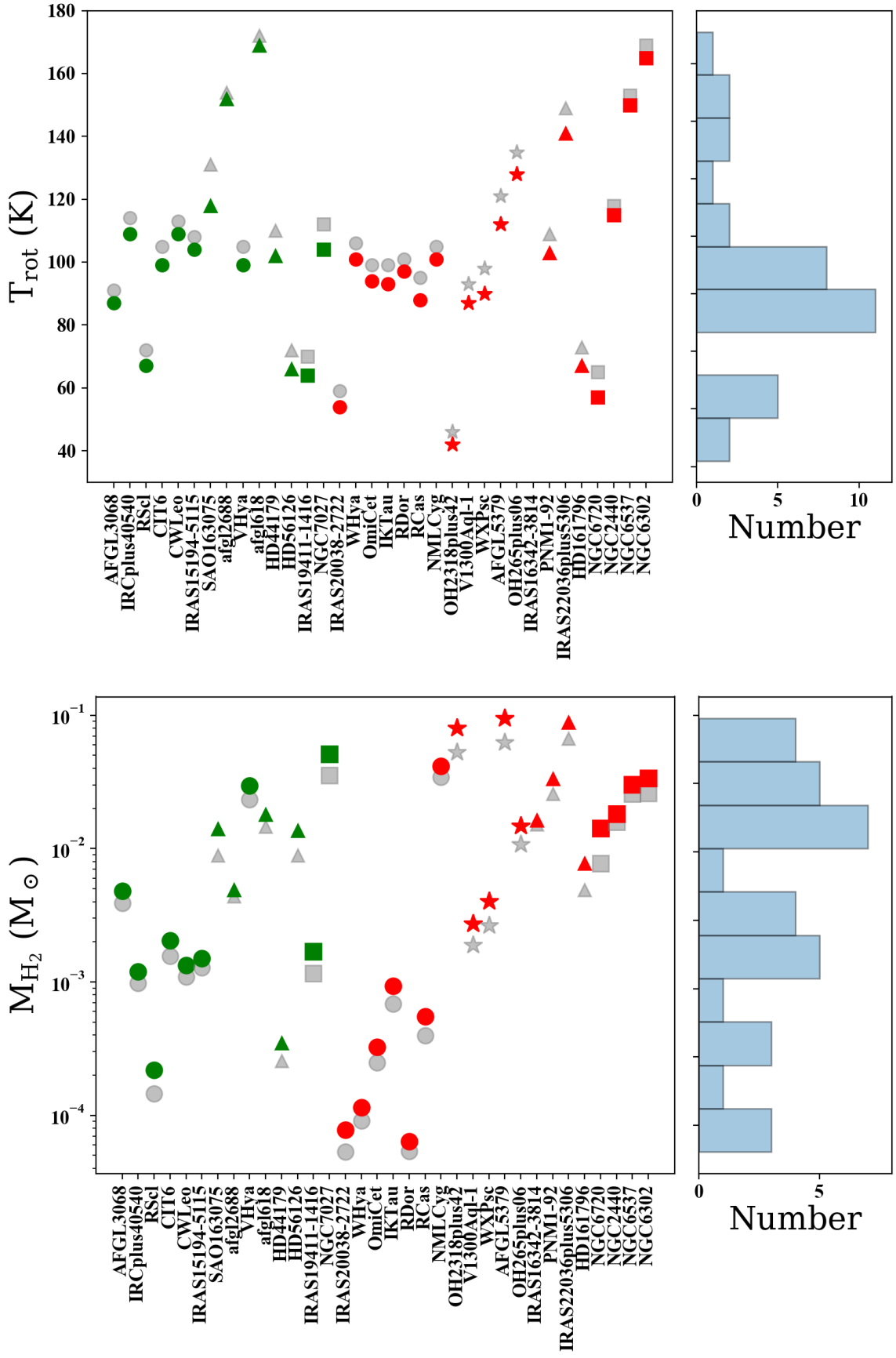

FIGURE 6.7: Values of T_{rot} and M_{tot} from our CO rotational diagram analysis (single fit; Sect. 6.5) before and after applying the opacity correction (grey and coloured symbols, respectively).

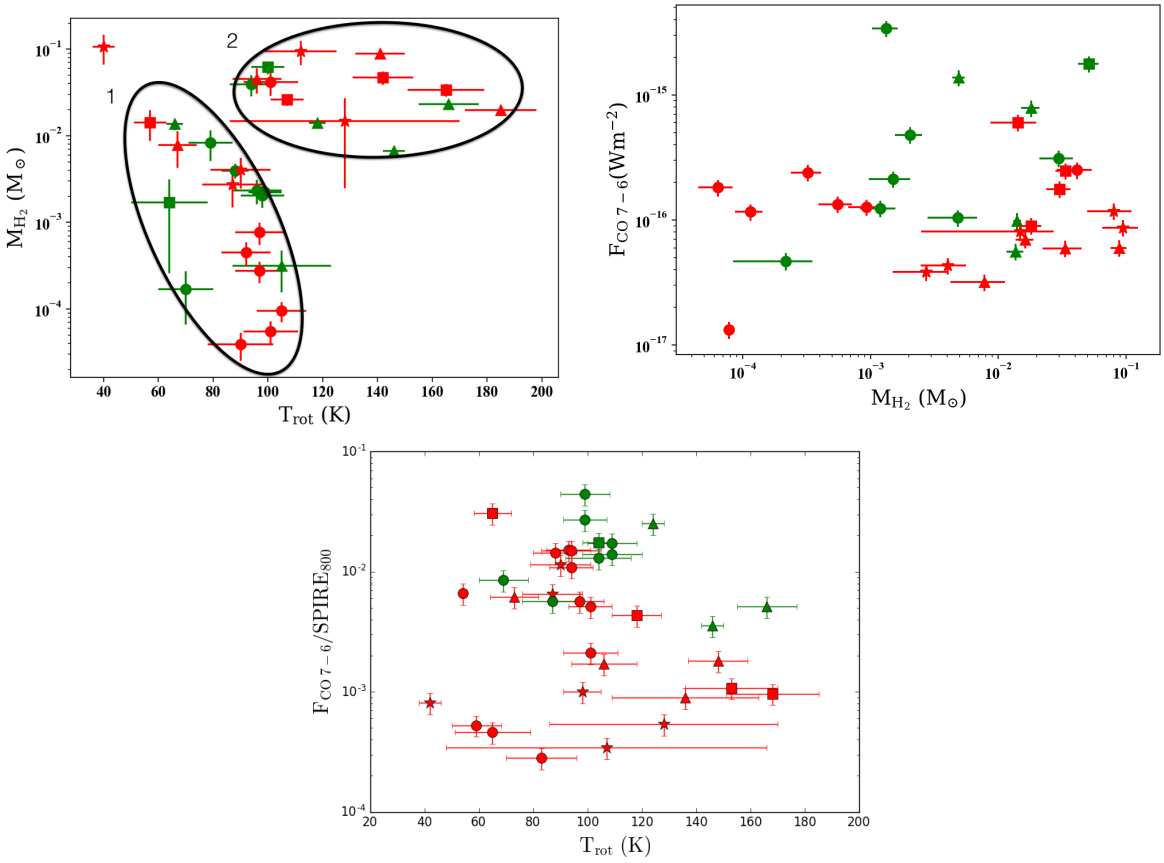

FIGURE 6.8: Relation between M_{H_2} and T_{rot} derived from our CO rotational diagram analysis and other magnitudes. Top-left) M_{H_2} vs T_{rot} (single-fit values), two different groups of sources are highlighted, see text for details. Top-right) Integrated fluxes of CO (J=7-6) vs M_{H_2} (single-fit) Bottom) Integrated fluxes of CO (J=7-6) line normalised to its adjacent continuum versus T_{rot}.

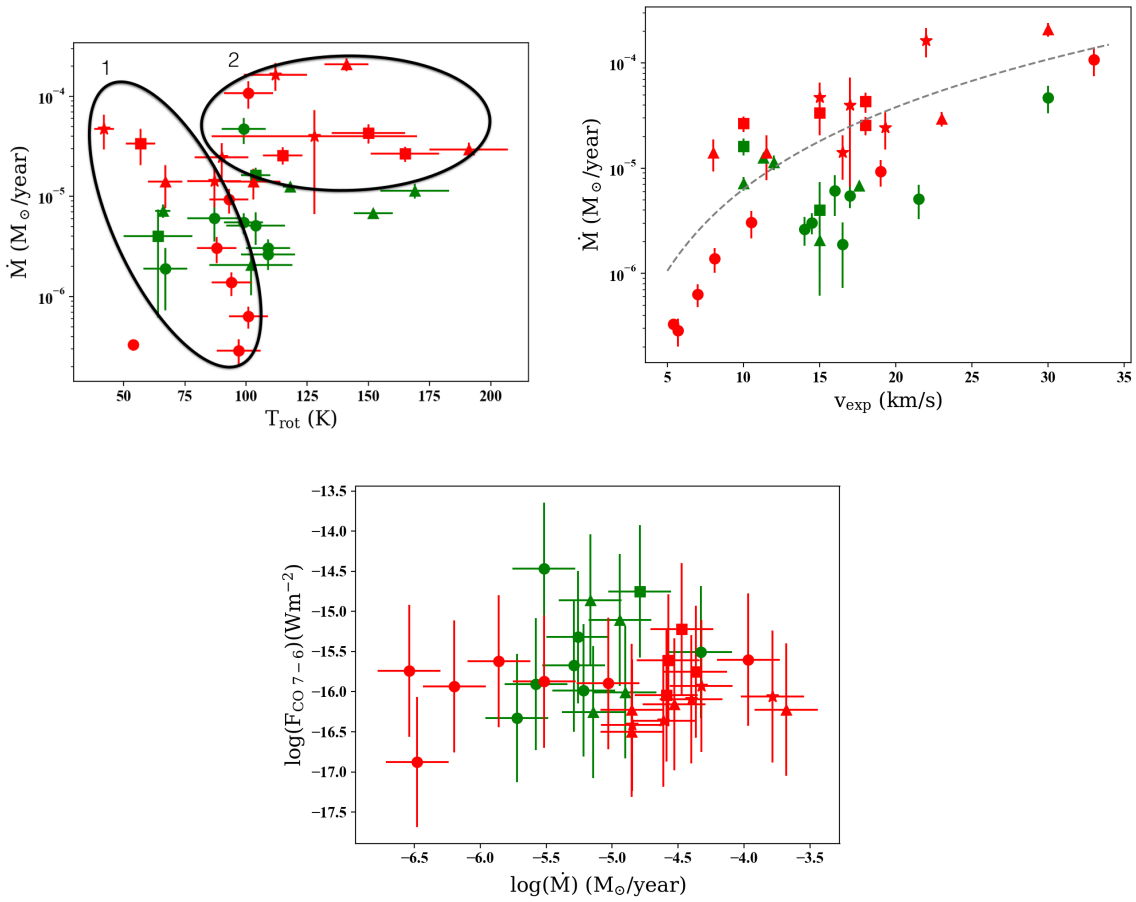

FIGURE 6.9: Top left) Relation between $\dot{M}$ and $T_{\rm rot}$. Single-fit. Two different groups of sources are highlighted, see text for details. Top right) Relation between $\dot{M}$ and $V_{\rm exp}$. Bottom) Integrated flux of the CO J=7-6 line versus $\dot{M}$ in a logarithmic scale.

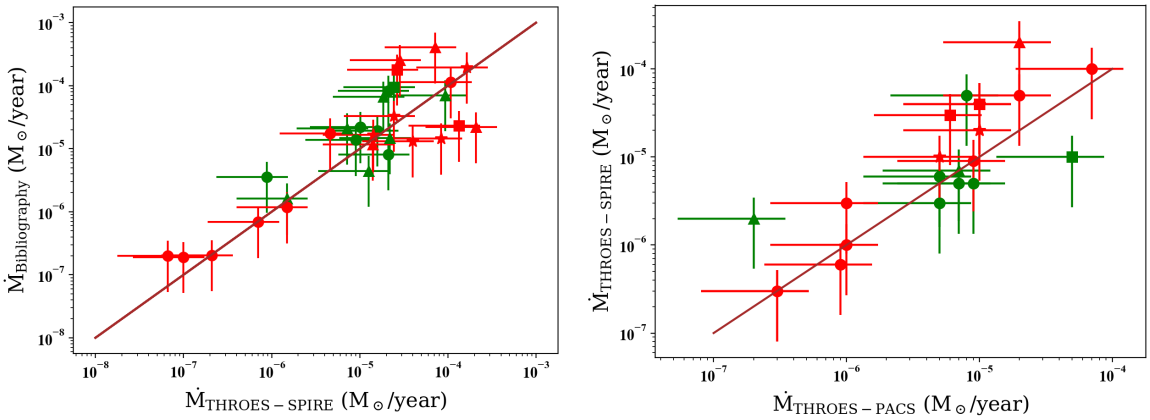

FIGURE 6.10: Left) Comparison of the mass-loss rates estimations using SPIRE data with those from the literature (Tables 4.1 and 6.3). The solid line represents a 1:1 ratio. Right) The same but comparing SPIRE and PACS $\dot{M}$, estimations for targets common to both studies.

The comparison between our mass-loss rates and those found in the bibliography is in good agreement for all the objects, both O-rich and C-rich subsamples occupy a narrow region around the 1:1 relation, this could also be seen in Appendix C.4.1 (Figs. C.14a-C.15a). As expected, some post-AGBs and PNe objects are more scattered due to the difficulty of estimating the mass-loss rates for post-AGB objects and PNs as it is not easy to define essential parameters like r_{CO} or V_{exp} for these spatio-kinematical and morphologically complex objects. Finally, the comparison between SPIRE and PACS $\dot{M}$, estimations are also in good agreement as shown in Fig. 6.10 (right-panel).

6.6 Analysis and interpretation of the results

6.6.1 Rotational temperature and total mass

For most of our sources, a single-T_{rot} component was enough to obtain a good fit of the CO RD, leading to rotational temperatures ~60-170 K for O-rich sources and ~40-190 K for C-rich ones. On the other hand, the total masses of the CO-emitting region range from ~6×10^{-5}-9×10^{-2} $M_\odot$, for O-rich objects and from ~2×10^{-4} to 5×10^{-2} $M_\odot$, for C-rich stars. (Sect. 6.5).

The rotational temperatures of around 100 K derived in this chapter using CO-SPIRE data (J_u=4-3, and up to J_u=13-12 lines) are in concordance with the typical values of $T_{rot}\approx$10-100 K found in previous studies from bibliography that made use of low-J CO lines detected at radio and mm wavelength ranges. This emission comes from the external layers of the CSE around evolved stars, at $\approx10^{16}$-10^{17} cm from the center (e.g. Teyssier et al., 2006a; Ramstedt et al., 2008a; Danilovich et al., 2015, and references therein). Compared to the T_{rot} derived from PACS data, these SPIRE values are clearly smaller than PACS ones. This corroborates that with SPIRE we are tracing outer layers of the envelopes bridging the inner ones studied with PACS and the cold regions observed in the sub-mm and mm wavelength regions.

For a total of 17 sources (ten O-rich and seven C-rich objects), a double-$T_{\rm rot}$ slope is more appropriate to fit all data points. This is interpreted as a consequence of a temperature stratification along the line of sight. The presence of non-LTE effects in some sources could also contribute to reinforce this double-slope trend.

The rotational temperatures and masses of the cold and mild components of these 17 sources are shown in Table. 6.4 (together with the single-fit $T_{\rm rot}$ and the rest of magnitudes derived for the whole sample). The difference between the mass of the cold and mild component is interpreted, again, as a consequence of a CO-emitting volume smaller for the mild component than for the warm cold. At this point it is interesting to highlight the smooth transition in terms of $T_{\rm rot}$ that we could trace connecting the "cold" (∼40 K) SPIRE component to the "hot" one of PACS (∼750 K), going through the "mild" and "warm" (∼150-350 K) regions. From the 11 objects of the SPIRE sample, with a double-component fit, that have also been studied with PACS data, only five sources present a double-slope structure in their PACS-CO RDs. This 5 objects represent a 41% of the total objects of PACS with two different regions of temperature.

We also compare in detail the mild-to-cold M and $T_{\rm rot}$ ratios in Fig. 6.11 as we did for the warm and hot CO-PACS components. From the fitting we obtain α=0.6±0.1, this value is in full agreement with exponents found in the literature for AGB CSEs which present values of α ∼0.5-1 (e.g. De Beck et al., 2010a; Maercker et al., 2016b; Danilovich et al., 2015, and references therein). This exponent is a bit higher than that obtained with PACS data ($\alpha_{\rm PACS}$=0.5±0.1). In spite of the marginal differences, the values obtained from PACS and SPIRE analysis seems to be in line with recent works that suggest a steeper profile in the temperature distributions for the most external regions of the CSEs.

This implies that the temperature profile is steeper at longer distances than as it is in inner regions. Based on that, we reinforce our idea about the temperature stratification present along the CSE layers that is being reflected in this empirical relation between the mild-to-cold ratio of M and $T_{\rm rot}$.

6.6.2 Mass/mass-loss rate vs T$_{rot}$

As shown in Fig. 6.8, we find an interesting distribution of the sources as two main groups can be identified. As expected, a similar trend is present between the mass-loss rate, $\dot{M}$, and $T_{\rm rot}$ (Fig. 6.9) (top-left panel). We consider that the first region represents a diagonal strip ranging between 10^{-4}-10^{-7} $M_{\odot}$ yr^{-1} and 40-100 K while the second region is a nearly horizontal cloud of points located between 10^{-4}-10^{-5} $M_{\odot}$ yr^{-1}, and 100-200 K.

If we concentrate on the sources located in the first region, we could infer an anti-correlation similar to what was reported in Chapters 4 and 5 in coincidence, also, to that found by Teyssier et al., 2006a and Danilovich et al., 2015 in previous works. The objects located in this region are, typically, the less evolved objects from both O-rich and C-rich subsamples. On the other hand, in region 2, the most evolved and massive objects are more abundant, although there are some exceptions like NML Cyg which is a red supergiant (Teyssier et al., 2012).

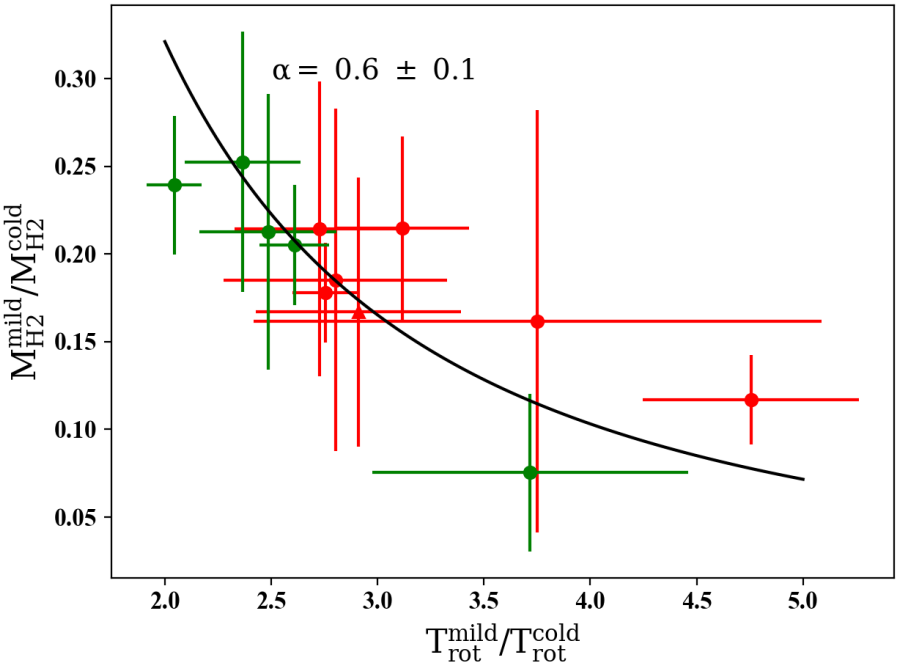

FIGURE 6.11: Ratio of the mass and rotational temperatures for the mild and cold components, $M_{H_2}^{mild}/M_{H_2}^{cold}$ vs ${T_{rot}}^{mild}/{T_{rot}}^{cold}$, for the O-rich and C-rich sources with a double-T_{rot} component in SPIRE. The solid line is a fit by a power-law function ($y \sim x^{-1/\alpha}$) to the AGB stars' data (see text in Sect.,6.6.1). A similar trend is found from our analysis of the PACS-CO emission in Chapters 4 and 5.

The anti-correlation found in first region could be explained attending to the three main factors discussed in Sect. 4.6: A more efficient line cooling, the heating due to the friction between dust and gas and, finally, an optical depth effect. The fact that the most evolved object (post-AGBs and PNe) do not follow this trend could be related to the more complex heating processes, such as shocks, which take place in this kind of objects.

6.6.3 Other trends

In Sect. 6.5 we highlighted the presence of evident correlations between $\dot{M}$ and V_{exp} (Fig. 6.9). This correlation reinforces the interpretation given in previous Chapters. The more massive the star is the more efficient the acceleration mechanisms are. We have fitted a power-law function to the observed distribution (dashed line in Fig. 6.9-top right panel) which implies an index of about 3 (i.e., $\dot{M} \propto {V_{exp}}^{2.5}$, similar to that found for PACS data) although the uncertainties associated to the fitting are important (±1).

As shown in Sect. 6.5, in contrast to what we found in Chapters 4 and 5 the correlations found between the J_u=7-6 line ($F_{CO\ 7-6}$) and M_{tot} and $\dot{M}$ (Fig.6.8 and 6.9, respectively) are not as evident as the ones found for PACS data. The weakness of the correlation found between the magnitudes studied could be associated to a higher opacity associated to the J=7-6 line.

On the other hand, the influence of the excitation temperature in the resulting strength of the CO lines relative to the continuum becomes evident in Fig. 6.9-bottom panel, where we see a weak anti-correlation between $F_{CO\,7-6}$/SPIRE$_{800}$ and T_{rot}, which are both distance independent parameters. We find that objects with the highest values of T_{rot} show small line-to-continuum ($F_{CO\ 7-6}$/SPIRE$_{800}$) ratios.

This distribution of points can be explained attending to the variation of the population of the rotational level J=7-6 with temperature. Under LTE condition, around 150 K, the population of this rotational level starts to decrease and, due to that, the intensity of the line fluxes and the M_{tot} derived decrease as the T_{rot} increases.

6.7 Analysis of the Non-LTE effects

The determination of the critical densities for the transitions involved in our study and their comparison with the real densities estimated for our sources is, again, a good diagnosis element to evaluate the presence of major Non-LTE effects. Almost all of the sources included in the SPIRE study (90%) have emitting CO lines ranging from 100 to 500 K above the ground level i.e transitions with quantum number $J_u\sim$ 4 to 13. Based on the estimations presented by (Yang et al., 2010), the critical densities of these rotational levels and the range of temperatures covered in our study (~40-190 K) are n_{crit} ~1.5×10^4 cm^{-3} (J_u=4) and n_{crit} ~9×10^5 cm^{-3} (J_u=13).

Once determined the critical densities, we have estimated the densities corresponding to the lowest and the highest mass-loss rate objects of the sample (3×10^{-7} and 2×10^{-4} $M_\odot$ yr^{-1}) taking into account the range of r_{CO}, used (4×10^{15}-4×10^{16} cm). The values found are $n_{H_2} \gtrsim$ 8×10^{5}cm^{-3} which implies that most of the CO population levels are thermalized or close to thermalization.

As we have shown in Table. 6.3, most of the sources analysed in this study have previous estimations of mass-loss rates in the literature based on radiative transfer models that take into account non-LTE effects. It is good to see how our estimations are compatible with the ones of the bibliography which corroborates that RD approach provides reasonably reliable estimates of the warm gas content and average temperature in the envelope regions under study (at least for the range of mass-loss rates in our sample objects).

6.8 Conclusions

In this chapter we have presented SPIRE spectra for a sample of 34 evolved stars (20 O-rich and 14 C-rich). The CO rotational emission lines found in these spectra have been analysed using the RD method. From this analysis we have derived the following main conclusions:

The SPIRE spectrometer data allow us to study and characterize intermediate regions of the CSEs (r_{CO}~10^{16} cm) with typical values of T_{rot}, around 100K, varying from 40 to 180 K.

TABLE 6.4: Results from our CO RD analysis (Sect.6.5). Col. 1: Target name; col. 2: distance (d); col. 3: expansion velocity (V_{exp}); col. 4: radius of the CO-emitting region(r_{CO}); col. 5: rotational temperature (T_{rot}); col. 6: column density of CO (N_{col}); col. 7: total mass of H_2 (M_{tot}); col. 8: mass-loss rate ($\dot{M}$); and col. 9: ratio between M_{tot} after and before the opacity correction was applied.

Target Name	d (pc)	V_{exp} (km/s)	r_{CO} (cm)	T_{rot} (K)	N_{col} (cm^{-2})	M_{tot} ($M_\odot$)	$\dot{M}$ ($M_\odot$ yr^{-1})	Correction$_{M_{H_2}}$
AFGL 3068	1100	16.0	4×10^{16}	90±10	$(4.6 \pm 1.9)\times10^{17}$	$(4.8 \pm 2.0)\times10^{-3}$	6×10^{-6}	1.2
IRC +40540	630	14.0	2×10^{16}	110±10	$(4.5 \pm 1.4)\times10^{17}$	$(1.2 \pm 0.4)\times10^{-3}$	3×10^{-6}	1.2
R Scl	290	16.5	6×10^{15}	70±10	$(9.2 \pm 5.6)\times10^{17}$	$(2.2 \pm 1.3)\times10^{-4}$	2×10^{-6}	1.5
CIT 6	400	17.0	2×10^{16}	100±10	$(7.7 \pm 1.9)\times10^{17}$	$(2.0 \pm 0.5)\times10^{-3}$	5×10^{-6}	1.3
CW Leo	120	14.5	2×10^{16}	110±10	$(5.0 \pm 1.1)\times10^{17}$	$(1.3 \pm 0.3)\times10^{-3}$	3×10^{-6}	1.2
IRAS 15194-5115	500	21.5	2×10^{16}	100±10	$(5.7 \pm 2.0)\times10^{17}$	$(1.5 \pm 0.5)\times10^{-3}$	5×10^{-6}	1.2
SAO 163075	2400	11.3	4×10^{16}	120±0	$(1.3 \pm 0.1)\times10^{18}$	$(1.4 \pm 0.1)\times10^{-2}$	10^{-5}	1.6
AFGL 2688	420	17.6	4×10^{16}	150±10	$(4.6 \pm 0.5)\times10^{17}$	$(4.9 \pm 0.6)\times10^{-3}$	7×10^{-6}	1.1
V Hya	2160	30.0	6×10^{16}	100±10	$(1.3 \pm 0.4)\times10^{18}$	$(3.0 \pm 0.9)\times10^{-2}$	5×10^{-5}	1.3
AFGL 618	1000	12.0	6×10^{16}	170±10	$(7.6 \pm 1.2)\times10^{17}$	$(1.8 \pm 0.3)\times10^{-2}$	10^{-5}	1.2
Red Rectangle	710	15.0	8×10^{15}	100±20	$(8.3 \pm 4.1)\times10^{17}$	$(3.5 \pm 1.7)\times10^{-4}$	2×10^{-6}	1.4
HD 56126	2400	10.0	6×10^{16}	70±0	$(5.7 \pm 0.9)\times10^{17}$	$(1.4 \pm 0.2)\times10^{-2}$	7×10^{-6}	1.5
IRAS 19411-1416	2000	15.0	2×10^{16}	60±10	$(6.4 \pm 5.4)\times10^{17}$	$(1.7 \pm 1.4)\times10^{-3}$	4×10^{-6}	1.5
NGC 7027	1000	10.0	10^{17}	100±10	$(7.8 \pm 1.4)\times10^{17}$	$(5.1 \pm 1.0)\times10^{-2}$	2×10^{-5}	1.4
IRAS 20038-2722	197	5.4	4×10^{15}	50±0	$(1.8 \pm 0.2)\times10^{17}$	$(7.8 \pm 0.6)\times10^{-5}$	3×10^{-7}	1.5
W Hya	98	7.0	4×10^{15}	100±10	$(2.7 \pm 0.7)\times10^{17}$	$(1.1 \pm 0.3)\times10^{-4}$	6×10^{-7}	1.3
o Cet	110	8.1	6×10^{15}	90±10	$(3.4 \pm 0.9)\times10^{17}$	$(3.2 \pm 0.9)\times10^{-4}$	10^{-6}	1.3
IK Tau	260	19.0	6×10^{15}	90±10	$(9.8 \pm 2.7)\times10^{17}$	$(9.3 \pm 2.6)\times10^{-4}$	9×10^{-6}	1.4
R Dor	59	5.7	4×10^{15}	100±10	$(1.5 \pm 0.5)\times10^{17}$	$(6.4 \pm 1.9)\times10^{-5}$	3×10^{-7}	1.2
R Cas	176	10.5	6×10^{15}	90±10	$(5.8 \pm 1.7)\times10^{17}$	$(5.5 \pm 1.6)\times10^{-4}$	3×10^{-6}	1.4
NML Cyg	1220	33.0	4×10^{16}	100±10	$(9.8 \pm 3.0)\times10^{17}$	$(4.1 \pm 1.3)\times10^{-2}$	10^{-4}	1.2
OH 231.8+4.2	1500	15.0	8×10^{16}	40±0	$(4.7 \pm 1.8)\times10^{17}$	$(8.0 \pm 3.0)\times10^{-2}$	5×10^{-5}	1.5
V1300 Aql	620	16.5	10^{16}	90±10	$(1.0 \pm 0.5)\times10^{18}$	$(2.7 \pm 1.2)\times10^{-3}$	10^{-5}	1.4
WX Psc	700	19.3	10^{16}	90±10	$(1.5 \pm 0.6)\times10^{18}$	$(4.0 \pm 1.6)\times10^{-3}$	2×10^{-5}	1.5
AFGL 5379	2750	22.0	4×10^{16}	110±10	$(2.2 \pm 0.7)\times10^{18}$	$(9.5 \pm 3.0)\times10^{-2}$	2×10^{-4}	1.5
OH 26.5+0.6	1370	17.0	2×10^{16}	130±40	$(1.4 \pm 1.2)\times10^{18}$	$(1.5 \pm 1.2)\times10^{-2}$	4×10^{-5}	1.4
IRAS 16342-3814	2000	23.0	4×10^{16}	190±20	$(3.8 \pm 0.6)\times10^{17}$	$(1.6 \pm 0.3)\times10^{-2}$	3×10^{-5}	1.1
M1-92	2500	8.0	6×10^{16}	100±10	$(3.5 \pm 1.2)\times10^{17}$	$(3.4 \pm 1.1)\times10^{-2}$	10^{-5}	1.3
IRAS 22036+5306	4000	30.0	4×10^{16}	140±10	$(2.1 \pm 0.3)\times10^{18}$	$(8.8 \pm 1.3)\times10^{-2}$	2×10^{-4}	1.3
HD 161796	1500	11.5	2×10^{16}	70±10	$(7.4 \pm 3.4)\times10^{17}$	$(7.8 \pm 3.6)\times10^{-3}$	10^{-5}	1.6
NGC 6720	450	15.0	2×10^{16}	60±10	$(1.4 \pm 0.5)\times10^{18}$	$(1.4 \pm 0.6)\times10^{-2}$	3×10^{-5}	1.8
NGC 2440	1500	18.0	4×10^{16}	120±10	$(4.3 \pm 0.9)\times10^{17}$	$(1.8 \pm 0.4)\times10^{-2}$	3×10^{-5}	1.1
NGC 6537	1500	18.0	4×10^{16}	150±20	$(7.2 \pm 1.6)\times10^{17}$	$(3.0 \pm 0.7)\times10^{-2}$	4×10^{-5}	1.2
NGC 6302	1170	10.0	4×10^{16}	170±10	$(8.0 \pm 1.4)\times10^{17}$	$(3.4 \pm 0.6)\times10^{-2}$	3×10^{-5}	1.3

No difference has been found between O-rich and C-rich samples in terms of temperature. These values are in concordance with precious estimations found in bibliography.

The total mass of the intermediate CSE layers where the SPIRE CO lines arise ranges from $M_{\rm tot}\approx10^{-4}$ to $10^{-1}\,M_{\odot}$ in our sample, with the most evolved objects being the most massive.

The mass-loss rates estimated are in the range $\dot{M}\approx10^{-7}$-$10^{-4}M_{\odot}$ yr^{-1}, in agreement (within uncertainties) with values found in the literature and with previous estimations with PACS (see Chapters 4 and 5).

For 17 objects in our sample a double temperature (cold and mild) component has been identified. The temperatures of the cold and mild components are ∼40-60 K and ∼180-220 K, respectively. The mass of the cold component ($\sim10^{-2}$-$8\times10^{-4}M_{\odot}$) is always larger than that of the mild component, by a factor ∼2-10.

The warm-to-hot M and $T_{\rm rot}$ ratios in our sample are correlated and are consistent with an average temperature radial profile of $\propto r^{-0.6\pm0.1}$, that is in agreement with previous studies and slightly steeper than that derived with PACS data.

We find two different groups of sources when comparing $M_{\rm tot}$, and $\dot{M}$ versus $T_{\rm rot}$. The first one, which include the AGB stars, presents a clear anti-correlation while the second one (populated with the most evolved objects) occupies a wide region of $T_{\rm rot}$, from 100 to 200K, and high and constant values of $M_{\rm tot}$, and $\dot{M}$.

The $M_{\rm tot}$, and $T_{\rm rot}$, anticorrelation observed for AGBs was found in PACS analysis as well as in previous works based on low-J CO line observations. No, evident, interpretation has been found for the objects of the second group although it would be probably related to the more complex excitation and heating methods, such as shocks, that are characteristic of post-AGBs and PNe.

A strong correlation has been found, also, between $\dot{M}$ and $V_{\rm exp}$, mainly for AGBs . This trend, which is also observed in PACS studies using high-J CO transitions, is consistent with the wind acceleration mechanism being more efficient in the more luminous and massive stars.

Chapter 7

Conclusions and future research

Ain´t no mountain high enough

Marvin Gaye, Tammi Terrell

7.1 Conclusions

In this thesis I have analysed spectroscopic observations corresponding to 182 evolved low to intermediate mass stars, observed with PACS (114) and SPIRE (68) instruments on-board *Herschel*. For all of them I have applied a high level reduction process, which included specific tasks created to improve the flux calibration for semi-extended and extended sources, as well as, other ones to deal with mispointed observations. At the end of the reduction process, final science-ready products in FITS and CSV formats were generated. To check the goodness of the reduction process applied to PACS data, I cross-validated the final products with other photometric (IRAS and AKARI), and spectroscopic (ISO) data. Finally, all the reduced observations were included in two different web-based catalogues: *https://throes.cab.inta-csic.es* (PACS) and *https://throes-spire.cab.inta-csic.es* (SPIRE), where they are available for the whole scientific community.

The objects included in both catalogues cover evolutionary stages, from AGB to PN as well as three different types of chemistry (O-rich stars, S-stars and C-rich stars). The PACS and SPIRE spectra explore a wide wavelength range from 50 to 650 μm that has enabled us to properly study and understand the physical and chemical properties of the CSEs associated to these objects at different regions which had never been systematically studied until this work.

The scientific analysis carried on in this thesis has been focused on the CO rotational emission lines. To do that, rotational diagrams have been generated for all the sources with a minimum of 3 CO lines detected with S/N ratio>3. Due to PACS and SPIRE capabilities, the range of detected ^{12}CO transitions has been extended to higher rotational levels, up to J=45-44, compared to previous observations including a relatively low/modest number of lines using ISO. For each source included in our analysis, we have estimated a characteristic radius of CO emission as well as performed a moderate opacity correction to the CO rotational lines. In total 75 rotational diagrams, 41 based on PACS data and the remaining 34 based on SPIRE

spectra, have been created. These RDs, which include a broad range of J rotational levels (from J=4-3 to J45-44; E_u=55 to 5700 K) have allowed us to derive fundamental physical parameters such as: rotational temperature (T_{rot}), total molecular mass in the CO-emitting layers (M_{tot}) and average mass-loss rates ($\dot{M}$) from "inner" layers of the CSEs ($\sim 5\times10^{15}$ cm; PACS) and from the intermediate ones ($\sim 4\times10^{16}$ cm; SPIRE) which bridge with the outermost ones ($\sim 10^{17}$ cm, which have been typically studied with J_u<3).

Focusing on PACS results, the rotational temperatures found for both O-rich and C-rich sub-samples vary from ~200 K to ~700 K, no substantial difference was found attending to the chemical type. In terms of evolutionary stage, we estimated higher temperatures, around T_{rot}~500 K, for less-evolved objects, like AGB and OH/IR stars, than for the most evolved ones, post-AGBs and PNs (T_{rot}~200 K). The rotational temperatures derived from the SPIRE rotational diagrams are, typically, one order of magnitude lower ranging from ~50 K to ~180 K. The difference between PACS and SPIRE T_{rot} values is expected because thanks to the PACS far-infrared range we have access to hotter gas that is closer to the central star ($\approx 10^{15}$ cm for AGBs and $\approx 10^{16}$ cm for post-AGBs and PNs) than that traced by SPIRE at typical distances of $\approx 10^{16}$ cm for AGBs and $\approx 10^{17}$ cm for more evolved objects.

The total mass of the inner CSE regions where the PACS CO lines arise ranges from $M_{tot}\approx 10^{-6}$ to $10^{-2}\,M_\odot$ in our O-rich sub-sample, this range is fully compatible with that found for the C-rich objects, although for these ones the range is narrower ($M_{tot}\approx 10^{-5}$ to $10^{-3}\,M_\odot$). In both sub-samples the most evolved objects are also the most massive. The values of M_{tot} derived from CO-PACS rotational diagrams are, typically, 100 to 1000 times lower than the total envelope mass obtained from CO-SPIRE analysis whose M_{tot} values range from $M_{tot}\approx 10^{-4}$ to $10^{-1}\,M_\odot$ for both O-rich and C-rich sub-samples. Again, the most evolved objects are also found to be the most massive ones.

The mass-loss rate is another magnitude that has been estimated using both PACS and SPIRE spectra. The values estimated for the O-rich sub-sample using PACS data range from $\dot{M}\approx 10^{-8}$-$10^{-5} M_\odot$ yr^{-1}, while the mass-loss rates derived for the C-rich objects are, globally, an order of magnitude higher ($\dot{M}\approx 10^{-7}$-$10^{-4} M_\odot$ yr^{-1}). The values derived are in agreement (within uncertainties) with values found in the literature which, in most cases, are deduced from lower-J transitions. In a few targets, detailed radiative transfer studies using higher J-CO lines have been developed, we have paid particular attention to these cases and also a good agreement has been found with our estimations. Focusing now in the SPIRE rotational diagram analysis, the mass-loss rates derived for the O-rich sub-sample are $\dot{M}\approx 10^{-7}$-$10^{-4} M_\odot$ yr^{-1}meanwhile those for the C-rich objects are $\dot{M}\approx 10^{-6}$-$10^{-4} M_\odot$ yr^{-1}. In both sub-samples the mass-loss rates estimated are in perfect agreement with previous estimations found in bibliography based on the same CO lines. These results let us to conclude that, taking into account the uncertainties, mas-loss rates keep constant along different epochs of these evolved low to intermediate mass stars.

For 23 sources out of 75 studied in this thesis, a double temperature component has been inferred from their PACS or SPIRE rotational diagrams. Particularly interesting are those double components found in the PACS-RDs of both O-rich and C-rich sub-samples as an, even hotter, gas component has been analysed for the very first time. The temperatures of the *warm* and *hot* components are independent of the chemical type of the objects and they

range between ~400-500 K and ~600-900 K, respectively. The mass of the warm component (~10^{-5}-8×10^{-2} $M_{\odot}$) is always larger than that of the hot component, by a factor ~2-10. In the case of SPIRE-RDs the double components found have been called *cold* and *mild* components as the typical $T_{\rm rot}$ values found are ~60 and ~200 K, respectively. The mass of the mild CO component is always larger than the mass of the warm component, for both O-rich and C-rich samples. For the cold component, these values vary from M= 7.4×10^{-5} to ~0.19 $M_{\odot}$ being typically 5 times larger than that of the mild component. The detection of these double-component structure suggests the presence of a stratified CSE with a smooth transition of temperatures, at least for less evolved objects.

The detection of the double-components mentioned above has allowed us to analyse the distribution of the warm-to-hot M and $T_{\rm rot}$ ratios, as well as, those of the mild-to-warm components. We have found an strong correlation between the M and $T_{\rm rot}$ ratios for the O-rich and C-rich objects detected with PACS, this trend could be consistent with an average temperature radial profile of $\propto r^{-0.5\pm0.1}$. This value is in agreement with recent studies which indicate that the temperature profile in the inner regions of the CSE are shallower than in the outer envelope layers. This point is in line with the correlation found between cold-to-mild M and $T_{\rm rot}$ ratios as the temperature profile found is $\propto r^{-0.6\pm0.1}$.

The distributions of the different magnitudes and physical parameters of these objects have been explored. An anti-correlation between the total mass and the mass-loss rate, with $T_{\rm rot}$, has been found making use of CO-PACS RDs. This is interpreted as a combination of three different processes: CO line cooling, dust friction heating and opacity effects. This anti-correlation is also evident when analysing the $M_{\rm tot}$, $\dot{M}$ and $T_{\rm rot}$ values estimated through SPIRE-RDs for AGB stars. The most evolved objects like the PNe are located in a relatively wide region in terms of $T_{\rm rot}$, while $M_{\rm tot}$, values are very similar for all of them. Previous works also reported similar $T_{\rm rot}$, vs $M_{\rm tot}$, anti-correlations based on low-J CO line observations.

For both PACS and SPIRE sub-samples, a strong correlation has been found, also, between $M_{\rm tot}$ and $V_{\rm exp}$, particularly for AGB stars (of both chemical types). This correlation is also present in the $\dot{M}$ vs. $V_{\rm exp}$ distribution, as expected. This trend, which is observed in past studies using low-J CO transitions, is consistent with the wind acceleration mechanism being more efficient the more luminous/massive the star is. The relation found, $\dot{M} \propto {V_{\rm exp}}^{2.5}$, is slightly smaller but compatible with those found in previous works $\dot{M} \propto {V_{\rm exp}}^{3.4}$ (Young, 1995), $\dot{M} \propto {V_{\rm exp}}^{3.3}$ (Ramstedt, Schöier, and Olofsson, 2009) $\dot{M} \propto {V_{\rm exp}}^{2.7}$ (Danilovich et al., 2015).

In this thesis we show that a global study using intermediate-to-high J CO emission lines probed by *Herschel*/SPIRE and *Herschel*/PACS (from J=4-3 to $J = 45 - 44$) is enormously useful to trace the different layers of the CSEs from the outer cold ($T_{\rm rot}$ ~70 K) to the inner and hot ones ($T_{\rm rot}$ ~900 K). Using simple and fair assumptions we have provided systematic and homogeneous insight into the physical properties of the CSEs of evolved low to intermediate mass stars. Apart from that, we have also found interesting trends like the change in the temperature profile along the different regions of the CSE, and the anticorrelation between $M_{\rm tot}$, and $T_{\rm rot}$. Both trends have to be deeply studied in the future using more sophisticated techniques. Finally, this thesis has demonstrated that RD technique could be a valid method to obtain a first order estimation of fundamental parameters such as: $M_{\rm tot}$, and $\dot{M}$. Besides,

for the range of $\dot{M}$, studied in this thesis, the values of $T_{\rm rot}$, derived do not significantly deviate from the temperature of the gas in most of the regions of the CSE.

7.2 Future prospects

One of the next future projects that could be developed would be focused on the observation of a great number of CO lines detected in a bigger, unbiased, sample using other space observatories like *SOFIA*. Following on the observational side, ALMA interferometer could be also used to obtain very detailed information of the intermediate regions of the CSEs as CO lines up to J=8-7, are observable. In this way, we could developed new radiative transfer analysis to be compared with the one carried out in this thesis using SPIRE.

In this thesis we have explored the physical properties of the inner and intermediate layers of CSEs concerning a wide variety of evolved low to intermediate mass stars. To develop our analysis we have made use of Rotational Diagrams which have demonstrated to be very useful to obtain reliable, first order estimations. Despite of that, to go in deep in the analysis of these data, as well as, in the characterization of the CSEs new steps can be taken. However, it is important to note that ALMA as well as *SOFIA* are not very efficient observatories to carry out multi-lines studies.

A more detailed study would incorporate radiative transfer models. These models are very demanding in terms of time of computing and resources so they are typically used to study individual targets. In future analysis, the use of radiative transfer models is considered a good opportunity to derive the physical properties of the CSE ($M_{\rm tot}$, $T_{\rm rot}$, and $\dot{M}$) dealing with the presence of Non-LTE effects in the gas.

The application of radiative transfer models could be useful to validate, again, the RD method. We can develop a model to create "synthetic" RDs by including a grid of physical parameters as input which allow us to understand how the changes in the initial parameters (like the temperature profile) affect the final RD obtained. Furthermore the comparison between the real and the synthetic parameters could helps us to estimate basic input parameters such as: the kinetic temperature of the gas, its expansion velocity of its column density. Apart from this kind of study, more detailed Non-LTE Radiative Transfer Model such as those found in literature (e.g. Teyssier et al., 2006a, Danilovich et al., 2015 or Maercker et al., 2016b, among others) are crucial to properly understand the physical and chemical process that take place in the inner regions of the CSEs.

In next years, future space missions, focussed in the infrared range, are scheduled, some of them are: James Webb Space Telescope (JWST-NASA/ESA; launch 2021) and SPICA (JAXA/ESA; launch late 2020s). Both telescopes present Mid-Infrared (MIR) instruments covering typical wavelength ranges from: 4.9-28.8 μm(JWST) and 12-36 μm(SPICA) but the spectral resolution defined is not high enough to resolve the CO rotational lines presented in this thesis. Moving to the FIR domain, only SPICA will cover it with the SAFARI instrument (34-230 μm) unfortunately, again, the spectral resolution will not be high enough to feed Non-LTE transfer models like the ones mentioned above.

Considering all these circumstances the PACS and SPIRE data reprocessed and presented in this thesis will be the unique FIR data available in the evolved low to intermediate mass topic during the next 10 years, as minimum.

Apart from the molecular analysis of CO, the spectra presented in this manuscript have a huge amount of chemical species which can be analysed in future works. Some examples are:

Forsterite (Mg_2SiO_4): This oxygen rich dust specie is easily detected at 69 μm, using PACS spectra. This crystalline olivine has been previously detected and studied by Blommaert et al., 2014a or de Vries et al., 2015 in different PACS spectra. The properly analysis of the forsterite 69 μm, feature is very interesting as its width and its wavelength position are very sensitive to the temperature and the composition of this element so it could be interesting to compare $T_{\rm dust}$ with $T_{\rm gas}$.

Water-ice: The detection of water-ice feature at 62 μm, is expected in some PACS spectra as its detection was reported in Molinari et al., 1999 using ISO data. However no identification has been found in PACS bibliography regarding this feature. This could be a very interesting challenge to face in future studies as some candidates have been identified in our THROES sample, such as MWC 922.

Appendix A

Appendix I

A.1 Multicomponent RD analysis: Bayesian Information Criterion

Here we describe the method used to automatically find a break point in the linear relation in the rotational diagram using the Bayesian information criterion (BIC)[1].

Our approach concerns the minimization of the RSS (residual sum of squares) by computing the BIC for a range of possible locations of break points. The BIC can be regarded as a rough estimate of the Bayes factor (Schwarz, 1978), and it is given by:

$$BIC = n \ln(RSS/n) + k \ln(n) \tag{A.1}$$

where a penalty term, $k \ln(n)$, penalizes model complexity depending on the number of parameters k and data points n (see also Maindonald and Braun, 2010). We also tested the Akaike's information criterion (AIC) (Akaike, 1974), but we concluded that for this particular application it tends to overfit essentially because the penalty term is smaller. In fact, due to the small number of data points, we are not interested in splitting the rotational diagram too much in order to obtain robust results. It can happen that BIC suggests more than one breakpoint due to the smaller accuracy of the higher J line fluxes, and in that case only the first break point is taken into account. Obvious line blends were excluded upon the computation of both statistics.

In figure A.1 we show the BIC test in a graphical way where we see that the BIC curve is usually minimal at 0 or 1 breakpoints. For example for AFGL 2513 it is shown that the residuals of the fit keep decreasing with 2 breakpoints, although this is strongly penalized by the BIC, so a 2-component fit is favored. On the contrary, in AFGL 3068, IRAS 15194-5115 and IRC+10216 a single temperature component suffices to reproduce the data.

Beware that these methods do not prove that a double temperature component is physically true, neither they provide an alternative explanation for the trends in the data. They simply highlight hidden patterns in the residuals which can be caused by many effects, being line blend the most obvious among them, or heteroscedasticity which can, in fact, invalidate

[1] Implemented in R using the package *strucchange* (Zeileis et al., 2002).

statistical tests of significance. Hence, supervision is required.

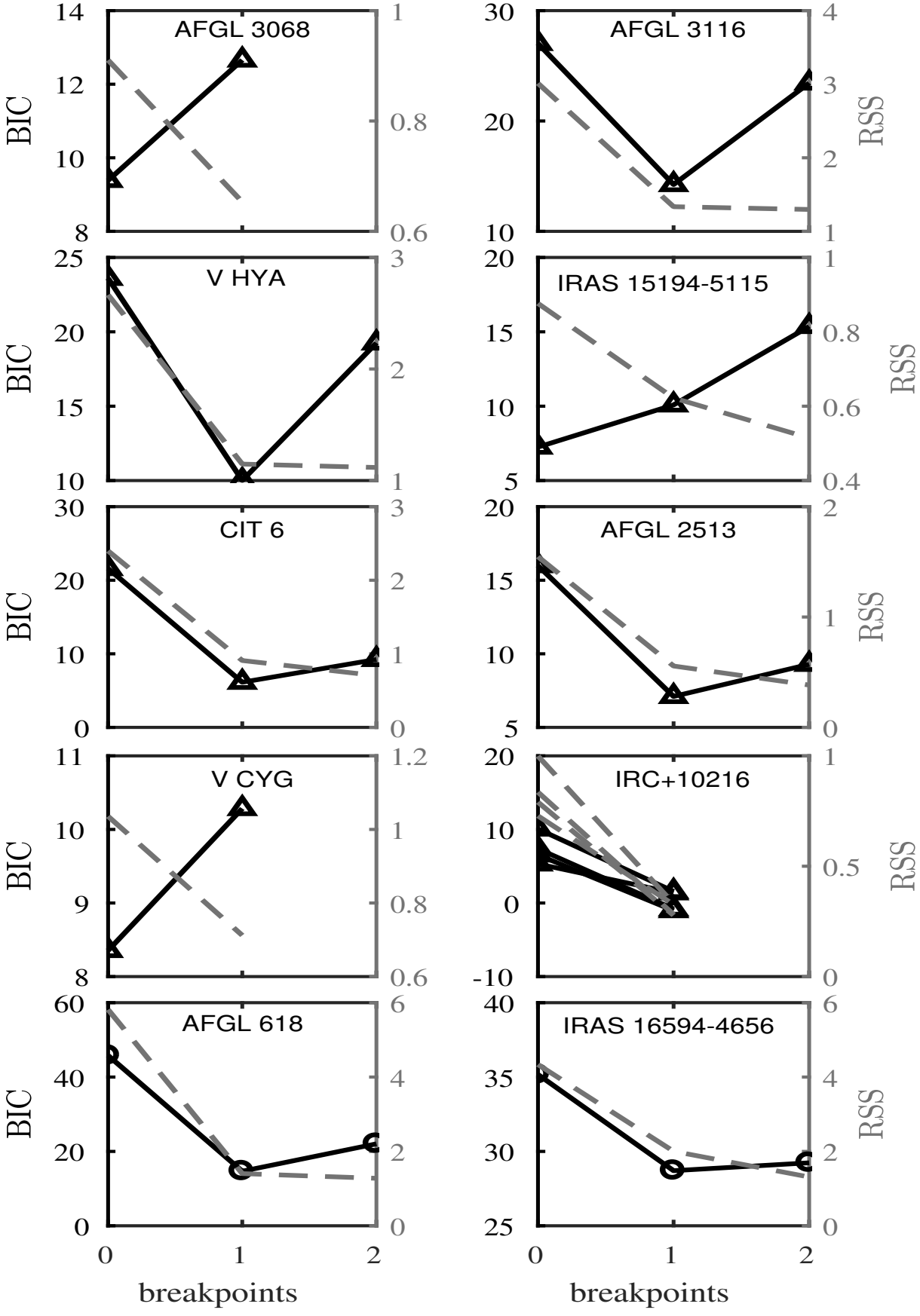

FIGURE A.1: Bayesian information criterion and residual sum of squares as a function of number of breakpoints, for a subset of sources with two-slopes components. The minimum of the BIC (solid line) suggests a slope change at a given breakpoint. The dashed lines show the residual sum of squares (RSS).

Appendix B

Appendix II. Supplementary tables

In this appendix we present different tables which contains relevant information about the sources included in the THROES catalogues, see Table. B.1. The fluxes of the fitted lines of the O-rich sources studied with PACS (Table B.2), as well as those of the C-rich sample (Tables. B.3 and B.4) are also shown in this appendix. Finally there is another table which contains the fluxes of the fitted lines of both O-rich and C-rich sources studied with SPIRE (Tables. B.5, B.5a and B.6).

B.1 Sources of PACS and SPIRE samples

All the targets observed with PACS Spectroscopy or SPIRE Spectrometer are resumed in the next table:

TABLE B.1: Basic information about all the observations reprocessed in THROES. Column 1: Target Name; Columns 2 and 3: Equatorial coordinates (J2000) in degrees; Columns 4, 5, 6 and 7: Complementary data for each observation in IRAS, AKARI, ISO or SPIRE; Column 8: Comments on complementary information about the PACS and SPIRE observations object: 1) Incomplete PACS wavelength coverage; 2) Mispointing (target not in the central spaxel); 3) Semiextended object (size ~3x3 central spaxels or 'SemiExtended' correction in SPIRE); 4) Extended object (size ~5x5 spaxels or 'Extended' correction in SPIRE); 5) Contamination in ISO data due to interstellar emission; 6) Faint source (≤10 Jy at 60 μm or ≤10 Jy at 60 μm); 7) Multi epochs observations. If the observation presents a complete spectral coverage in PACS and SPIRE wavelength range, is well pointed, Chop/Nod, with the SPIRE point correction applied and the source is point like and intense, there is no comment in the column (-); Column 9: ObsIds PACS; Column 10: ObsIDs SPIRE.

Target Name	RA(deg)	Dec(deg)	IRAS	AKARI	ISO	SPIRE	Comments	ObsIDs PACS	ObsIDs SPIRE
AC Her	277.5676	21.8668	Yes	Yes	Yes	No	1,6	1342208896	-
AFGL 618	70.7236	36.1147	Yes	Yes	Yes	Yes	-	1342225838 1342225839 1342225840	1342191214
AFGL 2019	268.3282	-26.9436	Yes	Yes	No	No	1,6	1342252253	-
AFGL 2403	292.6228	19.8447	Yes	Yes	No	No	1	1342245226	-
AFGL 2513	302.3093	31.4291	Yes	Yes	No	No	-	1342270010 1342269936	-
AFGL 2688	315.5781	36.6938	No	No	Yes	Yes	-	1342199233 1342199234 1342199235	1342189123
AFGL 3068	349.8016	17.1931	Yes	Yes	Yes	Yes	-	1342199417 1342199418 1342257635	1342189126
AFGL 3116	353.6152	43.5506	Yes	Yes	No	No	-	1342212512 1342212513	-
AFGL 4106	155.8311	-59.5346	Yes	Yes	Yes	Yes	1,3	1342207818	1342189115

TABLE B.1: Continued.

Target Name	RA(deg)	Dec(deg)	IRAS	AKARI	ISO	SPIRE	Comments	ObsIDs PACS	ObsIDs SPIRE
AFGL 4202	223.1012	-62.0721	Yes	Yes	No	No	1,6	1342250004	-
AFGL 4259	301.5947	27.0362	Yes	Yes	No	No	1,6	1342244918	-
AFGL 5379	266.0942	-31.9276	Yes	Yes	Yes	Yes	2,3	1342228537 1342228538	1342268287
AFGL 6815	259.5830	-32.4556	Yes	Yes	No	No	-	1342216629 1342216630	-
AQ Sgr	293.5791	-16.3741	Yes	Yes	No	No	-	1342268751 1342268752	-
BD +30 3639	293.6884	30.5163	Yes	Yes	Yes	Yes	3	1342220600 1342220601	1342243605
CIT 6	154.0094	30.5718	Yes	No	Yes	Yes	-	1342197799 1342197800	1342198264
CPD-568032	257.2536	-56.9133	Yes	Yes	Yes	Yes	-	1342228201 1342228202	1342191234
CPD-642939	219.2920	-64.8013	Yes	Yes	No	No	1,6	1342250006	-
EP Aqr	326.6327	-2.2127	Yes	Yes	No	No	-	1342270639 1342270684	-
G Her	247.1606	41.8816	Yes	Yes	No	No	1	1342247780	-
HD 56126	109.0427	9.9966	Yes	Yes	Yes	Yes	-	1342220930 1342220931	1342193664
HD 101584	175.2450	-55.5738	-	-	-	Yes	-	-	1342248418

TABLE B.1: Continued.

Target Name	RA(deg)	Dec(deg)	IRAS	AKARI	ISO	SPIRE	Comments	ObsIDs PACS	ObsIDs SPIRE
HD 161796	266.2311	50.0443	Yes	Yes	Yes	Yes	-	1342208881 1342208882	1342189117
HD 235858	337.2932	54.8517	Yes	Yes	No	No	-	1342196686 1342196687	-
HD 331319	297.3731	31.4545	Yes	Yes	No	No	1	1342245232	-
Helix Nebula	337.2917	-20.8561	-	-	-	Yes	-	-	1342256097 1342256098 1342256099 1342256100
Hen 2-90	197.4009	-61.3266	Yes	Yes	Yes	No	1,5,6	1342248308	-
Hen 2-113	224.9730	-54.3020	Yes	Yes	Yes	Yes	3	1342225142 1342225143 1342249211	1342251280
Hen 3-401	154.8852	-60.2248	Yes	Yes	No	No	-	1342225588 1342225589	-
Hen 3-1475	266.3090	-17.9462	Yes	Yes	Yes	No	-	1342229719 1342229720	-
IC 418	81.8675	-12.6973	Yes	No	Yes	No	3	1342265942 1342265943	-
IRAS 05280-6910	81.9171	-69.1345	-	-	-	Yes	-	-	1342247097 1342247098
IRAS 07027-7934	104.8599	-79.6463	Yes	Yes	Yes	No	1,6	1342245248	-

TABLE B.1: Continued.

Target Name	RA(deg)	Dec(deg)	IRAS	AKARI	ISO	SPIRE	Comments	ObsIDs PACS	ObsIDs SPIRE
IRAS 08011-3627	120.7568	-36.5966	Yes	Yes	No	Yes	3	1342210381 1342256781 1342256782	1342245844
IRAS 08544-4431	134.0591	-44.7196	Yes	Yes	No	Yes	3	1342245956 1342245957	1342247558
IRAS 09256-6324	141.7220	-63.6302	Yes	Yes	No	Yes	-	1342210386 1342248357 1342248358	1342247559
IRAS 09371+1212	144.9749	11.9814	Yes	Yes	No	Yes	-	1342245647 1342245648	1342198263
IRAS 09425-6040	146.0066	-60.9072	Yes	Yes	No	No	-	1342225563 1342225564	-
IRAS 10456-5712	161.91	-57.4674	Yes	Yes	No	Yes	3	1342211823 1342248928 1342248929	1342247562
IRAS 13428-6232	206.5854	-62.8000	Yes	Yes	No	No	2	1342212212 1342212213	-
IRAS 15194-5115	230.7704	-51.4330	Yes	Yes	Yes	Yes	3	1342215685 1342215686	1342251281
IRAS 16122-5128	244.0190	-51.5989	Yes	Yes	No	No	1	1342240167	-
IRAS 16279-4757	247.9087	-48.0677	Yes	Yes	No	No	2	1342228203 1342228204	-

TABLE B.1: Continued.

Target Name	RA(deg)	Dec(deg)	IRAS	AKARI	ISO	SPIRE	Comments	ObsIDs PACS	ObsIDs SPIRE
IRAS 16342-3814	249.417	-38.3380	Yes	Yes	Yes	Yes	-	1342216627 1342216628	1342251319
IRAS 16594-4656	255.7917	-47.0076	Yes	Yes	Yes	No	5	1342228414 1342228415	-
IRAS 17010-3840	256.1179	-38.7396	Yes	Yes	No	No	1,6	1342216176	-
IRAS 17251-2821	262.0770	-28.3991	Yes	Yes	No	No	1,6	1342228535	-
IRAS 17276-2846	262.7012	-28.8172	Yes	Yes	No	No	1,6	1342228536	-
IRAS 17323-2424	263.8583	-24.4422	Yes	Yes	No	No	1,6	1342228532	-
IRAS 17347-3139	264.5054	-31.6827	Yes	No	No	No	2	1342229696 1342229697	-
IRAS 17521-2938	268.8404	-29.6536	Yes	No	No	No	1,6	1342229802	-
IRAS 18433-0228	281.4800	-2.4189	Yes	No	No	No	1	1342231743	-
IRAS 18488-0107	282.8592	-1.0645	Yes	No	No	Yes	4	1342268791 1342268792	1342268317
IRAS 19067+0811	287.2845	8.2770	Yes	Yes	No	Yes	4	1342268797 1342268798	1342268308
IRAS 19306+1407	293.2295	14.2269	Yes	Yes	No	No	1,6	1342244921	-
IRAS 19411-1416	295.9910	-14.1533	-	-	-	Yes	-	-	1342268315
IRAS 19474-0744	297.5264	-7.6145	Yes	Yes	No	No	-	1342268638 1342268449	-
IRAS 20000+3239	300.4980	32.7924	Yes	Yes	No	No	-	1342270612	-

TABLE B.1: Continued.

Target Name	RA(deg)	Dec(deg)	IRAS	AKARI	ISO	SPIRE	Comments	ObsIDs PACS	ObsIDs SPIRE
								1342270344	
IRAS 20038-2722	301.7301	-27.2249	Yes	Yes	No	Yes	-	1342268730 1342268569	1342268314
IRAS 21282+5050	322.4934	51.0666	Yes	Yes	Yes	No	5	1342223375 1342220741	-
IRAS 21554+6204	329.2424	62.3121	Yes	Yes	No	No	1,6	1342245813 1342247150	-
IRAS 22036+5306	331.3761	53.3591	Yes	Yes	Yes	Yes	3,5	1342221882 1342221883	1342257338
IRC +10216	146.9892	13.2787	Yes	No	No	Yes	1,7	1342245395 1342221889 1342253754 1342256262	1342197466 1342245849 1342221713 1342253661 1342256105
IRC +10216 Arc	147.1250	13.2644	-	-	-	Yes	-	-	1342254036
IRC -10529[1]	302.6142	-6.2710	Yes	Yes	Yes	Yes	2	1342208931 1342208932	1342216902
IRC +40540	353.6147	43.5503	-	-	-	Yes	-	-	1342246288
IRC +50137	77.831	52.8758	Yes	Yes	No	No	1	1342249315	-
χ Cyg	297.6413	32.9140	Yes	Yes	Yes	No	-	1342198176 1342198177	-
M 1-92	294.0787	29.5472	-	-	-	Yes	-	-	1342243606

TABLE B.1: Continued.

Target Name	RA(deg)	Dec(deg)	IRAS	AKARI	ISO	SPIRE	Comments	ObsIDs PACS	ObsIDs SPIRE
MGE 4602	271.1620	-20.6242	Yes	Yes	No	Yes	1,4,6	1342243506	1342268285
MWC 922	275.3162	-13.0241	Yes	Yes	Yes	No	5	1342229805 1342229806	-
Mz 3	244.3058	-51.9862	Yes	Yes	Yes	Yes	4	1342243109 1342243110	1342251318
Mz 3 Off	244.2859	-52.0332	-	-	-	Yes	-	-	1342251316
Mz 3 SLobe	244.3051	-51.9904	-	-	-	Yes	-	-	1342251317
NGC 40	3.2542	72.5219	Yes	Yes	Yes	Yes	4,6	1342236879 1342236880	1342243640
NGC 40 Off	3.2300	72.4250	-	-	-	Yes	-	-	1342243641
NGC 40 WRim	3.2399	72.5240	-	-	-	Yes	-	-	1342245122
NGC 2022	85.5258	9.0861	-	-	-	Yes	-	-	1342227518
NGC 2392	112.2948	20.9118	Yes	Yes	No	Yes	4,6	1342229792 1342229816	1342245121
NGC 2392 Off	112.3037	20.9587	-	-	-	Yes	-	-	1342245119
NGC 2392 SRim	112.2937	20.9075	-	-	-	Yes	-	-	1342245120
NGC 2440	115.4787	-18.2082	-	-	-	Yes	-	-	1342221712
NGC 3242	156.1920	-18.6411	Yes	Yes	Yes	Yes	3,4,6	1342232278 1342232279	1342245847
NGC 3242 Off	156.2312	-18.5513	-	-	-	Yes	-	-	1342245845
NGC 3242 SFlier	156.1938	-18.6464	-	-	-	Yes	-	-	1342245846
NGC 6302	258.4342	-37.1044	Yes	Yes	Yes	Yes	2,3	1342230150	1342191224

Table B.1: Continued.

Target Name	RA(deg)	Dec(deg)	IRAS	AKARI	ISO	SPIRE	Comments	ObsIDs PACS	ObsIDs SPIRE
								1342230151	
NGC 6445	267.3133	-20.0095	Yes	Yes	Yes	Yes	4,6	1342242440 1342242441	1342243630
NGC 6445 Off	267.3100	-20.1110	-	-	-	Yes	-	-	1342243628
NGC 6445 WLobe	267.3095	-20.0060	-	-	-	Yes	-	-	1342243629
NGC 6537	271.3045	-19.8430	No	Yes	Yes	Yes	3,5	1342231322 1342231323	1342243627
NGC 6543	269.6385	66.6330	No	Yes	Yes	Yes	3,4	1342238388 1342238389 1342212264	1342227789 1342237028
NGC 6543 Off	269.6279	66.7304	-	-	-	Yes	-	-	1342227788
NGC 6543 WKnot	269.5722	66.6356	No	No	No	Yes	-	1342235679 1342235680	1342227787 1342237027
NGC 6720	283.3961	33.0291	Yes	Yes	Yes	Yes	1,4,6	1342208920	1342243616
NGC 6720 Off	283.3925	32.9344	-	-	-	Yes	-	-	1342243618
NGC 6720 NRim	283.3928	33.0358	-	-	-	Yes	-	-	1342243617
NGC 6720 OFFCenter	283.3937	33.0326	Yes	Yes	Yes	No	-	1342233716 1342233717	-
NGC 6781	289.6170	6.5386	Yes	No	Yes	Yes	4,6	1342230999 1342231000	1342243612
NGC 6781 Off	289.6349	6.4422	-	-	-	Yes	-	-	1342243610

TABLE B.1: Continued.

Target Name	RA(deg)	Dec(deg)	IRAS	AKARI	ISO	SPIRE	Comments	ObsIDs PACS	ObsIDs SPIRE
NGC 6781 Rim	289.6313	6.5388	No	No	No	Yes	-	1342231001 1342231002	1342243611
NGC 6826	296.2006	50.5250	Yes	Yes	Yes	Yes	3,4,6	1342238926 1342238927	1342237006
NGC 6826 Off	296.1140	50.6191	-	-	-	Yes	-	-	1342221686
NGC 6826 Rim	296.2207	50.5290	No	No	No	No	-	1342235850 1342235851	-
NGC 6853 Offset	299.8862	22.7102	-	-	-	Yes	-	-	1342270195
NGC 7009	316.0450	-11.3635	Yes	Yes	Yes	Yes	3,4	1342232300 1342232301	1342221681 1342245079
NGC 7009 EFlier	316.0518	-11.3621	-	-	-	Yes	-	-	1342245078
NGC 7009 Off	316.0178	-11.2705	-	-	-	Yes	-	-	1342221680
NGC 7026	316.5773	47.8519	Yes	Yes	No	Yes	3	1342234268 1342234269	1342239347
NGC 7026 NLobe	316.5771	47.8554	-	-	-	Yes	-	-	1342239346
NGC 7026 Off	316.5215	47.8831	-	-	-	Yes	-	-	1342239345
NGC 7027	316.7566	42.2361	-	-	-	Yes	-	-	1342189124 1342189125 1342221698
NGC 7293	337.2916	-20.8315	-	-	-	Yes	-	-	1342257353
NML Cyg	311.606	40.1165	No	Yes	Yes	Yes	3	1342198174 1342198175	1342243592

TABLE B.1: Continued.

Target Name	RA(deg)	Dec(deg)	IRAS	AKARI	ISO	SPIRE	Comments	ObsIDs PACS	ObsIDs SPIRE
NML Tau	58.3701	11.4062	Yes	Yes	Yes	Yes	-	1342203679 1342203680 1342203681	1342192176
OH 21.5+0.5	277.1316	-9.9696	No	No	No	Yes	2,4,7	1342242438 1342268778 1342268748	1342268311
OH 26.5+0.6	279.3852	-5.3998	Yes	Yes	Yes	Yes	3,5	1342207776 1342207777	1342243624
OH 30.1-0.7	282.1746	-2.8411	Yes	Yes	No	Yes	4	1342216207 1342269304 1342269305	1342268316
OH 30.7+0.4	281.5241	-1.9881	Yes	No	No	Yes	4,6	1342268789 1342268790	1342268309
OH 32.8-0.3	283.0924	-0.2371	Yes	No	Yes	Yes	4,5,7	1342209738 1342268793 1342268794	1342268318
OH 104.91+2.41	334.8645	59.8560	Yes	Yes	Yes	No	1	1342212261	-
OH 127.8+0.0	23.4633	62.4481	-	-	-	Yes	-	-	1342268319
OH 231.8+4.2	115.5701	-14.7144	Yes	Yes	No	Yes	3	1342196694 1342196695	1342193665
o Cet	34.8366	-2.9776	Yes	Yes	No	Yes	-	1342213286	1342189546

TABLE B.1: Continued.

Target Name	RA(deg)	Dec(deg)	IRAS	AKARI	ISO	SPIRE	Comments	ObsIDs PACS	ObsIDs SPIRE
								1342213287	
π Gru	335.6842	-45.9479	Yes	Yes	Yes	No	-	1342210397 1342210398	-
R Aql	286.5927	8.2300	Yes	Yes	Yes	No	1,5	1342243900	-
R Cas	359.6036	51.3888	Yes	Yes	Yes	Yes	-	1342212576 1342212577	1342246981
R Dor	69.1899	-62.0771	Yes	Yes	Yes	Yes	3	1342197794 1342197795	1342245114
R Lep	74.9014	-14.8062	Yes	Yes	No	No	1,6	1342249509	-
RAFGL 2374	290.4021	9.4656	Yes	Yes	No	No	1,6	1342244920	-
Red Rectangle	94.9925	-10.6374	Yes	Yes	Yes	Yes	3	1342220928 1342220929	1342192835 1342227779 1342227781
Red Rectangle Off	94.9870	-10.6226	-	-	-	Yes	-	-	1342227780
RR Aql	299.4002	-1.8864	Yes	Yes	No	No	1	1342269414	-
RT Cap	304.2772	-21.3179	Yes	Yes	No	No	6	1342269308 1342269355	- -
R Scl	21.7420	-32.5431	-	-	-	Yes	-	-	1342189545
S Aur	81.7810	34.1496	Yes	Yes	No	No	1,6	1342250896	-
SAO 163075	298.2195	-17.0306	-	-	-	Yes	-	1342216903	
ST Her	237.6942	48.4830	Yes	Yes	No	No	1,6	1342247537	-
T Cep	317.3824	68.4908	Yes	Yes	No	No	1	1342246557	-

TABLE B.1: Continued.

Target Name	RA(deg)	Dec(deg)	IRAS	AKARI	ISO	SPIRE	Comments	ObsIDs PACS	ObsIDs SPIRE
T Mic	306.9799	-28.2610	Yes	Yes	No	No	-	1342268729 1342268788 1342269458	-
Tc 1	266.3970	-46.0899	Yes	Yes	No	No	6	1342231319 1342231320	-
TX Cam	75.2099	56.1812	Yes	Yes	Yes	Yes	3,4	1342225855 1342225856	1342251300
U Hya	159.3886	-13.3845	Yes	Yes	No	No	1,6	1342256947	-
U Mon	112.6977	-9.7768	Yes	Yes	No	Yes	3	1342206993 1342245243 1342245244	1342251307
V384 Per	51.6229	47.5301	Yes	Yes	Yes	No	1,6	1342250572	-
V438 Oph	258.6657	11.0694	Yes	Yes	No	No	1,6	1342252326	-
V1300 Aql	302.6161	-6.2704	Yes	Yes	Yes	Yes	-	1342269516 1342269910	1342216902
V Cyg	310.3261	48.1413	Yes	Yes	Yes	No	5	1342208939 1342208940	-
V Hya	162.9052	-21.2500	Yes	Yes	Yes	Yes	-	1342197790 1342197791	1342247570
W Aql	288.8476	-7.0471	Yes	Yes	Yes	No	-	1342209731 1342209732	-

TABLE B.1: Continued.

Target Name	RA(deg)	Dec(deg)	IRAS	AKARI	ISO	SPIRE	Comments	ObsIDs PACS	ObsIDs SPIRE
W Hya	207.2583	-28.3676	Yes	Yes	Yes	Yes	-	1342212604 1342223808	1342189116
W Ori	76.3488	1.1776	Yes	Yes	No	No	1,6	1342249503	-
WX Psc	16.6082	12.5980	Yes	Yes	Yes	Yes	-	1342202121 1342202122	1342246973
X Her	240.6632	47.2403	Yes	Yes	No	No	-	1342197802 1342197803 1342202120	-
Y CVn	191.2826	45.4402	Yes	Yes	Yes	No	1,6	1342254305	-

B.2 Fluxes of CO lines measured with the PACS Spectrometer

TABLE B.2: Integrated fluxes of ^{12}CO lines for 26 sources studied in Chapter 4. Column 1: Quantum numbers; Column 2: Wavelength of the emission lines; Column 3: Einstein's coefficient; Column 4: Energy of the upper level of the transition; Columns 5 to 10: Integrated fluxes of the emission lines. †symbol indicates blended lines. ⋆ marks a bad determination of the continuum level. ‡ means a bad fit.

Line	λ (μm)	A_{ul} (s^{-1})	E_{up} (K)	Flux (10^{-16} W/m^2)	Flux (10^{-16} W/m^2)	Flux (10^{-16} W/m^2)	Flux (10^{-17} W/m^2)	Flux (10^{-17} W/m^2)	Flux (10^{-16} W/m^2)
				RR Aql	*o* Cet	W Hya	IRAS 20038-2722	T Cep	NML Tau
14-13	186.0	2.74×10^{-4}	580.5	-	3.0±0.1	2.2±0.2	1.9±0.4	-	3.4±0.1
15-14	173.6	3.35×10^{-4}	663.4	-	3.3±0.1	2.7±0.2	2.9±0.2	-	4.6±0.1
16-15	162.8	4.05×10^{-4}	751.7	-	3.8±0.1	9.0±1.1 ‡	1.0±0.4 †	-	3.4±0.5
17-16	153.3	4.83×10^{-4}	845.6	-	3.6±0.2	2.9±0.3	2.8±0.5	-	
18-17	144.8	5.70×10^{-4}	945.0	0.18±0.04	4.2±0.1	3.1±0.2	3.8±0.6 †	7.0±0.5	4.4±0.1
19-18	137.2	6.65×10^{-4}	1049.9	0.17±0.04	3.7±0.3	3.3±0.3 †	2.6±0.6	5.6±0.4	5.0±0.1
20-19	130.4	7.70×10^{-4}	1160.2	0.20±0.04	4.2±0.3	7.0±0.4 †	3.2±0.5	8.7±1.0	4.1±0.1
21-20	124.2	8.83×10^{-4}	1276.1	0.18±0.03	3.8±0.6	2.5±0.3	3.0±0.6	6.0±0.8	4.9±0.2
22-21	118.6	1.01×10^{-3}	1397.4	0.77±0.04 †	19±1.0 †	8.8±0.5 †	13±1.0 †	64±1.0 †	3.7±0.1
23-22	113.5	1.14×10^{-3}	1524.2	1.9±0.1 †	6.5±0.5 †	16±1.0 †	19±1.0 †	32±2.0 †	5.2±0.3
24-23	108.8	1.28×10^{-3}	1656.5	4.8±0.5	3.2±0.5	5.8±1.1 †	12±2.0 †	24±0.1 †	
25-24	104.5	1.43×10^{-3}	1794.3	-	1.7±0.5 †	1.3±1.0 †	2.7±0.9	3.6±1.1	3.6±0.2
28-27	93.4	1.94×10^{-3}	2240.3	-	5.3±0.4 †	6.9±0.5 †	6.7±0.8 †	-	2.4±0.4
29-28	90.2	2.13×10^{-3}	2399.9	-	2.4±0.3 †	2.6±0.5	2.5±0.4	-	11±0.1 †
30-29	87.2	2.32×10^{-3}	2564.9	-	3.6±0.8 †	1.3±0.5	1.8±0.8	-	2.5±0.1 [2]‡
31-30	84.4	2.52×10^{-3}	2735.3	-	4.7±0.5 †	3.0±0.6	3.8±1.1 †	-	2.4±0.2
32-31	81.8	2.74×10^{-3}	2911.2	-	-	3.2±0.7	-	-	5.5±1.3 †
33-32	79.4	2.95×10^{-3}	3092.5	-	-	-	-	-	1.7±0.5
34-33	77.1	3.18×10^{-3}	3279.2	-	-	-	-	-	2.2±0.5
35-34	74.9	3.40×10^{-3}	3471.3	-	-	-	-	-	-
36-35	72.9	3.64×10^{-3}	3668.9	-	-	-	-	-	-
37-36	70.9	3.88×10^{-3}	3871.8	-	-	-	-	-	-
38-37	70.9	4.12×10^{-3}	4080.1	-	-	-	-	-	-
39-38	67.3	4.37×10^{-3}	4293.7	-	-	-	-	-	-
40-39	65.7	4.61×10^{-3}	4512.8	-	-	-	-	-	-
41-40	64.1	4.86×10^{-3}	4737.2	-	-	-	-	-	-
42-41	62.6	5.11×10^{-3}	4966.9	-	-	-	-	-	-

TABLE B.2: Continued.

Line	λ (μm)	Flux (10^{-16} W/m^2)	Flux (10^{-16} W/m^2)	Flux (10^{-17} W/m^2)	Flux (10^{-17} W/m^2)	Flux (10^{-17} W/m^2)	Flux (10^{-16} W/m^2)
		R Dor	TX Cam	X Her	IRAS 19474-0744	T Mic	R Cas
14-13	186.0	2.6±0.1	1.9±0.1	4.5±0.7	4.7±0.7	1.9±0.3	1.4±0.1
15-14	173.6	3.0±0.2	2.0±0.1	2.7±0.4	5.5±0.4	3.5±0.2	1.6±0.1
16-15	162.8	69±2.0 ‡	1.9±0.1	2.9±0.8	6.0±0.4	3.3±0.4	1.6±0.1
17-16	153.3	4.2±0.4	2.1±0.1	5.9±0.8	6.8±0.5	3.9±0.3	1.7±0.1
18-17	144.8	5.1±0.3	1.8±0.1	8.5±0.7 †	6.3±0.5	4.6±0.4	1.9±0.1
19-18	137.2	4.7±0.5	1.6±0.1	4.5±0.8	5.4±0.8	27±2 ‡	1.5±0.1
20-19	130.4	4.7±0.5	1.6±0.2	4.4±2.1	7.4±0.5	5.3±0.7	1.6±0.1
21-20	124.2	3.9±0.4	9.0±1.5	4.1±0.6	6.0±0.3	3.4±0.3	1.4±0.1
22-21	118.6	13±1.0 †	3.3±0.2 †	10±2 †	40±1 †	21±1 †	3.1±0.1 †
23-22	113.5	32±1.0 †	7.9±0.3 †	42±1 †	42±1 †	23±1 †	13±1 †
24-23	108.8	6.4±0.6	-	5.5±1.8	8.3±0.7	5.3±0.9	1.1±0.1
25-24	104.5	-	-	-	11±3 †	-	0.5±0.1 †
28-27	93.4	10±1 †	-	4.5±1.0	8.7±1.5 †	-	2.1±0.2 †
29-28	90.2	3.6±0.3	-	3.0±1.4	-	5.0±0.9	0.6±0.1
30-29	87.2	2.8±0.8	-	5.4±1.7	-	2.7±1.0	1.0±0.2
31-30	84.4	6.3±0.7 †	-	9.5±2.4 †	-	5.5±1.2 †	1.5±0.2 †
32-31	81.8	6.0±1.6	-	-	-	-	0.9±0.2 †
33-32	79.4	-	-	-	-	-	-
34-33	77.1	-	-	-	-	-	-
35-34	74.9	-	-	-	-	-	-
36-35	72.9	-	-	-	-	-	-
37-36	70.9	-	-	-	-	-	-
38-37	70.9	-	-	-	-	-	-
39-38	67.3	-	-	-	-	-	-
40-39	65.7	-	-	-	-	-	-
41-40	64.1	-	-	-	-	-	-
42-41	62.6	-	-	-	-	-	-

TABLE B.2: Continued.

Line	λ (μm)	Flux (10^{-17} W/m^2)	Flux (10^{-16} W/m^2)	Flux (10^{-16} W/m^2)	Flux (10^{-16} W/m^2)	Flux (10^{-16} W/m^2)	Flux (10^{-16} W/m^2)
		EP Aqr	NML Cyg	χ Cyg	π Gru	W Aql	WX Psc
14-13	186.0	6.4±0.7	4.2±0.2	2.4±0.1	3.8±0.1	3.5±0.1	1.6±0.1
15-14	173.6	6.3±0.5	4.5±0.2	2.9±0.1	3.6±0.1	3.5±0.1	1.2±0.1
16-15	162.8	23±3 †	4.8±0.5	3.2±0.1	3.8±0.1	4.3±0.1	1.3±0.2
17-16	153.3	9.0±0.8	5.4±0.1	3.2±0.1	4.5±0.1	4.8±0.1	1.8±0.1
18-17	144.8	12±1 †	8.2±0.1 †	3.9±0.1	4.6±0.1	4.7±0.1	1.7±0.1
19-18	137.2	12±1 †	4.6±0.2	3.6±0.1	4.6±0.1	4.5±0.1	1.1±0.1
20-19	130.4	8.5±0.9	6.4±0.3	4.4±0.1	4.8±0.1	5.6±0.1	1.9±0.2
21-20	124.2	8.4±1.0	3.9±1.0	3.3±0.1	4.7±0.1	5.0±0.0	1.1±0.2
22-21	118.6	3.2±0.1 †	6.7±0.7 ‡	4.1±0.1	4.8±0.1	4.9±0.1	2.3±0.1
23-22	113.5	56±1 †	35±1 †	11±1 †	9.1±0.3 †	7.8±0.2 †	9.2±0.2 †
24-23	108.8	8.2±0.8	6.9±0.2	4.1±0.2	4.7±0.1	4.0±0.1	1.7±0.2
25-24	104.5	3.5±2.7 †	7.9±2.9 †	4.0±0.2	4.8±0.1	4.1±0.2	-
28-27	93.4	18±1 †	26±1 †	3.7±0.1	3.9±0.1	3.1±0.1	5.4±0.2 †
29-28	90.2	11±3 †	4.2±0.3	3.9±0.1	3.5±0.1	3.3±0.1	3.3±0.9
30-29	87.2	4.1±1.2	2.4±0.5	3.0±0.1	3.9±0.1	3.0±0.2	0.81±0.09
31-30	84.4	16±1 †	-	4.3±0.1 †	4.4±0.1 †	2.7±0.2	-
32-31	81.8	-	-	2.5±0.1	2.9±0.1	2.0±0.1	-
33-32	79.4	-	-	2.4±0.2	3.0±0.2	1.7±0.2	-
34-33	77.1	-	-	2.6±0.2	2.6±0.1	1.7±0.1	-
35-34	74.9	-	-	2.6±0.4	6.7±0.2 †	3.5±0.3 †	-
36-35	72.9	-	-	2.8±0.3 †	2.4±0.1	1.4±0.3	-
37-36	70.9	-	-	1.5±0.2	1.7±0.5	0.80±0.18	-
38-37	70.9	-	-	1.1±0.2	1.9±0.1	0.79±0.15	-
39-38	67.3	-	-	9.6±0.7 †	3.5±0.7 †	3.8±0.3 †	-
40-39	65.7	-	-	2.6±0.6 †	1.8±0.3	0.37±0.11	-
41-40	64.1	-	-	0.56±0.17	1.4±0.2	0.18±0.17	-
42-41	62.6	-	-	1.6±0.5 †	0.94±0.35	0.34±0.12 †	-

Table B.2: Continued.

Line	λ (μm)	Flux (10^{-17} W/m^2)	Flux (10^{-17} W/m^2)	Flux (10^{-17} W/m^2)	Flux (10^{-17} W/m^2)	Flux (10^{-16} W/m^2)	Flux (10^{-15} W/m^2)
		V1300 Aql	OH 231.8+4.2	OH 26.5+0.6	IRAS 22036+5306	AFGL 6815	IRAS 17347-3139
14-13	186.0	7.5±0.4	4.1±1.6	4.1±1.3 †	11±1 †	3.2±0.1	0.90±0.1
15-14	173.6	11±1	28±13	7.1±1.0	6.4±0.6	3.3±0.1	1.1±0.1
16-15	162.8	9.2±1.6	23±12	-	8.2±1.0 †	2.5±0.1	1.2±0.1
17-16	153.3	12±1	4.4±1.8	11±1	9.2±0.9 †	2.3±0.1	1.4±0.1
18-17	144.8	14±1	8.3±1.7 †	15±2	1.0±0.2 †	2.5±0.1	1.3±0.1
19-18	137.2	8.2±0.5	2.2±1.2	0.70±0.71 ⋆	4.9±1.7 †	2.0±0.1	1.4±0.1
20-19	130.4	9.5±0.7	3.5±1.5	7.1±1.1	3.9±0.5	2.2±0.1	1.4±0.1
21-20	124.2	6.9±1.0 †	-	7.5±1.7	5.4±1.1 †	1.6±0.1	1.4±0.1
22-21	118.6	12±1	-	4.8±2.4	3.0±0.8	1.2±0.1	1.5±0.1
23-22	113.5	44±1 †	-	49±5 †	6.6±0.9 †	3.0±0.1 †	2.2±0.1 †
24-23	108.8	17±1 †	-	15±2	-	0.38±0.07 ‡	1.3±0.1
25-24	104.5	2.8±3.0 †	-	-	-	0.91±0.38 †	1.2±0.1
28-27	93.4	-	-	-	-	0.43±0.10	0.93±0.02
29-28	90.2	6.0±1.0	-	-	-	-	0.92±0.02
30-29	87.2	5.6±0.6	-	-	-	-	0.68±0.02
31-30	84.4	4.6±1.8 †	-	-	-	-	1.5±0.1 †
32-31	81.8	3.5±1.0	-	-	-	-	0.57±0.02
33-32	79.4	4.4±0.9 †	-	-	-	-	0.52±0.03
34-33	77.1	2.7±0.6	-	-	-	-	0.48±0.02
35-34	74.9	-	-	-	-	-	0.47±0.02
36-35	72.9	-	-	-	-	-	0.42±0.03
37-36	70.9	-	-	-	-	-	0.54±0.10 †
38-37	70.9	-	-	-	-	-	0.24±0.04
39-38	67.3	-	-	-	-	-	0.34±0.03
40-39	65.7	-	-	-	-	-	0.21±0.03
41-40	64.1	-	-	-	-	-	0.26±0.05
42-41	62.6	-	-	-	-	-	-

TABLE B.2: Continued.

Line	λ (μm)	Flux (10^{-16} W/m^2)	Flux (10^{-16} W/m^2)
		NGC 6302	IRAS NGC 6537
14-13	186.0	9.9±0.3	2.9±0.3
15-14	173.6	9.0±0.4	3.4±0.2
16-15	162.8	8.4±0.4	2.3±0.2
17-16	153.3	8.3±0.3	3.2±0.2
18-17	144.8	9.7±0.4	2.1±0.1
19-18	137.2	5.5±0.2	1.4±0.1
20-19	130.4	6.5±0.3	1.4±0.1
21-20	124.2	4.2±0.3	0.70±0.06
22-21	118.6	3.2±0.5	0.37±0.07
23-22	113.5	2.8±0.5	0.82±0.31 †
24-23	108.8	1.7±1.0 †	-
25-24	104.5	2.4±0.3	-
28-27	93.4	-	-
29-28	90.2	-	-
30-29	87.2	-	-
31-30	84.4	-	-
32-31	81.8	-	-
33-32	79.4	-	-
34-33	77.1	-	-
35-34	74.9	-	-
36-35	72.9	-	-
37-36	70.9	-	-
38-37	70.9	-	-
39-38	67.3	-	-
40-39	65.7	-	-
41-40	64.1	-	-
42-41	62.6	-	-

TABLE B.3: Line fluxes of ^{12}CO lines of C-rich stars studied in Chapter 5. The ellipsis mark absent or noisy (SNR<3) lines, and asterisks (*) flag line blends.

Transition	ν_{rest} (MHz)	λ_{rest} (μm)	E_{up}/k (K)	A_{ij} (s^{-1})	F ($\times10^{-16}$ W m^{-2})				
^{12}CO (v = 0)					CIT 6	V HYA	IRAS 15194-5115	AFGL 2513	V CYG
$J = 14 \rightarrow 13$	1611794	185.999	580.497	0.00027	8.9±0.3	4.3±0.2	4.3±0.4	0.88±0.07	1.8±0.2
$J = 15 \rightarrow 14$	1726603	173.631	663.361	0.00034	7.7±0.3	4.6±0.2	3.9±0.5	0.96±0.05	1.8±0.1
$J = 16 \rightarrow 15$	1841346	162.812	751.733	0.00041	9.2±0.5	5.6±0.2	5.0±0.3	1.07±0.06	2.6±0.1
$J = 17 \rightarrow 16$	1956018	153.267	845.608	0.00048	11.3±0.6	6.1±0.2	4.9±0.3	1.29±0.08	2.3±0.1
$J = 18 \rightarrow 17$	2070616	144.784	944.983	0.00057	9.6±0.7	5.3±0.2	3.7±0.5	0.99±0.07	2.7±0.1
$J = 19 \rightarrow 18$	2185135	137.196	1049.854	0.00067	8.1±0.6	5.0±0.2	4.1±0.3	0.84±0.08	2.7±0.2
$J = 20 \rightarrow 19$	2299570	130.369	1160.217	0.00077	16.2±0.9	8.9±0.3	7.4±0.6	1.7±0.1	3.9±0.3
$J = 21 \rightarrow 20$	2413917	124.193	1276.068	0.00088	11±1.0	6.4±0.3	4±1	1.0±0.1	2.6±0.2
$J = 22 \rightarrow 21$	2528172	118.581	1397.402	0.00101	10.9±0.6	5.9±0.2	4.3±0.8	1.0±0.07	2.7±0.2
$J = 23 \rightarrow 22$	2642330	113.458	1524.215	0.00114	16±2	9±1	5±2	1.5±0.2	4.1±0.4
$J = 24 \rightarrow 23$	2756388	108.763	1656.502	0.00128	11±2	5.6±0.5	5±2*	0.9±0.1	1.9±0.3
$J = 25 \rightarrow 24$	2870339	104.445	1794.258	0.00143	9±1	5.9±0.5	3.8±0.8	0.8±0.1	2.7±0.4*
$J = 28 \rightarrow 27$	3211519	93.349	2240.286	0.00194	6.8±0.4	5.3±0.3	2.5±0.4*	0.7±0.1	1.2±0.2
$J = 29 \rightarrow 28$	3325005	90.163	2399.862	0.00213	11±1.0	5.3±0.4	1.6±0.4	0.8±0.1	1.8±0.2
$J = 30 \rightarrow 29$	3438365	87.19	2564.879	0.00232	9.7±0.9	6.4±0.5*	3.2±0.8	1.5±0.2*	2.1±0.4*
$J = 31 \rightarrow 30$	3551592	84.411	2735.331	0.00252	9.8±0.9	4.9±0.3	1.7±0.6	0.9±0.1	1.6±0.3
$J = 32 \rightarrow 31$	3664684	81.806	2911.209	0.00274	6.1±0.9	4.1±0.6	...	0.7±0.2	1.0±0.3
$J = 33 \rightarrow 32$	3777636	79.359	3092.509	0.00295	5.4±0.9	5.2±0.6	...	0.7±0.2	0.96±0.3
$J = 34 \rightarrow 33$	3890443	77.059	3279.223	0.00318	9±1	4.6±0.4	...	0.7±0.1*	1.1±0.3*
$J = 35 \rightarrow 34$	4003101	74.89	3471.344	0.0034	8±2*	3.9±0.8	...	0.8±0.1*	1.2±0.3*
$J = 36 \rightarrow 35$	4115606	72.843	3668.864	0.00364	4.7±0.9*	3.2±0.3	...	...	...
$J = 37 \rightarrow 36$	4227953	70.907	3871.775	0.00388	5±1	3.0±0.6*	...	...	...
$J = 38 \rightarrow 37$	4340138	69.074	4080.071	0.00412	3.7±0.4	2.8±0.3	...	...	...
$J = 39 \rightarrow 38$	4452157	67.336	4293.743	0.00437	3±1*	2.5±0.5*	...	...	...
$J = 40 \rightarrow 39$	4564006	65.686	4512.783	0.00461	3.2±1.0*	2.9±0.7	...	...	...
$J = 41 \rightarrow 40$	4675679	64.117	4737.183	0.00486	1.1±0.6*	1.4±0.4	...	...	...
$J = 42 \rightarrow 41$	4787174	62.624	4966.933	0.00511	2±1*	0.9±0.5*	...	...	...
$J = 43 \rightarrow 42$	4898485	61.201	5202.026	0.00536	3.3±0.9*	1.8±0.4*	...	...	...
$J = 44 \rightarrow 43$	5009608	59.843	5442.452	0.00561	1.7±0.6	1.9±0.5	...	...	...
$J = 45 \rightarrow 44$	5120539	58.547	5688.201	0.00585	...	...	...	...	...

TABLE B.3A: Continued.

AFGL 3068	AFGL 3116	AFGL 618	HD 44179	IRAS 16594-4656	AFGL 2688	Hen 2-113	CPD-568032	IRAS 21282+5050
2.1±0.2	2.7±0.2	39±1	0.4±0.1	4.1±0.1	41±1	2.24±0.09	2.4±0.1	2.96±0.06
2.1±0.2	2.9±0.2	33±1	0.39±0.09	4.1±0.1	36±1	2.16±0.07	2.3±0.1	2.92±0.05
2.3±0.1	2.8±0.1	40±1	0.4±0.1	3.9±0.3	33±1	2.3± 0.5	2.2±0.1	2.42±0.06
2.5±0.2	4.1±0.3	37±1	0.53±0.09	3.2±0.1	26±1	2.3± 0.1	2.0±0.07	1.63±0.04
2.7±0.3	3.5±0.2	38±1	0.6±0.1	2.76±0.06	25±1	2.1± 0.1	1.9±0.1	1.04±0.07
2.5±0.2	3.0±0.2	39±2	0.45±0.09	2.42±0.01	22±1	2.0± 0.1	1.6±0.1	0.9±0.1
3.9±0.2	6.1±0.4	44±1	0.4±0.1	2.5±0.1	24±1	2.2± 0.1	2±0.2	0.59±0.09
2.3±0.3	4.3±0.5	34±2	0.4±0.1	2.8±0.1	17±1	2.0± 0.1	1.7±0.2	0.50±0.08
2.7±0.2	3.6±0.2	36±2	0.7±0.1	2.2±0.2	18±1	2.4± 0.3	1.3±0.2	...
2.5±0.6	4.6±0.9	46±2	0.4±0.2	2.7±0.1	14±2	2.2±0.3	1.9±0.2	...
1.6±0.4	3.7±0.6	28±2*	...	1.9±0.1	11±2	1.2±0.2	1.0±0.2	...
1.3±0.5	3.4±0.2	31±2	...	2.1±0.2	6±2	1.6±0.2	1.2±0.3	...
1.2±0.3	3.2±0.3	21±1	...	1.6±0.1	6±1	0.7±0.2	0.9±0.1	...
1.9±0.4*	3.3±0.3	25±1	...	1±2*	11±2*	...	bad fit	...
...	4.5±0.5*	20±1	...	1.3±0.1	bad fit*	...	...	...
...	2.9±0.3	26±2	...	4.9±0.8*	4±2	...	...	...
...	2.0±0.2	17±2	...	0.9±0.1	...	...	...	...
...	2.4±0.5	15±2*	...	0.8±0.8*	...	...	...	...
...	2.4±0.7*	16±2	...	0.7±0.1	...	...	...	...
...	2.2±0.4	16±2	...	0.8±0.1*	...	...	...	...
...	2.3±0.5	11±1	...	...	...	...	...	...
...	3±1*	13±3*	...	...	...	...	...	...
...	1.3±0.2*	11±1	...	...	...	...	...	...
...	0.9±0.3	6±5	...	...	...	...	...	...
...	0.9±0.3	5±2	...	...	...	...	...	...
...	...	10±2	...	...	...	...	...	...
...	...	37±20*	...	...	...	...	...	...
...	...	9±3	...	...	...	...	...	...
...	...	6±2	...	...	...	...	...	...
...	...	3±2	...	...	...	...	...	...

TABLE B.4: Line fluxes, F, of CO rotational transitions of seven observations of IRC+10216. Asterisks flag known line blends.

Transition	$\nu_{\rm rest}$ (MHz)	$\lambda_{\rm rest}$ (μm)	$E_{\rm up}/k$ (K)	$A_{\rm ij}$ (s^{-1})	F ($\times10^{-16}$ W m^{-2})						
^{12}CO (v = 0)					OD 745	OD 894	OD 1087	OD 1113	OD 1257	OD 1288	OD 1296
$J = 14 \rightarrow 13$	1611794	185.99	580.5	0.00027	85±3	98±10	92±4	90±5	97±3	86±8	100±3
$J = 15 \rightarrow 14$	1726603	173.63	663.36	0.00034	74±5	103±13	80±6	108±30	82±5	88±8	80±5
$J = 16 \rightarrow 15$	1841346	162.81	751.73	0.00041	89±4	100±24	93±3	93±12	78±2	89±12	79±3
$J = 17 \rightarrow 16$	1956018	153.27	845.61	0.00048	92±7		99±7		92±7		89±6
$J = 18 \rightarrow 17$	2070616	144.78	944.98	0.00057	82±7		85±6		110±5		102±5
$J = 28 \rightarrow 27$	3211519	93.35	2240.29	0.00194	69±2	104±18	97±3	104±18	64±2	59±15	62±2
$J = 29 \rightarrow 28$	3325005	90.16	2399.86	0.00213	72±4	124±15	95±6	124±15	80±5	78±10	77±5
$J = 30 \rightarrow 29$	3438365	87.19	2564.88	0.00232	55±7	82±12	82±9	82±12	72±6	50±9	55±4
$J = 31 \rightarrow 30$	3551592	84.41	2735.33	0.00252	57±7	108±11	101±9	108±11	52±5	60±6	55±5
$J = 32 \rightarrow 31$	3664684	81.81	2911.21	0.00274	37±8	54±18	68±6	54±18	47±5	26±11	39±4
$J = 33 \rightarrow 32$	3777636	79.36	3092.51	0.00295	43±8	80±15	79±10	80±15	42±5	39±7	40±4
$J = 34 \rightarrow 33$	3890443	77.06	3279.22	0.00318	38±8		64±9		30±5		35±5
$J = 35 \rightarrow 34$	4003101	74.89	3471.34	0.0034	34±8*		64±9*		39±8*		38±7*
$J = 36 \rightarrow 35$	4115606	72.84	3668.86	0.00364	19±7		32±9		23±5		18±4
$J = 37 \rightarrow 36$	4227953	70.91	3871.78	0.00388	20±6		45±10		20±6		22±6

B.3 Fluxes of CO lines detected with the SPIRE Spectrometer

TABLE B.5: Integrated fluxes of ^{12}CO lines for the 20 O-rich sources studied in Chapter 6. Column 1: Quantum numbers of the transition; Column 2: Log of Einstein's coefficient; Column 3: Energy of the upper level of the transition; Column 4: Frequency corresponding to the emission lines in microns; Columns 5 to 10: Integrated fluxes of the emission lines in $W\,m^{-2}$. †, symbol indicates blended lines.

Line	log(A_{ul})	E_{up} (K)	Frequency (GHz)	Flux (10^{-17} W/m^2)	Flux (10^{-16} W/m^2)	Flux (10^{-16} W/m^2)	Flux (10^{-16} W/m^2)	Flux (10^{-16} W/m^2)	Flux (10^{-16} W/m^2)
				IRAS 20038-2722	W Hya	*o* Cet	IK Tau	R Dor	R Cas
4-3	-5.2	55.3	461.0	-	(0.4 ± 0.1)	(1.1 ± 0.1)	(0.5 ± 0.1)	(0.7 ± 0.1)	(0.6 ± 0.1)
5-4	-4.9	83.0	576.3	(0.8 ± 0.2)	(0.6 ± 0.1)	(1.4 ± 0.1)	(0.8 ± 0.1)	(1.0 ± 0.1)	(1.1 ± 0.1)
6-5	-4.7	116.2	691.5	(1.1 ± 0.1)	(1.2 ± 0.1)	(1.9 ± 0.1)	(0.9 ± 0.1)	(2.2 ± 0.1)	(1.3 ± 0.1)
7-6	-4.5	154.9	806.7	(1.3 ± 0.1)	(1.2 ± 0.1)	(2.4 ± 0.1)	(1.3 ± 0.1)	(1.8 ± 0.1)	(1.3 ± 0.1)
8-7	-4.3	199.1	921.8	(1.2 ± 0.1)	(1.2 ± 0.1)	(2.6 ± 0.1)	(1.4 ± 0.1)	(1.7 ± 0.1)	(1.2 ± 0.1)
9-8	-4.1	248.9	1036.9	(1.2 ± 0.1)	(1.5 ± 0.1)	(2.8 ± 0.1)	(1.2 ± 0.1)	(1.9 ± 0.1)	(1.6 ± 0.1)
10-9	-4.0	304.2	1152.0	-	(6.7 ± 0.1)†	(4.3 ± 0.1)†	-	(13 ± 1) †	(5.5 ± 0.1)
11-10	-3.9	365.0	1267.0	(1.9 ± 0.1)	(1.6 ± 0.1)	(3.1 ± 0.1)	(1.2 ± 0.1)	(2.3 ± 0.1)	(1.7 ± 0.1)
12-11	-3.7	431.3	1382.0	-	(1.7 ± 0.1)	(3.0 ± 0.0)	(1.5 ± 0.1)	(2.3 ± 0.1)	-
13-12	-3.6	503.1	1497.0	-	(1.9 ± 0.1)	(3.3 ± 0.0)	(1.8 ± 0.1)	(3.0 ± 0.1)	(1.7 ± 0.1)
Line	log(A_{ul})	E_{up} (K)	Frequency (GHz)	Flux (10^{-16} W/m^2)	Flux (10^{-16} W/m^2)	Flux (10^{-17} W/m^2)	Flux (10^{-17} W/m^2)	Flux (10^{-17} W/m^2)	Flux (10^{-17} W/m^2)
				NML Cyg	OH 231.8+4.2	V1300 Aql	WX Psc	AFGL 5379	OH 26.5+0.6
4-3	-5.2	55.3	461.0	(1.2 ± 0.1)	(1.2 ± 0.1)	(4.7 ± 1.3)	(4.5 ± 0.6)	(4.4 ± 1.3)	(6.7 ± 1.3)
5-4	-4.9	83.0	576.3	(1.7 ± 0.1)	(0.9 ± 0.1)	(2.8 ± 0.5)	(3.6 ± 0.3)	(6.0 ± 0.2)	(5.1 ± 0.4)
6-5	-4.7	116.2	691.5	(2.4 ± 0.0)	(1.1 ± 0.0)	(3.3 ± 0.1)	(5.0 ± 0.2)	(8.1 ± 0.2)	(2.5 ± 0.2)
7-6	-4.5	154.9	806.7	(2.5 ± 0.0)	(1.2 ± 0.0)	(3.8 ± 0.1)	(4.3 ± 0.1)	(8.7 ± 0.2)	(8.1 ± 0.4) †
8-7	-4.3	199.1	921.8	(2.7 ± 0.0)	(0.9 ± 0.2)	-	(5.7 ± 0.1)	(9.5 ± 0.2)	(2.4 ± 0.5)
9-8	-4.1	248.9	1036.9	(3.0 ± 0.0)	(0.9 ± 0.2)	(5.1 ± 0.1)	(6.8 ± 0.1)	(15 ± 3)	(7.5 ± 0.3)
10-9	-4.0	304.2	1152.0	(12 ± 2) †	(4.6 ± 0.5) †	(1.2 ± 0.0) †	-	(88 ± 10)†	(48 ± 6) †
11-10	-3.9	365.0	1267.0	(3.8 ± 0.0)	(0.2 ± 0.1)	-	(5.8 ± 0.1)	(8.4 ± 0.1)	-
12-11	-3.7	431.3	1382.0	(4.4 ± 0.0)	(1.3 ± 0.0) †	(7.1 ± 0.1)	(7.5 ± 0.1)	(31 ± 6)	(34 ± 7)
13-12	-3.6	503.1	1497.0	(4.6 ± 0.0)	-	(5.8 ± 0.1)	(9.5 ± 0.0)	-	(30 ± 7)

TABLE B.5A: Integrated fluxes of ^{12}CO lines for the 20 O-rich sources studied in Chapter 6. Continued. Column 1: Quantum numbers of the transition; Column 2: Frequency corresponding to the emission lines in microns; Columns 3 to 10: Integrated fluxes of the emission lines in $W\,m^{-2}$.

Line	Frequency (GHz)	Flux (10^{-16} W/m^2)	Flux (10^{-17} W/m^2)	Flux (10^{-16} W/m^2)	Flux (10^{-17} W/m^2)	Flux (10^{-16} W/m^2)	Flux (10^{-16} W/m^2)	Flux (10^{-16} W/m^2)	Flux (10^{-16} W/m^2)
		IRAS 16342	M1-92	IRAS 22036+5306	HD 161796	NGC 6720	NGC 2440	NGC 6537	NGC 6302
4-3	461.0	(0.5 ± 0.1)	(2.2 ± 0.6)†	(0.4 ± 0.1)	-	(1.5 ± 0.2)	(0.3 ± 0.1)	(0.4 ± 0.1)	(0.6 ± 0.2)
5-4	576.3	-	(4.7 ± 0.3)	(0.3 ± 0.1)	-	(1.7 ± 0.3)	(0.4 ± 0.1)	(0.6 ± 0.2)	(1.1 ± 0.3)
6-5	691.5	(0.4 ± 0.1)	(4.6 ± 0.8)	(0.4 ± 0.1)	(1.7 ± 0.4)	(3.1 ± 0.4)	(0.6 ± 0.2)	(1.1 ± 0.5)	(1.7 ± 0.5)
7-6	806.7	(0.7 ± 0.2)	(5.9 ± 0.6)	(0.6 ± 0.2)	(3.2 ± 0.6)	(6.0 ± 0.0)	(0.9 ± 0.3)	(1.8 ± 0.5)	(2.5 ± 0.6)
8-7	921.8	(0.8 ± 0.3)	(5.6 ± 0.5)	(0.7 ± 0.2)	(1.9 ± 0.5)	(5.0 ± 0.6)	(1.1 ± 0.4)	(1.6 ± 0.3)	(3.4 ± 0.5)
9-8	1036.9	(1.2 ± 0.4)	(5.6 ± 0.6)	(1.3 ± 0.4)	(4.4 ± 0.7)	(1.7 ± 0.4)	(1.7 ± 0.4)	(3.3 ± 0.6)	(5.3 ± 0.8)
10-9	1152.0	(3.1 ± 0.6) †	(7.8 ± 1.0)†	(2.0 ± 0.4)†	-	(1.5 ± 0.3)	(1.8 ± 0.5)	(4.2 ± 0.7)	(7.1 ± 1.5)
11-10	1267.0	(1.7 ± 0.5)	(7.1 ± 0.8)	(1.6 ± 0.5)	(2.4 ± 0.4)	(2.7 ± 0.5)	(1.8 ± 0.6)	(4.3 ± 0.6)	(8.5 ± 1.8)
12-11	1382.0	(2.5 ± 0.6)	(9.0 ± 1.2)	(2.0 ± 0.3)	(0.6 ± 0.2)	-	(1.8 ± 0.5)	(5.2 ± 0.8)	(10 ± 2.7)
13-12	1497.0	(2.6 ± 0.6)	(8.5 ± 1.5)	(1.5 ± 0.4)	(1.1 ± 0.2)†	-	(1.6 ± 0.5)	(5.9 ± 0.9)	(12 ± 4.1)

TABLE B.6: Integrated fluxes of ^{12}CO lines for the 14 C-rich sources studied in Chapter 6. Column 1: Quantum numbers of the transition; Column 2: Frequency corresponding to the emission lines in microns; Columns 3 to 10: Integrated fluxes of the emission lines in $W\,m^{-2}$. †, symbol indicates blended lines.

Line	Frequency (GHz)	Flux (10^{-16} W/m^2)	Flux (10^{-16} W/m^2)	Flux (10^{-17} W/m^2)	Flux (10^{-16} W/m^2)	Flux (10^{-15} W/m^2)	Flux (10^{-16} W/m^2)	Flux (10^{-16} W/m^2)
		AFGL 3068	IRC +40540	R Scl	CIT 6	CW Leo	IRAS 15194-5115	SAO 163075
4-3	461.0	(1.1 ± 0.3)	-	(5.8 ± 0.5)	(2.0 ± 0.5)	(1.3 ± 0.4)	(1.0 ± 0.3)	-
5-4	576.3	(0.9 ± 0.3)	(1.1 ± 0.3)	(4.8 ± 0.6)	(2.5 ± 0.5)	(1.9 ± 0.4)	(1.6 ± 0.5)	(0.4 ± 0.1)
6-5	691.5	(0.9 ± 0.3)	(1.1 ± 0.4)	(3.6 ± 0.2)	(3.6 ± 0.7)	(3.0 ± 0.7)	(2.3 ± 0.9)†	(0.6 ± 0.2)
7-6	806.7	(1.0 ± 0.3)	(1.2 ± 0.4)	(4.7 ± 0.3)†	(4.8 ± 0.8)	(3.4 ± 0.7)	(2.1 ± 0.6)	(0.9 ± 0.3)
8-7	921.8	(1.3 ± 0.4)	(1.4 ± 0.3)	-	(5.1 ± 0.4)	(4.6 ± 0.9)	(2.2 ± 0.7)	(1.4 ± 0.4)
9-8	1036.9	(1.3 ± 0.4)	(1.7 ± 0.5)	(3.2 ± 0.2)	(6.2 ± 0.9)	-	(3.5 ± 0.9)	(1.6 ± 0.5)
10-9	1152.0	(2.1 ± 0.6)	(3.0 ± 0.8)†	(5.3 ± 0.2)†	(9.6 ± 1.5)†	(8.7 ± 2.0)†	(5.4 ± 2.3)†	(1.8 ± 0.7)
11-10	1267.0	(1.2 ± 0.3)	(1.9 ± 0.6)	(2.5 ± 0.1)	(6.7 ± 1.1)	(5.6 ± 0.7)	(3.5 ± 0.9)	(1.9 ± 0.5)
12-11	1382.0	(1.5 ± 0.4)	(2.3 ± 0.6)	(2.3 ± 0.1)	(7.2 ± 1.2)	(6.9 ± 0.8)	(4.7 ± 1.6)	(1.8 ± 0.6)
13-12	1497.0	(1.4 ± 0.4)	(2.3 ± 0.7)	(3.8 ± 0.1)	(7.1 ± 1.0)	(6.8 ± 0.9)	(4.1 ± 1.2)	(1.9 ± 0.7)
Line	Frequency (GHz)	Flux (10^{-15} W/m^2)	Flux (10^{-16} W/m^2)	Flux (10^{-15} W/m^2)	Flux (10^{-17} W/m^2)	Flux (10^{-17} W/m^2)	Flux (10^{-18} W/m^2)	Flux (10^{-15} W/m^2)
		AFGL 2688	V Hya	AFGL 618	Red Rectangle	HD 56126	IRAS 19411-1416	NGC 7027
4-3	461.0	(0.3 ± 0.1)	(0.9 ± 0.4)	(0.2 ± 0.1)	-	(2.7 ± 0.8)	(37 ± 16)†	(0.6 ± 0.2)
5-4	576.3	(0.6 ± 0.2)	(1.5 ± 0.5)	(0.3 ± 0.1)	(2.6 ± 0.5)	(4.0 ± 1.2)	(17 ± 4)	(1.0 ± 0.4)
6-5	691.5	(0.9 ± 0.3)	(1.8 ± 0.6)	(0.5 ± 0.2)	(1.8 ± 0.7)	(4.6 ± 1.6)	(4.8 ± 0.6)	(1.3 ± 0.4)
7-6	806.7	(1.4 ± 0.5)	(3.1 ± 1.1)†	(0.8 ± 0.3)	-	(5.6 ± 1.8)	-	(1.8 ± 0.7)
8-7	921.8	(2.1 ± 0.6)	(2.4 ± 0.9)	(1.2 ± 0.4)	(2.1 ± 0.6)	(7.5 ± 2.4)	(30 ± 9)†	(2.2 ± 0.8)
9-8	1036.9	-	(2.7 ± 0.9)	(1.5 ± 0.6)	-	(5.9 ± 1.9)	(8.0 ± 1.7)	(2.6 ± 0.7)
10-9	1152.0	(4.0 ± 1.1)†	(4.3 ± 1.1)	(2.9 ± 1.3)†	(3.9 ± 1.2)	(5.9 ± 1.8)	(8.4 ± 2.1)	(3.0 ± 0.8)
11-10	1267.0	(3.8 ± 0.9)	(3.3 ± 1.2)	(2.7 ± 0.8)	(4.1 ± 1.5)	(3.8 ± 1.3)	(9.8 ± 3.5)	(3.1 ± 0.9)
12-11	1382.0	(4.4 ± 1.2)	(3.6 ± 1.2)	(3.2 ± 0.9)	-	(2.8 ± 0.9)	(4.7 ± 2.6)†	(3.2 ± 0.8)
13-12	1497.0	(4.6 ± 1.3)	(3.8 ± 1.2)	(3.7 ± 1.2)	(4.4 ± 1.3)	(1.3 ± 0.5)†	-	(3.1 ± 0.9)

Appendix C

Appendix III. Supplementary figures

C.1 THROES-PACS SEDs

In this section we present the PACS Spectroscopy data corresponding to each source contained in the THROES-PACS catalogue. When available, complementary IRAS, AKARI and ISO photometric and spectroscopic data are included.

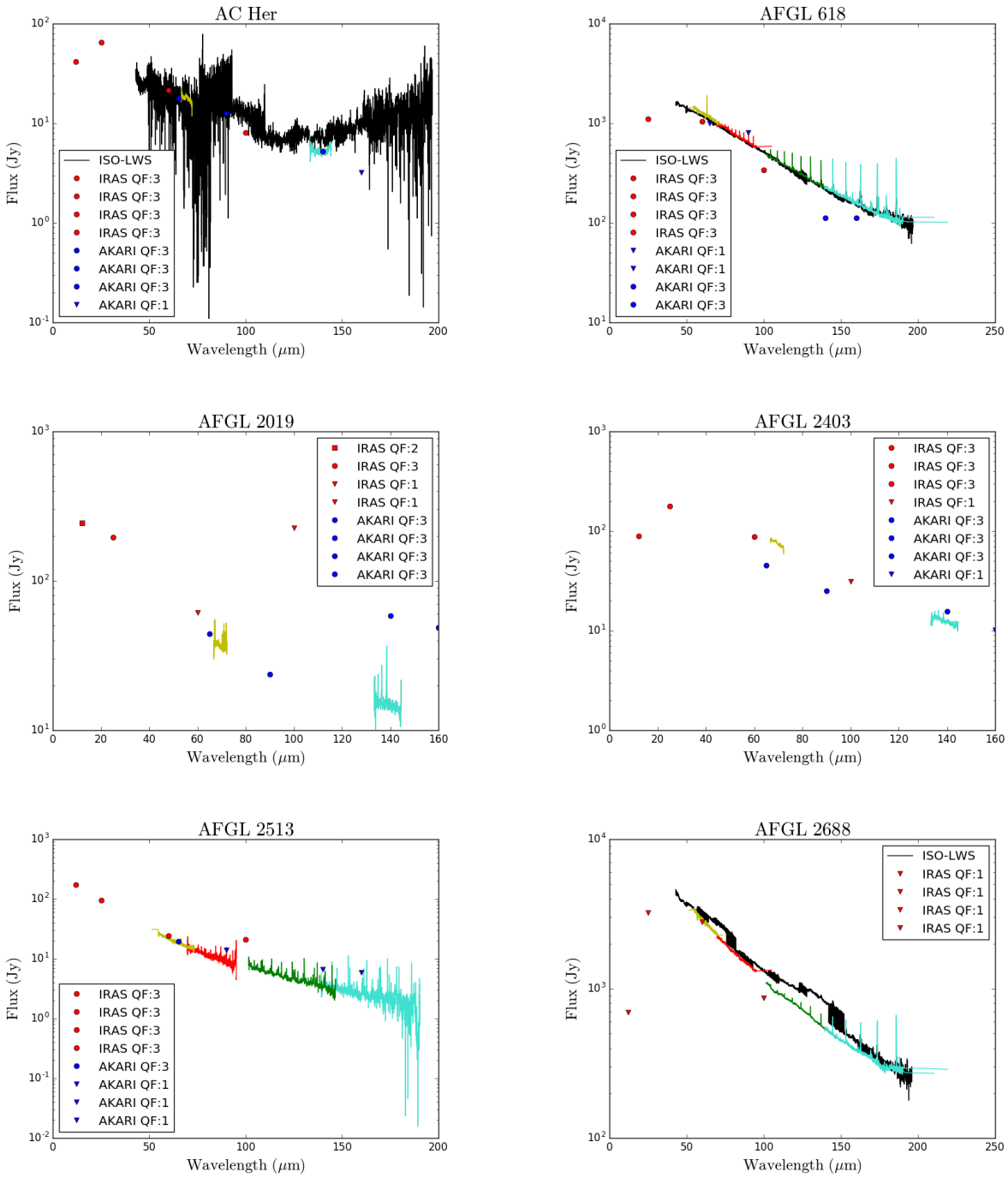

FIGURE C.1: PACS spectroscopy SED of well-pointed, non-extended sources, after applying PSFLC and semi-extended 3x3 correction (PSFLC-3x3). PACS data is colour-coded according to the spectral region covered by each subrange, as follows: ~50-70 μm (yellow), ~70-100 μm (red), ~100-145 μm (green), and ~145-200 μm (turquoise). IRAS (red points) and AKARI (blue points) photometric data and ISO (black) spectroscopic data are also displayed when available. We do not show those observations pointed to a specific region in the case of very extended sources such as rims or knots.

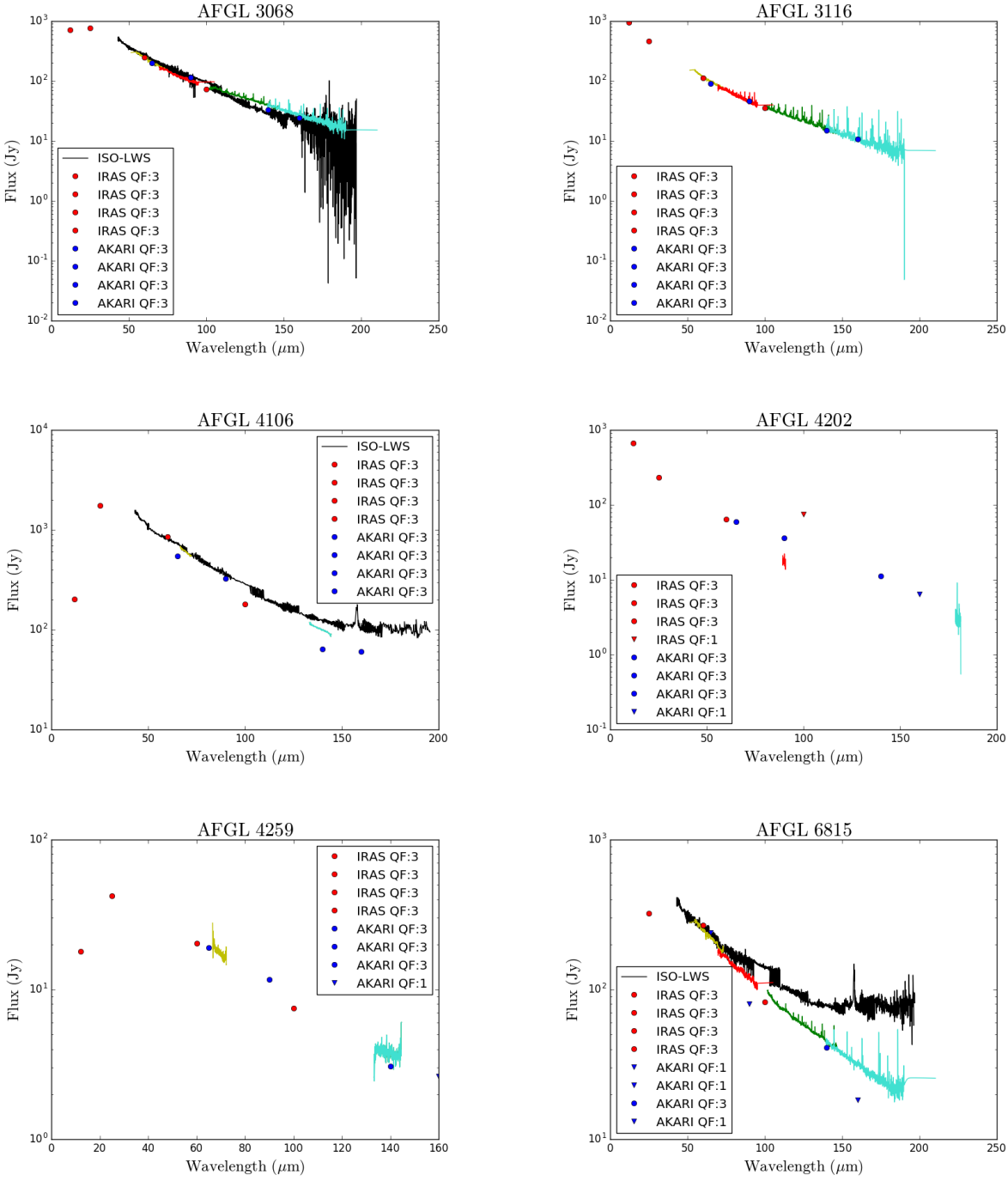

FIGURE C.1: Continued.

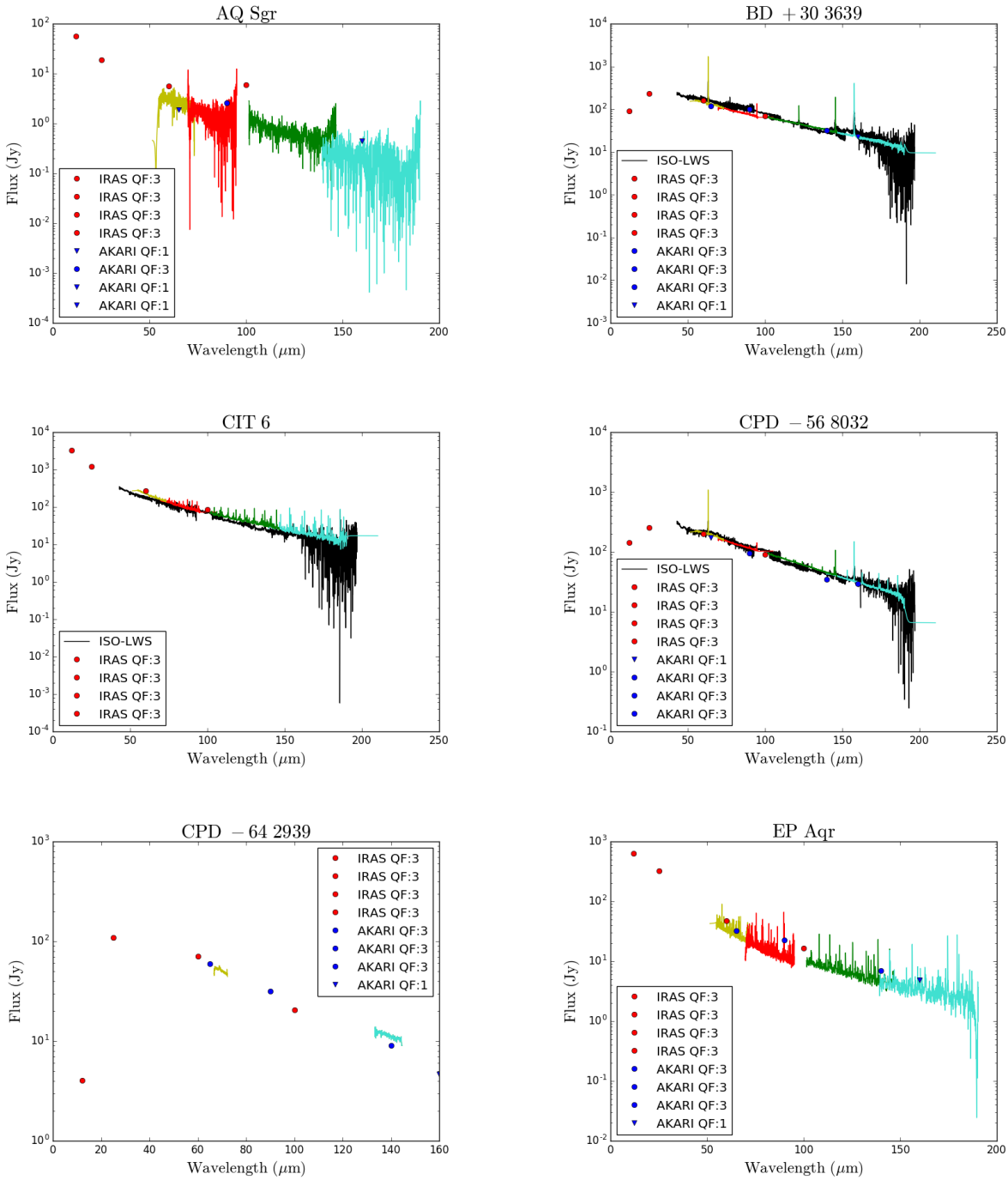

FIGURE C.1: Continued.

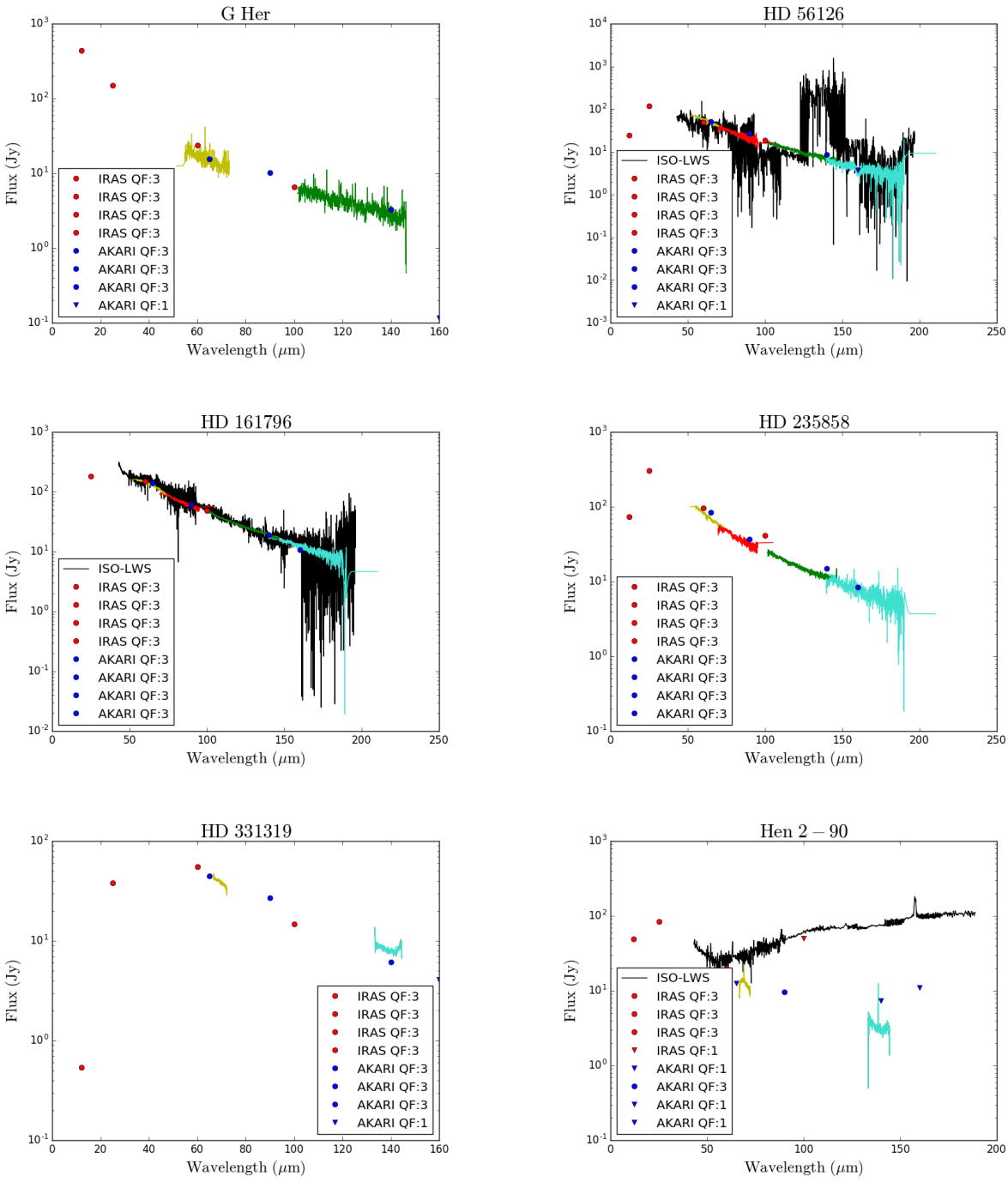

FIGURE C.1: Continued.

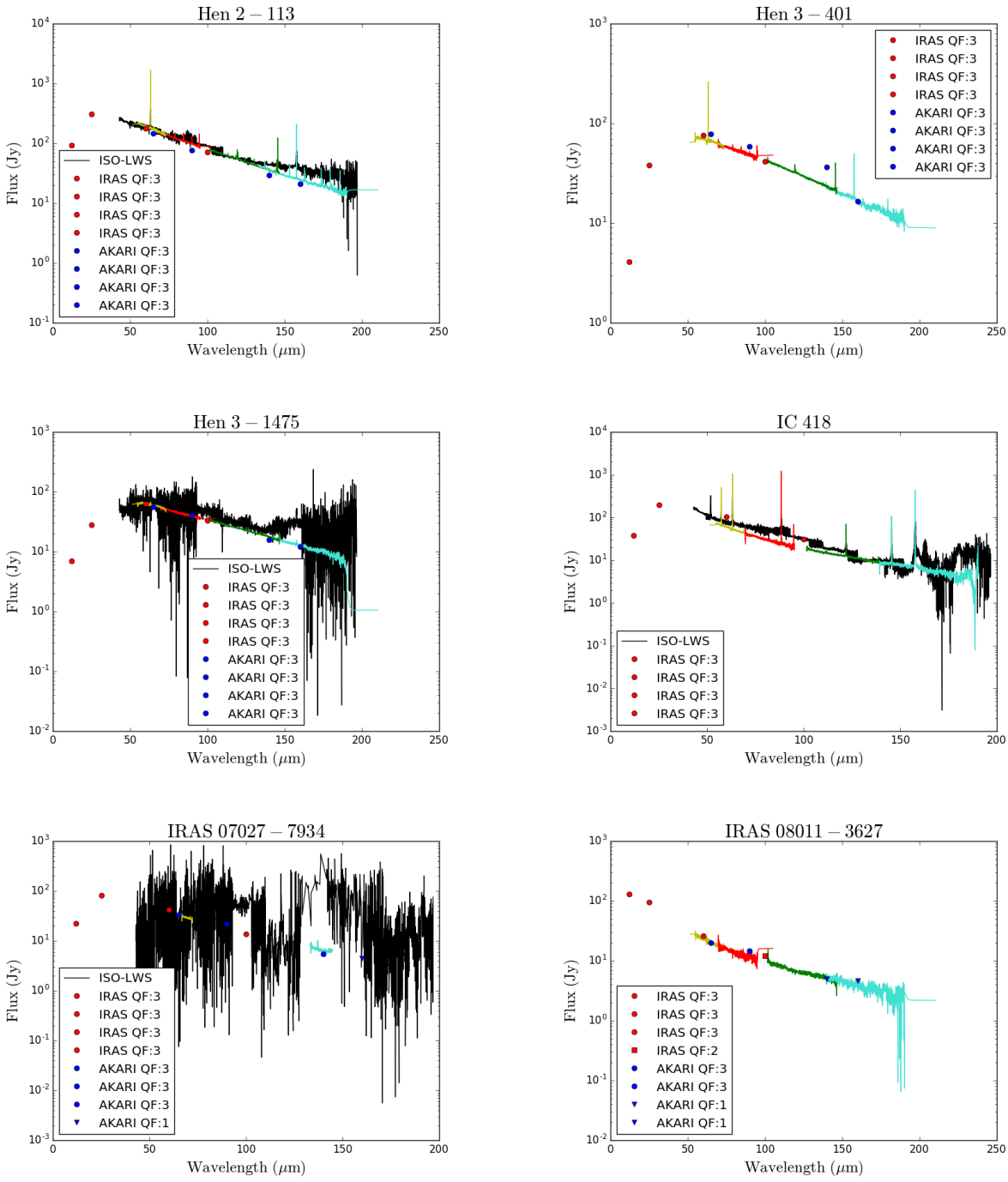

FIGURE C.1: Continued.

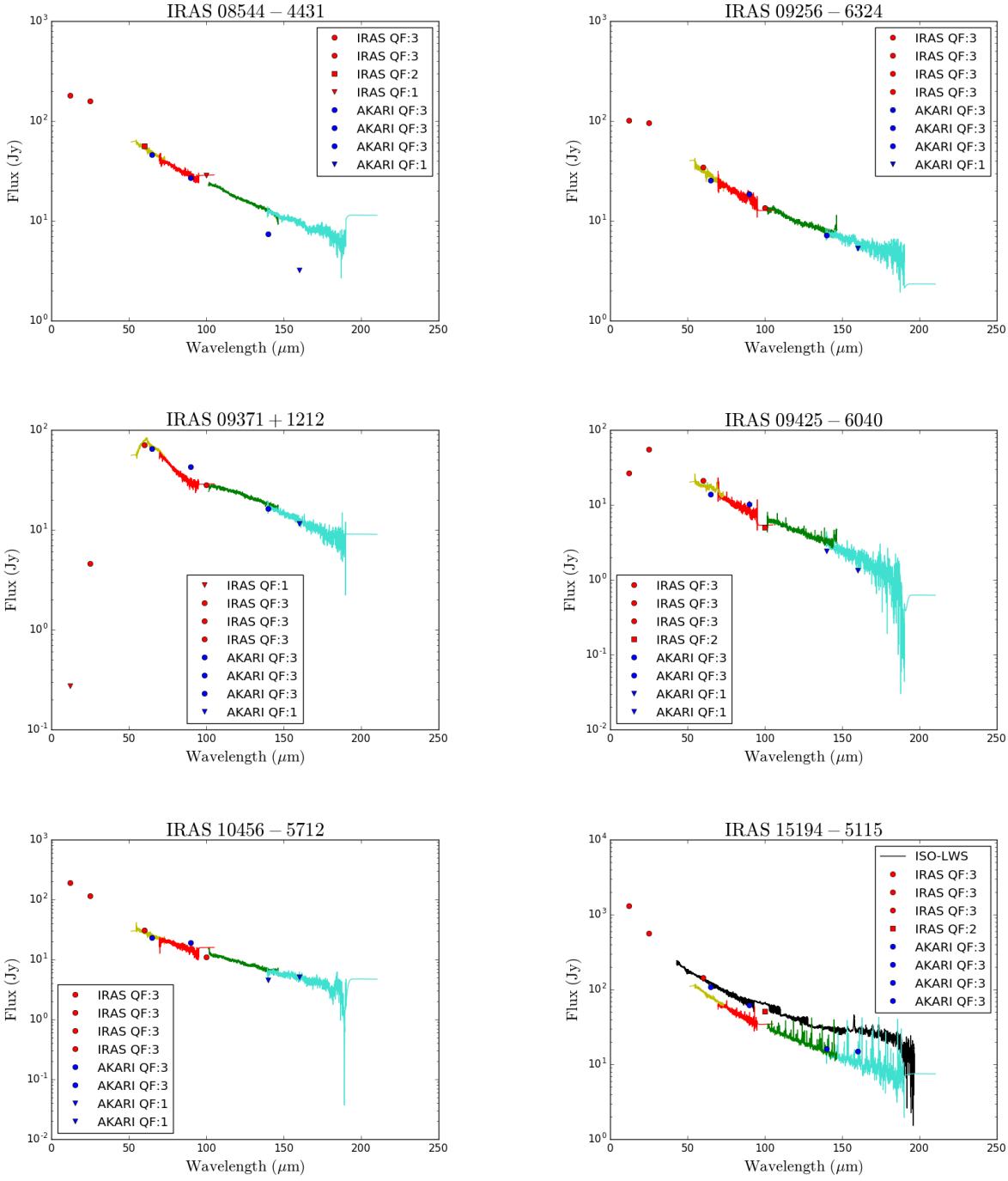

FIGURE C.1: Continued.

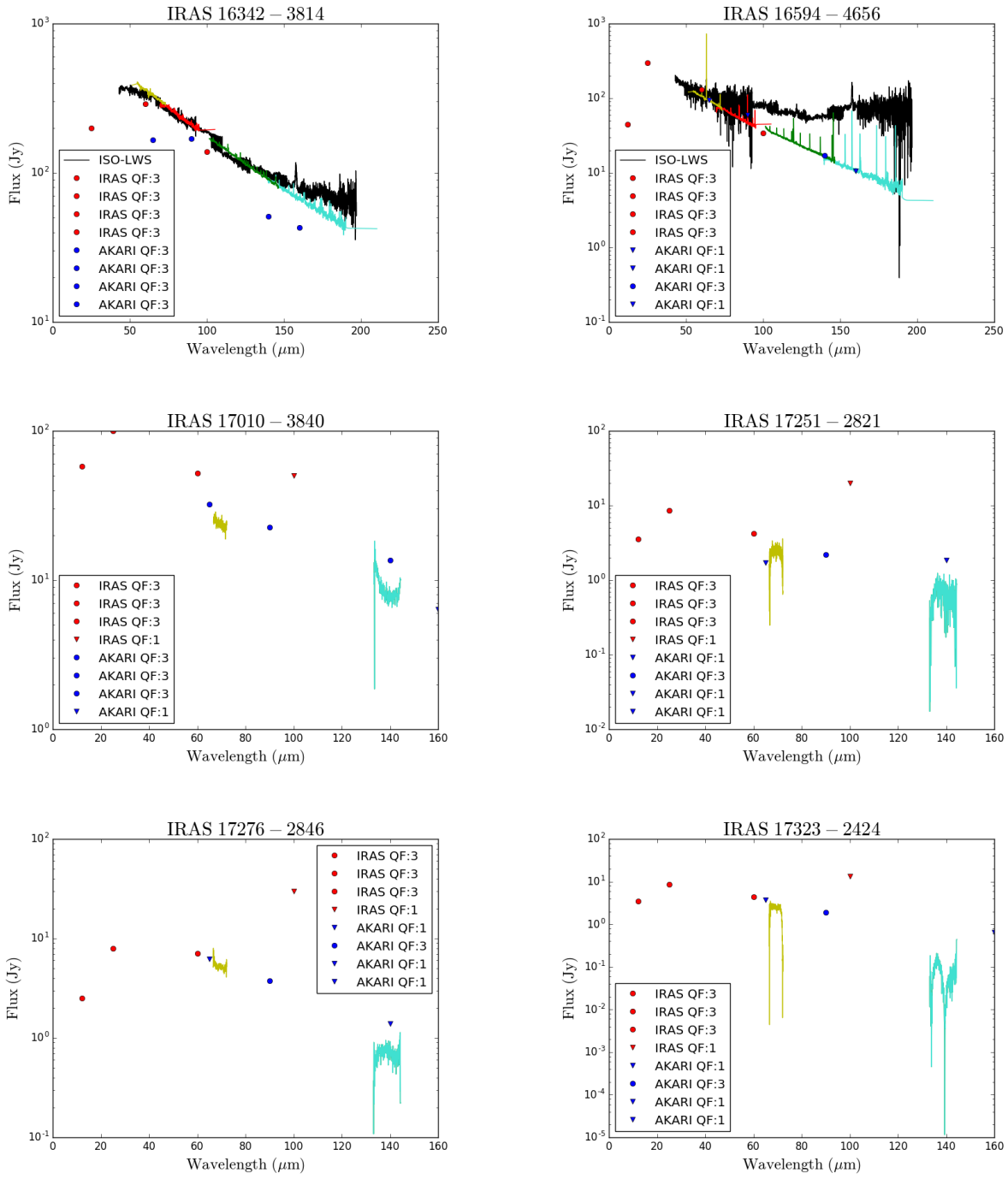

FIGURE C.1: Continued.

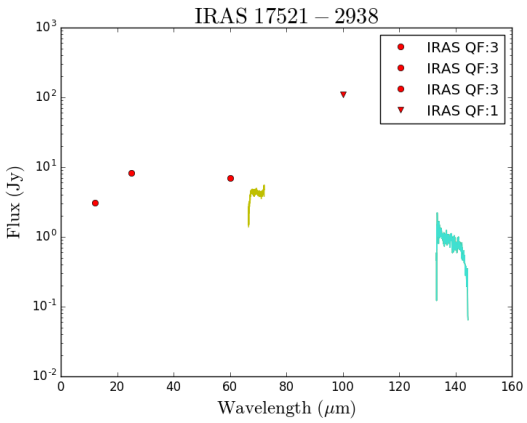

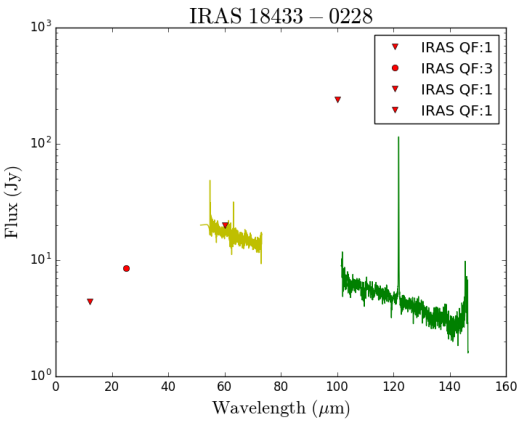

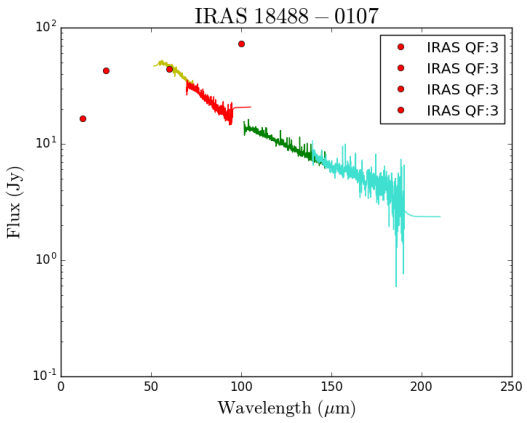

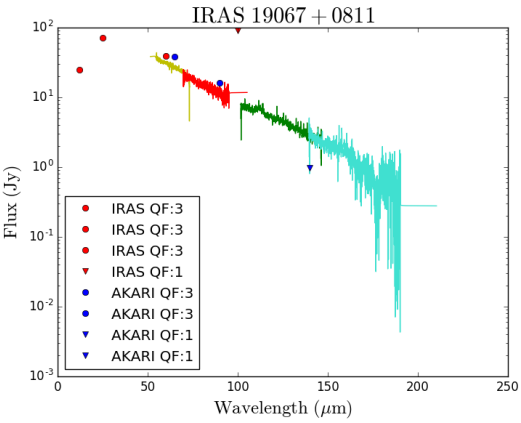

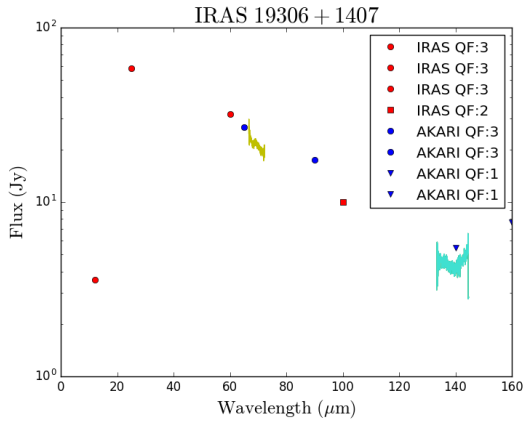

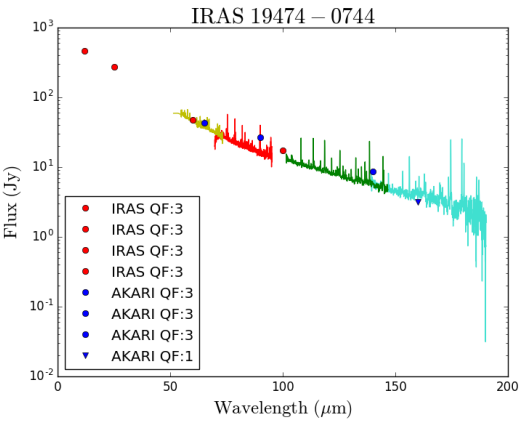

FIGURE C.1: Continued.

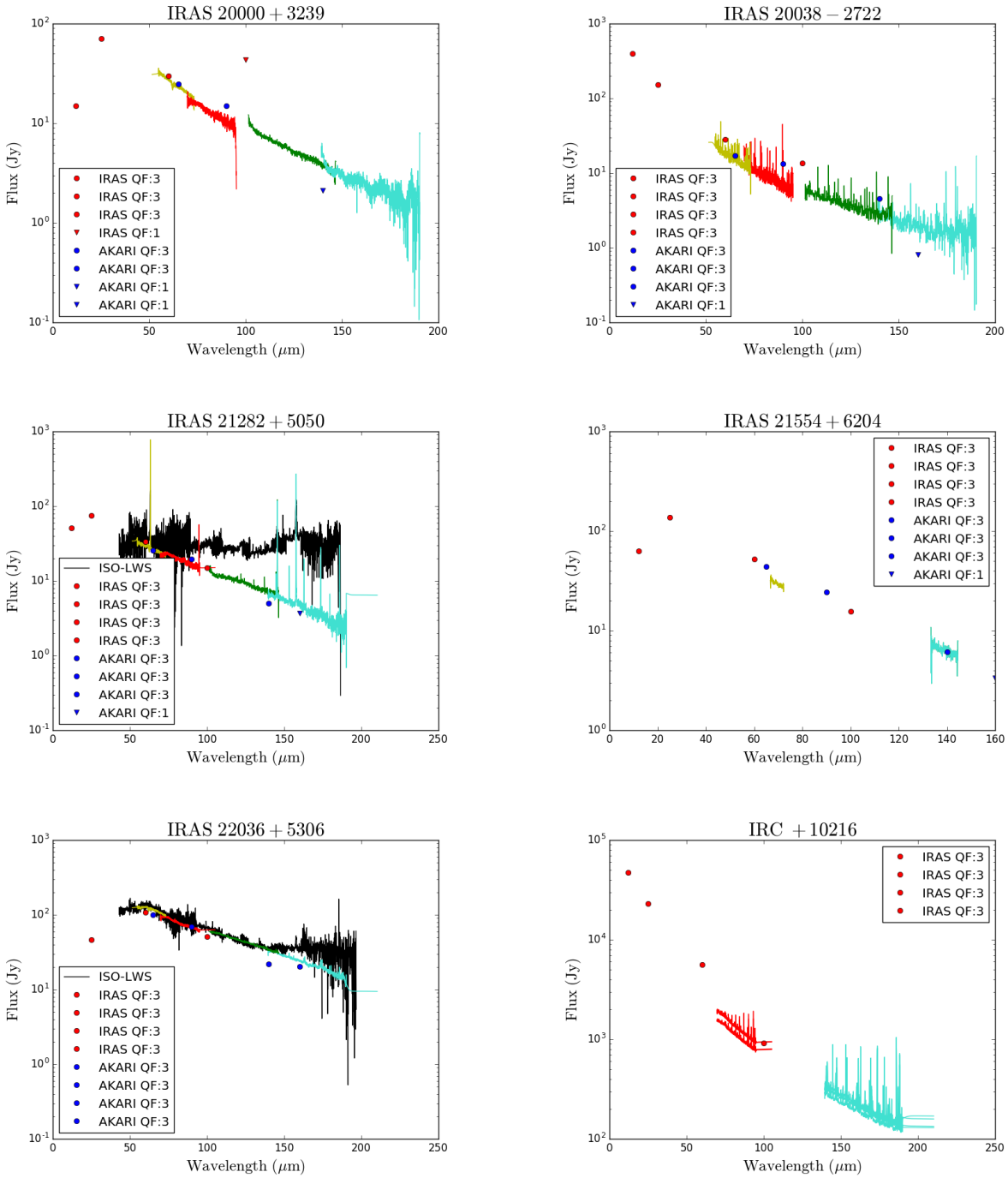

FIGURE C.1: Continued.

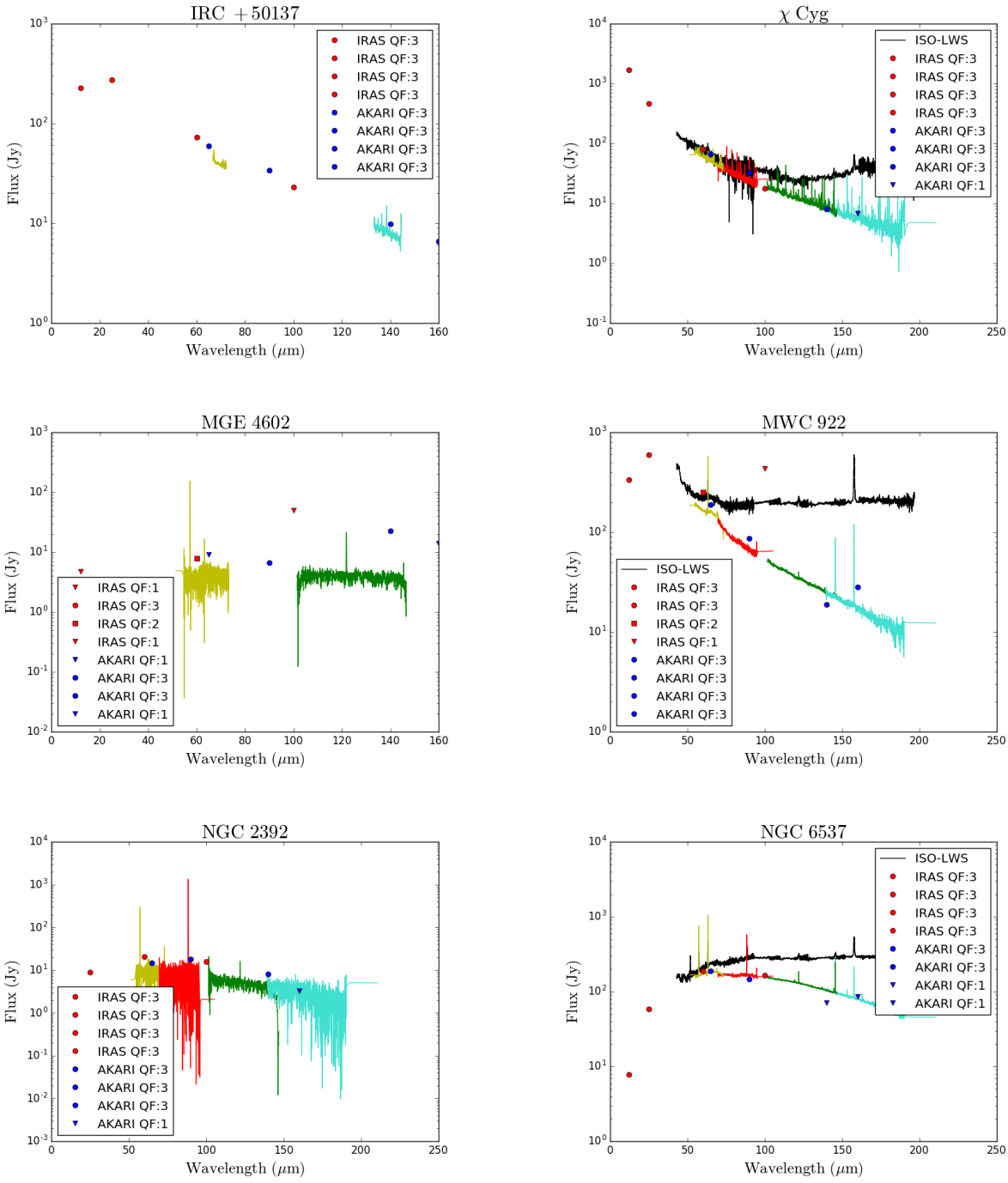

FIGURE C.1: Continued.

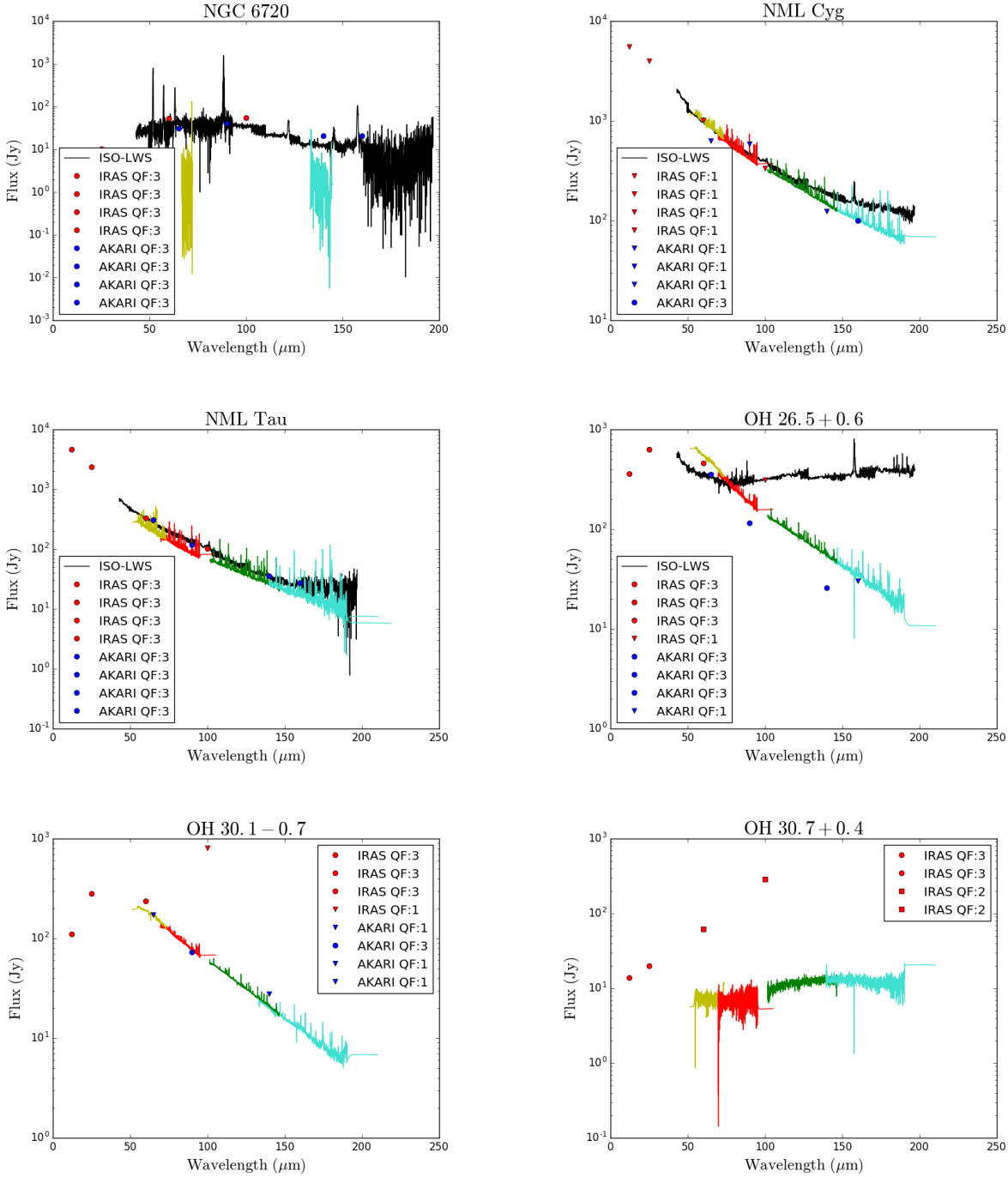

FIGURE C.1: Continued.

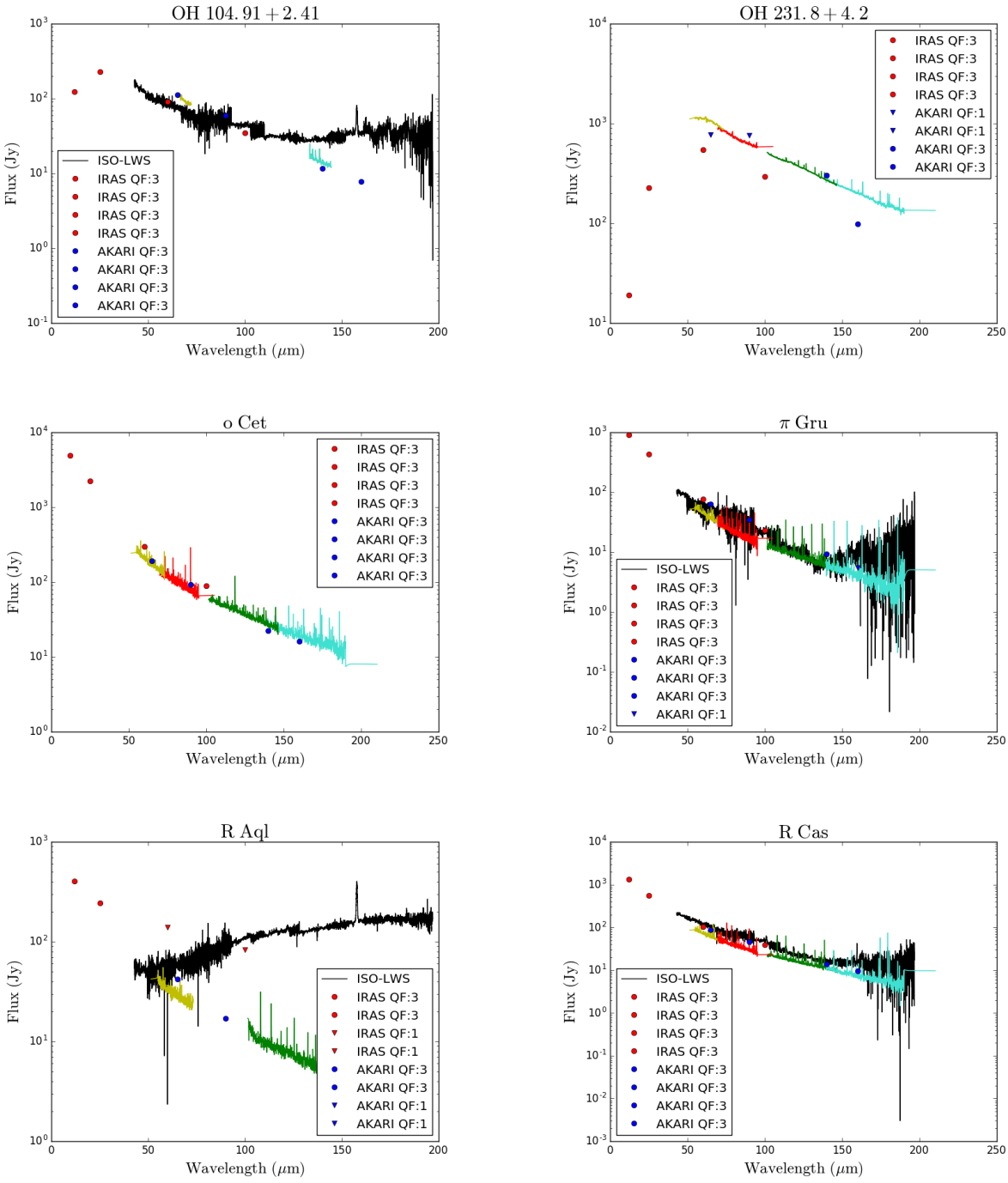

FIGURE C.1: Continued.

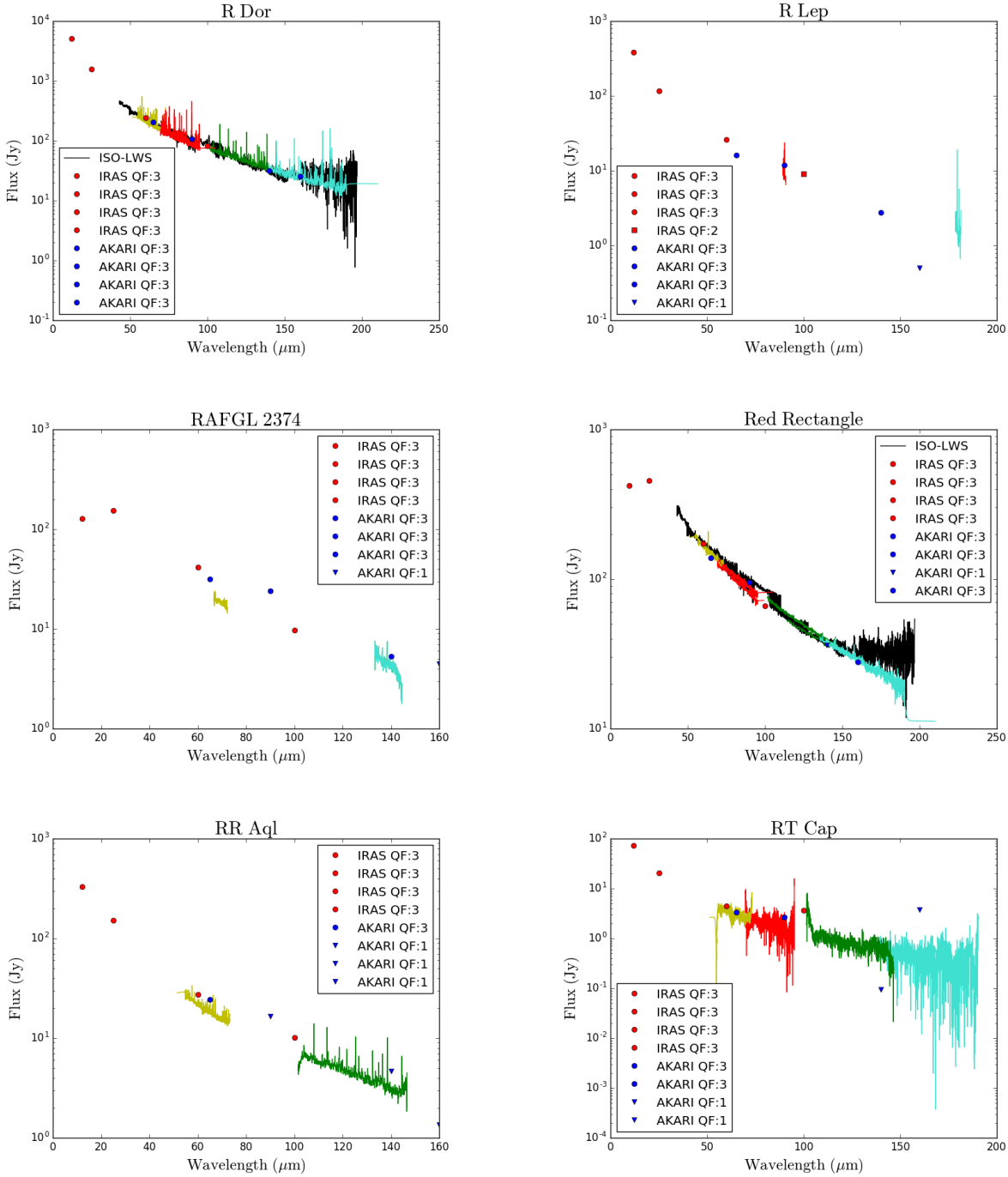

FIGURE C.1: Continued.

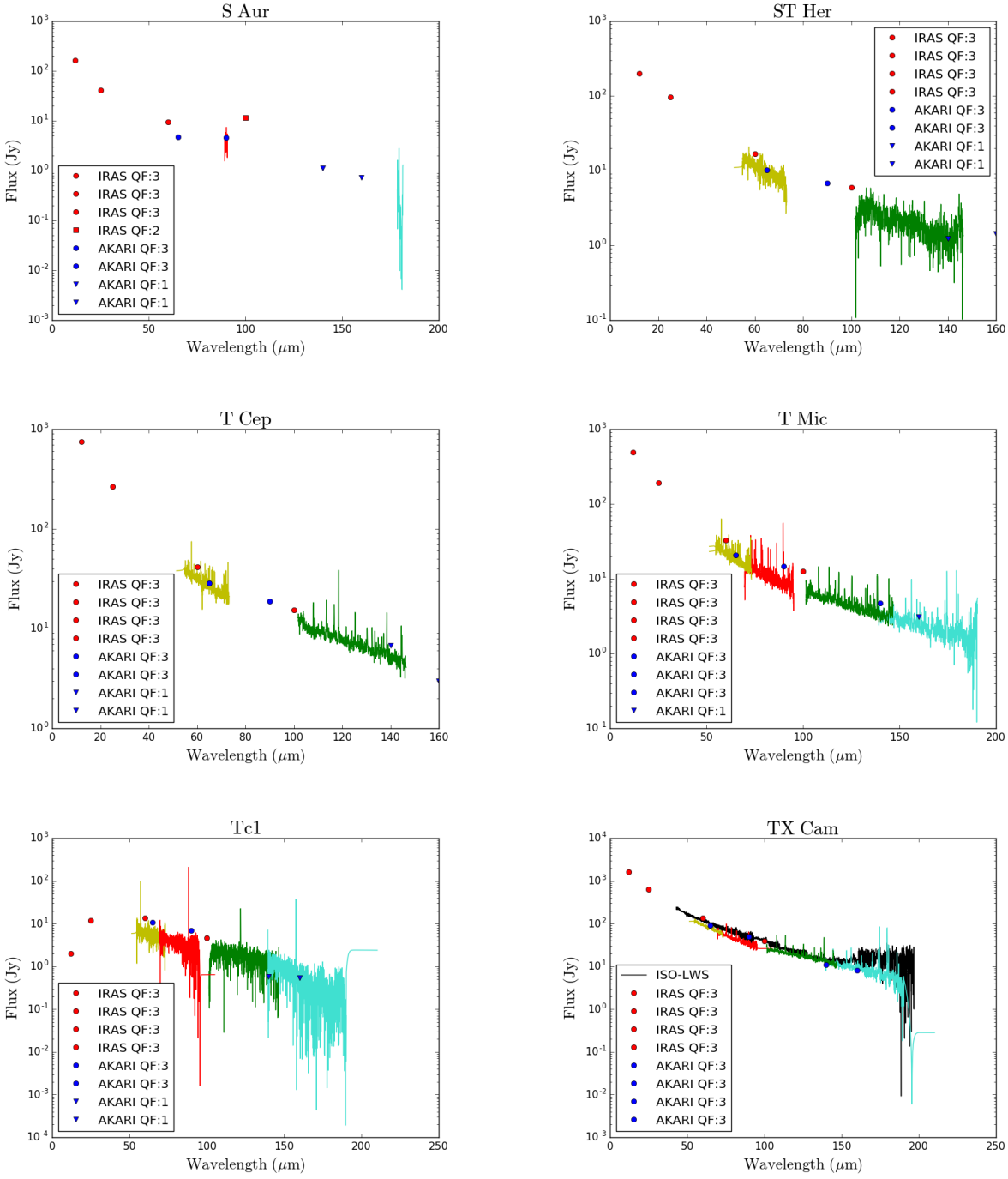

FIGURE C.1: Continued.

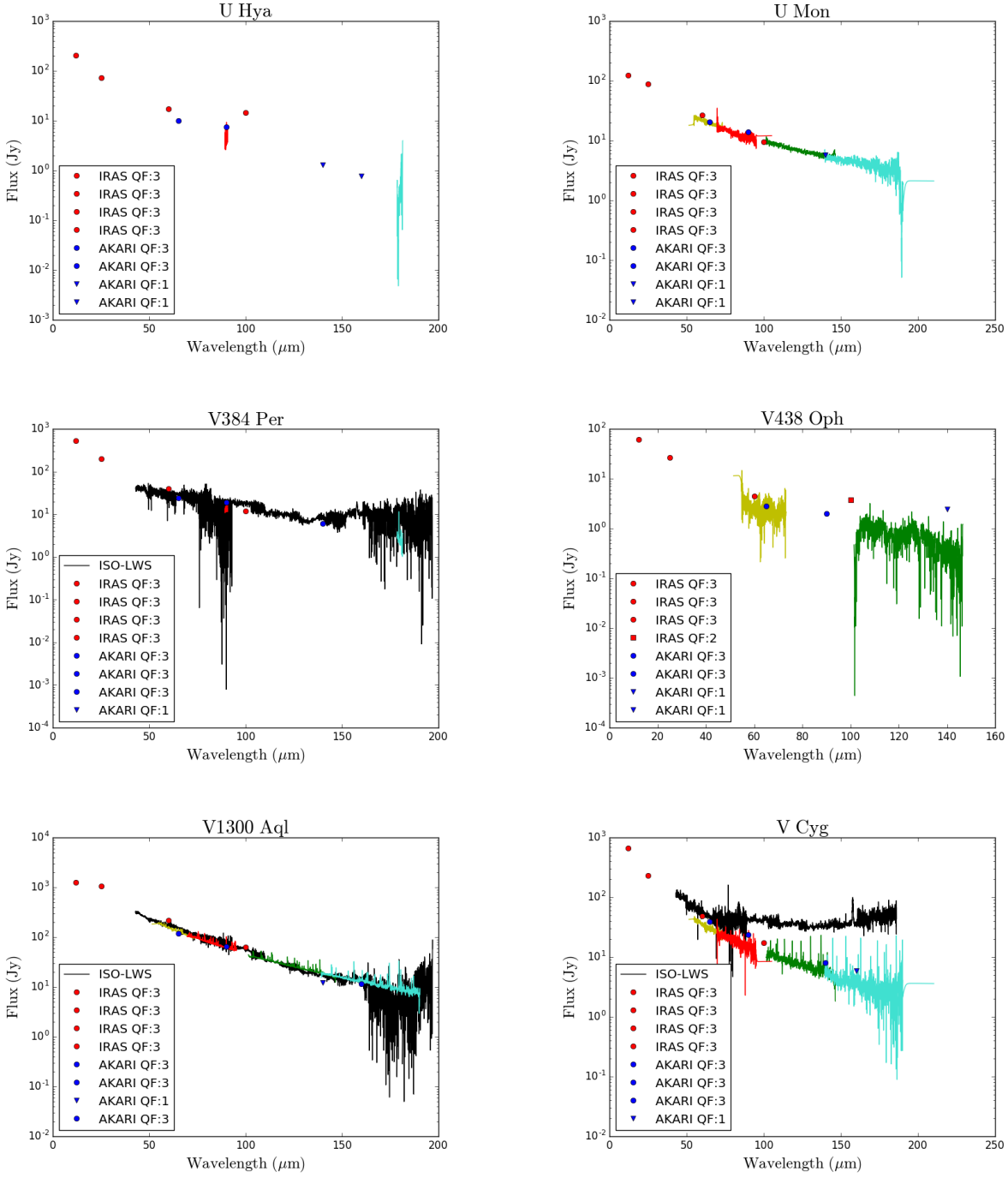

FIGURE C.1: Continued.

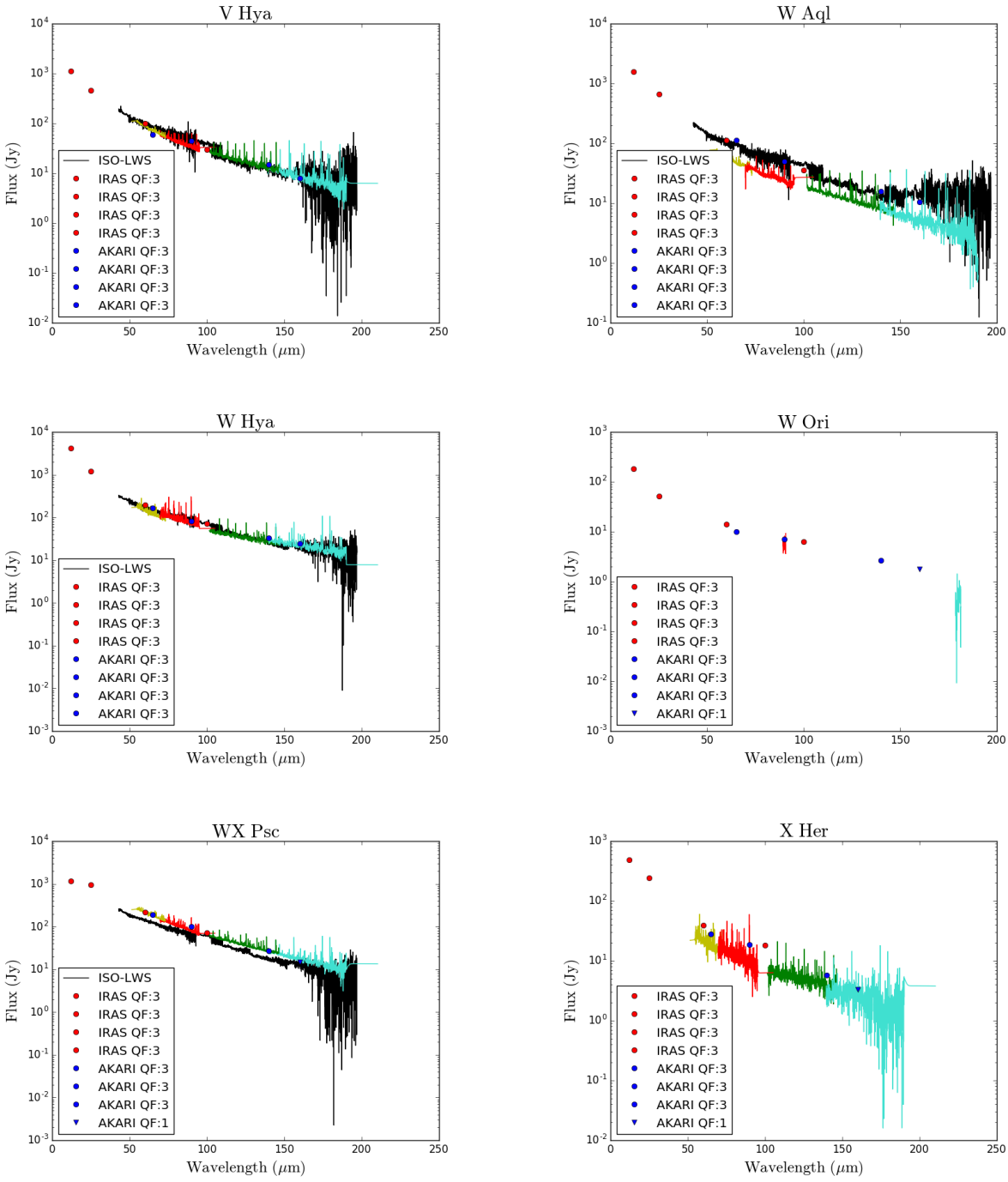

FIGURE C.1: Continued.

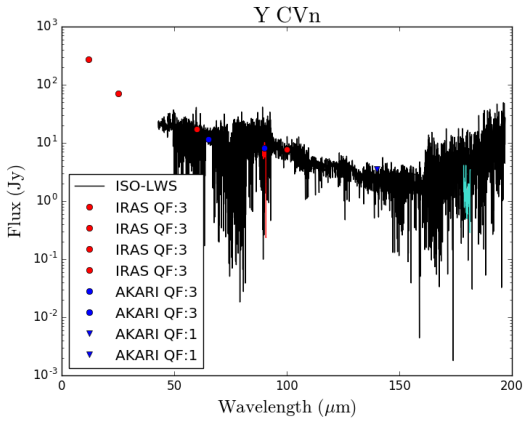

FIGURE C.1: Continued.

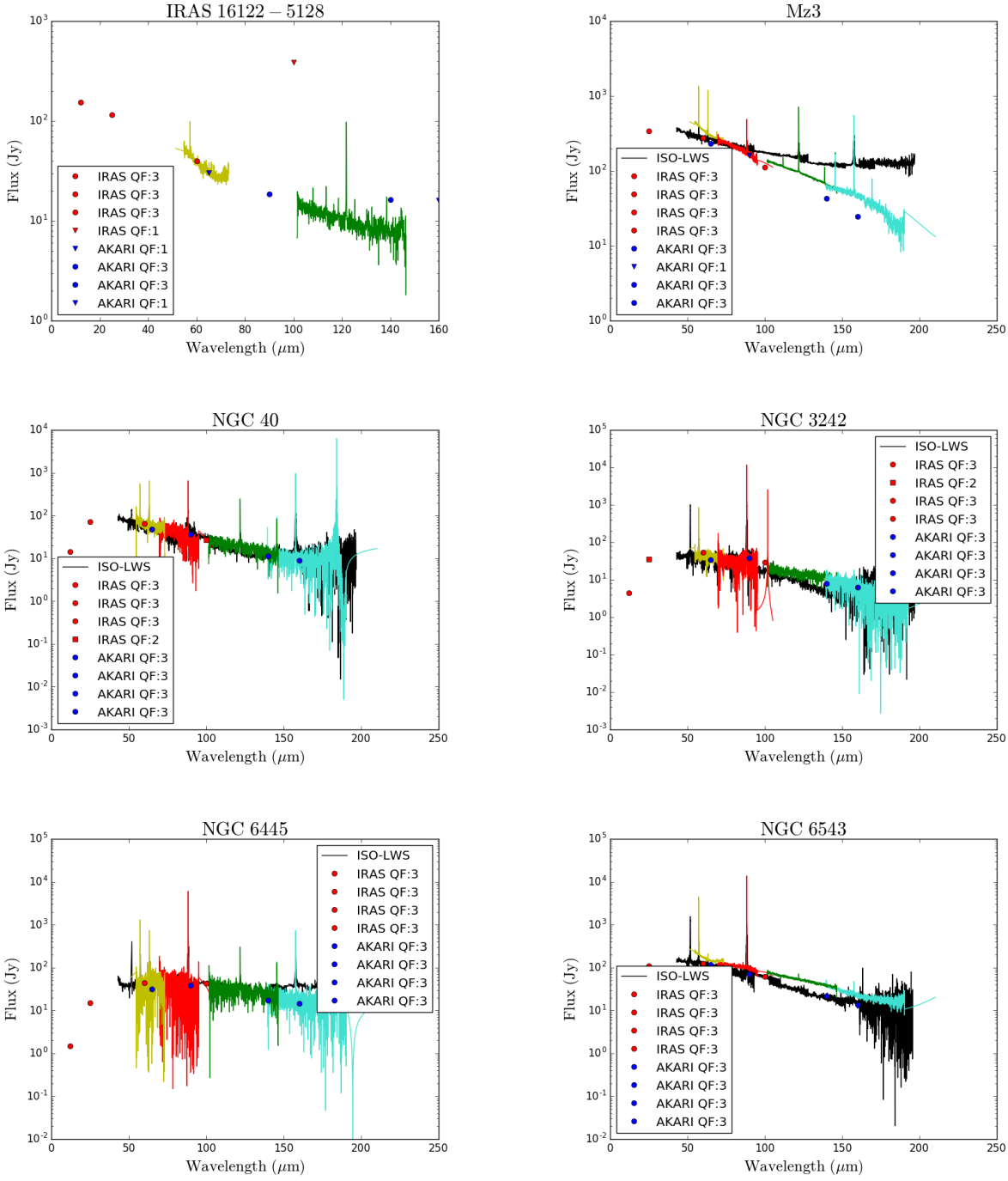

FIGURE C.2: As in Fig. C.1 but for extended objects after applying point source flux loss correction and extended 5x5 correction. IRAS 16122-5128 appears in THROES catalogue and in HSA as MGE 4218.

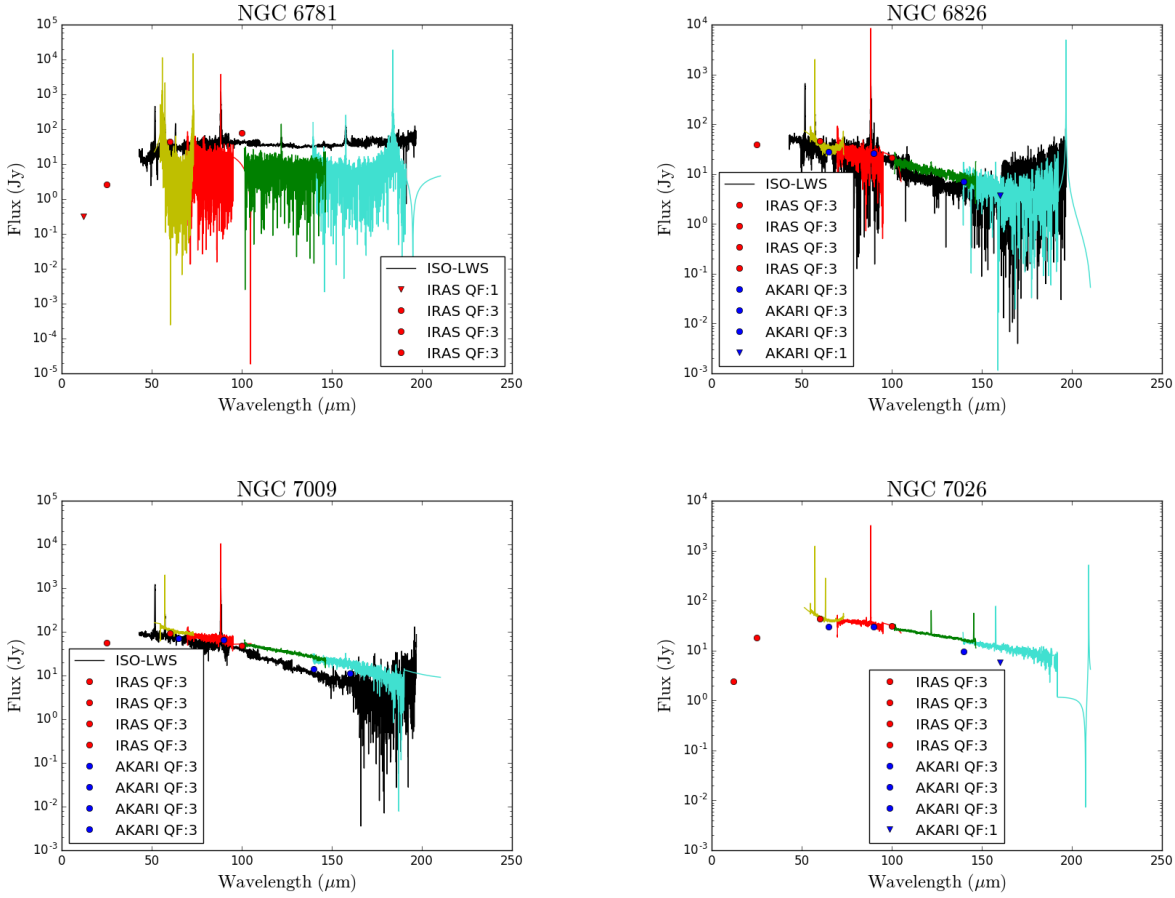

FIGURE C.2: Continued.

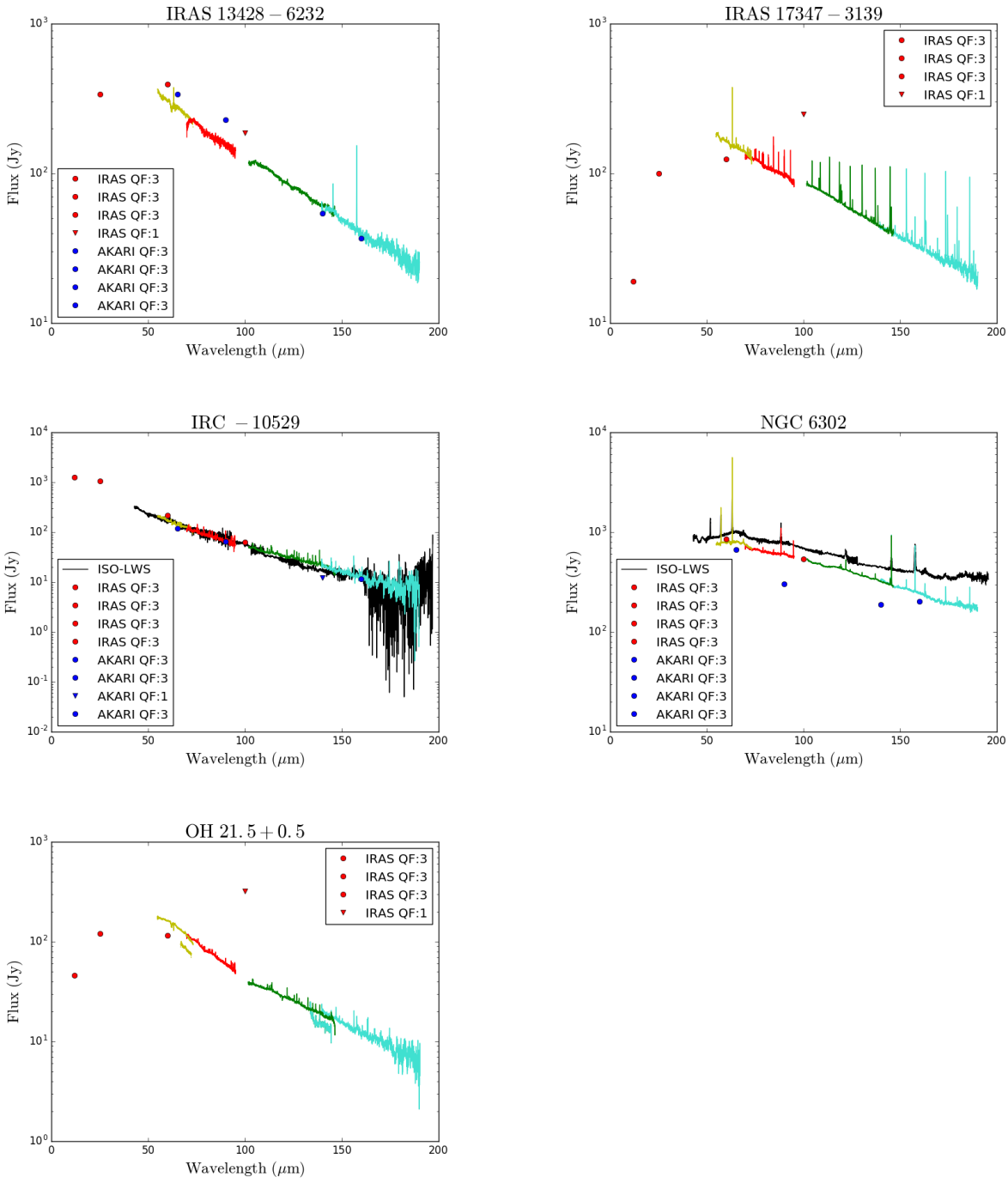

FIGURE C.3: As in Fig. C.1 but for mispointed sources after applying point sources correction and semi-extended 3x3 correction.

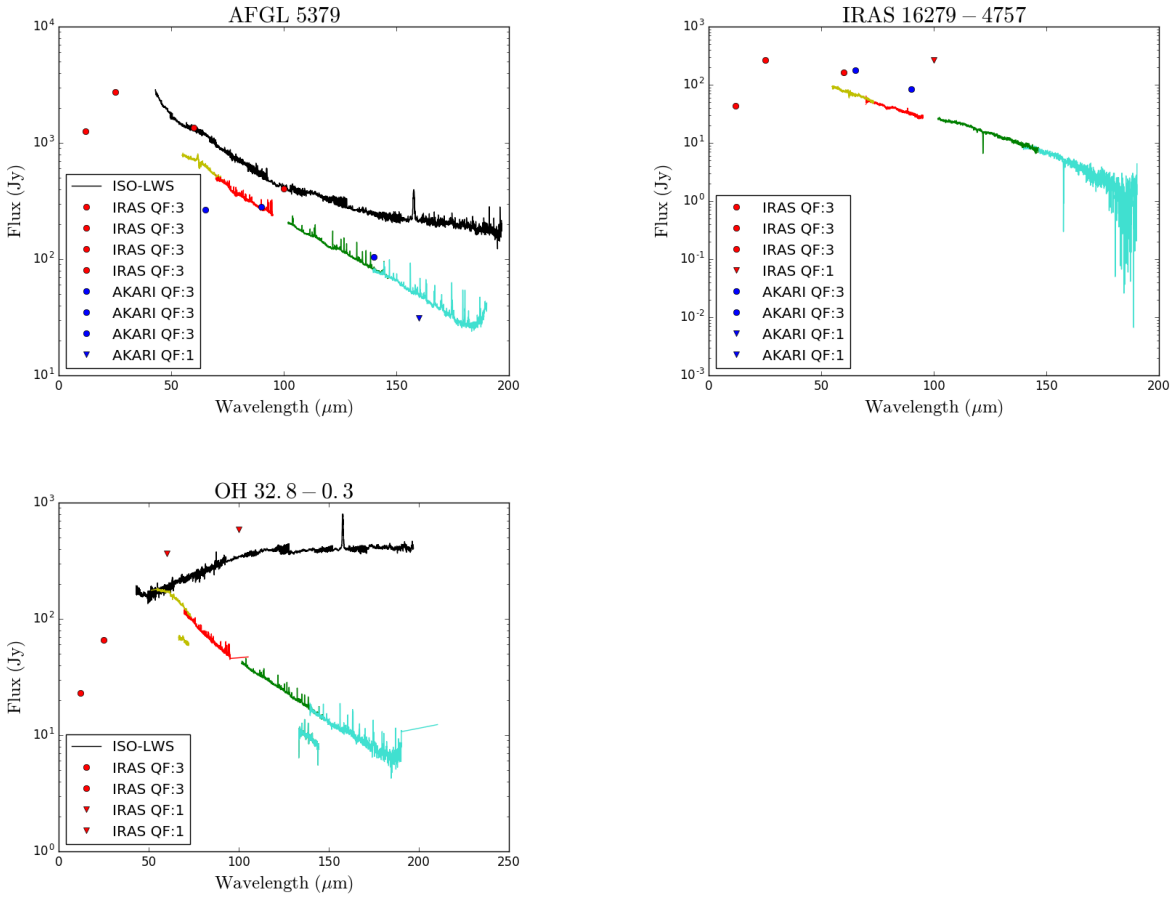

FIGURE C.4: As in Fig. C.1 but for those sources corrected only by point sources correction. AFGL 5379 and IRAS 16279-4757 are mispointed targets for which the semi-extended 3x3 correction could not be applied as they are located in one of the outermost spaxels. The well-pointed object OH 32.8-0.3 shows, for unknown reasons probably related to problems during the observations, negative fluxes in some of the 3x3 central spaxels, so the semi-extended 3x3 correction produced a wrong final 1D spectrum.

C.2 THROES-SPIRE SEDs

In this section, the un-apodized SPIRE spectroscopic data corresponding to each object contained in the THROES-SPIRE catalogue is shown.

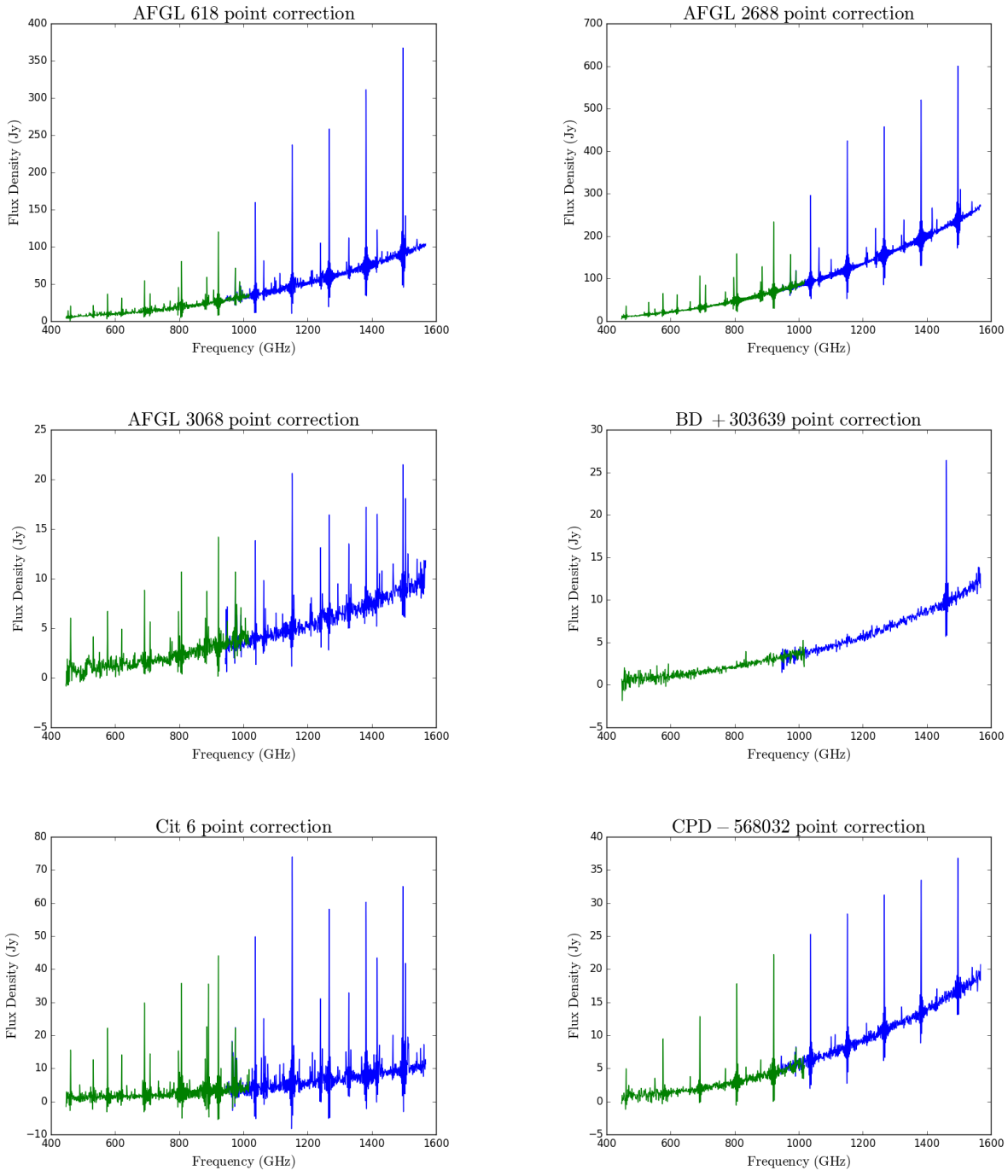

FIGURE C.5: SPIRE Spectrometer SED of those sources with 'Point Correction' applied. Both sub-ranges, SSW and SLW, blue and green respectively, are shown.

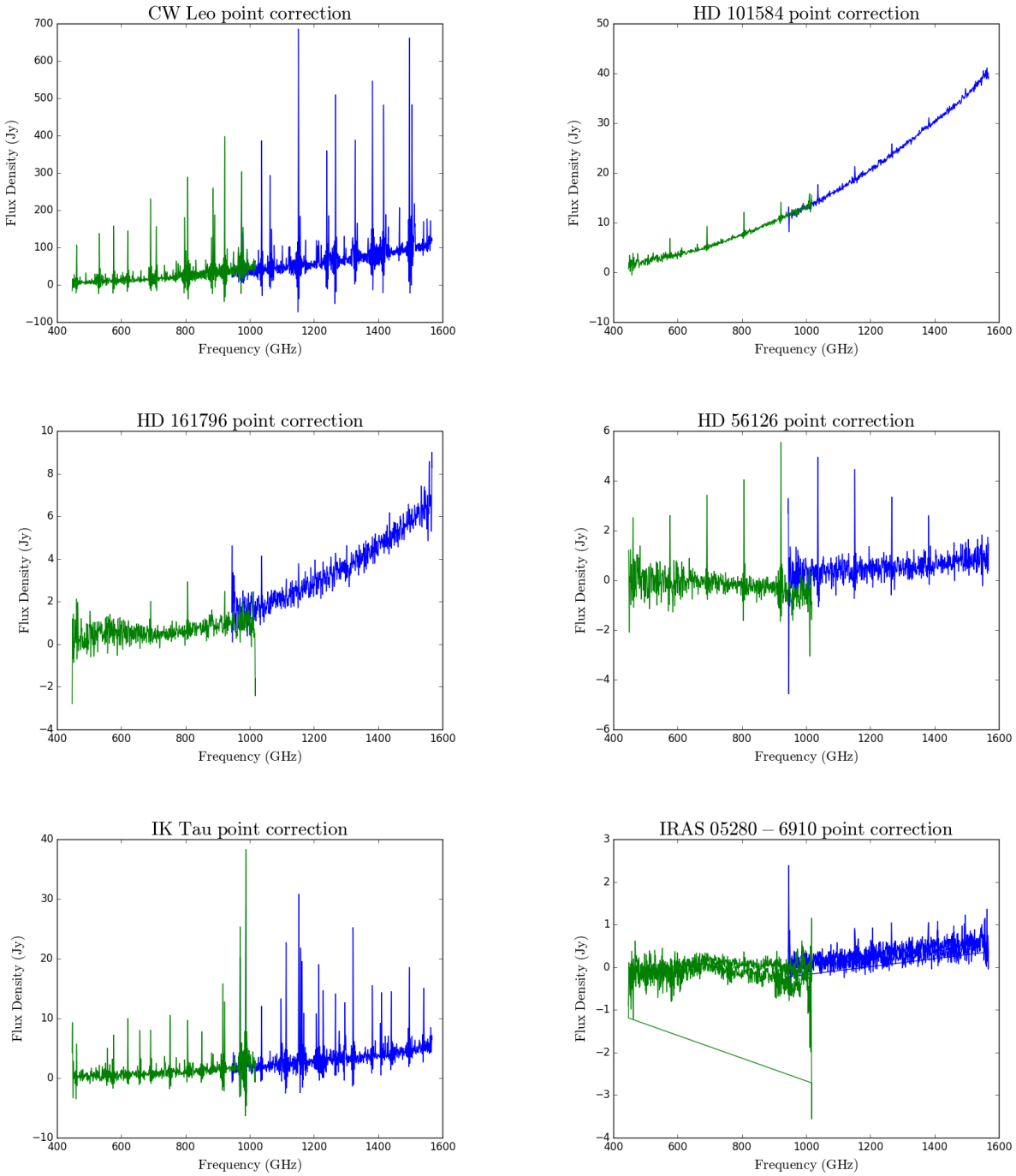

FIGURE C.5: Continued.

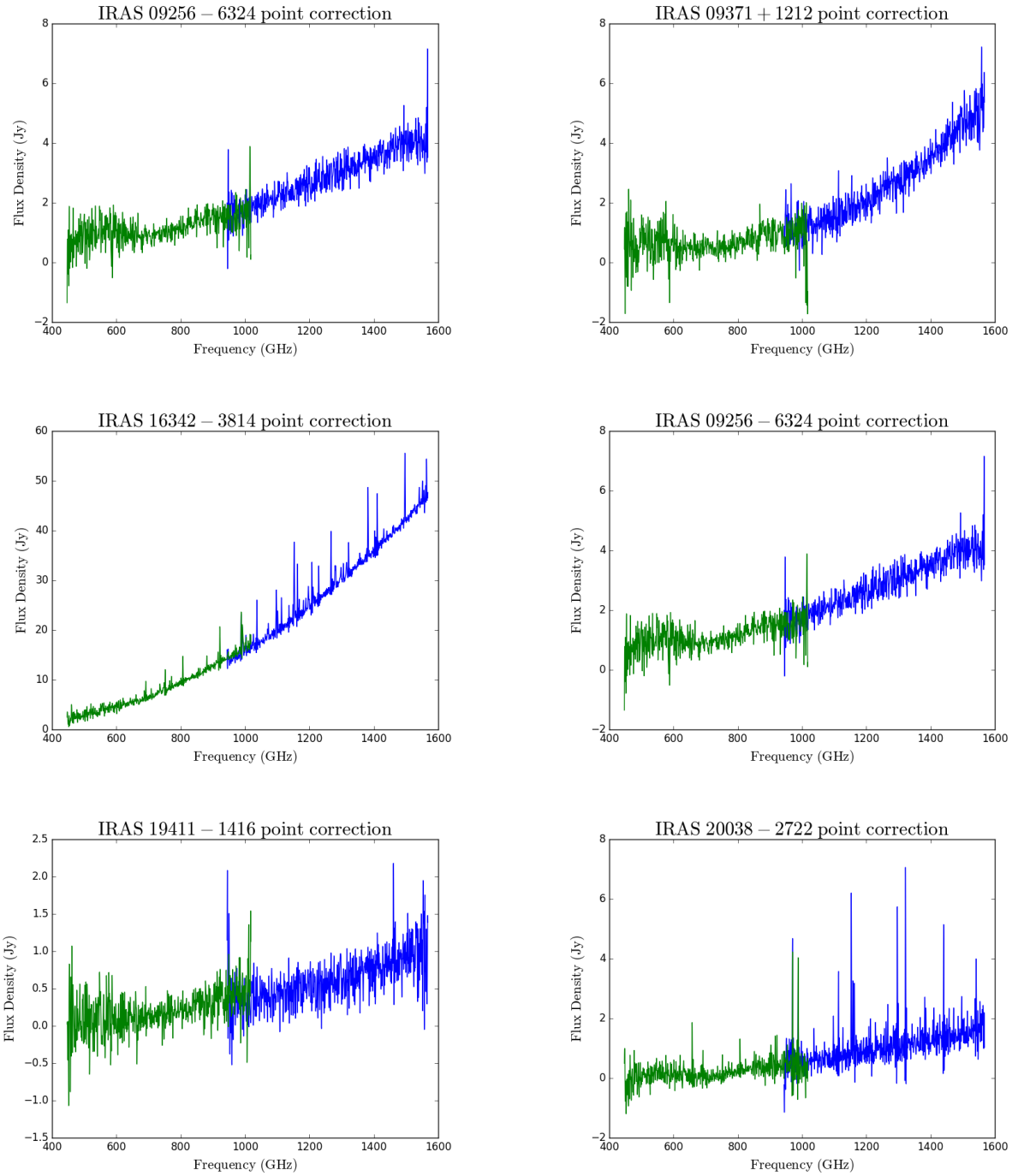

FIGURE C.5: Continued.

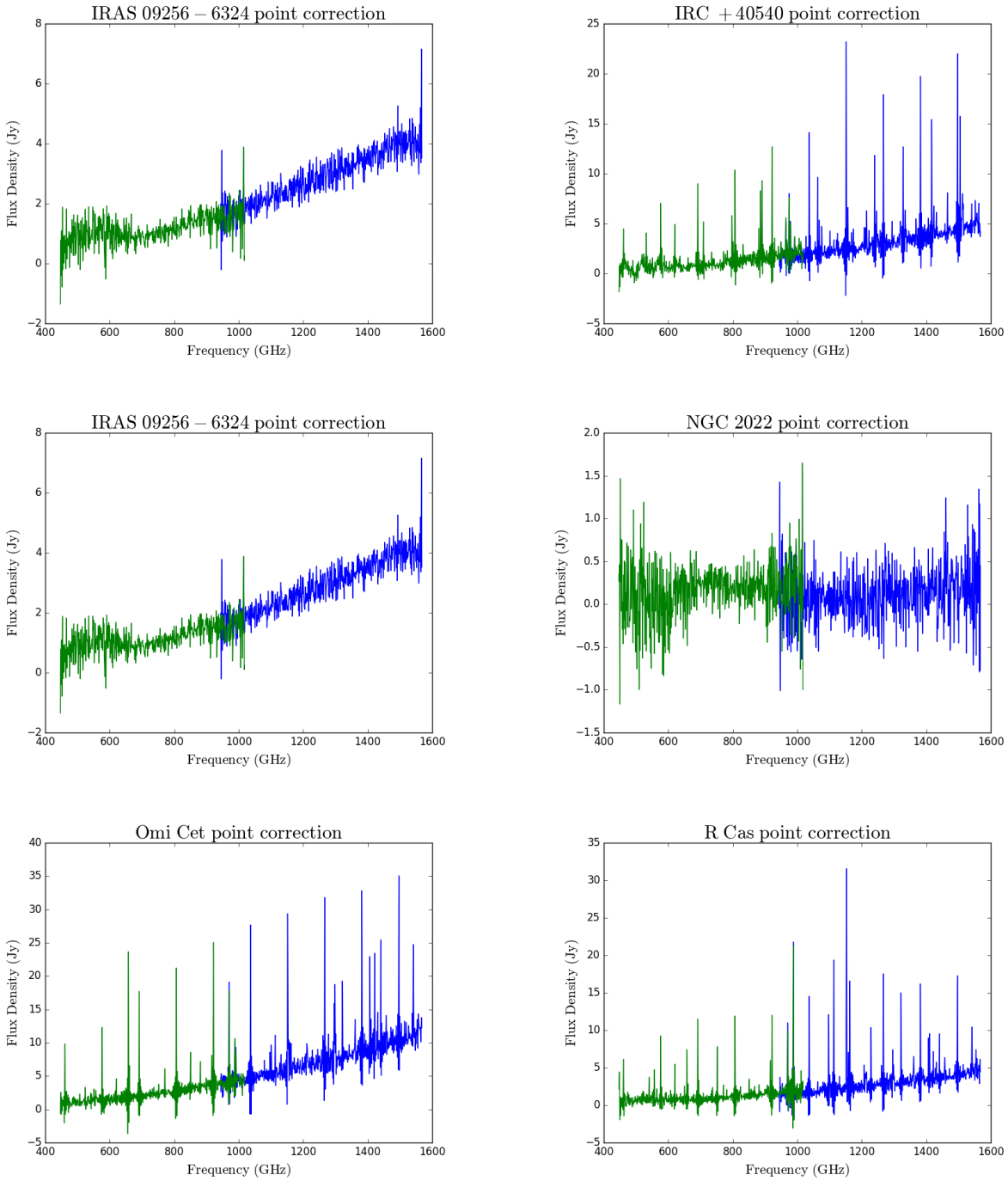

FIGURE C.5: Continued.

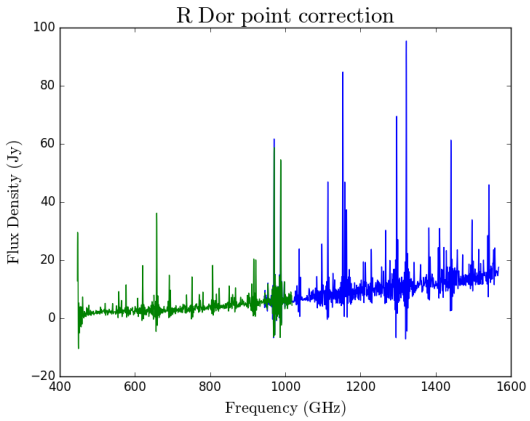

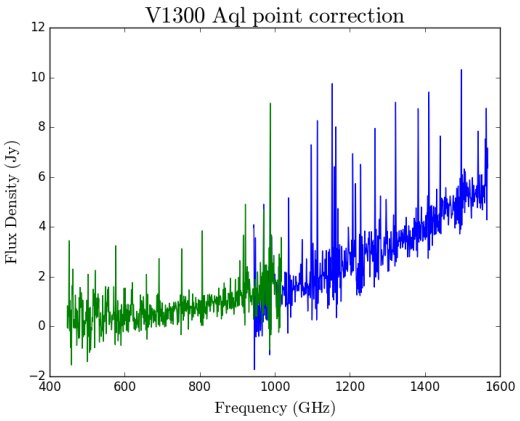

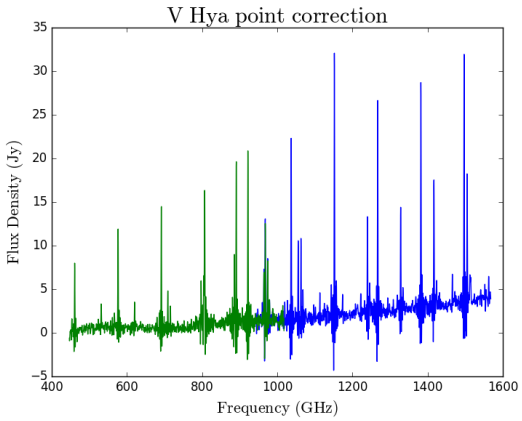

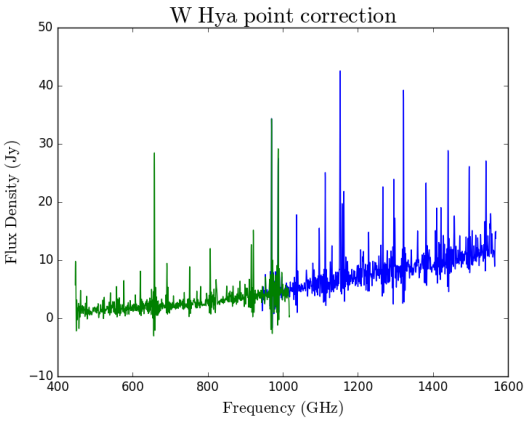

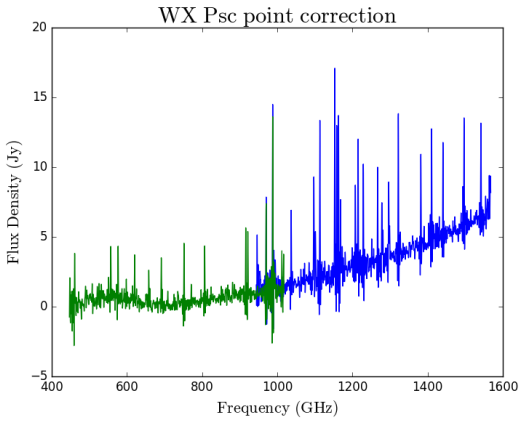

FIGURE C.5: Continued.

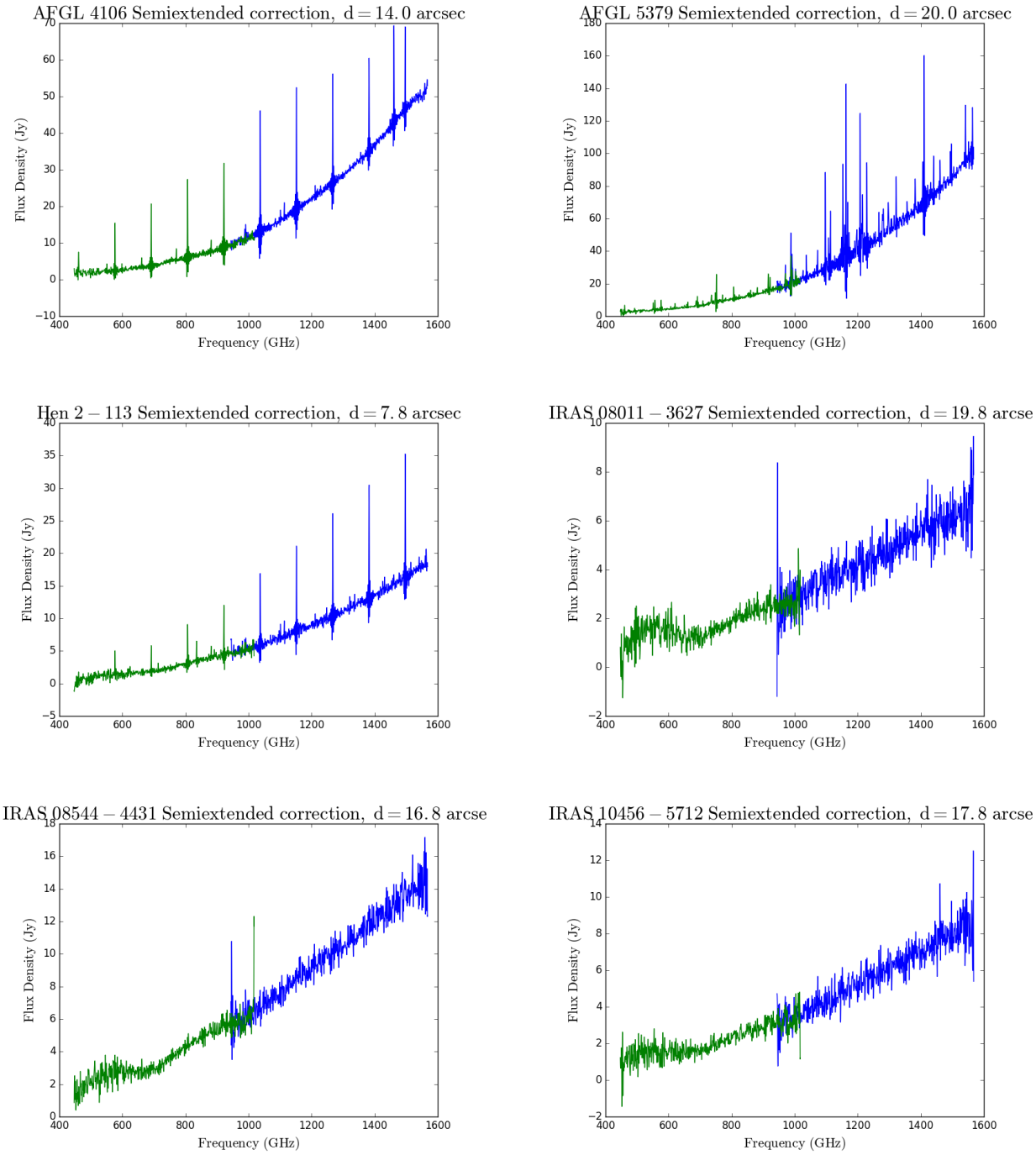

FIGURE C.6: SPIRE Spectrometer SED of those sources with 'Semiextended Correction' applied. Both subranges, SSW and SLW, blue and green respectively, are shown.

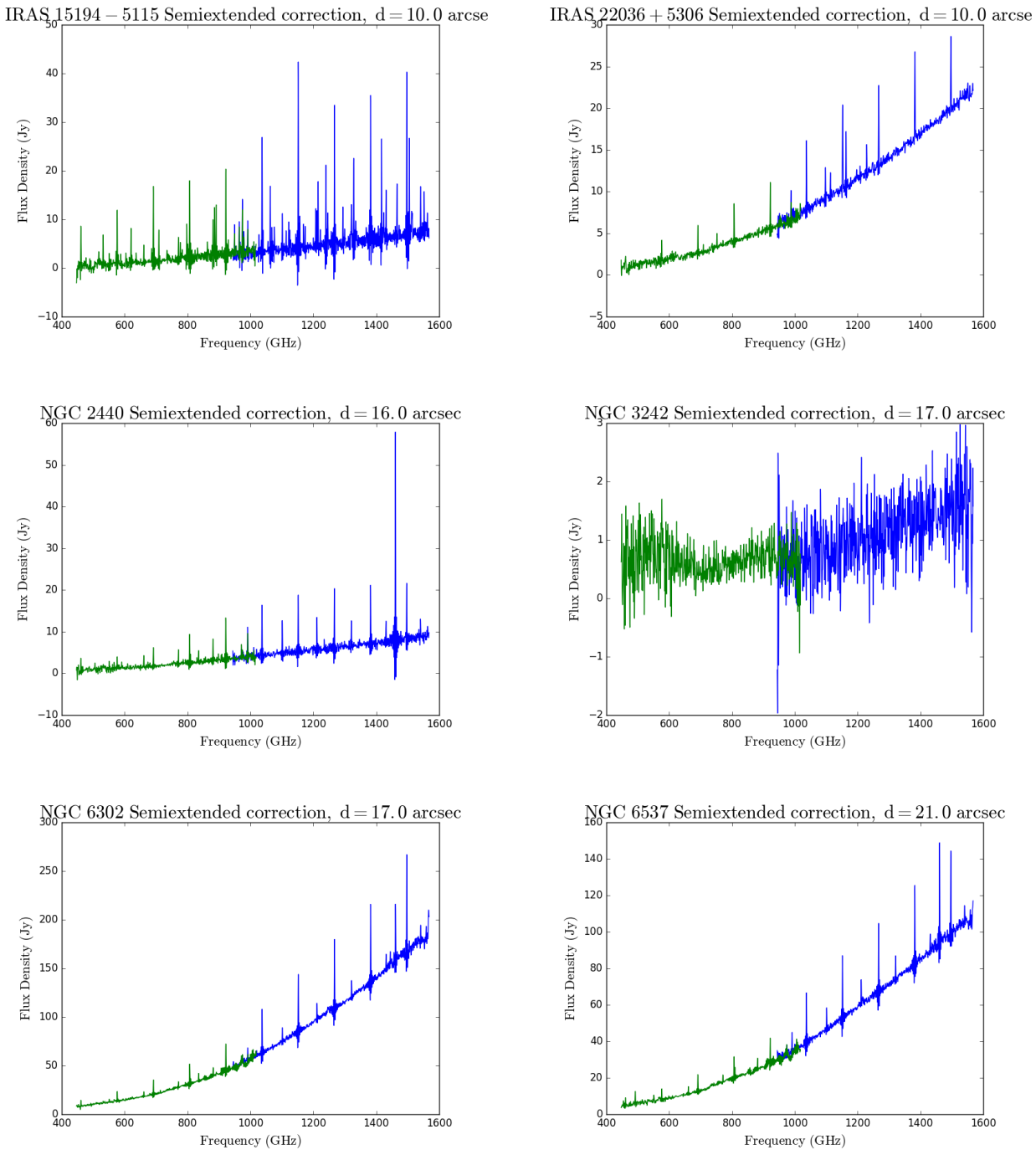

FIGURE C.6: Continued.

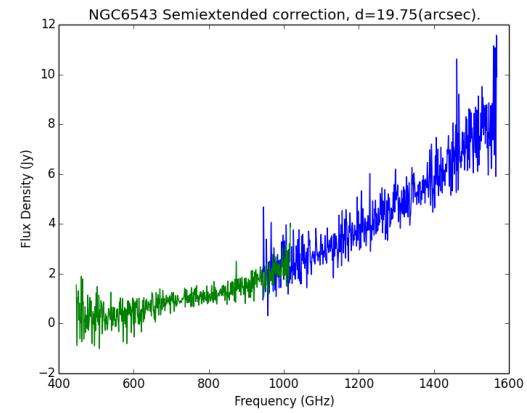

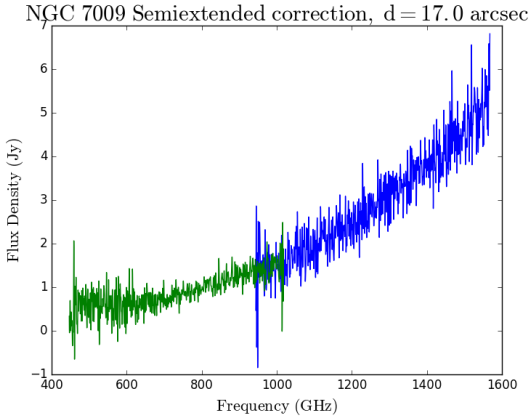

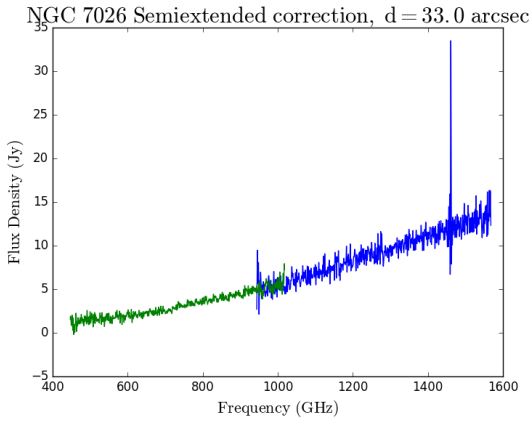

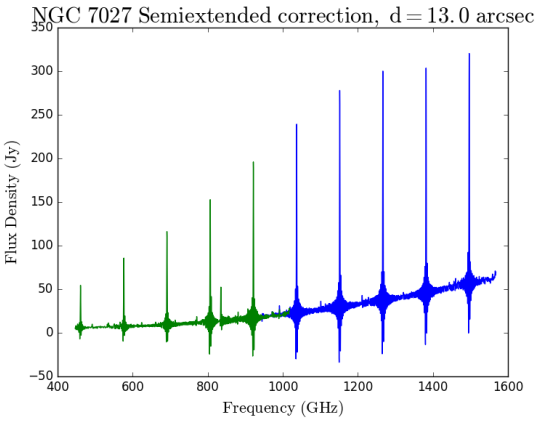

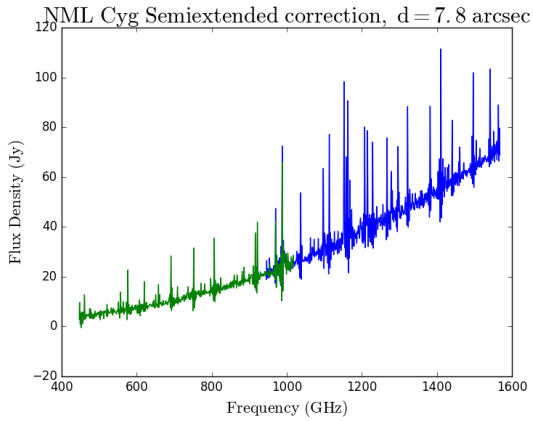

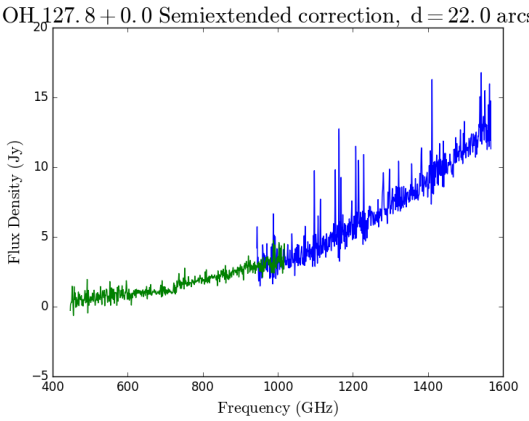

FIGURE C.6: Continued.

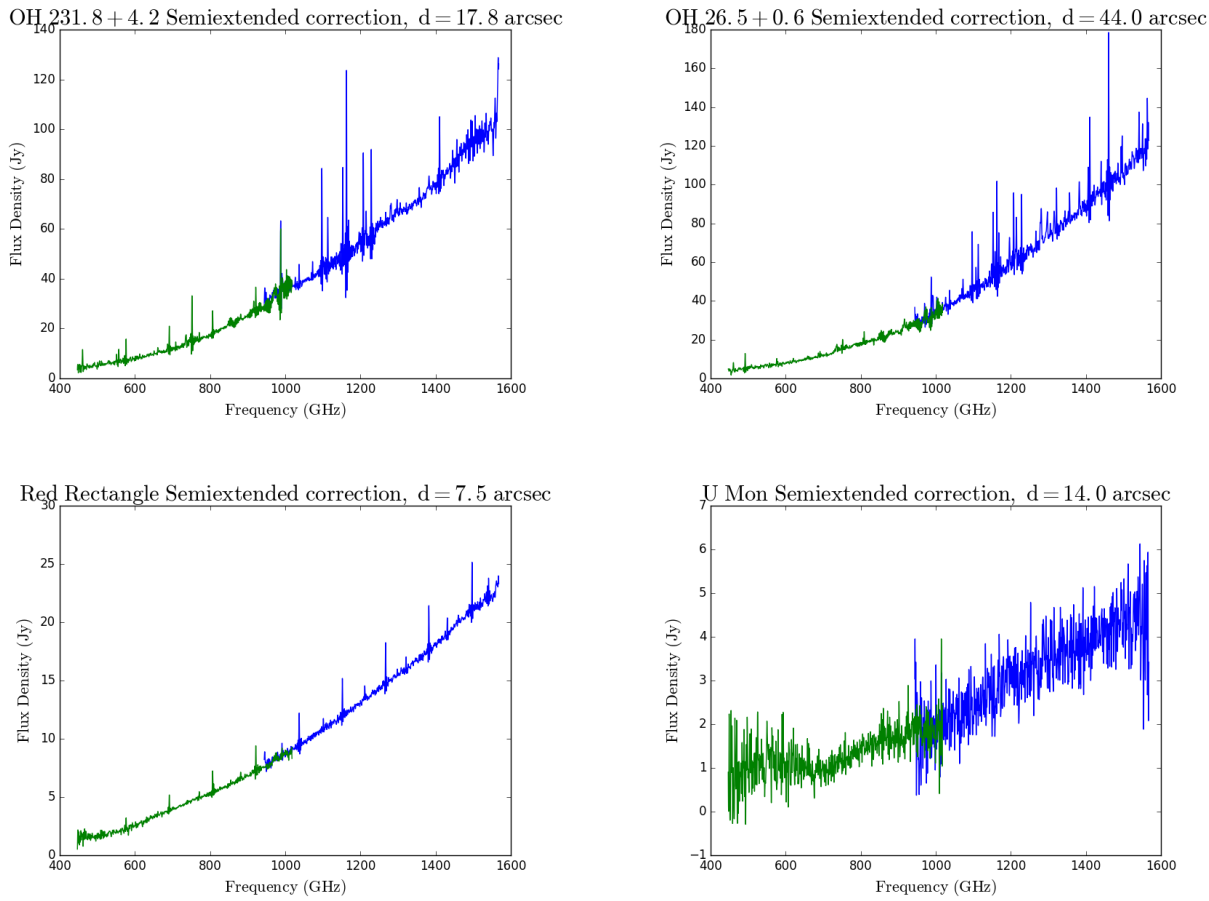

FIGURE C.6: Continued.

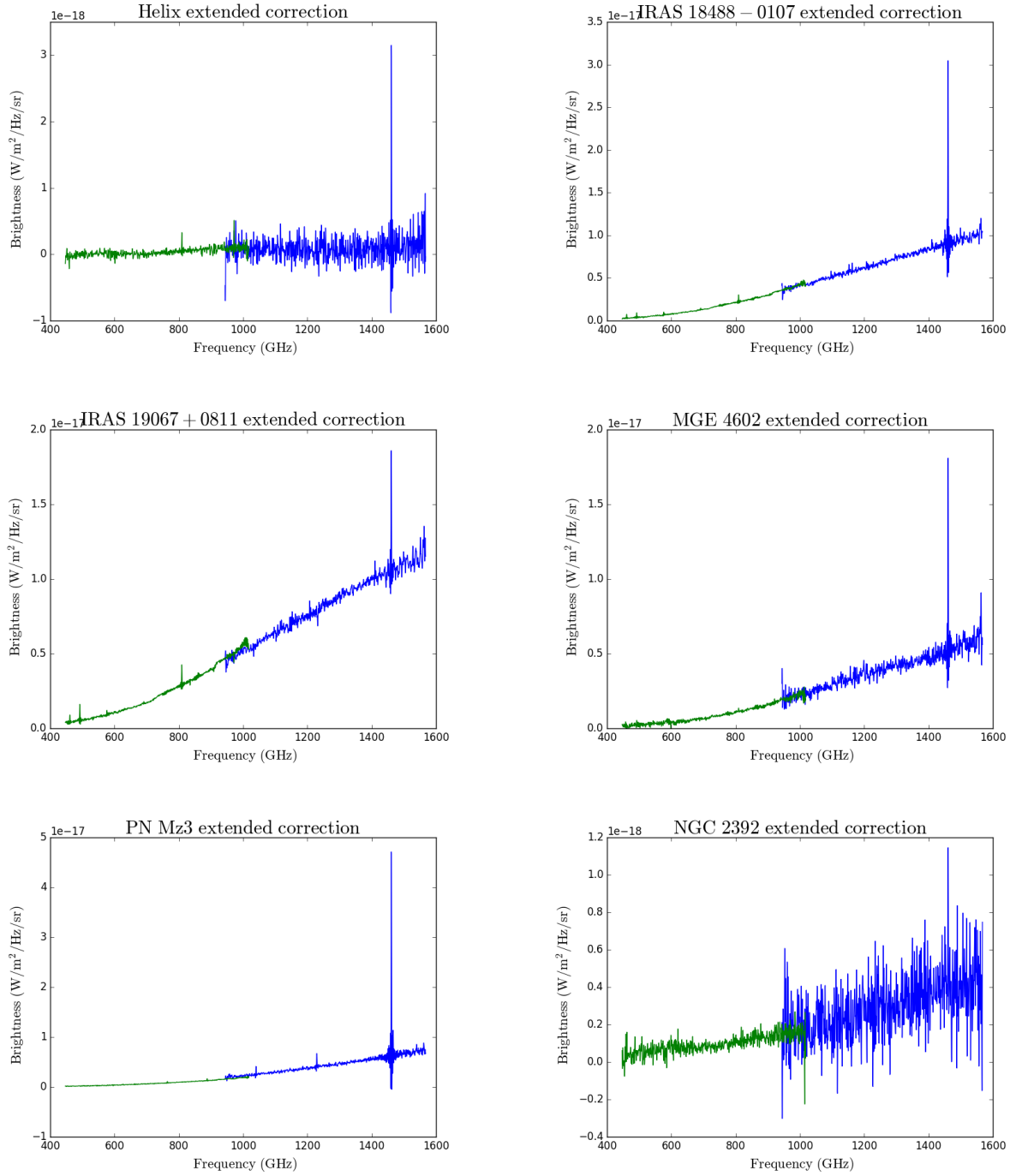

FIGURE C.7: SPIRE Spectrometer SED of those sources with 'Extended Correction' applied. Both subranges, SSW and SLW, blue and green respectively, are shown. Note that the spectra are in units of brightness.

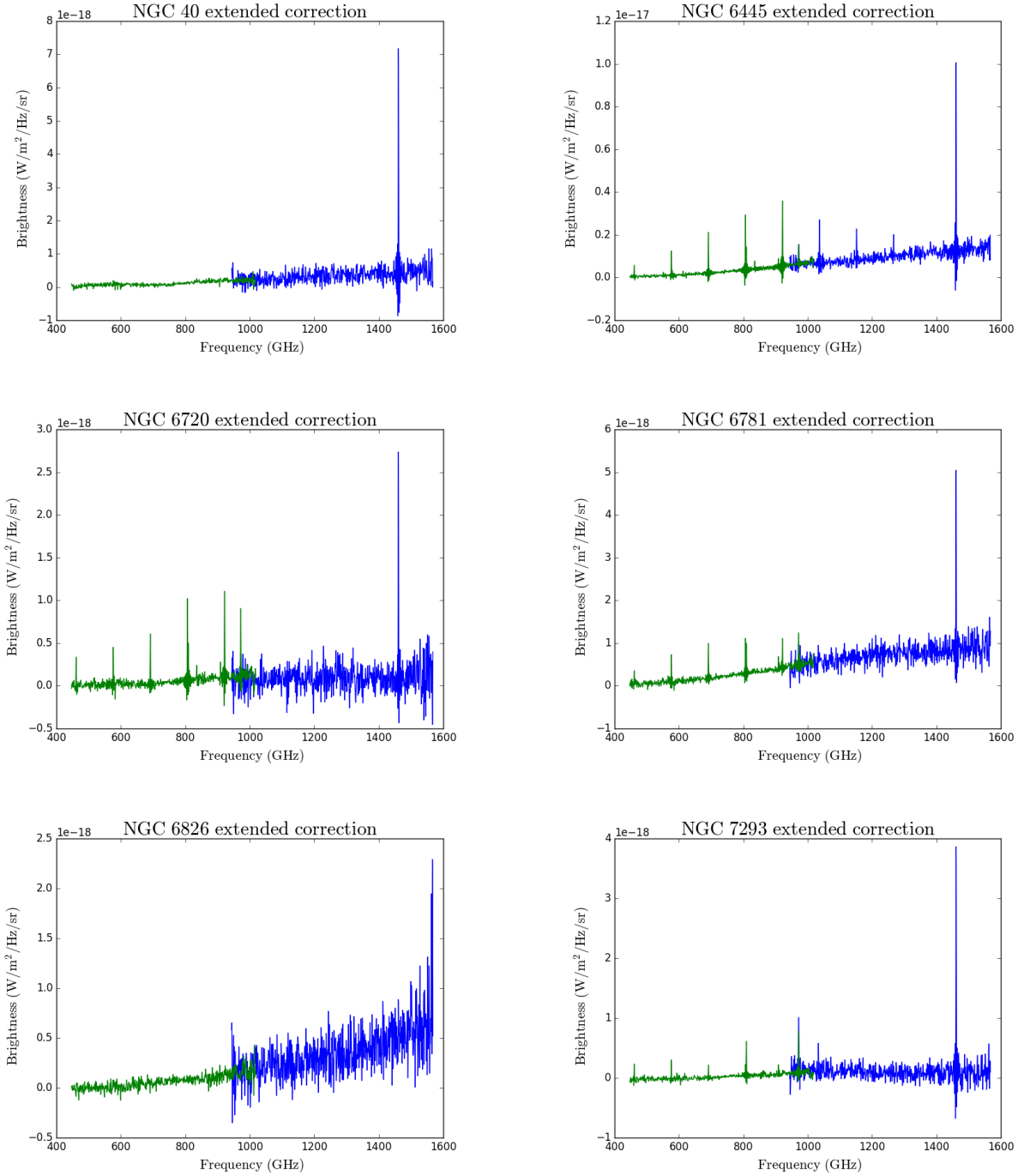

FIGURE C.7: Continued.

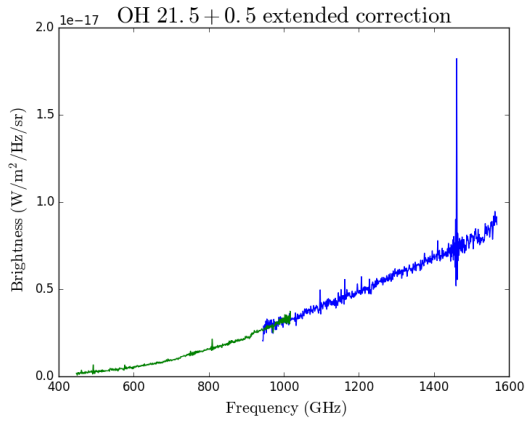

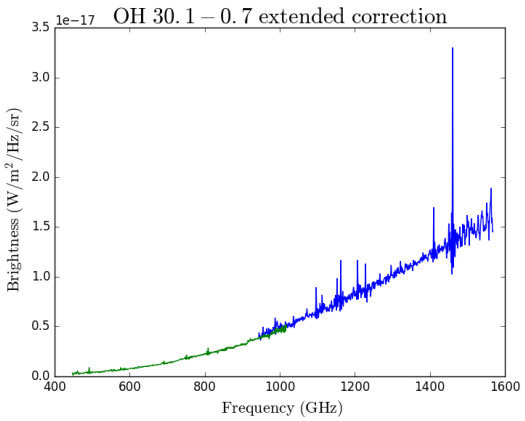

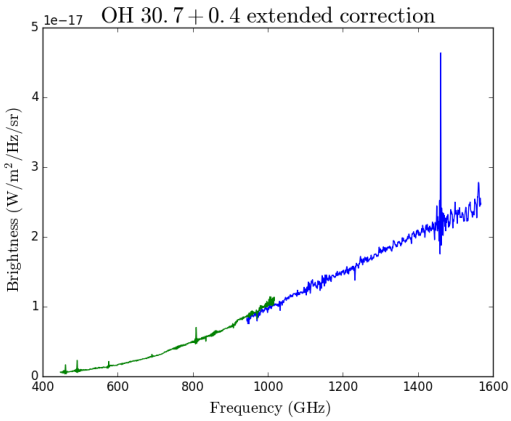

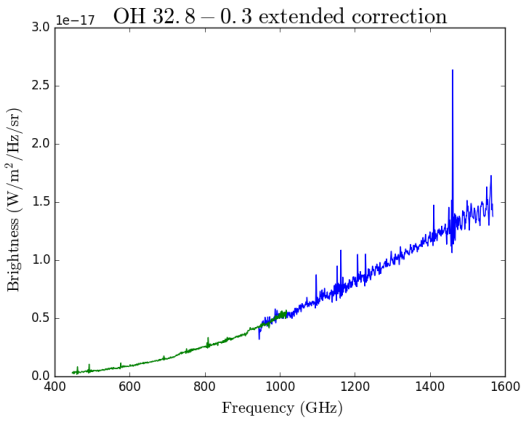

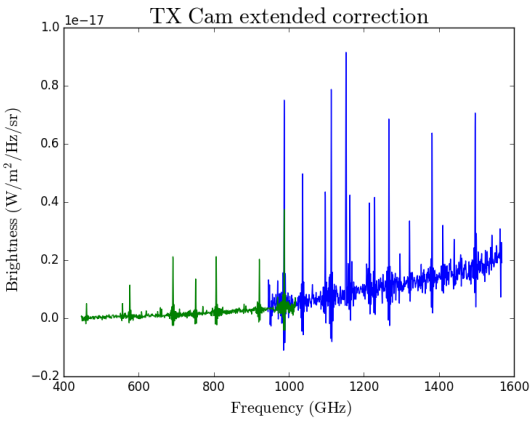

FIGURE C.7: Continued.

C.3 SEDs of common sources in THROES-PACS and THROES-SPIRE

In this section the PACS and SPIRE spectroscopic data are plotted together for those objects in common among both samples.

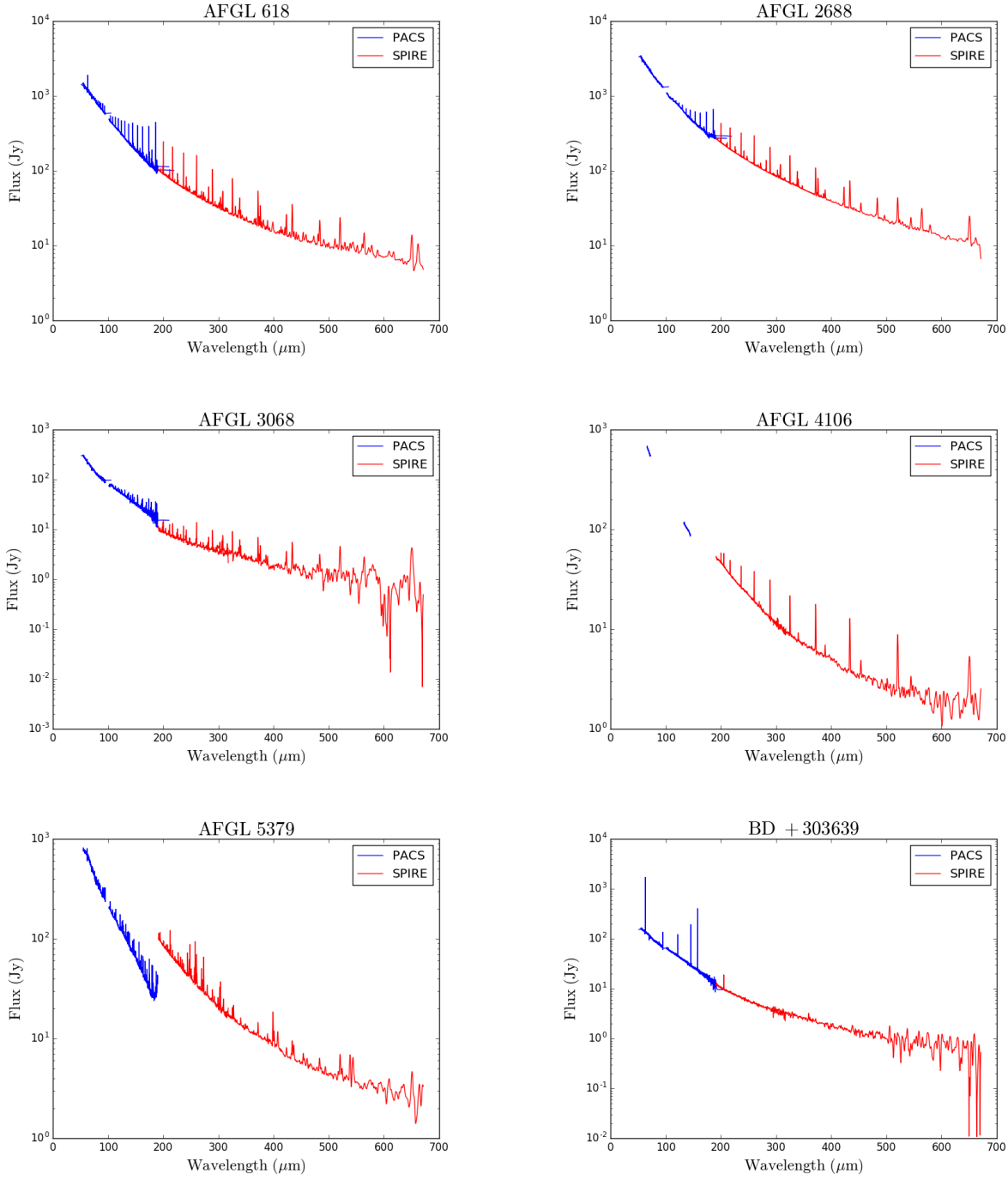

FIGURE C.8: PACS (blue) and SPIRE (red) spectroscopic data of those sources in common among THROES-PACS and THROES-SPIRE samples.

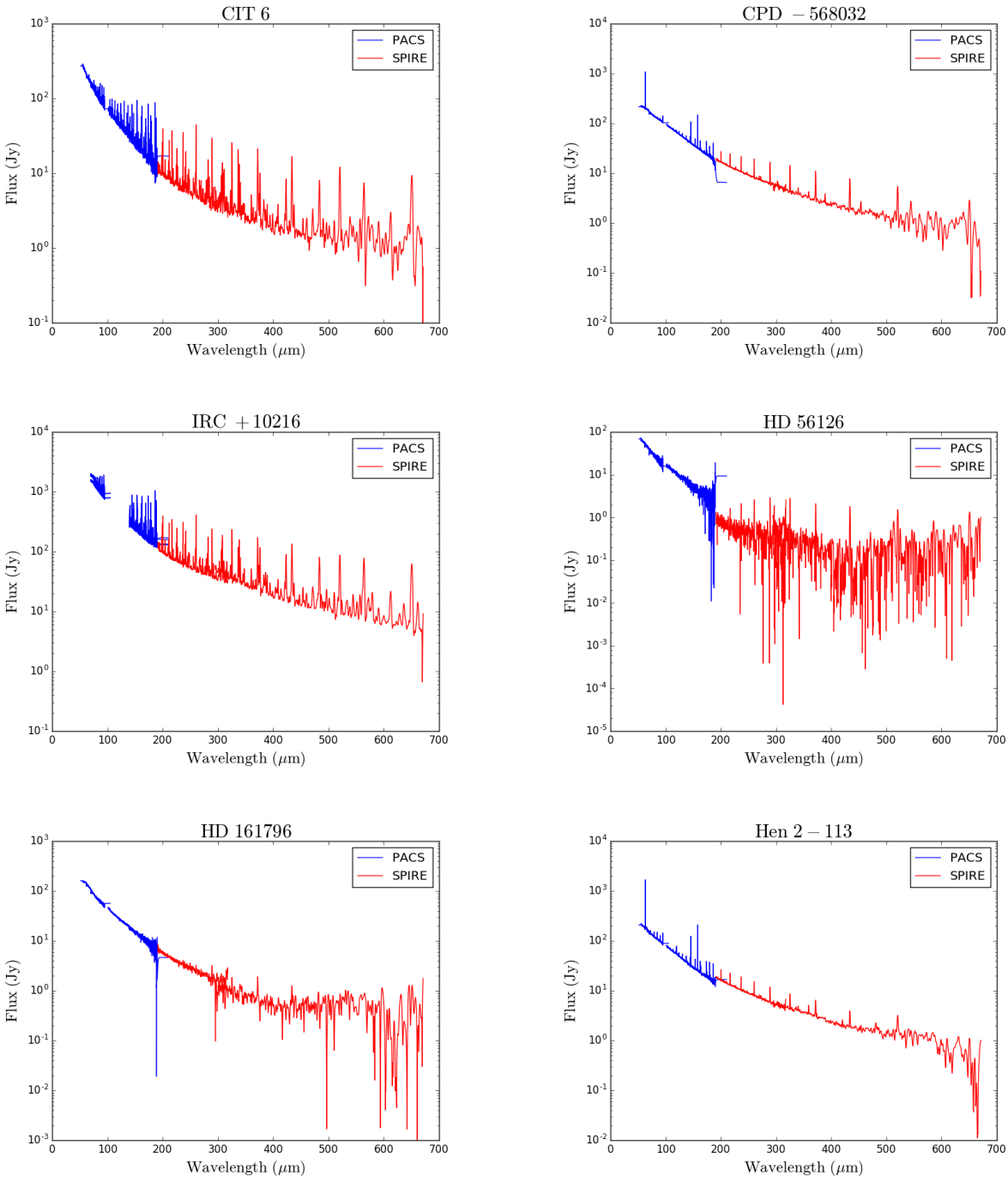

FIGURE C.8: Continued.

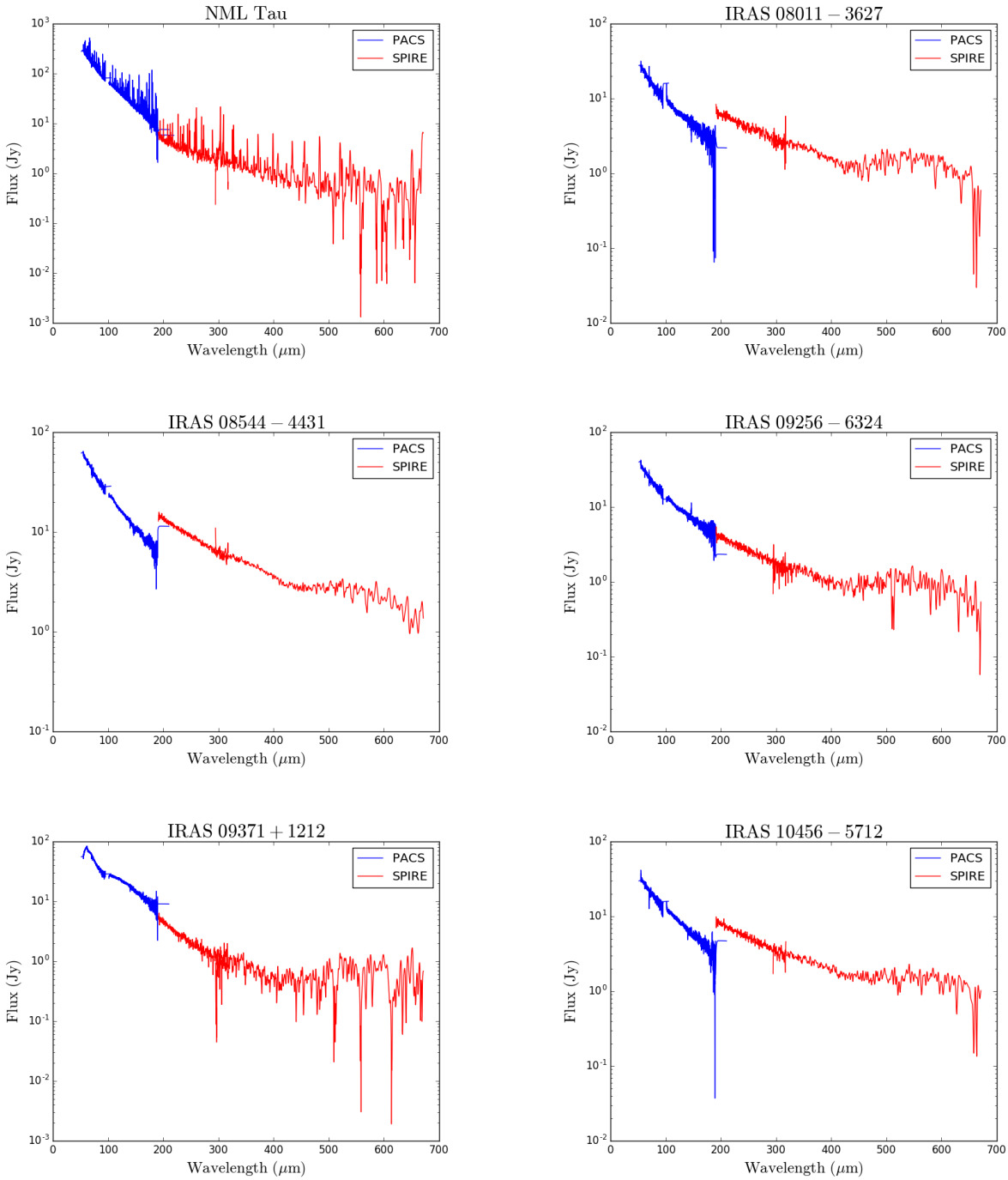

FIGURE C.8: Continued.

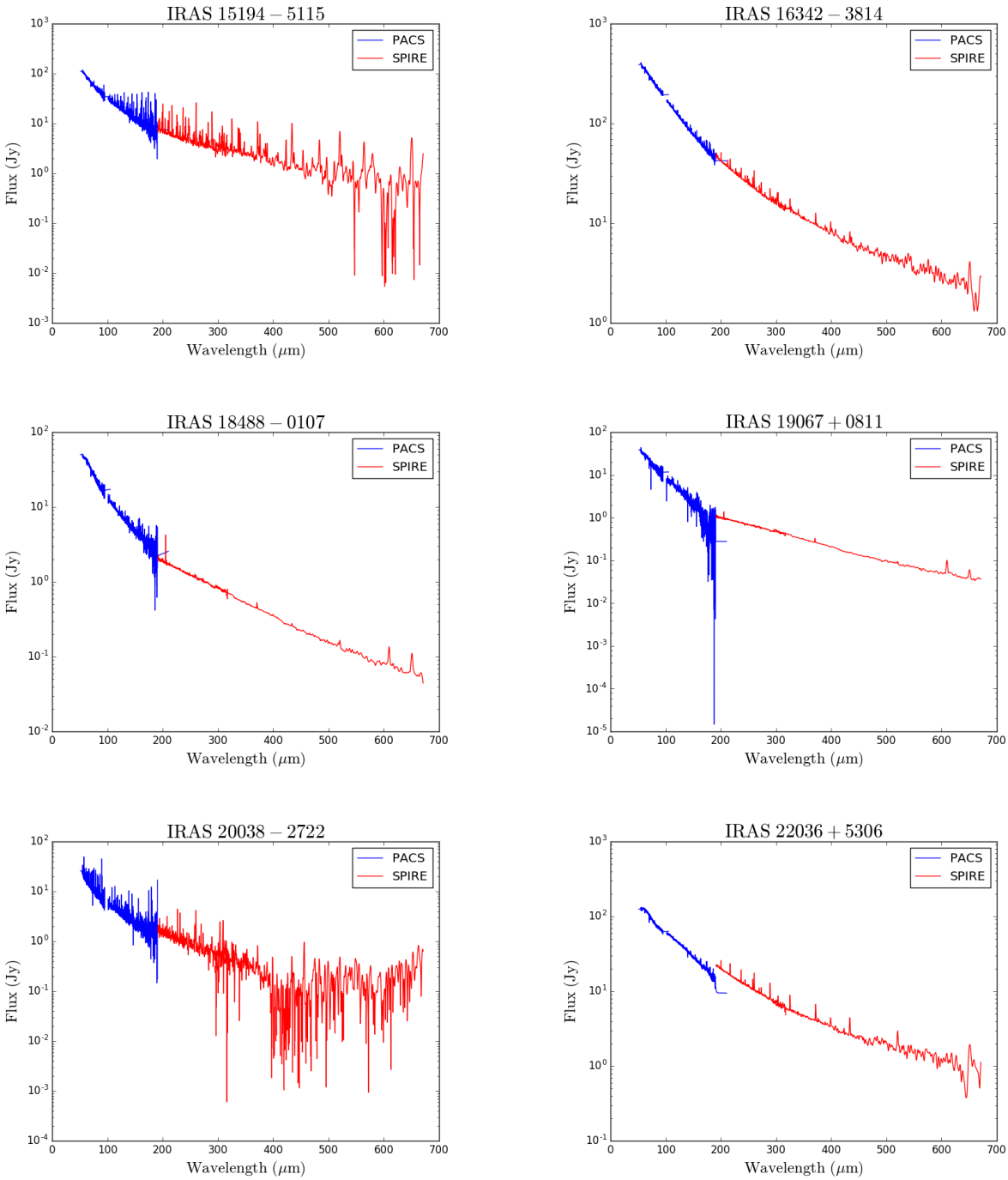

FIGURE C.8: Continued.

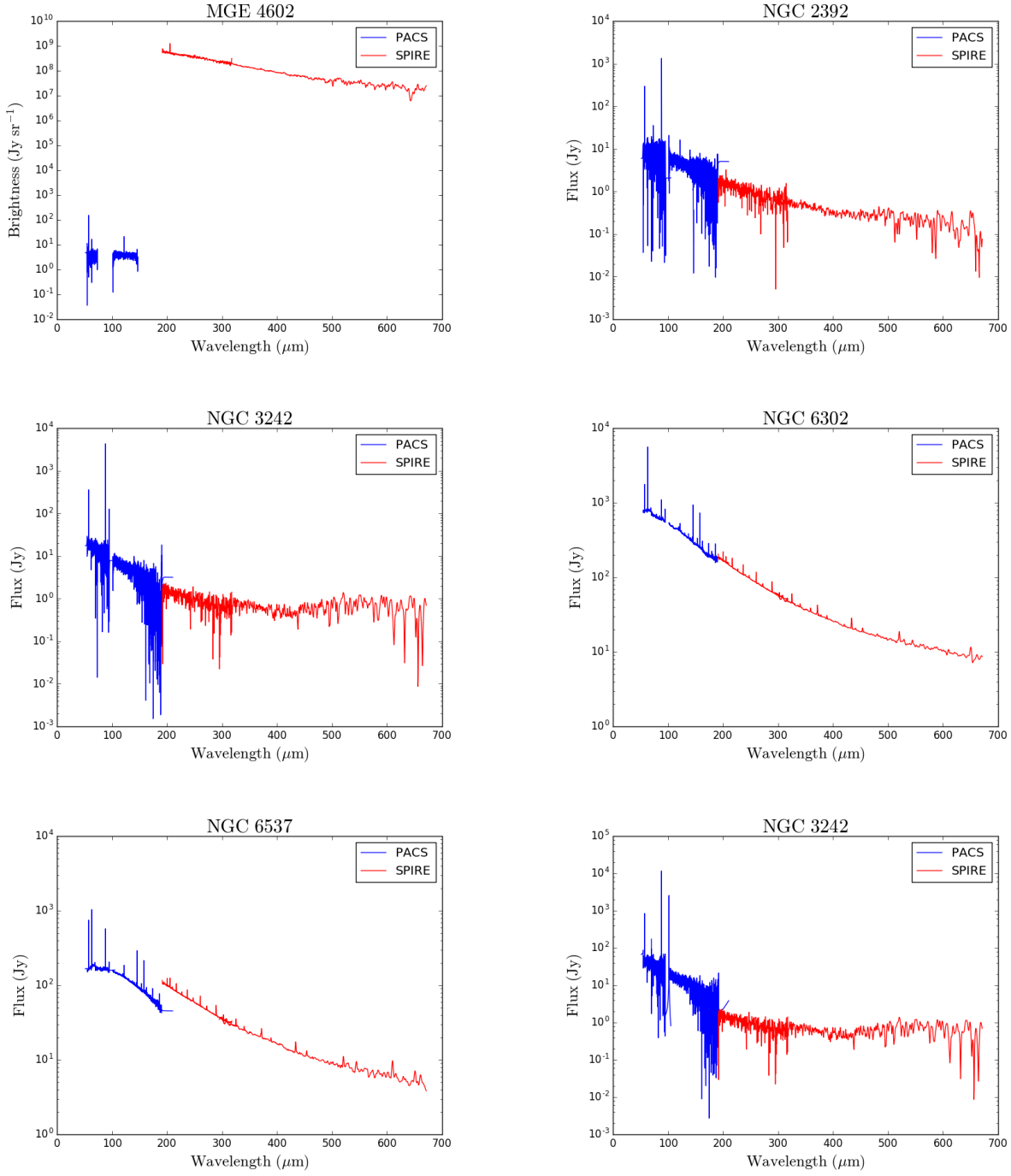

FIGURE C.8: Continued.

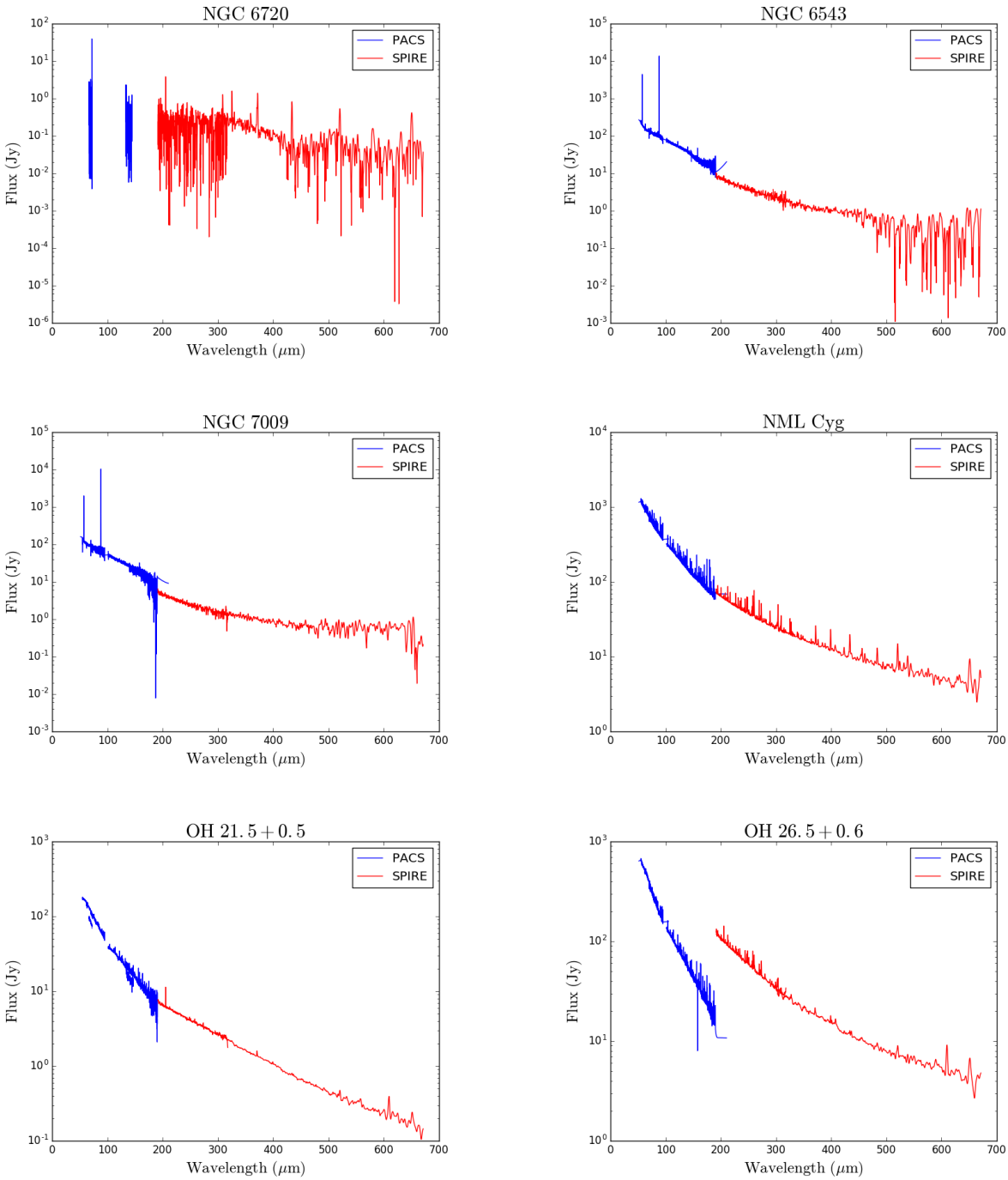

FIGURE C.8: Continued.

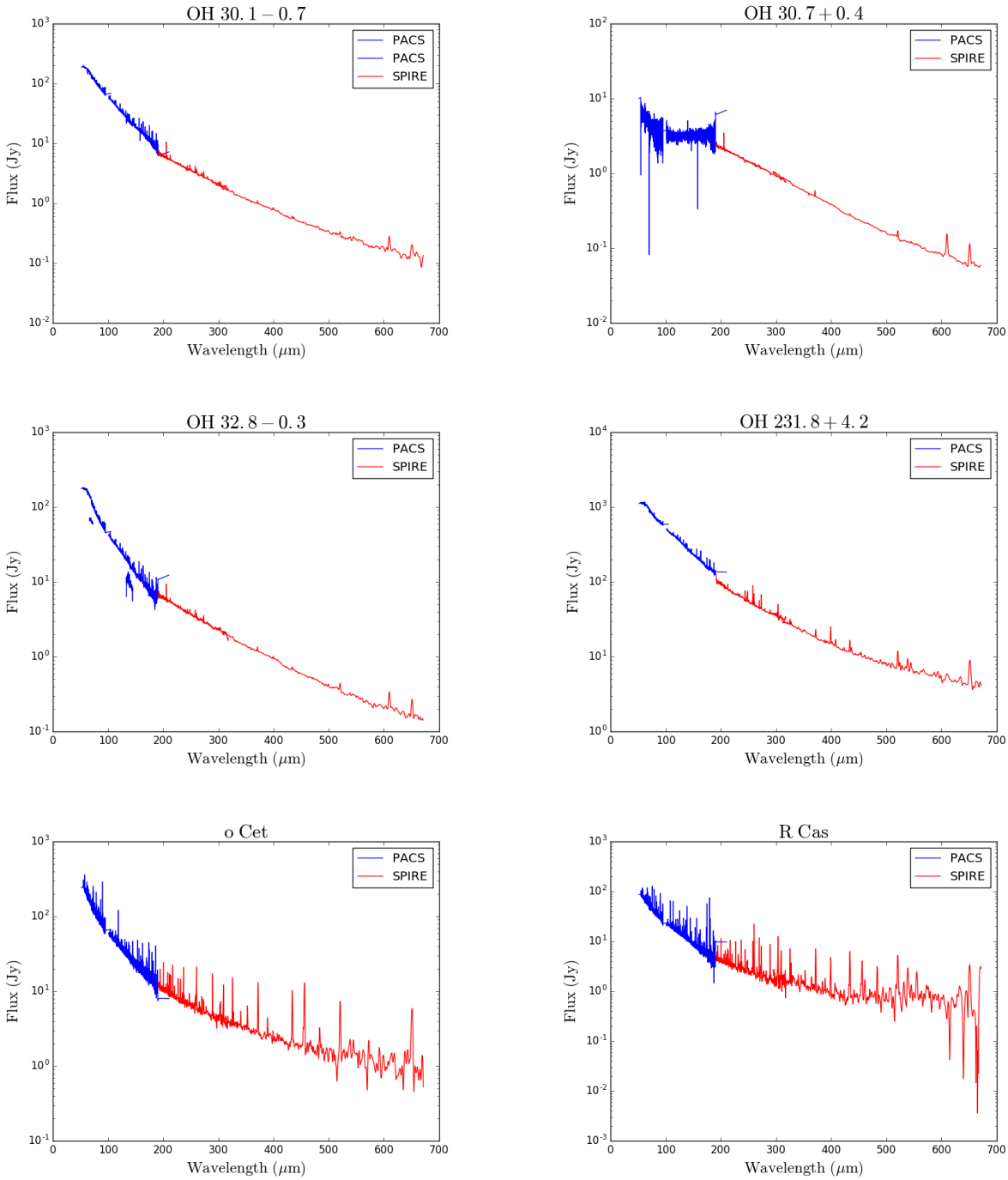

FIGURE C.8: Continued.

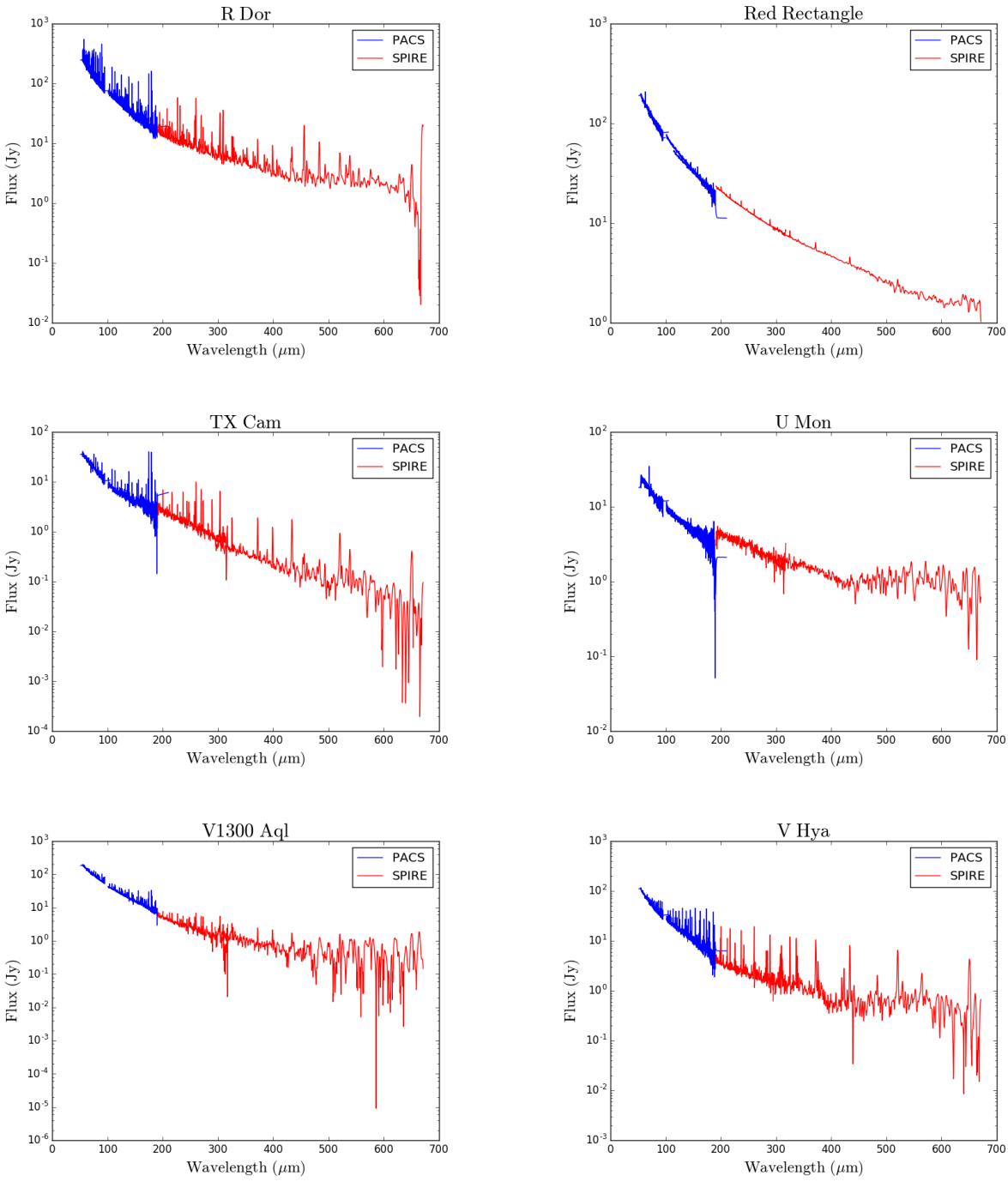

FIGURE C.8: Continued.

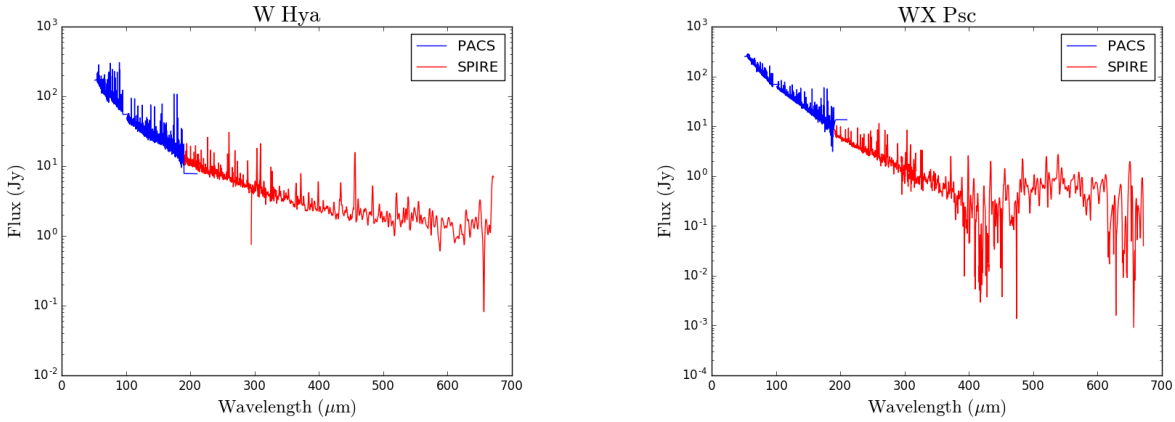

(A) 1d (B) 1b

FIGURE C.8: Continued.

C.4 Opacity correction

C.4.1 Opacity and mass-loss rate plots: PACS

In this section we present, for each source studied in Chapter 4, the values of the optical depth (τ, defined in § 4.4.1) of the different CO transitions used to build the RDs for a range of values of the characteristic radius ($r_{\rm CO}$) of the CO-emitting volume (Fig. C.9). As we can see in this figure, the radius adopted implies a moderate value of τ and, therefore, a moderate opacity correction. The radius of the PACS CO-emitting region is the major source of uncertainty in the computation of τ and, therefore, of the emitting mass and mass-loss rates. It also has an effect on the rotational temperature. The values of $M_{\rm tot}$ and $T_{\rm rot}$ for a range of $r_{\rm CO}$ are plotted inside the boxes in Fig. C.9. The resulting mass-loss rates, $\dot{M}$, are shown in Fig. C.11, together with the broad range of mass-loss rates found in the literature for each object, typically derived from low-J CO line studies (references are provided in Table 4.3).

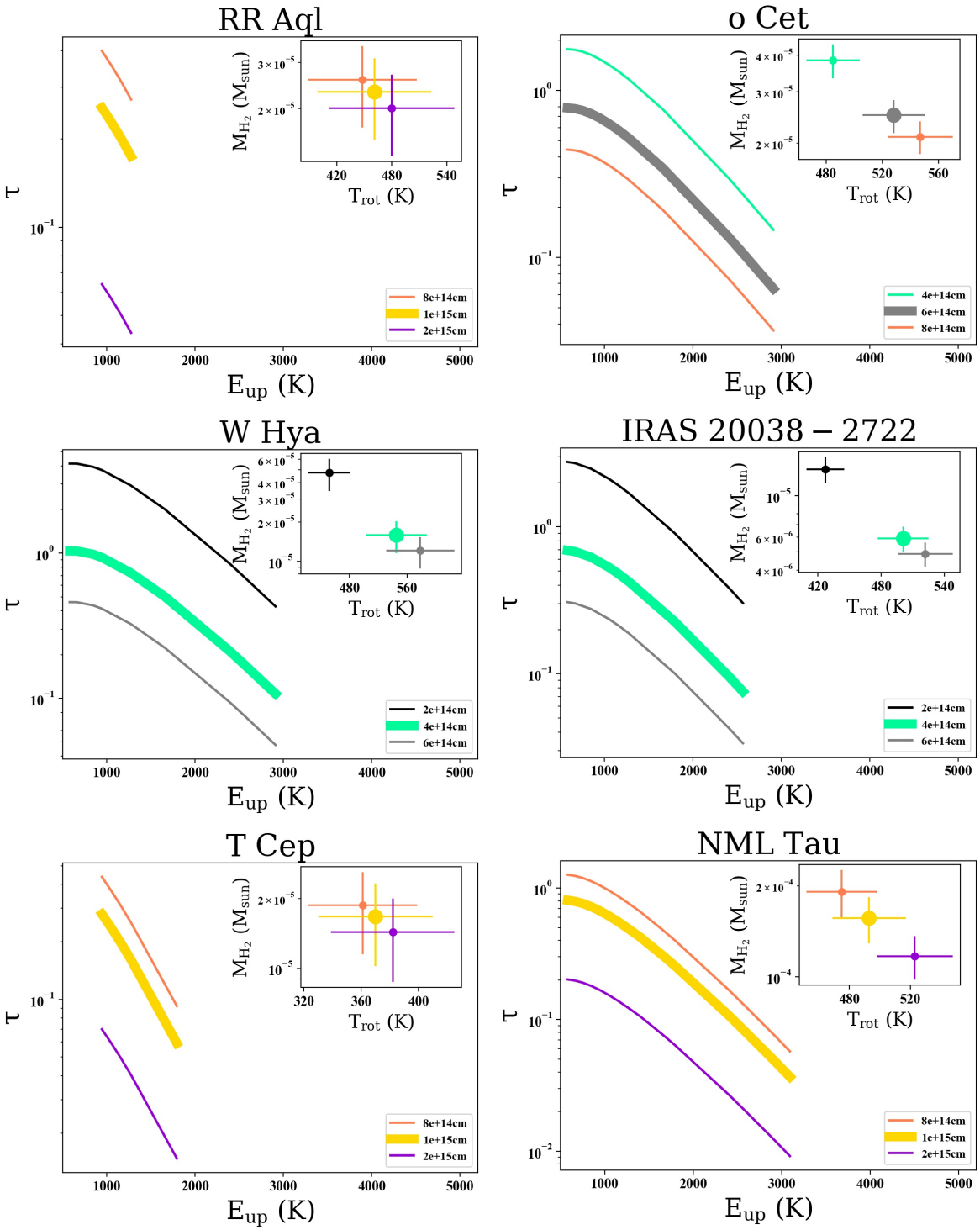

FIGURE C.9: Plots of τ vs E_{up} corresponding to different linear radii. In each chart there is a subgraphic showing M_{H_2} vs T_{rot}. The thickest curve and the biggest point are those associated to the r_{CO} shown in Table. 4.1.

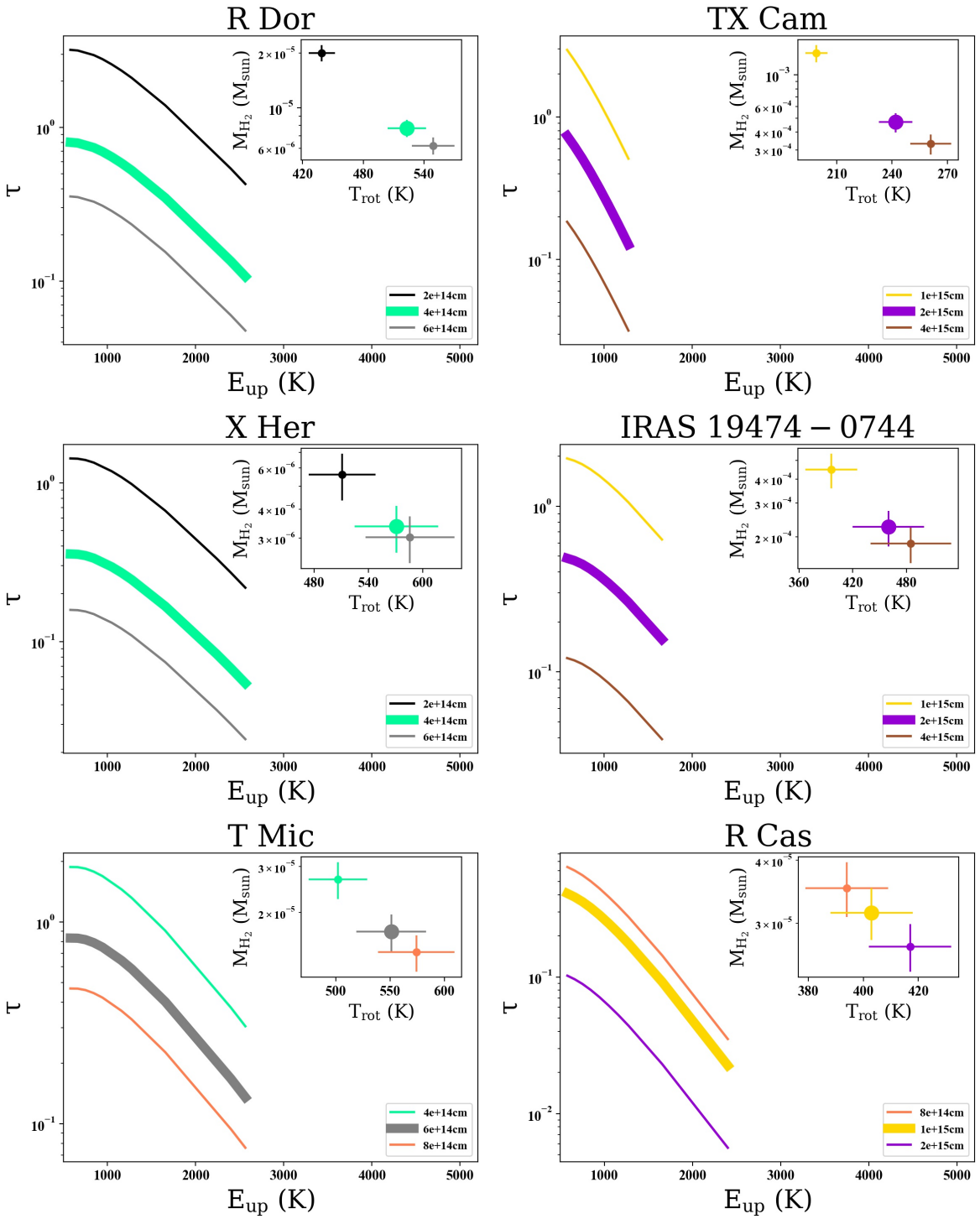

FIGURE C.9: Continued.

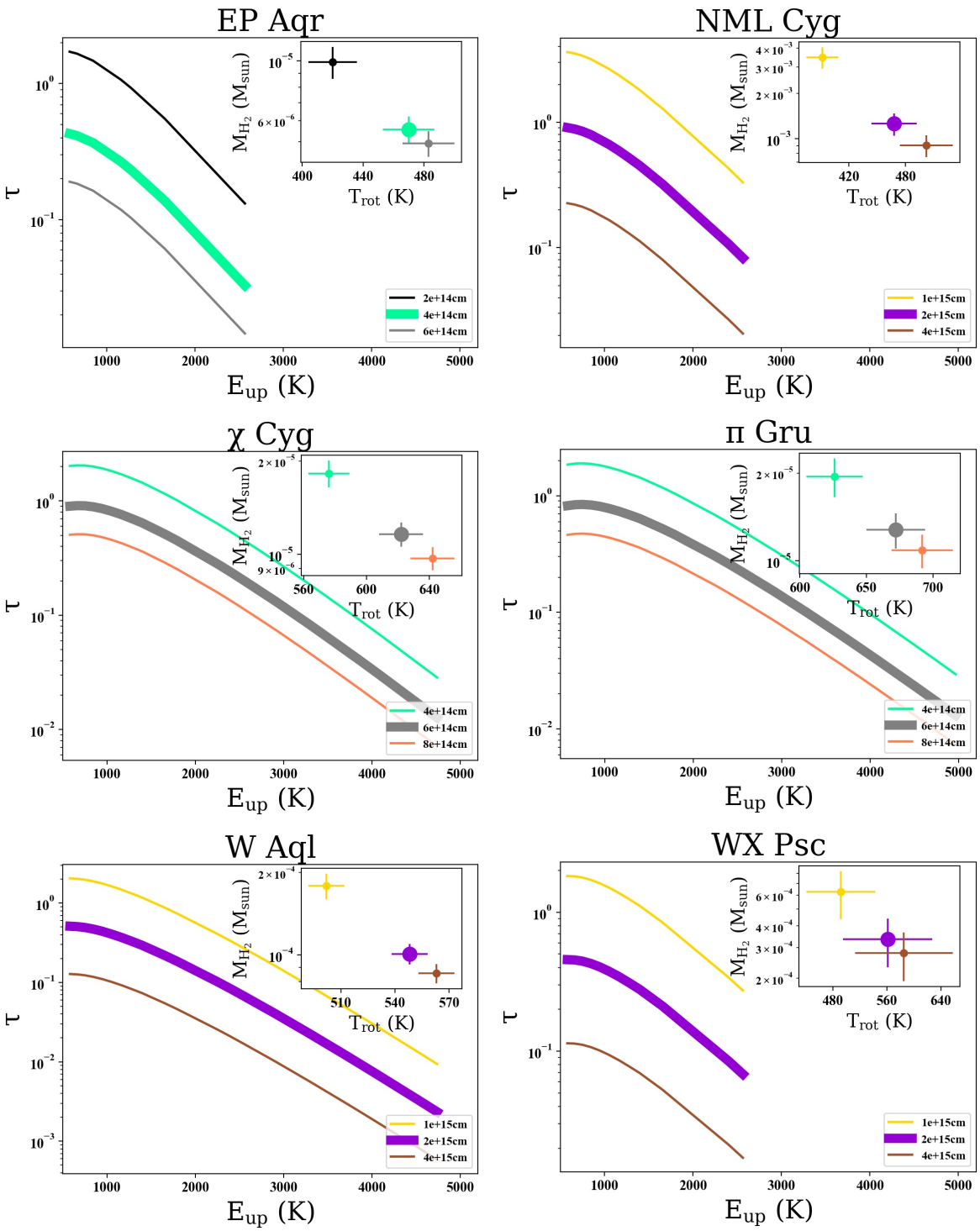

FIGURE C.9: Continued.

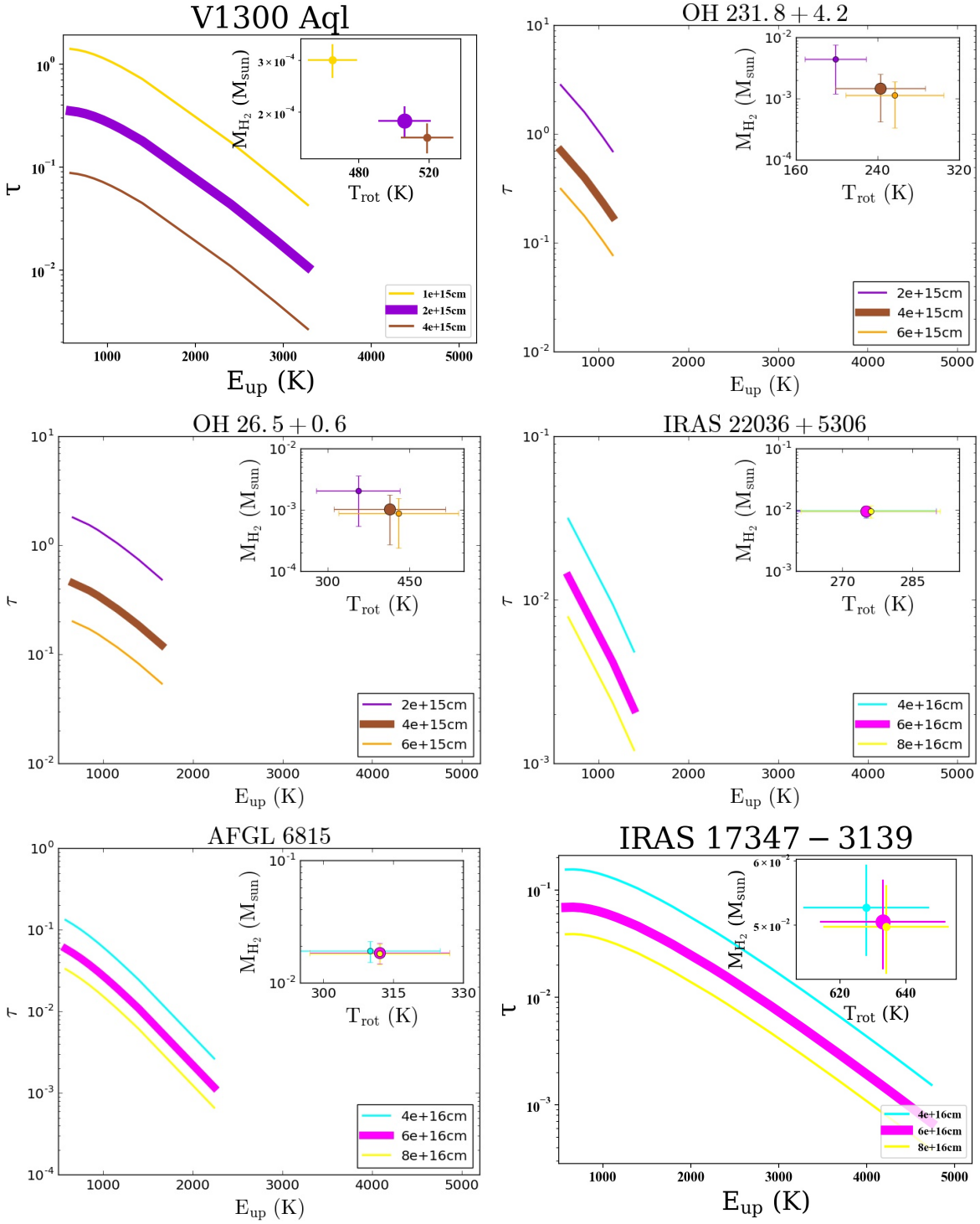

FIGURE C.9: Continued.

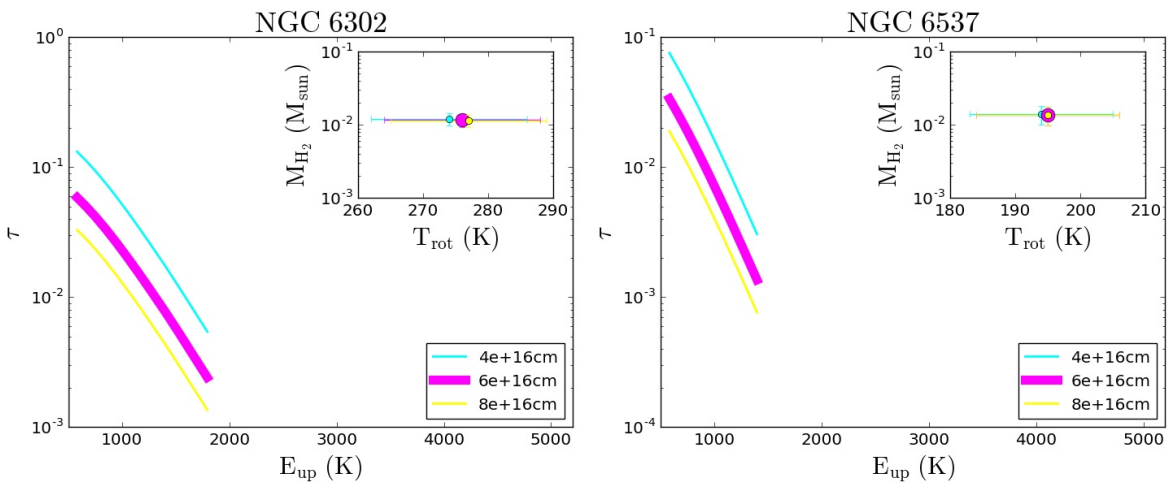

FIGURE C.9: Continued.

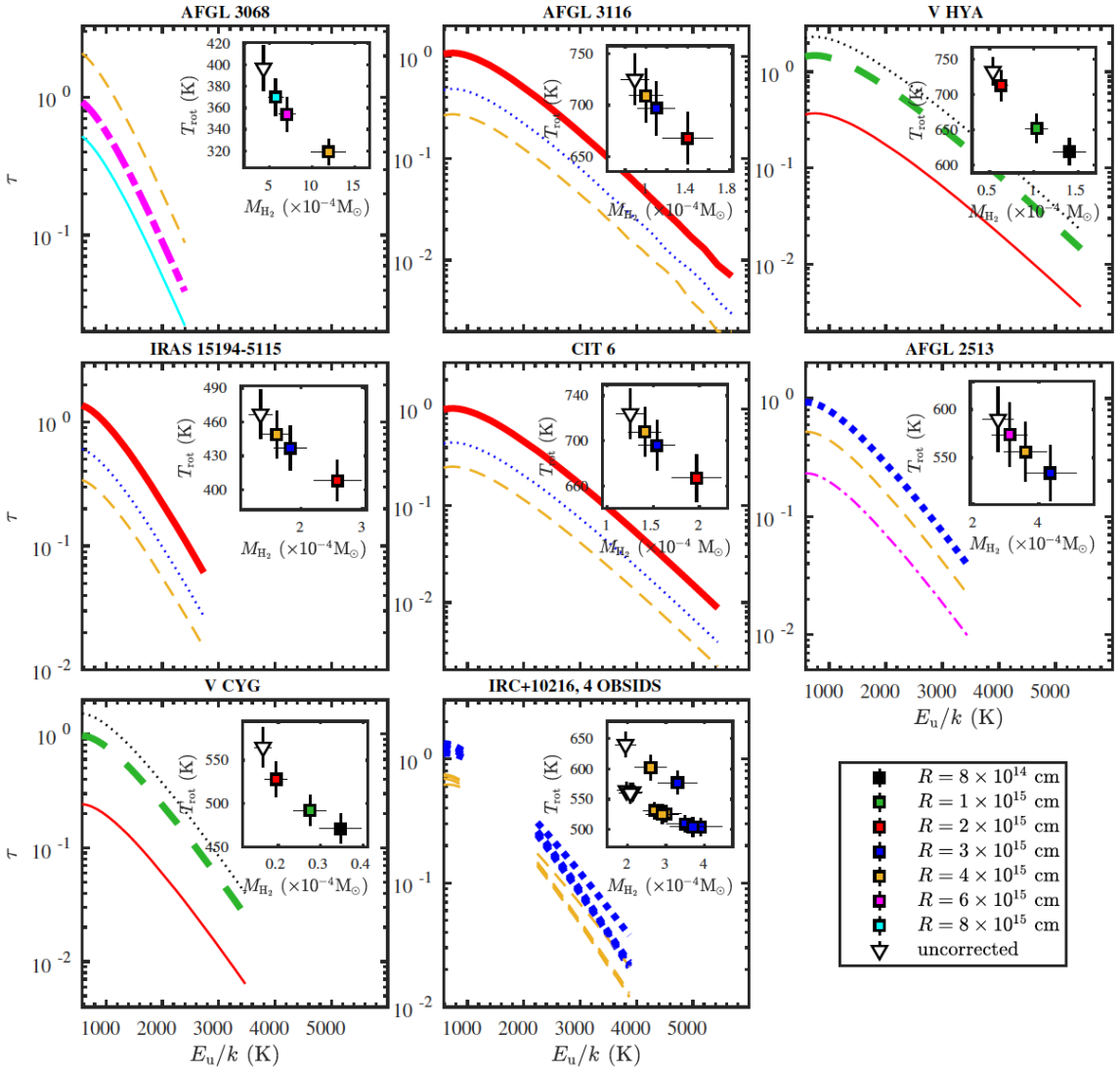

FIGURE C.10: As in Fig. C.9 but C-rich sources.

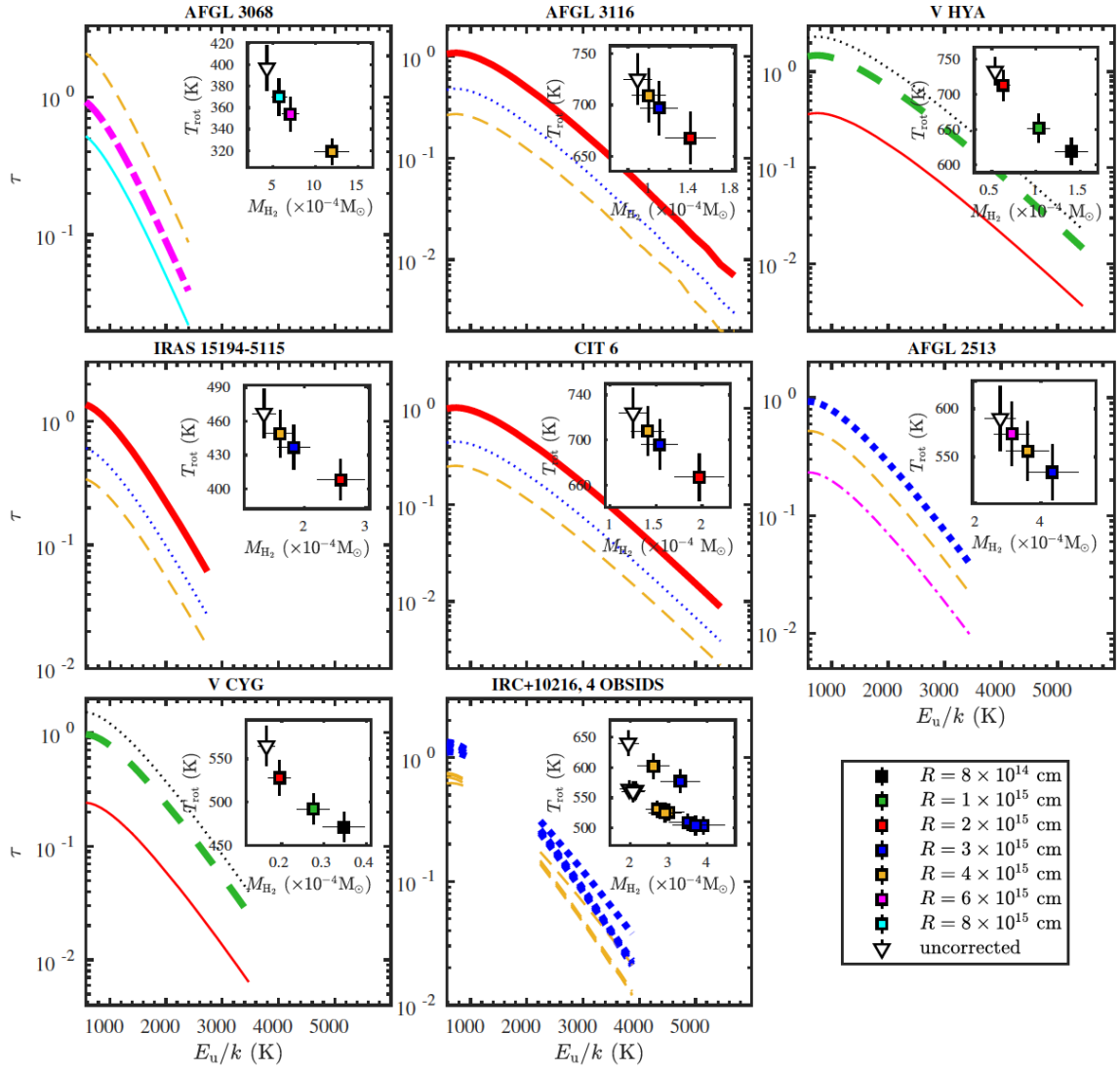

FIGURE C.10: Continued.

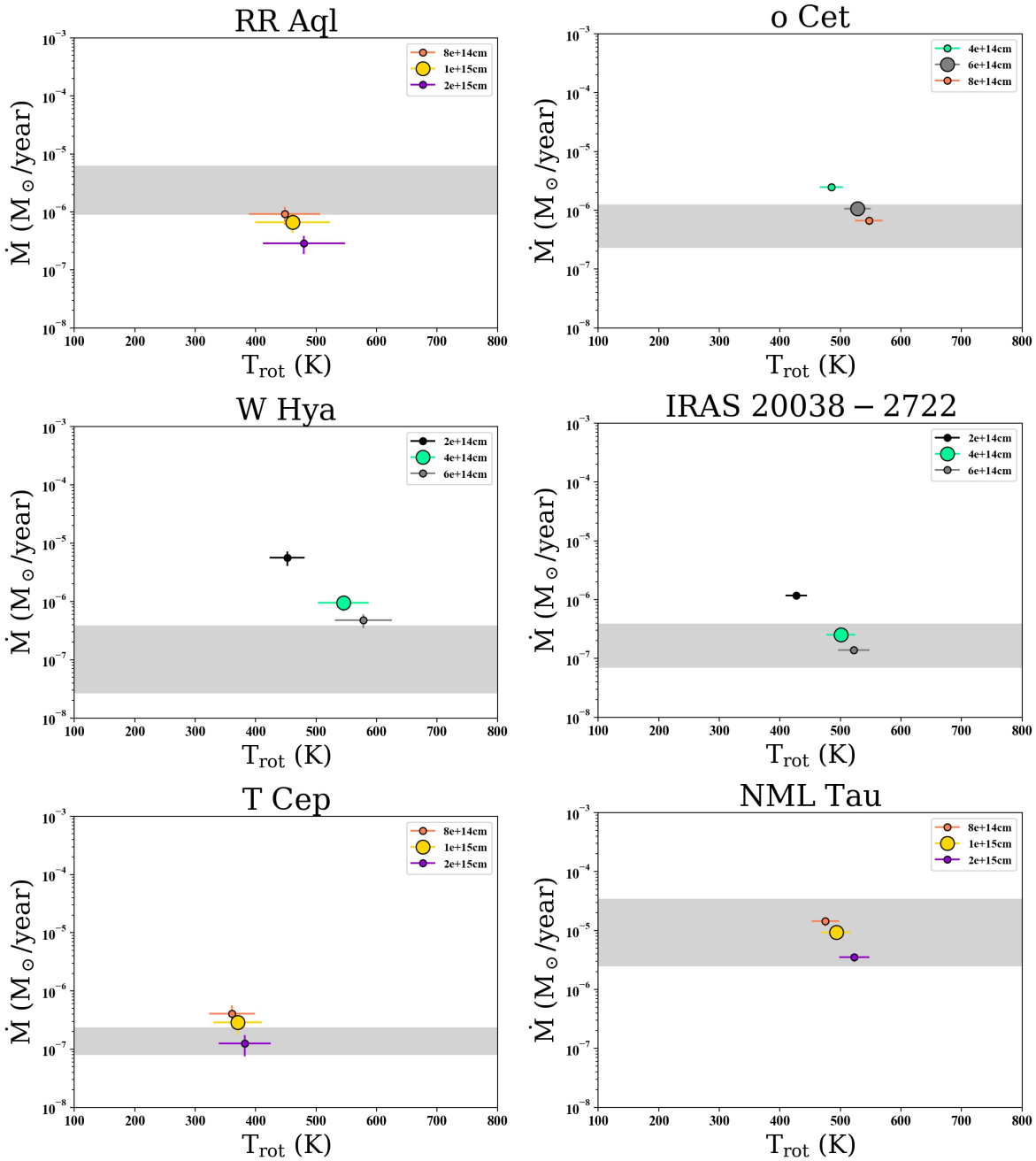

FIGURE C.11: Plots of $\dot{M}$ vs T_{rot}. In each panel three different points, corresponding to three different r_{CO} are shown. The point of the r_{CO} shown in Table 4.1 is bigger than the rest. The grey region represents the interval of mass-loss rates covered by previous works found in bibliography. For more details see Section 4.5. The linear radii explored are the same as the ones shown in Fig. C.9.

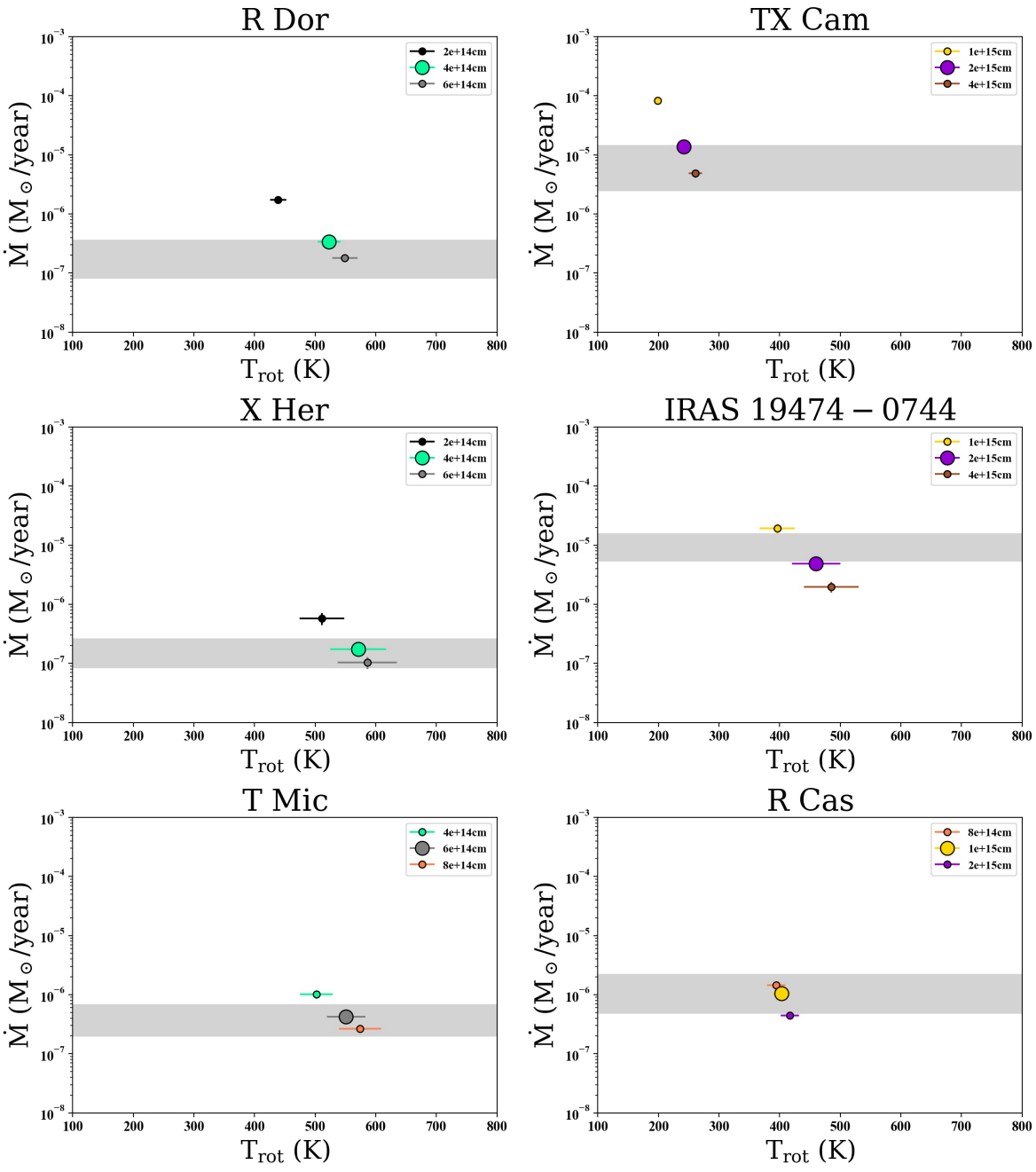

FIGURE C.11: Continued.

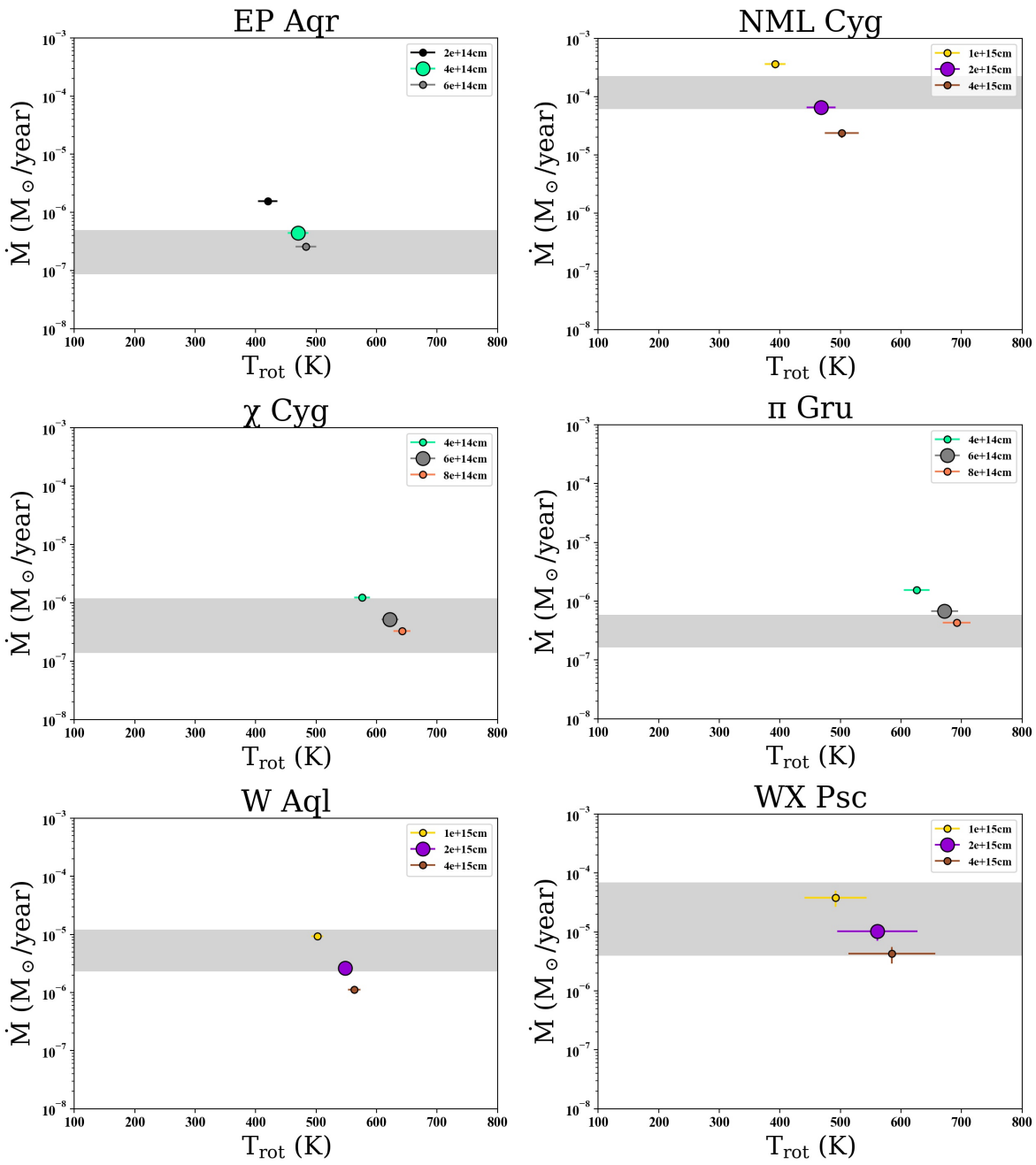

FIGURE C.11: Continued.

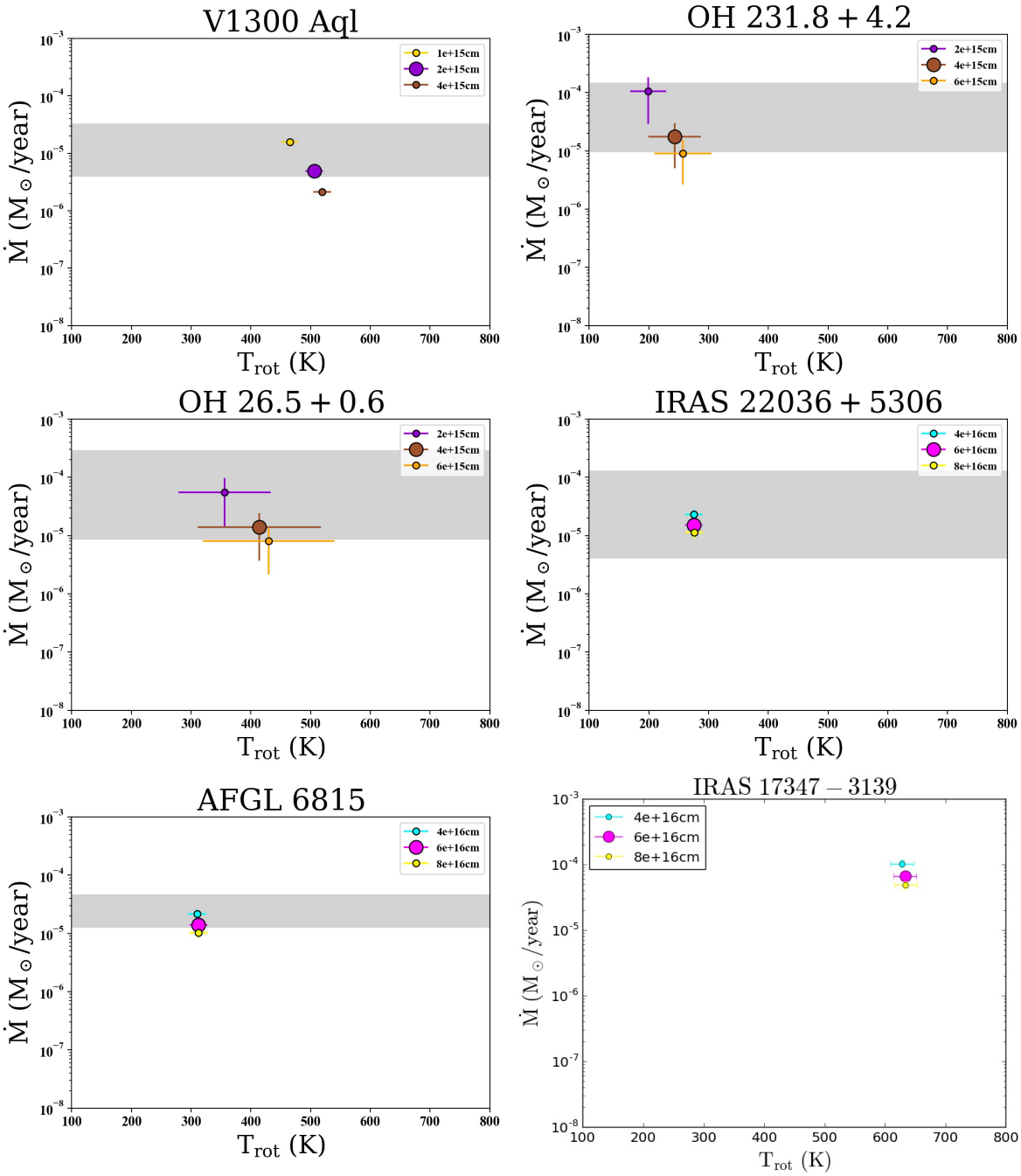

FIGURE C.11: Continued.

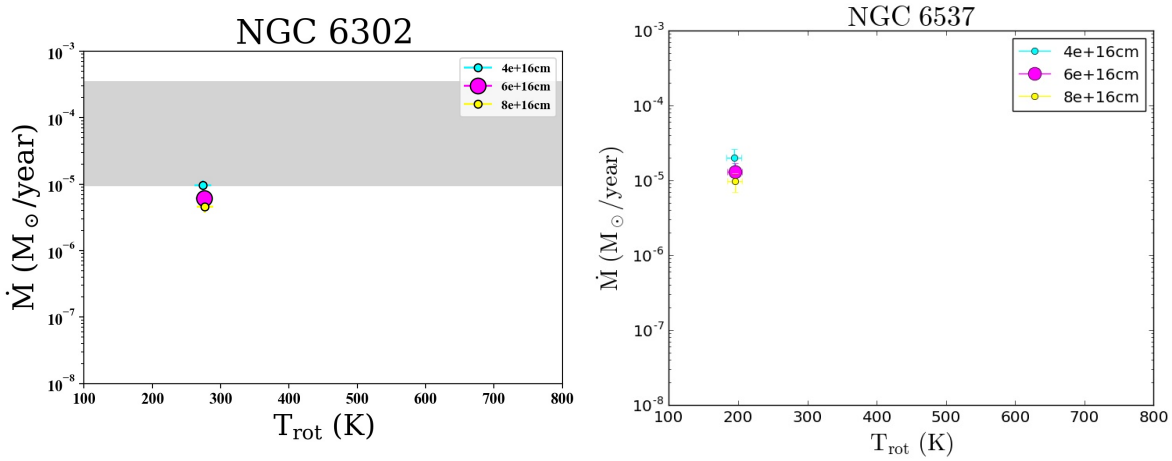

FIGURE C.11: Continued.

C.4.2 Opacity and mass-loss rate plots: SPIRE

In this section we present analogue plots to the one shown in previous section but regarding SPIRE data.

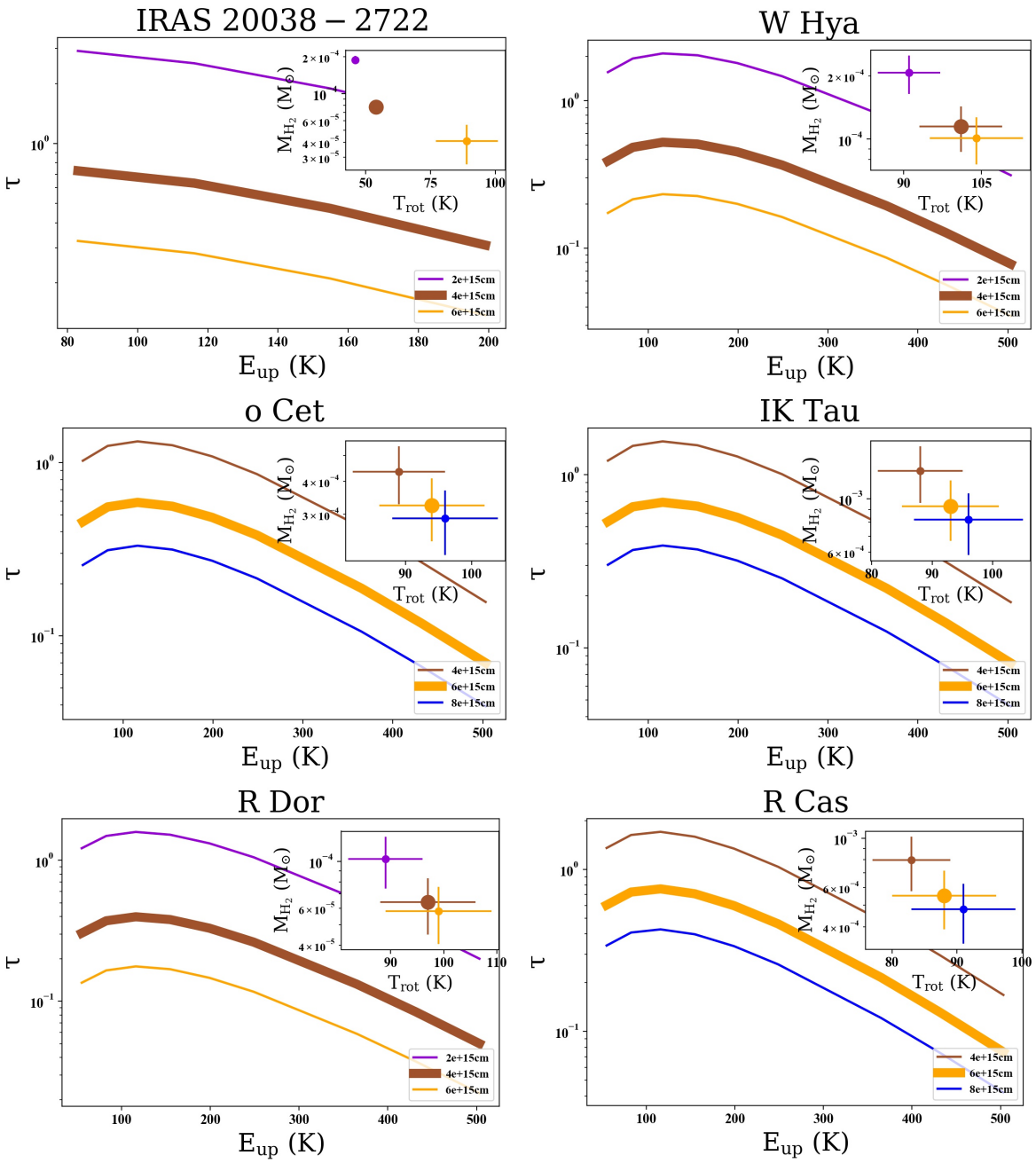

FIGURE C.12A: Similar to Fig. C.9 but regarding O-rich sources studied in Chapter 6.

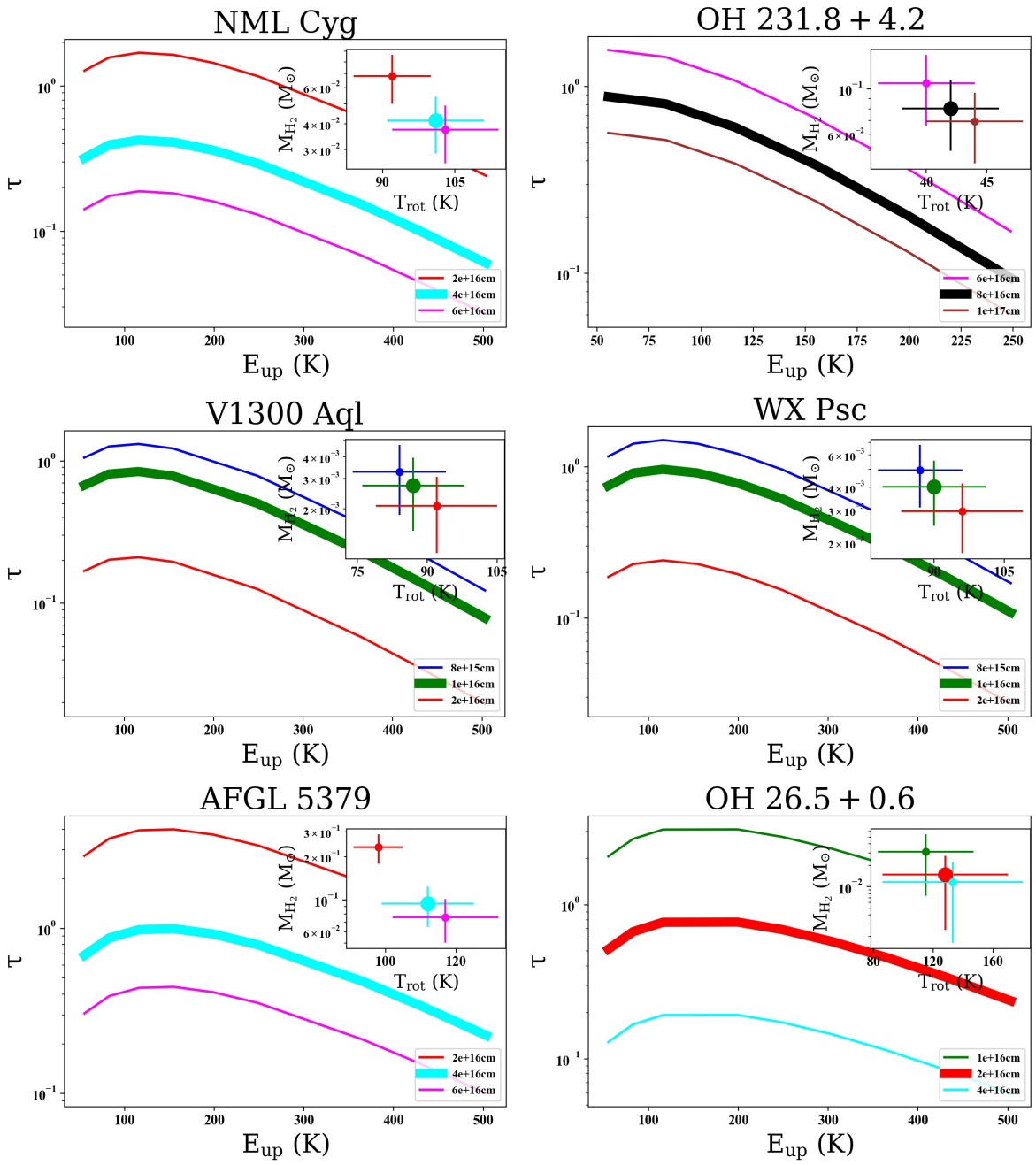

FIGURE C.12: Continued. O-rich sources.

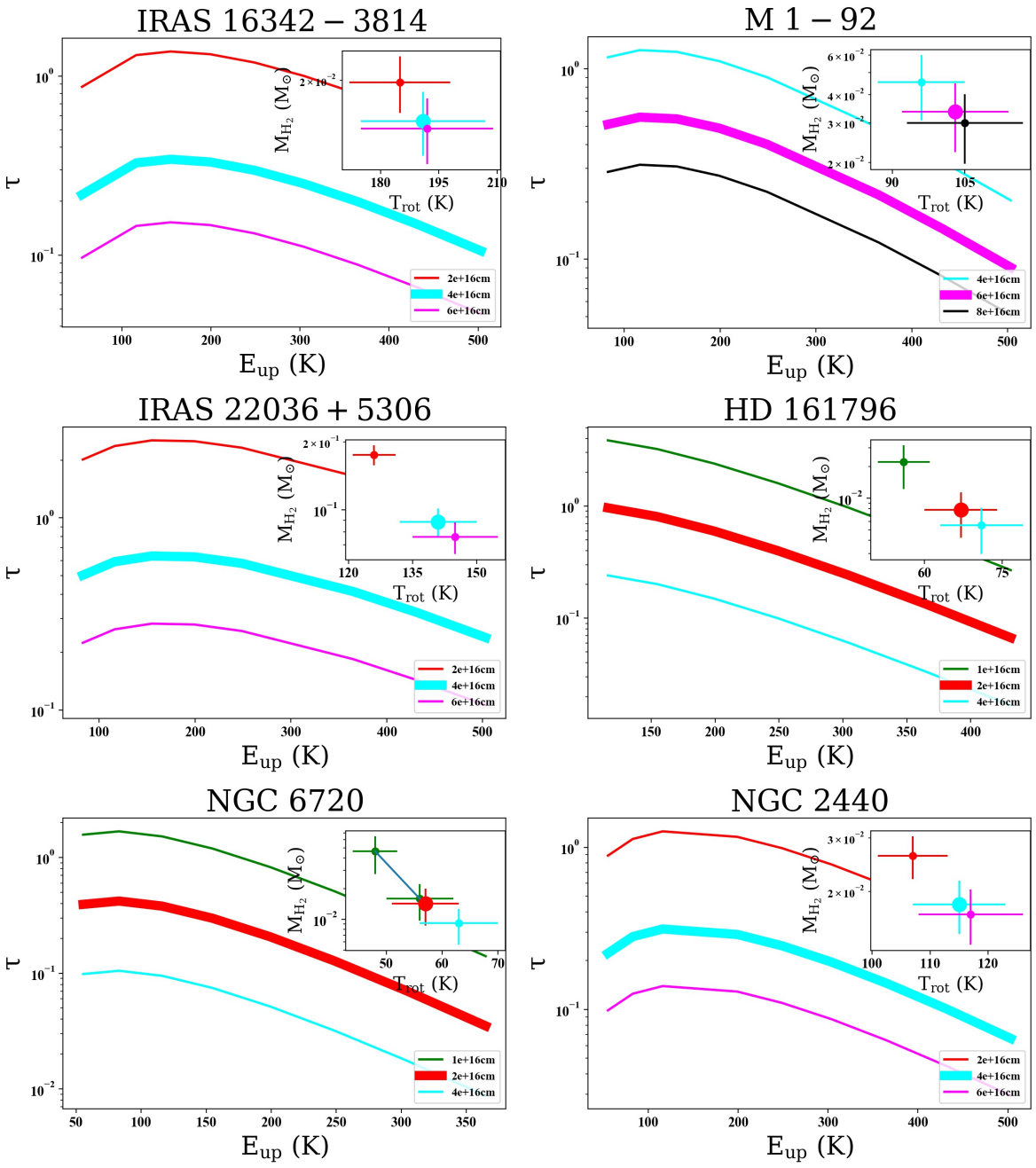

FIGURE C.12A: Continued O-rich sources.

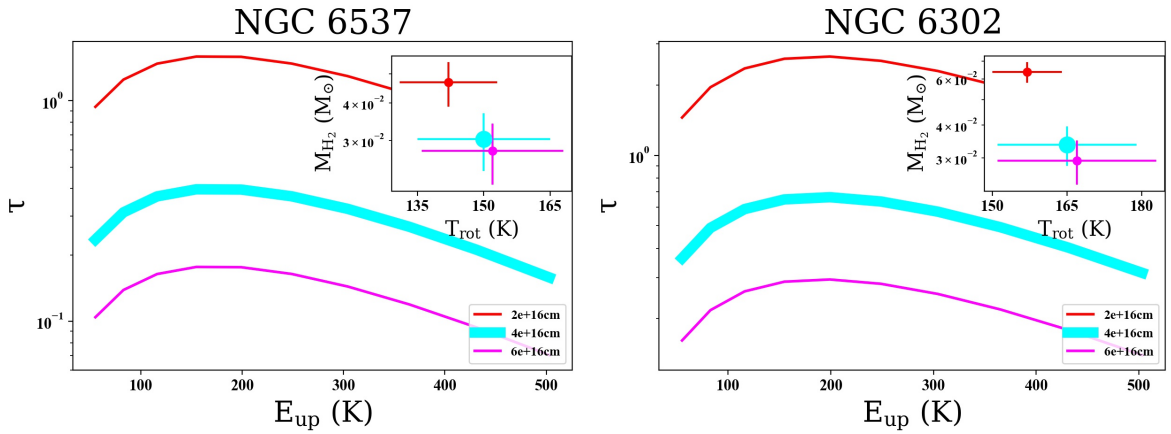

FIGURE C.12A: Continued O-rich sources.

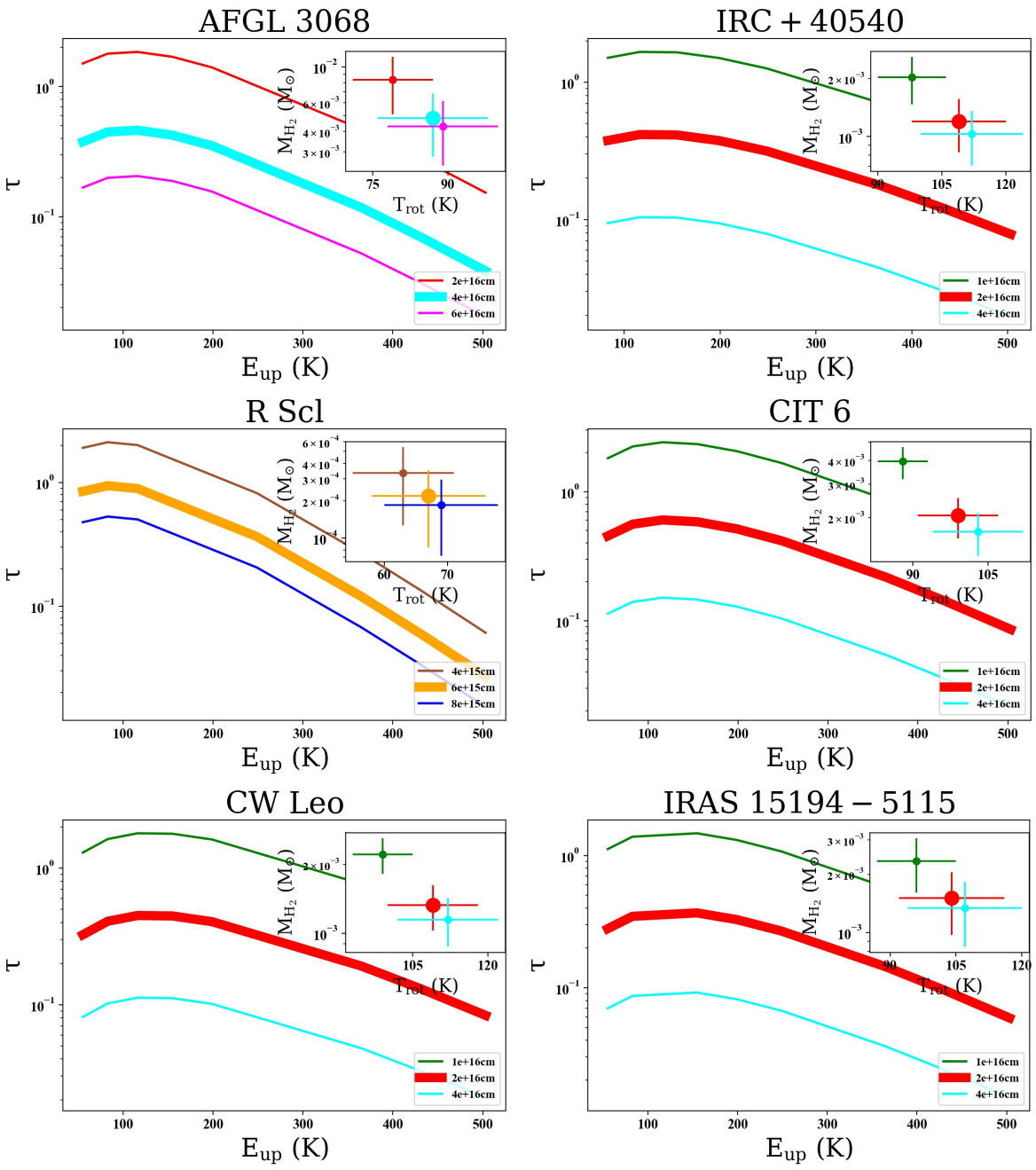

FIGURE C.13A: Similar to Figs. C.12a-C.12a regarding C-rich sources.

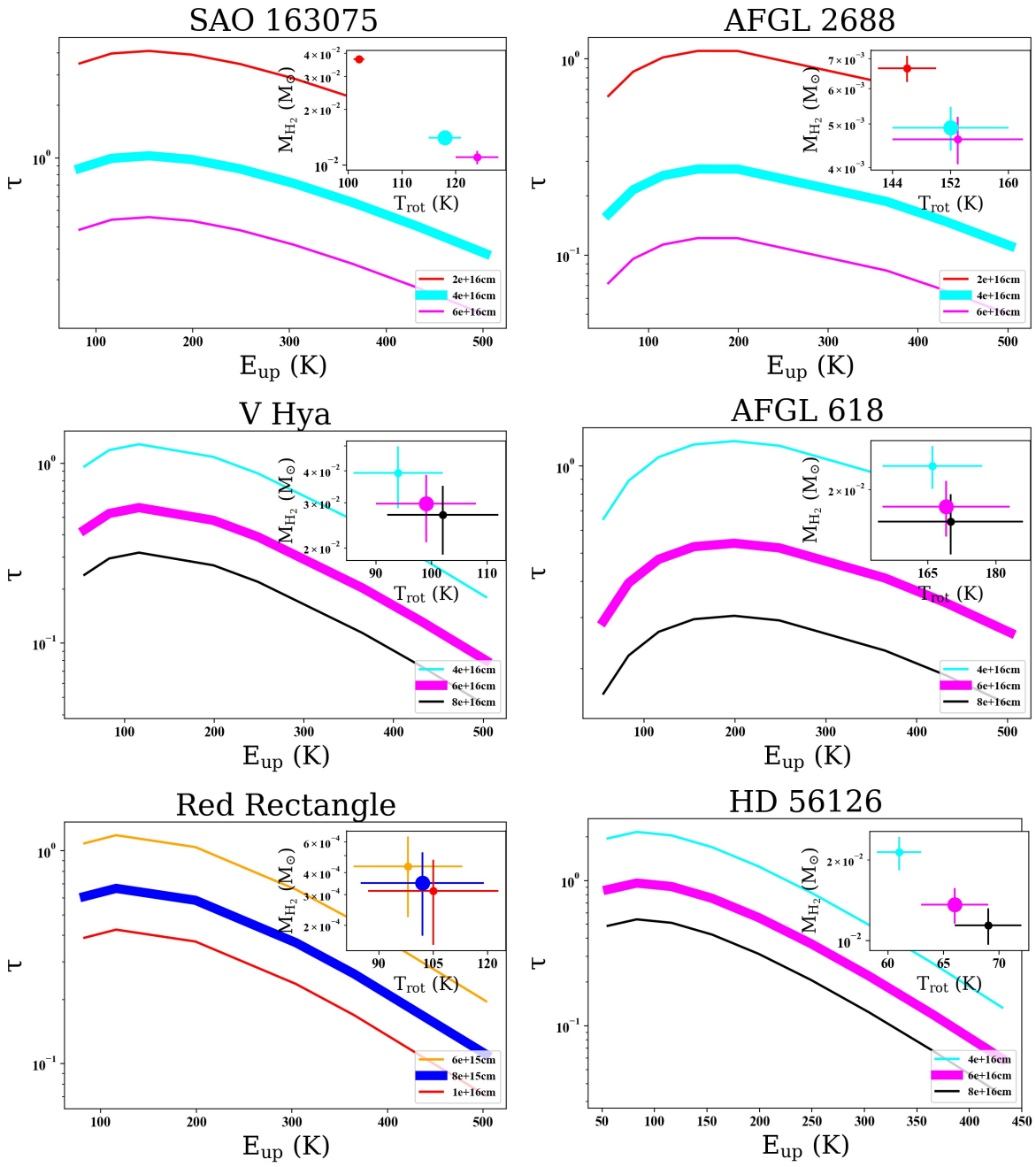

FIGURE C.13A: Continued C-rich sources.

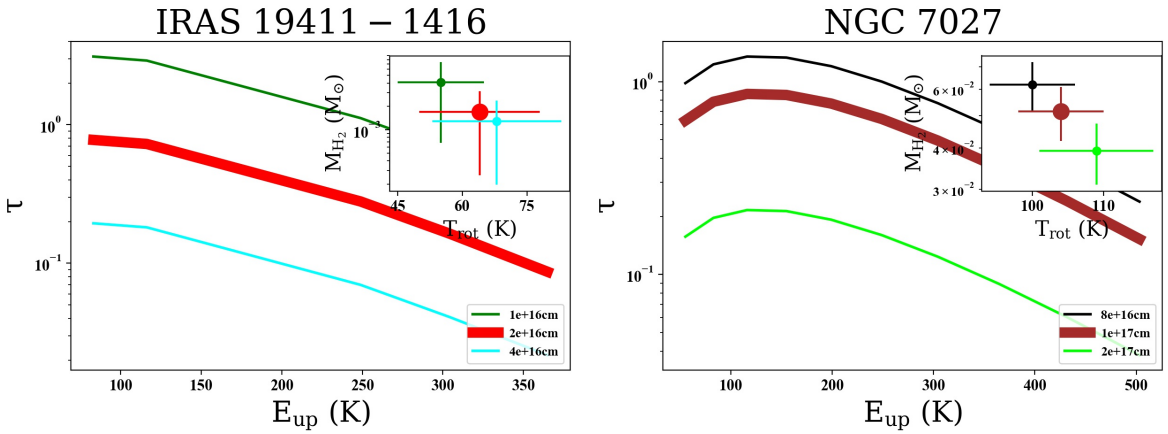

FIGURE C.13A: Continued C-rich sources.

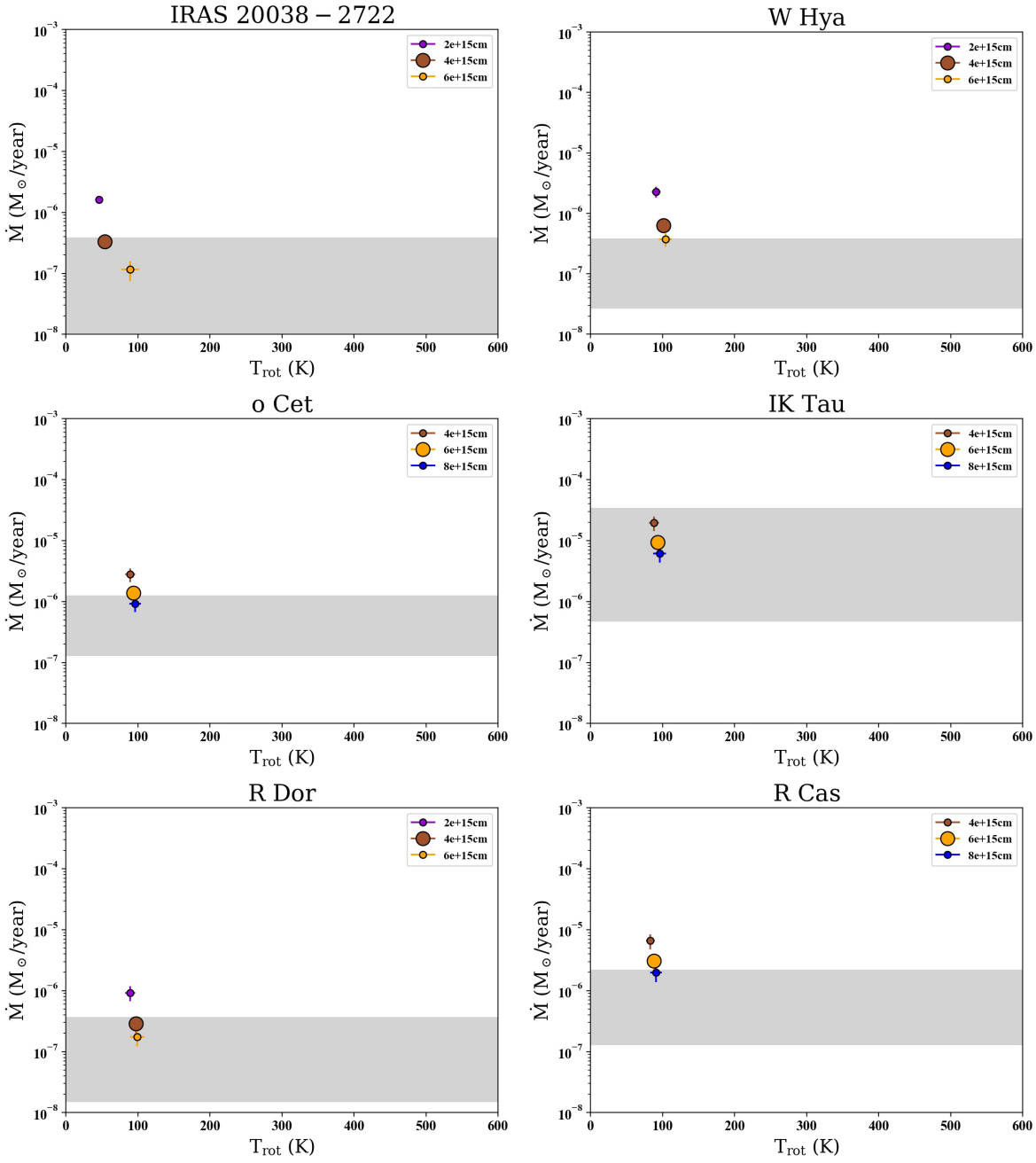

FIGURE C.14A: Similar to C.11 but regarding O-rich sources studied in Chapter 6.

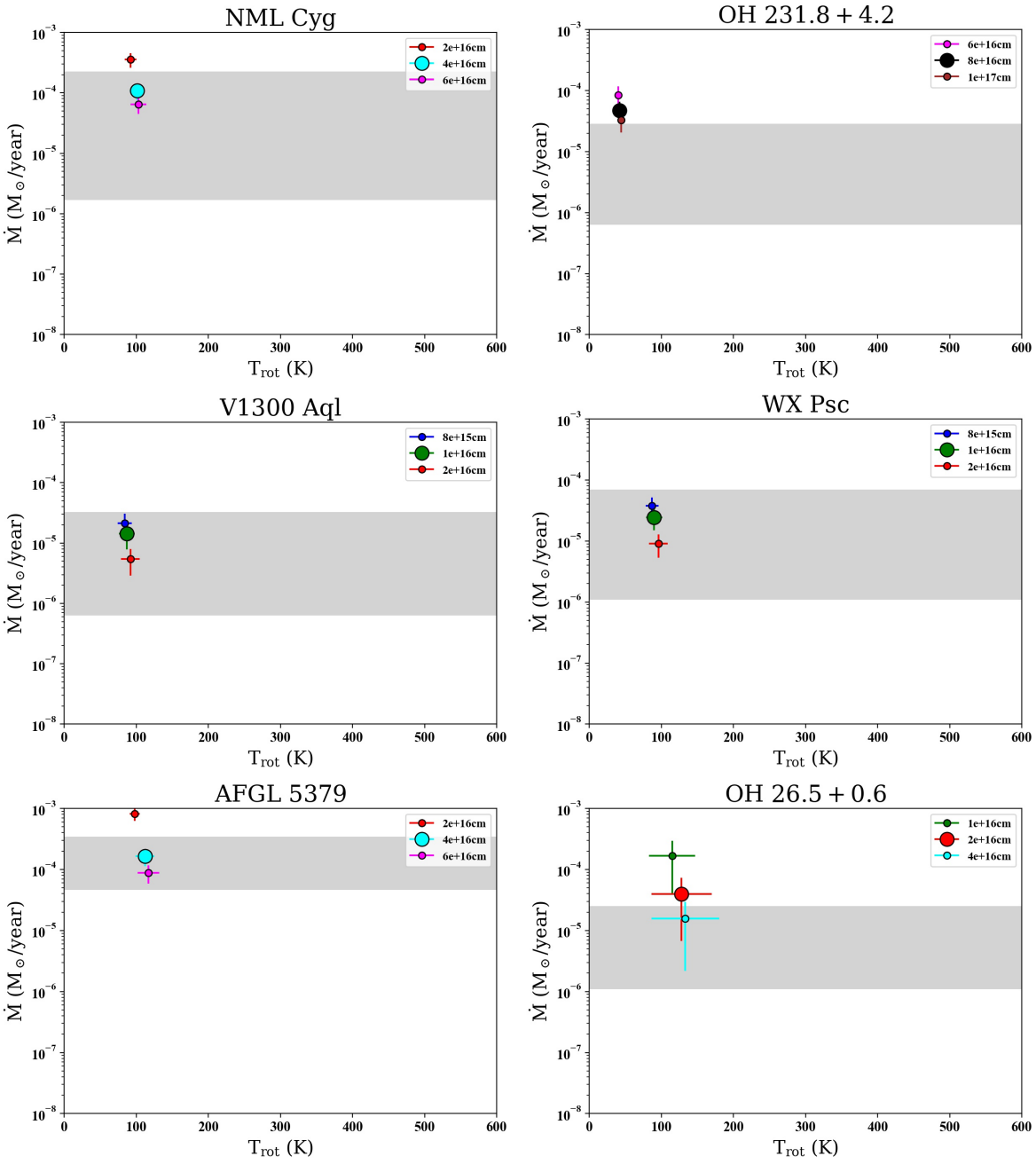

FIGURE C.14A: Continued O-rich sources.

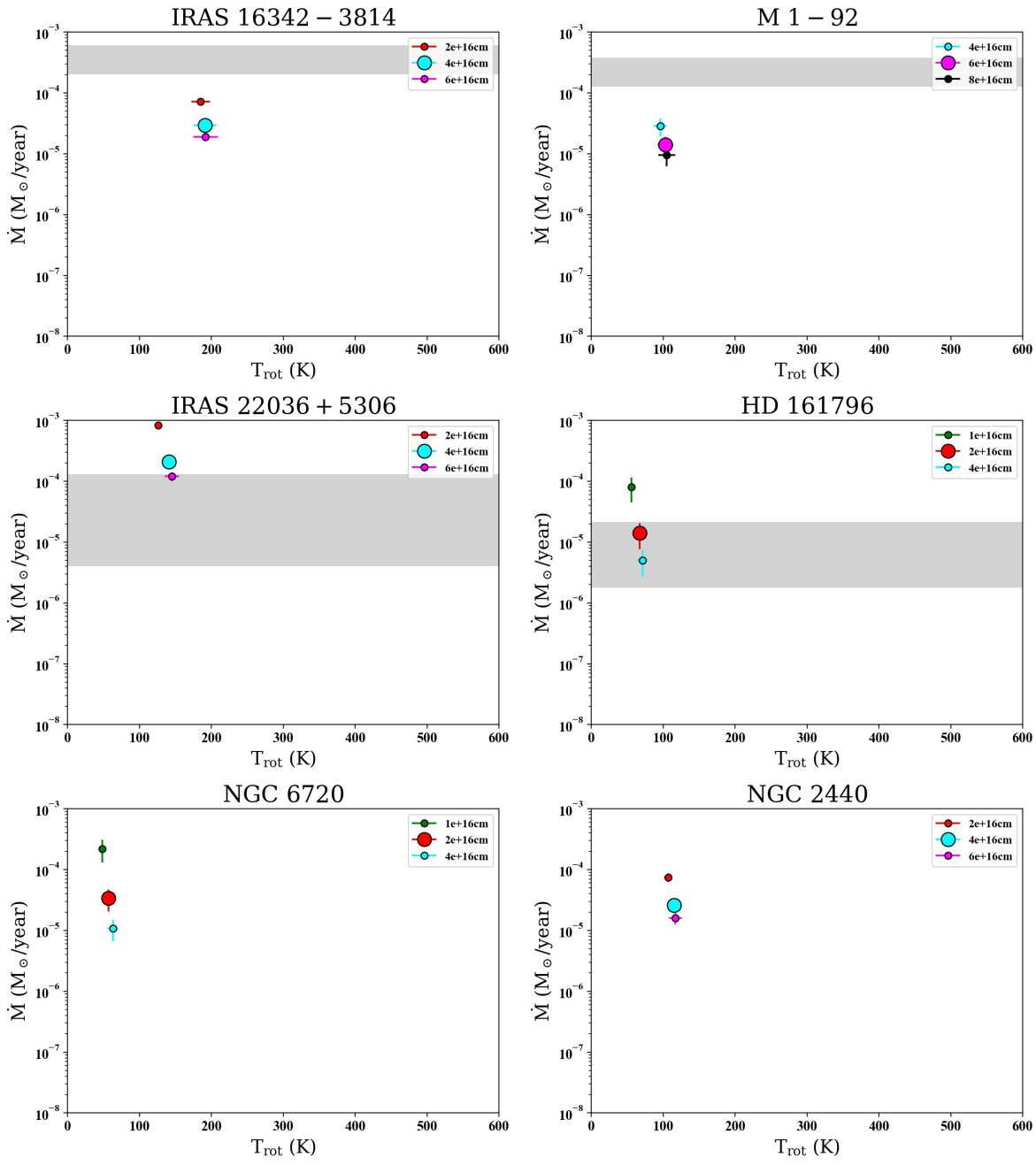

FIGURE C.14A: Continued O-rich sources.

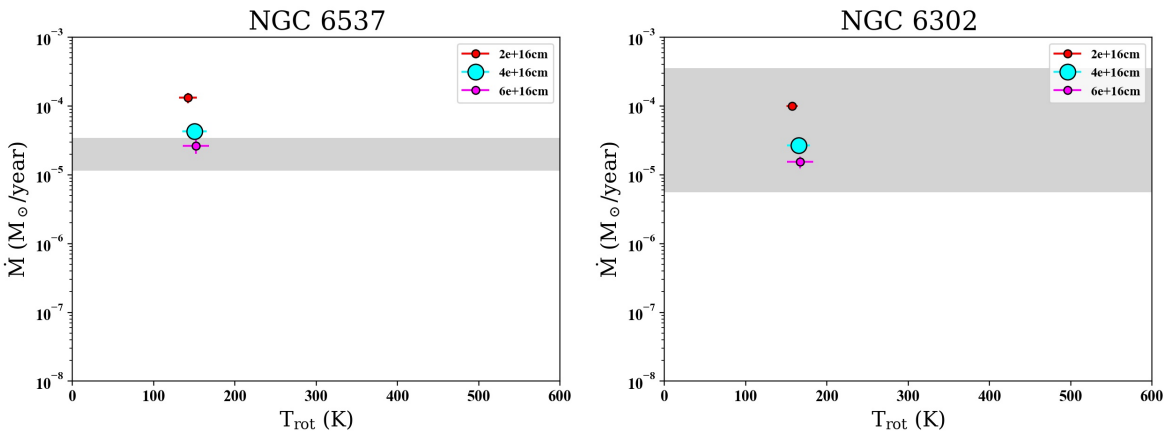

FIGURE C.14A: Continued O-rich sources.

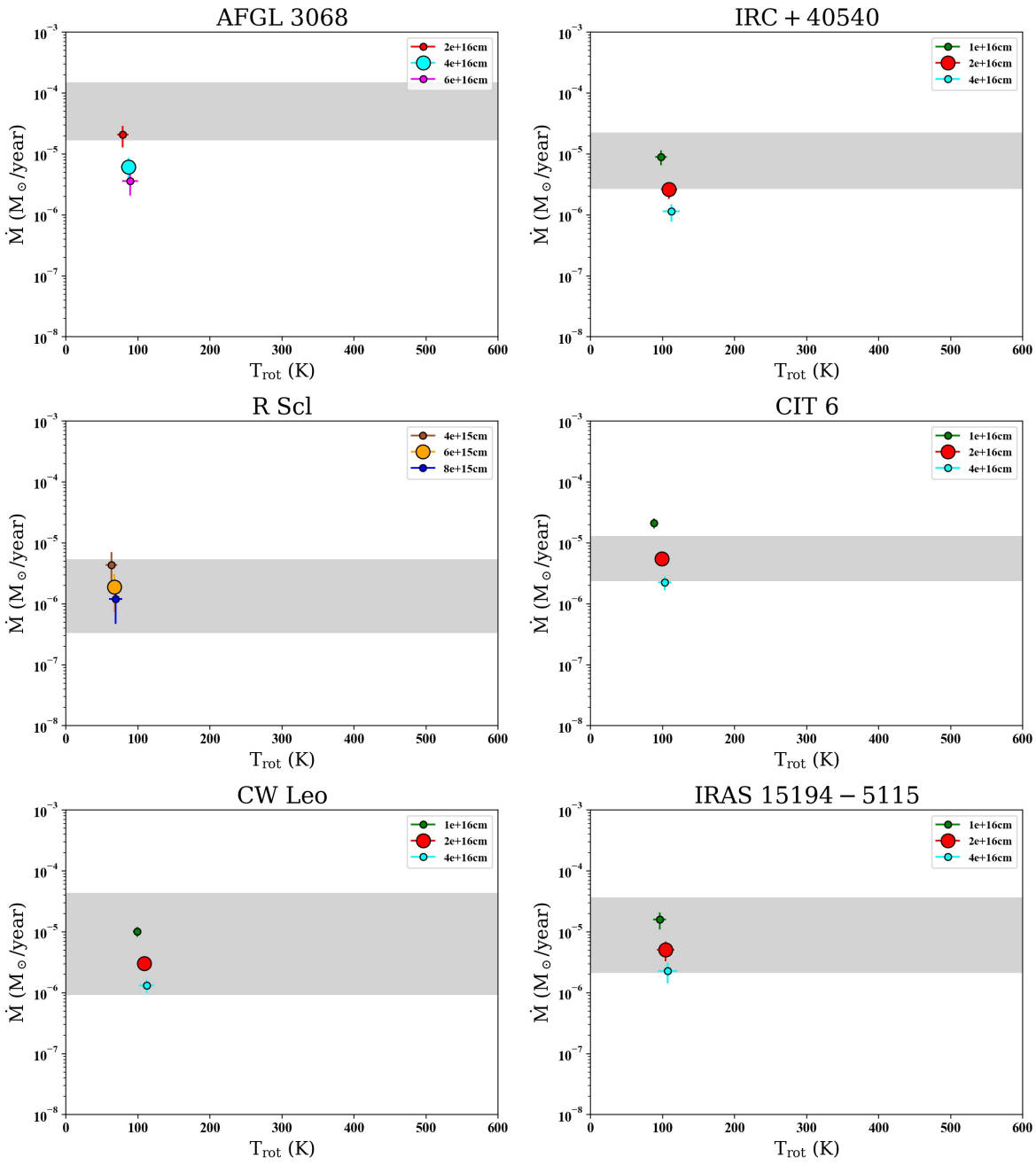

FIGURE C.15A: Similar to Figs. C.14a-C.14a regarding C-rich sources.

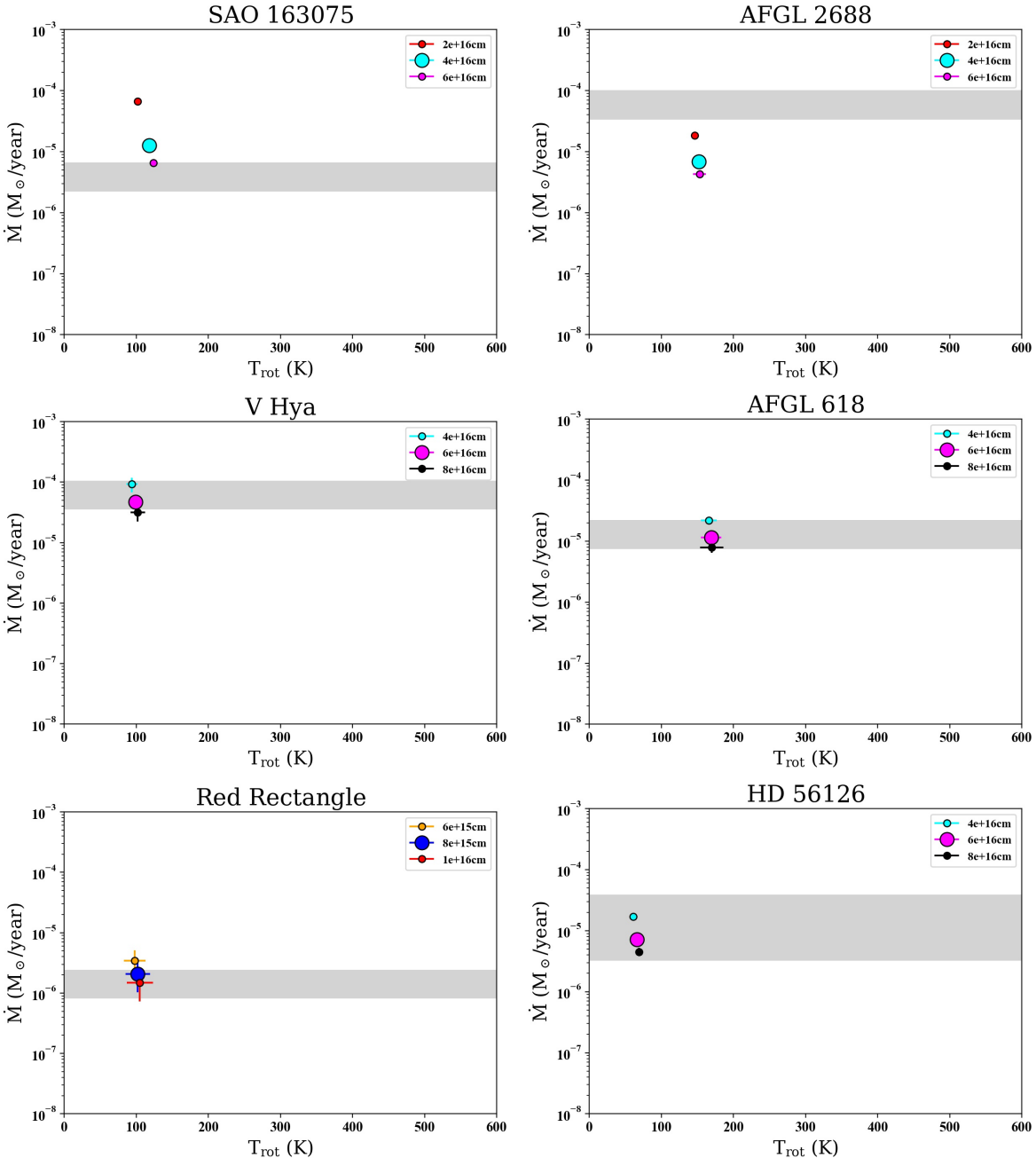

FIGURE C.15A: Continued C-rich sources.

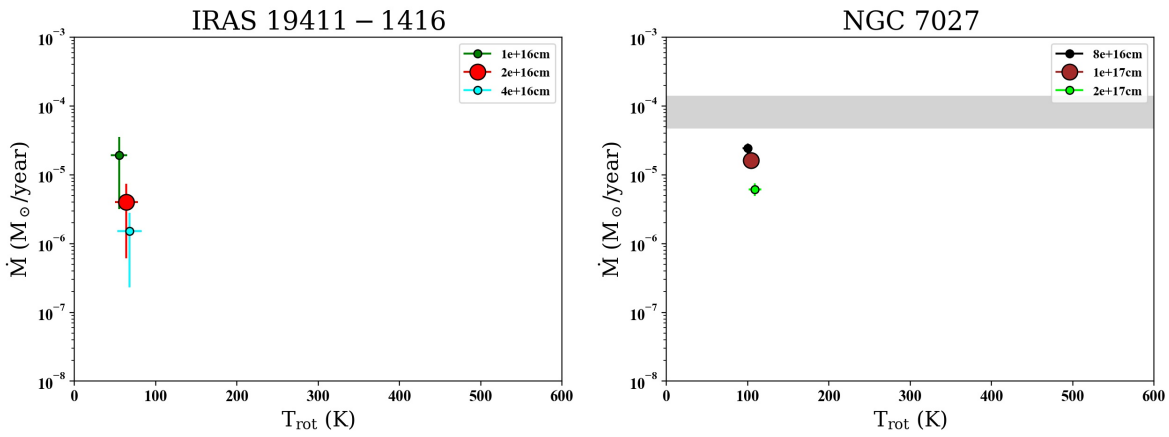

FIGURE C.15A: Continued C-rich sources.

Appendix D

Appendix IV. Publications

Astronomy & Astrophysics manuscript no. THROES-catalogueFinalVersion
November 6, 2018

THROES: a caTalogue of HeRschel Observations of Evolved Stars

I. PACS range spectroscopy

J. Ramos-Medina[1], C. Sánchez Contreras[1], P. García-Lario[2], C. Rodrigo[1], J. da Silva Santos[1] and E. Solano[1]

[1] Department of Astrophysics, Astrobiology Center (CSIC-INTA), ESAC campus, PO Box 78, 28691 Villanueva de la Cañada, Madrid, Spain
e-mail: jramos@cab.inta-csic.es
[2] European Space Astronomy Centre, European Space Agency, PO Box 78, 28691, Villanueva de la Cañada, Madrid, Spain

Received September 13, 2017; accepted October 27, 2017

ABSTRACT

This is the first of a series of papers presenting the THROES (A caTalogue of HeRschel Observations of Evolved Stars) project, intended to provide a comprehensive overview of the spectroscopic results obtained in the far-infrared (55-670 μm) with the *Herschel* space observatory on low-to-intermediate mass evolved stars in our Galaxy. Here we introduce the catalogue of interactively reprocessed PACS (Photoconductor Array Camera and Spectrometer) spectra covering the 55-200 μm range for 114 stars in this category for which PACS range spectroscopic data is available in the *Herschel* Science Archive (HSA). Our sample includes objects spanning a range of evolutionary stages, from the asymptotic giant branch to the planetary nebula phase, displaying a wide variety of chemical and physical properties. The THROES/PACS catalogue is accessible via a dedicated web-based interface (https://throes.cab.inta-csic.es/) and includes not only the science-ready Herschel spectroscopic data for each source, but also complementary photometric and spectroscopic data from other infrared observatories, namely IRAS (Infrared Astronomical Satellite), ISO (Infrared Space Observatory) or AKARI, at overlapping wavelengths. Our goal is to create a legacy-value *Herschel* dataset that can be used by the scientific community in the future to deepen our knowledge and understanding of these latest stages of the evolution of low-to-intermediate mass stars.

Key words. evolved stars – infrared radiation – PACS spectroscopy – catalogue – Herschel

1. Introduction

Herschel [1] (Pilbratt et al. 2010), launched in May 2009, has provided a new vision of the whole Universe in the far infrared (FIR) thanks to the capabilities of the three instruments on board: HIFI (The Heterodyne Instrument for the Far-Infrared) (de Graauw et al. 2010), SPIRE (Spectral and Photometric Imaging Receiver) (Griffin et al. 2010) and PACS (Poglitsch et al. 2010). In particular, *Herschel* has been extremely useful in the study of the complex physical and chemical processes that take place in the final stages of stellar evolution. For example, observations from the MESS (Mass-loss of Evolved Stars) observing programme (Groenewegen et al. 2011) have demonstrated the capability of *Herschel* to image the circumstellar envelopes (CSEs) of evolved stars and the interaction regions between the stellar winds and the interstellar medium with unprecedented detail. In the spectroscopic area, studies have addressed the analysis of the circumstellar forsterite (e.g. de Vries et al. (2011)) and the CO line emission (e.g. De Beck et al. 2010; Danilovich et al. 2015; Maercker et al. 2016). The detection of rotational emission lines of OH^+ for the first time in three planetary nebulae (PNe) (Aleman et al. 2014) with observations taken as part of the HerPlans observing programme (Ueta et al. 2014), or the detection of warm water vapour around IRC +10216 (Decin et al. 2010), the closest C-rich star to our solar system, are also good examples of the contribution of *Herschel* to our understanding of the chemical complexity of these CSEs and can also be considered as important highlights of the mission in the field.

Towards the end of their lives, low-to-intermediate mass stars (1 $M_\odot \leq$ M $\leq$ 8 $M_\odot$) have burnt up their central hydrogen and helium, leaving a quiescent C-O core with H and He fusion reactions taking place in thin shells surrounding the inner core. These objects are ascending the asymptotic giant branch (AGB), a phase of stellar evolution during which their atmospheres expand and cool down, characterized by an intense mass loss (from 10^{-7} to 10^{-4} $M_\odot$ yr^{-1}) that results in the formation of a CSE of gas and dust around the central star, which emits very strongly in the mid-to far-infrared wavelengths (Habing 1996). Once the star terminates the AGB phase, the mass-loss rate suddenly decreases and the temperature of the central object becomes, progressively, high enough to induce the onset of the ionization of the gas in the surrounding CSE. If the temperature increases on a timescale shorter than the dispersion time of the matter previously ejected, we will observe an ionized planetary nebula (PN) (Kwok 2005).

The intermediate stage between the AGB and PN phases is called the post-AGB phase. This phase is also known as pre-PN phase, although it is not clear whether all post-AGB stars will develop a PN. During the post-AGB phase, the shell, formed in the AGB phase, detaches from the central star, the spherical symmetry is broken, and fast bipolar or multi-polar winds appear

[1] Herschel is an ESA space observatory with science instruments provided by European-led Principal Investigator consortia and with important participation from NASA.

(see e.g. Balick & Frank 2002, for a review). This is a very short-lived phase (~ 1000 years) and, as a consequence of it, a not very well understood stage of stellar evolution.

The infrared and sub-millimetre regions offer a rich variety of diagnostic, atomic, ionic, molecular, and solid-state spectral features, and are particularly well suited to study the complex physical and chemical properties found in AGBs, post-AGBs, and PNe, which may be very different from source to source, depending on critical parameters like the initial mass or the metallicity. A large sample of low- and intermediate-mass evolved stars in our Galaxy were observed by the PACS instrument on-board *Herschel* under many different observing programmes, and the associated automatically pipeline-processed data are now publicly available from the Herschel Science Archive[2](HSA) after the end of the proprietary period of one year. In the vast majority of cases, unfortunately, the PACS spectroscopy pipeline products in the HSA cannot be considered science-ready, and they would strongly benefit from dedicated interactive data reduction to help remove the residual instrument artefacts and to improve the absolute flux calibration as a necessary further step in order to become publication-quality products.

With this aim, we have interactively processed in a systematic and homogeneous way all PACS range spectroscopic observations contained in the HSA corresponding to stars that can be identified as low- or intermediate-mass evolved stars, with the exception of a small subset of nearby sources that show very extended emission and a few cases where the unchopped observing mode was used, as they require a special case-by-case treatment, which is beyond the scope of this project. The result of this interactive data reduction effort has been used to compile the first version of THROES: "a caTalogue of HeRschel Observations of Evolved Stars", through which our final data products are made available to the community for scientific exploitation. We are currently working on a second version of the THROES catalogue that will also incorporate spectroscopic data from the Herschel/SPIRE instrument (Ramos Medina et al., in preparation).

This paper is organized as follows. In Section 2 we describe how the observations were performed, the building of the THROES sample, and the main characteristics of the sources included in it. In Section 3 the main data reduction steps applied are described. In Section 4, we introduce the contents of the THROES catalogue and its web interface. In Section 5, we try to characterize the quality of our science data products through comparisons with the standard pipeline products contained in the HSA and with observations taken by other space-based facilities in the past, like IRAS, AKARI, and ISO. The final summary is given in Section 6.

2. Observations

2.1. PACS spectroscopy

2.1.1. The PACS spectrometer

The PACS spectrometer covers nominally the wavelength range from 51 to 210 μm in two different channels that operate simultaneously in the so-called blue (51 to 105 μm) and red (102 to 220μm) bands. The field of view (FoV) covers a 47"×47" region in the sky using an array composed of 5×5 square spatial pixels (hereinafter ″spaxels"), each one 9.4"×9.4" in size, with 16 pixels along the spectral dimension that are shifted to sample the whole wavelength range to be covered. PACS provides a resolving power between 940 and 5500 (i.e. a spectral resolution of 75 to 300 km/s) depending on the wavelength range. As shown in the PACS Observer's Manual [3], the PSF (point spread function) of the PACS spectrometer ranges from ~ 9" in the blue band to ~ 14" in the red band.

2.1.2. Astronomical observing templates (AOTs)

Two different observation schemes or AOTs (astronomical observing templates) were offered to the users of the PACS spectrometer. The LineScan Mode was intended for the observation of one or a limited number of narrow spectral line features, while the RangeScan Mode was optimized for the observation of broad spectral lines or features, including the possibility to observe the full spectral range of the selected orders in 'SED (Spectral Energy Distribution) mode'. Both configurations generate data in a 3D cube format (flux versus wavelength and spatial position).

2.1.3. Observing modes

For each of the AOTs above described, PACS also offered two different observing modes: "Standard chopping-nodding mode" (hereafter 'Chop/Nod') and "Unchopped grating scan mode" (hereafter 'Unchopped'); the difference between these two modes lies in the observing technique used to allow the telescope and astronomical background to be subtracted from the signal coming from the source. 'Chop/Nod' observations point, alternatively, to the On- and Off- positions and collect the On- and Off- data in a common 'ObsID'. The 'Unchopped' ones take one observation for the On-source position and another different observation for the Off-source pointing; they are then processed independently. After that, the user has to carry out the required On-Off subtraction.

2.1.4. Pointing modes

Every observation was also defined by the pointing mode, which could be 'pointed' using a single pointing on the source; or 'mapping', a composition of different pointings that, combined, were used to generate maps with improved beam sampling and a larger FoV. More information about the different instrument AOTs, observing, and pointing modes can be found in the PACS Observer's Manual.

2.2. Building the THROES sample

Herschel successfully performed more than 37,000 science observations during its operational lifetime. The full list can be found in the Herschel Observing Log, available at `http://herschel.esac.esa.int/obslog/`. The Herschel Observing Log contains a total of 530 PACS spectroscopy observations executed successfully, associated to 44 science proposals that were submitted under the 'Evolved Stars/Planetary Nebulae/Supernova Remnants' category by the original proposers. Out of these original 530 observations, 347 were identified as corresponding to low- or intermediate-mass stars, according to the information available in the bibliography, of which a subset of 258 were taken in PACS RangeScan mode.

All these observations were originally included in the THROES sample. However, in the final version of the catalogue,

[2] http://archives.esac.esa.int/hsa/whsa.

[3] herschel.esac.esa.int/Docs/PACS/pdf/pacs_om.pdf.

we discarded 7 observations of a small group of extended, nearby sources taken in PACS 'mapping' mode, as they would require a dedicated reprocessing adapted to the specific characteristics of each source, an effort that in most cases has been or is being carried out by the research groups that requested the original observations. Similarly, we excluded 20 additional observations taken in 'Unchopped' mode from our reprocessing as these are in general more complex observations affected by technical problems that would deserve a special case-by-case treatment, beyond the scope of this project. Finally, 11 observations failed during the reprocessing for different reasons and were not included in this first version of the THROES catalogue. In particular, one observation of the planetary nebula NGC 6153 (ObsID 1342249998) and another one of NGC 7662 (ObsID 1342246642) both failed because of the too narrow spectral range covered, centred at the forbidden [O III] emission line at 52 μm, at the edge of the spectral coverage of the PACS blue detector where the spectral response function is not well characterized; six observations (ObsIDs: 1342230895 and 1342230905 to 1342230909) associated to the Red Rectangle failed because they cover very narrow spectral regions affected by leakage; an observation of the post-AGB star HR 4049 (ObsID 1342247550), covering a very short wavelength region between 103 and 116 μm, was extremely noisy in the red channel and failed reprocessing in the blue channel; and finally, we could not reprocess two very long exposure SED mode observations of the proto-planetary nebula IRAS 01005+7910 (ObsIDs 1342247005 and 1342247006) as they demanded too much memory, exceeding the capacity of our local hardware environment. In summary, a total of 220 Herschel observations (ObsIDs) were finally considered for interactive data reduction, corresponding to 114 individual targets (see full list in Table 1), comprising a total of 440 individual spectral ranges.

2.3. Characteristics of the THROES sample

2.3.1. Evolutionary stage and IRAS colours

Information on the evolutionary stage of each object in the THROES sample was extracted from the SIMBAD (Set of Indications, Measurements, and Bibliography for Astronomical Data) database and from the literature. Accordingly, we have classified our objects into four main groups: AGB stars, OH/IR stars (extreme O-rich AGB stars with high mass-loss rates and long variability periods), post-AGB stars (or pre-PNe), and PNe. In its current version, the catalogue contains PACS range spectra for 43 (38 %) AGB stars, 17 (15 %) OH/IR stars, 29 (25 %) post-AGB stars, and 25 (22 %) PNe (see Fig. 1).

Figure 2 shows the distribution of our targets in the IRAS two-colour diagram, where the location of various types of sources is indicated, following the original description presented by van der Veen & Habing (1988). This diagram illustrates the variety of evolutionary stages covered by the THROES sample. The AGB stars are distributed along a sequence of increasing infrared excess, which represents the evolution expected during the AGB as a result of the formation of thick and dense shells of dust and gas around these mass-losing stars, with the reddest IRAS colours corresponding to the most extreme OH/IR stars. Once the mass-loss phase ends, objects evolve towards the right in the two-colour diagram (region IV, V, and VIII in the plot), which are the areas populated by most of the sources in our sample classified as post-AGB stars and PNe, surrounded by detached cool dust shells.

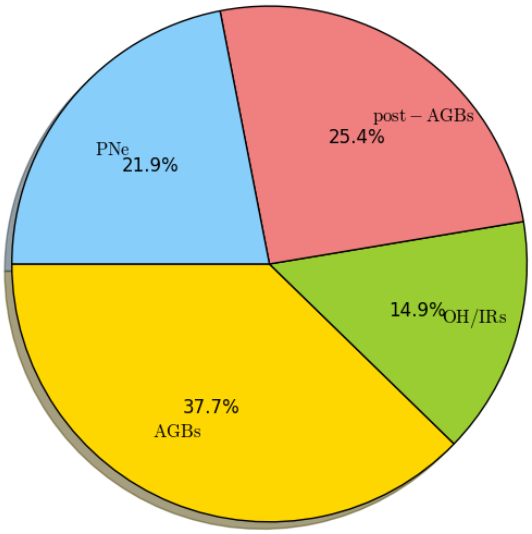

Fig. 1: Pie chart illustrating the distribution of stars in the THROES sample according to their evolutionary stage.

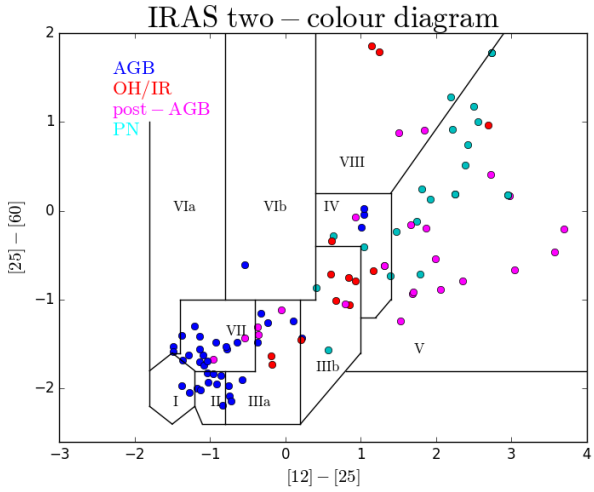

Fig. 2: IRAS colour-colour diagram of the THROES sample with good quality IRAS data (Quality Flag=3) in the 12, 25, and 60 μm bands. The diagram is divided into different boxes where sources with different characteristics and evolutionary stage are contained (see van der Veen & Habing 1988, for a detailed description).

2.3.2. Galactic distribution

The galactic distribution of the THROES sample is shown in Fig. 3. Our sources are strongly concentrated at relatively low galactic latitudes, as expected from a distant population of luminous sources concentrated in the galactic disk, although a significant number of them are also observed at high galactic latitudes, corresponding to the small fraction of bright, nearby sources. Interestingly, most of the OH/IR stars are found at very low galactic latitudes, as they correspond to a population of stars that are proposed to represent the most massive precursors of PNe (García-Hernández et al. 2007).

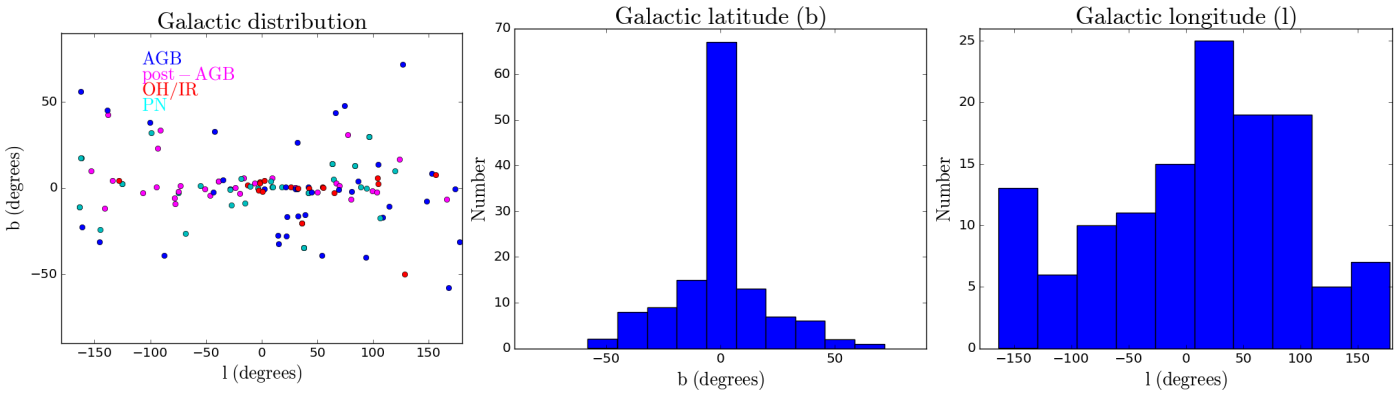

Fig. 3: Galactic distribution of the THROES targets. Colour code as in Fig. 2.

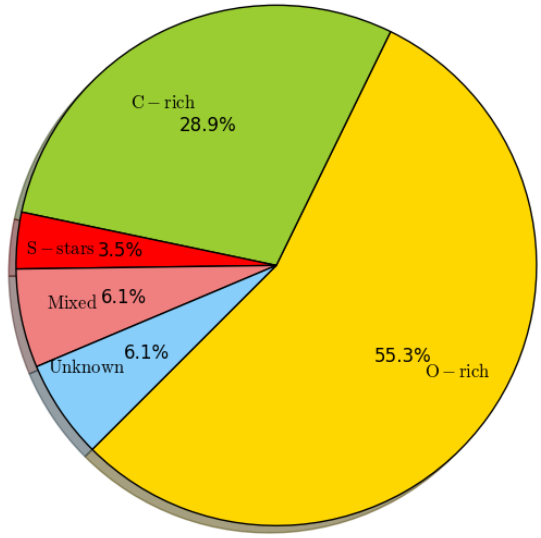

Fig. 4: Pie chart illustrating the distribution of stars in the THROES sample according to their dominant chemistry.

2.3.3. Dominant chemistry

Asymptotic giant branch stars are generally classified as O-rich (M-type) or C-rich (C-type) based on the C/O ratio found in their outer envelope. Objects with C/O > 1 are considered C-rich stars under this criterion while objects with C/O < 1 are considered O-rich stars. Those sources showing C/O ratios of approximately one. are denoted as S-stars. In addition, there are also objects that present chemical indicators from both kinds of chemistries, such as the simultaneous presence of crystalline silicates, typical of O-rich chemistry, and policyclic aromatic hidrocarbons (PAHs), expected in C-rich targets, in their mid-infrared spectra. The C/O ratio in this kind of source may be different depending on the region of the source considered. Some of them are known to be objects in transition between O-rich and C-rich objects (Herwig 2005); others display a strong bipolar morphology, and may be surrounded by disks that could explain the mixed chemistry observed. In our sample, 29% of sources are C-rich stars, 55% are O-rich stars, 3% are S-stars, 7% are sources with mixed chemistry, and 6% are sources with unknown chemistry (see Fig. 4).

3. Data reduction

The data available in the HSA have been generated using the latest version of the Standard Product Generator (SPG), an automated pipeline that takes the data from level 0 (raw) to level 2 (spectral cubes). At the time of starting this project, the archive was populated with products generated with HIPE 13.0.0. A complete explanation of the pipeline processing steps applied in this version of the pipeline can be found in the PACS Data Reduction Guide: Spectroscopy. [4]

Interactive data reduction can help improve the quality of the final products by applying certain data reduction tasks not available in the automated pipeline because they require a direct interaction of the user. Therefore, we used HIPE 13.0 and version 65 of the PACS calibration files to interactively reprocess all the observations in our sample, introducing those tasks that at the moment of starting this project were not applied by the standard data reduction pipeline (version 13 at that time), with the aim of obtaining better quality products than those offered by the pipeline.

For PACS range spectroscopy observations, the interactive data reduction tasks that we have applied to improve the quality of the data can be split into two main groups:

- i) tasks applied to the spectral cubes before the level 2 data are generated, so-called, interactive re-processing.
- ii) tasks applied to the level 2 data products to extract the best 1D spectrum, so-called, post-processing.

The interactive re-processing tasks comprise:

- FlatField correction: This correction fits an n-grade polynomium to the PACS spectra to obtain a higher signal-to-noise ratio (S/N) and a better shape of the continuum.
- Telescope background correction: This correction uses the telescope background emission to flux calibrate the spectra instead of using the relative spectral response function (RSRF) applied in the SPG. This correction was later implemented in version 14 of the SPG pipeline.

To extract the final 1D spectrum from the level 2 data cubes, the following post-processing corrections were applied:

- Point source flux loss correction (PSFLC): This is needed to extract the correctly-calibrated spectrum of a point source to account for PSF losses.

[4] herschel.esac.esa.int/twiki/pub/Public/PacsCalibrationWeb/pacs_spec_Hipe13.pdf.

– Correction for semi-extended sources (which we refer to as "semi-extended 3x3" correction): To recover the whole flux of semi-extended sources, defined as those sources with a FWHM (Full Width Half Maximum) larger than a single spaxel (9.4") but small enough to fill the field of view of a single pointing (about 47"x47"). This correction is also applied to try to minimize the effects of pointing jitter. The so-called semi-extended 3x3 correction is always applied after the PSFLC and the final product is a 1D spectrum labelled as "PSFLC-3x3" corrected.
– Correction for extended sources (which we refer to as "extended 5x5" correction): This correction was also never made available in HIPE, but we had to create it to deal with sources extended beyond the central 3x3 spaxels. It works in a similar way to the semi-extended 3x3 correction, and is also applied after PSFLC. In this case the final product is a 1D spectrum labelled as "PSFLC-5x5" corrected.

In addition, several objects in our sample were significantly mispointed, that is, the main target was clearly not located in the central spaxel of the 5×5 spaxel array of PACS. To extract the 1D spectra of these sources, we had to use a modified version of the semi-extended 3x3 correction, as we will explain in Section 3.3 in more in detail.

3.1. Spectral flatfielding

As explained in the PACS Data Reduction Guide, spectral flatfielding can be crucial for improving the continuum of the final spectra. For range scan observations, flatfielding will result in general in a better S/N, especially for the longer wavelength ranges. It will also remove the "fringing"-like pattern that the SPG cubes often have and it will improve the appearance of sharp rises or drops in the data.

The HIPE task used for flatfield correction is *specFlatFieldRange*, where the user can select the order of the polynomial to fit. The default value is five but from our experience, a lower value (three or four) usually yields better results. For PacsRange observations that do not cover the whole SED of PACS, the best results are obtained using an even lower value for the order of the polynomial (normally one). We have configured the *specFlatFieldRange* task to exclude the regions affected by leakage (70-73 μm, 98-105 μm, and 190-220 μm); by setting the option *excludeLeaks* to "True" we obtained "clean" spectra. The exclusion of the regions affected by leaks is actually very important to obtain a correct shape of the continuum and to improve the results obtained with the *specFlatFieldRange* range. We note that the improvement in the S/N ratio after flatfielding is most remarkable in relatively faint sources.

3.2. Telescope background correction

This correction is needed to remove the sky and telescope background contribution. Furthermore, it uses the telescope background spectrum to flux calibrate the data, instead of using the standard calibration blocks. This process is applied using the HIPE task *specDiffChop*. This task computes the pairwise difference ratio: 2*(On-Off)/(On+Off), rather than the pairwise differences (On-Off) as is the case for the standard pipeline. This computation eliminates in an optimal way the detector drifts that appear in both On- and Off- positions. After this step, the flux density in the cubes is in units of "telescope background".

3.3. THROES post-processing

All the observations have been post-processed in different ways taking into account the nature of the object (extended or not) and the position of the source in the PACS FoV. The main goal of the post-processing was to extract, from the spectral cubes previously reduced, a 1D spectrum recovering the whole emission of the source. Depending on the post-processing tasks applied, the sources can be grouped into five main families:

– **Pointed observations, good pointing, point, or semi-extended sources (PSFLC-3x3)**: To recover the absolute flux of a point source from PACS data, it is necessary to apply first the point source flux loss correction (PSFLC) to the spectrum extracted from the central spaxel of the final (level 2) spectral cube. This correction is needed to take into account the flux losses derived from the fraction of the PSF that falls out of the central spaxel. A theoretical PSF model is used to compute the fraction of flux seen by the central spaxel and then recover the emission that has not been detected. After this, we also need to apply the semi-extended 3x3 correction in order to recover the emission received by the spaxels around the central one in case of semi-extended sources. Both corrections are performed by the HIPE task *extractCentralSpectrum*, which generates three different 1D spectra:
1) The first 1D spectrum returned by the task is simply the spectrum from the central spaxel corrected for point source flux losses.
2) The second 1D spectrum returned contains the integrated flux of the 3x3 central spaxels (also known as "superspaxel") with the point source flux loss correction applied to the central one.
3) Finally, the third 1D spectrum is the same as the first one, corresponding to the central spaxel with the point source flux loss correction applied, scaled to the flux level of the second spectrum, that of the 3x3 superspaxel. The result is the so-called semi-extended 3x3 corrected spectrum.
Using the Semi-extended 3x3 corrected spectrum, the whole flux from sources that are slightly extended is fully recovered. An example of the differences between the 1D spectrum generated after applying this correction and the spectrum taken directly from the central spaxel of the level 2 cube before post-processing is shown in Fig. 5. The vast majority of the sources in our sample have been reprocessed in this standard way and the resulting 1D spectra are displayed in Fig. 8. An exceptional case is OH 32.8−0.3, for which some spaxels around the central one show negative flux values and therefore these observations have only been corrected for PSFLC (i.e. the semi-extended 3x3 correction has not been applied).

– **Pointed observations, extended sources (PSFLC-5x5):** Based on PACS photometric data, when this was available, the existing PACS spectroscopy, and the bibliography, we identified those sources in our sample that appeared more extended than just the central 3x3 spaxels. These 'extended' objects are: IRAS 16122−5122, NGC 3242, NGC 40, NGC 6445, NGC 6543, NGC 6781, NGC 6826, NGC 7009, NGC 7026, and Mz3. Due to their extension, their emission can spread sometimes over the whole PACS FoV and, therefore, for these objects, we developed a new task, the extended 5x5 correction, to scale the spectrum from the central spaxel, after applying the point source flux loss correction, to the continuum level of the 5x5 spectrum, as we did for the

semi-extended 3x3 correction.

As we will see in Section 5, with this new task we were able to obtain a more realistic spectrum of the extended sources in our sample, better than the spectrum generated with the semi-extended 3x3 correction, as in. this way we recovered the whole emission from the source. In Fig. 9, we show the final 1D spectra of these extended sources after applying the PSFLC and the extended 5x5 correction. The effect of this task in terms of continuum flux level recovery can be seen in Fig. 5.

– **Pointed observations, mispointing (PSFLC-3x3):** In our sample there were also seven cases of mispointed observations, namely, IRAS17347−3139, NGC 6302, IRC−10529, OH21.5+0.5, AFGL 5379, IRAS 16279−4757, and IRAS 13428−6232, for which the source is located on a spaxel different than the central one. In these cases, *extractCentralSpectrum* cannot be applied because, in this task, the 3x3 superspaxel is always built around the central spaxel, instead of around the one where the source is located.

  To deal with these mispointed cases, we developed a script that works in a similar way to the HIPE task *extractCentralSpectrum* but which allows the user to select the spaxel (other than the central one) where the source is located. Our task was successfully applied to IRC−10529, OH 21.5+0.5, IRAS 13428-6232, NGC 6302, and IRAS 17347-3139. In Fig. 10 we show the final 1D spectra obtained after applying this correction.
  For AFGL 5379 and IRAS16279−4757 this correction did not work correctly as, due to the position of the sources being too far away from the central spaxel, it was impossible to generate the 3x3 superspaxel around the off-centred spaxel where the source was located.
  As was done for other observations in our sample, it is also necessary to correct these mispointed observations from PSF losses before applying the semi-extended 3x3 correction described above. To do that, HIPE provides two different tasks: *extractSpaxelSpectrum* and *pointSourceLossCorrection*. The first one takes the spectrum from the spaxel where the source is located and, after that, the second one corrects for the point source flux losses.
  Again in Fig. 5 we show the significant improvement of the final 1D spectra after applying the semi-extended 3x3 correction to mispointed observations.

– **Sources corrected only for PSFLC:** Three additional sources(AFGL 5379, IRAS 16279-4757, and OH 32.8-0.3) were only corrected for PSFLC, due to different issues that prevented the application of the semi-extended 3x3 correction. These issues are related to the position of the source in the 5×5 spaxels array and the presence of corrupted data in some of the spaxels needed to create the 3×3 superspaxel. Their spectra are displayed in Fig. 11. For these three sources the absolute flux level of the final 1D spectrum available in the THROES catalogue should be considered only as a lower limit.

To summarize, after our interactive data reduction process, we generated for each object the following final products:

– 1) Final spectral cubes (level 2) with the improvements that result from flatfielding and telescope background correction.
– 2) 1D spectra with the PSFLC applied, as well as the specific correction for slightly extended sources (semi-extended 3x3 correction) or extended sources (extended 5x5 correction). As a word of caution, we note that the scaling strategy followed assumes that the extension of the continuum and of the line-emitting region is roughly the same and that the spectral lines emission does not vary within the nebula, which may not be the case in some of the more extended objects. For those sources showing a more complex and extended morphology (particularly the PSFLC-5x5 corrected targets), we recommend the users to create their own 1D spectra making use of the final cubes provided in the THROES catalogue if they want to perform a more detailed analysis.

4. THROES catalogue

All the reprocessed PACS range spectroscopy observations have been compiled in a catalogue that is accessible via a web interface available at `https://throes.cab.inta-csic.es/`. On this web page all the reprocessed data are publicly available, including some general information about the objects and the observations made, as well as plots with the reduced PACS spectroscopy data and complementary spectroscopic and photometric observations from other observatories. A screenshot of the 'Data Retrieval' interface of the catalogue is shown in Fig. 6.

The tool used to create the web-based catalogue is *SVOCat*[5]. This application, developed by the Spanish Virtual Observatory (SVO[6]) is designed to make the publication of an astronomical catalogue easier, both as a web page and as a Virtual Observatory *Cone Search* service. Our archive system has been designed following the IVOA (International Virtual Observatory Alliance)[7] standards and requirements. In particular, it implements the *Cone Search* protocol, a standard defined by the IVOA for retrieving records from a catalogue of astronomical sources. Queries made through the *Cone Search* service are based on the description of a sky position and an angular distance, defining a cone on the sky. The response returns a list of astronomical sources from the catalogue whose positions in the sky lie within the pre-defined cone, formatted as a VOTable (Virtual Observatory Table). The system as a whole is included in the IVOA Registry and can therefore be discovered by any VO-tool.

To structure our catalogue in a homogeneous and logical way, all the observations with the same pointing have been grouped into a unique entry in the archive. Therefore, there is a single line per region in the sky observed. As we can see in Fig. 6, there are 13 columns for each entry, each providing information about the object or the observation as well as links to plots and to the reprocessed data. Each of the columns contains the following information:

– **Columns 1 to 4**: The equatorial coordinates (right ascension and declination) of the observation in different units: decimal degrees in columns 1 and 2, and hh:mm:ss and dd:mm:ss in columns 3 and 4.
– **Column 5**: Name of the object in the THROES catalogue.
– **Column 6**: The astronomical observation template (AOT). This could be PacsRange or PacsLine. For some objects there are spectra taken in both modes. These cases appear in the catalogue as PacsLine/PacsRange. Only the PacsRange spectra have been reprocessed in the current version of the THROES catalogue.

[5] http://svo2.cab.inta-csic.es/vocats/SVOCat-doc/.
[6] http://svo.cab.inta-csic.es.
[7] http://www.ivoa.net.

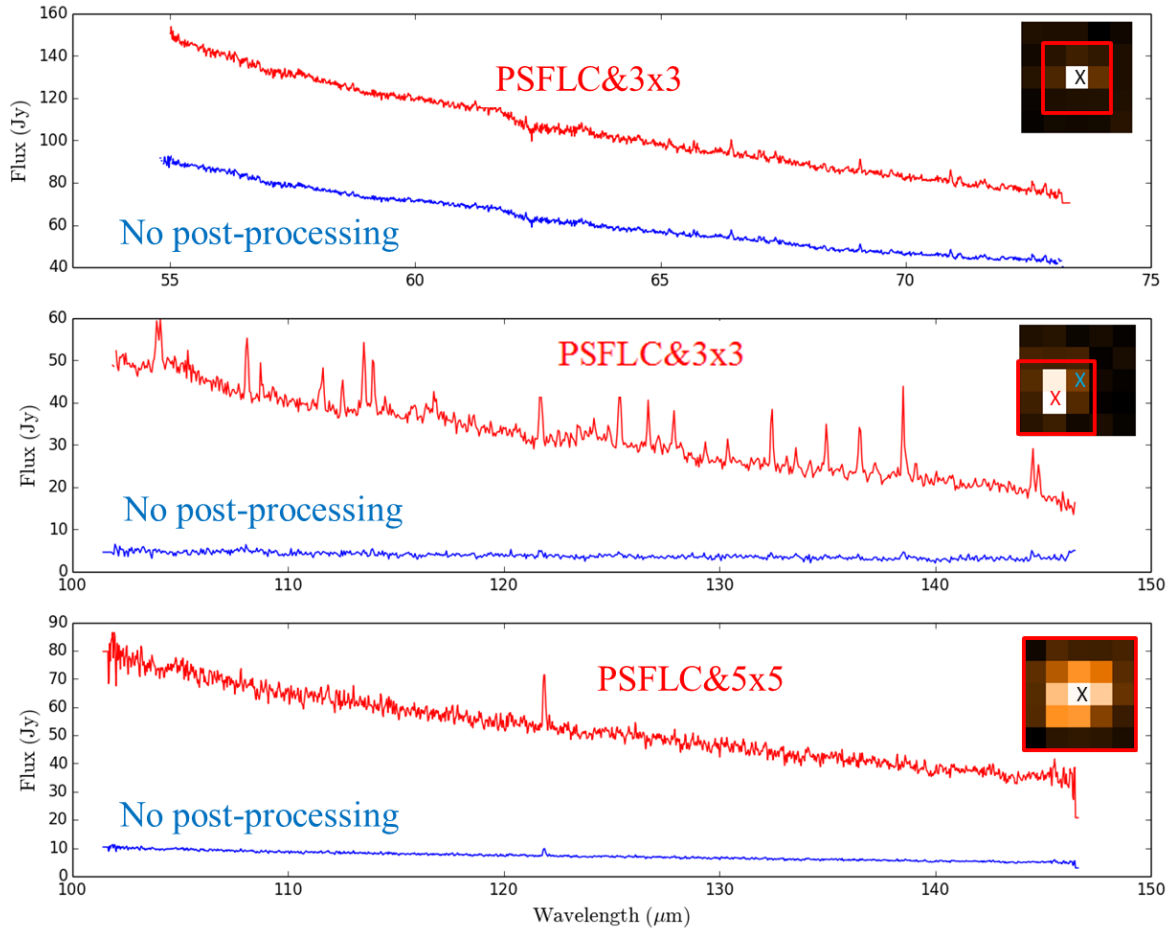

Fig. 5: One-dimensional spectra extracted for three different targets in the THROES catalogue following the procedures described in Section 3 (red). The flux corrections and apertures have been chosen depending on the source extent and its location in the 5x5 spaxels FoV of PACS. For comparison, we show the corresponding spectrum obtained in each case from the central spaxel before post-processing (blue). At the top right corner of each box, we show a layer of the *FinalCube* with the 5x5 spaxels of the PACS spectrometer of the observation. The crosses indicate the spaxel from which the spectra were taken; a black cross means that both spectra were extracted from the central spaxel. The squares (red and blue) enclose the spaxels used for the 3x3 correction or for the 5x5 correction. **Top)** AFGL 3116, blue camera of PACS (ObsID: 1342212512): well pointed and semi-extended source; PSFLC-3x3 correction has been applied. **Centre)** Same as above but for IRC−10529, red camera of PACS (ObsID: 1342208931): this is a mispointed observation where the blue spectrum corresponds to that extracted from the central spaxel without post-processing, while the red one is the spectrum taken from the brightest spaxel and with the post-processing applied (PSFLC-3x3). **Bottom)** Same as the first two panels but for NGC 6543, red camera (ObsID: 1342238389): this is an extended source; PSFLC-5x5 correction applied.

- **Column 7**: The number of observations taken in that position of the sky. By clicking on the number shown in this column, a new table is deployed with detailed information for each observation, such as: target name, equatorial coordinates (RA and Dec), proposal name, AOT, observation ID, observing date and time, and original AOR (Astronomical Observation Request) label.
- **Column 8**: Mass classification (based on the bibliography and SIMBAD[8]). The options are: evolved low-intermediate mass star, evolved massive star, or unknown.
- **Column 9**: Object classification including the evolutionary stage and its dominant chemistry (based on the bibliography and SIMBAD), the options are: O-rich AGBs, C-rich AGBs, S stars, OH/IR stars, O-rich post-AGBs, C-rich post-AGBs, mixed chemistry post-AGBs, O-rich PNe, C-rich PNe, mixed chemistry PNe, or Unknown.
- **Column 10**: This column indicates if the observations have been reprocessed under the THROES project or not. This is because THROES may be expanded in the future to other observing modes of PACS and/or massive evolved stars.
- **Column 11**: By double clicking on 'SED', a pop-up window is displayed showing the 1D PACS spectra generated after the interactive data reduction and subsequent

[8] http://simbad.u-strasbg.fr/simbad/.

post-processing, together with complementary photometric (IRAS and AKARI) and spectroscopic (Infrared Space Observatory-Long-Wave Spectrometer (ISO-LWS)) data, when available.
- **Column 12**: By double clicking on 'CSV' (Comma-Separated Values), a compressed folder with the name of the target is downloaded containing a gzipped tar file with the 1D PACS spectra, in CSV format.
- **Column 13**: Similarly, by double clicking on 'FITS' (Flexible Image Transport System), a compressed gzipped tar file is downloaded containing the THROES reprocessed final spectral cubes (level2) in FITS format and the 1D PACS spectra, also in FITS format, derived from these final spectral cubes after post-processing.

More information about how to query the catalogue through the different search fields is available in the documentation available on the THROES catalogue web page.

5. Characterization of the THROES sample

All the individual THROES spectra are shown from Figs. 8 to 11. To illustrate the quality of the resulting spectra, every plot contains not only the final PACS 1D spectra, but also the photometric (IRAS and AKARI) and spectroscopic ISO-LWS data, whenever these are available. In Table. 1 we display information associated to the PACS, ISO (Infrared Space Observatory), IRAS, and AKARI data used for the generation of the SEDs.

5.1. Comparison with IRAS and AKARI photometry

All the objects in the THROES catalogue have complementary IRAS photometric information while, for AKARI data, the percentage of common objects decrease to 89%. The Infrared Astronomical Satellite (IRAS) (http://irsa.ipac.caltech.edu/IRASdocs/iras.html) point source catalogue presents photometric data in four bands centred at 12, 25, 60, and 100 μm. The beam size of IRAS observations, which is much larger than that of PACS, varies from 2' at shorter wavelengths to 5' at longer ones (Jeong et al. 2007). AKARI (http://www.ir.isas.jaxa.jp/AKARI/index.html) covers longer wavelengths, 65, 90, 140, and 160 μm, and the beam size varies from 0.5' to 0.9' (Jeong et al. 2007). The different beam sizes of the instruments is a key point that has to be kept in mind when comparing PACS spectroscopy to IRAS and AKARI photometric data.

In order to check the quality of the final processed PACS spectroscopy data and to obtain information about the effect of the post-processing tasks applied to generate the final 1D spectra, a comparison between the synthetic photometry derived from the PACS spectroscopic data and the IRAS and AKARI photometric data at 100 and 160 μm, respectively, has been done.

Synthetic photometry is generated by convolving the transmission curve of the photometric filters, $IRAS_{100}$ and $AKARI_{160}$, with the 1D PACS spectra. The transmission curve of $IRAS_{100}$ has been obtained from: `http://irsa.ipac.caltech.edu/IRASdocs/exp.sup/ch2/tabC5.html` and the transmission curve of $AKARI_{160}$ has been estimated from the relative response function available in: `http://svo2.cab.inta-csic.es/theory/fps3/?id=AKARI/FIS.N160`.

As the synthetic photometry requires a convolution between the 1D PACS spectrum and the curve of the photometric filters, it is necessary that the PACS spectrum spectral coverage extends, at least, along the whole wavelength subrange covered by the photometric filters. For this reason, the synthetic photometry can be estimated for the subsample of 71 THROES targets with full spectral coverage of the PACS wavelength range.

As mentioned in Section 3, due to the instrument configuration and the exclusion of some sub-regions affected by leakage, all the 1D PACS spectra show a small gap (less than 10 μm) around 100 μm, even for those sources that present a complete spectral coverage. As the photometric curve of IRAS 100 μm is centred on this region, it is important to find a solution. To cope with that in the synthetic photometry estimation, a linear interpolation was done to approximate the continuum flux level in this region. This assumption is good enough as intense emission lines are not expected in this region.

On the AKARI 160 μm side, due to the exclusion of the wavelength regions affected by leakage, there are no PACS data to cover the wavelength range from 190 to 220 μm. To solve that, a power law (λ^{α}) was fitted to the red bands of the PACS SED and, after that, we extrapolated the flux values to the 190-220 μm region. At these wavelengths, we are mainly tracing the Rayleigh-Jeans emission, so this extrapolation is reasonable.

To show the effect of the post-processing tasks applied in the THROES reduction process, the synthetic photometry has been estimated for 1D PACS spectra before and after applying the post-processing tasks. In Fig. 7 the comparison between $IRAS_{100}$ and $AKARI_{160}$ photometric data and their synthetic counterparts using PACS data with and without post-processing is shown. We can see clearly that a disagreement between the photometric and the synthetic photometric data, before post-processing, is obtained. This disagreement is significantly reduced after post-processing tasks are applied, so it confirms that the tasks introduced in the reduction process of THROES are needed for reliable absolute flux calibration. The few points that fall out of a one-to-one observational-to-synthetic photometry relation are points that have bad IRAS and/or AKARI photometric data, (Quality Flag≠3, red triangles) or are associated to extended objects (blue crosses).

5.2. ISO-LWS spectroscopy

It is interesting to compare our PACS spectroscopic data to ISO-LWS spectra, since this instrument covers a wavelength range from 43 to 197 μm that almost fully overlaps with PACS. However, it is important to keep in mind that ISO-LWS presents a worse spectral resolution, R=200 (medium resolution) and R=1000 (high resolution), and a larger beam size (80"×100").

Whenever available, ISO spectra are shown in Figs 8 to 11 together with our 1D PACS spectra and IRAS/AKARI photometry points. After a visual inspection of those objects which present both PACS and ISO data, objects can be grouped into five main families:

1. Good agreement between PACS and ISO: For most of the sources, a good agreement between PACS and ISO-LWS spectroscopic data is found. For example, HD 161796, CIT 6, AFGL 618, or CPD -568032 (see Fig. 8).

2. Mispointed PACS observations without 3x3 correction: Due to its location close to the edge of the PACS 5×5 array, it was not possible to apply the semi-extended 3x3 correction to one source, AFGL 5379. This could explain why the continuum flux level of the ISO-LWS is higher than that of the PACS spectrum (see Fig. 11).

3. Background contamination of the ISO spectra: One of the most remarkable facts found with this comparison is

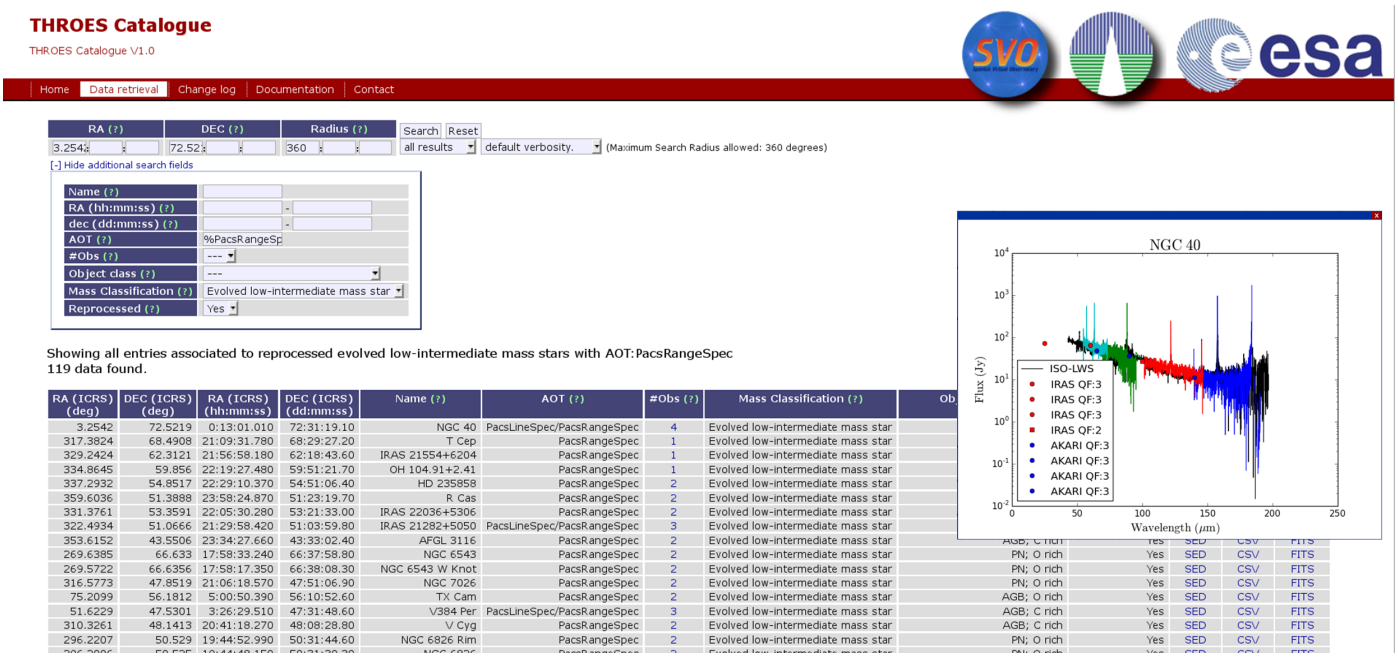

RA (ICRS) (deg)	DEC (ICRS) (deg)	RA (ICRS) (hh:mm:ss)	DEC (ICRS) (dd:mm:ss)	Name (?)	AOT (?)	#Obs (?)	Mass Classification (?)	Ob				
3.2542	72.5219	0:13:01.010	72:31:19.10	NGC 40	PacsLineSpec/PacsRangeSpec	4	Evolved low-intermediate mass star					
317.3824	68.4908	21:09:31.780	68:29:27.20	T Cep	PacsRangeSpec	1	Evolved low-intermediate mass star					
329.2424	62.3121	21:56:58.180	62:18:43.60	IRAS 21554+6204	PacsRangeSpec	1	Evolved low-intermediate mass star					
334.8645	59.856	22:19:27.480	59:51:21.70	OH 104.91+2.41	PacsRangeSpec	1	Evolved low-intermediate mass star					
337.2932	54.8517	22:29:10.370	54:51:06.40	HD 235858	PacsRangeSpec	2	Evolved low-intermediate mass star					
359.6036	51.3888	23:58:24.870	51:23:19.70	R Cas	PacsRangeSpec	2	Evolved low-intermediate mass star					
331.3761	53.3591	22:05:30.280	53:21:33.00	IRAS 22036+5306	PacsRangeSpec	2	Evolved low-intermediate mass star					
322.4934	51.0666	21:29:58.420	51:03:59.80	IRAS 21282+5050	PacsLineSpec/PacsRangeSpec	3	Evolved low-intermediate mass star					
353.6152	43.5506	23:34:27.660	43:33:02.40	AFGL 3116	PacsRangeSpec	2	Evolved low-intermediate mass star					
269.6385	66.633	17:58:33.240	66:37:58.80	NGC 6543	PacsRangeSpec	2	Evolved low-intermediate mass star	PN; O rich	Yes	SED	CSV	FITS
269.5722	66.6356	17:58:17.350	66:38:08.30	NGC 6543 W Knot	PacsRangeSpec	2	Evolved low-intermediate mass star	PN; O rich	Yes	SED	CSV	FITS
316.5773	47.8519	21:06:18.570	47:51:06.90	NGC 7026	PacsRangeSpec	2	Evolved low-intermediate mass star	PN; O rich	Yes	SED	CSV	FITS
75.2099	56.1812	5:00:50.390	56:10:52.60	TX Cam	PacsRangeSpec	2	Evolved low-intermediate mass star	AGB; O rich	Yes	SED	CSV	FITS
51.6229	47.5301	3:26:29.510	47:31:48.60	V384 Per	PacsLineSpec/PacsRangeSpec	3	Evolved low-intermediate mass star	AGB; C rich	Yes	SED	CSV	FITS
310.3261	48.1413	20:41:18.270	48:08:28.80	V Cyg	PacsRangeSpec	2	Evolved low-intermediate mass star	AGB; C rich	Yes	SED	CSV	FITS
296.2207	50.529	19:44:52.990	50:31:44.60	NGC 6826 Rim	PacsRangeSpec	2	Evolved low-intermediate mass star	PN; O rich	Yes	SED	CSV	FITS

Fig. 6: Screenshot of the THROES catalogue web interface. All the columns and search fields described in Section 4 are shown as well as an example of a complete SED with IRAS and AKARI data overplotted.

that, for some sources, the ISO-LWS spectra show a continuum level higher than the one of PACS. This effect seems to be more evident at longer wavelengths (> 100 μm). Besides, for all these spectra we find an emission line at 158 μm associated to [C II] due to interstellar emission, so the origin of this extra contribution could be the contamination of the interstellar medium. There are 11 sources that have been classified in this group: AFGL6815, IRAS 16342-3814, IRAS 16594-4656, IRAS 22036+5306, IRAS 21282+5050, MWC 922, NGC 6537, NML Cyg, OH 26.5+0.6, OH 32.8-0.3, and V Cyg. The reason why ISO-LWS spectra show this contamination is the larger FoV of ISO-LWS with respect to the PACS FoV (see Figs. 8 to 11).

4. Very extended sources: Extended sources in THROES sample have been corrected using the extended 5x5 correction to recover the whole flux taken by PACS spectroscopy. However, there are some objects, such as NGC 6781, that are even larger than the PACS FoV and, therefore, PACS spectroscopic data do not measure all the flux emission from the source in contrast to ISO-LWS, which has a larger beam. For that reason, for these very extended sources, the continuum flux level of the ISO-LWS spectra is higher than that of PACS (see Fig. 9).

5. Bad ISO data: Finally, for some sources like IRAS 07027-7934 or HD 56126, ISO-LWS data present evident artefacts that make the ISO spectroscopic data unreliable (see Fig. 8).

6. Summary

We made an inventory of all the observations of all evolved stars taken in standard mode by *Herschel* with PACS spectroscopy. From all of them, we selected pointed, Chop/Nod, and PacsRange observations of evolved low-to-intermediate mass stars and we interactively processed the resulting 220 individuals *Herschel*/PACS Obs IDs, corresponding to 114 different targets.

Along the reduction process we introduced new tasks to improve the final PACS spectroscopy products. These tasks can be divided into two main groups:

- 1) Tasks applied to the spectral cubes before the level 2 data are generated: flatfield correction and telescope background correction.
- 2) Tasks applied to the level 2 data products to extract the best 1D spectrum (post-processing). These tasks try to recover the whole flux of the sources within the PACS 5×5 spaxels array, taking into account the extension of the emission and the position of the object in the PACS FoV. They are: point source flux loss correction (PSFLC), semi-extended 3x3 correction, and extended 5x5 correction.

After the interactive data reduction, we generated synthetic photometry to compare our final THROES 1D spectra to photometric, $IRAS_{100}$, and $AKARI_{160}$ photometric data. THROES 1D spectra were compared also with spectroscopic (ISO-LWS) data. From these comparisons we can conclude that our re-processing generates improved quality products compared with those routinely generated by the SPG in an automated mode, available in the HSA, and are in good agreement with IRAS and AKARI photometric data. Furthermore, the comparison of PACS with ISO-LWS spectra has highlighted the presence of interstellar contamination in some ISO-LWS data.

To ease the access to the final spectral cubes (level 2) and to the post-processed 1D spectra, we have created a web-based interface using *SVOCat*. Through `https://throes.cab.inta-csic.es/`, all the products generated as a result of the THROES interactive data reduction process are available. The THROES catalogue is expected to be updated in the near future by extending the analysis to new spectroscopic data from other instruments such as SPIRE. Furthermore, there is the potential to extend the analysis to evolved massive stars.

Acknowledgements. The *Herschel* spacecraft was designed, built, tested, and launched under a contract to ESA managed by the Herschel/Planck Project team by an industrial consortium under the overall responsibility of the prime contractor Thales Alenia Space (Cannes), and including Astrium (Friedrichshafen) responsible for the payload module and for system testing at spacecraft level, Thales Alenia Space (Turin) responsible for the service module, and Astrium

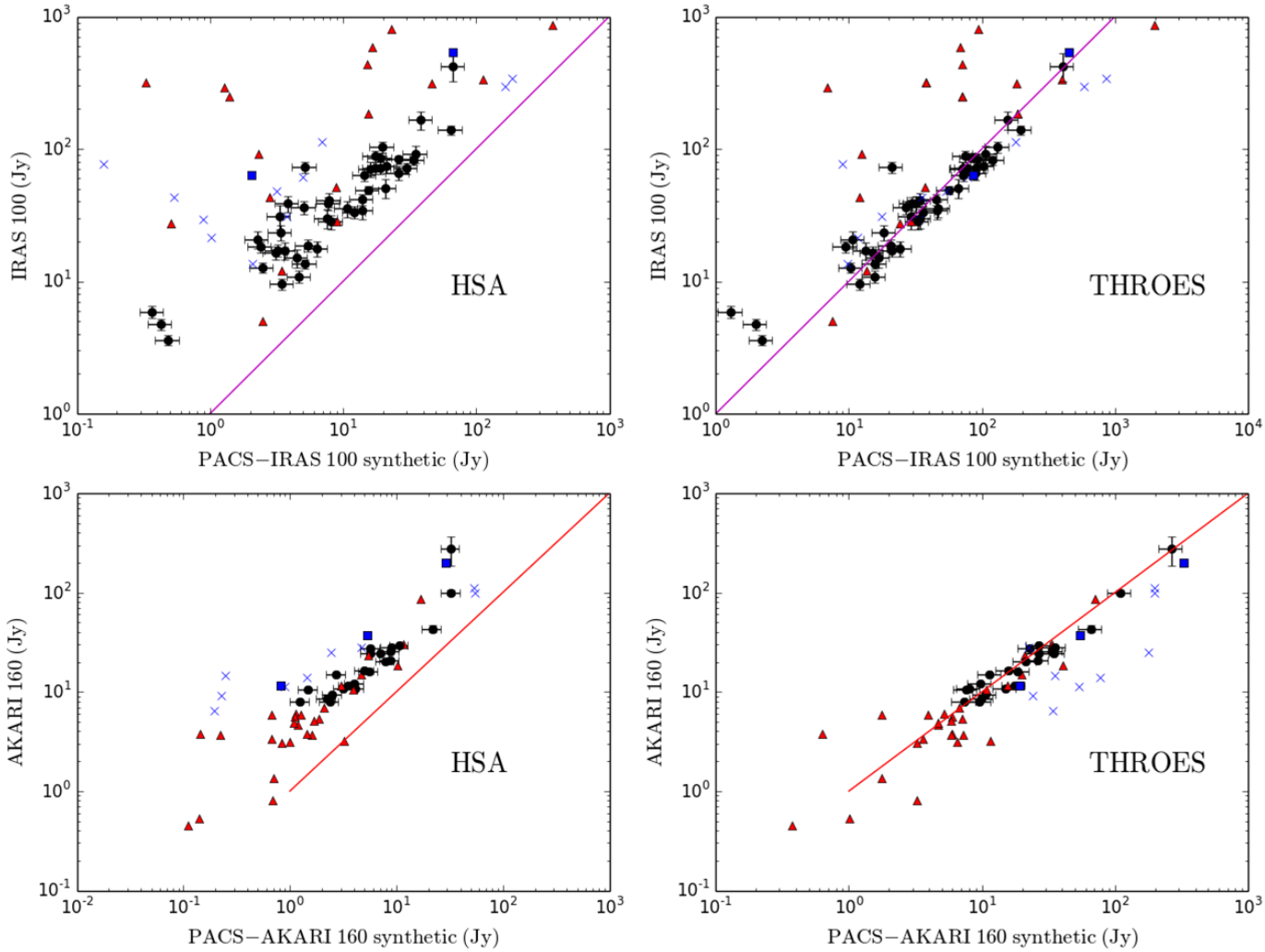

Fig. 7: Comparison of IRAS (100 μm) and AKARI (160 μm) photometry with synthetic PACS photometry at these wavelengths before (left) and after (right) the interactive reprocessing of the data carried out in this work and that is available through the THROES catalogue. The objects plotted here are those which present a complete coverage of the PACS spectral range. We have established a code to distinguish the extended objects (blue crosses), the mispointed ones (red squares), the objects with bad $IRAS_{100}$ or $AKARI_{160}$ data (Quality Flag≠3, red triangles), and objects with good $IRAS_{100}$ or $AKARI_{160}$ data (Quality Flag=3, black circles with error bars). The solid line represents a perfect match (1:1 ratio) of the synthetic (PACS) and observational photometric (IRAS and AKARI) points.

(Toulouse) responsible for the telescope, with in excess of a hundred subcontractors. HCSS and HIPE are joint developments by the Herschel Science Ground Segment Consortium, consisting of ESA, the NASA Herschel Science Center, and the HIFI, PACS, and SPIRE consortia. We are grateful to the entire spectroscopy group of PACS for their help and support, especially to E. Puga and K. Exter, as well as the anonymous referee for their careful reading of the manuscript and very useful suggestions. This research has been supported by the funding of the ESAC Faculty and the Herschel Science Division. CSC is partially funded by the Spanish MINECO through grants AYA2012-32032 and AYA2016-750066-C2-1-P. This research has made use of the Spanish Virtual Observatory (svo.cab.inta-csic.es) supported from the Spanish MINECO through grants AyA2014-55216.

References

Aleman, I., Ueta, T., Ladjal, D., et al. 2014, A&A, 566, A79
Balick, B. & Frank, A. 2002, ARA&A, 40, 439
Danilovich, T., Teyssier, D., Justtanont, K., et al. 2015, A&A, 581, A60
De Beck, E., Decin, L., de Koter, A., et al. 2010, A&A, 523, A18
de Graauw, T., Helmich, F. P., Phillips, T. G., et al. 2010, A&A, 518, L6
de Vries, B. L., Klotz, D., Lombaert, R., et al. 2011, in Astronomical Society of the Pacific Conference Series, Vol. 445, Why Galaxies Care about AGB Stars II: Shining Examples and Common Inhabitants, ed. F. Kerschbaum, T. Lebzelter, & R. F. Wing, 621
Decin, L., Justtanont, K., De Beck, E., et al. 2010, A&A, 521, L4
García-Hernández, D. A., Perea-Calderón, J. V., Bobrowsky, M., & García-Lario, P. 2007, ApJ, 666, L33
Griffin, M. J., Abergel, A., Abreu, A., et al. 2010, A&A, 518, L3
Groenewegen, M. A. T., Waelkens, C., Barlow, M. J., et al. 2011, in Astronomical Society of the Pacific Conference Series, Vol. 445, Why Galaxies Care about AGB Stars II: Shining Examples and Common Inhabitants, ed. F. Kerschbaum, T. Lebzelter, & R. F. Wing, 567
Habing, H. J. 1996, A&A Rev., 7, 97
Herwig, F. 2005, ARA&A, 43, 435
Jeong, W.-S., Nakagawa, T., Yamamura, I., et al. 2007, PASJ, 59, S429
Kwok, S. 2005, Journal of Korean Astronomical Society, 38, 271
Maercker, M., Danilovich, T., Olofsson, H., et al. 2016, A&A, 591, A44
Pilbratt, G. L., Riedinger, J. R., Passvogel, T., et al. 2010, A&A, 518, L1
Poglitsch, A., Waelkens, C., Geis, N., et al. 2010, A&A, 518, L2
Ueta, T., Ladjal, D., Exter, K. M., et al. 2014, A&A, 565, A36
van der Veen, W. E. C. J. & Habing, H. J. 1988, A&A, 194, 125

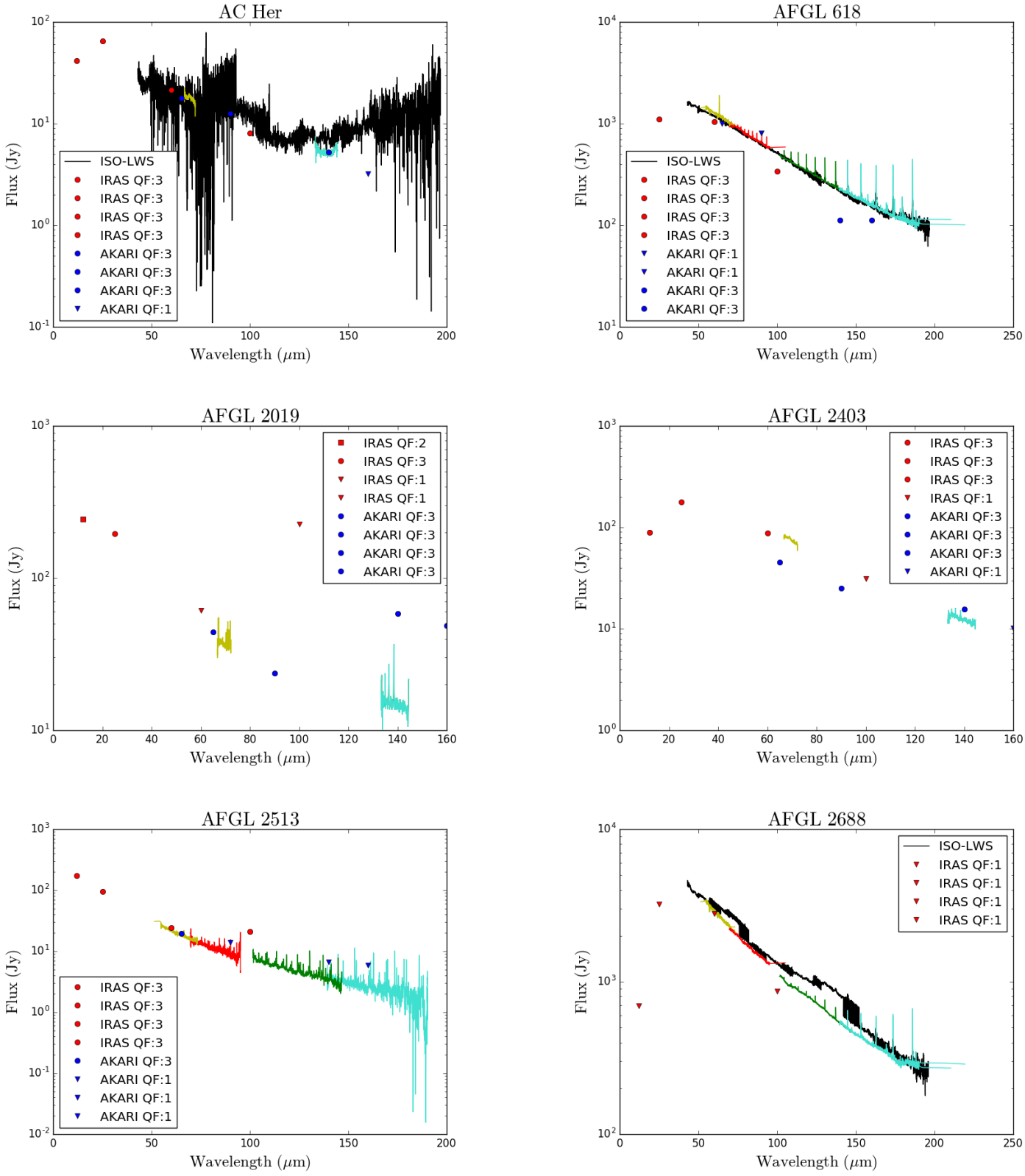

Fig. 8: PACS spectroscopy SED of well-pointed, non-extended sources, after applying PSFLC and semi-extended 3x3 correction (PSFLC-3x3). PACS data is colour-coded according to the spectral region covered by each subrange, as follows: ~50-70 μm (yellow), ~70-100 μm (red), ~100-145 μm (green), and ~145-200 μm (turquoise). IRAS (red points) and AKARI (blue points) photometric data and ISO (black) spectroscopic data are also displayed when available. We do not show those observations pointed to a specific region in the case of very extended sources such as rims or knots.

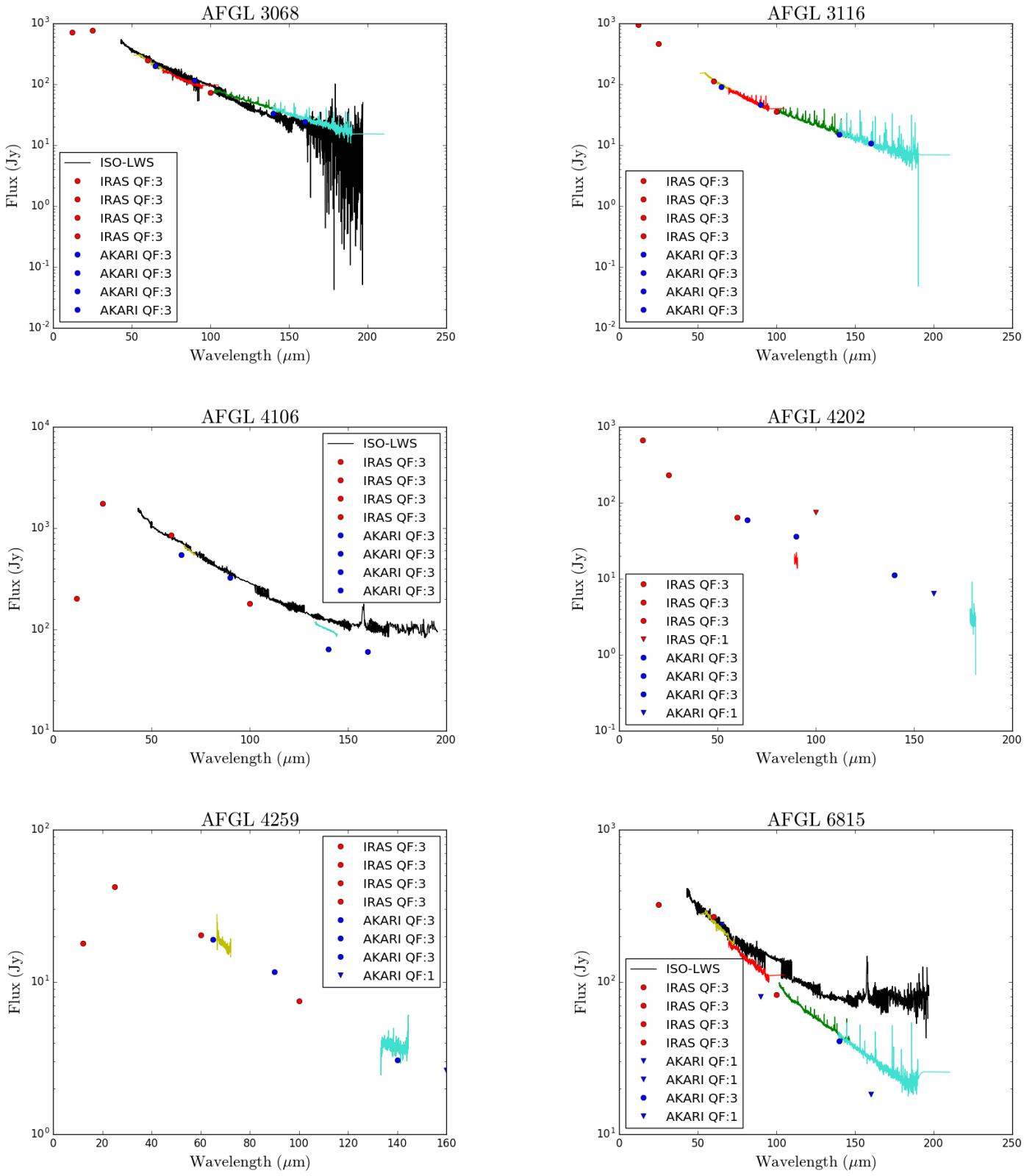

Fig. 8: Continued.

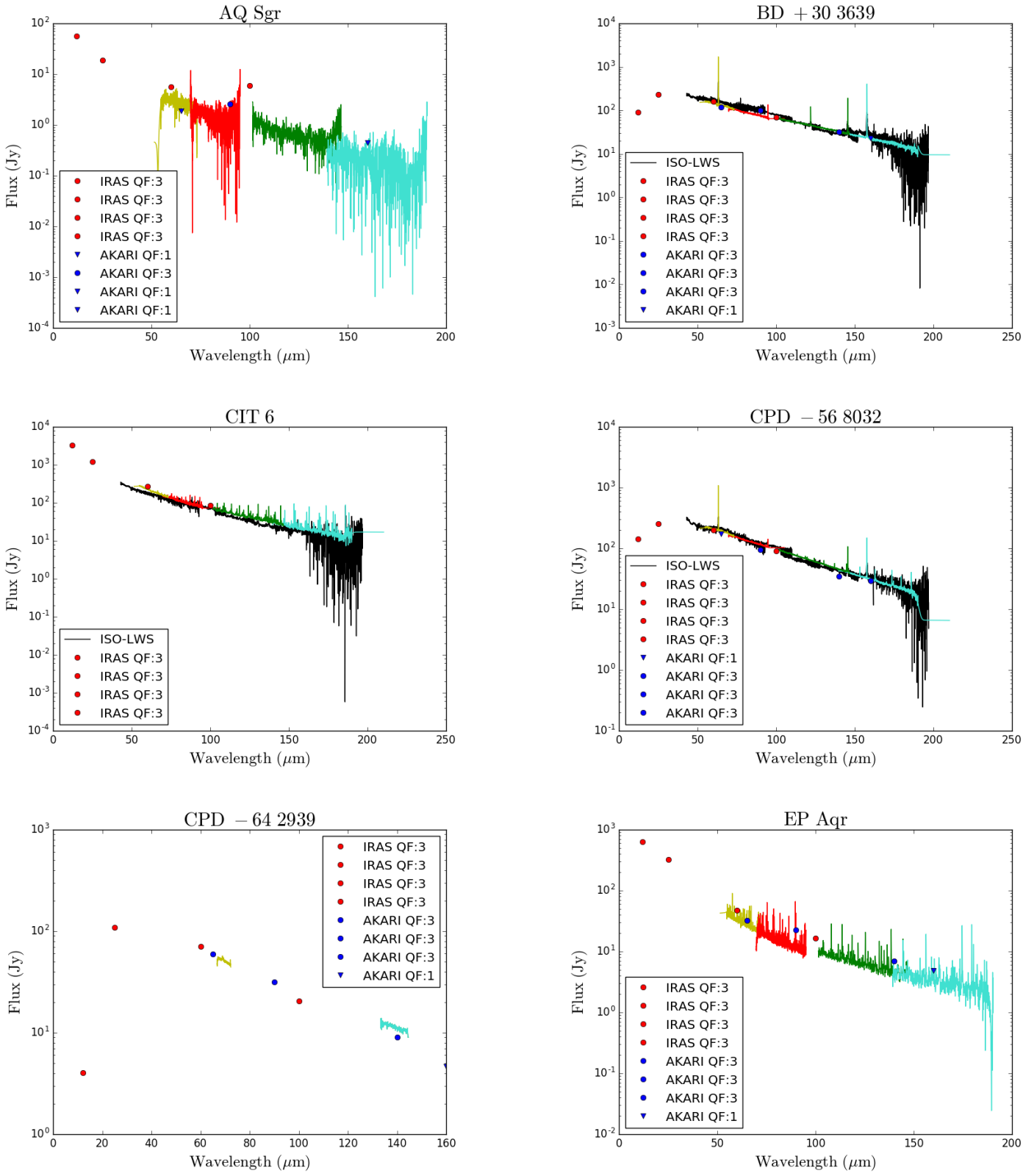

Fig. 8: Continued.

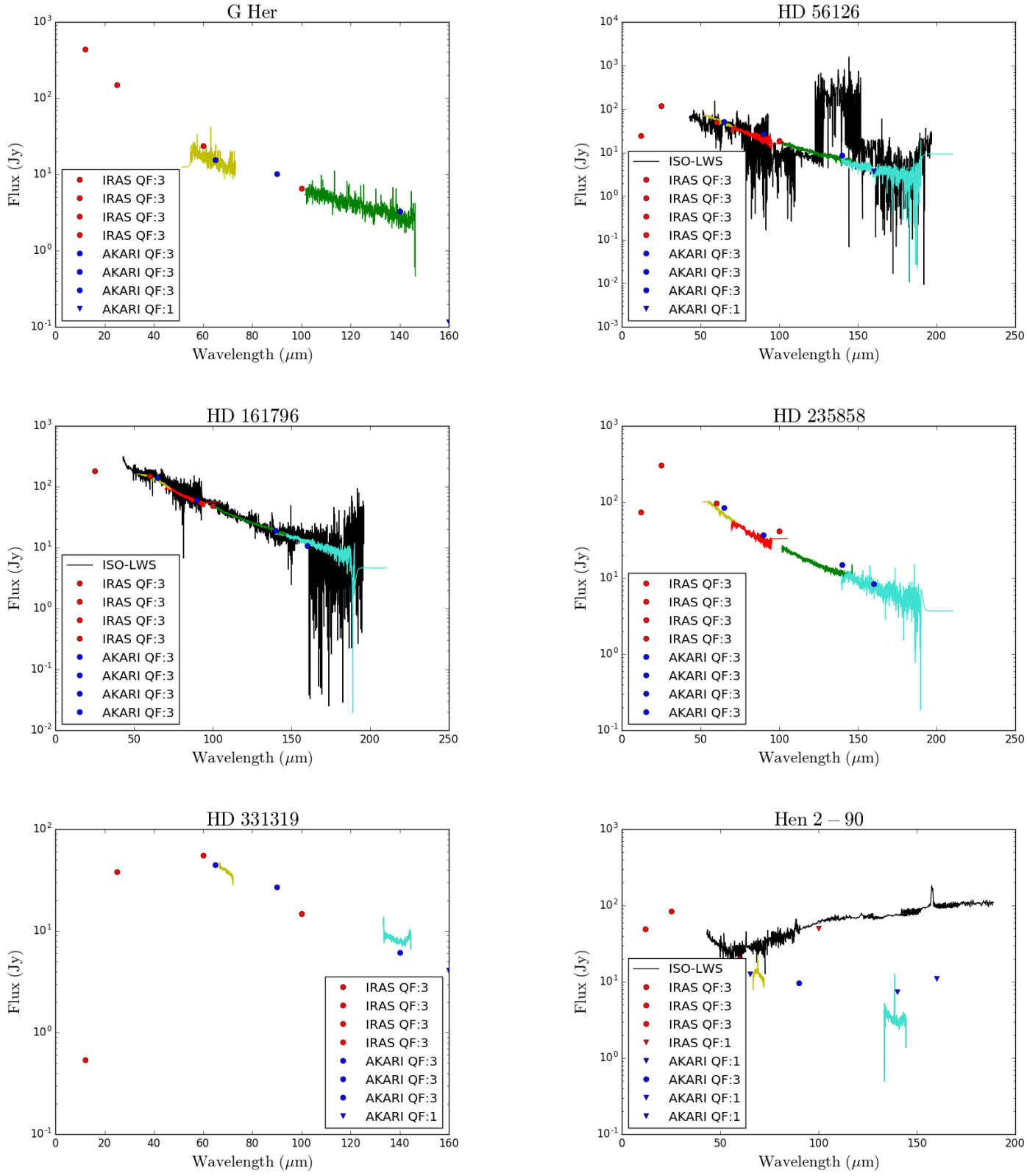

Fig. 8: Continued.

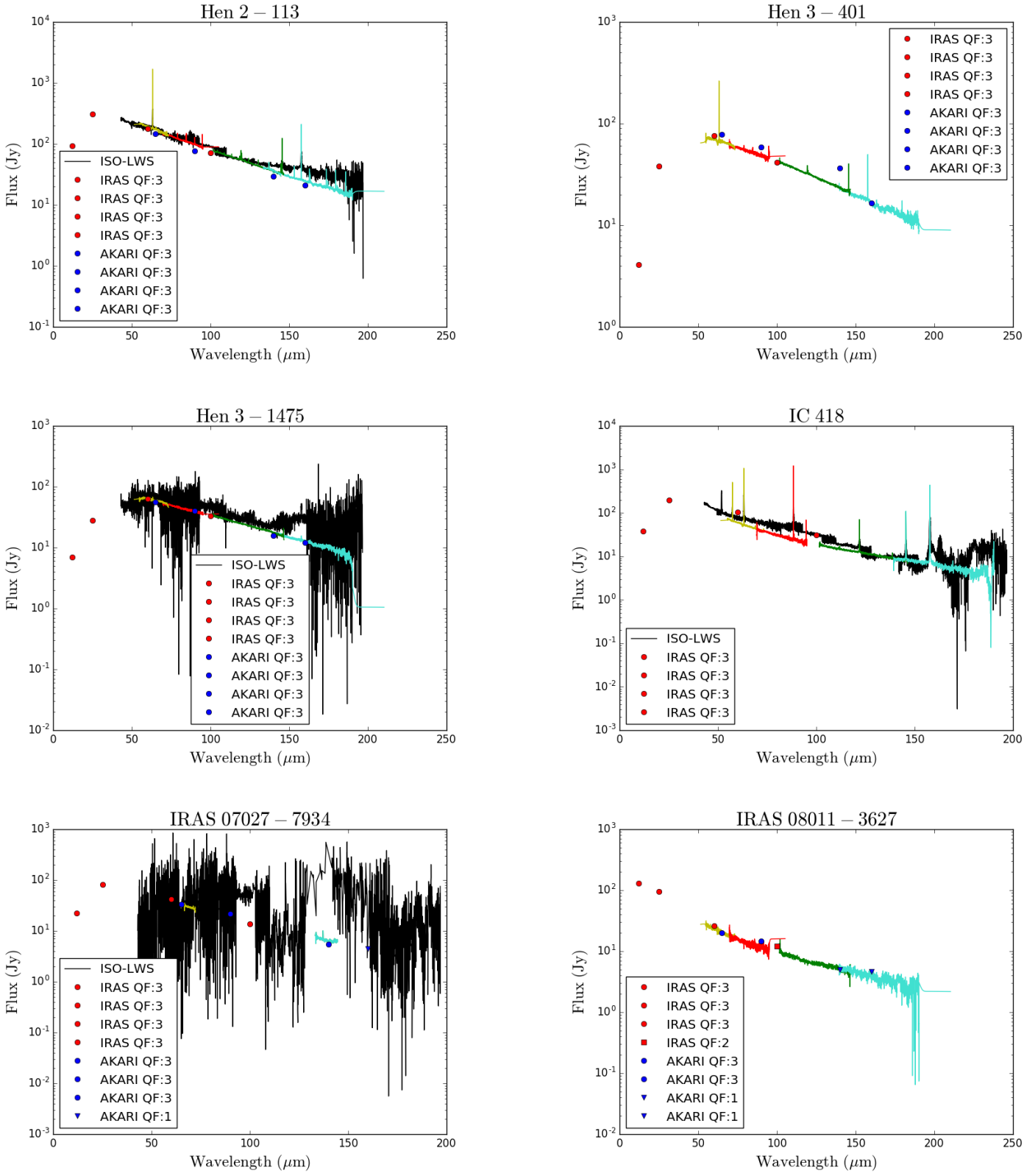

Fig. 8: Continued.

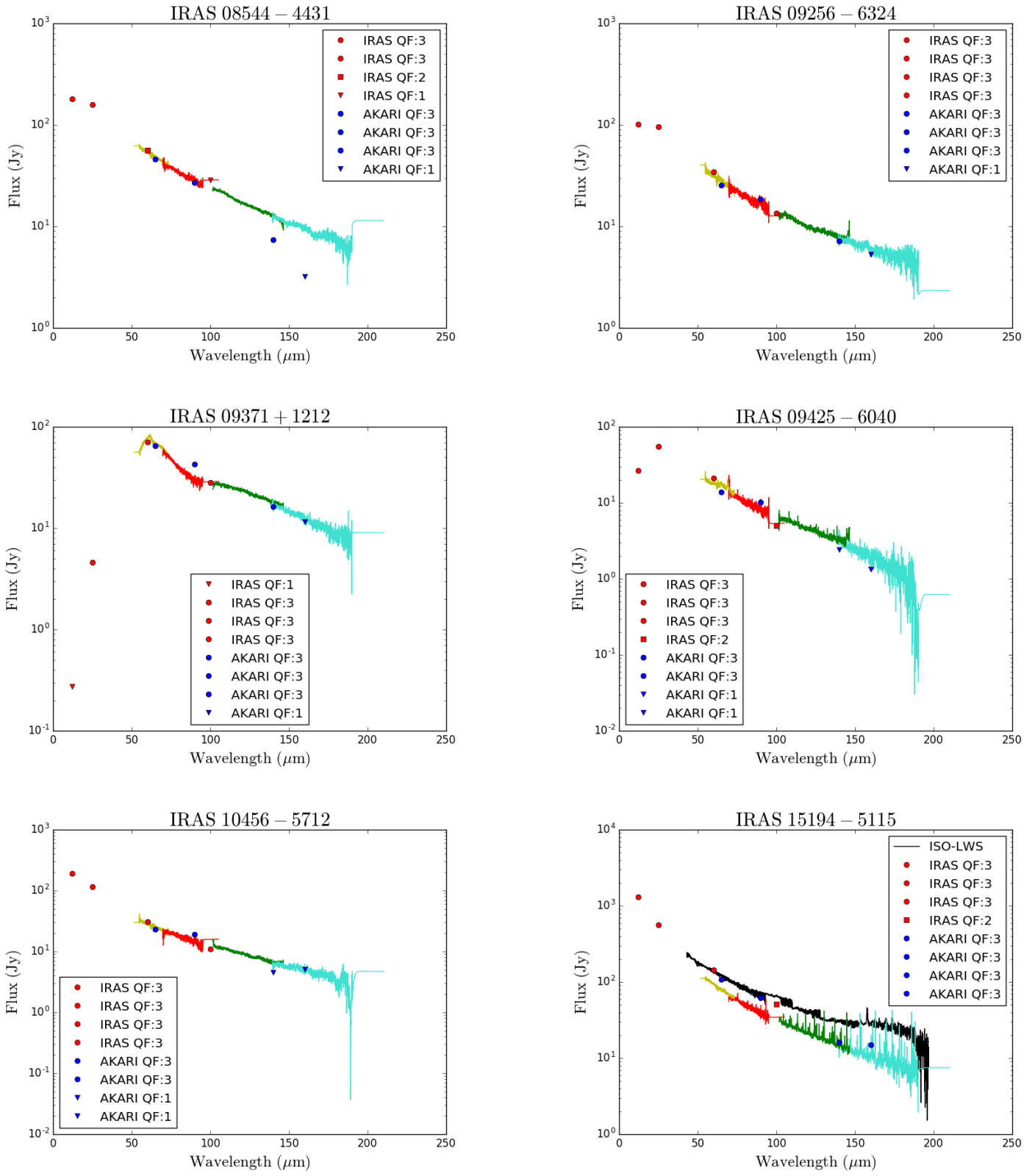

Fig. 8: Continued.

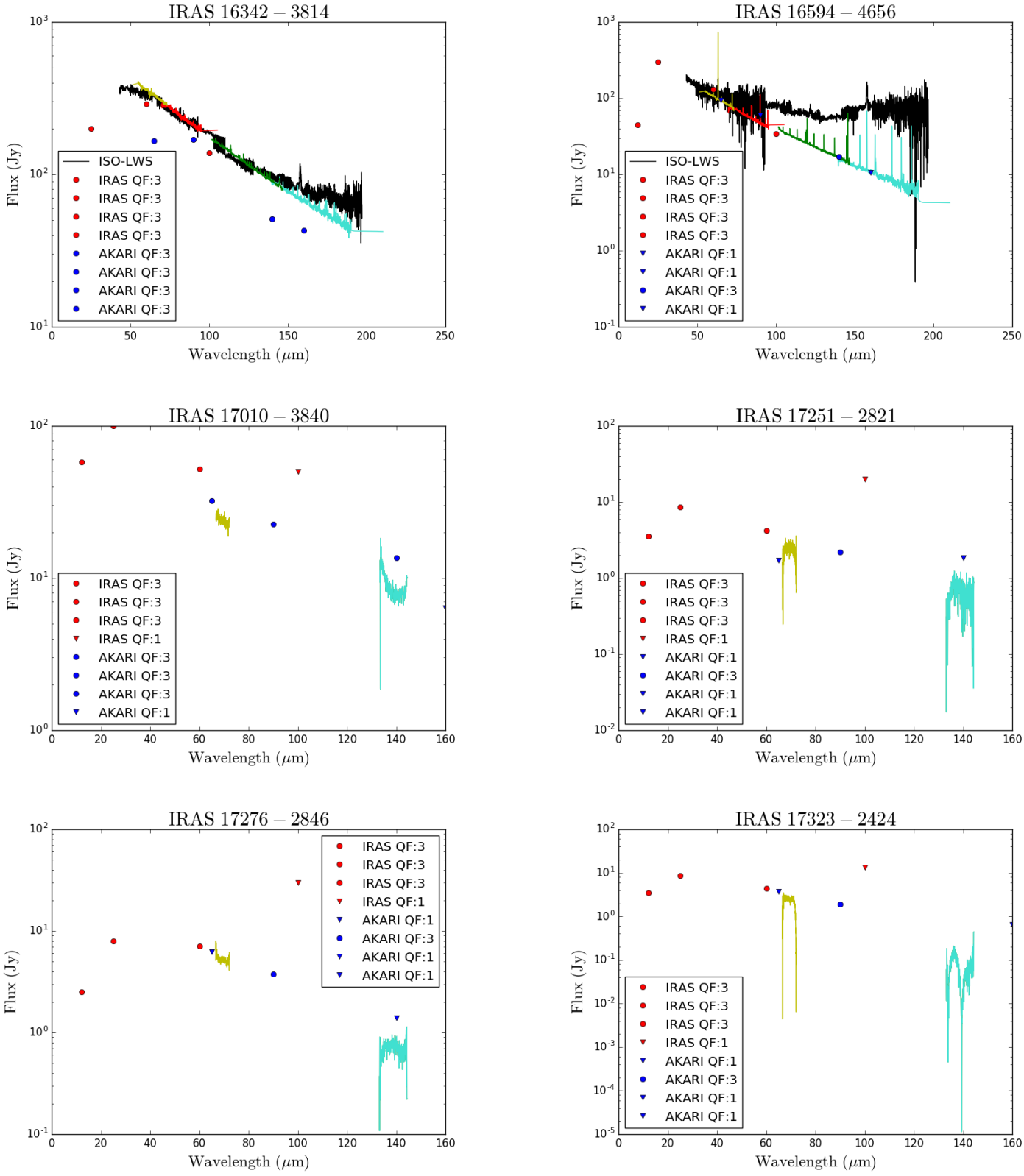

Fig. 8: Continued.

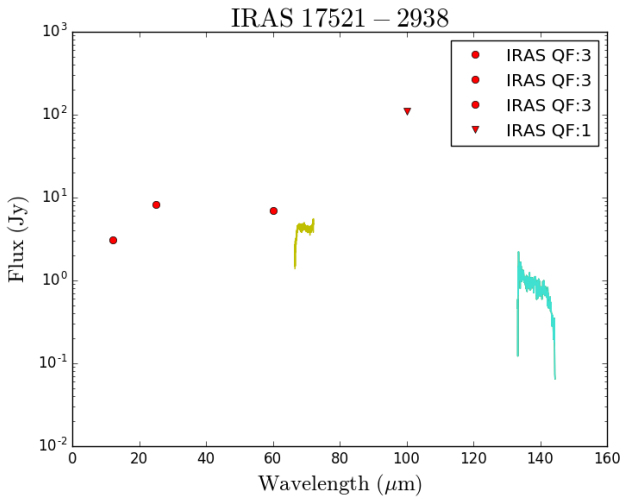

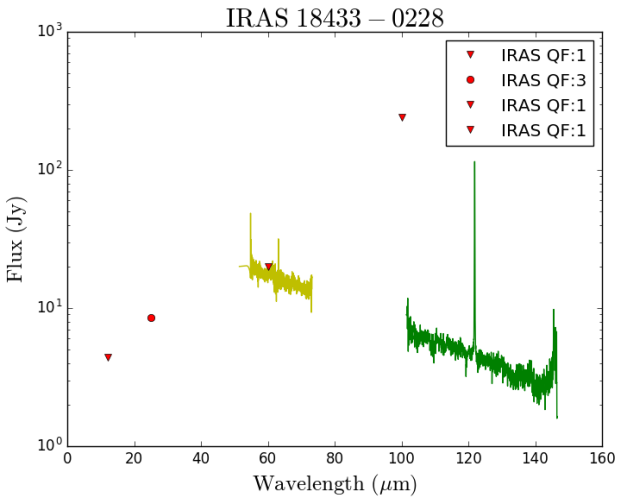

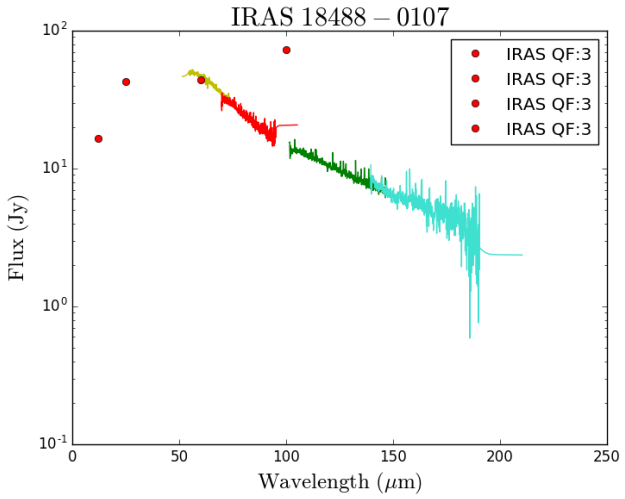

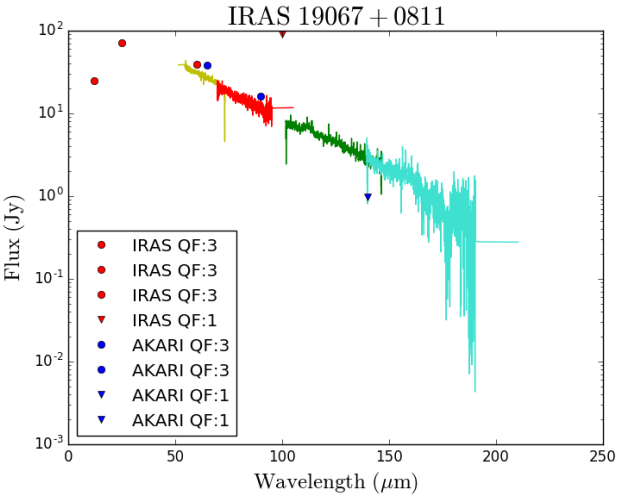

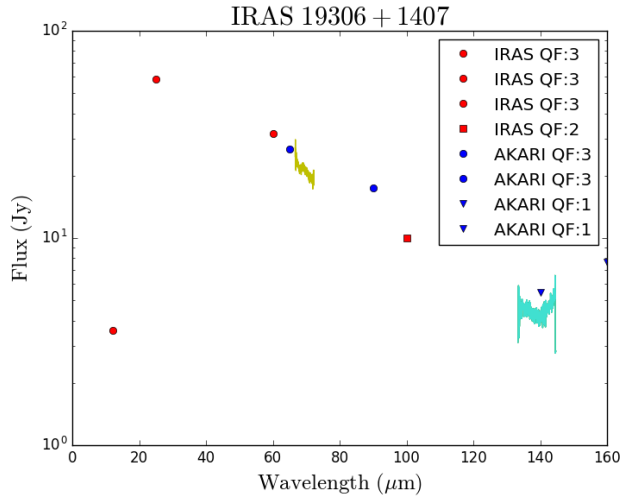

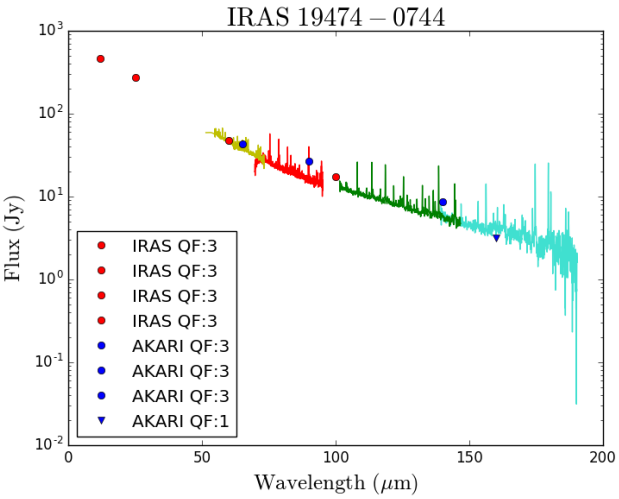

Fig. 8: Continued.

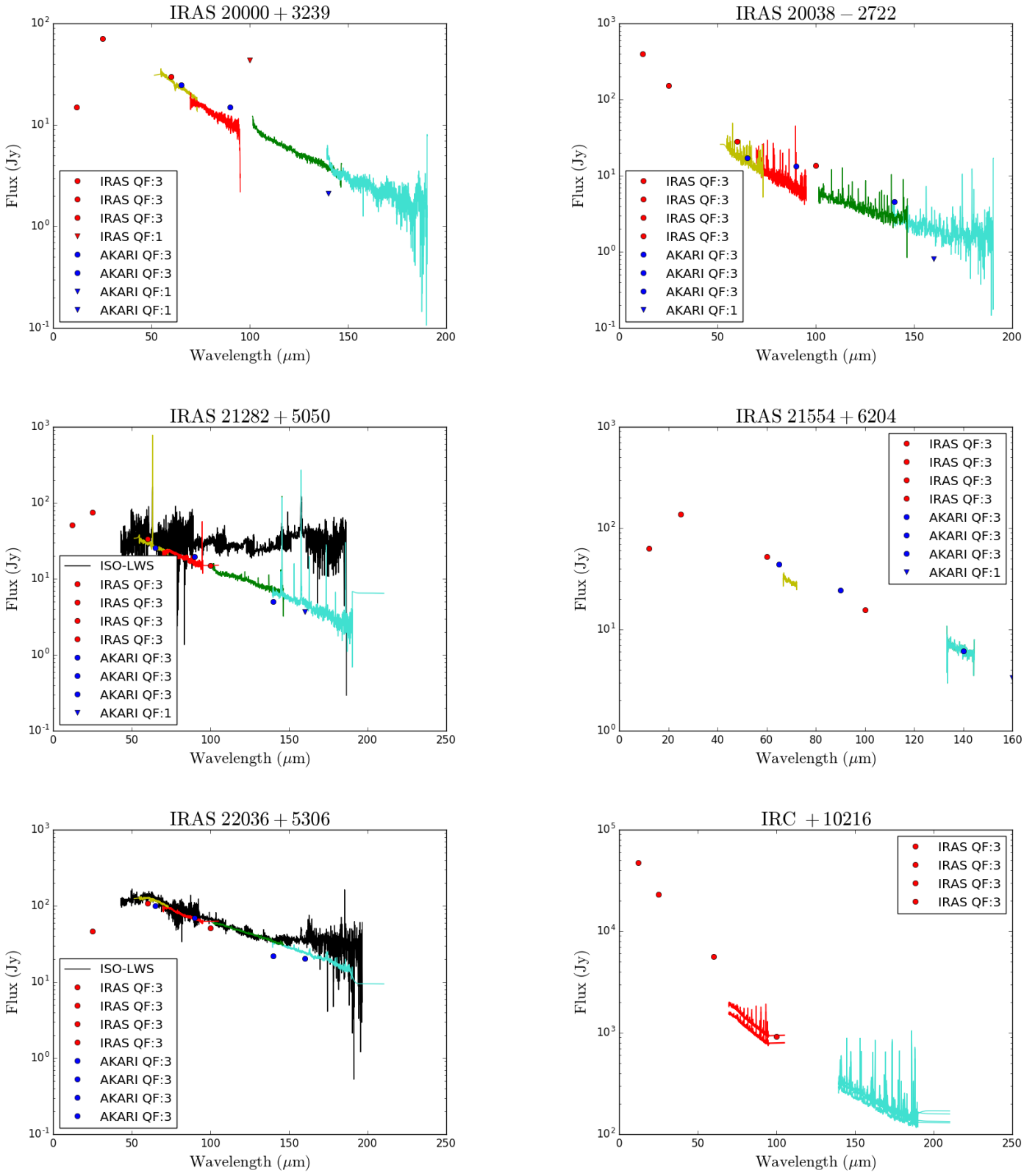

Fig. 8: Continued.

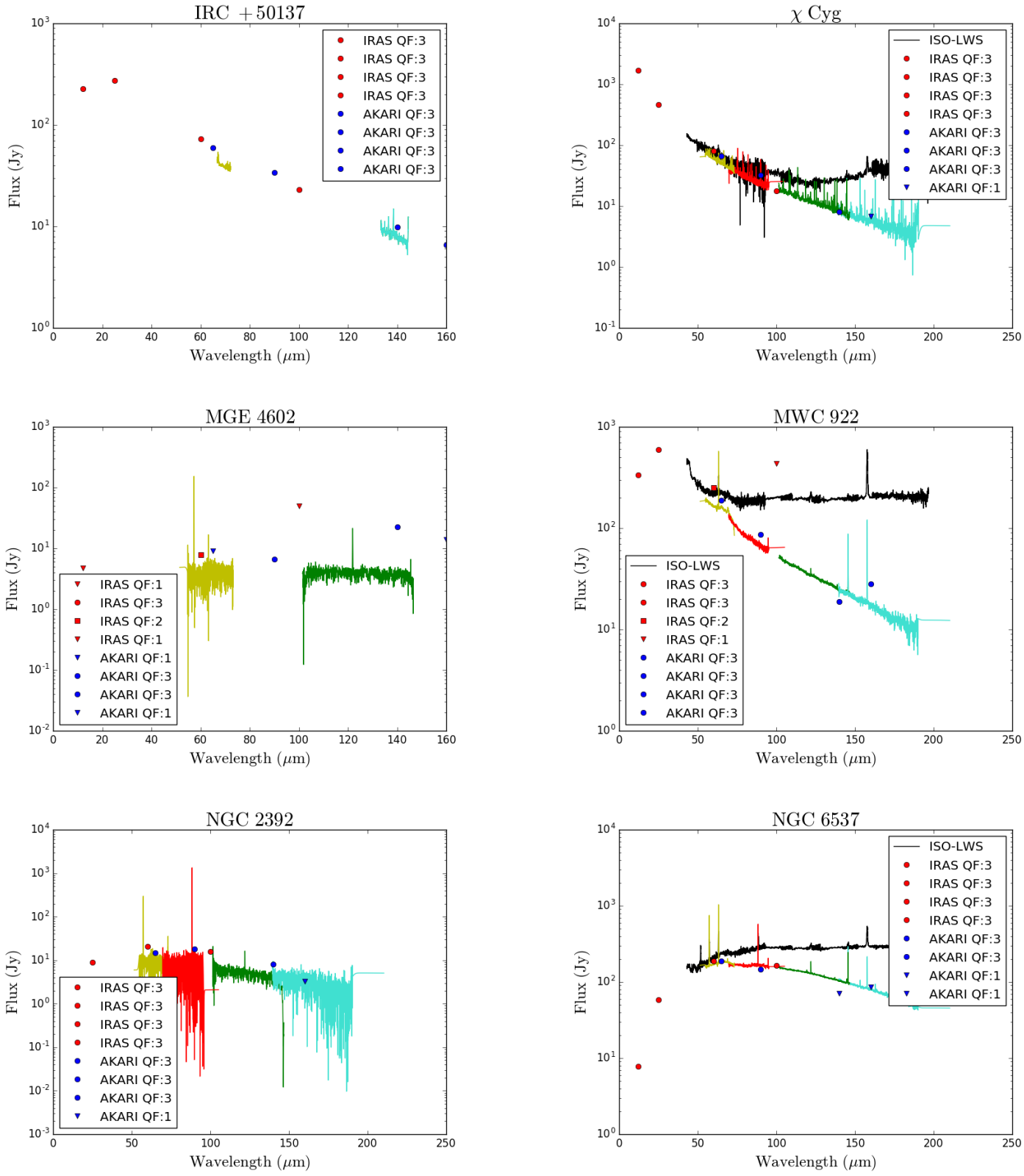

Fig. 8: Continued.

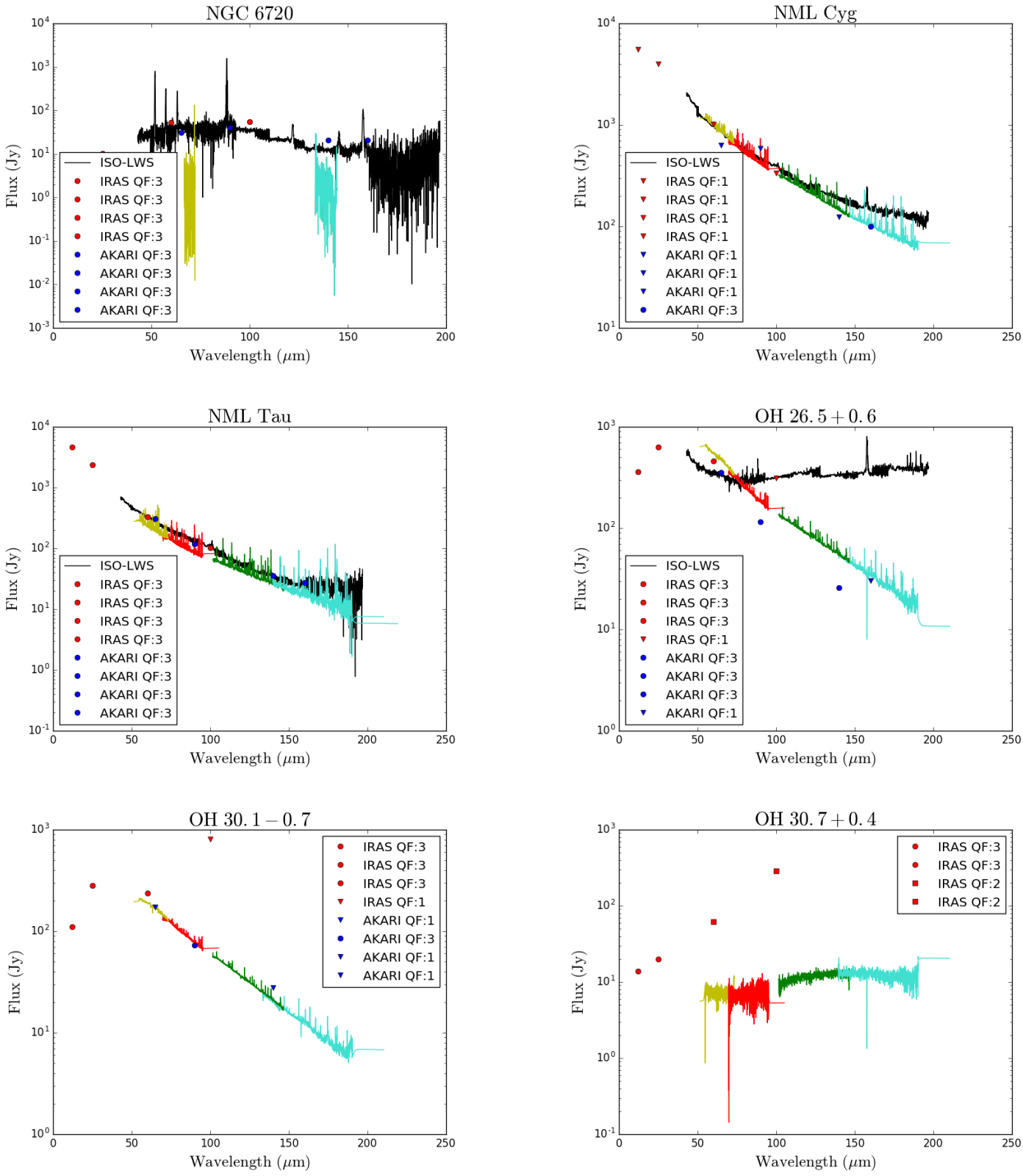

Fig. 8: Continued.

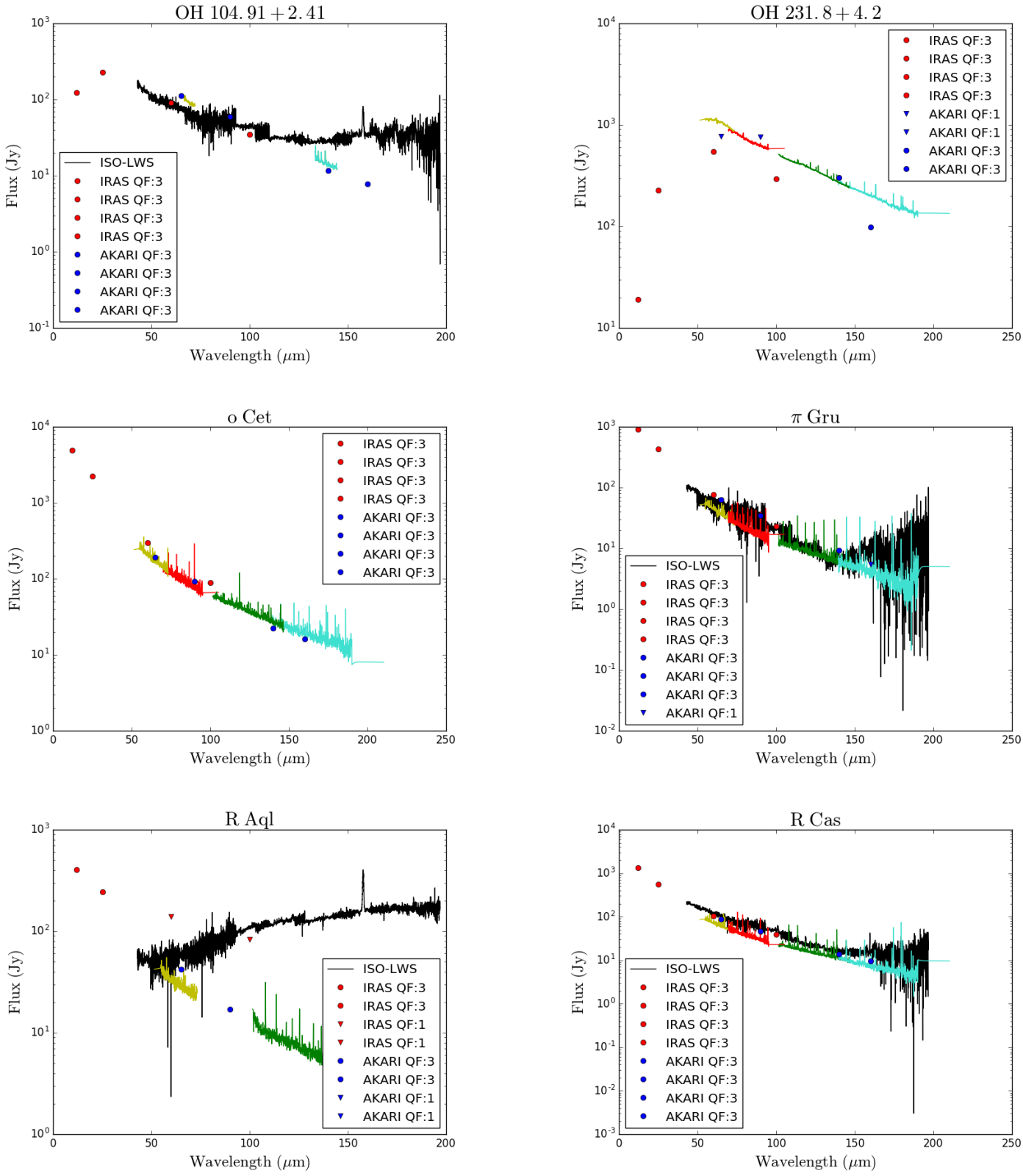

Fig. 8: Continued.

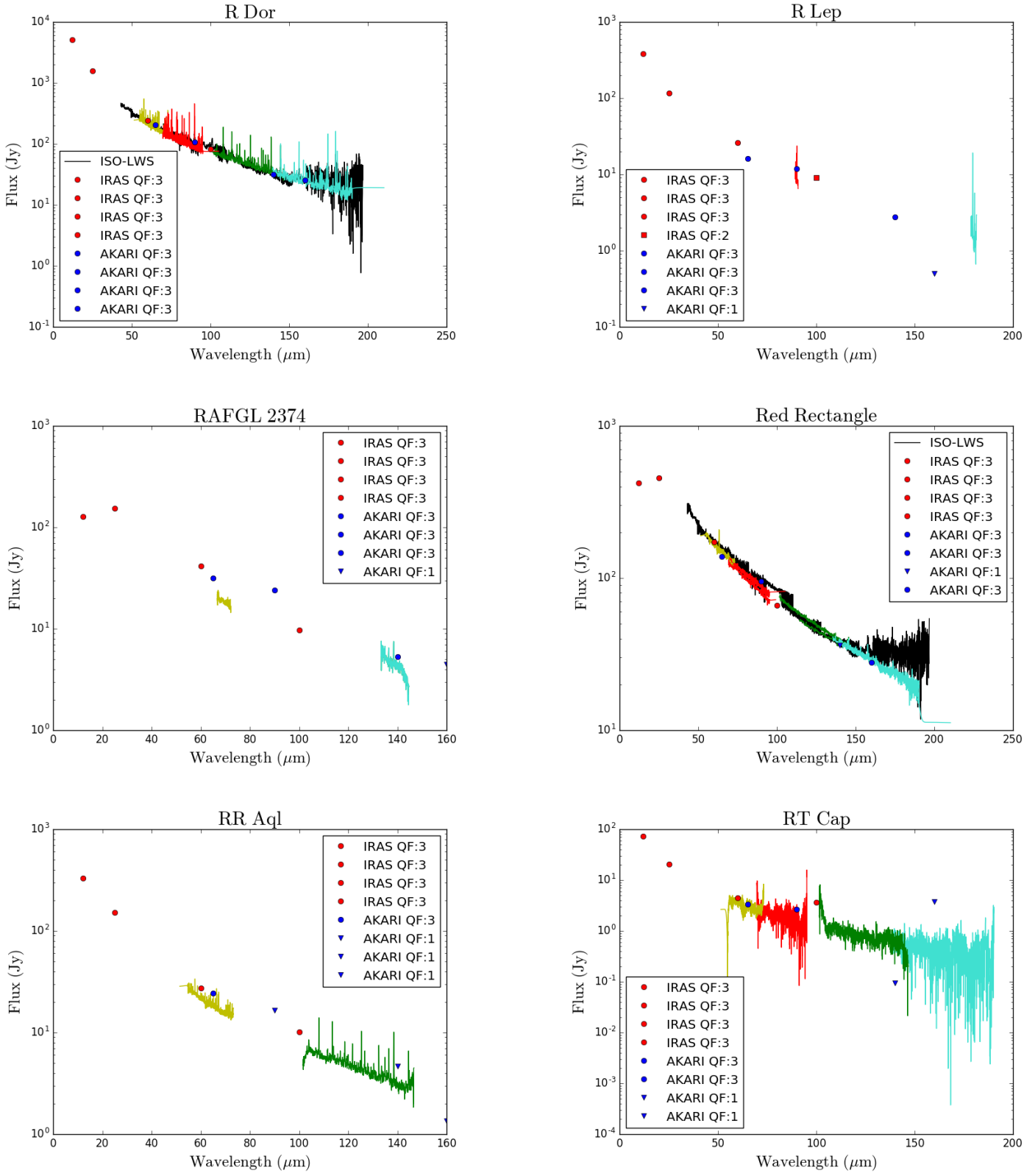

Fig. 8: Continued.

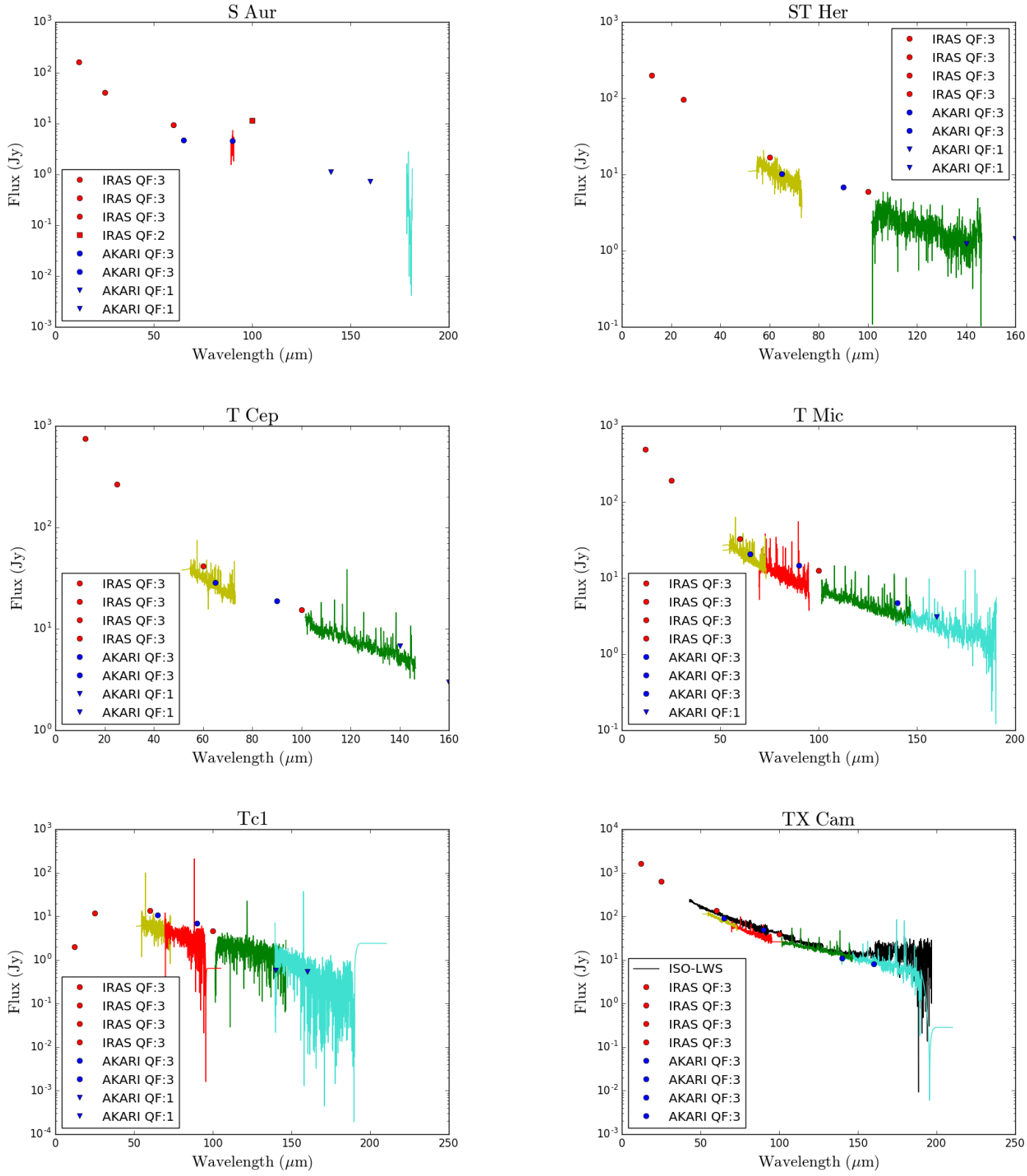

Fig. 8: Continued.

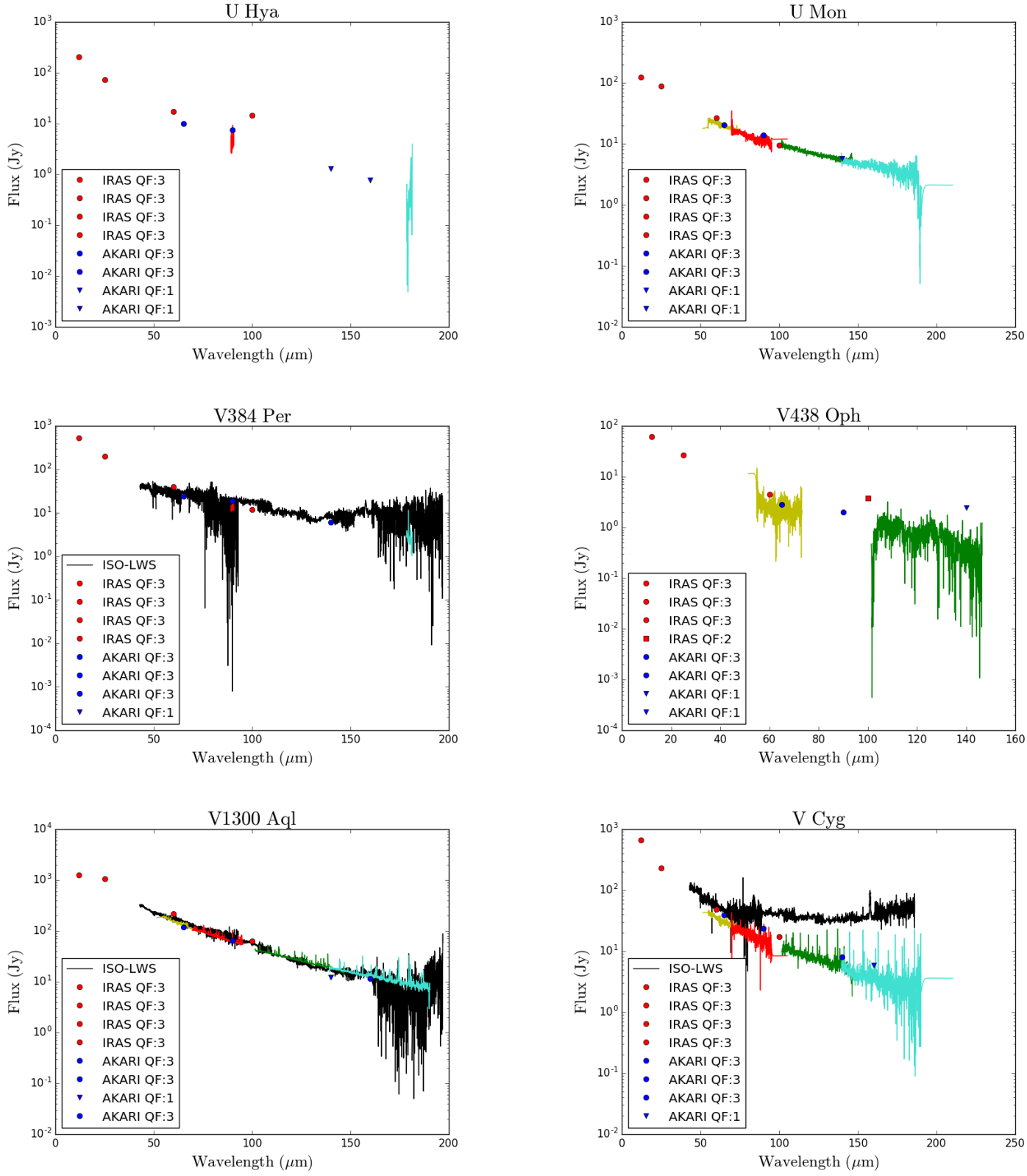

Fig. 8: Continued.

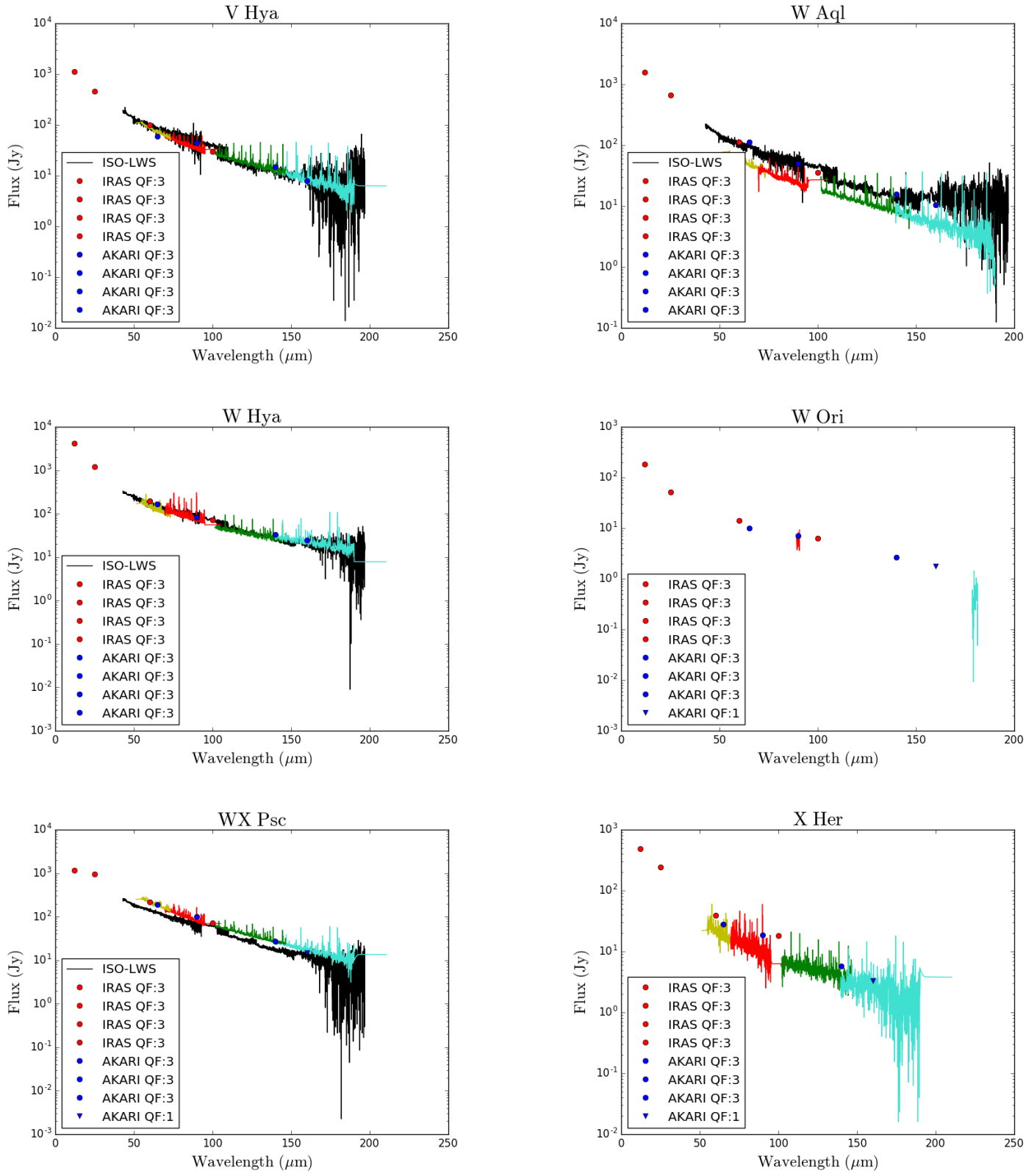

Fig. 8: Continued.

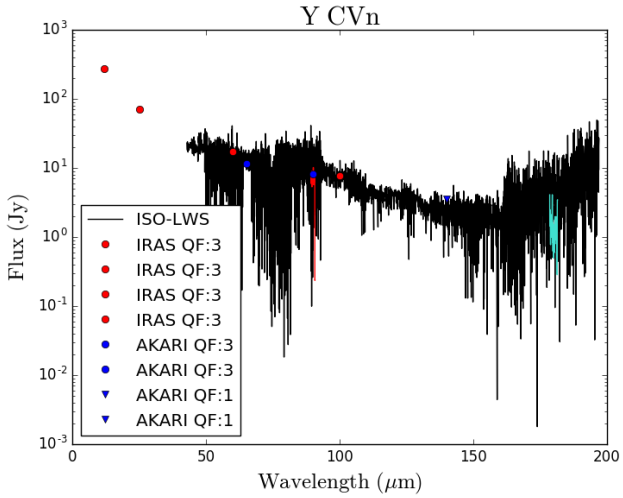

Fig. 8: Continued.

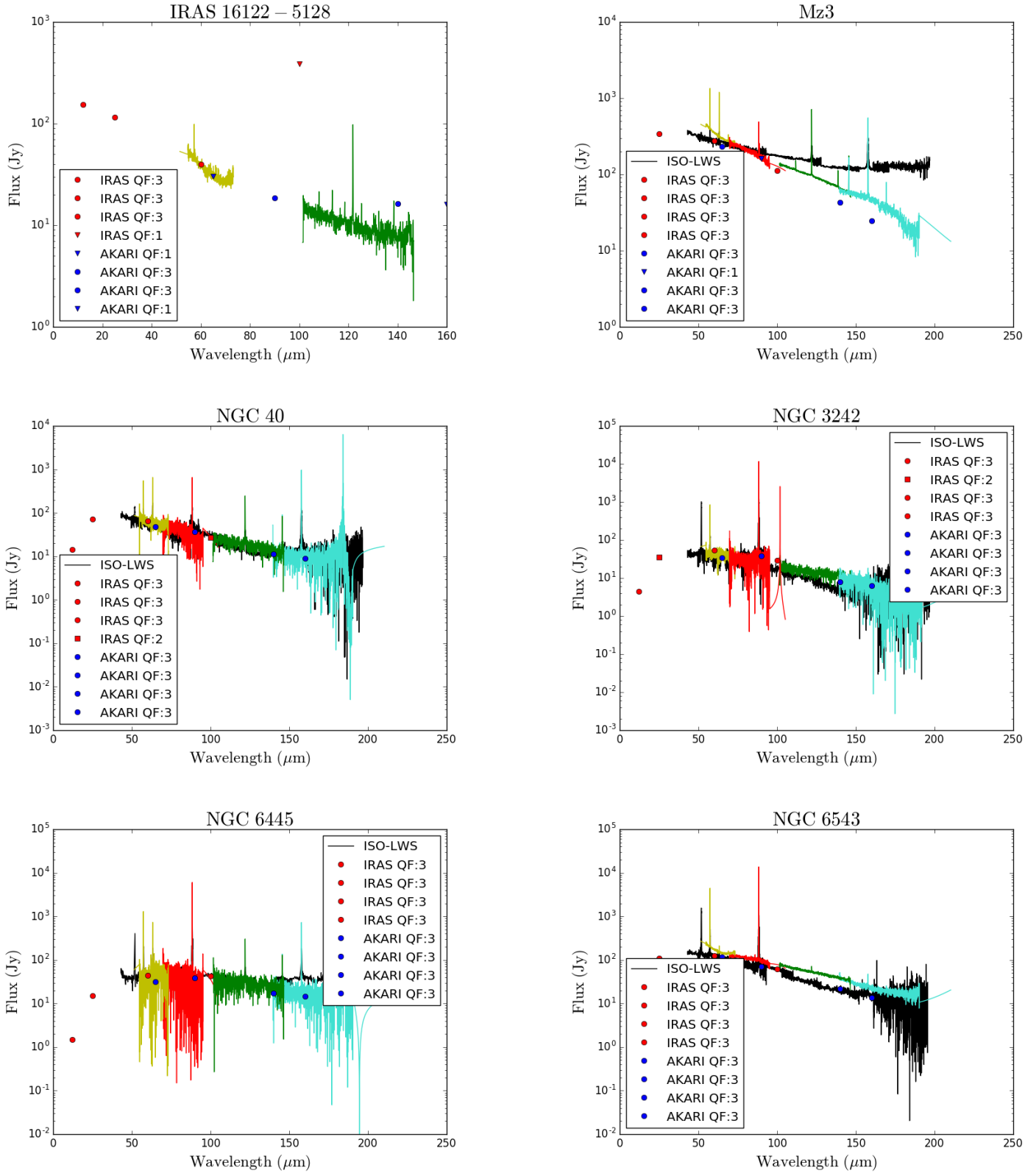

Fig. 9: As in Fig. 8 but for extended objects after applying point source flux loss correction and extended 5x5 correction. IRAS 16122-5128 appears in THROES catalogue and in HSA as MGE 4218.

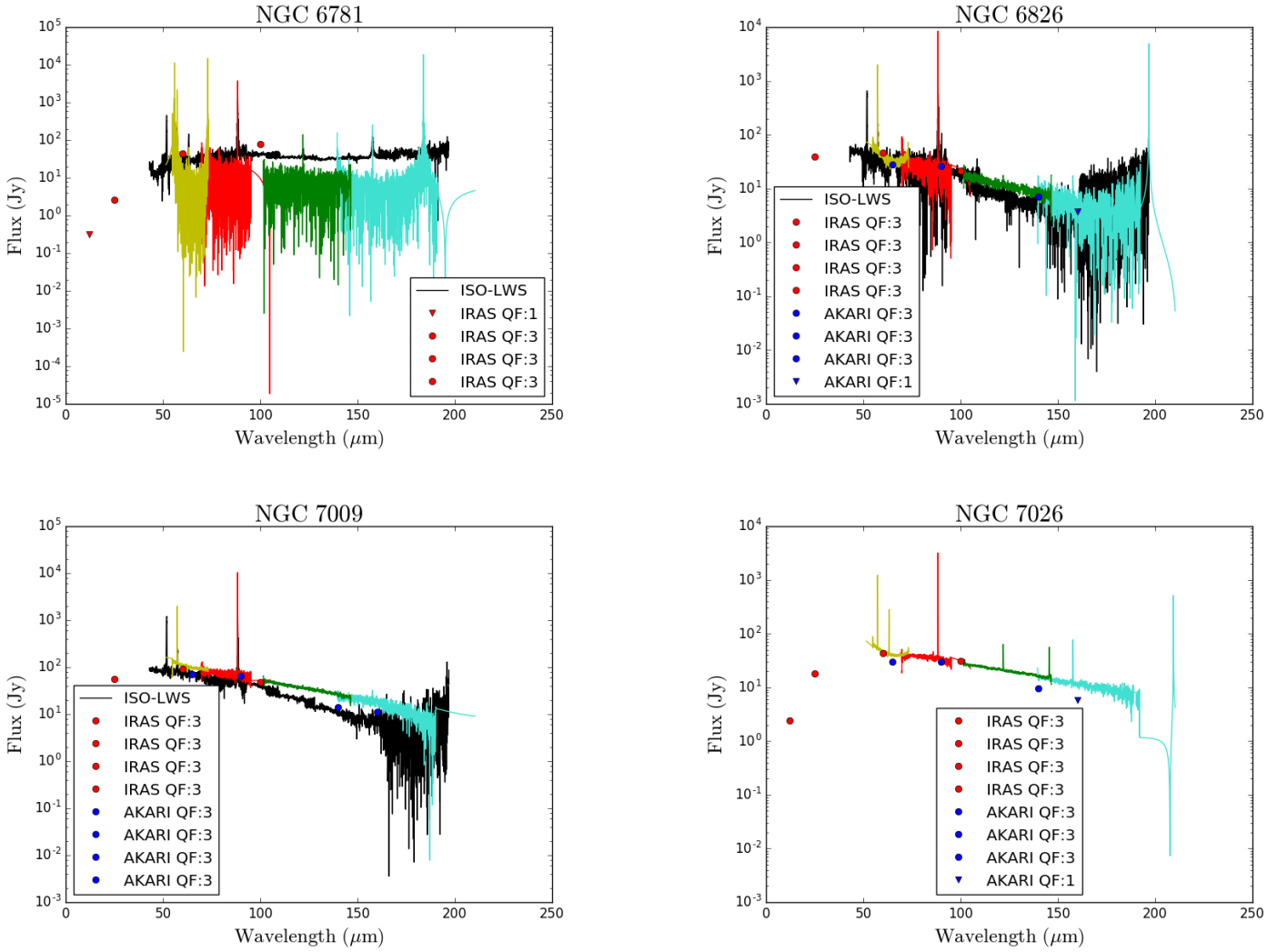

Fig. 9: Continued.

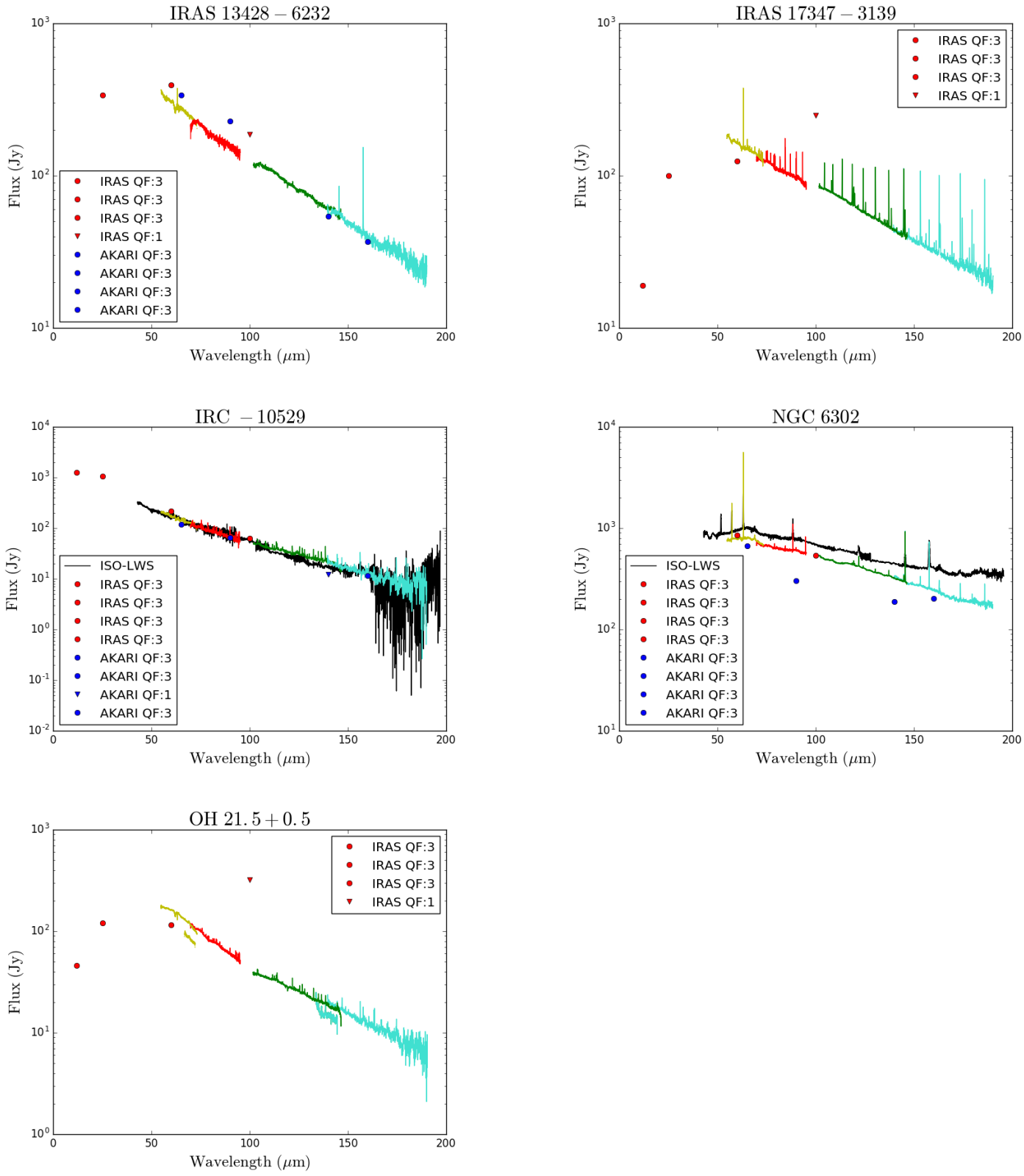

Fig. 10: As in Fig. 8 but for mispointed sources after applying point sources correction and semi-extended 3x3 correction.

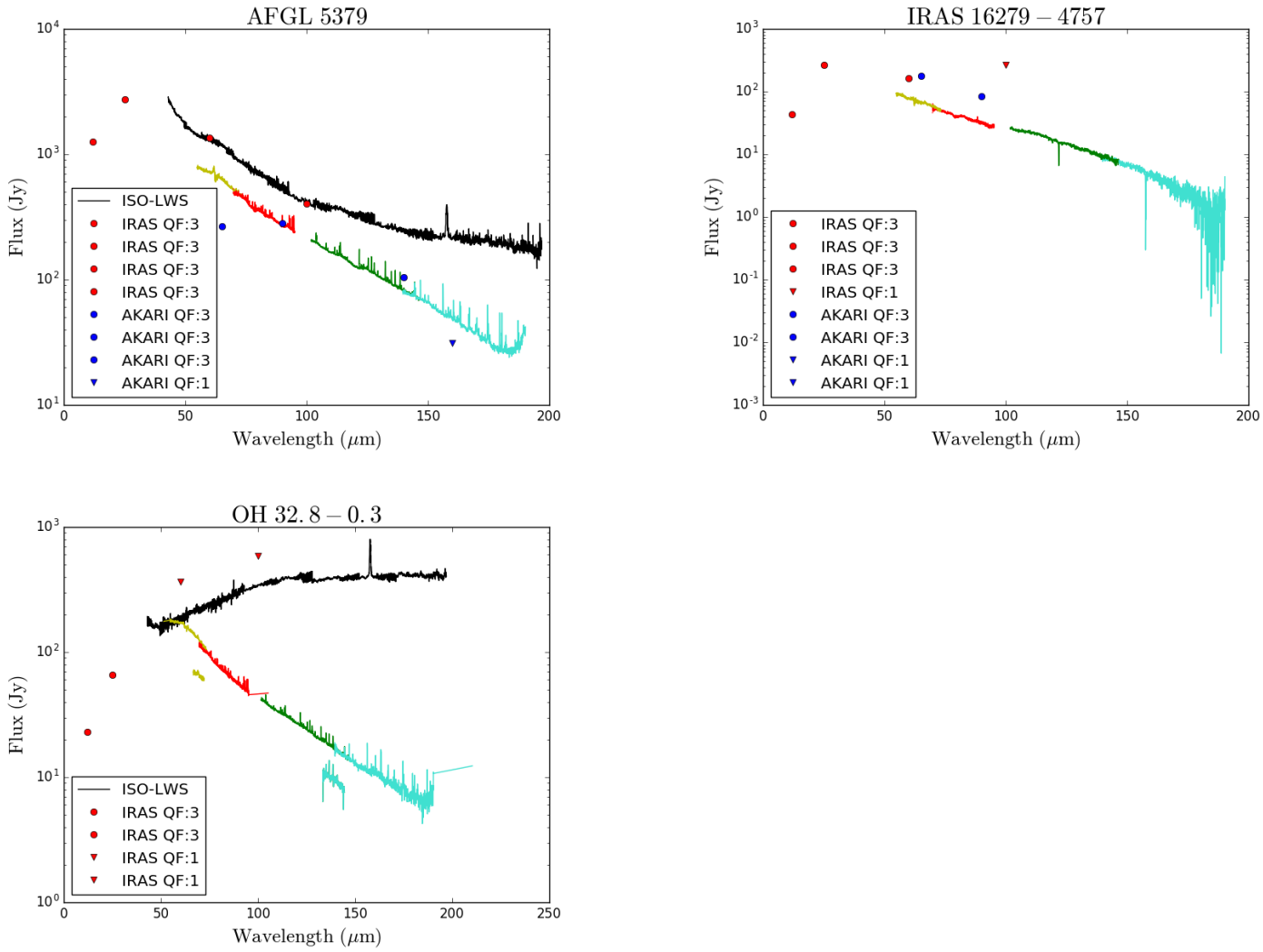

Fig. 11: As in Fig. 8 but for those sources corrected only by point sources correction. AFGL 5379 and IRAS 16279-4757 are mispointed targets for which the semi-extended 3x3 correction could not be applied as they are located in one of the outermost spaxels. The well-pointed object OH 32.8-0.3 shows, for unknown reasons probably related to problems during the observations, negative fluxes in some of the 3x3 central spaxels, so the semi-extended 3x3 correction produced a wrong final 1D spectrum.

Table 1: Basic information about all observations reprocessed in THROES. Column 1: Target name; Columns 2 and 3: Equatorial coordinates (J2000) in degrees; Columns 4, 5, and 6: Complementary data for each observation in IRAS, AKARI, or ISO; Column 7: Comments on complementary information about the PACS observations object: 1) Incomplete PACS wavelength coverage; 2) Mispointing (target not in the central spaxel); 3) Semi-extended object (size ∼3x3 central spaxels); 4) Extended object (size ∼5x5 spaxels); 5) Contamination in ISO data due to interstellar emission; 6) Faint source (≤10 Jy at 60 μm); 7) Multi epochs observations. If the observation presents a complete spectral coverage in PACS wavelength range, is well pointed, Chop/Nod and the source is point-like and intense, there is no comment in the column (-); Column 8: ObsIds; Column 9: Date of observation.

Target name	RA(deg)	Dec(deg)	IRAS	AKARI	ISO	Comments	ObsIDs	Date
AC Her	277.5676	21.8668	Yes	Yes	Yes	1,6	1342208896	2010-11-13
AFGL 618	70.7236	36.1147	Yes	Yes	Yes	-	1342225838	2011-08-07
							1342225839	2011-08-07
							1342225840	2011-08-07
AFGL 2019	268.3282	-26.9436	Yes	Yes	No	1,6	1342252253	2012-10-05
AFGL 2403	292.6228	19.8447	Yes	Yes	No	1	1342245226	2012-05-01
AFGL 2513	302.3093	31.4291	Yes	Yes	No	-	1342270010	2013-04-14
							1342269936	2013-04-12
AFGL 2688	315.5781	36.6938	No	No	Yes	-	1342199233	2010-06-26
							1342199234	2010-06-26
							1342199235	2010-06-27
AFGL 3068	349.8016	17.1931	Yes	Yes	Yes	-	1342199417	2010-06-30
							1342199418	2010-06-30
							1342257635	2012-12-21
AFGL 3116	353.6152	43.5506	Yes	Yes	No	-	1342212512	2011-01-11
							1342212513	2011-01-11
AFGL 4106	155.8311	-59.5346	Yes	Yes	Yes	1	1342207818	2010-11-03
AFGL 4202	223.1012	-62.0721	Yes	Yes	No	1,6	1342250004	2012-08-21
AFGL 4259	301.5947	27.0362	Yes	Yes	No	1,6	1342244918	2012-04-24
AFGL 5379	266.0942	-31.9276	Yes	Yes	Yes	2	1342228537	2011-09-13
							1342228538	2011-09-13
AFGL 6815	259.5830	-32.4556	Yes	Yes	No	-	1342216629	2011-03-22
							1342216630	2011-03-22
AQ Sgr	293.5791	-16.3741	Yes	Yes	No	-	1342268751	2013-03-28
							1342268752	2013-03-28
BD +30 3639	293.6884	30.5163	Yes	Yes	Yes	3	1342220600	2011-05-04
							1342220601	2011-05-04
CIT 6	154.0094	30.5718	Yes	No	Yes	-	1342197799	2010-06-05
							1342197800	2010-06-05
CPD-568032	257.2536	-56.9133	Yes	Yes	Yes	-	1342228201	2011-09-06
							1342228202	2011-09-06
CPD-642939	219.2920	-64.8013	Yes	Yes	No	1,6	1342250006	2012-08-21
EP Aqr	326.6327	-2.2127	Yes	Yes	No	-	1342270639	2013-04-20
							1342270684	2013-04-21
G Her	247.1606	41.8816	Yes	Yes	No	1	1342247780	2012-07-09
HD 56126	109.0427	9.9966	Yes	Yes	Yes	-	1342220930	2011-04-30
							1342220931	2011-04-30
HD 161796	266.2311	50.0443	Yes	Yes	Yes	-	1342208881	2010-11-12
							1342208882	2010-11-12
HD 235858	337.2932	54.8517	Yes	Yes	No	-	1342196686	2010-05-18
							1342196687	2010-05-18
HD 331319	297.3731	31.4545	Yes	Yes	No	1	1342245232	2012-05-01
Hen 2-90	197.4009	-61.3266	Yes	Yes	Yes	1,5,6	1342248308	2012-07-16
Hen 2-113	224.9730	-54.3020	Yes	Yes	Yes	-	1342225142	2011-08-02
							1342225143	2011-08-02
							1342249211	2012-08-07
Hen 3-401	154.8852	-60.2248	Yes	Yes	No	-	1342225588	2011-08-03
							1342225589	2011-08-03
Hen 3-1475	266.3090	-17.9462	Yes	Yes	Yes	-	1342229719	2011-09-24
							1342229720	2011-09-24
IC 418	81.8675	-12.6973	Yes	No	Yes	3	1342265942	2013-03-04
							1342265943	2013-03-04
IRAS 07027-7934	104.8599	-79.6463	Yes	Yes	Yes	1,6	1342245248	2012-05-02

Table 1: Continued.

Target name	RA(deg)	Dec(deg)	IRAS	AKARI	ISO	Comments	ObsIDs	Date
IRAS 08011-3627	120.7568	-36.5966	Yes	Yes	No	-	1342210381	2010-11-27
							1342256781	2012-12-04
							1342256782	2012-12-04
IRAS 08544-4431	134.0591	-44.7196	Yes	Yes	No	-	1342245956	2012-05-21
							1342245957	2012-05-21
IRAS 09256-6324	141.7220	-63.6302	Yes	Yes	No	-	1342210386	2010-11-27
							1342248357	2012-07-20
							1342248358	2012-07-20
IRAS 09371+1212	144.9749	11.9814	Yes	Yes	No	-	1342245647	2012-05-12
							1342245648	2012-05-12
IRAS 09425-6040	146.0066	-60.9072	Yes	Yes	No	-	1342225563	2011-07-25
							1342225564	2011-07-25
IRAS 10456-5712	161.91	-57.4674	Yes	Yes	No	-	1342211823	2010-12-28
							1342248928	2012-07-31
							1342248929	2012-07-31
IRAS 13428-6232	206.5854	-62.8000	Yes	Yes	No	2	1342212212	2010-12-31
							1342212213	2010-12-31
IRAS 15194-5115	230.7704	-51.4330	Yes	Yes	Yes	-	1342215685	2011-03-10
							1342215686	2011-03-10
IRAS 16122-5128	244.0190	-51.5989	Yes	Yes	No	1	1342240167	2012-02-18
IRAS 16279-4757	247.9087	-48.0677	Yes	Yes	No	2	1342228203	2011-09-06
							1342228204	2011-09-06
IRAS 16342-3814	249.417	-38.3380	Yes	Yes	Yes	-	1342216627	2011-03-22
							1342216628	2011-03-22
IRAS 16594-4656	255.7917	-47.0076	Yes	Yes	Yes	5	1342228414	2011-09-10
							1342228415	2011-09-10
IRAS 17010-3840	256.1179	-38.7396	Yes	Yes	No	1,6	1342216176	2011-03-16
IRAS 17251-2821	262.0770	-28.3991	Yes	Yes	No	1,6	1342228535	2011-09-13
IRAS 17276-2846	262.7012	-28.8172	Yes	Yes	No	1,6	1342228536	2011-09-13
IRAS 17323-2424	263.8583	-24.4422	Yes	Yes	No	1,6	1342228532	2011-09-13
IRAS 17347-3139	264.5054	-31.6827	Yes	No	No	2	1342229696	2011-09-24
							1342229697	2011-09-24
IRAS 17521-2938	268.8404	-29.6536	Yes	No	No	1,6	1342229802	2011-09-27
IRAS 18433-0228	281.4800	-2.4189	Yes	No	No	1	1342231743	2011-11-01
IRAS 18488-0107	282.8592	-1.0645	Yes	No	No	-	1342268791	2013-03-30
							1342268792	2013-03-30
IRAS 19067+0811	287.2845	8.2770	Yes	Yes	No	-	1342268797	2013-03-31
							1342268798	2013-03-31
IRAS 19306+1407	293.2295	14.2269	Yes	Yes	No	1,6	1342244921	2012-04-24
IRAS 19474-0744	297.5264	-7.6145	Yes	Yes	No	-	1342268638	2013-03-25
							1342268449	2013-03-26
IRAS 20000+3239	300.4980	32.7924	Yes	Yes	No	-	1342270612	2013-04-18
							1342270344	2013-04-17
IRAS 20038-2722	301.7301	-27.2249	Yes	Yes	No	-	1342268730	2013-03-29
							1342268569	2013-03-27
IRAS 21282+5050	322.4934	51.0666	Yes	Yes	Yes	5	1342223375	2011-06-30
							1342220741	2011-05-12
IRAS 21554+6204	329.2424	62.3121	Yes	Yes	No	1,6	1342245813	2012-05-15
							1342247150	2012-06-20
IRAS 22036+5306	331.3761	53.3591	Yes	Yes	Yes	5	1342221882	2011-05-29
							1342221883	2011-05-29
IRC +10216	146.9892	13.2787	Yes	No	No	1,7	1342245395	2012-05-05
							1342221889	2011-05-29
							1342253754	2012-10-21
							1342256262	2012-11-30
IRC -10529[9]	302.6142	-6.2710	Yes	Yes	Yes	2	1342208931	2010-11-14
							1342208932	2010-11-14
IRC +50137	77.831	52.8758	Yes	Yes	No	1	1342249315	2012-08-10

Table 1: Continued.

Target name	RA(deg)	Dec(deg)	IRAS	AKARI	ISO	Comments	ObsIDs	Date
χ Cyg	297.6413	32.9140	Yes	Yes	Yes	-	1342198176	2010-06-02
							1342198177	2010-06-02
MGE 4602	271.1620	-20.6242	Yes	Yes	No	1,6	1342243506	2012-03-24
MWC 922	275.3162	-13.0241	Yes	Yes	Yes	5	1342229805	2011-09-27
							1342229806	2011-09-27
Mz 3	244.3058	-51.9862	Yes	Yes	Yes	4	1342243109	2012-03-21
							1342243110	2012-03-21
NGC 40	3.2542	72.5219	Yes	Yes	Yes	4,6	1342236879	2012-01-08
							1342236880	2012-01-08
NGC 2392	112.2948	20.9118	Yes	Yes	No	6	1342229792	2011-09-26
							1342229816	2011-09-27
NGC 3242	156.1920	-18.6411	Yes	Yes	Yes	4,6	1342232278	2011-11-12
							1342232279	2011-11-12
NGC 6302	258.4342	-37.1044	Yes	Yes	Yes	2	1342230150	2011-10-05
							1342230151	2011-10-05
NGC 6445	267.3133	-20.0095	Yes	Yes	Yes	4,6	1342242440	2012-03-26
							1342242441	2012-03-26
NGC 6537	271.3045	-19.8430	No	Yes	Yes	3,5	1342231322	2011-10-22
							1342231323	2011-10-22
NGC 6543	269.6385	66.6330	No	Yes	Yes	4	1342238388	2012-01-29
							1342238389	2012-01-29
							1342212264	2011-01-02
NGC 6543 WKnot	269.5722	66.6356	No	No	No	-	1342235679	2011-12-27
							1342235680	2011-12-27
NGC 6720	283.3961	33.0291	Yes	Yes	Yes	1,6	1342208920	2010-11-14
NGC 6720 OFFCenter	283.3937	33.0326	Yes	Yes	Yes	-	1342233716	2011-12-07
							1342233717	2011-12-07
NGC 6781	289.6170	6.5386	Yes	No	Yes	4,6	1342230999	2011-10-14
							1342231000	2011-10-14
NGC 6781 Rim	289.6313	6.5388	No	No	No	-	1342231001	2011-10-15
							1342231002	2011-10-15
NGC 6826	296.2006	50.5250	Yes	Yes	Yes	3,6	1342238926	2012-02-10
							1342238927	2012-02-10
NGC 6826 Rim	296.2207	50.5290	No	No	No	-	1342235850	2011-12-31
							1342235851	2011-12-31
NGC 7009	316.0450	-11.3635	Yes	Yes	Yes	4	1342232300	2011-11-13
							1342232301	2011-11-13
NGC 7026	316.5773	47.8519	Yes	Yes	No	3	1342234268	2011-12-06
							1342234269	2011-12-06
NML Cyg	311.606	40.1165	No	Yes	Yes	-	1342198174	2010-06-02
							1342198175	2010-06-02
NML Tau	58.3701	11.4062	Yes	Yes	Yes	-	1342203679	2010-08-28
							1342203680	2010-08-28
							1342203681	2010-08-28
OH 21.5+0.5	277.1316	-9.9696	No	No	No	2,7	1342242438	2012-03-26
							1342268778	2013-03-29
							1342268748	2013-03-30
OH 26.5+0.6	279.3852	-5.3998	Yes	Yes	Yes	5	1342207776	2010-10-31
							1342207777	2010-10-31
OH 30.1-0.7	282.1746	-2.8411	Yes	Yes	No	-	1342216207	2011-03-04
							1342269304	2013-04-03
							1342269305	2013-04-03
OH 30.7+0.4	281.5241	-1.9881	Yes	No	No	6	1342268789	2013-03-30
							1342268790	2013-03-30
OH 32.8-0.3	283.0924	-0.2371	Yes	No	Yes	5,7	1342209738	2010-11-07
							1342268793	2013-03-30
							1342268794	2013-03-30
OH 104.91+2.41	334.8645	59.8560	Yes	Yes	Yes	1	1342212261	2011-01-01

Table 1: Continued.

Target name	RA(deg)	Dec(deg)	IRAS	AKARI	ISO	Comments	ObsIDs	Date
OH 231.8+4.2	115.5701	-14.7144	Yes	Yes	No	-	1342196694	2010-05-19
							1342196695	2010-05-19
o Cet	34.8366	-2.9776	Yes	Yes	No	-	1342213286	2011-01-25
							1342213287	2011-01-25
π Gru	335.6842	-45.9479	Yes	Yes	Yes	-	1342210397	2010-11-28
							1342210398	2010-11-28
R Aql	286.5927	8.2300	Yes	Yes	Yes	1,5	1342243900	2012-04-08
R Cas	359.6036	51.3888	Yes	Yes	Yes	-	1342212576	2011-01-12
							1342212577	2011-01-12
R Dor	69.1899	-62.0771	Yes	Yes	Yes	3	1342197794	2010-06-05
							1342197795	2010-06-05
R Lep	74.9014	-14.8062	Yes	Yes	No	1,6	1342249509	2012-08-14
RAFGL 2374	290.4021	9.4656	Yes	Yes	No	1,6	1342244920	2012-04-24
Red Rectangle	94.9925	-10.6374	Yes	Yes	Yes	-	1342220928	2011-04-30
							1342220929	2011-04-30
RR Aql	299.4002	-1.8864	Yes	Yes	No	1	1342269414	2013-04-05
RT Cap	304.2772	-21.3179	Yes	Yes	No	6	1342269308	2013-04-03
							1342269355	2013-04-04
S Aur	81.7810	34.1496	Yes	Yes	No	1,6	1342250896	2012-09-11
ST Her	237.6942	48.4830	Yes	Yes	No	1,6	1342247537	2012-06-30
T Cep	317.3824	68.4908	Yes	Yes	No	1	1342246557	2012-06-01
T Mic	306.9799	-28.2610	Yes	Yes	No	-	1342268729	2013-03-29
							1342268788	2013-03-30
							1342269458	2013-04-06
Tc 1	266.3970	-46.0899	Yes	Yes	No	6	1342231319	2011-10-22
							1342231320	2011-10-22
TX Cam	75.2099	56.1812	Yes	Yes	Yes	3	1342225855	2011-08-08
							1342225856	2011-08-08
U Hya	159.3886	-13.3845	Yes	Yes	No	1,6	1342256947	2012-12-11
U Mon	112.6977	-9.7768	Yes	Yes	No	-	1342206993	2010-10-23
							1342245243	2012-05-02
							1342245244	2012-05-02
V384 Per	51.6229	47.5301	Yes	Yes	Yes	1,6	1342250572	2012-09-04
V438 Oph	258.6657	11.0694	Yes	Yes	No	1,6	1342252326	2012-10-07
V1300 Aql	302.6161	-6.2704	Yes	Yes	Yes	-	1342269516	2013-04-07
							1342269910	2013-04-11
V Cyg	310.3261	48.1413	Yes	Yes	Yes	5	1342208939	2010-11-15
							1342208940	2010-11-15
V Hya	162.9052	-21.2500	Yes	Yes	Yes	-	1342197790	2010-06-05
							1342197791	2010-06-05
W Aql	288.8476	-7.0471	Yes	Yes	Yes	-	1342209731	2010-11-06
							1342209732	2010-11-07
W Hya	207.2583	-28.3676	Yes	Yes	Yes	-	1342212604	2011-01-14
							1342223808	2011-07-09
W Ori	76.3488	1.1776	Yes	Yes	No	1,6	1342249503	2012-08-14
WX Psc	16.6082	12.5980	Yes	Yes	Yes	-	1342202121	2010-07-28
							1342202122	2010-07-28
X Her	240.6632	47.2403	Yes	Yes	No	-	1342197802	2010-06-05
							1342197803	2010-06-05
							1342202120	2010-07-28
Y CVn	191.2826	45.4402	Yes	Yes	Yes	1,6	1342254305	2012-11-02

Table 2: . Photometric data of THROES targets. Target name (Col. 1), as it appears in HSA, galactic coordinates (Cols. 2 and 3), IRAS (100 μm) and AKARI (160 μm) photometric data (Cols. 4 and 5), and PACS synthetic photometry at 100 and 160 μm (Cols. 6 and 7)

Target name	b(deg)	l(deg)	$IRAS_{100}$ (Jy)	$AKARI_{160}$ (Jy)	$PACS_{IRAS100}$ (Jy)	$PACS_{AKARI160}$ (Jy)
AC Her	14.2415	50.4928	8.0	<3.2	-	-
AFGL 618	-6.5275	166.4460	340.0	111.7	859.0	195.9
AFGL 2019	-0.4324	2.5826	<227.0	48.6	-	-
AFGL 2403	0.7353	54.9494	<31.3	<10.1	-	-
AFGL 2513	-0.8653	69.3522	20.8	<5.8	10.7	3.9
AFGL 2688	-6.5032	80.1675	<863.0	-	1969.1	467.8
AFGL 3068	-40.3540	93.5266	73.7	24.4	102.0	34.3
AFGL 3116	-17.1467	108.4549	35.5	10.9	46.8	14.9
AFGL 4106	-1.8789	285.1439	181.0	60.1	-	-
AFGL 4202	-2.4514	316.5887	<75.3	<6.5	-	-
AFGL 4259	-2.7141	65.3167	7.5	<2.6	-	-
AFGL 5379	-1.3330	357.3084	406.0	<31.2	-	-
AFGL 6815	2.9842	353.8442	82.4	<18.37	120.0	40.3
AQ Sgr	-16.7007	22.7377	5.9	<0.5	1.3	0.4
BD +30 3639	5.0194	64.7853	70.1	<23.1	70.6	21.0
CIT 6	55.9641	197.7148	86.1	-	83.5	24.2
CPD-568032	-9.9082	332.9152	91.7	29.4	106.2	26.7
CPD-642939	-4.2026	313.8867	20.6	<4.7	-	-
EP Aqr	-39.2603	54.2000	16.4	<4.9	15.0	4.7
G Her	43.7146	66.1579	6.6	<0.1	-	-
HD 56126	9.9947	206.7457	18.7	<3.8	20.5	6.0
HD 161796	30.8696	77.1331	48.7	10.7	56.1	8.0
HD 235858	-2.5181	103.3488	41.0	8.5	34.0	10.0
HD 331319	2.7327	67.1633	14.8	<4.1	-	-
Hen 2-90	1.4683	305.1099	<50.2	<11.1	-	-
Hen 2-113	3.9885	321.0483	71.3	20.9	90.7	26.0
Hen 3-401	-2.7162	285.1194	41.5	16.6	45.2	15.7
Hen 3-1475	5.7788	9.3644	33.4	12.1	36.2	9.7
IC 418	-24.2837	215.2120	31.2	-	29.1	9.5
IRAS 07027-7934	-26.2939	291.3749	13.6	<4.4	-	-
IRAS 08011-3627	-2.9959	253.0207	12.0	<4.7	13.6	4.6
IRAS 08544-4431	0.3864	265.5011	<28.4	<3.2	29.3	11.5
IRAS 09256-6324	-9.2362	282.4206	13.5	<5.3	15.6	7.1
IRAS 09371+1212	42.7271	221.8893	28.2	<11.6	32.7	15.5
IRAS 09425-6040	-5.8842	282.0386	5.1	<1.3	7.5	1.8
IRAS 10456-5712	1.4921	286.8707	10.9	<5.1	15.6	5.8
IRAS 13428-6232	-0.5939	309.1588	<186.0	36.9	-	-
IRAS 15194-5115	4.6593	325.5339	51.0	15.0	37.0	11.4
IRAS 16122-5128	-0.6095	331.8689	<387.0	<16.1	-	-
IRAS 16279-4757	0.0851	336.1433	<265.0	-	-	-
IRAS 16342-3814	5.8464	344.0739	139.0	43.2	193.9	65.4
IRAS 16594-4656	-3.2887	340.3924	34.4	<10.6	45.7	10.8
IRAS 17010-3840	1.5481	347.1050	<50.1	<6.3	-	-

Table 2: Continued.

Target name	b(deg)	l(deg)	$IRAS_{100}$ (Jy)	$AKARI_{160}$ (Jy)	$PACS_{IRAS100}$ (Jy)	$PACS_{AKARI160}$ (Jy)
IRAS 17251-2821	3.4922	358.4142	<19.9	-	-	-
IRAS 17276-2846	2.8046	358.3664	<30.0	-	-	-
IRAS 17323-2424	4.3084	2.6112	<13.5	<0.7	-	-
IRAS 17347-3139	-0.0557	356.8018	<249.0	-	-	-
IRAS 17521-2938	-2.1916	0.4718	<110.0	-	-	-
IRAS 18433-0228	0.1239	30.1503	<240.0	-	-	-
IRAS 18488-0107	-0.4851	31.9844	72.8	-	20.9	6.9
IRAS 19067+0811	-0.1323	42.3093	<91.1	-	12.4	2.4
IRAS 19306+1407	-2.4774	50.3034	10.0	<7.6	-	-
IRAS 19474-0744	-16.4859	32.7232	17.2	<3.2	20.8	6.5
IRAS 20000+3239	1.1609	69.6792	<43.1	-	12.0	3.4
IRAS 20038-2722	-27.6822	14.7708	13.6	<0.8	9.8	3.3
IRAS 21282+5050	-0.1178	93.9871	15.0	<3.7	16.6	7.2
IRAS 21554+6204	5.9916	104.1301	15.6	<3.3	-	-
IRAS 22036+5306	-1.8353	99.6333	50.7	20.3	66.1	21.2
IRC +10216	45.0604	221.4467	922.0	-	-	-
IRC -10529[10]	-20.4151	36.3565	63.7	11.4	-	-
IRC +50137	7.8349	156.4379	23.0	6.6	-	-
χ Cyg	3.2762	68.5386	17.7	<6.9	24.2	6.8
MGE 4602	0.4734	9.3523	<50.0	<14.0	-	-
Mz 3	-1.0113	331.7275	113.0	24.7	77.5	28.3
NGC 40	9.8680	120.0162	27.5	9.1	11.5	4.8
NGC 2392	17.4002	197.8784	16.1	<3.3	-	-
NGC 3242	32.0509	261.0499	29.6	6.4	15.4	3.6
NGC 6302	1.0558	349.5075	537.0	201.7	-	-
NGC 6445	3.9051	8.0758	43.2	14.6	13.4	3.5
NGC 6537	0.7395	10.0989	166.0	<85.5	155.4	70.9
NGC 6543	29.9548	96.4680	60.9	13.9	48.5	13.0
NGC 6543 WKnot	29.9810	96.4712	-	-	-	-
NGC 6720	13.9782	63.1700	54.6	20.6	-	-
NGC 6720 OFFcenter	13.9814	63.1725	54.6	20.6	-	-
NGC 6781	-2.9878	41.8407	77.0	-	0.6	1.6
NGC 6781 Rim	-3.0000	41.8475	77.0	-	-	-
NGC 6826	12.7923	83.5616	21.3	<3.7	11.7	5.8
NGC 6826 Rim	12.7828	83.5713	-	-	-	-
NGC 7009	-34.5713	37.7621	48.1	11.3	29.0	8.6
NGC 7026	0.3753	89.0020	30.9	<5.8	17.8	1.7
NML Cyg	-1.9208	80.7982	<334.0	100.1	400.0	109.2
NML Tau	-31.4120	177.9545	103.0	27.4	131.1	22.9
OH 21.5+0.5	0.4893	21.4588	<319.0	-	-	-
OH 26.5+0.6	0.6179	26.5434	<311.0	<30.25	181.0	33.5
OH 30.1-0.7	-0.6862	30.0911	<807.0	-	93.6	15.0
OH 30.7+0.4	0.2813	30.5537	290.0	-	6.9	12.7

[10] Also appears as V1300 Aql. We keep two different entries as the coordinates are different.

Table 2: Continued.

Target name	b(deg)	l(deg)	$IRAS_{100}$ (Jy)	$AKARI_{160}$ (Jy)	$PACS_{IRAS100}$ (Jy)	$PACS_{AKARI160}$ (Jy)
OH 32.8-0.3	-0.3154	32.8271	<583.0	-	68.6	14.0
OH 104.91+2.41	2.4134	104.9083	35.0	7.8	-	-
OH 231.8+4.2	4.2196	231.8354	294.0	98.9	586.2	198.0
o Cet	-57.9827	167.7549	88.4	16.1	74.3	18.5
π Gru	-55.1638	350.2822	23.3	<5.5	18.4	6.0
R Aql	0.4539	41.9524	<83.1	-	-	-
R Cas	-10.6191	114.5608	38.8	9.5	29.6	10.5
R Dor	-39.3424	272.6713	83.4	25.5	92.8	33.2
R Lep	-31.3270	214.3244	9.1	<0.5	-	-
RAFGL 2374	-2.3064	44.7947	9.8	<4.5	-	-
Red Rectangle	-11.7648	218.9680	66.2	<28.0	88.4	35.0
RR Aql	-15.5601	38.9171	10.1	<1.4	-	-
RT Cap	-27.9386	21.9411	3.6	<3.8	2.2	0.6
S Aur	-0.5112	173.4866	11.6	<0.7	-	-
ST Her	49.4432	76.9788	6.0	<1.4	-	-
T Cep	13.8449	104.8050	15.3	<3.0	-	-
T Mic	-32.4287	15.1857	12.7	<3.1	10.4	3.2
Tc 1	-8.8349	345.2375	4.7	<0.5	2.0	1.0
U Hya	38.0741	259.9663	14.5	<0.8	-	-
U Mon	4.1536	226.1413	9.5	-	12.0	4.9
V384 Per	-7.5975	148.1771	11.9	-	-	-
V438 Oph	26.4554	32.1306	3.7	-	-	-
V1300 Aql	-20.4165	36.3580	63.7	11.4	72.7	17.5
V Cyg	3.7667	86.5361	17.2	<6.0	13.3	5.2
V Hya	33.6014	268.9648	29.9	8.0	33.9	9.6
W Aql	-8.5161	29.3389	36.0	10.6	26.6	7.6
W Hya	32.8108	318.0223	72.2	24.3	72.3	26.6
W Ori	-22.8179	199.0092	6.27	<1.8	-	-
WX Psc	-50.1074	128.6416	72.1	<15.0	77.5	19.8
X Her	47.7855	74.4639	18.3	<3.3	9.5	3.6
Y CVn	71.6450	126.4472	7.8	-	-	-

A&A 619, C2 (2018)
https://doi.org/10.1051/0004-6361/201833177e

Astronomy & Astrophysics

Warm CO in evolved stars from the THROES catalogue

I. *Herschel*-PACS spectroscopy of O-rich envelopes

(Corrigendum)

J. Ramos-Medina[1], C. Sánchez Contreras[1], P. García-Lario[2], and J. M. da Silva Santos[1,3]

[1] Department of Astrophysics, Astrobiology Centre (CSIC-INTA), ESAC campus, PO Box 78, 28691 Villanueva de la Cañada, Madrid, Spain
e-mail: jramos@cab.inta-csic.es
[2] European Space Astronomy Centre, European Space Agency, PO Box 78, 28691 Villanueva de la Cañada, Madrid, Spain
[3] Institute for Solar Physics, Department of Astronomy, Stockholm University, AlbaNova University Centre, 106 91 Stockholm, Sweden

A&A, 618, A171 (2018), https://doi.org/10.1051/0004-6361/201833177

Key words. stars: AGB and post-AGB – circumstellar matter – stars: mass-loss – planetary nebulae: general – infrared: stars – errata, addenda

Following a production error, many powers of ten were incorrectly displayed in the original version of this paper. Here we republish the paper in its entirety, correcting the errors.

A&A 618, A171 (2018)
https://doi.org/10.1051/0004-6361/201833177

Astronomy & Astrophysics

Warm CO in evolved stars from the THROES catalogue

I. *Herschel*-PACS spectroscopy of O-rich envelopes⋆

J. Ramos-Medina[1], C. Sánchez Contreras[1], P. García-Lario[2], and J. M. da Silva Santos[1,3]

[1] Department of Astrophysics, Astrobiology Centre (CSIC-INTA), ESAC campus, PO Box 78, 28691 Villanueva de la Cañada, Madrid, Spain
e-mail: jramos@cab.inta-csic.es
[2] European Space Astronomy Centre, European Space Agency, PO Box 78, 28691 Villanueva de la Cañada, Madrid, Spain
[3] Institute for Solar Physics, Department of Astronomy, Stockholm University, AlbaNova University Centre, 106 91 Stockholm, Sweden

Received 6 April 2018 / Accepted 1 August 2018

ABSTRACT

In this work (Paper I), we analyse *Herschel*-PACS spectroscopy for a subsample of 23 O-rich and 3 S-type evolved stars, in different evolutionary stages from the asymptotic giant branch (AGB) to the planetary nebula (PN) phase, from the THROES catalogue. (C-rich targets are separately studied in Paper II). The broad spectral range covered by PACS (~55–210 μm) includes a large number of high-J CO lines, from J = 14–13 to J = 45–44 (v = 0), that allow us to study the warm inner layers of the circumstellar envelopes (CSEs) of these objects, at typical distances from the star of $\approx 10^{14}$–10^{15} cm and $\approx 10^{16}$ cm for AGBs and post-AGB-PNe, respectively. We have generated CO rotational diagrams for each object to derive the rotational temperature, total mass within the CO-emitting region and average mass-loss rate during the ejection of these layers. We present first order estimations of these basic physical parameters using a large number of high-J CO rotational lines, with upper-level energies from $E_{\rm up} \sim 580$ to 5000 K, for a relatively big set of evolved low-to-intermediate mass stars in different AGB-to-PN evolutionary stages. We derive rotational temperatures ranging from $T_{\rm rot} \sim 200$ to 700 K, with typical values around 500 K for AGBs and systematically lower, ~200 K, for objects in more advanced evolutionary stages (post-AGBs and PNe). Our values of $T_{\rm rot}$ are one order or magnitude higher than the temperatures of the outer CSE layers derived from low-J CO line studies. The total mass of the inner CSE regions where the PACS CO lines arise is found to range from $M_{\rm H_2} \sim 10^{-6}$ to $\approx 10^{-2}\,M_\odot$, which is expected to represent a small fraction of the total CSE mass. The mass-loss rates estimated are in the range $\dot{M} \sim 10^{-7}$–$10^{-4}\,M_\odot\,{\rm yr}^{-1}$, in agreement (within uncertainties) with values found in the literature. We find a clear anticorrelation between $M_{\rm H_2}$ and $\dot{M}$ vs. $T_{\rm rot}$ that probably results from a combination of most efficient line cooling and higher line opacities in high mass-loss rate objects. For some strong CO emitters in our sample, a double temperature (hot and warm) component is inferred. The temperatures of the warm and hot components are ~400–500 K and ~600–900 K, respectively. The mass of the warm component ($\sim 10^{-5}$–$8\times10^{-2}\,M_\odot$) is always larger than that of the hot component, by a factor of between two and ten. The warm-to-hot $M_{\rm H_2}$ and $T_{\rm rot}$ ratios in our sample are correlated and are consistent with an average temperature radial profile of $\propto r^{-0.5\pm0.1}$, that is, slightly shallower than in the outer envelope layers, in agreement with recent studies.

Key words. stars: AGB and post-AGB – circumstellar matter – stars: mass-loss – planetary nebulae: general – infrared: stars – stars: evolution

1. Introduction

The asymptotic giant branch (AGB) is one of the late stages in the evolution of low and intermediate mass stars ($1\,M_\odot \lesssim M \lesssim 8\,M_\odot$). At this phase, stars are very luminous ($\sim 10^4\,L_\odot$) and cool, with effective temperatures ranging from $T_{\rm eff} \sim 2000$ to 4000 K. The stellar radius of a typical AGB star is of about 1 AU, i.e. $R_\star \approx 10^{13}$ cm. AGB stars are dominated by an intense mass loss process with rates that range, typically, between 10^{-7} and $10^{-4}\,M_\odot\,{\rm yr}^{-1}$. For complete reviews see, for example, Habing (1996), Herwig (2005), Höfner & Olofsson (2018).

The vigorous mass loss generates a circumstellar envelope (CSE) of gas and dust around these evolved objects. The mass loss is thought to be produced by the combination of two mechanisms: pulsations and radiation pressure on dust (Bowen 1988; Simis et al. 2001). Both mechanisms work together driving a slow, dense stellar wind. The wind is strongly accelerated from the dust condensation region (at a few stellar radii, $\approx 10^{14}$ cm), reaching terminal velocities of about 5 to 25 km s^{-1} at distances from the star of $\gtrsim$10–20 $R_\star$. The temperature of the gas decreases along the CSE from 2000–2500 K, close to the stellar atmosphere, to ~1000 K in the dust condensation region, and progressively falling down to just a few tens of K in the most external envelope layers, at $\approx 10^{16}$–10^{17} cm (e.g. Decin 2012).

The material ejected due to the mass loss process, is expected to enrich the interstellar medium (ISM) with stellar nucleosynthesis products. It is believed that about half of the elements heavier than Fe are formed in the AGB phase (Herwig 2005). The analysis of the molecular products found in the AGB CSEs is very useful to derive information on the nucleosynthesis history of the central star and to improve our current understanding of the complex circumstellar chemistry (e.g. Millar 2016).

The relative abundance of carbon and oxygen in the CSE completely determines the dominant chemistry of these envelopes. According to the ratio of carbon over oxygen atoms,

⋆ *Herschel* is an ESA space observatory with science instruments provided by European-led Principal Investigator consortia and with important participation from NASA.

we identify envelopes with a carbon-rich (C/O > 1) or oxygen-rich (C/O < 1) chemistry, with a few objects (known as S-stars) showing C/O ratios very close to unity. This chemical branching is very important and depends on the nucleosynthesis processes that have taken place in the interior of these stars during their AGB evolution, which are basically determined by the mass of the progenitor star and its initial metallicity. All stars are born with a C/O ∼ 0.5 and therefore O-rich. However, this chemical composition may change during their AGB evolution. According to theoretical models (Marigo et al. 2003; Karakas et al. 2009), low-mass progenitors ($M < 2\,M_{\odot}$) remain as O-rich objects throughout the whole AGB evolution, while those stars with higher initial masses, between 2 and 4 $M_{\odot}$, may become C-rich objects during the AGB phase due to the thermal pulses and convective processes (dredge-ups) that enrich the surface of the AGB star with carbon, produced as a result of nuclear reactions. Finally, the most massive objects (AGB stars with initial masses in the range $4\,M_{\odot} < M < 8\,M_{\odot}$) remain also O-rich throughout their evolution in the AGB as they do not produce so much carbon, instead they convert carbon into nitrogen via the CN cycle (in a process known as hot bottom burning).

After the AGB phase the convective envelope is expelled and the hot core starts to ionize the surrounding material. When the bulk of the gas in the CSE is ionized the object is recognized as a planetary nebula (PN), see Kwok (2005).

The transition phase between AGBs and PNe is called the post-AGB phase. It is a very fast (≈10^3–10^4 yr) phase when the shell, formed in the AGB phase, detaches from the central star and the spherical symmetry is usually broken due to the effect of the onset of fast bipolar or multi-polar winds (Balick & Frank 2002).

The CO molecule is one of the most abundant species found in these objects as it is quickly and easily formed from the O and C atoms present in the envelope and it is also the most stable at the typical conditions found in these envelopes, CO molecules develop strong rotational emission lines which are very useful to trace the physical properties of the molecular envelopes around evolved stars in different evolutionary stages, from the AGB to the PN phase.

The molecular emission of CO has been studied over the last decades mainly at mm and sub-mm wavelength ranges using the low-J transitions that trace outer (>10^{16} cm) relatively cold (10–50 K) regions of the CSE (Bujarrabal 1999; Schöier & Olofsson 2001; Teyssier et al. 2006; Ramstedt et al. 2009). Studying the hotter layers of the envelope, presumably closer to the central star, traced by high-J CO transitions has only been possible with space telescopes like the Infrared Space Observatory (ISO; see, for example Justtanont et al. 2000) and in more recent times with *Herschel*, particularly, making use of PACS spectroscopy data (see, Groenewegen et al. 2011; Ueta et al. 2014).

Here, we analyse, in a uniform and systematic way, PACS spectroscopy data of a sample of O-rich (and a few S-type) evolved stars from the THROES catalogue (Ramos-Medina et al. 2018). We focus our study on the high-excitation rotational transitions of the CO molecule detected in these stars. In Sect. 2, a general description of our sample is provided. After that, in Sect. 3, we present the main characteristics of the PACS instrument and provide a brief description of the major data reduction steps. In Sect. 4 we show the principal observational results, including our measurements of the CO line fluxes. The rotational diagram (RD) analysis method used in this work and the results derived can be found in Sects. 5 and 6, respectively. The analysis of our results is presented in Sect. 7. Finally, in Sect. 8 we summarize our main conclusions.

2. Sample information

In this work we have studied 26 evolved stars at different evolutionary stages, from the AGB to PN phase, taken from the THROES catalogue (Ramos-Medina et al. 2018). In its current version, the THROES catalogue contains PACS spectroscopic cubes for a total of 114 low-to-intermediate mass evolved stars. In this study, we focus on non C-rich targets, with most of our sources being O-rich objects but also including a few S-type AGB stars (Table D.1). Sources with a dominant C-rich chemistry are studied separately by da Silva Santos et al. (in prep., Paper II). Our sources are grouped in five main categories as originally defined in the THROES catalogue: classical O-rich and S-type AGB stars, OH/IR stars (strong far-IR emitters with intense OH maser lines, typically late-AGB or early post-AGB stars heavily obscured by dust at optical wavelengths), post-AGB objects, and PNe. For this study, we have selected objects with a minimum of three CO transitions detected with a ratio of $S/N > 3$, a total of 26 out of 66 non C-rich targets in the THROES catalogue.

In Fig. 1 we present IRAS fluxes and colours of the sources of our sample in comparison with the rest of objects (C-rich or CO non-detections of any chemical type) contained in the THROES catalogue. IRAS colours in this diagram are defined as: $[12]-[25] = 2.5\log_{10}\frac{\mathrm{IRAS}_{25}}{\mathrm{IRAS}_{12}}$ and $[25]-[60] = 2.5\log_{10}\frac{\mathrm{IRAS}_{60}}{\mathrm{IRAS}_{25}}$. In the colour–colour diagram, the sources included in the THROES catalogue follow a well-known evolutionary sequence, with the AGBs located at the bottom left region (boxes: I, II, IIIa and VII) and the post-AGBs and PNe occupying the upper right area (boxes: V and VIII); more details can be found in van der Veen & Habing (1988). We note that the only OH/IR star located close to other PNe in region V is OH 231.8+4.2, which is a peculiar AGB star with a massive outflow with physical and chemical particularities uncommon for the AGB stage but approaching those of post-AGB objects (e.g. Alcolea et al. 2001; Sánchez Contreras et al. 2015).

All the objects of our sample except two, IRAS 17347-3139 and NGC 6537, have previous estimations of the mass loss rate but using low-J CO lines detected in the sub-millimetre and millimetre ranges (see Table D.2). Only for six objects namely, NML Tau, TX Cam, R Dor, R Cas, W Hya and W Aql, the mass loss rates provided come from recent works (Danilovich et al. 2014; Khouri et al. 2014; Maercker et al. 2016; Van de Sande et al. 2018) which are based on detailed non-local thermal equilibrium (non-LTE) radiative transfer models which make use of a combination of different sets of CO lines taken from several telescopes and including HIFI and PACS observations that, eventually, cover CO rotational lines up to $J = 24$–23. We have paid particular attention to the mass loss rates estimations derived in these works in order to test the results obtained with the rotational diagram method, used in this paper.

3. Observations and data reduction

PACS (Poglitsch et al. 2010) is an instrument onboard *Herschel* (Pilbratt et al. 2010) with photometric and spectroscopic capabilities in the FIR wavelength region. The PACS spectrometer covers the wavelength range from 51 to 210 μm in two different channels that operate simultaneously in the blue (51–105 μm) and red (102–220 μm) bands. The Field of View (FoV) covers a $47'' \times 47''$ region in the sky, it is structured in an array of 5×5 spatial pixels ("spaxels"), each spaxel is a $9.4'' \times 9.4''$ square. PACS provides a resolving power between 5500 and 940 (i.e.

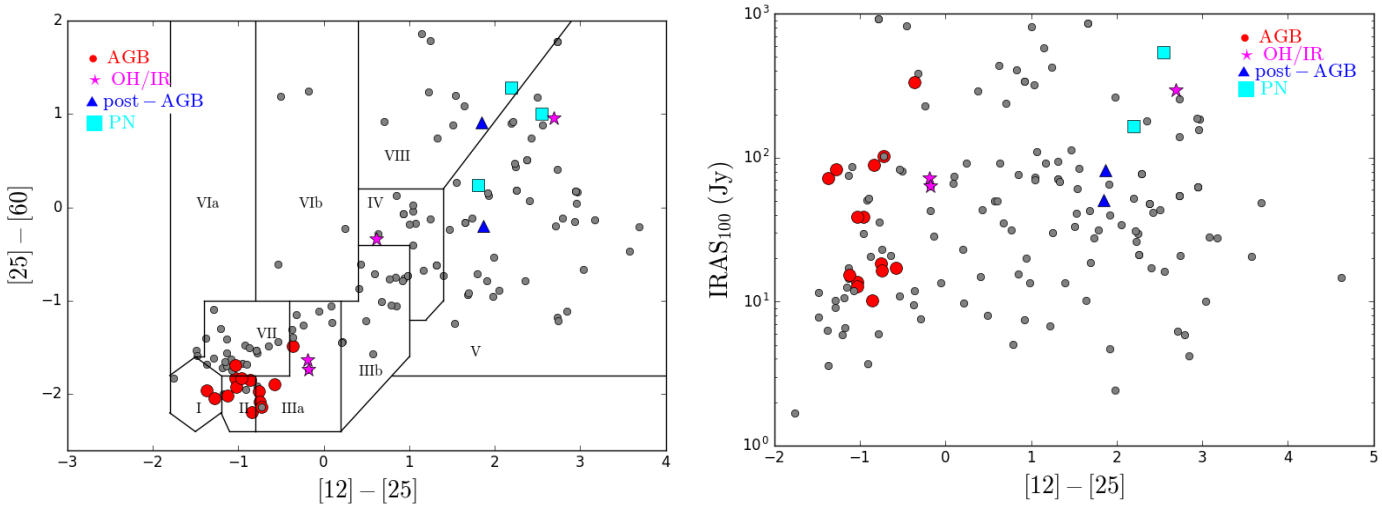

Fig. 1. IRAS colour–colour diagram (*left*) and 100 μm flux vs. [12]−[25] IRAS colour (*right*) of the THROES targets with good quality IRAS data (Quality Flag = 3) in the 12, 25, 60 and 100 μm bands. The colour–colour diagram is divided in different boxes where sources with common characteristics and evolutionary stages are located (see van der Veen & Habing 1988, for details). Objects with CO line detections, studied in this work, are highlighted using the symbol and colour code shown in the figure. In the rest of the plots presented throughout this paper, AGBs, OH/IRs, post-AGBs and PNe are coloured and symbol-coded as indicated in this figure.

a spectral resolution of 55–320 km s^{-1}) at short and long wavelengths, respectively, and the point spread function (PSF) of the PACS spectrometer ranges from ∼9″ in the blue band to ∼13″ in the red band. The PSF is described in da Silva Santos (2016) and Bocchio et al. (2016). Complete details about PACS instrument can be found in the PACS Observer's Manual[1].

In this work we have used one-dimensional (1D) PACS spectra, integrated over the emitting source, taken from the THROES catalogue (Ramos-Medina et al. 2018). THROES is a web-based catalogue that contains fully reduced PACS spectra, in 3D cubes structure (FITS files) and 1D spectra format (FITS and CSV files), for 114 low-to-intermediate mass evolved stars, covering a range of evolutionary stages from the AGB to the PN phase. The THROES catalogue is public and can be accessed online[2].

The main goal of the THROES project was the production of enhanced PACS spectroscopic data through the systematic careful interactive reprocessing, for full science exploitation of the spectra. Apart from the standard data reduction steps (most of them) common to the pipeline, some extra corrections were added such as: flat-field, background correction and other post-processing corrections applied in particular cases to extract the science-ready 1D PACS spectra from the 3D data cubes. In this process, the extent of the sources and their precise position in the FoV of PACS were taken into account. Particular attention was given to the mispointed cases (those objects not perfectly centred on the central spaxel of the PACS field of view). Full details on the data reduction process of the THROES targets can be found in Ramos-Medina et al. (2018).

The complete 1D spectra reported here are formed by four individual sub-spectra that cover four different wavelength sub-ranges resulting in a final spectral coverage that ranges from 55 to 95 μm (blue band) and from 105 to 190 μm (red band). All the objects included in this work have a full spectral coverage except RR Aql and T Cep, whose 1D PACS spectra cover only two of the spectral subranges: from 55 to 73 μm and from 105 to 147 μm.

[1] herschel.esac.esa.int/Docs/PACS/pdf/pacs_om.pdf
[2] https://throes.cab.inta-csic.es

4. Observational results

In Figs. 2 and 3 we display the continuum subtracted PACS spectra of the sources studied in this paper from 55 to 95 μm and from 110 to 190 μm, respectively. The continuum was fitted using a non-parametric method after identifying the line-free regions of the spectrum for each target.

The sources are sorted in Figs. 2 and 3 attending to their classification with the O-rich AGBs at the top, followed by S-type stars, OH/IR stars, post-AGB stars and PNe. Inside each group, the objects are sorted attending to the effective temperature of the central star, with the coolest object at the top and the hottest one at the bottom. The way the objects have been sorted evidences how different the spectra are along the different evolutionary stages from AGB phase to the PN stage. While the spectra of the envelopes around AGB stars show hundreds of molecular emission lines the density of emission lines in post-AGB objects is clearly lower. Finally, the most evolved objects, with highest temperatures of central stars, the PNe, show intense atomic emission lines in their envelopes and a lack of molecular features compared to the AGBs.

Rotational CO transitions in the ground vibrational state (v = 0) are the most prominent molecular lines found in all the spectra. We have detected and measured the integrated flux of CO v = 0 rotational lines with high-J levels, up to J = 42 ($E_{\rm up}$ ∼ 4700 K). We have checked that, as expected, the resolving power of PACS (of a few 100 km s^{-1}) does not allow us to spectrally resolve the line profiles, which are expected to have full widths at half intensity similar to the terminal expansion velocity of the envelopes, $FWHM$ ∼ 20–40 km s^{-1} in the majority of our sample. The PACS CO line profiles are also unresolved for a few post-AGB objects and PNs in our sample that are known to have fast outflows sampled by low-J transitions, that is OH 231.8+4.2 (Alcolea et al. 2001).

Apart from CO, we have also detected molecular emission lines from H_2O, including orto- and para- configurations, OH, HCN or SiO amongst others. Some of these lines have been reported for some objects of our subsample in (e.g. Danilovich et al. 2014; Maercker et al. 2016). Atomic lines such

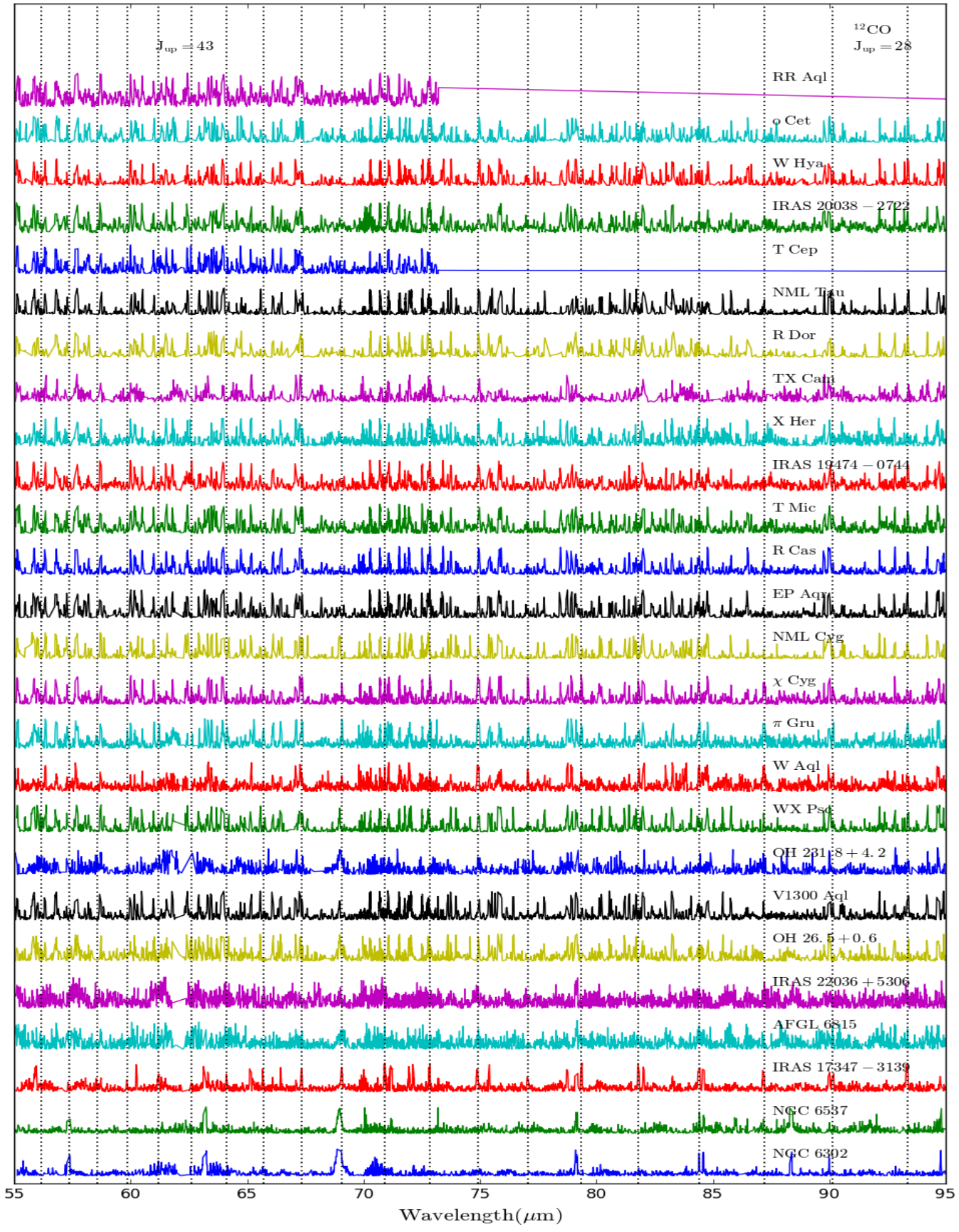

Fig. 2. PACS continuum subtracted spectra of our sample in the 55–75 μm range. The ^{12}CO rotational lines are indicated by vertical dotted lines (see Table D.4). The upper-level rotational quantum number J_u of a few selected CO transitions are shown as a reference. The sources are sorted from top to bottom in these five groups: AGBs, S-type stars, extreme OH/IR stars, post-AGBs, and PNe. Within each category, targets are ordered based on the stellar effective temperature from the coolest source to the hottest one.

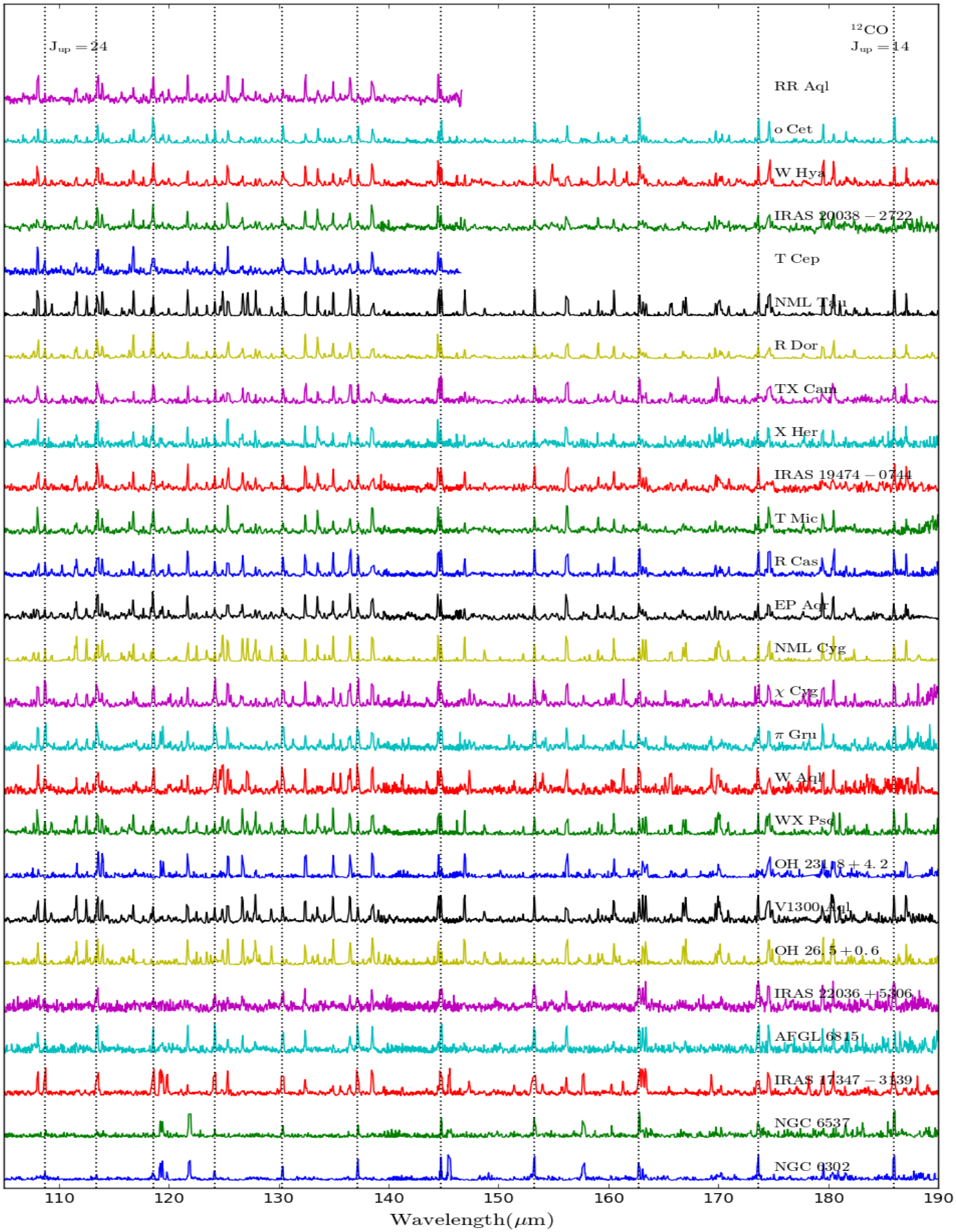

Fig. 3. The same as in Fig. 2 but covering the spectral range from 110 to 190 μm.

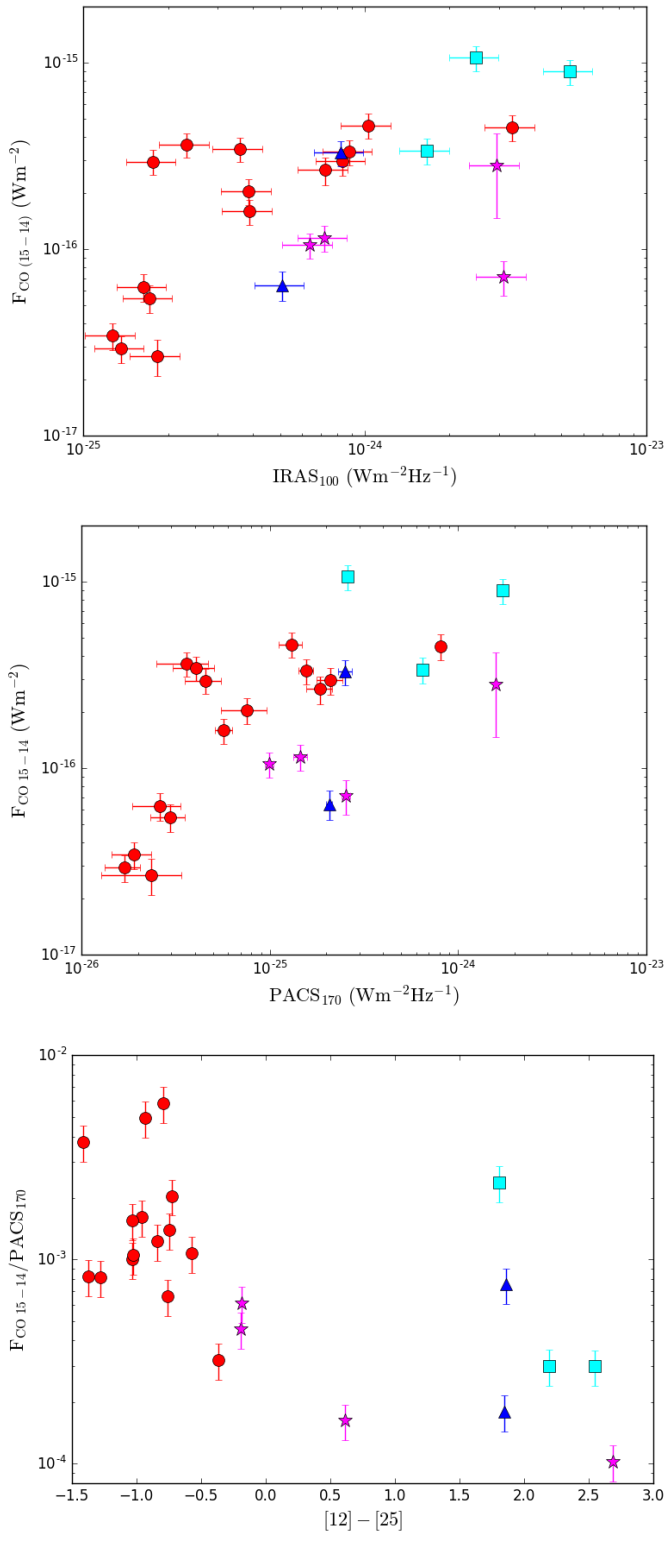

Fig. 4. *Top*: integrated flux of the CO J = 15−14 transition at 173.6 μm ($F_{CO\ 15-14}$) against the IRAS 100 μm flux. Targets with no PACS data beyond ~145 μm (i.e. not covering this CO transition; RR Aql and T Cep – see Fig. 3) or with bad quality (Quality Flag≠3) IRAS$_{100}$ data (OH 26.5+0.6) are excluded. *Middle*: fluxes of the CO J = 15−14 transition and the adjacent continuum (PACS$_{170}$). In this diagram, OH 26.5+0.6 is included. *Bottom*: line-to-continuum ($F_{CO\ 15-14}$-to-PACS$_{170}$) flux ratio against the IRAS colour [12]−[25].

as OI (63 μm), OIII (88 μm), NII (122 μm) and CII (158 μm) are also identified in post-AGBs and PNe, but not in AGBs. Finally, broad dust emission features associated to forsterite at 69 μm are also found in 4 objects: NGC 6537, NGC 6302, OH 231.8+4.2 and OH 26.5+0.6. Previous detections of forsterite in evolved stars with *Herschel* are shown, for example, in de Vries et al. (2015) and Blommaert et al. (2014). The integrated fluxes of the CO rotational emission lines detected in our sample are shown in Table D.4.

Certain CO rotational lines are known to be blended with transitions by other abundant species that lie within the same PACS spectral resolution element. We have identified, for example, the blend of CO (J = 23−22) with o–H_2O (414–303), and that of CO(J = 22−21) with the ^{13}CO(J = 23−22) and HNC (J = 28−27) transitions. Line blends were excluded in our RD analysis, but these lines are listed and integrated fluxes are reported in Table D.4 for completeness. In this table, we also list the lines that present a poor estimation of the underlying continuum level, although they have not been used for the rotational diagram analysis given their very large flux error bars. Finally, we note that the CO (J = 27−26) and (J = 26−25) transitions are missing for all targets since there is a gap in the 95–102 μm region of the PACS detector where these lines lie. The errors in the CO line fluxes are derived using the error associated to the fitting, estimated using the rms value of the continuum adjacent to the line, and assuming a flux calibration error of 15%.

In Fig. 4 we compare the integrated flux of the CO (J = 15−14) transition at 173.6 μm ($F_{CO\ 15-14}$) with other observational parameters, in particular, with the IRAS 100 μm flux (IRAS$_{100}$), the PACS continuum at 170 μm (PACS$_{170}$), i.e. near the CO (J = 15−14) line, and the [12]–[25] IRAS colour. As expected, there is a correlation between the CO line strength and the IRAS$_{100}$ and PACS$_{170}$ continuum fluxes, which confirms that objects with stronger molecular emission show, typically, stronger continuum emission from dust as well. Of course, in addition to an intrinsic relation between these two observational parameters, there is also a dependence with the distance to the sources, which is partially responsible of the observed relation. The scatter of the points is significantly larger in the $F_{CO\ 15-14}$ vs. IRAS$_{100}$ distribution, which partially reflects the variability of the majority of the targets (pulsating AGB stars) given that PACS and IRAS observations were obtained at different epochs, as well as different instrument calibration uncertainties, background contamination sources, beam size and pointing, etc. These effects are discussed for the whole sample of the THROES catalogue in Ramos-Medina et al. (2018). We find an anticorrelation between the line-to-continuum ($F_{CO\ 15-14}$/PACS$_{170}$) ratio and the IRAS [12]–[25] colour, which are both distant-independent parameters. In general, we find that the ratio between the molecular emission and the dust emission is higher in less evolved objects than in the most evolved ones.

5. CO emission analysis: rotational diagrams (RD)

The CO rotational lines provide a fundamental diagnostic of the physical conditions of the molecular gas. As a first approximation, we calculated the rotational population diagrams of the CO (J_u–J_l) v = 0 transitions observed with PACS assuming optically thin emission under LTE conditions. We have used the approach presented by Justtanont et al. (2000), where the total flux observed is used to derive the total mass of the CO-emitting volume adopting the distance to the source indicated in Table D.2.

The concept of the RD analysis is very simple, see Goldsmith & Langer (1999). Assuming LTE, the population of each level N_u can be described by a single rotation temperature

$T_{\rm rot}$, which is expected to be the same as the kinetic temperature, and given by the Boltzmann distribution:

$$N_{\rm u} = \frac{N_{\rm CO}}{Q(T_{\rm rot})} g_{\rm u} {\rm e}^{-E_{\rm u}/(\kappa T_{\rm rot})}, \quad (1)$$

where $N_{\rm CO}$ is the total number of CO molecules in the emitting volume, $Q(T_{\rm rot})$ is the rotational partition function and $g_{\rm u}$ are the statistical weights for each upper level. Equation (1) can be rewritten in the following form:

$$\ln\left(\frac{N_{\rm u}}{g_{\rm u}}\right) = \ln\left(\frac{N_{\rm CO}}{Q(T_{\rm rot})}\right) - \frac{E_{\rm u}}{\kappa T_{\rm rot}} - \ln C_\tau, \quad (2)$$

where C_τ is the opacity correction term defined as $C_\tau = \frac{\tau_\lambda}{1-{\rm e}^{-\tau_\lambda}}$ by, e.g, Goldsmith & Langer (1999). The left hand side of Eq. (2) can be estimated using the relation between the observed flux of a single line and the number of molecules at the upper level ($N_{\rm u}$):

$$N_{\rm u} = \frac{4\pi F \lambda_{\rm ul} d^2}{A_{\rm ul} hc}, \quad (3)$$

where F is the integrated line flux, λ is the rest wavelength of the transition, d is the distance to the source, $A_{\rm ul}$ is the Einstein's spontaneous emission coefficient associated to the transition, h is the Planck's constant and c represents the speed of light.

In our RDs we represent $\ln\left(\frac{N_{\rm u}}{g_{\rm u}}\right)$ against $\frac{E_{\rm u}}{\kappa}$ and we apply a linear regression that allow us to obtain $T_{\rm rot}$ (derived from the slope) and $N_{\rm CO}$ (estimated from the intercept in the y-axis) following Eq. (2).

With the values of $N_{\rm CO}$ and $T_{\rm rot}$ derived from this first fitting we estimate those of τ and C_τ from Eq. (4) in Sect. 5.1. This initial estimation is used to obtain new values of $\ln\left(\frac{N_{\rm u}}{g_{\rm u}}\right)$ applying the correction shown in Eq. (2). Then we can apply a new linear fit to this new set of values to derive the so-called opacity corrected values for $T_{\rm rot}$ and $N_{\rm CO}$ that are the ones adopted for the rest of the analysis. We want to highlight that the opacity correction derived is moderate being the τ values estimated for each object close to 1 (see Sect. 5.1). Very high values of τ would lead to unreliable results from the RD analysis, see Goldsmith & Langer (1999) for details.

5.1. Opacity correction

The optical depth (τ_λ) of a CO line is given by:

$$\tau_\lambda = \frac{A_{\rm ul}\lambda_{\rm ul}^3 N_{\rm u}^{\rm col}}{8\pi v_{\rm exp}\sqrt{\pi}/(2\sqrt{\log 2})} \times ({\rm e}^{(hc/(\lambda_{\rm ul}\kappa T_{\rm rot}))} - 1), \quad (4)$$

where $N_{\rm u}^{\rm col}$ is the column density of CO in the upper level of the transition.

We need an estimation of $T_{\rm rot}$ and $N_{\rm CO}^{\rm col}$ to calculate τ. $T_{\rm rot}$ is directly extracted from the RDs and $N_{\rm CO}^{\rm col}$ is derived from the total number of CO molecules, $N_{\rm CO}$, through the following, simplified, equation: $N_{\rm CO}^{\rm col} = \frac{N_{\rm CO}}{\pi r_{\rm CO}^2}$. Where $r_{\rm CO}$ represents the characteristic radius of the region where the bulk of the CO emission is produced.

The value of $r_{\rm CO}$ is one of the main sources of uncertainty to compute the optical depth and the subsequent opacity correction term. Unfortunately, as mentioned in Sect. 3, the inner envelope layers where the CO PACS lines are produced are unresolved or barely resolved in the PACS spectroscopy cubes for most of the sources given the large PSF (~9″–13″) and pixel size (9.″4) of the instrument (see Sect. 3). Therefore, the value of $r_{\rm CO}$ needs to be adopted based on several criteria. These criteria are described in detail in Appendix B, and a summary is offered in the following paragraphs.

For AGB stars, an estimate of $r_{\rm CO}$ is obtained by comparing the values of $T_{\rm rot}$ deduced from our analysis, ~200–700 K, with the radial temperature distribution $T(r)$ in the envelopes of a number of AGB stars with detailed non-LTE excitation and radiative transfer studies of their CO emission. The gas temperature can be up to 2000 K near the dust condensation radius (~10^{14} cm), and decreases gradually towards the outermost layers following, approximately, a power-law of the type ~$1/r^{\alpha}$, with $\alpha \sim 0.5$–1.0, see Van de Sande et al. (2018), Maercker et al. (2016), Danilovich et al. (2014), Khouri et al. (2014). For our sample, we deduce a range of values of $r_{\rm CO}$ from about 2×10^{14} cm to [2–4]$\times10^{15}$ cm, with the highest mass-loss rate objects requiring the largest values of $r_{\rm CO}$. The values of $r_{\rm CO}$ adopted for our targets are given in Table D.3.

The CO column densities derived from our RD analysis adopting a range of $r_{\rm CO}$ from ~10^{14} to ~10^{15} cm are moderate, $N_{\rm CO}^{\rm col} <\sim 10^{19}$ cm^{-2}, resulting in line optical depths of the order of ~0.9, and even lower in some cases, for the CO $J = 14\rightarrow13$ transition, which is the line with the largest opacity in our study. For AGBs, we have tuned $r_{\rm CO}$ to a value slightly larger than the radius of the wind layer where $\tau_{J=14\rightarrow13} \sim 1$; the latter is indeed the deepest region of the envelope observationally accessible, because of the almost null escape probability ($1/C_\tau = \frac{(1-{\rm e}^{-\tau})}{\tau} \rightarrow 0$) from much deeper, optically thicker ($\tau \gg 1$) layers of the wind.

Not only for the AGB stars but also for the OH/IR stars, we find that values of the radius around $r_{\rm CO} \sim$ [2–4]$\times10^{15}$ cm result in line optical depths close to, but smaller than, unity (typically $\tau_{J=14\rightarrow13}$ ~0.5–0.7) that result in moderate C_τ opacity correction factors. For all the objects studied in this work, the opacity correction is typically negligible for lines higher than $J = 19$–18.

Unlike for AGBs and OH/IR stars, for post-AGBs/PNe there are no theoretical or observationally constrained temperature profiles of the molecular gas component available in the literature. For these targets, we find that $\tau_{J=14\rightarrow13}$ approaches a value of ~1 at distances of $r_{\rm CO} \sim 1\times10^{16}$ cm, which therefore have been taken as a lower limit to the radius of the CO emitting volume detected with PACS. The PACS spectroscopy cubes indeed show extended, partially resolved nebulosities consistent with a linear diameter of $\lesssim$[1–2]$\times10^{17}$ cm (da Silva Santos 2016), in some of these cases. Using additional information on the molecular envelope extent from the literature and aiming to treat the sources as homogeneously as possible, we have adopted a common value of $r_{\rm CO} = 6\times10^{16}$cm for the 5 post-AGBs/PNe in our sample, resulting in column densities of $N_{\rm CO} \lesssim 1$–5×10^{17} cm^{-2} and small line optical depths of $\tau_{J=14\rightarrow13}$ ~0.02–0.07.

It must be noted that, in addition, we have completed our analysis by systematically exploring a range of radii around the value of $r_{\rm CO}$ adopted in each case to investigate the impact of this uncertain parameter in our results (see Fig. C.1). As expected, the smaller the $r_{\rm CO}$, the larger the opacity correction, which results in lower values of $T_{\rm rot}$ and larger values of $N_{\rm CO}$. We note that after applying the C_τ correction, the slope of the RD increases, as a direct result of the frequency-dependence of C_τ and the typical values of $T_{\rm rot}$ in our sample, see Appendix B. For example, in AGBs and OH/IR stars, values of $r_{\rm CO} \gtrsim 5\times10^{15}$ cm always result in negligible opacity corrections, whereas for values of $r_{\rm CO} \lesssim 8\times10^{14}$ cm the opacity becomes larger than one for most targets, except for the sources with the lowest mass-loss rates ($\dot{M} \sim 10^{-8} M_\odot$ yr^{-1}, see

Table D.2) where the CO lines remain optically thin at these radii.

6. Results

6.1. Rotational temperatures and total emitting mass of H_2

The CO RDs of our targets, from which we derive the rotational temperature ($T_{\rm rot}$) and the total number of CO molecules ($N_{\rm CO}$) in the emitting volume, are shown in Figs. 5a–c. For most objects, the RDs include CO transitions with upper-level energies that range from $E_{\rm up} \sim 580$ K to $E_{\rm up} \lesssim 2500$ K and are well fitted using a single temperature component. The single-fit rotational temperatures obtained range from ~200 K (NGC 6537) to ~700 K (π Gru), with an average value of $T_{\rm rot} \sim 450$ K.

For a number of strong CO emitters (NML Tau, χ Cyg, W Aql, NML Cyg and IRAS 17347-3139) transitions with upper-level energies of up to $E_{\rm up} \sim 5000$ K are also detected. In these cases, the data points in the RD over the full $E_{\rm up}$ covered are not well reproduced by a single straight-line fit. A double-slope in the RD is expected if a range of temperatures occur along the line of sight.

We have formally tested that a double-slope fit is indeed most appropriate in these cases using statistical tools for model selection: F statistics and Bayesian Information Criterion (BIC), implemented in R programming language in the *strucchange*[3] package (see Paper II for more details). We refer to the CO emitting regions with the lowest and highest $T_{\rm rot}$ values derived from the double-fit as the "warm" and "hot" CO components, respectively (Figs. 5a–c). The rotational temperatures of the warm and hot components are in the range ~370–480 K and ~570–900 K, respectively. As expected, the values of $T_{\rm rot}$ obtained from a single-fit to the RDs are intermediate to those of the warm and hot components.

The total number of CO molecules in the emitting volume, $N_{\rm CO}$, derived from the RDs has been converted to total mass of molecular hydrogen using:

$$M_{\rm H_2} = \frac{N_{\rm CO}}{\chi_{\rm CO}} m_{\rm H_2}, \quad (5)$$

where $m_{\rm H_2}$ is the mass of a molecule of hydrogen ($m_{\rm H_2}$ = 2.0159 a.u. = 3.3475×10^{-24} g) and $\chi_{\rm CO}$ is the CO-to-H_2 fractional abundance, assumed to be 2×10^{-4} for O-rich objects (Ramstedt & Olofsson 2014) and 6×10^{-4} for S-type stars (Ramstedt & Olofsson 2014; Danilovich et al. 2014).

The resulting values of $M_{\rm H_2}$ and $T_{\rm rot}$ are listed for each target in Table D.3, together with a few other relevant parameters (such as the adopted $r_{\rm CO}$ for the moderate opacity correction applied, Sect. 5.1). In Fig. 6 we show the $M_{\rm H_2}$ and $T_{\rm rot}$ values for each target, with and without the opacity correction, and the final histogram distributions.

The single-fit values of the total mass of the CO-emitting volume range between $M_{\rm H_2} \sim 3 \times 10^{-6}\,M_\odot$ (X Her) and $\sim 5 \times 10^{-2}\,M_\odot$ (IRAS 17347-3139), with an average value of $M_{\rm H_2} \sim 4 \times 10^{-3}\,M_\odot$. The opacity correction applied in all cases is small-to-moderate, which results in a mass-correction factor less than 20% in most sources. The source with the largest opacity correction (of a factor ~1.5) is NML Cyg, the AGB star with the largest $M_{\rm H_2}$, and highest mass-loss rate, in our sample (Table D.2).

The mass of the warm CO component is always larger than the mass of the hot component. For the warm component, these values vary from $M_{\rm H_2} \sim 1.3 \times 10^{-5}$ to $7.8 \times 10^{-2} M_\odot$, and for the hot between 3.7×10^{-6} and $1.6 \times 10^{-2} M_\odot$. The warm-to-hot $M_{\rm H_2}$ and $T_{\rm rot}$ ratio, and their relation, is further examined in Sect. 7.

We have investigated if there are any trends between $T_{\rm rot}$ and $M_{\rm H_2}$, derived for our RD analysis, and other observational parameters, such as the terminal expansion velocity of the envelope ($v_{\rm exp}$) and the strength of the CO (J = 15−14) transition (Fig. 7). First, we notice that objects in the most advances stages of the evolution, namely, post-AGBs and PNe, systematically have the lowest temperatures, $T_{\rm rot} \sim 200$–300 K, and the highest masses, $M_{\rm H_2} > 0.01\,M_\odot$ (see also Fig. 6). IRAS 17347-3139 is the only object with an exceptionally large $T_{\rm rot}$ for its class. The distribution of $T_{\rm rot}$ and $M_{\rm H_2}$ for post-AGB and PNe is also much narrower than for AGBs and OH/IR. The latter show a broad range of $T_{\rm rot} \sim 200$–700 K and $M_{\rm H_2} \sim 10^{-6}$–$10^{-3}\,M_\odot$. This segregation of the sources exists before and after the opacity correction has been applied; the opacity correction is indeed marginal for post-AGBs and PNe (grey symbols in Fig. 6). The observed bias in favour of massive post-AGB/PNe could reflect that, in our sample, post-AGB/PNe are on average more distant ($d > 1$ kpc) than AGBs and OH/IRs stars, which hampers CO line detections in the less massive post-AGB/PNe.

We observe an anticorrelation between $M_{\rm H_2}$ and $T_{\rm rot}$ (Fig. 7, top-left panel). This is most clearly noticed amongst AGB and OH/IRs, which are more numerous and cover a broader range of $T_{\rm rot}$ and $M_{\rm H_2}$ values, but it is also followed by post-AGB/PNe. We note that for objects for which a double-$T_{\rm rot}$ component has been identified (NML Tau, χ Cyg, W Aql, NML Cyg and IRAS 17347-3139), both the double- and the single-fit values (connected with dashed lines in Fig. 7, top-left panel) follow the trend. The object IRAS 17347-3139 is an outlier, since it has a much larger $T_{\rm rot}$ than anticipated based on the overall properties of the rest of our sample. This object is known to be at the earliest stages of the post-AGB evolution and making a fast transition to the PN phase at present (Table D.2, see Gómez et al. 2005; Tafoya et al. 2009).

For AGBs and OH/IRs stars, there is also an evident linear correlation between $M_{\rm H_2}$ and the terminal expansion velocity of the envelope (from the literature – Table D.3). As we will see in Sect. 7.4, this is linked to an analogue $\dot{M}$-to-$v_{\rm exp}$ relation, which is known to exist based on previous low-J CO studies of AGB CSEs (e.g. Danilovich et al. 2015) and that we corroborate in this work using higher-J CO lines. The post-AGB objects and PNe in our sample, however, show very similar values of the mass over a the full range of velocities.

As expected, the integrated flux of the CO lines correlate with the total mass of the CO-emitting volume and, as we will see later, with the average mass-loss rate of the envelopes. As an example we show this relation for the CO J = 15−14 transition ($E_{\rm up} \sim 660$ K) in Fig. 7 (bottom-left). There is a significant scatter in the line flux vs. $M_{\rm H_2}$ relation since the latter also depends on the excitation temperature ($T_{\rm rot}$), the velocity field in the envelope, the optical depth, etc. (Sect. 5).

Finally, we investigated if a correlation exist between the CO J = 15−14 line integrated flux normalized to the underlying ~170 μm-continuum observed with PACS ($F_{\rm CO\,15-14}$/PACS$_{170}$) and the parameters derived from the RD analysis. The strongest correlation is found with $T_{\rm rot}$ (Fig. 7, bottom-right), which is somewhat expected since the mass and the distance dependence is removed in the line-to-continuum flux ratio. The relation between $F_{\rm CO\,15-14}$/PACS$_{170}$ with $M_{\rm H_2}$ (not shown) has a much larger scatter and suggests a certain anticorrelation (given that $T_{\rm rot}$ anticorrelates with $M_{\rm H_2}$ in our sample).

In Sect. 7 we further discuss the observed trends.

[3] https://cran.r-project.org/web/packages/strucchange/index.html

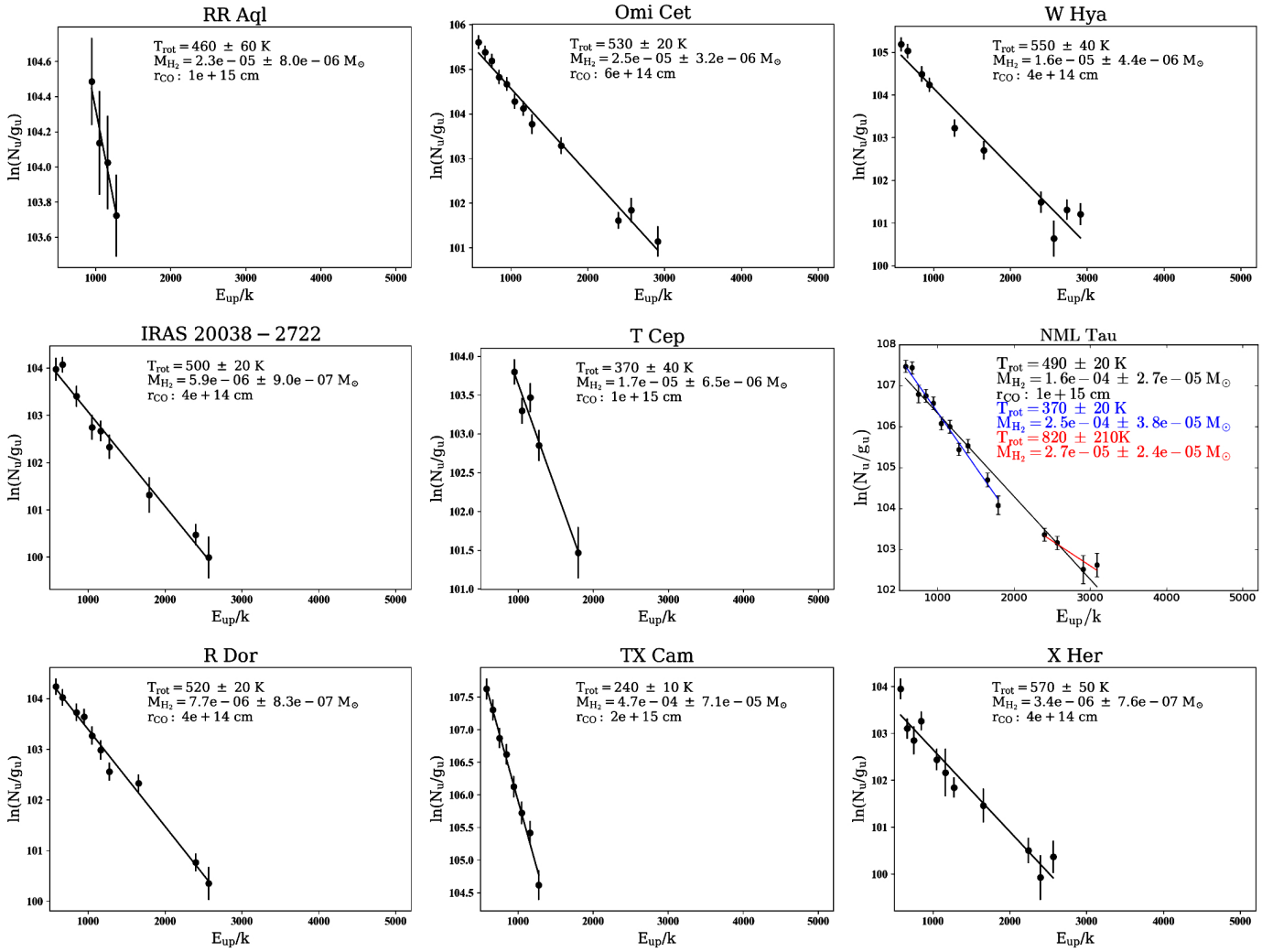

Fig. 5. RDs of CO for our targets (continues in 5b and 5c). For each source, the values of $T_{\rm rot}$ and $M_{\rm H_2}$ derived from the fits (solid lines) as well as the characteristic radius of the emitting envelope layers adopted ($r_{\rm CO}$) are shown (Sect. 5). The errors of $T_{\rm rot}$ and $M_{\rm H_2}$ represent the uncertainty of the fit considering the error bars of the individual points, which include formal errors due to the noise and absolute flux uncertainty of the PACS spectra. For a few sources, a double component fit was necessary. For these cases, the values of $T_{\rm rot}$ and $M_{\rm H_2}$ for the so-called warm (blue) and hot (red) components are also indicated.

6.2. Mass-loss rate

Using the values of the total emitting mass, we calculate the mass-loss rates ($\dot{M}$) for each source in a simplified manner dividing the total mass by the crossing time of the CO-emitting layers, that is:

$$\dot{M} = \frac{M_{\rm H_2}\, v_{\rm exp}}{r_{\rm CO}}, \tag{6}$$

Apart from $M_{\rm H_2}$, derived from the RDs, we need to adopt a value for the expansion velocity ($v_{\rm exp}$), which has been taken from literature, as well as for the characteristic radius of the CO emitting region, for which we use the same value used for the estimation of the opacity correction, $r_{\rm CO}$. The values of $\dot{M}$ are given in Table D.2.

In Sect. 5, we already mentioned the uncertainties associated to the adoption of a particular linear radius for the emitting region of each source and the importance of exploring a wide range of values to determine a reasonable estimation of the opacity correction and, thus, of $M_{\rm H_2}$. The same kind of analysis is even more important now, as the impact of $r_{\rm CO}$ in the mass-loss rate estimation is larger than in the calculation of the opacity correction (it affects $M_{\rm H_2}$ but also directly $\dot{M}$ as $\sim 1/r_{\rm CO}$). Another uncertainty arises in $v_{\rm exp}$, however, this parameter is rather well known (from previous works), to an accuracy of ~10–20% typically.

In Fig. C.2, we show, for every object, the different values of $\dot{M}$ and $T_{\rm rot}$ that correspond to three different values of the radius around the adopted value. For each source, we have also plotted a grey region that represents the broad interval of mass-loss rates found in the literature. The latter are usually derived from the analysis of low-J CO lines and, therefore, they represent the average mass-loss rate in the outer envelope layers. These values of $\dot{M}$ from the literature have been re-scaled after matching the expansion velocity ($v_{\rm exp}$), the distance (d) and the relative abundance of CO ($\chi_{\rm CO}$) to the values adopted here, which is needed for a proper comparison with our estimates of $\dot{M}$. The values of the mass-loss rates reported in the bibliography for each object are displayed in Table D.2 together with the associated interval range of mass-loss rates after scaling and relevant references. To our knowledge, for IRAS 17347-3139 and NGC 6537 there are no previous estimates of the gas mass-loss rate in the literature.

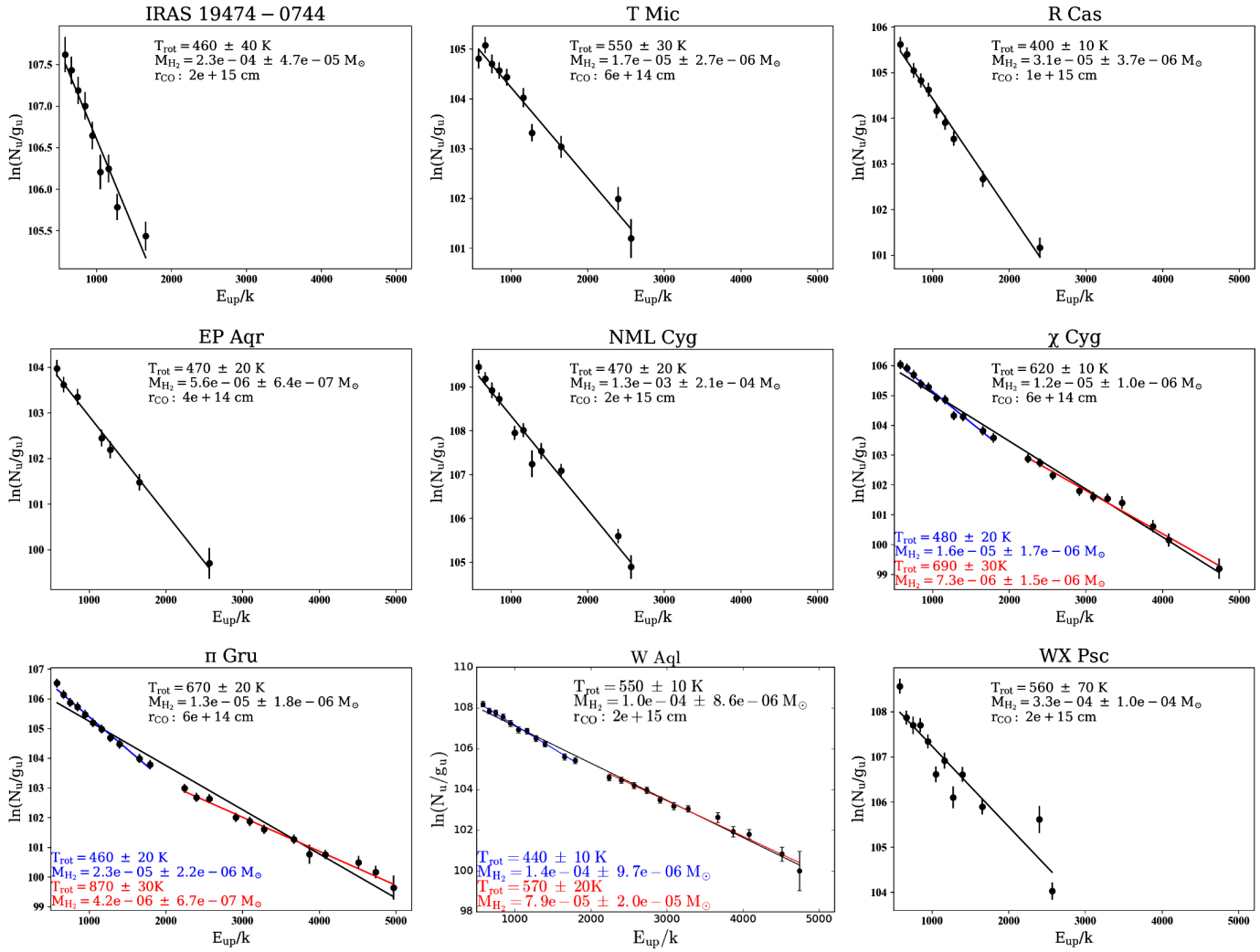

Fig. 5. continued.

Our estimates of the mass-loss rates are shown in Fig. 8 plotted against the rotational temperature, the expansion velocity, and the CO (J = 15–14) line strength to explore any trends that may be present. In the $\dot{M}$ vs. $T_{\rm rot}$ diagram we also include the mass-loss rates associated to the warm and hot component for objects with a double-slope in their RDs. There is an anti-correlation between $\dot{M}$ and $T_{\rm rot}$, which was expected based on a similar trend observed directly between $M_{\rm H_2}$ and $T_{\rm rot}$ (Fig. 7). This trend together with the clear correlation between $\dot{M}$ and $v_{\rm exp}$ and, more scattered, trend with $F_{\rm CO\,15-14}$ are briefly discussed in Sect. 7.

7. Analysis and interpretation of the results

In this section, we analyse and discuss the results obtained from the RDs as well as the correlations found between different magnitudes.

7.1. Rotational temperature and total mass

For most of our sources, a single-$T_{\rm rot}$ component was sufficient to obtain a good fit of the CO RD, leading to single-fit rotational temperatures and total (H_2) masses of the CO-emitting region of $T_{\rm rot} \sim 200$–700 K and $M_{\rm H_2} \sim 3\times10^{-6} - 5\times10^{-2}\ M_\odot$, respectively (Sect. 6).

The rotational temperatures of a few 100 K derived in this work using CO-PACS data ($J_{\rm u} \sim 14$–27, and up to $J_{\rm u} = 40$ lines in some cases) are clearly larger than the typical values of $T_{\rm rot} \sim 10$–100 K found from CO low-J line studies (most commonly using $J_{\rm u} < 4$ lines at mm and sub-mm wavelengths) in the external layers of the CSE around evolved stars, at $\approx 10^{16}$–10^{17} cm from the center (e.g. Teyssier et al. 2006, and references therein). This corroborates that, as anticipated, the CO-PACS lines sample the warm, presumably inner, regions of the CSEs, probably at a typical/average distance from the central star of about $\approx 10^{15}$ cm for AGB stars (e.g. Danilovich et al. 2014).

We find that the total mass of the warm inner layers where the PACS CO ($J_{\rm u} > 14$) lines mainly arise is typically a factor ~100–1000 lower than the masses deduced from low-J CO line studies in the literature, reinforcing the idea that CO PACS lines sample mainly the inner part of the envelopes, which contains a small fraction of the total envelope mass.

For a total of five targets in our sample (NML Tau, π Gru, W Aql, χ Cyg and IRAS 17347-3139), the RD diagram shows a double slope and, thus, a double-$T_{\rm rot}$ fit is most appropriate. Deviations from a single straight line fit of the RDs, most likely denoting a temperature stratification along the line of sight (see below), are not uncommon and have been previously found in a number of AGB and post-AGB CSEs using ISO and/or SPIRE

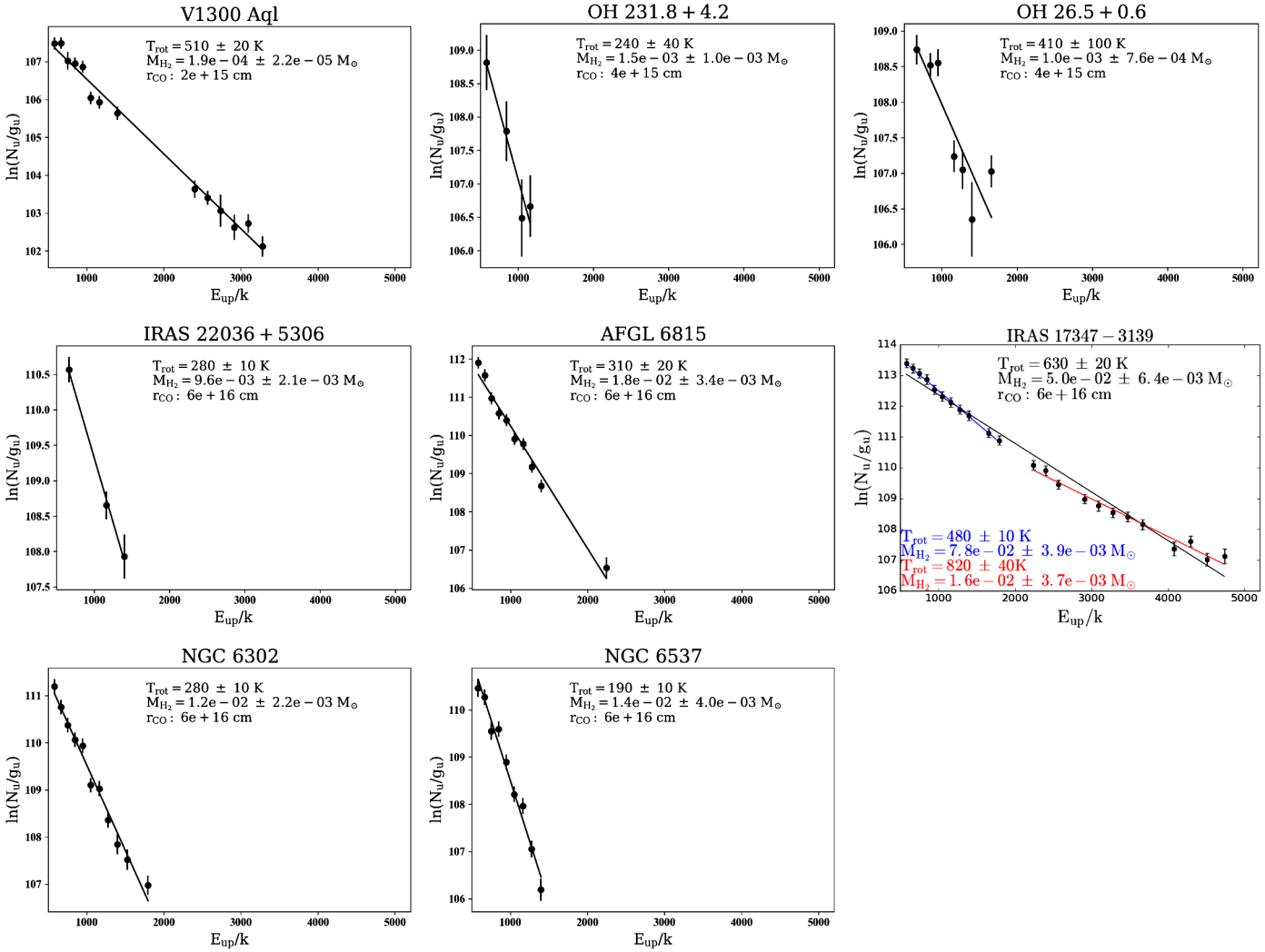

Fig. 5. continued.

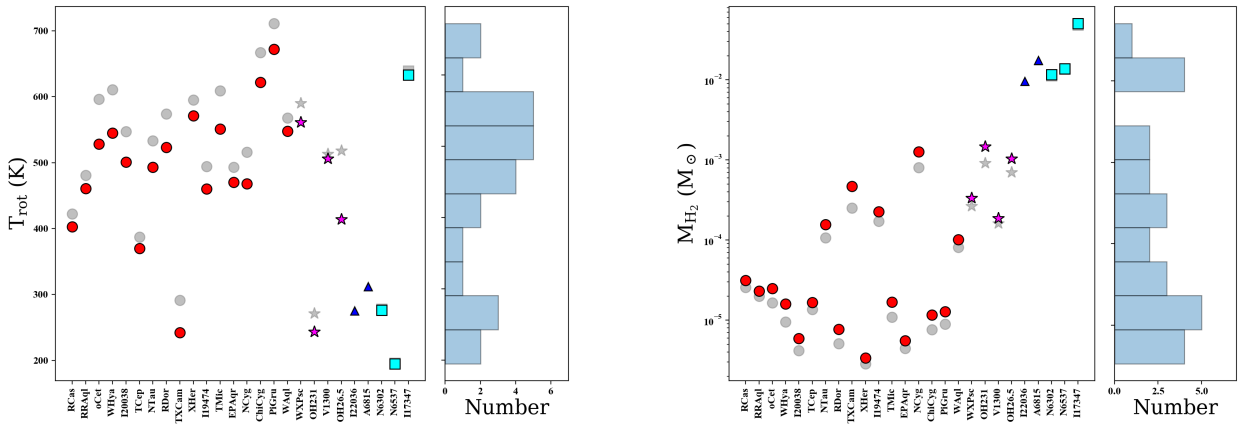

Fig. 6. Values of $T_{\rm rot}$ and $M_{\rm H_2}$ from our CO rotational diagram analysis (single fit; Sect. 6) before and after applying the opacity correction (grey and coloured symbols, respectively).

CO spectra (e.g. Justtanont et al. 2000; Wesson et al. 2010; Matsuura et al. 2014; Cernicharo et al. 2015; Cordiner et al. 2016).

The rotational temperatures and masses of the hot and warm components of these five objects are displayed in Fig. 7 (together with the single-fit $T_{\rm rot}$ and $M_{\rm H_2}$ values derived for the whole sample). The mass of the warm component is always larger (by a factor 2–10) than that of the hot component. Adopting a constant mass-loss rate and a gas temperature that decreases with the distance, the difference between the mass of the warm and hot component suggests a CO-emitting volume smaller for the hot component than for the warm one.

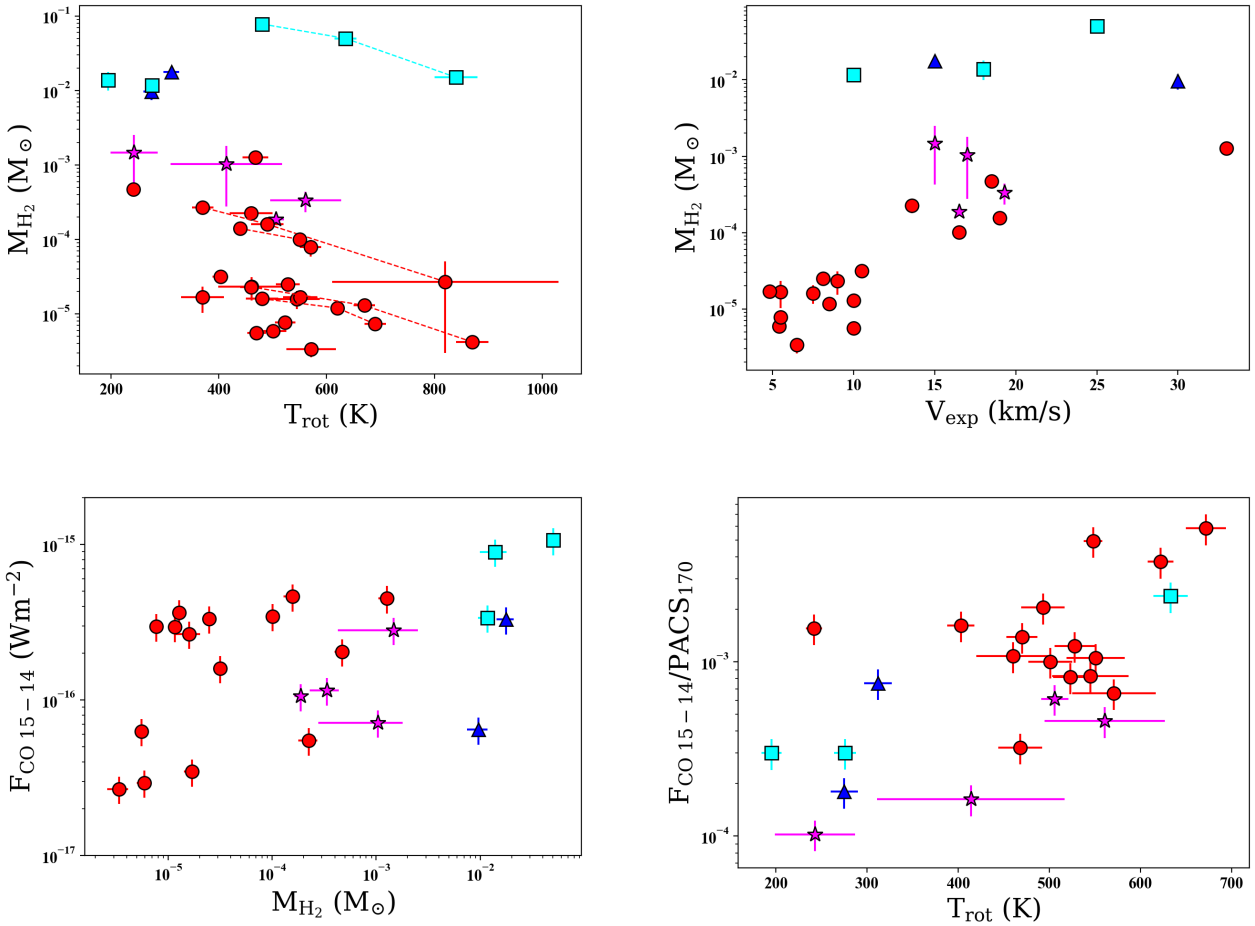

Fig. 7. Relation between M_{H_2} and T_{rot} derived from our CO RD analysis and other magnitudes. *Top-left*: M_{H_2} vs. T_{rot}. For objects (a total of five) with a double-T_{rot} component, both the single-fit and double-fit values are connected with dashed lines for an easier identification. *Top-right*: values of M_{H_2} (single-fit) vs. v_{exp} taken from the literature. *Bottom panels*: integrated fluxes of CO (J = 15−14) line vs. M_{H_2} (*left*) and the same line normalized to its adjacent continuum vs. T_{rot} (*right*).

We compare in detail the hot-to-warm M_{H_2} and T_{rot} ratios in Fig. 9. We find that the mass and temperature ratios are well correlated and follow approximately a power-law function. For AGB CSE with an inverse-square density profile, the latter is indeed expected if the temperature stratification within the emitting layers is described by a power-law function, $T(r) \sim 1/r^{\alpha}$. This is because, in this case, the total mass within a given CO-emitting volume is roughly proportional to its radius ($M_{H_2} \propto$ r) and, therefore, it is easy to derive that:

$$\frac{T_{rot}^{hot}}{T_{rot}^{warm}} \sim \left(\frac{M_{H_2}^{hot}}{M_{H_2}^{warm}}\right)^{-\frac{1}{\alpha}}, \quad (7)$$

Fitting a power-law function to the set of points corresponding to our AGB stars[4], we obtain $\alpha = 0.5 \pm 0.1$. This value is at the low end of the range of exponents found in the literature (from a combination of theoretical modelling and observational works) for AGB CSEs, typically $\alpha \sim 0.5 - 1$ (e.g. De Beck et al. 2010; Maercker et al. 2016; Danilovich et al. 2015, and references therein). There is some indication from recent works that the kinetic temperature distribution is shallower, with values of α down to ~0.4, for the inner CSE layers (~5×10^{14}–3×10^{15} cm; De Beck et al. 2012; Lombaert et al. 2016) than for the outer regions, where the steepest temperature variations (α ~1–1.2) are found ($\gtrsim$10^{16} cm; Teyssier et al. 2006). This is indeed in very good agreement with the small value of α found in the inner envelope layers from our analysis. (The hot-to-warm mass vs. T_{rot} trend with a similar value of α is also deduced in our sample of C-rich targets studied in Paper II). We believe that the empirical relation between the hot-to-warm ratio of M_{H_2} and T_{rot} therefore supports that the double-T_{rot} component identified in some of our objects (and possibly also present in more targets for which CO $J_u > 27$ transitions remain undetected), is a natural consequence of the temperature stratification across the inner envelope layers. Detailed non-LTE excitation and radiative transfer of the CO emission including high-J transitions, $J_u \sim$ 14–40, are needed for a proper characteriztion of the temperature structure in the warm inner-wind regions of AGB stars. See Appendix A for a discussion of non-LTE effects on the RD analysis.

7.2. Comparison with other works: $\dot{M}_{THROES}$ vs. $\dot{M}_{Bibliography}$

In Fig. 10 we show, for each source, the mass-loss rate estimated in this work for the adopted radius (r_{CO}) against a mean value of gas mass-loss rates found in the bibliography ($\dot{M}_{Bibliography}$). We assign error bars of a factor 3 to our estimates of the mass-loss rate; this is a common uncertainty value adopted in most

[4] Although IRAS 17347-3139 does not deviate significantly from the observed hot-to-warm M_{H_2} vs. T_{rot} trend, we excluded this object from the fit because, being a young PNe, it does not necessarily follows the same density and temperature profiles of the AGB CSEs.

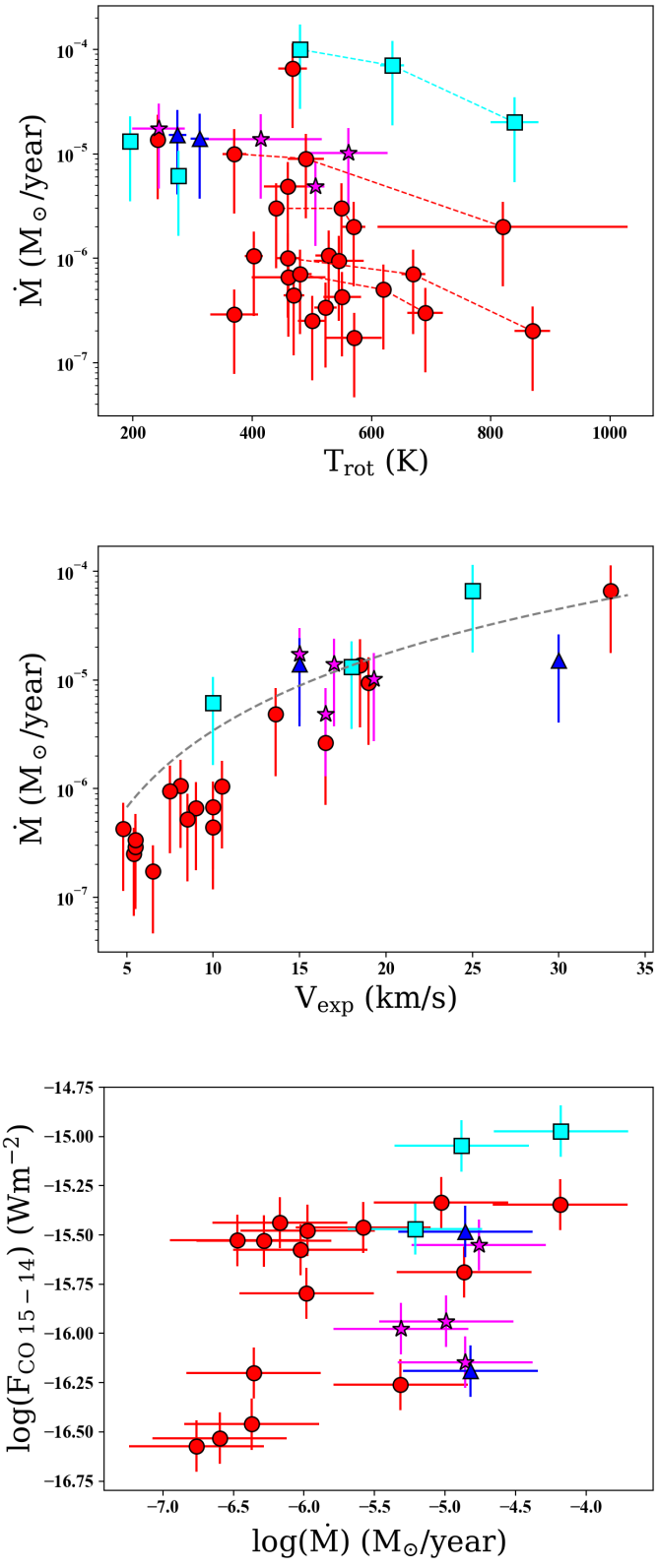

Fig. 8. *Top*: relation between $\dot{M}$ and $T_{\rm rot}$. Single- and double-fit (warm and hot) values, whenever these exist, are connected using dashed lines. *Middle*: relation between $\dot{M}$ and $v_{\rm exp}$. The distribution approaches a power-law of the type $\dot{M} \propto v_{\rm exp}^{2.5}$ (dashed line). *Bottom*: integrated flux of the CO $J = 15-14$ line vs. $\dot{M}$ in a logarithmic scale.

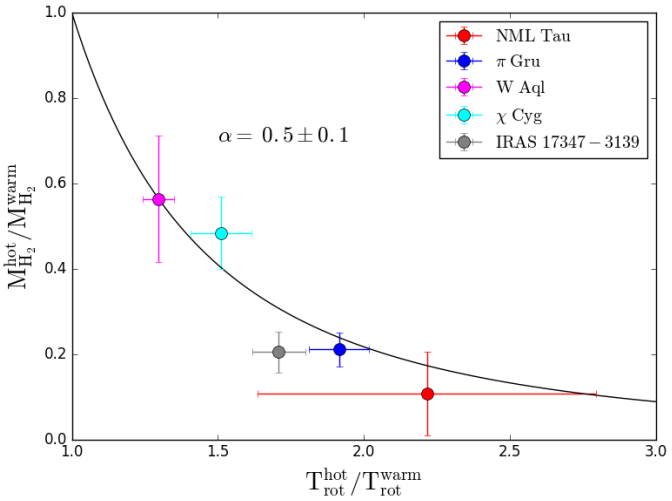

Fig. 9. Ratio of the mass and rotational temperatures for the hot and warm components, $M_{\rm H_2}^{\rm hot}/M_{\rm H_2}^{\rm warm}$ vs. $T_{\rm rot}^{\rm hot}/T_{\rm rot}^{\rm warm}$, for sources with a double-$T_{\rm rot}$ component, namely, the AGB stars NML Tau, π Gru, W Aql, and χ Cyg and the yPN IRAS 17347-3139. The solid line is a fit by a power-law function ($y \sim x^{-1/\alpha}$) to the AGB stars' data – see text in Sect. 7.1. A similar trend is found in our analogue study of the THROES C-rich sample reported in Paper II.

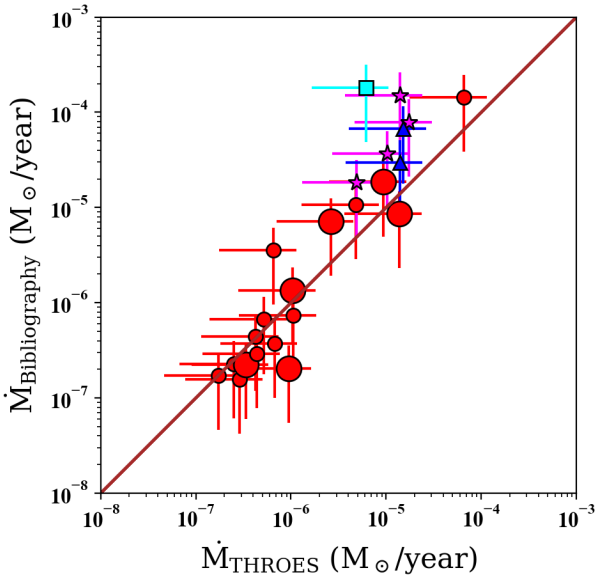

Fig. 10. Comparison of the mass-loss rates from this work and from the literature (Tables D.2 and D.3, respectively). The solid line represents a 1:1 ratio. Target colour and symbol code as in Fig. 1. The big circles are used to locate a few targets with previous $\dot{M}_{\rm Bibliography}$ estimates obtained from non-LTE excitation and radiative transfer analysis of CO lines, including some of the PACS transitions.

molecular line-emission studies (e.g. Maercker et al. 2016). The error bars of $\dot{M}_{\rm Bibliography}$ represent the low and high ends of the broad range of values found in bibliography after scaling to our d, $v_{\rm exp}$ and $\chi_{\rm CO}$ values, and is always ~3 or more. For objects with only one value of $\dot{M}$ from the literature, an uncertainty factor of 3 has also been assumed after scaling.

The comparison between our mass-loss rates and those found in the bibliography is in quite good agreement for all the objects, see also Fig. C.2. As already mentioned, we are particularly interested in the comparison of our $\dot{M}$ with those obtained from comprehensive non-LTE excitation and radiative transfer models that make use of some CO rotational lines (normally, $J < 20$) measured with PACS, which exist for a small

sample of objects: for R Cas, NML Tau, TX Cam, R Dor, W Hya and W Aql (Van de Sande et al. 2018; Maercker et al. 2016; Khouri et al. 2014; Danilovich et al. 2014). We find that, also in these cases, discrepancies with our values are always within 50% for all sources except W Hya, demonstrating that the simple and approximate RD approach and the assumptions (e.g. the adopted size of the emitting layers) used in this work yield reasonable first estimate results.

Considering again our sample as a whole, our mass-loss rate estimations of post-AGBs and PNe seem to be systematically lower than those in the literature by a ∼20%. In principle, this small difference could suggest that the radius of the CO-emitting region is slightly smaller than the value of r_{CO} adopted by us (at least in some objects). As it is shown in Fig. C.2, a fine tuning of r_{CO} can be performed to obtain a perfect match between $\dot{M}_{\rm Bibliography}$ and our estimates for each individual object. However, we prefer to treat the sources as homogeneously as possible and to be conservative avoiding the use of very small values of r_{CO}, which would result in large opacities ($\tau \gg 1$) and would consequently lead to unreliable opacity corrections.

A similar discrepancy is reported by Danilovich et al. (2015) from a CO-line study (including non-LTE radiative transfer modelling) of AGB CSEs in the SUCCESS programme including CO transitions from $J = 1{-}0$ to $J = 9{-}8$, as well as $J = 14{-}13$ in some targets. Their models give mass-loss rates that are on average 40% lower than those derived from past studies (see their Fig. 7). Danilovich et al. (2015) note that, as already mentioned here, most past studies are based on observations of a small number of low-J CO transitions (with similar excitation conditions, i.e., $E_{\rm up}$), and conclude that taking a large sample of CO transitions, including high-J lines, properly into account when modelling mass-loss rates, results in lower derived values.

It is important to stress that the mass-loss rates derived in this work represent average values during the period of time when the warm, inner envelope layers were ejected, that is, during the last <50–100 years, for AGBs, and the last ∼600–2000 years, for PNe (considering the values of r_{CO} and $v_{\rm exp}$ given in Table D.3). Since the low-J lines commonly used in the previous studies to derive $\dot{M}_{\rm Bibliography}$ mainly trace the outer envelope layers, the discrepancies observed with respect to past studies could reflect a real time variation of the mass-loss rate in some cases. This is indeed the case of OH 231.8+4.2, where mass-loss rate when the bulk of the nebula was ejected during the last ≈1000 yr (∼$2{\times}10^{-4}\,M_{\odot}$, Alcolea et al. 2001) is much larger than the present-day mass-loss rate (<$2{\times}10^{-5}\,M_{\odot}$), Sánchez Contreras et al. 2002). The upper limit to the present-day mass-loss rate of OH 231.8+4.2 is indeed in very good agreement with our estimate using high-J CO transitions.

Finally, as a word of caution we note that the mass-loss rates estimated for post-AGB objects and PNs are particularly uncertain as it is not easy to define essential parameters like r_{CO} or $v_{\rm exp}$ for these spatio-kinematically and morphologically complex objects. This makes the comparison with values from past studies subject to larger uncertainties. In spite of this, the agreement is reasonably good for the two post-AGBs and one PN in our sample with values of $\dot{M}$ reported in the literature.

7.3. Mass and mass-loss rate vs. $T_{\rm rot}$

As shown in Fig. 7, we find a statistically significant anticorrelation between the total mass of the PACS-CO emitting region, $M_{\rm H_2}$, and the rotational temperature, $T_{\rm rot}$, derived from our RD analysis. As expected, a similar trend is present between the mass-loss rate, $\dot{M}$, and $T_{\rm rot}$ (Fig. 8).

Prior to this work, Teyssier et al. (2006) and Danilovich et al. (2015) noticed a tentative $\dot{M}$ vs. $T_{\rm rot}$ anticorrelation based on their studies of the intermediate-to-outer regions of the envelopes of AGB and post-AGB stars using submm/mm-wavelength CO transitions. Particularly, Danilovich et al. (2015) reported $\dot{M}$ and $T_{\rm kin}$ at a representative distance of $\approx 10^{16}$ cm (i.e. ∼100 times the dust condensation radius) for a sample of 53 AGB stars. From their analysis, using self-consistent non-LTE radiative transfer models of the dust continuum emission and the CO emission transitions over a range of excitations (from $J = 1{-}0$ to $J = 9{-}8$, and in a few cases, up to $J = 14{-}13$), Danilovich et al. (2015) found that in general high mass-loss rate objects show relatively low temperatures (see their Fig. 6).

The temperatures of the regions studied by Danilovich et al. (2015), at distances ∼$[1{-}2]{\times}10^{16}$ cm, range between ∼10 and 80 K to be compared with the larger temperatures, ∼200–600 K, found by us at distances typically a factor ∼10 smaller in our AGB+OH/IR targets. This indicates that this trend is preserved from the inner envelope layers, traced by $J_{\rm u} \geq 14$ CO lines, through the outer parts of the CSE, sampled by lower-J transitions.

As discussed by Danilovich et al. (2015), a possible reason for the anticorrelation observed is the more efficient line cooling expected for high mass-loss rate objects (see also Groenewegen 1994, and references therein). In addition to this, we believe that optical depth effects can partially contribute to, and reinforce, the observed anticorrelation. This is because for high mass-loss rate objects, the τ_{CO} ∼1 surface layer, which is the deepest region that can be observationally sampled by a given CO line, is located at larger distances from the star where the gas kinetic temperature is lower.

7.4. Mass and mass-loss vs. expansion velocities

In Sect. 6 we already mentioned the presence of evident correlations between $M_{\rm H_2}$ and $v_{\rm exp}$ and between $\dot{M}$ and $v_{\rm exp}$ (Figs. 7 and 8, respectively).

The correlation found between $M_{\rm H_2}$ and $v_{\rm exp}$ is stronger if we consider only the AGB and OH/IR stars in our sample. In AGB and OH/IRs stars, the observed correlation could be telling us about the processes which are responsible for the acceleration of the stellar wind. Since AGB winds are primarily driven by radiation pressure on dust, the most luminous objects (which are also the most massive) will exhibit the largest expansion velocities.

The fact that post-AGB and PNs deviate from the observed trend is probably related with the different mass-loss mechanism (not driven by radiation pressure on dust) in these latest stages (Bujarrabal et al. 2001).

Moreover, the expansion velocities of post-AGBs and PNs do not represent the terminal velocity of the present-day stellar wind but the result from the complex hydrodynamical interaction between the stellar high-velocity winds, that appear beyond the AGB phase, and the slow ambient circumstellar material (expelled in the previous AGB stage).

Based on the above conclusion that, in AGB stars, $v_{\rm exp}$ correlates with $M_{\rm H_2}$ via the stellar luminosity, the trend found between $v_{\rm exp}$ and $\dot{M}$ is not surprising (Fig. 8). In this case, however, the post-AGBs and PNs in our sample do not deviate significantly from the general trend, although, as we mentioned above, the values and interpretation of $v_{\rm exp}$ as well as the $\dot{M}$ derived (under simplifying assumptions) have to be regarded with caution.

The $\dot{M}$-to-$v_{\rm exp}$ relation has been observed before in other CO line studies in AGB CSEs. For example, Danilovich et al. (2015)

report a correlation between $\dot{M}$ and $v_{\rm exp}$ including stars of different chemical types (O-rich, C-rich and S-stars), which is in very good agreement with our data-points (in spite of the lower-J transitions, $J < 14$, used by these authors). We have fitted a power-law function to the observed distribution (dashed line in Fig. 8-middle panel), the best fit gives an index of about 3 (i.e., $\dot{M} \propto {v_{\rm exp}}^{2.5}$) although the uncertainties associated to the fitting are important (2.5 ± 1).

7.5. Other trends

As shown in Sect. 6, we find a clear and expected correlation between the strength of the CO line emission, in particular, of the $J = 15{-}14$ line ($F_{\rm CO\ 15-14}$), with $M_{\rm H_2}$ and $\dot{M}$ (Figs. 7 and 8, respectively). The correlation found by us is in very good agreement with that reported recently by Lombaert et al. (2016) using a number of CO transitions observed with PACS to model the envelopes of a sample of C-rich AGB CSEs with H_2O emission. The dependence with the distance to the sources of $F_{\rm CO\ 15-14}$, $M_{\rm H_2}$ and $\dot{M}$ partially explain the observed trend; additionally, the line flux is proportional to the amount of mass in the emitting volume (Eq. (3)), although other factors, such as the opacity and the excitation temperature, have an important influence.

The influence of the excitation temperature in the resulting strength of the CO lines relative to the continuum becomes evident in Fig. 8-bottom panel, where we see a clear correlation between $F_{\rm CO\,15-14}/{\rm PACS}_{170}$ and $T_{\rm rot}$, which are both distance independent parameters. We find that objects with the lowest values of $T_{\rm rot}$ show small line-to-continuum ($F_{\rm CO\ 15-14}/{\rm PACS}_{170}$) ratios. We have found from this work that post-AGBs and PNs have the most massive envelopes in our sample (>0.01–0.1 $M_\odot$), but in spite of this, they are relatively weak high-J CO emitters as a consequence of the relatively low excitation conditions prevailing in their envelopes ($T_{\rm rot} \sim 200$–300 K). Other factors, such as a different gas-to-dust mass fraction at different evolutionary stages, may also lie behind the observed trend.

8. Summary

We have analysed *Herschel*-PACS 1D spectra of 26 evolved low-to-intermediate mass stars, in different evolutionary stages from the AGB to the PN phase, contained in the THROES catalogue[5]. Our sample includes 23 O-rich and 3 S-type objects (C-rich targets are separately studied in Paper II).

RDs using high-excitation CO $v = 0$ rotational emission lines, with upper-level energies $E_{\rm up} \sim 580$–5000 K, have been created to study the warm inner layers of the CSEs of these objects. We derive fundamental physical parameters such as: rotational temperatures ($T_{\rm rot}$), total molecular mass in the CO-emitting layers ($M_{\rm H_2}$) and average mass-loss rates during the ejection of these layers ($\dot{M}$).

The rotational temperatures are found to vary from ~200 K to ~700 K. For AGB and OH/IR stars, which represent ~80% of our sample, the rotational temperatures are around $T_{\rm rot} \sim 500$ K and systematically larger than for the most evolved objects, post-AGBs and PNs ($T_{\rm rot} \sim 200$ K). These temperatures are one order of magnitude higher than estimated from past low-J CO line studies of the outer envelope. This is expected as, in the PACS far-infrared range, we are tracing gas that is closer to the central star ($\approx 10^{15}$ cm for AGBs and $\approx 10^{16}$ cm for post-AGBs and PNs).

The total mass of the inner CSE regions where the PACS CO lines arise ranges from $M_{\rm H_2} \sim 10^{-6}$ to $10^{-2}\ M_\odot$ in our sample, with the most evolved objects being the most massive. The values of $M_{\rm H_2}$ found in this work are typically 100–1000 times lower than the total envelope mass obtained from previous low-J CO line studies.

The mass-loss rates estimated are in the range $\dot{M} \approx 10^{-7}{-}10^{-4}\ M_\odot\ {\rm yr}^{-1}$, in agreement (within uncertainties) with values found in the literature.

For some strong CO emitters in our sample (NML Tau, χ Cyg, W Aql, NML Cyg and IRAS 17347−3139) a double temperature (hot and warm) component is inferred. The temperatures of the warm and hot components are ~400–500 K and ~600–900 K, respectively. The mass of the warm component ($\sim 10^{-5} - 8 \times 10^{-2}\ M_\odot$) is always larger than that of the hot component, by a factor ~2–10.

The warm-to-hot $M_{\rm H_2}$ and $T_{\rm rot}$ ratios in our sample are correlated and are consistent with an average temperature radial profile of $\propto r^{-0.5\pm0.1}$, that is, slightly shallower than in the outer envelope layers, in agreement with recent studies.

We have explored the distributions of the different magnitudes and physical parameters of these objects and if any trends exist. We find that $M_{\rm H_2}$ and $\dot{M}$ are both anticorrelated with $T_{\rm rot}$. This is interpreted as a combination of two different processes: CO line cooling and opacity effects. Previous works have also reported similar trends based on low-J CO line observations.

A strong correlation has been found, also, between $M_{\rm H_2}$ and $v_{\rm exp}$, particularly for AGB stars. This correlation is also present in the $\dot{M}$ vs. $v_{\rm exp}$ distribution, as expected. This trend, which is observed in past studies using low-J CO transitions, is consistent with the wind acceleration mechanism being more efficient in the more luminous and massive stars.

Acknowledgements. We acknowledge support from the Faculty of the European Space Astronomy Centre (ESAC). C.S.C. acknowledges financial support by the Spanish MINECO through grants AYA2016-75066-C2-1-P and by the European Research Council through ERC grant 610256: NANOCOSMOS. We also acknowledge our referee, Kay Justtanont, for her useful and precise comments which have helped to improve our work.

[5] https://throes.cab.inta-csic.es

References

Alcolea, J., Bujarrabal, V., Sánchez Contreras, C., Neri, R., & Zweigle, J. 2001, A&A, 373, 932
Balick, B., & Frank, A. 2002, ARA&A, 40, 439
Blommaert, J. A. D. L., de Vries, B. L., Waters, L. B. F. M., et al. 2014, A&A, 565, A109
Bocchio, M., Bianchi, S., & Abergel, A. 2016, A&A, 591, A117
Bowen, G. H. 1988, ApJ, 329, 299
Bujarrabal, V. 1999, in Asymptotic Giant Branch Stars, eds. T. Le Bertre, A. Lebre, & C. Waelkens, IAU Symp., 191, 363
Bujarrabal, V., Castro-Carrizo, A., Alcolea, J., & Sánchez Contreras, C. 2001, A&A, 377, 868
Cernicharo, J., Teyssier, D., Quintana-Lacaci, G., et al. 2014, ApJ, 796, L21
Cernicharo, J., McCarthy, M. C., Gottlieb, C. A., et al. 2015, ApJ, 806, L3
Choi, Y. K., Brunthaler, A., Menten, K. M., & Reid, M. J. 1999, in Cosmic Masers – from OH to H0, eds. R. S. Booth, W. H. T. Vlemmings, & E. M. L. Humphreys, IAU Symp., 287, 407
Cordiner, M. A., Boogert, A. C. A., Charnley, S. B., et al. 2016, ApJ, 828, 51
Cox, N. L. J., Kerschbaum, F., van Marle, A.-J., et al. 2012, A&A, 537, A35
Danilovich, T., Bergman, P., Justtanont, K., et al. 2014, A&A, 569, A76
Danilovich, T., Teyssier, D., Justtanont, K., et al. 2015, A&A, 581, A60
da Silva Santos, J. M. 2016, Master's Thesis, University of Porto, Portugal
De Beck, E., Decin, L., de Koter, A., et al. 2010, A&A, 523, A18
De Beck, E., Lombaert, R., Agúndez, M., et al. 2012, A&A, 539, A108
Decin, L. 2012, Adv. Space Res., 50, 843
Decin, L., Hony, S., de Koter, A., et al. 2007, A&A, 475, 233
Decin, L., Justtanont, K., De Beck, E., et al. 2010, A&A, 521, L4
de Vries, B. L., Maaskant, K. M., Min, M., et al. 2015, A&A, 576, A98
Dinh-V-Trung, Bujarrabal, V., Castro-Carrizo, A., Lim, J., & Kwok, S. 2008, ApJ, 673, 934
Doan, L., Ramstedt, S., Vlemmings, W. H. T., et al. 2017, A&A, 605, A28

Goldsmith, P. F., & Langer, W. D. 1999, ApJ, 517, 209
Gómez, J. F., de Gregorio-Monsalvo, I., Lovell, J. E. J., et al. 2005, MNRAS, 364, 738
Groenewegen, M. A. T. 1994, A&A, 290, 531
Groenewegen, M. A. T., Waelkens, C., Barlow, M. J., et al. 2011, A&A, 526, A162
Habing, H. J. 1996, A&ARv, 7, 97
He, J. H., Szczerba, R., Hasegawa, T. I., & Schmidt, M. R. 2014, ApJS, 210, 26
He, J. H., Dinh-V-Trung, J. H., & Hasegawa, T. I. 2017, ApJ, 845, 38
Heras, A. M., & Hony, S. 2005, A&A, 439, 171
Herwig, F. 2005, ARA&A, 43, 435
Höfner, S., & Olofsson, H. 2018, A&ARv, 26, 1
Justtanont, K., Barlow, M. J., Tielens, A. G. G. M., et al. 2000, A&A, 360, 1117
Justtanont, K., Decin, L., Schöier, F. L., et al. 2010, A&A, 521, L6
Justtanont, K., Teyssier, D., Barlow, M. J., et al. 2013, A&A, 556, A101
Karakas, A. I., van Raai, M. A., Lugaro, M., Sterling, N. C., & Dinerstein, H. L. 2009, ApJ, 690, 1130
Khouri, T., de Koter, A., Decin, L., et al. 2014, A&A, 561, A5
Knapp, G. R., Phillips, T. G., Leighton, R. B., et al. 1982, ApJ, 252, 616
Kwok, S. 2005, J. Korean Astron. Soc., 38, 271
Lombaert, R., Decin, L., Royer, P., et al. 2016, A&A, 588, A124
Loup, C., Forveille, T., Omont, A., & Paul, J. F. 1993, A&AS, 99, 291
Maercker, M., Schöier, F. L., Olofsson, H., Bergman, P., & Ramstedt, S. 2008, A&A, 479, 779
Maercker, M., Danilovich, T., Olofsson, H., et al. 2016, A&A, 591, A44
Marigo, P., Bernard-Salas, J., Pottasch, S. R., Tielens, A. G. G. M., & Wesselius, P. R. 2003, A&A, 409, 619
Matsuura, M., Zijlstra, A. A., Gray, M. D., Molster, F. J., & Waters, L. B. F. M. 2005, MNRAS, 363, 628
Matsuura, M., Yates, J. A., Barlow, M. J., et al. 2014, MNRAS, 437, 532
Meaburn, J., Lloyd, M., Vaytet, N. M. H., & López, J. A. 2008, MNRAS, 385, 269
Millar, T. J. 2016, J. Phys. Conf. Ser., 728, 052001
Nhung, P. T., Hoai, D. T., Winters, J. M., et al. 2015, A&A, 583, A64
Olofsson, H., González Delgado, D., Kerschbaum, F., & Schöier, F. L. 2002, A&A, 391, 1053
Pilbratt, G. L., Riedinger, J. R., Passvogel, T., et al. 2010, A&A, 518, L1
Poglitsch, A., Waelkens, C., Geis, N., et al. 2010, A&A, 518, L2
Ramos-Medina, J., Sánchez Contreras, C., García-Lario, P., et al. 2018, A&A, 611, A41
Ramstedt, S., & Olofsson, H. 2014, A&A, 566, A145
Ramstedt, S., Schöier, F. L., Olofsson, H., & Lundgren, A. A. 2006, A&A, 454, L103
Ramstedt, S., Schöier, F. L., Olofsson, H., & Lundgren, A. A. 2008, A&A, 487, 645
Ramstedt, S., Schöier, F. L., & Olofsson, H. 2009, A&A, 499, 515
Sánchez Contreras, C., & Sahai, R. 2012, ApJS, 203, 16
Sánchez Contreras, C., Desmurs, J. F., Bujarrabal, V., Alcolea, J., & Colomer, F. 2002, A&A, 385, L1
Sánchez Contreras, C., Velilla Prieto, L., Agúndez, M., et al. 2015, A&A, 577, A52
Santander-García, M., Bujarrabal, V., Koning, N., & Steffen, W. 2015, A&A, 573, A56
Schöier, F. L., & Olofsson, H. 2001, A&A, 368, 969
Schöier, F. L., Maercker, M., Justtanont, K., et al. 2011, A&A, 530, A83
Simis, Y. J. W., Icke, V., & Dominik, C. 2001, A&A, 371, 205
Tafoya, D., Gómez, Y., Patel, N. A., et al. 2009, ApJ, 691, 611
Teyssier, D., Hernandez, R., Bujarrabal, V., Yoshida, H., & Phillips, T. G. 2006, A&A, 450, 167
Teyssier, D., Cernicharo, J., Quintana-Lacaci, G., et al. 2015, in Why Galaxies Care about AGB Stars III: A Closer Look in Space and Time, eds. F. Kerschbaum, R. F. Wing, & J. Hron, ASP Conf. Ser., 497, 43
Ueta, T., Ladjal, D., Exter, K. M., et al. 2014, A&A, 565, A36
van der Veen, W. E. C. J., & Habing, H. J. 1988, A&A, 194, 125
Van de Sande, M., Decin, L., Lombaert, R., et al. 2018, A&A, 609, A63
Vickers, S. B., Frew, D. J., Parker, Q. A., & Bojičić, I. S. 2015, MNRAS, 447, 1673
Wesson, R., Cernicharo, J., Barlow, M. J., et al. 2010, A&A, 518, L144
Woods, P. M., Nyman, L.-Å., Schöier, F. L., et al. 2005, A&A, 429, 977
Yang, B., Stancil, P. C., Balakrishnan, N., & Forrey, R. C. 2010, ApJ, 718, 1062

Appendix A: Non-LTE effects

The rotational diagram (RD) method is a classical and widely used line-emission analysis technique useful to obtain a first estimate of the excitation temperature and mass of the gas in the line emitting region (Goldsmith & Langer 1999; Justtanont et al. 2000). As explained in Sect. 5, it is based on two major assumptions: optically thin emission and excitation under LTE conditions. A canonical opacity correction factor, C_τ, has been included to take into account moderate optical depth effects (Sect. 5). Here, we examine whether non-LTE excitation effects are expected to be significant in our sample and, if this is the case, what is the impact on the values of $M_{\rm H_2}$ and $T_{\rm rot}$ inferred from our RD analysis. We present several arguments that suggest that although small LTE deviations cannot be ruled out (particularly, in the lowest mass-loss rate objects), we expect a negligible impact on the derived values of $M_{\rm H_2}$. Additionally, the double slope in the RD observed for some targets predominantly reflects the temperature stratification in the emitting layers.

A first simple evaluation of LTE deviations is obtained from the comparison of the critical densities of the CO transtions studied here and the densities expected in the CO-emitting regions in our sample. For most (80%) of our targets, the far-IR CO transitions detected and used in our RD analysis arise from states ~500–2000 K above the ground, i.e. with upper-level rotational quantum numbers $J_{\rm u} \sim 14$–27. According to most recent collisional rate coefficients computed by Yang et al. (2010)[6], these transitions have critical densities of $n_{\rm crit} \sim 5{\times}10^5$ and $3{\times}10^6$ cm^{-3}, for $J_{\rm u} = 14$ and $J_{\rm u} = 27$, respectively, for a range of temperatures consistent with our estimates, ~200 and 700 K, see Fig. 10 in Yang et al. (2010).

From the lowest to the highest mass-loss rate objects in our sample ($\dot{M} \sim 2{\times}10^{-7}$–$1{\times}10^{-4}\,M_\odot\,{\rm yr}^{-1}$, Fig. 8), densities of $n_{\rm H_2} \gtrsim 10^6$–10^8 cm^{-3} are expected at the typical radius adopted (from $r_{\rm CO} \sim 4{\times}10^{14}$ to $r_{\rm CO} \sim [1\text{–}4]{\times}10^{15}$ cm, respectively – see Table D.2, Appendix B) consistent with CO population levels predominantly thermalized in most cases.

As already pointed out in pioneering studies of ISO-LWS observations of high-J CO lines using the RD approach, see Justtanont et al. 2000, the mere fact that we detect CO $J_{\rm u} \sim 14$–27 transitions together with a roughly linear distribution in the RD is a hint of high-density gas and level populations in this range of $J_{\rm u}$ close to thermal equilibrium.

For a few targets, we also detect CO lines with upper-levels above $J_{\rm u} > 27$, which have critical densities of $n_{\rm crit} \sim 10^6$–10^7 cm^{-3} and, therefore, some LTE deviations cannot be rule out (but we note that these transitions presumably arise from regions closer to the center, within the dust formation layers).

The simple calculations above are indeed corroborated by non-LTE excitation and radiative transfer analysis computations of a selection of high-J CO transitions observed with PACS (from $J_{\rm u} = 14$ to 38) on a sample of C-rich AGB CSEs by Lombaert et al. (2016). These authors conclude that over the broad range of mass-loss rates studied in their work, $\dot{M} \sim 10^{-7}$–$2{\times}10^{-5}\,M_\odot\,{\rm yr}^{-1}$, which is comparable to the range in our sample, the CO molecule is predominantly excited through collisions with H_2, with a minor effect of far-IR radiative pumping due to the dust radiation field.

We stress that even under non-LTE conditions, for a simple diatomic molecule like CO, the RD method provides a reliable measure of the total mass within the emitting volume. This is because, although $T_{\rm rot}$ may deviate from the kinetic temperature, $T_{\rm kin}$, in regions where the local density is lower than the critical densities of the transitions considered, it does describe quite precisely the molecular excitation (i.e. the real level population). To test this idea and to check the reliability of our analysis, we have compared our values of $M_{\rm H_2}$ and $\dot{M}$ with those obtained from state-of-the-art line excitation and radiative transfer models of high-J CO transitions, sometimes including PACS data, performed by other authors in objects of our sample. To our knowledge, these have been published for a total of 6 sources: R Cas, R Dor, TX Cam, NML Tau, W Hya and W Aql (see Van de Sande et al. 2018; Maercker et al. 2016; Danilovich et al. 2014; Khouri et al. 2014 and references therein). For these objects, the CO emission over a broad range of $E_{\rm up}$ has been modelled to derive the temperature, density and velocity profile across their ~10^{14}–10^{17} cm CSE layers, as well as the mass-loss rate of the stellar wind. As shown in Sect. 6, discrepancies between our values of $\dot{M}$ and those obtained from comprehensive non-LTE radiative transfer analysis are very small, always within 50%, demonstrating that the simple and approximate RD approach and the assumptions (e.g. the adopted size of the emitting layers) used in this work yield reasonable results.

An additional test of the reliability and uncertainties of the RD method is presented in Paper II, where we perform our RD analysis using multi-epoch CO-PACS spectra for the C-rich AGB star IRC+10216. This object shows prominent line variability (mainly of high-excitation transitions of CO and other molecules) denoting radiative farIR (ro-vibrational) pumping via the dust radiation field modulated by the stellar pulsation (Cernicharo et al. 2014; Teyssier et al. 2015; He et al. 2017). This object, thus, serves as a benchmark for testing the effect of radiative vs. collisional excitation and its impact of the values of $M_{\rm H_2}$ and $T_{\rm rot}$ derived from our RD analysis. We corroborate that, in spite of strong CO line flux variations and confirmed changes in the relative level population, the total number of emitting molecules (adding up all levels) from the RD analysis remains constant (within uncertainties, <15%) at multiple epochs. This is true for both the warm and hot components (both identified in IRC+10216) and, thus, for the single-fit value of $M_{\rm H_2}$.

We also find that line variability has also a small impact on the value of $T_{\rm rot}$ derived at multiple epochs in IRC+10216. The values of $T_{\rm rot}$ from the single-fit and warm component (using $J_{\rm u} < 27$ transitions) remain essentially constant within uncertainties, consistent with negligible impact of non-LTE effects (if any). The highest-excitation CO lines ($J_{\rm u} > 27$) show stronger variations and, as a consequence, the variations of $T_{\rm rot}$ for the hot component are larger, of $\lesssim \pm 15\%$ about the average, maybe denoting some repercussion of LTE deviations on $T_{\rm rot}$ in this case.

Although it is improbable given our previous discussion, let us now consider whether the double slope in the RD diagram found for a few objects in our sample could predominantly result from non-LTE effects, with $T_{\rm rot}$ deviating most significantly from $T_{\rm kin}$ for the highest-J CO transitions, and what would be the implications in this case.

Among our targets (O-rich and S-type), we find a double-$T_{\rm rot}$ component in a total of five sources, covering a broad range of mass-loss rates, from $\dot{M} \sim 2{\times}10^{-7}$ to $8{\times}10^{-5}\,M_\odot\,{\rm yr}^{-1}$. The mass-loss rate distribution of these sources is the same as the sources for which only one $T_{\rm rot}$ component is found. Moreover, we do not find any correlation between $\dot{M}$ and the properties of the hot and warm components (also including C-rich targets, see e.g. Fig. A.1), which makes improbable the double $T_{\rm rot}$ component being predominantly a non-LTE effect (expected to be most remarkable in low mass-loss rate objects).

[6] Also available from the Leiden Lambda Database web page.

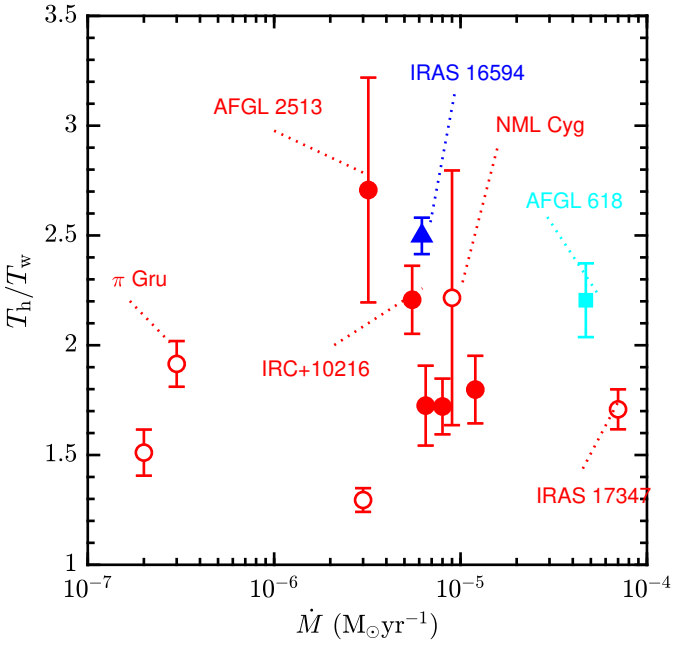

Fig. A.1. Ratio of the hot-to-warm rotational temperature vs. the mass-loss rates for objects with a double-T_{rot} component: targets from this work (Paper I) are represented by open symbols, C-rich objects (from Paper II) are plotted using filled symbols.

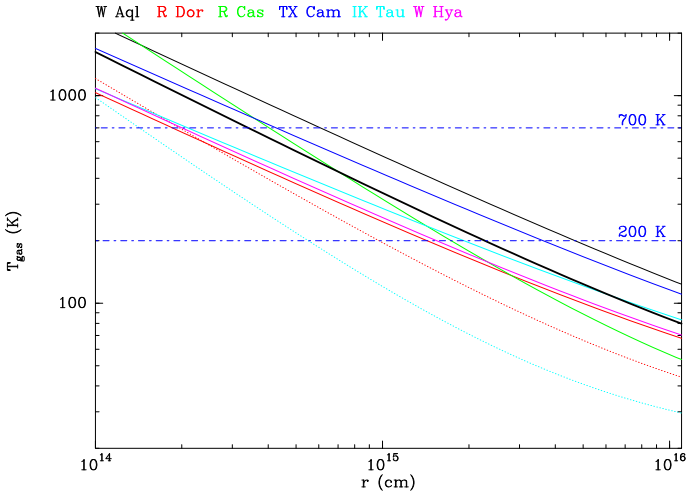

Fig. B.1. Power-law radial distribution of the gas kinetic temperature estimated from non-LTE excitation and radiative transfer models of the CO emission in a number of AGB envelopes (indicated at the top of the box using the same colour for the temperature laws) from the literature. References: Van de Sande et al. (2018), Maercker et al. (2016), Khouri et al. (2014), Decin et al. (2010). The solid and dotted lines of R Dor and IK Tau are different temperature profiles derived by different authors (solid from Maercker et al. 2016, and dotted from Van de Sande et al. 2018 – R Dor and Decin et al. 2010 – IK Tau). The thick black line is an average temperature law.

Moreover, to explain the observed double slope as a purely non-LTE effect, two conditions need to be simultaneously met in all double-T_{rot} targets. First, a very specific value of the number density, in a narrow range around $\sim 10^7$ cm^{-3}, is needed to have $J_u < 27$ levels close to thermal equilibrium but $J_u > 27$ levels deviating perceivably from LTE (this would generate the double slope in the RD diagram). Second, a strong background radiation source $T_{bg} > T_{kin}$ is required to reproduce a T_{rot} that is higher for $J_u > 27$ transitions than for $J_u < 27$ lines. Dust mixed with the gas in the CO-emitting volume and heated by the stellar radiation to 800 K could produce the required T_{bg}. If this is the case, then it would also imply similarly high gas temperatures in the emitting region since the difference between the gas and dust temperature across these inner wind layers is expected to be moderate (of <100 K) and to follow a similar radial dependence based on detailed dust-continuum and non-LTE radiative transfer CO emission models (e.g. for W Aql, $T_{kin} \sim T_{dust} \sim 300$ K at $r_{CO} = 2{\times}10^{15}$ cm Danilovich et al. 2014). In the extreme case (e.g. maybe for very low mass-loss rate objects with densities $<10^6$ cm^{-3}) that T_{rot} is totally decoupled from T_{kin} but very close to T_{bg} for all transitions from $J_u = 14$ to 40, then the double-slope of the RDs would most likely reflect the stratification of the *dust* temperature (rather than the gas) across the envelopes.

Summarizing, a minor impact of small LTE deviations on the values of M_{H_2} and $\dot{M}$ is expected, even for the targets with the lowest mass-loss rates, $\dot{M} \approx 10^{-7}\ M_\odot$ yr^{-1}. The double slope of the RD is unlikely to be primarily due to large LTE deviations and points to a temperature stratification in the warm inner layers of the envelopes probed by PACS CO line emission. The temperature profile deduced is further discussed in Sect. 7.1.

Appendix B: The characteristic radius of the CO-emitting volume

In this appendix, we provide a more detailed description of the procedure that we have followed to decide on a "characteristic" radius of the CO-emitting volume (r_{CO}) to be used to compute, and correct for, the CO line opacities (Sect. 5.1) and to obtain an estimate of the mean mass-loss rate of our targets (Sect. 6.2).

For AGB CSEs (also including OH/IRs), a first estimate of the size of the CO-emitting volume is derived using the envelope temperature structure estimated from detailed non-LTE excitation and radiative tranfer calculations in the literature. These exist for many AGB CSEs using low-J CO transitions (typically $J_u \lesssim 6$), and, for more reduced samples, also using certain CO transitions from higher J levels.

In Fig. B.1 we show temperature power-law radial profiles in the form

$$T(r) = T_i \times (\tfrac{r}{R_i})^\alpha$$

that have been deduced in a number of previous works (references are given in the figure caption) for the *few* targets in our sample that include at least one high-J CO line observed with any of the three *Herschel* instruments (HIFI, SPIRE, or PACS). As we see in this figure, the full range of rotation temperatures deduced from our RD analysis, $T_{rot} \sim 200$–700 K (Sect. 6), is consistent with the bulk of the PACS CO emission studied here arising from layers between $\sim 2{\times}10^{14}$ and $\sim 5{\times}10^{15}$ cm, if we take together all the $T(r)$ distributions in Fig. B.1 (coloured lines), or between $\sim 3{\times}10^{14}$ and $\sim 3{\times}10^{15}$ cm, if we use an average $T(r)$ power-law (thick black line, in Fig. B.1). The quadratic mean of these two ranges is $r_{CO} \sim 10^{15}$ cm, which we uniformly use as the reference value in most AGB stars to compute M_{H_2}, T_{rot}, and $\dot{M}$ (but see more details below). Since the radius is, in any case, uncertain, we offer additional estimates of these parameters for a larger range of radius around the default r_{CO} (Appendix C). As we will see next, for the lowest (larger) mass-loss rate AGB stars in our sample, the characteristic CO-radius could be a factor of ~2–4 smaller (larger) than the $r_{CO} \sim 10^{15}$ cm reference value.

In the following, we perform a case-by-case RD analysis of three targets (R Dor, W Aql, and TX Cam) that are representative of three main mass-loss regimes in our sample: low, medium

and high ($\dot{M} \approx 10^{-7}\ M_\odot\ \mathrm{yr}^{-1}$, $\approx 10^{-6}\ M_\odot\ \mathrm{yr}^{-1}$, and $\gtrsim 10^{-5}\ M_\odot\ \mathrm{yr}^{-1}$, respectively) and for which detailed non-LTE excitation and radiative transfer studies of the CO emission including some mid-to-high J_u-CO transitions exist in the literature. The purpose is twofold: (1) to better illustrate our method to constrain r_{CO} in our sample (needed to decide on a plausible reference value for a uniform analysis), and (2) to compare the mass-loss rates from our approximate RD analysis with those computed using more sophisticated modelling tools.

R Dor. Precise CO-modelling studies of the molecular envelope of this object, including CO transitions up to $J_u = 16$ ($E_{up} = 750$ K), have been carried out by Maercker et al. (2016) and Van de Sande et al. (2018; references to other molecular line studies using lower-J_u transitions are given in Table D.2). The gas temperature structure deduced from these works, which use the same set of CO lines, are not fully coincident (dotted and solid red lines in Fig. B.1). Van de Sande et al. (2018) claim that their model achieves a better fit to more lines, and therefore, we adopt the $T(r)$ power-law determined by these authors, with an exponent $\alpha = 0.65$.

Our general procedure to determine an optimal/acceptable value of r_{CO} is as follows. From a linear fit to the CO datapoints in the RD diagram (dotted line and black dots, respectively, in the top panel of Fig. B.2) we find a first or iteration-zero estimate of $T_{rot}(i = 0)$ before any opacity correction is applied. Assuming that $T_{rot}(i = 0) \sim 570$ K represents (or is close to) the average gas temperature within the CO-emitting volume and using the $T(r)$ function depicted in Fig. B.1, we derive an initial value of $r_{CO}(i = 0) \sim 2.5{\times}10^{14}$ cm. We use this radius to compute the opacity of the different transitions. In this case, we obtain $\tau_{14\rightarrow13} \sim 1.8$ for the CO $J = 14{-}13$ line, and smaller for higher-J lines (see Eq. (4)). After applying the opacity correction, through the frequency-dependent factor $C_\tau = \tau/(1{-}e^{-\tau})$, a second linear fit to the opacity-corrected datapoints is performed (pink line and dots, respectively, in top panel of Fig. B.2), resulting in a new estimate of $T_{rot}(i = 1)$. The latter always is smaller than the iteration-zero value because after applying the C_τ correction, the slope of the RD increases, as a direct result of the frequency-dependence of C_τ and the typical values of T_{rot} that we measure in our sample. Comparing again the value of $T_{rot}(i = 1) \sim 480$ K with the $T(r)$ law, we deduce a *new* value of $r_{CO}(i = 1) \sim 3.4{\times}10^{14}$ cm, where the gas would have such a temperature.

This exercise indicates that an intermediate value between $r_{CO}(i = 0)$ and $r_{CO}(i = 1)$ is needed to reach full consistency between the r_{CO} value used for the opacity correction and the one that reproduces the opacity-corrected T_{rot} derived (according to the $T(r)$ adopted). In the particular case of R Dor, we find a *perfect* match between $r_{CO}(i = 0)$ and $r_{CO}(i = 1)$ for $r_{CO} \sim 3.15{\times}10^{14}$ cm (leading to $T_{rot}(i = 1) \sim 500$ K at this radius – Fig. B.1, middle panel).

An additional constrain to the radius is obtained from the fact that, as already explained in Sect. 5, the deepest layer traced by the observed CO emission must be such that $\tau < 1$. In order to satisfy this moderate-opacity condition, a value of r_{CO} slightly larger than the "perfect-match" r_{CO} above is preferred. For R Dor, a value of $r_{CO} \sim 3.5{\times}10^{14}$ cm satisfies the opacity criteria ($\tau_{14\rightarrow13} < 1$) and is, within uncertainties, still fully consistent with the radius where the final value of T_{rot} is attained, adopting the $T(r)$ law from previous works – Fig. B.2, bottom panel). The mass-loss rate that results adopting this value of the radius $r_{CO} \sim 3.5{\times}10^{14}$ cm, which guarantees line opacities lower than 1, is $\dot{M} \sim 4{\times}10^{-7}\ M_\odot\ \mathrm{yr}^{-1}$.

In this and in most targets, in principle we cannot rule out a larger radius (leading to even lower line opacities), even if

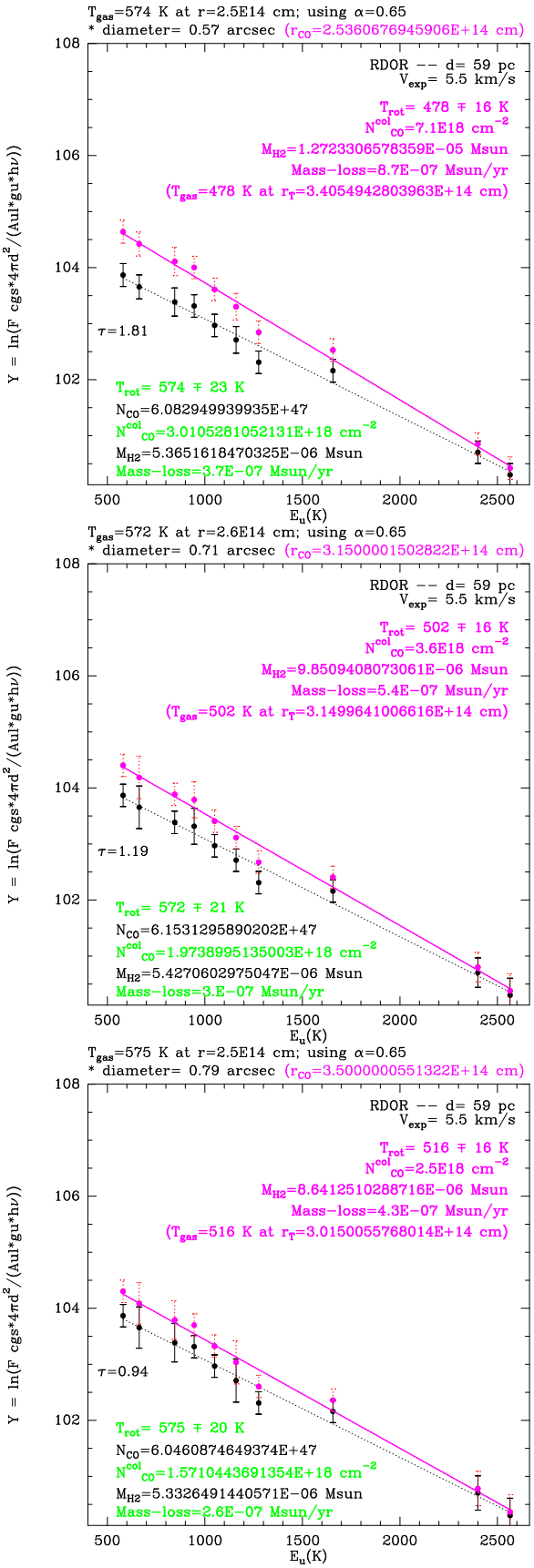

Fig. B.2. Rotational diagrams of the low mass-loss rate O-rich AGB star R Dor to illustrate the different steps that we have routinely followed to constrain r_{CO} in our sample. The *bottom panel* shows an optimal value of r_{CO} according to our temperature-opacity combined criteria (full details are given in the text, Appendix B).

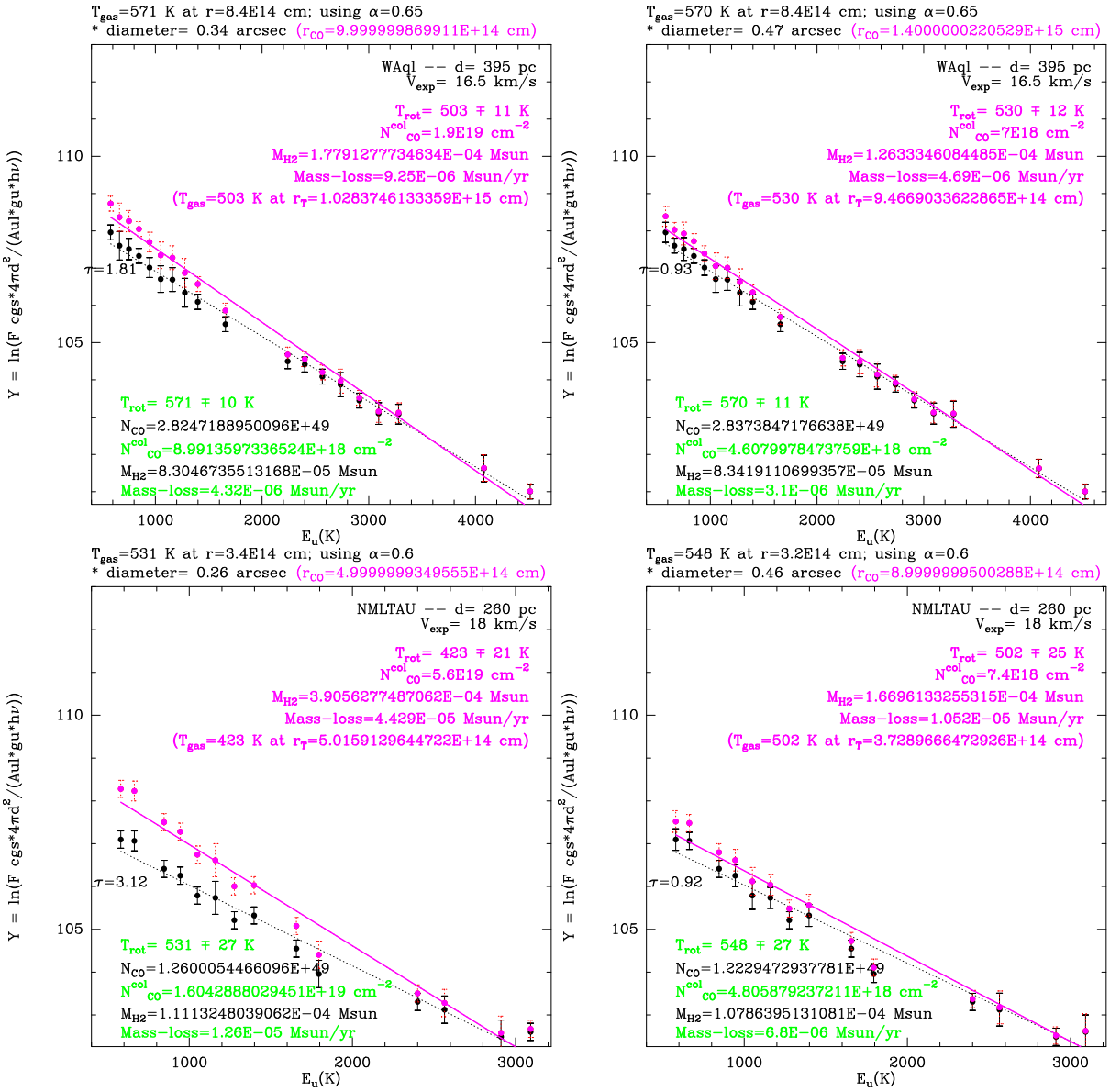

Fig. B.3. Rotational diagram of W Aql and NML Tau (*bottom*). *Left*: results of the RD for $r_{CO} = 1{\times}10^{15}$ cm, which results in a perfect match between the opacity- and temperature-radius (labelled as r_{CO} and r_T, respectively, in the plot) but results in an undesired large opacity correction, $\tau_{14\rightarrow13} > 1$. *Right*: results of the RD for $r_{CO} = 1.4{\times}10^{15}$ cm, which satisfies our $\tau_{14\rightarrow13} < 1$ criteria.

T_{rot} deviates from the gas temperature predicted at that radius based on the $T(r)$ law adopted. This is because there is no guarantee that the adopted $T(r)$ is a 100% accurate representation of the real temperature structure in these inner-wind regions and because T_{rot} may not be either a 100% accurate representation of the temperature of the gas (especially for low mass-loss rate objects). For R Dor, if we adopt the default radius of $r_{CO} \sim 1{\times}10^{15}$ cm previously established as a reasonable characteristic radius for the overall AGB class, we deduce a temperature of $T_{rot} \sim 570$ K and a mass-loss rate of $\dot{M} \sim 1{\times}10^{-7}\,M_{\odot}\,\mathrm{yr}^{-1}$.

For R Dor, the mass-loss rates derived from Van de Sande et al. (2018) and Maercker et al. (2016) from their non-LTE CO excitation and radiative transfer analysis are very similar in both cases ($\sim 2{\times}10^{-7}\,M_{\odot}\,\mathrm{yr}^{-1}$) and lie within the range of values estimated by us from our simple RD approach and the *plausible* range of r_{CO} explored, $\dot{M} \sim [1\text{–}4]{\times}10^{-7}\,M_{\odot}\,\mathrm{yr}^{-1}$.

W Aql. Non-LTE excitation and radiative transfer of the CO emission, including CO transitions up to $J_u = 25$ ($E_{up} = 1796$ K), have been carried out for this S-type AGB star by Danilovich et al. (2014). The mass-loss rate obtained in this work is $\dot{M} \sim 4{\times}10^{-6}\,M_{\odot}\,\mathrm{yr}^{-1}$ (as quoted in Table D.2, where we provide additional references to other molecular line studies using lower-J_u transitions). Danilovich et al. (2014) derive the gas and dust temperature profile in the $2{\times}10^{14}$–10^{17} cm envelope layers (see their Fig. 3). Both the gas and dust temperatures are quite similar throughout the whole envelope, with the dust being slighly cooler than the gas below $2{\times}10^{15}$ cm (i.e. the region sampled by the PACS CO data). In this region, the gas and dust temperatures do not differ by more than 50% (in particular, at $\sim 10^{15}$ cm, values of $T_{dust} \sim 400$ K and $T_{kin} \sim 500$ K are expected).

In Fig. B.1 we reproduce the gas temperature structure deduced by Danilovich et al. (2014); the exponent of this power-law function is $\alpha = 0.65$. We have used this profile

to constrain r_{CO} following the same procedure explained in the previous paragraphs for R Dor. As we can see in the left panel of Fig. B.3, a radius of $r_{CO} \sim 1{\times}10^{15}$ cm produces a perfect match between the final (opacity-corrected) temperature derived ($T_{rot} \sim 500$ K) and the radius where this temperature is expected (r_T) according to Danilovich et al. (2014). This value of the radius, however, results in line opacities larger than desirable and a mass-loss rate of $\dot{M} \sim 9{\times}10^{-6}\ M_{\odot}\ yr^{-1}$. In this case, the radius that produces $\tau_{14\rightarrow13}$ <1 and simultaneously satisfies (within uncertainties) the temperature criteria is $r_{CO} \sim 1.4{\times}10^{15}$ cm (right panel of Fig. B.3. This results in a somewhat smaller mass-loss rate of $\dot{M} \sim 5{\times}10^{-6}\ M_{\odot}\ yr^{-1}$, which is in excellent agreement with previous estimates.

IK Tau. The physical properties of the circumstellar gas, including the temperature, velocity and density structure, have been determined from the radiative transfer modelling of the multi-transitional (sub)millimetre CO line observations by Decin et al. (2010) and Maercker et al. (2016). The temperature distributions from these two works differ substantially (as for R Dor) and are shown in Fig. B.1 (solid and dotted cyan lines).

Adopting the $\alpha = 0.6$ distribution derived by Decin et al. (2010), we find that a radius of $r_{CO} \sim 5{\times}10^{14}$ cm produces a perfect match between the final (opacity-corrected) value of the temperature ($T_{rot} = 420$ K) and the radius r_T where this temperature is expected, however, it results in opaque lines (Fig. B.3, bottom-left). For IK Tau, a radius of $r_{CO} \sim 9{\times}10^{14}$ cm or larger is needed to meet the $\tau_{14\rightarrow13}$ <1 criteria (Fig. B.3, bottom-rigth). This results in a somewhat smaller mass-loss rate of $\dot{M} \sim 1{\times}10^{-5}\ M_{\odot}\ yr^{-1}$, also in agreement with the range of values from previous estimates ($\dot{M} \sim [0.2\text{–}3.5]{\times}10^{-5}\ M_{\odot}\ yr^{-1}$, Table D.2).

Rest of the targets. We have followed this procedure to constrain the range of r_{CO} values that are plausible (based on our opacity- and temperature- combined criteria) for each target individually. Whenever a $T(r)$ distribution was available in the literature (this happened for a few targets, see Fig. B.1) we used that specific law, and for the rest we used a mean $T(r)$ distribution represented by the thick black line in Fig. B.1 as a guide.

Remarks on the temperature profiles. The $T(r)$ profiles used and represented in Fig. B.1, although obtained from detailed non-LTE excitation and radiatiave transfer models of the CO emission, are not free from large uncertainties. This is denoted by the discrepancies between the temperature structure derived for the same targets when computed by different teams (notable cases are R Dor and IK Tau, in spite of these being among the most studied and best characterized AGB envelopes). Moreover, the power-law distribution is only an approximation to the real temperature structure. Indeed, the latter can deviate significantly from a simple power-law in some regions, in particular, $T(r)$ can have multiple-slopes as well as local minima and maxima as shown in De Beck et al. (2010, see their Fig. 9) and Maercker et al. (2016, see their Fig. 5).

Additionally, given the moderate range of J_u in the CO transitions predominantly modelled and published to date, the curves represented in Fig. B.1 are expected to be most reliable in the intermediate-to-outer envelope layers, beyond $\sim 10^{15}$ cm. Recently, Lombaert et al. (2016) performed non-LTE excitation and radiative transfer models of a sample of C-rich AGB CSEs using a selection of seven high-J CO transitions observed with PACS and SPIRE covering levels from $J_u = 15$ to 38, that is, higher than in the studies represented in Fig. B.1. One interesting result from this study is that the temperature of the gas falls off less steeply, with a power-law exponent close to $\alpha \sim 0.4\text{–}0.5$, in the inner-warm envelope regions sampled by these high-J CO transitions. This is indeed consistent with the crude estimate of α deduced in this work by comparing the hot and warm envelope components for a few targets in our sample (see Sect. 7). More dedicated non-LTE excitation and radiative transfer models of the high-J CO emission in larger samples is needed to confirm this result and to obtain a more precise description of the temperature distribution in these inner and warm regions of the envelopes of AGB stars.

Final remark on the reference values of r_{CO}. It is evident that the value of r_{CO} derived using a temperature criteria is very model-dependent since it fully relies on $T(r)$ and on T_{rot} being a perfect representation of T_{kin}. For this reason, we prefer to be cautious and, after having explored carefully the range of plausible r_{CO} values based on a temperature-opacity combined criteria for all targets, to use a set of (order-of-magnitude) estimates of r_{CO} for the whole sample, rather than using the best-match radius individually found for each target. As shown in Table D.2, we chose a reference radius: $r_{CO} = 1{\times}10^{15}$cm for most AGB CSEs, $r_{CO} = [2\text{–}4]{\times}10^{15}$ cm for high-$\dot{M}$ AGB CSEs ($>1{\times}10^{-5}\ M_{\odot}\ yr^{-1}$) and $r_{CO} = [4\text{–}6]{\times}10^{14}$ cm for low-$\dot{M}$ AGB CSEs ($<1{\times}10^{-6}\ M_{\odot}\ yr^{-1}$).

As discussed in Sect. 5, the temperature profile in the molecular envelopes of post-AGB objects and PN is extremely poorly characterized due to a much more limited number of CO emission cartography and, most importantly, modelling studies (especially using high-J CO transitions). Based on the systematically low values of T_{rot} in post-AGB objects and PNs found in this work (~200 K) as well as their generally larger dimensions, we chose a reference value of the radius of $r_{CO} = 6{\times}10^{16}$ cm in these cases (Table D.3), although we explored a larger range of r_{CO} (examples are given in Figs. C.1 and C.2). This range of r_{CO} resulted in negligible RD opacity corrections in all these sources.

Appendix C: Additional opacity and mass-loss rate plots

In this appendix we show, for each source, the values of the optical depth (τ, defined in Sect. 5.1) of the different CO transitions used to build the RDs for a range of values of the characteristic radius (r_{CO}) of the CO-emitting volume (Fig. C.1). As we can see in this figure, the radius adopted implies a moderate value of τ and, therefore, a moderate opacity correction. The radius of the PACS CO-emitting region is the major source of uncertainty in the computation of τ and, therefore, of the emitting mass and mass-loss rates. It also has an effect on the rotational temperature. The values of M_{H_2} and T_{rot} for a range of r_{CO} are plotted inside the boxes in Fig. C.1. The resulting mass-loss rates, $\dot{M}$, are shown in Fig. C.2, together with the broad range of mass-loss rates found in the literature for each object, typically derived from low-J CO line studies (references are provided in Table D.2).

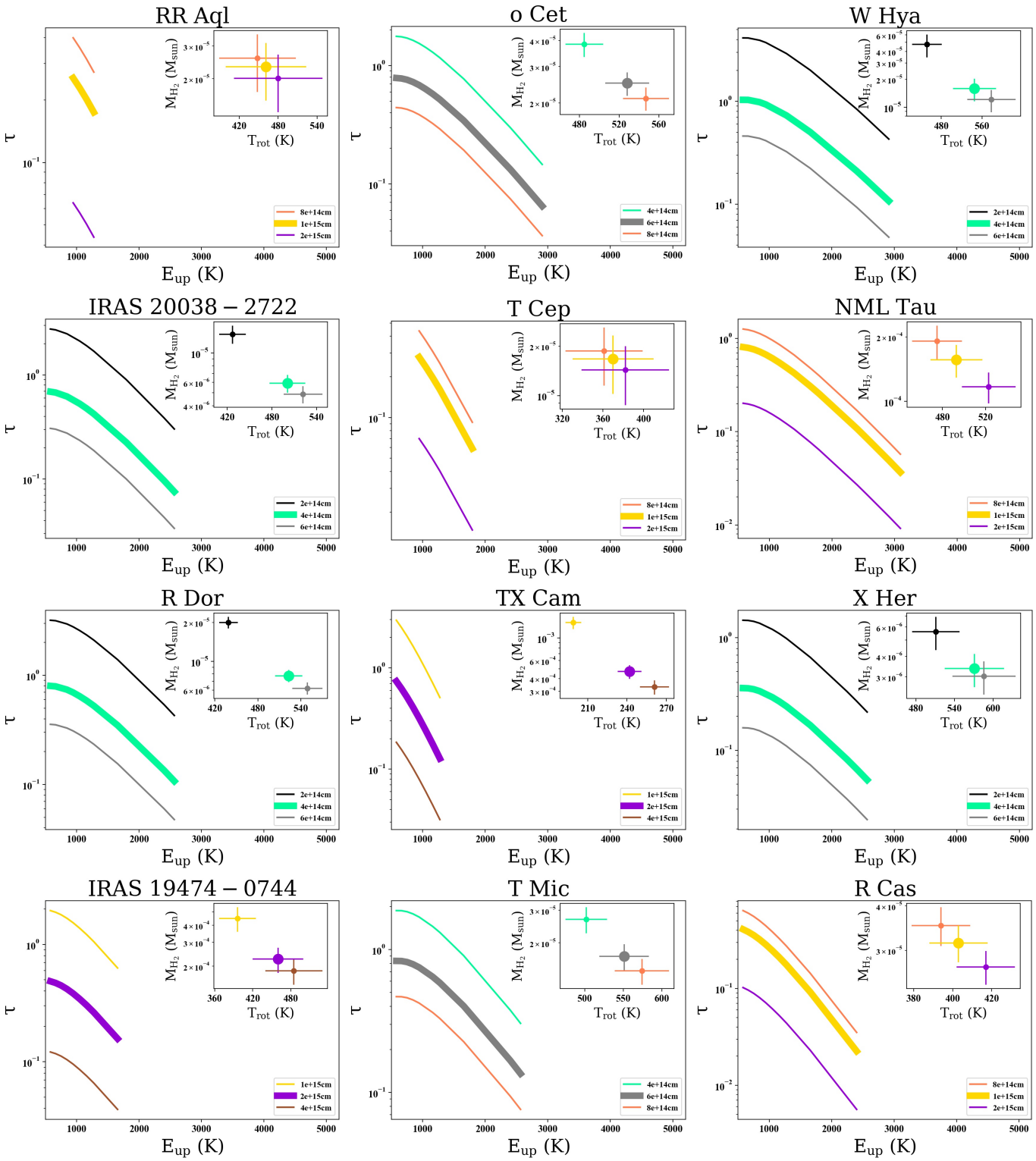

Fig. C.1. Plots of τ vs. E_{up} corresponding to different linear radii. In each chart there is a subgraphic showing M_{H_2} vs. T_{rot}. The thickest curve and the biggest point are those associated to the r_{CO} shown in Table D.3.

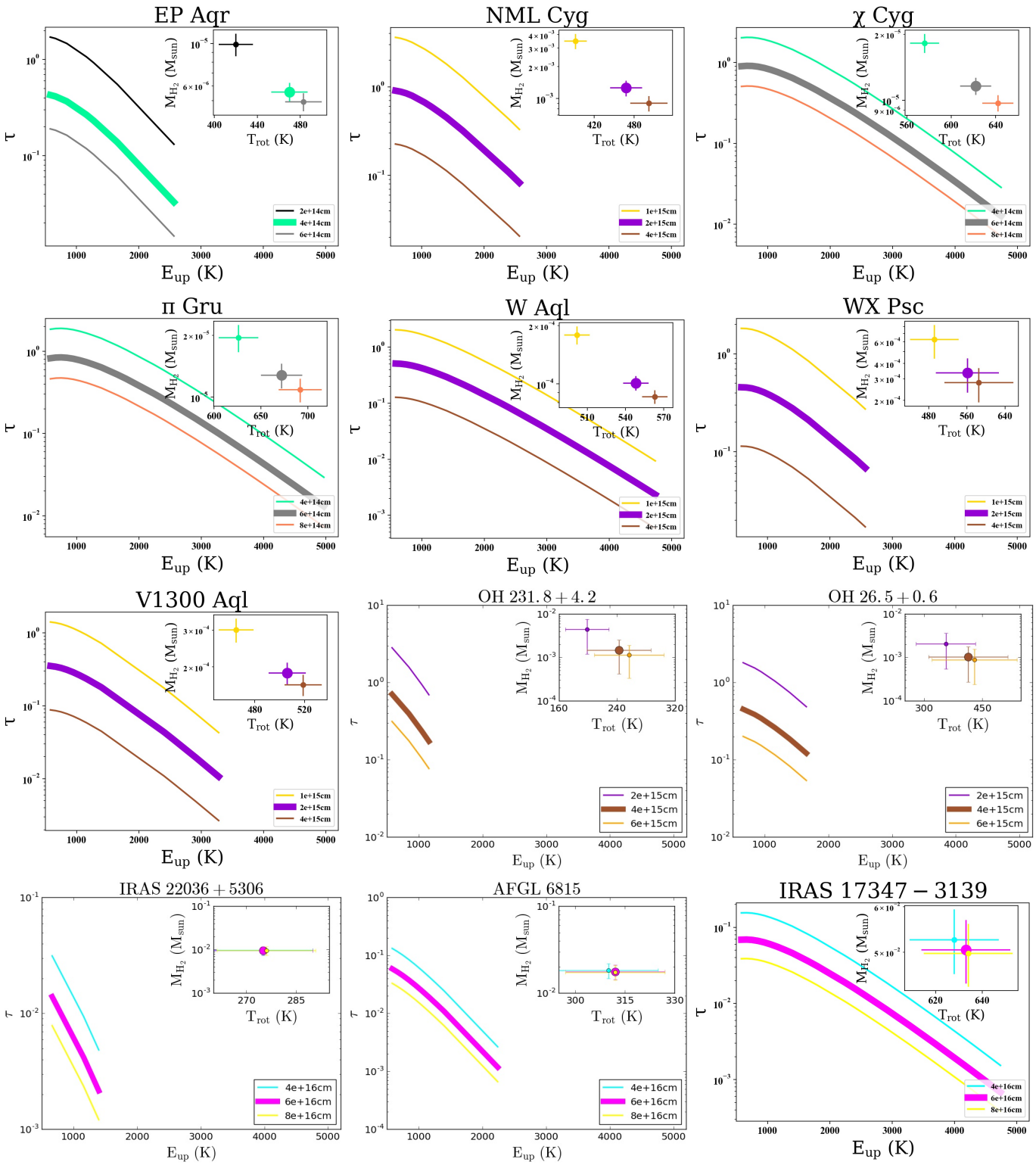

Fig. C.1. continued.

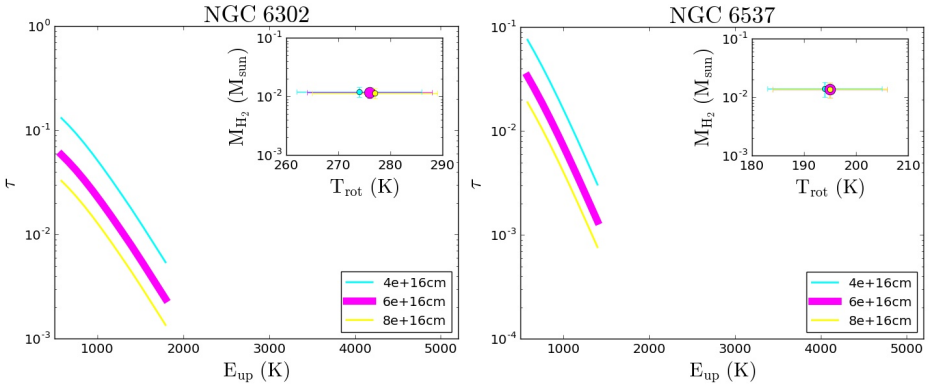

Fig. C.1. continued.

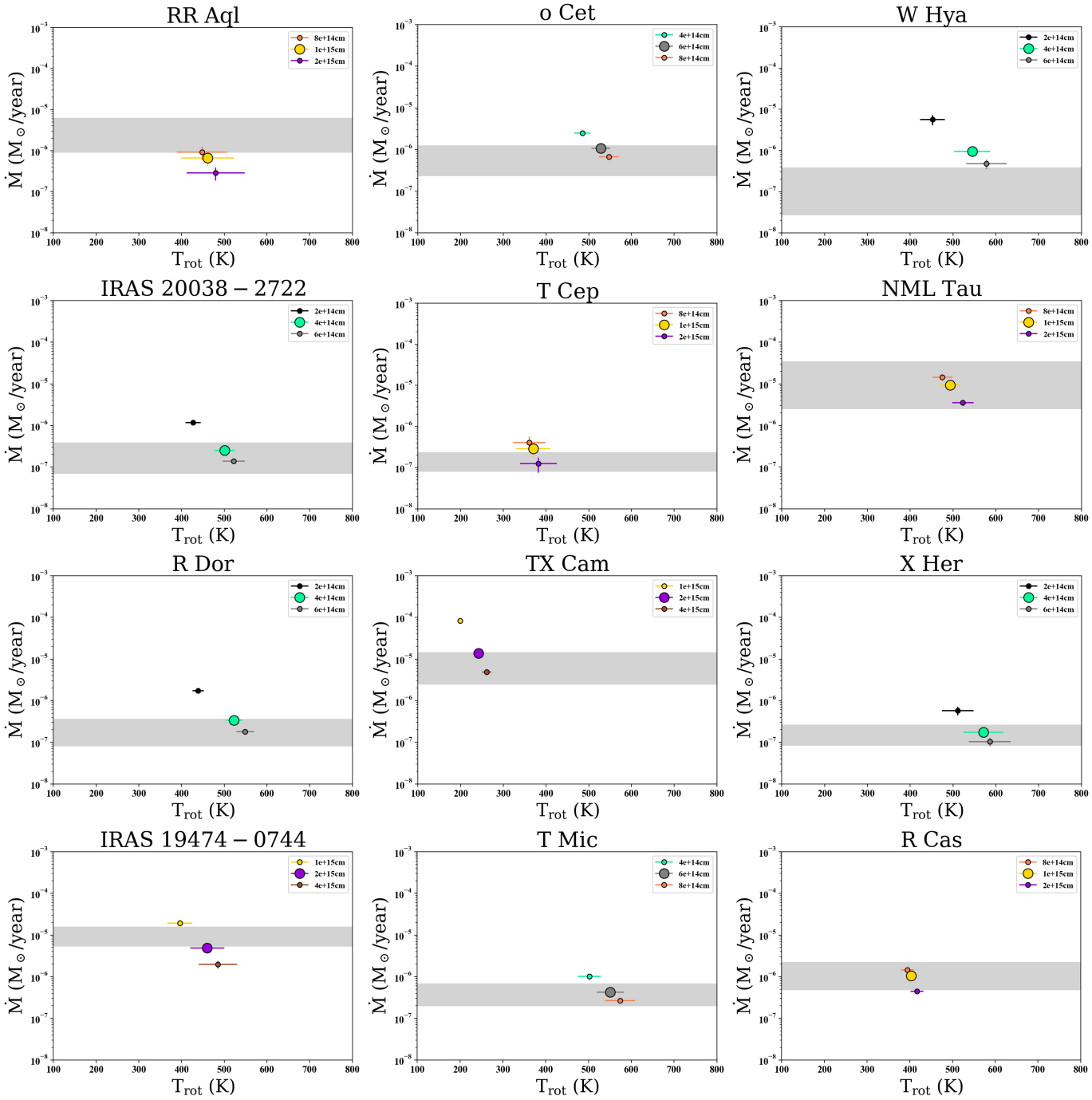

Fig. C.2. Plots of $\dot{M}$ vs. $T_{\rm rot}$. In each panel three different points, corresponding to three different $r_{\rm CO}$ are shown. The point of the $r_{\rm CO}$ shown in Table D.3 is bigger than the rest. The grey region represents the interval of mass-loss rates covered by previous works found in bibliography. For more details see Sect. 6. The linear radii explored are the same as the ones shown in Fig. C.1.

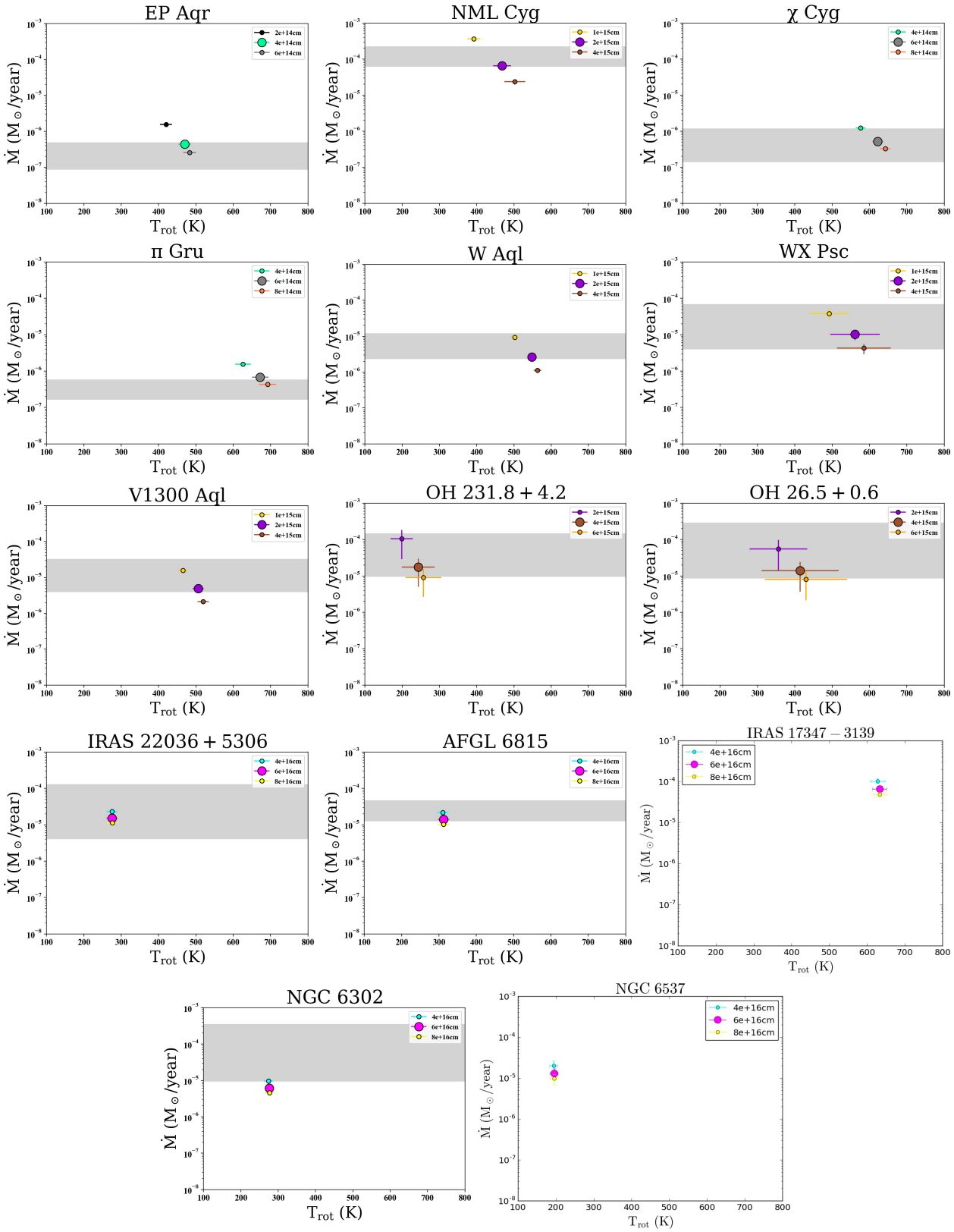

Fig. C.2. continued.

Appendix D: Tables

Table D.1. Observations log.

Target name	Alternative name	Class	RA (J2000) (hh:mm:ss.s)	Dec (J2000) (dd:mm:ss.s)	Obs IDs	Observing date (yyyy-mm-dd)
RR Aql	–	O-rich AGB	19:57:36.1	–1:53:11.3	1342269414	2013-04-05
Omi Cet	Mira	O-rich AGB	2:19:20.8	–2:58:39.5	1342213286 1342213286	2011-01-25 2011-01-25
W Hya	–	O-rich AGB	13:49:02.0	–28:22:03.5	1342212604 1342223808	2011-01-14 2011-07-09
IRAS 20038-2722	V1943 Sgr	O-rich AGB	20:06:55.2	–27:13:29.8	1342268730 1342268569	2013-03-29 2013-03-27
T Cep	–	O-rich AGB	21:09:31.8	68:29:27.2	1342246557	2012-06-01
NML Tau	IK Tau	O-rich AGB	3:53:28.8	11:24:22.6	1342203679 1342203680 1342203681	2010-08-28 2010-08-28 2010-08-28
R Dor	–	O-rich AGB	4:36:45.6	–62:04:37.8	1342197794 1342197794	2010-06-05 2010-06-05
TX Cam	–	O-rich AGB	5:00:50.4	56:10:52.6	1342225855 1342225856	2011-08-08 2011-08-08
X Her	–	O-rich AGB	16:02:39.2	47:14:25.3	1342197802 1342202120	2010-06-05 2010-07-28
IRAS 19474-0744	GY Aql	O-rich AGB	19:50:06.3	–7:36:52.5	1342268638 1342268449	2013-03-25 2013-03-26
T Mic	–	O-rich AGB	20:27:55.2	–28:15:39.8	1342268729 1342268788 1342269458	2013-03-29 2013-03-29 2013-04-06
R Cas	–	O-rich AGB	23:58:24.9	51:23:19.7	1342212576 1342212577	2011-01-12 2011-01-12
EP Aqr	–	O-rich AGB	21:46:31.9	–2:12:45.9	1342270639 1342270684	2013-04-20 2013-04-21
NML Cyg	–	O-rich AGB	20:46:25.5	40:06:59.6	1342198174 1342198174	2010-06-02 2010-06-02
χ Cyg	–	S-type	19:50:33.9	32:54:50.6	1342198176 1342198177	2010-06-02 2010-06-02
π Gru	–	S-type	22:22:44.2	–45:56:52.6	1342210397 1342210398	2010-11-28 2010-11-28
W Aql	–	S-type	19:15:23.4	–7:02:49.9	1342209731 1342209732	2010-11-06 2010-11-07
WX Psc	IRC +10011	OH/IR star	1:06:26.0	12:35:53.0	1342202121 1342202122	2010-07-28 2010-07-28
V1300 Aql	IRC -10529	OH/IR star	20:10:27.9	–6:16:13.6	1342269516 1342269910	2013-04-07 2013-04-11
OH 231.8+4.2	–	OH/IR star	7:42:16.8	–14:42:52.1	1342196694 1342196695	2010-05-19 2010-05-19
OH 26.5+0.6	V437 Sct	OH/IR star	18:37:32.5	–5:23:59.4	1342207776 1342207777	2010-10-31 2010-10-31
IRAS 22036+5306	–	O-rich p-AGB	22:05:30.3	53:21:33.0	1342221882 1342221883	2011-05-29 2011-05-29
AFGL 6815	Cotton Candy Nebula	O-rich p-AGB	17:18:19.9	–32:27:20.2	1342216629 1342216630	2011-03-22 2011-03-22
IRAS 17347-3139	–	O-rich PN	17:38:01.3	–31:40:58.0	1342229696 1342229697	2011-09-24 2011-09-24
NGC 6537	Red Spider Nebula	O-rich PN	18:05:13.1	–19:50:34.9	1342231322 1342231323	2011-10-22 2011-10-22
NGC 6302	Butterfly Nebula	O-rich PN	17:13:44.2	–37:06:15.9	1342230150 1342230151	2011-10-05 2011-10-05

Table D.2. Stellar and circumstellar information taken from the bibliography for the objects of the sample.

Target name	Variability	$T_{\rm eff}$ (K)	d (pc)	$v_{\rm exp}$ (km s^{-1})	$\dot{M}_{\rm Bibliography}$ ($M_\odot$ yr^{-1})		References
RR Aql	Mira	2000	530	9.0	2.4×10^{-6} 9.1×10^{-7}	$(0.9,6.2)\times10^{-6}$	7, 34
Omi Cet	Mira	2200	110	8.1	2.5×10^{-7} 5×10^{-7}	$(0.2,1.2)\times10^{-6}$	18, 29, 34
W Hya	SRa	2200	98	7.0	1.5×10^{-7} 7.8×10^{-8} 10^{-7} 7×10^{-8} 8.1×10^{-8}	$(0.3,3.8)\times10^{-7}$	10, 12, 18, 23, 32, 34
IRAS 20038-2722	SRb	2200	197	5.4	9.9×10^{-8} 1.3×10^{-7}	$(0.7,3.9)\times10^{-7}$	7, 14, 32
T Cep	Mira	2400	190	5.5	9.1×10^{-8}	$(0.8,2.4)\times10^{-7}$	7
NML Tau	Mira	2700	260	19.0	5×10^{-6} 8×10^{-6} 2×10^{-5} 4.5×10^{-6} 10^{-5} 4.7×10^{-6} 4.4×10^{-6}	$(0.2,3.5)\times10^{-5}$	3, 10, 18, 19, 23, 27, 34
R Dor	SRb	2800	59	5.7	1.6×10^{-7} 2×10^{-7} 1.3×10^{-7} 6.9×10^{-8}	$(0.9,4.2)\times10^{-7}$	1, 3, 10, 23, 32, 34
TX Cam	Mira	2800	380	18.5	4×10^{-6} 5.5×10^{-6} 7×10^{-6} 6.5×10^{-6}	$(0.2,1.5)\times10^{-5}$	3, 10, 18, 23, 24
X Her	SRV	2800	137	6.5	1.5×10^{-7} 10^{-6}	$(0.8,2.6)\times10^{-7}$	14, 32, 34
IRAS 19474-0744	SR	2800	810[a]	13.6	4.1×10^{-6}	$(0.5,1.6)\times10^{-5}$	34, 35
T Mic	SRb	2800	290	4.8	8×10^{-8} 2.7×10^{-7}	$(1.9,6.9)\times10^{-7}$	29, 32, 34
R Cas	Mira	3100	176	10.5	8×10^{-7} 9×10^{-7} 4×10^{-7}	$(0.5,2.2)\times10^{-6}$	3, 10, 18, 23
EP Aqr	SRb	3200	114	10.0	3.1×10^{-7} 1.2×10^{-7}	$(0.9,5.0)\times10^{-7}$	8, 18
NML Cyg	SRc	3800	620	33	8.7×10^{-5} 1.8×10^{-6}	$(0.6,2.3)\times10^{-4}$	18, 35
χ Cyg	Mira	2000	149	8.5	7×10^{-7} 4×10^{-7} 2.4×10^{-7}	$(0.1,1.2)\times10^{-6}$	10, 17, 18, 20, 27

Notes. Column 1: target name; Col. 2: variability of the central star; Col. 3: effective temperature of the star; Col. 4: adopted distance to the object; Col. 5: expansion velocity of the circumstellar envelope; Col. 6: left: mass loss rate taken from the literature. Right: range of mass loss rates shown at left after being scaled to the values of d, $v_{\rm exp}$ and $\chi_{\rm CO}$ used in this work. For those with only one previous estimation, the range cover a factor of 3 around that value after scaling. [(a)]Uncertain.

References. (1) Van de Sande et al. (2018) (2) Doan et al. (2017) (3) Maercker et al. (2016), (4) Santander-García et al. (2015), (5) Vickers et al. (2015), (6) Santander-García et al. (2015), (7) Danilovich et al. (2015), (8) Nhung et al. (2015), (9) He et al. (2014), (10) Ramstedt & Olofsson (2014), (11) Danilovich et al. (2014), (12) Khouri et al. (2014), (13) Justtanont et al. (2013), (14) Cox et al. (2012), (15) Choi et al. (2012), (16) Sánchez Contreras & Sahai (2012), (17) Schöier et al. (2011), (18) De Beck et al. (2010), (19) Decin et al. (2010), (20) Justtanont et al. (2010), (21) Ramstedt et al. (2009), (22) Meaburn et al. (2008), (23) Maercker et al. (2008), (24) Ramstedt et al. (2008), (25) Dinh-V-Trung et al. (2008), (26) Decin et al. (2007), (27) Teyssier et al. (2006), (28) Ramstedt et al. (2006), (29) Heras & Hony (2005), (30) Matsuura et al. (2005), (31) Woods et al. (2005), (32) Olofsson et al. (2002), (33) Alcolea et al. (2001), (34) Loup et al. (1993) and (35) Knapp et al. (1982).

Table D.2. continued.

Target name	Variability	$T_{\rm eff}$ (K)	d (pc)	$v_{\rm exp}$ (km s^{-1})	$\dot{M}_{\rm Bibliography}$ ($M_\odot$ yr^{-1})		References
π Gru	SRb	2300	152	10.0	8.5×10^{-7} 7.7×10^{-7}	$(1.6,4.9)\times10^{-7}$	2, 7, 18
W Aql	Mira	2800	395	16.5	2.7×10^{-6} 1.3×10^{-5} 2.2×10^{-6} 2.5×10^{-6} 4×10^{-6}	$(0.2,1.2)\times10^{-5}$	10, 11, 18, 21, 28
WX Psc	Mira	2000	700	19.3	1.7×10^{-5} 4×10^{-5} 1.9×10^{-5} 6×10^{-6} 8.5×10^{-6}	$(0.4,6.9)\times10^{-5}$	10, 13, 18, 26, 35
V1300 Aql	Mira	2000	620	16.5	10^{-5} 4.5×10^{-6} 1.6×10^{-5}	$(0.4,3.3)\times10^{-5}$	7, 10, 18, 24
OH 231.8+4.2	Mira	2500	1500	15.0	1.6×10^{-4}	$(0.9,2.8)\times10^{-4}$	15, 33
OH 26.5+0.6	Mira	2750	1370	17.0	1.0×10^{-4} 9.7×10^{-6}	$(3,0.8)\times10^{-4}$	13, 18
IRAS 22036+5306	No	6900	4000	30.0	7.5×10^{-5} 7×10^{-6}	$(0.04,1.3)\times10^{-4}$	16
AFGL 6815	No	7000	2900	15.0	2.1×10^{-5} 3×10^{-5}	$(1.3,4.7)\times10^{-5}$	5, 9, 18, 31
IRAS 17347-3139	No	30000[a]	3680[a]	25.0	–	–	5, 30
NGC 6537	No	200000	1500	18.0	–	–	31
NGC 6302	No	250000	1170	10.0	1.5×10^{-4} 2.7×10^{-5}	$(0.09,3.6)\times10^{-4}$	4, 6, 22, 25

Table D.3. Results from our CO RD analysis (Sect. 6), including double-fit (hot and warm) components for NML Tau, χ Cyg, π Gru, W Aql, and IRAS 17347-3139.

Target name	d (pc)	v_{exp} (km s^{-1})	r_{CO} (cm)	T_{rot} (K)	N_{CO}^{col} (cm^{-2})	M_{H_2} ($M_\odot$)	$\dot{M}$ ($M_\odot$ yr^{-1})	Correction$_{M_{H_2}}$
RR Aql	530	9.0	1×10^{15}	460 ± 60	$(8.8\pm3.0)\times10^{17}$	$(2.3\pm0.8)\times10^{-5}$	7×10^{-7}	1.2
o Cet	110	8.1	6×10^{14}	530 ± 20	$(2.6\pm0.3)\times10^{18}$	$(2.5\pm0.3)\times10^{-5}$	10^{-6}	1.6
W Hya	98	7.5	4×10^{14}	550 ± 40	$(3.8\pm1.0)\times10^{18}$	$(1.6\pm0.4)\times10^{-5}$	9×10^{-7}	1.6
IRAS 20038-2722	197	5.4	4×10^{14}	500 ± 20	$(1.4\pm0.2)\times10^{18}$	$(5.9\pm0.9)\times10^{-6}$	3×10^{-7}	1.4
T Cep	190	5.5	1×10^{15}	370 ± 40	$(6.3\pm2.5)\times10^{17}$	$(1.7\pm0.7)\times10^{-5}$	3×10^{-7}	1.2
NML Tau	260	18.0	1×10^{15}	490 ± 20	$(5.9\pm1.0)\times10^{18}$	$(1.6\pm0.3)\times10^{-4}$	9×10^{-6}	1.5
NML Tau	260	18.0	1×10^{15}	370 ± 20	$(9.5\pm1.4)\times10^{18}$	$(2.5\pm0.4)\times10^{-4}$	1×10^{-5}	–
NML Tau	260	18.0	1×10^{15}	820 ± 210	$(1.0\pm0.9)\times10^{18}$	$(2.7\pm2.4)\times10^{-5}$	2×10^{-6}	–
R Dor	59	5.5	4×10^{14}	520 ± 20	$(1.8\pm0.2)\times10^{18}$	$(7.7\pm0.8)\times10^{-6}$	3×10^{-7}	1.5
TX Cam	380	18.5	2×10^{15}	240 ± 10	$(4.4\pm0.7)\times10^{18}$	$(4.7\pm0.7)\times10^{-4}$	10^{-5}	1.5
X Her	137	6.5	4×10^{14}	570 ± 50	$(8.0\pm1.8)\times10^{17}$	$(3.4\pm0.8)\times10^{-6}$	2×10^{-7}	1.2
IRAS 19474-0744	810	13.6	2×10^{15}	460 ± 40	$(2.1\pm0.5)\times10^{18}$	$(2.3\pm0.5)\times10^{-4}$	5×10^{-6}	1.3
T Mic	290	4.8	6×10^{14}	550 ± 30	$(1.8\pm0.3)\times10^{18}$	$(1.7\pm0.3)\times10^{-5}$	4×10^{-7}	1.6
R Cas	176	10.5	1×10^{15}	400 ± 20	$(1.2\pm0.1)\times10^{18}$	$(3.1\pm0.4)\times10^{-5}$	10^{-6}	1.2
EP Aqr	114	10.0	4×10^{14}	470 ± 20	$(1.3\pm0.2)\times10^{18}$	$(5.6\pm0.6)\times10^{-6}$	4×10^{-7}	1.2
NML Cyg	620	33.0	2×10^{15}	470 ± 20	$(1.2\pm0.2)\times10^{19}$	$(1.3\pm0.2)\times10^{-3}$	7×10^{-5}	1.6
χ Cyg	149	8.5	6×10^{14}	620 ± 10	$(3.7\pm0.3)\times10^{18}$	$(1.2\pm0.1)\times10^{-5}$	5×10^{-7}	1.6
χ Cyg	149	8.5	6×10^{14}	480 ± 20	$(4.9\pm0.4)\times10^{18}$	$(1.6\pm0.2)\times10^{-5}$	7×10^{-7}	–
χ Cyg	149	8.5	6×10^{14}	690 ± 30	$(2.3\pm0.2)\times10^{18}$	$(7.3\pm1.5)\times10^{-6}$	3×10^{-7}	–
π Gru	152	10.0	6×10^{14}	670 ± 20	$(4.0\pm0.6)\times10^{18}$	$(1.3\pm0.2)\times10^{-5}$	7×10^{-7}	1.4
π Gru	152	10.0	6×10^{14}	460 ± 20	$(7.1\pm1.1)\times10^{18}$	$(2.3\pm0.2)\times10^{-5}$	10^{-6}	–
π Gru	152	10.0	6×10^{14}	870 ± 30	$(1.3\pm0.2)\times10^{18}$	$(4.2\pm0.7)\times10^{-6}$	2×10^{-7}	–
W Aql	395	16.5	2×10^{15}	550 ± 10	$(2.9\pm0.2)\times10^{18}$	$(1.0\pm0.1)\times10^{-4}$	3×10^{-6}	1.2
W Aql	395	16.5	2×10^{15}	440 ± 10	$(3.9\pm0.3)\times10^{18}$	$(1.4\pm0.1)\times10^{-4}$	3×10^{-6}	–
W Aql	395	16.5	2×10^{15}	570 ± 20	$(2.3\pm0.6)\times10^{18}$	$(7.9\pm2.0)\times10^{-5}$	2×10^{-6}	–
WX Psc	700	19.3	2×10^{15}	560 ± 70	$(3.2\pm1.0)\times10^{18}$	$(3.3\pm1.0)\times10^{-4}$	10^{-5}	1.0
V1300 Aql	620	16.5	2×10^{15}	510 ± 20	$(1.8\pm0.2)\times10^{18}$	$(1.9\pm0.2)\times10^{-4}$	5×10^{-6}	1.0
OH 231.8+4.2	1500	15.0	4×10^{15}	240 ± 40	$(3.5\pm2.5)\times10^{18}$	$(1.5\pm1.0)\times10^{-3}$	2×10^{-5}	1.0
OH 26.5+0.6	1370	17.0	4×10^{15}	410 ± 100	$(2.4\pm1.8)\times10^{18}$	$(1.0\pm0.8)\times10^{-3}$	10^{-5}	1.0
IRAS 22036+5306	4000	30.0	6×10^{16}	280 ± 20	$(1.0\pm0.2)\times10^{17}$	$(9.6\pm2.1)\times10^{-3}$	2×10^{-5}	1.1
AFGL 6815	2900	15.0	6×10^{16}	310 ± 20	$(1.9\pm0.4)\times10^{17}$	$(1.8\pm0.3)\times10^{-2}$	10^{-5}	1.1
IRAS 17347-3139	3680	25.0	6×10^{16}	630 ± 20	$(5.3\pm0.7)\times10^{17}$	$(5.0\pm0.6)\times10^{-2}$	7×10^{-5}	1.0
IRAS 17347-3139	3680	25.0	6×10^{16}	480 ± 10	$(8.2\pm0.4)\times10^{17}$	$(7.8\pm0.4)\times10^{-2}$	10^{-4}	–
IRAS 17347-3139	3680	25.0	6×10^{16}	820 ± 40	$(1.7\pm0.4)\times10^{17}$	$(1.6\pm0.4)\times10^{-2}$	2×10^{-5}	–
NGC 6302	1170	10.0	6×10^{16}	280 ± 10	$(1.2\pm0.2)\times10^{17}$	$(1.2\pm0.2)\times10^{-2}$	6×10^{-6}	1.1
NGC 6537	1500	18.0	6×10^{16}	200 ± 10	$(1.5\pm0.4)\times10^{17}$	$(1.4\pm0.4)\times10^{-2}$	10^{-5}	1.0

Notes. Column 1: target name; Col. 2: distance to the source (d); Col. 3: expansion velocity of the gas (v_{exp}); Col. 4: characteristic radius of the CO-emitting region adopted (r_{CO}); Col. 5: rotational temperature (T_{rot}); Col. 6: column density of CO (N_{CO}^{col}); Col. 7: total mass of H_2 within the CO-emitting volume (M_{H_2}); Col. 8: mass-loss rate ($\dot{M} = M_{H_2} \times v_{exp}/r_{CO}$); and Col. 9: ratio between M_{H_2} after and before the opacity correction was applied.

Table D.4. Integrated fluxes of ^{12}CO lines for 26 sources studied in this work.

Line	λ_{ul} (μm)	A_{ul} (s^{-1})	E_u (K)	Flux (10^{-16} W m^{-2})	Flux (10^{-16} W m^{-2})	Flux (10^{-16} W m^{-2})	Flux (10^{-17} W m^{-2})	Flux (10^{-17} W m^{-2})	Flux (10^{-16} W m^{-2})
				RR Aql	*o* Cet	W Hya	IRAS 20038-2722	T Cep	NML Tau
14-13	186.0	2.74×10^{-4}	580.5	–	3.0 ± 0.1	2.2 ± 0.2	1.9 ± 0.4	–	3.4 ± 0.1
15-14	173.6	3.35×10^{-4}	663.4	–	3.3 ± 0.1	2.7 ± 0.2	2.9 ± 0.2	–	4.6 ± 0.1
16-15	162.8	4.05×10^{-4}	751.7	–	3.8 ± 0.1	9.0 ± 1.1^{c}	1.0 ± 0.4^{a}	–	3.4 ± 0.5
17-16	153.3	4.83×10^{-4}	845.6	–	3.6 ± 0.2	2.9 ± 0.3	2.8 ± 0.5	–	
18-17	144.8	5.70×10^{-4}	945.0	0.18 ± 0.04	4.2 ± 0.1	3.1 ± 0.2	3.8 ± 0.6^{a}	7.0 ± 0.5	4.4 ± 0.1
19-18	137.2	6.65×10^{-4}	1049.9	0.17 ± 0.04	3.7 ± 0.3	3.3 ± 0.3^{a}	2.6 ± 0.6	5.6 ± 0.4	5.0 ± 0.1
20-19	130.4	7.70×10^{-4}	1160.2	0.20 ± 0.04	4.2 ± 0.3	7.0 ± 0.4^{a}	3.2 ± 0.5	8.7 ± 1.0	4.1 ± 0.1
21-20	124.2	8.83×10^{-4}	1276.1	0.18 ± 0.03	3.8 ± 0.6	2.5 ± 0.3	3.0 ± 0.6	6.0 ± 0.8	4.9 ± 0.2
22-21	118.6	1.01×10^{-3}	1397.4	0.77 ± 0.04^{a}	19 ± 1.0^{a}	8.8 ± 0.5^{a}	13 ± 1.0^{a}	64 ± 1.0^{a}	3.7 ± 0.1
23-22	113.5	1.14×10^{-3}	1524.2	1.9 ± 0.1^{a}	6.5 ± 0.5^{a}	16 ± 1.0^{a}	19 ± 1.0^{a}	32 ± 2.0^{a}	5.2 ± 0.3
24-23	108.8	1.28×10^{-3}	1656.5	4.8 ± 0.5	3.2 ± 0.5	5.8 ± 1.1^{a}	12 ± 2.0^{a}	24 ± 0.1^{a}	
25-24	104.5	1.43×10^{-3}	1794.3	–	1.7 ± 0.5^{a}	1.3 ± 1.0^{a}	2.7 ± 0.9	3.6 ± 1.1	3.6 ± 0.2
28-27	93.4	1.94×10^{-3}	2240.3	–	5.3 ± 0.4^{a}	6.9 ± 0.5^{a}	6.7 ± 0.8^{a}	–	2.4 ± 0.4
29-28	90.2	2.13×10^{-3}	2399.9	–	2.4 ± 0.3^{a}	2.6 ± 0.5	2.5 ± 0.4	–	11 ± 0.1^{a}
30-29	87.2	2.32×10^{-3}	2564.9	–	3.6 ± 0.8^{a}	1.3 ± 0.5	1.8 ± 0.8	–	2.5 ± 0.1^{c}
31-30	84.4	2.52×10^{-3}	2735.3	–	4.7 ± 0.5^{a}	3.0 ± 0.6	3.8 ± 1.1^{a}	–	2.4 ± 0.2
32-31	81.8	2.74×10^{-3}	2911.2	–	–	3.2 ± 0.7	–	–	5.5 ± 1.3^{a}
33-32	79.4	2.95×10^{-3}	3092.5	–	–	–	–	–	1.7 ± 0.5
34-33	77.1	3.18×10^{-3}	3279.2	–	–	–	–	–	2.2 ± 0.5
35-34	74.9	3.40×10^{-3}	3471.3	–	–	–	–	–	–
36-35	72.9	3.64×10^{-3}	3668.9	–	–	–	–	–	–
37-36	70.9	3.88×10^{-3}	3871.8	–	–	–	–	–	–
38-37	70.9	4.12×10^{-3}	4080.1	–	–	–	–	–	–
39-38	67.3	4.37×10^{-3}	4293.7	–	–	–	–	–	–
40-39	65.7	4.61×10^{-3}	4512.8	–	–	–	–	–	–
41-40	64.1	4.86×10^{-3}	4737.2	–	–	–	–	–	–
42-41	62.6	5.11×10^{-3}	4966.9	–	–	–	–	–	–

Notes. Column 1: quantum numbers of the transition; Col. 2: wavelength corresponding to the emission lines; Cols. 3 and 4: integrated fluxes of the emission lines. [(a)]Blended line. [(b)]Bad determination of the continuum level. [(c)]Bad fit.

Table D.4. continued.

Line	λ_{ul} (μm)	Flux (10^{-16} W m^{-2})	Flux (10^{-16} W m^{-2})	Flux (10^{-17} W m^{-2})	Flux (10^{-17} W m^{-2})	Flux (10^{-17} W m^{-2})	Flux (10^{-16} W m^{-2})
		R Dor	TX Cam	X Her	IRAS 19474-0744	T Mic	R Cas
14-13	186.0	2.6 ± 0.1	1.9 ± 0.1	4.5 ± 0.7	4.7 ± 0.7	1.9 ± 0.3	1.4 ± 0.1
15-14	173.6	3.0 ± 0.2	2.0 ± 0.1	2.7 ± 0.4	5.5 ± 0.4	3.5 ± 0.2	1.6 ± 0.1
16-15	162.8	69 ± 2.0^{c}	1.9 ± 0.1	2.9 ± 0.8	6.0 ± 0.4	3.3 ± 0.4	1.6 ± 0.1
17-16	153.3	4.2 ± 0.4	2.1 ± 0.1	5.9 ± 0.8	6.8 ± 0.5	3.9 ± 0.3	1.7 ± 0.1
18-17	144.8	5.1 ± 0.3	1.8 ± 0.1	8.5 ± 0.7^{a}	6.3 ± 0.5	4.6 ± 0.4	1.9 ± 0.1
19-18	137.2	4.7 ± 0.5	1.6 ± 0.1	4.5 ± 0.8	5.4 ± 0.8	27 ± 2^{c}	1.5 ± 0.1
20-19	130.4	4.7 ± 0.5	1.6 ± 0.2	4.4 ± 2.1	7.4 ± 0.5	5.3 ± 0.7	1.6 ± 0.1
21-20	124.2	3.9 ± 0.4	9.0 ± 1.5	4.1 ± 0.6	6.0 ± 0.3	3.4 ± 0.3	1.4 ± 0.1
22-21	118.6	13 ± 1.0^{a}	3.3 ± 0.2^{a}	10 ± 2^{a}	40 ± 1^{a}	21 ± 1^{a}	3.1 ± 0.1^{a}
23-22	113.5	32 ± 1.0^{a}	7.9 ± 0.3^{a}	42 ± 1^{a}	42 ± 1^{a}	23 ± 1^{a}	13 ± 1^{a}
24-23	108.8	6.4 ± 0.6	–	5.5 ± 1.8	8.3 ± 0.7	5.3 ± 0.9	1.1 ± 0.1
25-24	104.5	–	–	–	11 ± 3^{a}	–	0.5 ± 0.1^{a}
28-27	93.4	10 ± 1^{a}	–	4.5 ± 1.0	8.7 ± 1.5^{a}	–	2.1 ± 0.2^{a}
29-28	90.2	3.6 ± 0.3	–	3.0 ± 1.4	–	5.0 ± 0.9	0.6 ± 0.1
30-29	87.2	2.8 ± 0.8	–	5.4 ± 1.7	–	2.7 ± 1.0	1.0 ± 0.2
31-30	84.4	6.3 ± 0.7^{a}	–	9.5 ± 2.4^{a}	–	5.5 ± 1.2^{a}	1.5 ± 0.2^{a}
32-31	81.8	6.0 ± 1.6	–	–	–	–	0.9 ± 0.2^{a}
33-32	79.4	–	–	–	–	–	–
34-33	77.1	–	–	–	–	–	–
35-34	74.9	–	–	–	–	–	–
36-35	72.9	–	–	–	–	–	–
37-36	70.9	–	–	–	–	–	–
38-37	70.9	–	–	–	–	–	–
39-38	67.3	–	–	–	–	–	–
40-39	65.7	–	–	–	–	–	–
41-40	64.1	–	–	–	–	–	–
42-41	62.6	–	–	–	–	–	–

Table D.4. continued.

Line	λ_{ul} (μm)	Flux (10^{-17} W m^{-2})	Flux (10^{-16} W m^{-2})	Flux (10^{-16} W m^{-2})	Flux (10^{-16} W m^{-2})	Flux (10^{-16} W m^{-2})	Flux (10^{-16} W m^{-2})
		EP Aqr	NML Cyg	χ Cyg	π Gru	W Aql	WX Psc
14-13	186.0	6.4 ± 0.7	4.2 ± 0.2	2.4 ± 0.1	3.8 ± 0.1	3.5 ± 0.1	1.6 ± 0.1
15-14	173.6	6.3 ± 0.5	4.5 ± 0.2	2.9 ± 0.1	3.6 ± 0.1	3.5 ± 0.1	1.2 ± 0.1
16-15	162.8	23 ± 3^a	4.8 ± 0.5	3.2 ± 0.1	3.8 ± 0.1	4.3 ± 0.1	1.3 ± 0.2
17-16	153.3	9.0 ± 0.8	5.4 ± 0.1	3.2 ± 0.1	4.5 ± 0.1	4.8 ± 0.1	1.8 ± 0.1
18-17	144.8	12 ± 1^a	8.2 ± 0.1^a	3.9 ± 0.1	4.6 ± 0.1	4.7 ± 0.1	1.7 ± 0.1
19-18	137.2	12 ± 1^a	4.6 ± 0.2	3.6 ± 0.1	4.6 ± 0.1	4.5 ± 0.1	1.1 ± 0.1
20-19	130.4	8.5 ± 0.9	6.4 ± 0.3	4.4 ± 0.1	4.8 ± 0.1	5.6 ± 0.1	1.9 ± 0.2
21-20	124.2	8.4 ± 1.0	3.9 ± 1.0	3.3 ± 0.1	4.7 ± 0.1	5.0 ± 0.0	1.1 ± 0.2
22-21	118.6	3.2 ± 0.1^a	6.7 ± 0.7^c	4.1 ± 0.1	4.8 ± 0.1	4.9 ± 0.1	2.3 ± 0.1
23-22	113.5	56 ± 1^a	35 ± 1^a	11 ± 1^a	9.1 ± 0.3^a	7.8 ± 0.2^a	9.2 ± 0.2^a
24-23	108.8	8.2 ± 0.8	6.9 ± 0.2	4.1 ± 0.2	4.7 ± 0.1	4.0 ± 0.1	1.7 ± 0.2
25-24	104.5	3.5 ± 2.7^a	7.9 ± 2.9^a	4.0 ± 0.2	4.8 ± 0.1	4.1 ± 0.2	–
28-27	93.4	18 ± 1^a	26 ± 1^a	3.7 ± 0.1	3.9 ± 0.1	3.1 ± 0.1	5.4 ± 0.2^a
29-28	90.2	11 ± 3^a	4.2 ± 0.3	3.9 ± 0.1	3.5 ± 0.1	3.3 ± 0.1	3.3 ± 0.9
30-29	87.2	4.1 ± 1.2	2.4 ± 0.5	3.0 ± 0.1	3.9 ± 0.1	3.0 ± 0.2	0.81 ± 0.09
31-30	84.4	16 ± 1^a	–	4.3 ± 0.1^a	4.4 ± 0.1^a	2.7 ± 0.2	–
32-31	81.8	–	–	2.5 ± 0.1	2.9 ± 0.1	2.0 ± 0.1	–
33-32	79.4	–	–	2.4 ± 0.2	3.0 ± 0.2	1.7 ± 0.2	–
34-33	77.1	–	–	2.6 ± 0.2	2.6 ± 0.1	1.7 ± 0.1	–
35-34	74.9	–	–	2.6 ± 0.4	6.7 ± 0.2^a	3.5 ± 0.3^a	–
36-35	72.9	–	–	2.8 ± 0.3^a	2.4 ± 0.1	1.4 ± 0.3	–
37-36	70.9	–	–	1.5 ± 0.2	1.7 ± 0.5	0.80 ± 0.18	–
38-37	70.9	–	–	1.1 ± 0.2	1.9 ± 0.1	0.79 ± 0.15	–
39-38	67.3	–	–	9.6 ± 0.7^a	3.5 ± 0.7^a	3.8 ± 0.3^a	–
40-39	65.7	–	–	2.6 ± 0.6^a	1.8 ± 0.3	0.37 ± 0.11	–
41-40	64.1	–	–	0.56 ± 0.17	1.4 ± 0.2	0.18 ± 0.17	–
42-41	62.6	–	–	1.6 ± 0.5^a	0.94 ± 0.35	0.34 ± 0.12^a	–

Table D.4. continued.

Line	λ_{ul} (μm)	Flux (10^{-17} W m^{-2})	Flux (10^{-17} W m^{-2})	Flux (10^{-17} W m^{-2})	Flux (10^{-17} W m^{-2})	Flux (10^{-16} W m^{-2})	Flux (10^{-15} W m^{-2})
		V1300 Aql	OH 231.8+4.2	OH 26.5+0.6	IRAS 22036+5306	AFGL 6815	IRAS 17347-3139
14-13	186.0	7.5 ± 0.4	4.1 ± 1.6	4.1 ± 1.3[a]	11 ± 1[a]	3.2 ± 0.1	0.90 ± 0.1
15-14	173.6	11 ± 1	28 ± 13	7.1 ± 1.0	6.4 ± 0.6	3.3 ± 0.1	1.1 ± 0.1
16-15	162.8	9.2 ± 1.6	23 ± 12	–	8.2 ± 1.0[a]	2.5 ± 0.1	1.2 ± 0.1
17-16	153.3	12 ± 1	4.4 ± 1.8	11 ± 1	9.2 ± 0.9[a]	2.3 ± 0.1	1.4 ± 0.1
18-17	144.8	14 ± 1	8.3 ± 1.7[a]	15 ± 2	1.0 ± 0.2[a]	2.5 ± 0.1	1.3 ± 0.1
19-18	137.2	8.2 ± 0.5	2.2 ± 1.2	0.70 ± 0.71[b]	4.9 ± 1.7[a]	2.0 ± 0.1	1.4 ± 0.1
20-19	130.4	9.5 ± 0.7	3.5 ± 1.5	7.1 ± 1.1	3.9 ± 0.5	2.2 ± 0.1	1.4 ± 0.1
21-20	124.2	6.9 ± 1.0[a]	–	7.5 ± 1.7	5.4 ± 1.1[a]	1.6 ± 0.1	1.4 ± 0.1
22-21	118.6	12 ± 1	–	4.8 ± 2.4	3.0 ± 0.8	1.2 ± 0.1	1.5 ± 0.1
23-22	113.5	44 ± 1[a]	–	49 ± 5[a]	6.6 ± 0.9[a]	3.0 ± 0.1[a]	2.2 ± 0.1[a]
24-23	108.8	17 ± 1[a]	–	15 ± 2	–	0.38 ± 0.07[c]	1.3 ± 0.1
25-24	104.5	2.8 ± 3.0[a]	–	–	–	0.91 ± 0.38[a]	1.2 ± 0.1
28-27	93.4	–	–	–	–	0.43 ± 0.10	0.93 ± 0.02
29-28	90.2	6.0 ± 1.0	–	–	–	–	0.92 ± 0.02
30-29	87.2	5.6 ± 0.6	–	–	–	–	0.68 ± 0.02
31-30	84.4	4.6 ± 1.8[a]	–	–	–	–	1.5 ± 0.1[a]
32-31	81.8	3.5 ± 1.0	–	–	–	–	0.57 ± 0.02
33-32	79.4	4.4 ± 0.9[a]	–	–	–	–	0.52 ± 0.03
34-33	77.1	2.7 ± 0.6	–	–	–	–	0.48 ± 0.02
35-34	74.9	–	–	–	–	–	0.47 ± 0.02
36-35	72.9	–	–	–	–	–	0.42 ± 0.03
37-36	70.9	–	–	–	–	–	0.54 ± 0.10[a]
38-37	70.9	–	–	–	–	–	0.24 ± 0.04
39-38	67.3	–	–	–	–	–	0.34 ± 0.03
40-39	65.7	–	–	–	–	–	0.21 ± 0.03
41-40	64.1	–	–	–	–	–	0.26 ± 0.05
42-41	62.6	–	–	–	–	–	–

Table D.4. continued.

Line	λ_{ul} (μm)	Flux (10^{-16} W/m^2)	Flux (10^{-16} W/m^2)
		NGC 6302	IRAS NGC 6537
14-13	186.0	9.9 ± 0.3	2.9 ± 0.3
15-14	173.6	9.0 ± 0.4	3.4 ± 0.2
16-15	162.8	8.4 ± 0.4	2.3 ± 0.2
17-16	153.3	8.3 ± 0.3	3.2 ± 0.2
18-17	144.8	9.7 ± 0.4	2.1 ± 0.1
19-18	137.2	5.5 ± 0.2	1.4 ± 0.1
20-19	130.4	6.5 ± 0.3	1.4 ± 0.1
21-20	124.2	4.2 ± 0.3	0.70 ± 0.06
22-21	118.6	3.2 ± 0.5	0.37 ± 0.07
23-22	113.5	2.8 ± 0.5	0.82 ± 0.31^a
24-23	108.8	1.7 ± 1.0^a	–
25-24	104.5	2.4 ± 0.3	–
28-27	93.4	–	–
29-28	90.2	–	–
30-29	87.2	–	–
31-30	84.4	–	–
32-31	81.8	–	–
33-32	79.4	–	–
34-33	77.1	–	–
35-34	74.9	–	–
36-35	72.9	–	–
37-36	70.9	–	–
38-37	70.9	–	–
39-38	67.3	–	–
40-39	65.7	–	–
41-40	64.1	–	–
42-41	62.6	–	–

Astronomy & Astrophysics manuscript no. rotdiag
December 20, 2018

Warm CO in evolved stars from the THROES catalogue

II. Herschel⋆/PACS spectroscopy of C-rich envelopes

J. M. da Silva Santos[1,2], J. Ramos-Medina[1], C. Sánchez Contreras[1], and P. García-Lario[3]

[1] Centro de Astrobiología (CSIC-INTA), ESAC, Camino Bajo del Castillo s/n, 28691 Villanueva de la Cañada, Madrid, Spain
[2] Institute for Solar Physics, Department of Astronomy, Stockholm University, AlbaNova University Centre, SE-106 91 Stockholm, Sweden. e-mail: joao.dasilva@astro.su.se
[3] European Space Astronomy Center, PO Box 78, 28691, Villanueva de la Cañada, Madrid, Spain

December 20, 2018

ABSTRACT

Context. This is the second paper of a series making use of *Herschel*/PACS spectroscopy of evolved stars in the THROES catalogue to study the inner warm regions of their circumstellar envelopes (CSEs).
Aims. We analyze the CO emission spectra, including a large number of high-J CO lines (from J=14-13 to J=45-44, v=0), as a proxy for the warm molecular gas in the CSEs of a sample of bright carbon-rich stars spanning different evolutionary stages from the Asymptotic Giant Branch (AGB) to the young planetary nebulae (PNe) phase.
Methods. We use the rotational diagram (RD) technique to derive rotational temperatures ($T_{\rm rot}$) and masses ($M_{\rm H_2}$) of the envelope layers where the CO transitions observed with PACS arise. Additionally, we obtain a first order estimate of the mass-loss rates and assess the impact of the opacity correction for a range of envelope characteristic radii. We use multi-epoch spectra for the well studied C-rich envelope IRC+10216 to investigate the impact of CO flux variability on the values of $T_{\rm rot}$ and $M_{\rm H_2}$.
Results. PACS sensitivity allowed the study of higher rotational numbers than before indicating the presence of a significant amount of warmer gas (~200-900 K) not traceable with lower-J CO observations at sub-mm/mm wavelengths. The masses are in the range $M_{\rm H_2}$ ~ 10^{-2} – 10^{-5} $M_\odot$, anti-correlated with temperature. For some strong CO emitters we infer a double temperature (warm $\overline{T}_{\rm rot}$ ~400 K and hot $\overline{T}_{\rm rot}$ ~820 K) component. From the analysis of IRC+10216, we corroborate that the effect of line variability is perceptible on the $T_{\rm rot}$ of the hot component only, and certainly insignificant on $M_{\rm H_2}$ and, hence, the mass-loss rate. The agreement between our mass-loss rates and the literature across the sample is good. Therefore, the parameters derived from the RD are robust even when strong line flux variability occurs, with the major source of uncertainty in the estimate of the mass-loss rate being the size of the CO-emitting volume.

Key words. Stars: AGB and post-AGB – Stars: circumstellar matter – Stars: carbon – Stars: mass-loss – ISM: planetary nebulae

1. Introduction

The asymptotic giant branch (AGB) is a late evolutionary stage of low-to-intermediate mass stars ($1\,M_\odot \lesssim M_\star \lesssim 8 M_\odot$) which is largely dominated by mass-loss processes. AGB stars can shed significant portions of their outer atmospheric layers in a dust-driven wind, with mass-loss rates of up to $\dot{M}$~10^{-4} $M_\odot$ yr^{-1} (e.g. Habing 1996; Höfner & Olofsson 2018). The material expelled by the central star (with very low effective temperatures of $T_{\rm eff}$~2000-3000 K) forms a cool, dense circumstellar envelope (CSE) that is rich in dust grains and a large variety of molecules. After a significant decrease of the mass-loss rate, the AGB phase ends and the 'star+CSE' system begins to evolve to the Planetary Nebula (PN) phase, at which the CSE is fully or almost fully ionized due to the much higher central star temperatures ($T_{\rm eff}$≈10^4-10^5 K) and more diluted envelopes. During the AGB-to-PN transition, shocks – resulting from the interaction between slow and fast winds at the end of the AGB phase (or early post-AGB) – also play an important role changing the morphology, dynamics and chemistry of the CSEs (e.g. Kwok 2000; van Winckel 2003; Bujarrabal 2006).

The CO[1] molecule is an excellent tracer of the CSEs of AGB stars, post-AGB objects and PNe (e.g Groenewegen et al. 1996; Schöier & Olofsson 2001; Schöier et al. 2002; Teyssier et al. 2006). The rotational transitions of the ground vibrational level over a wide range of excitation energies sample from cold (~10 K) to hot gas (~1000 K). Literature on observations of the cold, extended CO $J = 1 - 0$ to $J = 6 - 5$ emission around many evolved stars is abundant at mm/sub-mm wavelengths (e.g. Knapp et al. 1982; Knapp & Morris 1985; Knapp & Chang 1985; Olofsson et al. 1993; Bujarrabal et al. 1989; Jorissen & Knapp 1998; Castro-Carrizo et al. 2010; Sánchez Contreras & Sahai 2012; Ramstedt & Olofsson 2014). Studies looking at far-infrared (FIR) observations of even higher J CO transitions probing the warmest gas (~200-1000 K) in deeper layers of CSEs are much more scarce. Pioneering works based on observations with the Infrared Space Observatory (*ISO*) (e.g. Justtanont et al. 2000; Schöier et al. 2002) have continued more recently with *Herschel* (e.g. Groenewegen et al. 2011; Bujarrabal et al. 2012; Khouri et al. 2014; Danilovich et al. 2015; Nicolaes et al. 2018).

⋆ *Herschel* is an ESA space observatory with science instruments provided by European-led Principal Investigator consortia and with important participation from NASA.

[1] We abbreviate $^{12}C^{16}O$ as simply CO throughout the paper.

This is the second of a series of papers (Ramos-Medina et al. 2018a, Paper I) where we analyze in an uniform and systematic way *Herschel*/PACS spectra of a large sample of evolved stars from the THROES catalogue (Ramos-Medina et al. 2018b) to study their warm inner envelope regions using high-J CO transitions at FIR wavelengths. As in other previous studies, we divide our sample in O-rich and C-rich targets (papers I and II, respectively) since these two major chemistry classes correspond to progenitor stars with different masses, which follow somewhat different evolutionary paths, and also have a dissimilar dust composition, both facts potentially affecting the mass-loss process. We include targets with different evolutionary stages: AGB, post-AGB (or pre-PNe) and young planetary nebulae (yPNe).

The goal of our study (papers I and II) is to obtain a first estimate of the average excitation temperature ($T_{\rm rot}$) and mass ($M_{\rm H_2}$) of the warm envelope layers traced by the PACS CO lines in a uniform way using a simple analysis technique, the well-known rotational diagram (RD) method. The RD technique is useful to rapidly analyze large data sets (large number of lines and/or large samples) and to provide some constraints on these fundamental parameters. With the aim of benchmarking the results of the RD approximation, we obtain rough estimates of mass-loss rates ($\dot{M}$) and compare them to values in the literature, paying particular attention to studies including at least a few high-J CO (FIR) transitions.

The impact of possible non-LTE effects on the results from the simple RD analysis was investigated in paper I. It was concluded that, though they are expected to be minor in general and probably only affecting the highest-J CO transitions studied here (J≳27) at most, their existence cannot be ruled out in the lowest mass-loss rate stars and/or the outermost layers of the PACS CO-emitting volume. We also showed that even under non-LTE conditions, the masses derived from the RDs are approximately correct (or, at the very least, not affected by unusually large uncertainties) since the average excitation temperature describes rather precisely the molecular excitation (i.e., the real level population). This is also corroborated by the good agreement found between our estimates of $\dot{M}$ and those from detailed non-LTE excitation and radiative transfer (nLTEexRT) studies that exist for a number of targets. We stress that the RD method enables a characterization of the warm CSEs of evolved stars in a first approximation and that for a more robust and detailed study of the radial structure of the density, temperature and velocity in the CSEs, as well as for establishing potential mass-loss rate variations with time, more sophisticated analysis is needed (e.g., Ryde et al. 1999; Schöier et al. 2002; De Beck et al. 2012).

Upon submission of this manuscript (and after our paper I was accepted for publication) we became aware of a recent work by Nicolaes et al. (2018) who independently presented *Herschel*/PACS (and SPIRE) range spectroscopy of a sample of 37 AGB stars. These authors perform a similar RD analysis of the CO spectra and focus on deriving excitation temperatures (in contrast to our study, estimates of the envelope mass or mass-loss rates are not reported). Other differences with respect to the work by Nicolaes et al. (2018) is that we introduce a canonical opacity correction in the RDs and that we include post-AGBs and PNe.

2. Observations

2.1. Observations and data reduction

PACS is a photometer and medium resolution grating spectrometer (Poglitsch et al. 2010) onboard the Herschel Space Telescope (Pilbratt et al. 2010) probing the FIR wavelength range. The PACS spectrometer covers the wavelength range from 51 to 210 μm in two different channels that operate simultaneously in the blue (51-105 μm) and red (102-220 μm) bands. The Field of View (FoV) covers a 47″×47″ region in the sky, structured in an array of 5×5 spatial pixels ("spaxels") with 9.4″×9.4″. PACS provides a resolving power between 5500 and 940, i.e. a spectral resolution of approximately 55-320 km s^{-1}, at short and long wavelengths, respectively, and the PSF of the PACS spectrometer ranges from ∼9″ in the blue band to ∼13″ in the red band. The PSF is described in da Silva Santos (2016) and Bocchio et al. (2016). The technical details of the instrument can be found in the *PACS Observer's Manual*[2].

The PACS (1D) spectral data were taken from the THROES (caTalogue of HeRschel Observations of Evolved Stars) website[3] which contains fully reduced PACS spectra of a collection of 114 stars, mostly low-to-intermediate mass AGB stars, post-AGB and PNe. The data reduction is explained in Ramos-Medina et al. (2018b) in full detail. The catalogue also consists of a compilation of previous photometry measurements at 12, 25, 60, 100 μm with the Infrared Astronomical Satellite (IRAS).

Table B.1 offers a description of the observations used here where we provide the target name as listed in the header of the PACS FITS files and an alternative name for which some of the stars are more well known in the literature. We only analyzed the spectra between [55-95] and [101-190] μm because the flux densities are unreliable above 190 μm, below 55 μm and between 95-101 μm due to spectral leakage. Two observation identifiers (OBSIDs) per target, corresponding to the bands B2A, B2B and R1, are necessary to cover the full PACS wavelength range. In the case of IRC+10216, band B2A data exists (see Decin et al. 2010), but these were acquired in a non-standard spectroscopy mode and have restricted access in the *Herschel* Science Archive and, thus, are not included in the THROES catalogue. Instead, we used 4+3 OBSIDs corresponding to seven different operational days: OD = [745, 1087, 1257 and 1296] covering the spectral range [69-95, 140-190] μm and OD = [894, 1113 and 1288] covering a narrower interval [77-95, 155-190] μm.

2.2. Sample overview

We searched for CO emission amongst the entire THROES catalog, but in this paper we focus on C-rich CSEs (29% of the entries) observed in PACS range mode. We found 15 evolved stars with at least three CO emission lines with signal-to-noise ratio above 3.

This sample contains bright infrared targets spanning a range of evolutionary stages from the AGB to the PN phase, but sharing similar carbon chemistry with strong CO emission at high excitation temperatures (up to $E_{\rm u}/k \approx 5688$ K). The AGBs, which are mostly Mira variables, are known for their high mass-loss rates compared to the mean value of $\dot{M} \sim 1.5\times10^{-7}$ M$_\odot$ yr^{-1} derived from studies with large samples of carbon stars (Olofsson et al. 1993). We also include two mixed-chemistry post-AGBs (Red Rectangle and IRAS 16594-4656, Waters et al. 1998; Woods et al. 2005) and two mixed-chemistry yPNes (Hen 2-113 and CPD-56°8032, De Marco & Crowther 1998; Danehkar & Parker 2015, and references therein), that is, they show both C-rich and O-rich dust grains. In the Appendix we provide Table B.2 with a summary of some relevant properties such as dis-

[2] herschel.esac.esa.int/Docs/PACS/html/pacs_om.html
[3] https://throes.cab.inta-csic.es

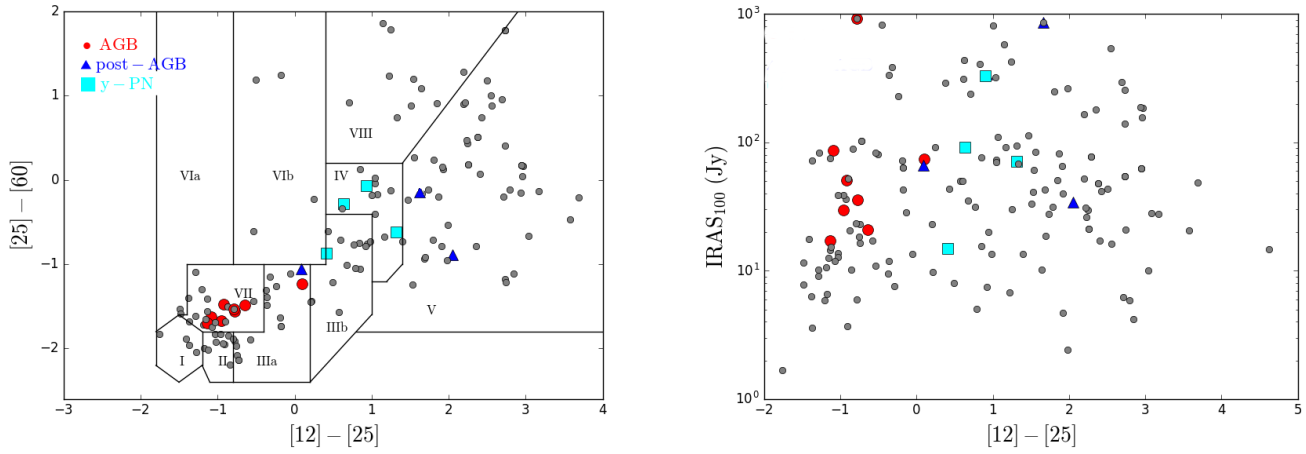

Fig. 1: IRAS color diagrams for the stars in the THROES catalogue. The colors are defined from the infrared fluxes at 12, 25 and 60 μm. The boxes on the left panel are the ones defined in van der Veen & Habing (1988), and the highlighted points correspond to the stars studied in this paper.

tance, effective temperature and gas mass-loss rate, along with additional references.

Figure 1 shows the classic IRAS color-color diagram (van der Veen & Habing 1988) featuring the colors [25] − [60] = $-2.5 \log \frac{IRAS_{25}}{IRAS_{60}}$ and [12] − [25] = $-2.5 \log \frac{IRAS_{12}}{IRAS_{25}}$ of all the stars in THROES. The stars here studied are highlighted with colored filled symbols which we will use consistently throughout the paper. This diagram is known to be a good indicator of the evolutionary stage of low-to-intermediate evolved stars, with AGBs populating the lower left corner and more advanced stages being located on the diametrically opposed, so-called cold, side of the diagram. It also shows an evolution in terms of the mass-loss rate and/or progressively increasing optical depths (Bedijn 1987). C-rich AGBs clearly constellate in a different box compared to the O-rich stars in Paper I, which has been interpreted as a consequence of different grains' emissivities (Zuckerman & Dyck 1986). The AGB star that falls outside the expected box with a clear 25 μm excess ([12] − [25] = 0.1) is AFGL 3068 (LL Peg), which is an "extreme carbon star": very dust-obscured by optically thick shells due to high mass-loss rate (Volk et al. 1992; Winters et al. 1997). The post-AGB object HD 44179, best known as The Red Rectangle, is also outlying in this same box with respect to objects in a similar evolutionary status beyond the AGB, which typically show much larger 25 μm excess indicative of detached cold dust (and gas) envelopes.

3. Observational results

3.1. Features in PACS spectra

The PACS continuum-subtracted spectra are plotted in Fig. 2 sorted in terms of stellar effective temperature ($T_{\rm eff}$ increases from top to bottom) and arbitrarily scaled for better comparison of the CO spectra. The continuum was fitted using a non-parametric method after identifying the line-free regions of the spectrum for each target. A brief line-detection statistics summary is given in Table B.3. Broad emission or absorption features due to instrumental artifacts are occasionally visible in some of the targets (e.g. near 62 μm). The spectra of IRC+10216 taken at seven different epochs are shown in the top panel of Fig. 3, and in more detail in Fig. C.2 in the Appendix.

Straightaway we see significant differences between the spectra of these targets such as the larger line density, resulting from a richer molecular content, in AGB stars compared to post-AGBs and yPNe as expected. In AGB stars the strongest spectral lines are due to CO emission, while post-AGBs and yPNe show much more prominent forbidden lines, except for AFGL 2688 and AFGL 618. Additional molecular features with intense emission are attributed to rotational transitions of common C-bearing species such as ^{13}CO, HCN, CS, etc.

Not so common in C-rich stars is the presence of OH, yet we identify several OH doublet lines (at 79, 84, 119 and 163 μm) in all yPNe and in the post-AGB star IRAS 16594-4656, with the highest $T_{\rm eff}$~10 000K in its class and where the presence of shocks is plausible. Two additional OH doublets at 65 and 71 μm, with high-excitation energy of about 500 and 600 K, respectively, are also observed in IRAS 16594-4656 and in the yPNe Hen 2-113. In those five ($T_{\rm eff}$>10 000 K) targets, we also identify pure rotational transitions of CH^+, with the J=3-2 line at 119.86 μm being one of the most clearly detected and best isolated lines[4]. The 179.61 μm CH^+ line could be blended with the water 2_{12}-1_{01} transition. The highest-J lines of CH^+ are also present in IRAS 16594-4656 and Hen 2-113. Interestingly, we do not see CH^+ in the spectrum of the Red Rectangle, where sharp emission features near 4225 Å were discovered and assigned to this ion by Balm & Jura (1992). The detection of CH^+ in AFGL 618 and the more evolved PNe NGC 7027 had been previously reported by Wesson et al. (2010, *Herschel*/SPIRE) and Cernicharo et al. (1997, *ISO* data). As we see below in this section, the targets with CH^+ and OH emission also show the strongest atomic/ionic fine-structure lines.

We identify lines due to H_2O (orto- and para-) transitions in all AGBs, in the post-AGB AFGL 2688 and in the yPNe AFGL 618. The study of water lines in the C-rich AGB stars of our sample (except for AFGL 2513) was already conducted by Lombaert et al. (2016) who suggested that both shocks and UV photodissociation may play a role in warm H_2O formation. Water lines had also been previously identified in the SPIRE spectrum of AFGL 618 and AFGL 2688 Wesson et al. (2010).

[4] The lines of CH^+ covered by PACS are J=2-1, 3-2, 4-3, 5-4 and 6-5 at 179.61, 119.86, 90.02, 72.15 and 60.26 μm, respectively.

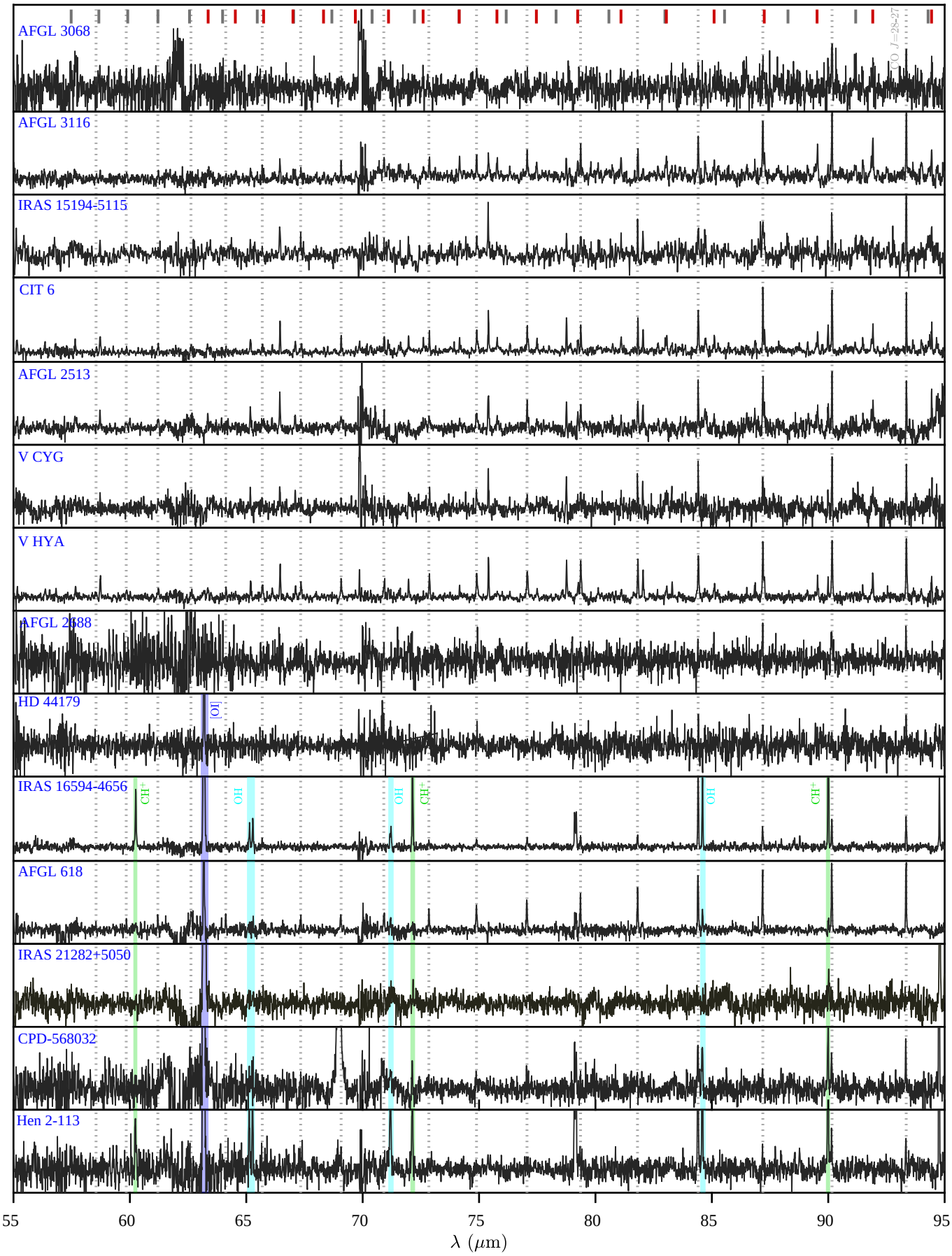

Fig. 2: Continuum-subtracted PACS spectra of our sample. The vertical segments (at the top) and bars indicate the rotational transitions of ^{12}CO (light gray, dotted lines), ^{13}CO (dark gray), HCN (red), CS (yellow), OH (cyan), CH^+ (green) and forbidden lines (blue) of [C II] 157.7 μm, [O I] 63.2, 145.5 μm, [N II] 121.9 μm.

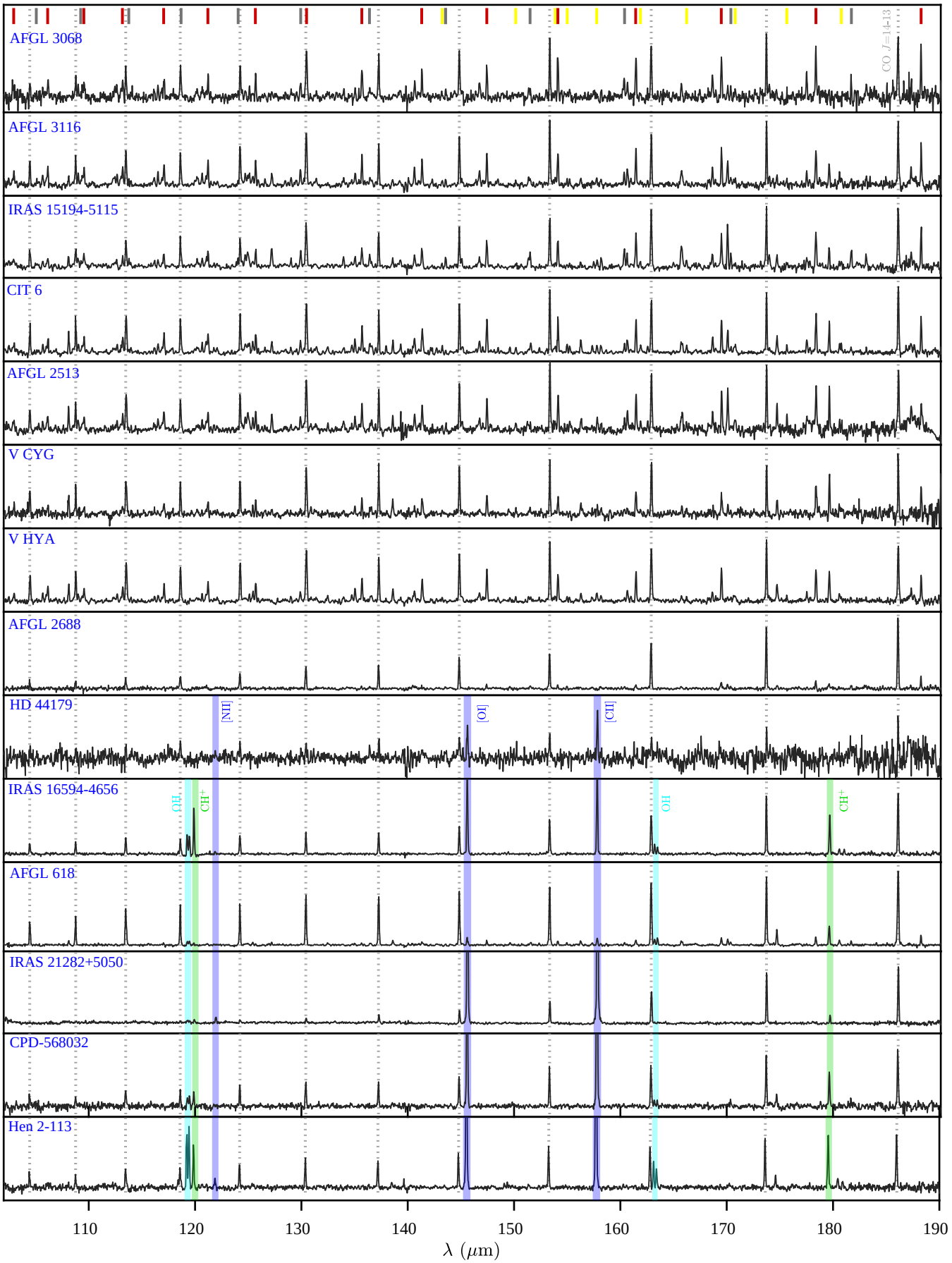

Fig. 2: Continued.

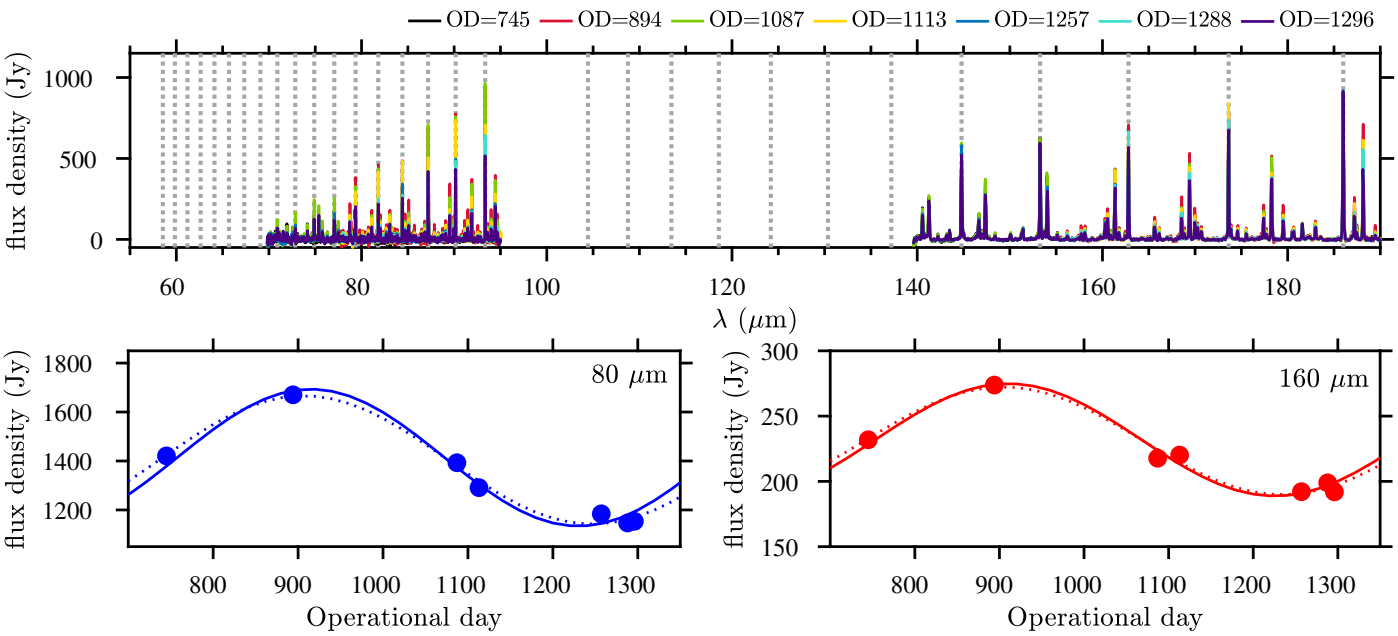

Fig. 3: Line and continuum variability of IRC+10216 in the FIR. Top: Continuum subtracted spectra at different epochs (see also Fig. C.2); the dotted lines sign the CO transitions. Bottom: Sine-wave fit to the continuum variability at two selected wavelengths for a fixed pulsation period of 630 days (solid lines) and free-period fit corresponding to 680 and 660 days for the blue and red dashed curves, respectively.

The fine-structure lines [O I] at 63.18 μm and 145.53 μm and [C II] at 157.74 μm are very prominent in the spectra of all post-AGBs and yPNe in our sample with the exception of AFGL 2688. The post-AGB object IRAS 16594-4656 demonstrates clear signs of ionization since it shows a [C II] line even stronger than that of AFGL 618, which has a hotter central star (Table B.1). Weak [N II] 121.89 μm emission is also detected in Hen 2-113 and IRAS 21282+5050, and, tentatively in IRAS 16594-4656 and HD 44179.

The 69 μm band of forsterite (Mg_2SiO_4) is visible in CPD-56°8032, Hen 2-113, and HD 44179, as already reported by Cohen et al. (2002) and Blommaert et al. (2014). The presence of O-rich dust in such C-rich objects corroborates a mixed chemistry nature.

3.2. Line flux variability in IRC+10216

Variability of the continuum at optical and IR wavelengths due to stellar pulsations is a common property of AGB stars. We present PACS spectra at multiple epochs of the Mira-type C-rich star IRC+10216 displaying periodic variations both in the continuum and in the lines (see Fig. 3 and Fig. C.2).

Cernicharo et al. (2014) first reported on the discovery of strong intensity variations in high-excitation lines of abundant molecular species towards IRC+10216 using *Herschel*/HIFI and IRAM 30m data. Line variability was attributed to periodic changes in the IR pumping rates and also possibly in the dust and gas temperatures in the innermost layers of the CSE. From the analysis of a 3 yr-long monitoring of the molecular emission of IRC+10216 with *Herschel* (including HIFI, SPIRE and PACS data), Teyssier et al. (2015) concluded that intensity changes of CO lines with rotational numbers up to J=18 are within the typical instrument calibration uncertainties, but in the higher PACS frequency range ($J \geq 28$), line strength variations of a factor $\gtrsim$1.6, and scaling with J, were found. More recently, He et al. (2017) reported 5%-30% intensity variability of additional mm lines with periodicities in the range 450-1180 days.

In section 5.3 we study in greater detail what is the impact of CO line variability on the estimate of $T_{\rm rot}$ and $M_{\rm H_2}$ from the rotational diagram analysis using PACS data for different epochs.

3.3. CO line fluxes

We now focus on the purely rotational spectrum of CO in the ground vibrational state (v=0), which we use to study the physical properties of the warm regions of the molecular CSEs of our targets. In the PACS range one can potentially find very high CO rotational transitions, from J = 14−13 ($E_{\rm u}$~581 K) to J = 45−44 ($E_{\rm u}$~5688 K). The lack of data between 95 and 101 μm means we cannot detect the transitions J=26-25 and J=27-26. In the case of IRC +10216, the much larger gap in the PACS coverage (~95-140 μm, Fig. 3) prevents detection of CO transitions with upper-level rotational number between $J_{\rm u}$=19 and $J_{\rm u}$=27.

The line fluxes are given in Table B.4. The quoted uncertainties correspond to the propagated statistical errors and do not contain absolute flux calibration errors (typically of ~15%-20%) or underlying continuum subtraction uncertainties.

As expected, the resolving power of PACS (~80-300 km s^{-1}) does not allow to spectrally resolve the CO profiles. This is true not only for AGB CSEs with full-widths-at-half-maximum (FWHM) similar to or smaller than the terminal expansion velocity of the envelopes (FWHM~10-25 km s^{-1}, Table B.2), but also for post-AGB objects and yPNe, even in targets that are known to have fast (≈100 km s^{-1}) molecular outflows like AFGL 618 (e.g. Bujarrabal et al. 2010). For this reason we measured CO fluxes by simply fitting a Gaussian function to the PACS lines.

Due to insufficient spectral resolution some reported line fluxes are affected by line blend. These are identified with asterisks in the tables and figures. Some of the well-known line blends are CO J=30-29 with HCN J=39-38 and CO J=20-19

with HCN J=26-25 at 87.2 and 130.4 μm, respectively. Also, the CO transitions J=21-20 and J=22-21 are blended with ^{13}CO J=22-21 and J=23-22 at 124.2 μm and 118.6 μm, respectively.

Figure 4 compares the integrated flux of the CO (J=15-14) line ($F_{\rm CO\,(15-14)}$) with the IRAS 100 μm flux (IRAS$_{100}$), the PACS continuum at 170 μm (PACS$_{170}$), i.e. near the CO (J=15-14) line, and the [12]-[25] IRAS color. The J=15-14 transition is a strong, non-blended line, detected towards all of our targets, and it was also used by Lombaert et al. (2016) who analyzed PACS data of most of the AGBs here studied, which facilitates comparison.

As for the O-rich sample (paper I), there is a positive correlation between the CO line strength and the IRAS$_{100}$ and PACS$_{170}$ continuum fluxes. The correlation between the CO J=1-0 line and the IRAS fluxes of evolved stars of various chemical types had been previously reported (Olofsson et al. 1987, 1988; Bujarrabal et al. 1992). We also confirm the anticorrelation between the line-to-continuum ($F_{\rm CO\ 15-14}$/PACS$_{170}$) ratio and the IRAS [12]-[25] color (both distance-independent) for the AGB stars, which was noted in Paper I. For the more evolved targets the trend is not so obvious, but the sample size is small. We also see that, in general, the ratio between the molecular emission and the dust emission is higher in less evolved objects than in the most evolved ones, which could be partially attributed to more prominent CO photodissociation as the objects evolves along the AGB-to-PNe track. AFGL 618 and IRAS 16594-4656 are two clear outliers in this relation since they show a line-to-continuum emission ratio as large as that of the AGB class. The Red Rectangle (HD 44179) is well isolated in all the panels due to its comparatively weak CO emission and low CO-to-dust ratio. This surely reflects the different nature of this object with respect to the rest of post-AGB and yPNe in our sample, which is well known from previous works. The Red Rectangle belongs to a special class of post-AGB objects with relatively weak CO emission coming from large (~1000-2000 AU) circumbinary rotating disks, with very prominent IR emission by warm/hot dust in the disk, but lacking massive molecular outflows found in many other evolved stars (e.g., Bujarrabal et al. 2016, and references therein).

4. Rotational diagram analysis

Following the same approach of Paper I, we have used the well-known and widely employed rotational diagram (RD) technique (e.g. Goldsmith & Langer 1999) to obtain a first estimate of the (average) excitation temperature ($T_{\rm rot}$) and total mass ($M_{\rm H_2}$) of the warm inner layers of the molecular envelopes of our sample. A canonical opacity correction factor, C_τ, as defined by Goldsmith & Langer (1999), has been included to take into account moderate optical depth effects (§ A.1). We refer to Paper I for a more detailed description of the method.

4.1. The characteristic size of the CO-emitting layers

To compute the optical depth of the line and to make the corresponding C_τ correction, we need an estimate of the column density of CO, which is computed in a simplified manner dividing the total number of CO molecules ($N_{\rm CO}$) by the projected area of the CO-emitting volume on the sky. The *characteristic* size of the envelope regions where the CO PACS emission is produced ($r_{\rm CO}$) is one of the main sources of uncertainty since, except for a few targets (see below), these high-J CO-emitting layers are unresolved by PACS. Therefore, the value of $r_{\rm CO}$ needs to be adopted based on several criteria. These criteria are described in much detail in paper I, Appendix B. In the following, we provide a brief summary of the general method and provide additional arguments particularized to the C-rich targets here under study.

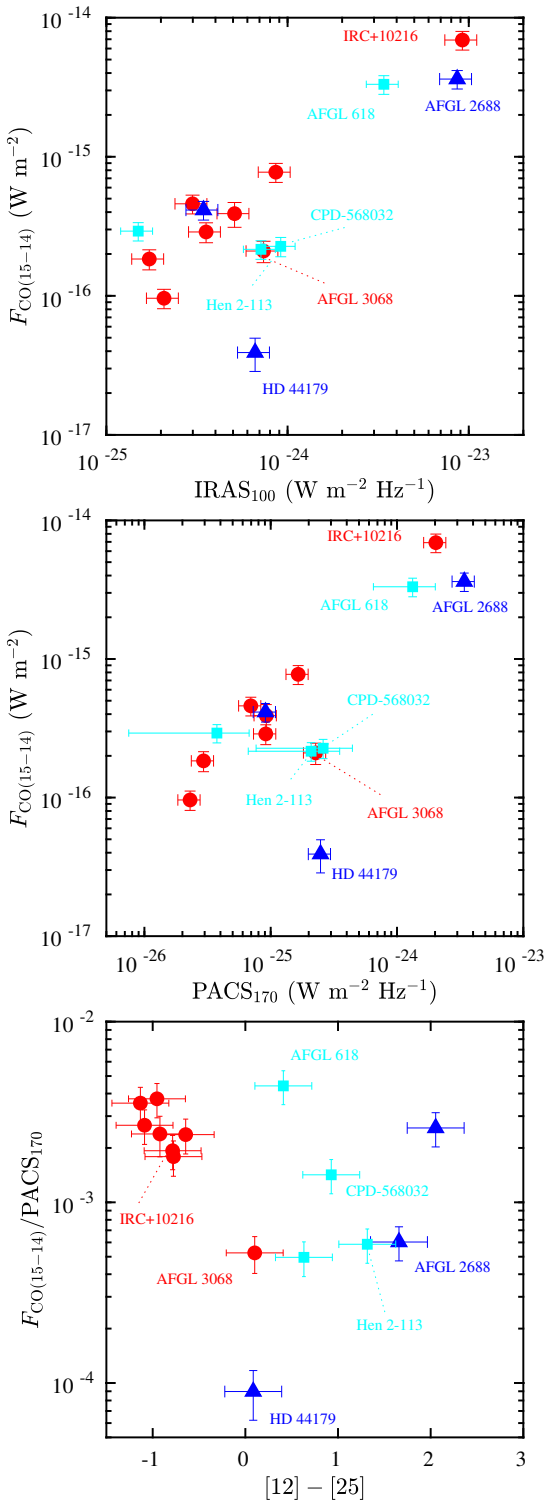

Fig. 4: Correlation between CO line flux and continuum intensities. Top: CO J = 15 − 14 vs IRAS 100 μm flux. Middle: CO J = 15 − 14 vs PACS 170 μm continuum flux. Bottom: continuum normalized CO J = 15 − 14 flux vs IRAS [12]-[25] color. The symbols and colors are the same as in Fig. 1.

For AGB CSEs, a first estimate of the size of the CO-emitting volume can be derived from the envelope temperature struc-

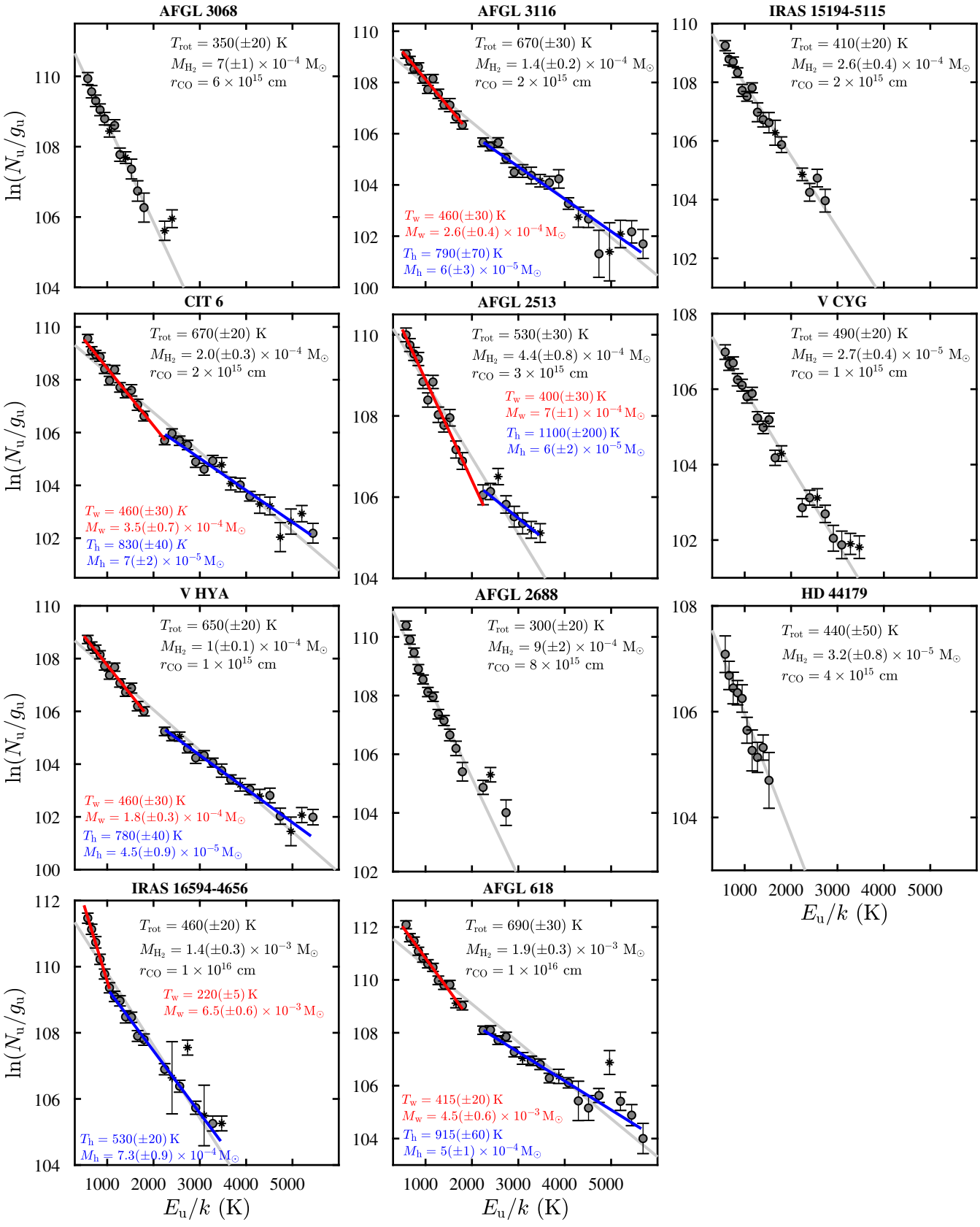

Fig. 5: Rotational diagrams of the CO molecule. The gray line correspond to a single least-squares fit to the full range of transitions from where a rotational temperature, $T_{\rm rot}$, and total gas mass, $M_{\rm H_2}$, is computed. The characteristic radius of the CO-emitting volume ($r_{\rm CO}$) adopted is indicated. The red and blue lines correspond to a two-component model consisting of a "warm" and "hot" region, respectively. Asterisks mark line blends that were excluded in the fit.

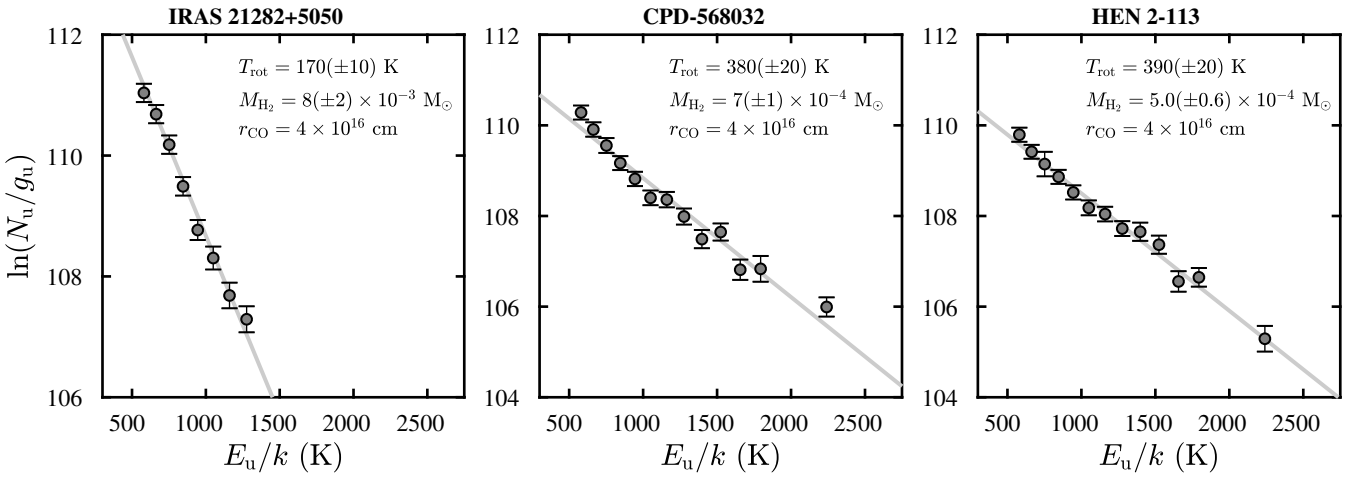

Fig. 5: Continued.

ture, $T(r)$, estimated from detailed non-LTE molecular excitation and radiative transfer (nLTExRT) calculations in the literature. These have been done for many AGB CSEs using low-J CO transitions (typically $J_{\rm u}\lesssim$6), and, for a few cases, also using certain CO transitions from higher J levels (see e.g., Decin et al. 2010; Khouri et al. 2014; Danilovich et al. 2014; Maercker et al. 2016; Van de Sande et al. 2018). As deduced from these studies, the gas temperature is approximately 1000-2000 K close to the dust condensation radius (~5-15 R$_\star$), and decreases gradually towards the outermost layers approximately following a power-law[5] of the type ~1/r$^\alpha$, with α ~0.5-1.0. Such models also exist in literature for three targets in our C-rich sample: IRAS 15194-5115, CIT 6 and IRC+10216 (Ryde et al. 1999; Schöier et al. 2002; De Beck et al. 2012). According to this, the high-excitation transitions observed with PACS require relative proximity to the central star and, in particular, we anticipate that regions with a few hundred kelvin, as deduced from our RDs (Figs. 5 and 6), should not extend much farther than a few 10^{15} cm ($\lesssim 10^2$ R$_\star$) in AGB stars.

An additional constraint on the radius can be imposed from the fact that the deepest layer traced by the observed CO emission must be such that $\tau < 1$ because of the almost null escape probability from deeper, very optically thick regions (§ A.1). For all our AGB CSEs, we have explored a range of radii around 1×10^{15} cm (Fig. A.1). We found that values around $r_{\rm CO}$~[1-4]×10^{15} cm result in line optical depths close to, but smaller than unity (typically $\tau_{J=14\rightarrow13}$ ~0.5-0.9) that yield moderate C_τ opacity correction factors for lines with $J_{\rm u}$<19 and negligible for higher-J transitions. For $r_{\rm CO}$<1×10^{15} cm, the opacity of the CO J=14-13 line, which is the optically thickest transition in our sample, becomes larger than 1 in all our targets (also including post-AGBs and yPNes).

We have checked that the range of plausible radii found for the AGB CSEs in our sample, $r_{\rm CO}$~[1-4]×10^{15} cm, is consistent with the upper limits to the size of their envelopes deduced from the PACS spectral cubes and/or photometric maps by da Silva Santos (2016) and with any other information on the molecular envelope extent from the literature. IRC+10216 is the only AGB CSE that is partially resolved in the PACS cubes, and it is also the closest in our sample. The PACS cubes show a slightly extended source (with a half-intensity size 4σ above the instrument PSF in both bands) that implies a deconvolved Gaussian radius of about 2″, that is ~ 4 × 10^{15} cm at d=150 pc. This value is in good agreement with the lower limit to $r_{\rm CO}$ needed to satisfy the $\tau_{J=14\rightarrow13}$ <1 criteria in this target, $r_{\rm CO}$~2×10^{15} cm. In this case, we then rather confidently use an intermediate value of $r_{\rm CO}$=3×10^{15} cm.

Contrary to AGBs, for post-AGBs and yPNe there are no model temperature profiles in the literature of the molecular gas in the CSEs (except for the rotating, circumbinary disk of the Red Rectangle, § 6.1.1).

The range of representative radius adopted for post-AGBs and yPNe is $r_{\rm CO}$=[0.4-4]×10^{16} cm (Table 1) based on a moderate opacity criteria, the extent of the emission in the PACS cubes and photometric maps, and on additional information on the extent of the intermediate-to-outer molecular envelope from the literature. In particular, in AFGL 2688, a deconvolved diameter of ~4″ in the PACS blue band suggests that $r_{\rm CO}\lesssim$ 1 × 10^{16} cm (at d=340 pc). Previous CO J=2-1 mapping observations identified a compact shell of radius ~2″ (~5×10^{15}cm) around the center of the nebula (Cox et al. 2000). Since the CO J=14-13 emission is optically thick at $r_{\rm CO}\lesssim$6×10^{15} cm (as shown in Fig. A.1), we adopt as representative radius an intermediate value of $r_{\rm CO}$=8×10^{15} cm. HD 44179 (The Red Rectangle) is a point-source in the PACS photometric maps, therefore, for a distance of 710 pc, $r_{\rm CO}$ should be of the same order as in AFGL 2688, which is roughly consistent with interferometric observations (e.g., Bujarrabal et al. 2016). For IRAS 16594-4656, only a very loose upper limit to the radius of $r_{\rm CO}$<3×10^{16} cm is inferred from optical images and H$_2$ emission maps in this object (e.g., Hrivnak et al. 2008). We explored the range, $r_{\rm CO}$ ~ 0.8 − 2 × 10^{16}, similar to AFGL 2688, and adopted as a reference value the midpoint value where $\tau_{J=14\rightarrow13}$ ~0.7.

All yPNe in our sample are point-sources in the PACS spectral cubes, which means that the upper limit to the radius is of about $r_{\rm CO}\lesssim$1″~[1-2]×10^{16} cm for AFGL 618, and ~[4-6]×10^{16} cm for the rest. They are known to have central H II regions that have recently formed as the star has become progressively hotter along the PNe evolution. Because the CO envelope surrounds the ionized nebula, a lower limit to $r_{\rm CO}$ can be established from the extent of the latter. Taking this into account, we set a representative radius to $r_{\rm CO}$=1×10^{16} cm for AFGL 618 (Sanchez Contreras et al. 2017; Lee et al. 2013), and $r_{\rm CO}$=4×10^{16} cm for the rest (see e.g., Danehkar & Parker 2015; Castro-Carrizo et al. 2010).

[5] See also the temperature profiles for the O-rich AGBs in Fig. B.1 of Paper I.

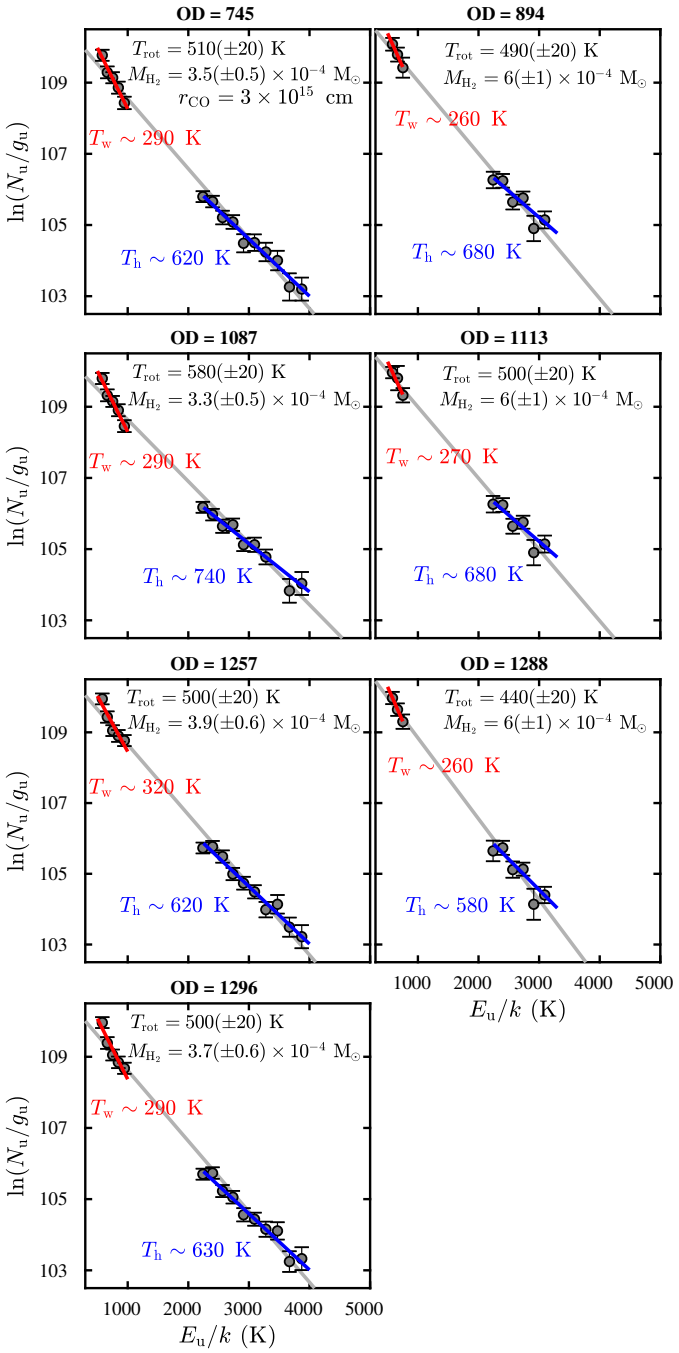

Fig. 6: Rotational diagram of the CO molecule in IRC+10216 at different epochs. Analogous to Fig. 5.

Given the uncertainty in $r_{\rm CO}$, we have systematically explored a range of radii around optimal/plausible values of $r_{\rm CO}$ to asses the impact of this parameter in our results (Fig. A.1). The opacity correction increases the smaller $r_{\rm CO}$ is, therefore the slope and y-intercept of the RD increase as a direct result of the frequency-dependence of C_τ (§ A.1), which results in lower values of $T_{\rm rot}$ and larger values of $N_{\rm CO}$, thus $M_{\rm H_2}$. This also means that, in practice, only the lowest-frequency-points are affected by C_τ, while the highest-frequency transitions (i.e., highest excitation energies) are unaltered regardless of the radius that we chose within the reasonable constraints that we have put.

4.2. Non-LTE effects

In Paper I we examine and discuss extensively the impact of non-LTE excitation effects (if present) on the values of $T_{\rm rot}$ and $M_{\rm H_2}$ derived from the RDs in a sample of 26 non C-rich evolved stars with mass-loss rates in the range $\dot{M}$~2×10^{-7}-1×10^{-4} M$_\odot$ yr^{-1}. The C-rich targets studied here have on average larger mass-loss rates than those in Paper I, therefore, using a similar reasoning, the CO population levels are also most likely close to thermalization in the inner dense regions of the CSEs under study.

This is further supported by nLTEexRT computations of a selection of high-J CO transitions observed with PACS (from $J_{\rm u}$=14 to 38) by Lombaert et al. (2016). Their sample included all our targets except for AFGL 2513 and IRC+10216. These authors conclude that over a broad range of mass-loss rates ($\dot{M}$~10^{-7}-2×10^{-5} M$_\odot$ yr^{-1}) the CO molecule is predominantly excited through collisions with H_2, with a minor effect of FIR radiative pumping due to the dust radiation field. The role of dust-excitation on FIR CO lines was also investigated by Schöier et al. (2002) and found to be of minor importance for AGBs with typical mass-loss rates of ~ 10^{-5} M$_\odot$ yr^{-1}. We assess the FIR pumping effect further in Section 5.3, where we study multi-epoch RDs of IRC+10216, which is a source with well-known CO line variability.

We stress that even under non-LTE conditions, for a simple diatomic molecule like CO, the RD method provides a reliable measure of the total mass within the emitting volume. Although $T_{\rm rot}$ may deviate from the kinetic temperature in regions where the local density is lower than the critical densities of the transitions considered ($n_{\rm crit}$~5×10^5-3×10^6 cm^{-3}, for $J_{\rm u}$=14 and 27, respectively, and $n_{\rm crit}$≈10^6-10^7 cm^{-3} for $J_{\rm u}$>27), it does describe quite precisely the molecular excitation, i.e. the real level population. Therefore, the total number of emitting molecules (and, thus, the mass) is quite robustly computed by adding up the populations of all levels. This is also supported by the good agreement (within uncertainties) between the mass-loss rates derived from this (and other works) using similar LTE approximations, and those obtained from nLTEexRT models (including PACS lines for a few targets) – see paper I and Section 6.2.

As discussed in paper I, conceivable LTE deviations would have its largest impact on the excitation temperature of the hot component, since high-J levels have the lowest critical densities (see above). If this is the case, in low mass-loss rate objects, the value of $T_{\rm rot}$ deduced for the hot component could deviate from the temperature of the gas and approach to that of the dust within the CO-emitting volume. We note that, in any case, the gas and dust temperatures, although not equal, are not excessively divergent in the warm envelope regions around ~10^{15} cm under study (e.g., Danilovich et al. 2014; Schöier et al. 2002).

5. Results

5.1. Gas temperatures and masses

The opacity-corrected RDs of the CO molecule are plotted in Fig. 5 and in Fig. 6, where multi-epoch RDs for IRC+10216 are separately shown, together with the best-fit parameters using a single-temperature component (gray line) and double-temperature component (red and blue lines). For 8 out of 14 sources, the RDs include CO transitions with upper-level energies that range from $E_{\rm u}$~580 K to $E_{\rm u}$≲2000-3000 K. For 6 targets, CO transitions with upper-level energies of up to $E_{\rm u}$~5000 K are also detected. Our temperatures for the group of AGBs are consistent with the ones reported in Nicolaes et al.

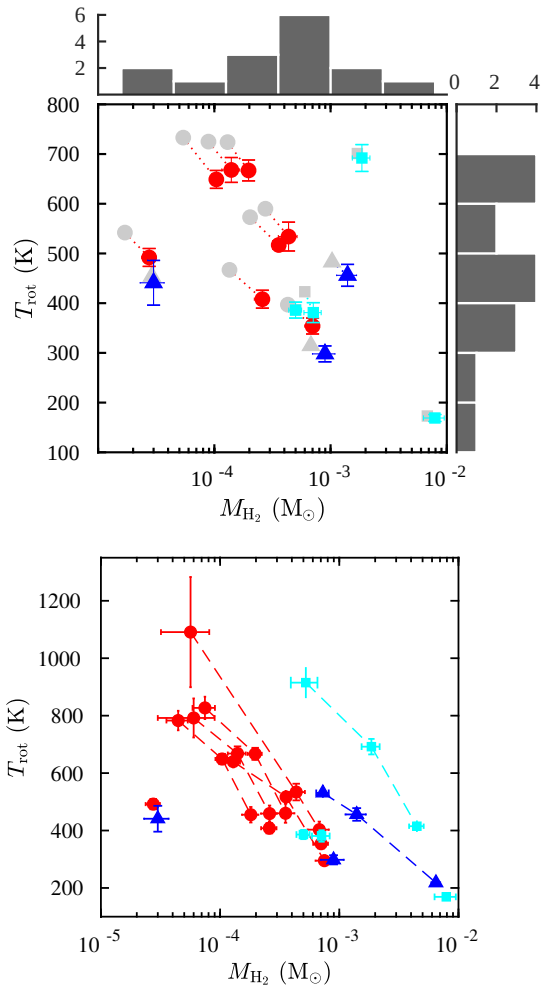

Fig. 7: Summary of the RD results. Top: The colored symbols correspond to the opacity corrected values (single fit) which are connected by dotted lines to the corresponding uncorrected values in gray; on the sides we show the histograms of temperature and mass of the single fits; in the case of IRC+10216 we show weighted averages of four observations. Bottom: temperature and mass of the warm and hot components connected by dashed lines for the same target (if applicable).

(2018) within the uncertainties, although for many AGBs we find lower values because of the opacity correction term that we have included.

There are cases where it is clear by the analysis of residuals that a single straight line does not fit the entire range of excitation energies. That is the case of V Hya, IRAS 16594-4656, AFGL 3116, CIT 6 and AFGL 618. Because it is not always clear by eye whether the slope changes and at which point it occurs, we used the Bayesian information criterion (BIC) to help us deciding where to split the diagram and to quantify significance. This is explained in the appendix A.2 and illustrated in the supplementary Fig. A.2.

We provide the fitting parameters in Table 1 corresponding to a single-fit and a double-component fit in targets where a single line does not equally fit all data points. As in Paper I, we call these two components "warm" and "hot" with $T_{\rm w} < T_{\rm single} < T_{\rm h}$. Their mean temperatures are $\overline{T}_{\rm w} \sim 400$ K and $\overline{T}_{\rm h} \sim 820$ K respectively. The corresponding masses are $M_{\rm w}$ and $M_{\rm h}$ with the former being 4-10 times larger than the latter. We find single-fit rotational temperatures in the range $T_{\rm rot}\sim$ 200-700 K with some of the post-AGBs and yPNe being the targets with the coolest gas, except for the yPNe AFGL 618 which has the largest rotational temperature in our sample similar to that of the warmest AGB CSEs.

The total number of CO molecules is in the range $N_{\rm CO}\sim 10^{49} - 10^{51}$, resulting in column densities of $N_{\rm CO}^{\rm col}\sim 10^{16} - 10^{19}$ cm^{-2} for the adopted radii (Table 1). To estimate the total gas mass from CO we assumed the same fractional abundance $X_{\rm CO} = 8 \times 10^{-4}$ (e.g. Teyssier et al. 2006) with respect to H_2 for all targets. The single-fit values of the total mass of the CO-emitting volume range between $M_{\rm H_2}\sim 3\times10^{-5}$ M$_\odot$ (V Cyg and HD 44179) and $\sim 8\times10^{-3}$ M$_\odot$ (IRAS 21282+5050), with a median value of $M_{\rm H_2}\sim 4\times10^{-4}$ M$_\odot$.

Figure 7 shows the single-fit temperature versus mass for the opacity corrected diagram (colored symbols) and uncorrected (gray symbols). The opacity-correction results in changes in $T_{\rm rot}$ of 10-15% in AGBs, and lower than 5% in post-AGBs and yPNe. In mass this typically corresponds to 60% in AGBs and lower in the post-AGBs and AFGL 618 (< 10% in $M_{\rm H_2}$), and negligible in the other three yPNes. Figure A.1 shows that $\tau_{J=14-13}$ is close to unity but it quickly falls off with increasing J meaning that $C_\tau \rightarrow 0$ for $E_{\rm u}/k > 2000$ K, and that $M_{\rm h}$, in particular, is not underestimated by opacity effects.

As in Paper I, we find an anti-correlation between $M_{\rm H_2}$ and $T_{\rm rot}$, especially if we consider only the group of AGBs (Fig. 7). In general, post-AGBs and yPNe have the the highest masses. One clear exception to trend is The Red Rectangle, which is one of the least massive targets (with only a few $\sim10^{-5}$ M$_\odot$ yr^{-1}) in contrast to the rest of post-AGBs and yPNe. This is not surprising given the nature of this object, which is the prototype of a special class of post-AGB objects with hot rotating disks and tenuous winds very different from the massive and fast (high-momentum) outflows of standard pre-PNe (Bujarrabal et al. 2016, and references therein).

We also investigated the correlation between the CO $J = 15 - 14$ flux and the gas mass and find that the strongest CO emitters have tendentially more massive envelopes, although there is a significant scatter (Fig. C.1). Also, the targets with the highest temperatures have the highest line-to-continuum ($F_{\rm CO\,15-14}$/PACS$_{170}$) ratios. IRAS 21282+5050, which has the most massive warm envelope in our sample, defies this trend since it shows relatively strong CO $J = 15 - 14$ emission, although its $T_{\rm rot}\sim$ 170 K is the lowest in the sample. The Red Rectangle appears isolated in a region of rather weak CO emission in spite of relatively high temperatures (~400-500 K). We compare these results to Paper I in Section 6.3.

5.2. Mass-loss rates

The mass-loss rates have been estimated by simply dividing the total mass by the crossing time of the CO-emitting layers, that is:

$$\dot{M} = \frac{M_{\rm H_2}\, v_{\rm exp}}{r_{\rm CO}} \qquad (1)$$

where $v_{\rm exp}$ is the expansion velocity of the gas, which has been taken from literature (Table B.2). For the characteristic radius of the CO-emitting region we use the same value ($r_{\rm CO}$) adopted for the opacity correction. We note that this estimate represents a mean or "equivalent" mass-loss rate assuming constant-velocity spherically-symmetric mass-loss during the time when

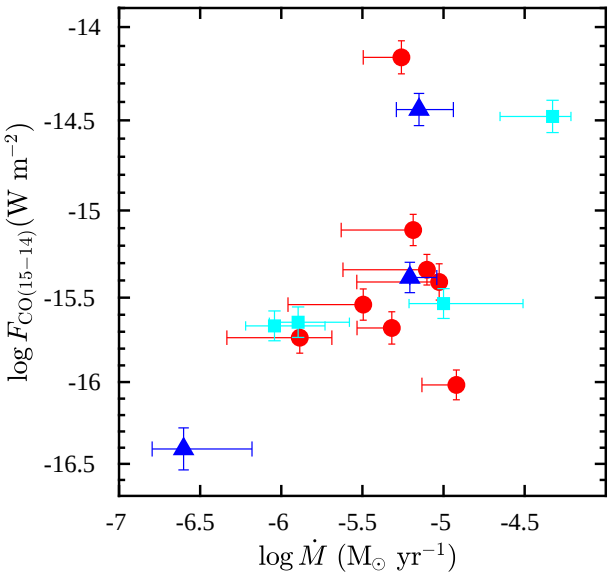

Fig. 8: Logarithm of the mass-loss rate versus total CO J =15-14 flux.

the warm-inner envelope layers where the CO PACS lines arise were ejected, that is, during the last ~20-50 yr and ≲300 yr for AGBs and post-AGBs/yPNe, respectively, given the values of v_{exp} and r_{CO}.

The mass-loss rates are listed in Table 1. We find a range of values of $\dot{M} \sim 10^{-7} - 10^{-5}$ M$_\odot$ yr^{-1}, with a median value in our AGB stars of $\dot{M} \sim 6 \times 10^{-6}$ M$_\odot$ yr^{-1}. These values are not to be taken as representative of the whole class of C-rich evolved stars, since our sample is small and not unbiased. This is because the objects in the THROES catalogue were originally selected for *Herschel* observations due to various reasons, probably including their strong CO emission.

As in Paper I, we investigated a possible correlation between $\dot{M}$, and T_{rot}, v_{exp}. We see little evidence of an anti-correlation between $\dot{M}$ and T_{rot}, although the relation is strongly influenced by AFGL 618, which is a strong outlier in this parameter space (Fig. C.1). In this, and maybe other objects (mainly post-AGB/yPNe), we expect departures from the simple (constant mass-loss rate, spherically symmetric) model adopted to estimate the "equivalent" $\dot{M}$. We compare the results obtained here and in Paper I in Section 6.3.

Figure 8 shows the logarithm of the integrated flux of the CO $J = 15 - 14$ line versus the logarithm of the mass-loss rate of the single component fit. The upper and lower limit of the errorbars in $\dot{M}$ correspond to a range of radii around the representative one (see Fig. A.1). We find a positive trend which is consistent with a power-law relation similar to that found by Lombaert et al. (2016) in their sample of C-rich AGB CSEs with H_2O FIR emission lines.

Separate values of $\dot{M}$ for the hot and warm components are computed for completeness, but the difference found ($M_h < M_w$) should not be overinterpreted as a recent decrease of the mass-loss rate. The hot and warm components most likely trace adjacent layers of the inner-winds of our targets, with the hot component presumably best sampling regions closer to the center. However, for simplicity and since we ignore the true CO excitation structure, we use the same radius to formally compute $\dot{M}$ for both components. We note that due to the $1/r_{CO}$ dependence, the values of M_h and M_w can be brought closer to the single-fit value if the warm and hot correspond to different r_{CO}. We refrain from discussing M_h and M_w separately since a more sophisticated analysis, including nLTEexRT modeling, is needed in order to assess mass-loss time variability. For this reason we only compare our single-component mass-loss rates to the literature (§ 6.2).

5.3. The influence of line variability on T_{rot} and M_{H_2}

We have shown in Fig. 3 the temporal variability of the continuum and line fluxes in the case of the Mira-type variable AGB star IRC+10216. The higher-J CO lines (E_u>2000 K) are the ones that show the strongest variations with time. Here, we are interested in studying how CO line variability affects the values of M_{H_2} and T_{rot} derived using the RD method but using data acquired at different epochs. We use the same seven available OBSIDS[6] of IRC+10216 as Teyssier et al. (2015), which span a time period of 551 days (Table B.1).

The RDs of IRC+10216 for these seven different observing epochs are shown in Fig. 6, and the results of the RD analysis are tabulated in Table 1, together with the remaining targets. Since three of the OBSIDs corresponding to the ODs 894, 1133 and 1288 have a more restricted wavelength coverage, the fits to the RDs have an inherently larger uncertainty because the fit is more sensitive to the low number statistics. The error-weighted mean (single-fit) rotational temperature and mass are T_{rot}~520 K and M_{H_2}~4×10^{-4} M$_\odot$, respectively.

In Fig. 9, we plot the temperature and the mass, for single- and double-temperature components, versus the operational day of the observations. The bottom panel shows that the total gas mass deduced from the single-fit of the RD or for the warm and hot components does not reflect the line flux variability since it stays essentially constant with time about the average value (dotted lines), well within the estimated uncertainties.

In a similar manner, the temperature of the warm component does not clearly reflect the CO line flux variations, since all multi-epoch values are in good agreement within uncertainties. The hot component is the one that shows the largest variations (perhaps periodic) of the temperature, with T_h going ~100 K (~16%) above the average (~ 640 K) at OD 1087, and then relaxing back to normal values in the remaining epochs. This variation is echoed in the single-fit value of T_{rot} (~12%).

Temperature variations are not necessarily expected to be periodic, but if we assume that to be true by fitting a sinusoidal function with the known pulsation period P = 630 days to the RD parameters, we find that such model accommodates reasonably well the data points corresponding to T_h (and also the single-fit T_{rot}). It is also possible that IRC+10216 underwent an abrupt change of the physical conditions in its inner wind layers at epoch OD 1087, since the remaining data points by themselves will not justify/indicate periodic variability.

In summary, probably due to a compensation between the changes in the y-intercept and the slope of the RD due to CO line flux variations, which are largest for transitions with the highest J, the total gas mass M_{H_2} appears to be quite robust to FIR pumping (non-LTE) effects. These, however, could have a measurable, yet moderate impact on the rotational temperatures.

[6] Which have been reprocessed and are part of the THROES catalogue.

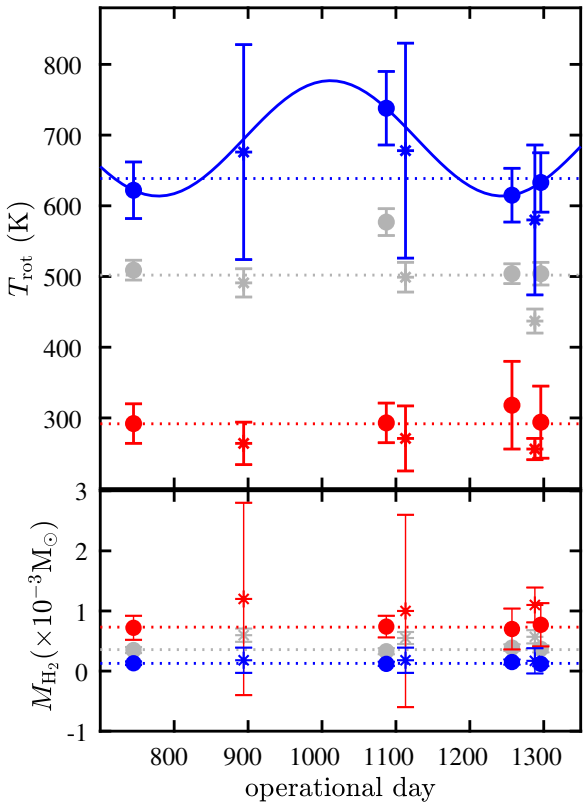

Fig. 9: Rotational temperature and mass versus operational day in IRC+10216. Top: sinusoidal fit to the T_{rot} variation with fixed period of 630 days (solid line). Bottom: total gas mass over time. In each panel, the dotted lines are the average of each component and the asterisks mark unused data points in the fit (see text). The color code is the same as in Fig. 6.

6. Discussion

6.1. Gas temperatures

The detection of high-J CO rotational lines is an indication of a significant amount of molecular gas under relatively high temperature conditions. From our simple RD analysis we inferred that the average gas temperatures of the layers sampled by FIR CO lines are much larger ($T_{rot} \sim 200 - 900$ K) than those typically derived from mm/sub-mm observations, which are sensitive to $\lesssim 100$ K gas from the intermediate-to-outer layers of the envelopes of evolved stars (at $\approx 10^{16}$-10^{17} cm, see e.g. De Beck et al. 2010; Schöier et al. 2011).

In a number of targets we identified a double-temperature ("warm" and "hot") component. Deviations from a single straight line fit to the RD have been found also in some of the O-rich objects in Paper I and in other previous works using, for example, ISO and/or *Herschel*/SPIRE CO spectra in a number of AGB and post-AGB CSEs (e.g., Justtanont et al. 2000; Wesson et al. 2010; Matsuura et al. 2014; Cernicharo et al. 2015b; Cordiner et al. 2016). AFGL 618 and IRAS 16594-4656 are the targets whose RDs show the most obvious departure from linearity. IRAS 16594-4656 is particularly interesting since we found a much cooler warm-component of just $T_w \sim 220$ K, and a breakpoint at lower energies ($E_u/k \approx 1049.9$ K) compared to other targets typically with $T_w \sim 450$ K up to $E_u/k \approx 1794.3$ K.

As in Paper I, in order to investigate if the double-temperature component is consistent with resulting from the temperature stratification within the inner layers of the CSEs, we compared the hot-to-warm M_{H_2} and T_{rot} ratios (Fig. 10), and find that they are correlated. If the temperature profiles in the envelope follow a power-law of the type $T(r) \propto r^{-\alpha}$, with α being a constant, then the trend in Fig. 10 should also follow approximately a power-law function. We find $\alpha \sim 0.4$, which is similar to the value found for the O-rich targets studied in Paper I. The value of α is in agreement with past works that suggested that the kinetic temperature distribution is shallower, with values of α down to ~0.4-0.5, for the inner (~5×10^{14}-3×10^{15} cm) CSE layers (De Beck et al. 2012; Lombaert et al. 2016; Matsuura et al. 2014) than for the outer regions, where the steepest temperature variations (α ~1-1.2) are found ($\gtrsim 10^{16}$ cm; Teyssier et al. 2006).

In addition to the average power-law exponent obtained by fitting all the targets simultaneously, we can also derive a value for each individual case applying:

$$\alpha = -\frac{\log(T_h/T_w)}{\log(M_h/M_w)} \quad (2)$$

as shown in the bottom panel of Fig. 10. In the case of IRC+10216, we find $\alpha = 0.45 \pm 0.06$ which is in good agreement with the power-law exponent in the inner CSE between 9 and 65 stellar radii (i.e., up to $\sim 3 \times 10^{15}$ cm) deduced from detailed non-LTE excitation and radiative transfer models (De Beck et al. 2012).

Therefore, the empirical relation found between the hot-to-warm ratio of M_{H_2} and T_{rot} is consistent with the double-T_{rot} component in some of our targets stemming (at least partially) from the temperature stratification across the inner envelope layers. The two components in the RD do not necessarily imply two distinct/detached shells of gas at different temperatures, but they most likely reflect the temperature decay laws. As explained in Paper I, in case of LTE deviations (not impossible in the lowest mass-loss rate objects), the value of α obtained from this simple approach would more closely represent the dust (rather than the gas) temperature distribution. This needs confirmation by detailed nLTEexRT models to the individual targets, which will be done in a future publication.

6.1.1. Individual targets: comparison with previous works

It is not possible to directly compare most of our results with literature because past studies have been focusing on the cold, outer components of CSEs. Prior to *Herschel* there was a study based on ISO LWS data in roughly the same wavelength range by Justtanont et al. (2000) who also performed RD analysis (without opacity correction). They found $T_{rot} \sim 700(\pm90)$ K and $T_{rot} \sim 380(\pm30)$ K for AFGL 618 and AFGL 2688 respectively. We obtained similar results without opacity correction, but introducing this effect lowered these values to $T_{rot} \sim 690(\pm30)$ K and $T_{rot} \sim 300(\pm20)$ K. In AFGL 618 the central star is hot enough ($T_{eff} \sim 33000$ K) to produce FUV photons that heat the gas. In AGFL 2688 this is probably not the case since the central star is much cooler ($T_{eff} \sim 7250$ K), so low-velocity shocks are the most likely heating mechanism.

Also partially based on ISO data, Ryde et al. (1999) used a number of spectral lines of CO between $J = 1 - 0$ and $J = 21 - 20$ to infer the kinetic temperature profile across the CSE of IRAS 15194-5115. According to their model, $T_{kin} \sim 400$ K at $r_{CO} \sim (1\text{-}2)\times10^{15}$ cm, which is in excellent agreement with our opacity-corrected single component $T_{rot} \sim 410$ K for $r_{CO} = 2\times10^{15}$ cm. This is because, as already pointed out by Ryde et al. (1999), these high-J levels are mainly populated by collisions, therefore they are proxies for the kinetic temperature, at least out

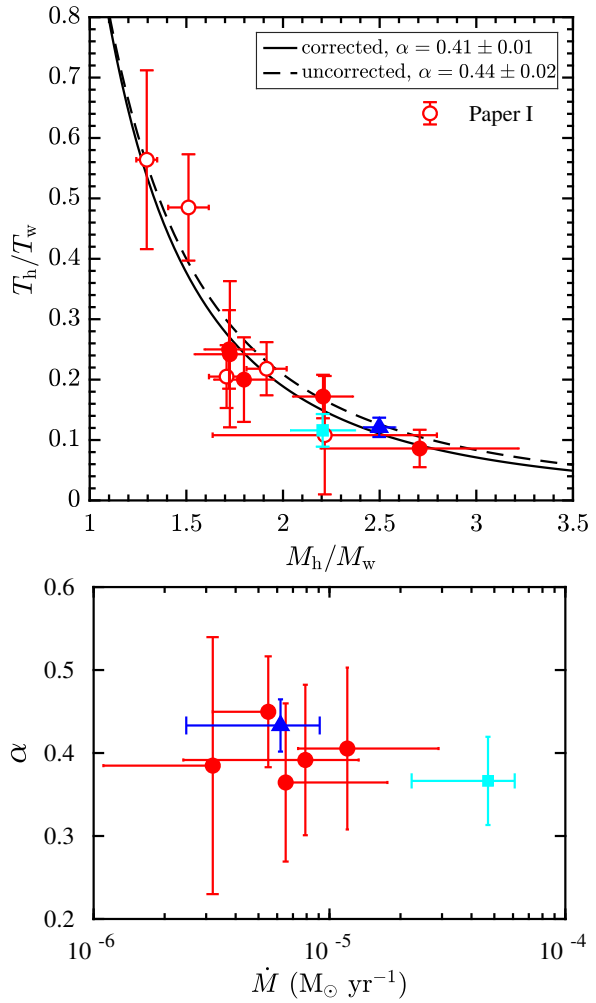

Fig. 10: Hot/warm temperature ratio versus hot/warm mass ratio for AGBs and post-AGBs and the power-law index. Top: the lines correspond to power-law fits with index $\alpha = 0.4$ for the opacity corrected RDs (solid) and $\alpha = 0.44$ for the uncorrected RDs (dashed); the open symbols correspond to the O-rich AGB stars in Paper I. Bottom: power law index for each individual target versus mass-loss rate (single fit).

to a few $\sim 10^{15}$ cm. Also using *ISO* data, Schöier et al. (2002) presented a kinetic temperature model for CIT 6 that shows that $T_{\rm kin} \sim 400-500$ K at approximately $r_{\rm CO} \sim$(1-2)×10^{15} cm, which is consistent with the warm component ($T_{\rm w} \sim 460$ K) that we infer and the representative radius $r_{\rm CO} = 2 \times 10^{15}$ cm adopted. The hot component ($T_{\rm w} \sim 830$ K) found by us would imply that regions closer to the star have an important contribution to the emission of the highest-J lines.

The only star whose inner/warmer (gaseous) CSE had been studied in detail before using *Herschel*/PACS data is IRC+10216. This was done by Decin et al. (2010) using high-J CO spectral lines to infer the kinetic temperature profile as a function of radial distance. They find $T_{\rm kin} \sim 500 - 600$ K at $r_{\rm CO} \sim$ (1-2)×10^{15} cm. Here we applied the opacity correction for $r_{\rm CO} = 3 \times 10^{15}$ cm which seems to be the layer at which $T_{\rm kin} \sim 300$ K in their model. This is also the average value of $T_{\rm w}$ that we found by fitting only the lowest J transitions, wich does not change appreciably with time despite strong line flux variability (Fig. 9). The hot component (~600-700 K) may correspond to $r_{\rm CO} \sim 1 \times 10^{15}$ cm according to their model.

Using *Herschel*/SPIRE data, Wesson et al. (2010) also performed RD analysis of CO spectra and derived $T_{\rm rot}$ ~70-230 K and $T_{\rm rot}$ ~100-200 K for AFGL 618 and AFGL 2688, respectively. The rotational temperatures we find are thus higher than the ones obtained in Wesson et al. (2010) as expected. Further Large-velocity gradient (LVG) calculations by those authors suggested that hot material at approximately 1000 K might exist at the high-velocity wind region of AFGL 618, which could be the one traced by PACS since we found $T_{\rm h} \sim 900$ K.

For HD 44179 (the Red Rectangle) we obtained $T_{\rm rot} \sim 440$ K, which is about 2-3 times larger than the range of values inferred by Bujarrabal & Alcolea (2013) from *Herschel*/HIFI lower-J CO observations. It is not surprising that we find a larger value since the higher J lines probed by PACS are probably formed deeper inside the rotating circum-binary disk at the core of this object. Meanwhile follow up analysis has shown more clearly an outflow with $\sim$ 500 K (Bujarrabal et al. 2016), but also seems that such temperature conditions could exist in a region of the inner disk with a radius of about $r_{\rm CO} \sim 2 \times 10^{15}$ cm, unresolved by PACS. The opacity correction would still be moderate for this value ($\tau_{J=14-13} \sim 0.67$), and it lowers the rotational temperature to $T_{\rm rot} \approx 410$ K which is still within the uncertainties. For the remaining yPNes (IRAS 21282+5050, CPD-568032, Hen 2-113) there are no kinetic temperature models in the literature that we could compare our results to.

6.2. Mass-loss rate

As in Paper I, we have compared the values of the mass-loss rates derived from our simple RD analysis with other values found in the literature mostly from low-J observations, paying special attention to a few targets with detailed non-LTE excitation and radiative transfer analysis of CO data including at least some high-J transitions observed with *Herschel*. This is also a way of ascertaining the robustness of the RD method.

Figure 11 shows our estimate of the mass-loss rate versus that found in the literature (see Table B.2). For each target the markers correspond to the single temperature component for the radius mentioned in Table 1, and the error bars represent the uncertainty in the radius for the adopted $v_{\rm exp}$. We show the computed opacities for the considered radii in each target in the supplementary Fig. A.1. The range of values found in literature are shown by the gray shaded area whose bounds are set by the maximum and minimum $\dot{M}$ plus uncertainties when reported (factor of ~3 in AGBs, Ramstedt et al. 2008; De Beck et al. 2010). Those values have been rescaled to the same distance, $v_{\rm exp}$ and $X_{\rm CO}$ here adopted.

Similarly to the non C-rich THROES targets in Paper I, our mass-loss rates are in good agreement with values in the literature within the large uncertainties. In our case, these are dominated by the uncertainty in $r_{\rm CO}$. We see that the range of radii we explored yields a $\dot{M}$ that fits within the shaded area. In many cases, the error bars are truncated at the upper limit above which the line opacities would be too large to allow reliable estimates of the masses and mass-loss rates (see Fig. A.1). For example, in the case of AFGL 3068 this seems to imply smaller radius than what we have adopted to better match the values in literature.

In the case of IRC+10216, the opacity correction for $r_{\rm CO} = 2 \times 10^{15}$ cm (instead of $r_{\rm CO}$=3×10^{15} cm) would result in a mass-loss of $\dot{M} \approx 1.4 \times 10^{-5}$ $M_\odot$ yr^{-1} (not displayed) that would best match the estimate from mm observations. However in these circumstances the expected opacities in the lowest J lines would be too large ($\tau \gg 1$). Nonetheless, the derived $T_{\rm w}$ and $T_{\rm h}$ are consistent with kinetic temperature profile models as explained

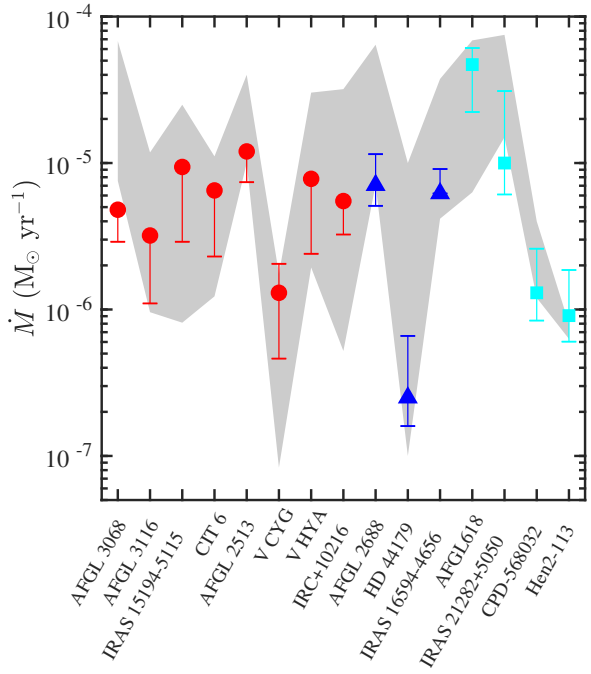

Fig. 11: Comparison between the mass-loss rate in this work and the literature. The markers correspond to the representative radii listed in Table 1 for each target and the error bars are mass-loss rates for a given range of radii. The shaded area encloses the range of values found in literature scaled to the same parameters here assumed (see text).

in Section 6.1. We find an average value of four OBSIDs of $\dot{M} \sim 5 \times 10^{-6}$ M$_\odot$ yr^{-1}, which is lower than the range $\dot{M} \sim$(1-3)$\times10^{-5}$ M$_\odot$ yr^{-1} scaled from Teyssier et al. (2006); De Beck et al. (2010, 2012); Guélin et al. (2017). However the value obtained for the warm component agrees with the lower limit of this range (because of the larger M_{H_2}). We obtain $T_w \sim 300$ K and $\dot{M}_w \sim 1\times10^{-5}$ M$_\odot$ yr^{-1} for a radius of $r_{CO} = 3 \times 10^{15}$ cm, in good agreement with the results of radiative transfer modeling of the same high J CO lines by Decin et al. (2010). Scaling their $\dot{M}$ to the same d and X_{CO} gives $\dot{M} \sim 1.2\times10^{-5}$ M$_\odot$ yr^{-1} with an uncertainty of a factor 2.

For V Hya we obtained $\dot{M} \sim 8 \times 10^{-6}$ M$_\odot$ yr^{-1} which is lower than $\dot{M} \sim 3 \times 10^{-5}$ M$_\odot$ yr^{-1} from Camps (2011) who performed radiative transfer calculations using the same PACS spectrum. In this case, however, the spatio-kinematic structure of the molecular outflow is more complex than assumed here. In particular, multiple kinematic (fast and slow) components seem to be present Hirano et al. (2004); Sahai et al. (2009), which not only translates into a larger uncertainty in the characteristic value of v_{exp} in the PACS CO-emitting layers, but also implies that the "equivalent" mass-loss rate is particularly questionable.

As for V Hya, for pPNe and yPNe, the assumption of constant-velocity spherically- symmetric mass loss may also not hold. For completeness, the mass-loss rates estimates for these targets are shown Table B.2, but they are subject to larger uncertainties and have to be interpreted with caution. We have checked that, even in these cases, our values are in good agreement with previous estimates (making similar simplifying assumptions) in the literature. For example, for the Red Rectangle, we obtained $\dot{M} \sim 2 \times 10^{-7}$ M$_\odot$ yr^{-1} which is within the (scaled) range of $\dot{M} \sim$(0.2-1.4)$\times10^{-7}$ M$_\odot$ yr^{-1} reported by De Beck et al. (2010).

In summary, our results are consistent with the literature within the typical uncertainties, but it is hard to tell what is the exact cause of the slight discrepancies from case to case. One obvious reason is that the simple RD method and our assumption of a characteristic value of r_{CO} (unknown, but crudely constrained from first principles and observations) only provides a rough estimate of the mass-loss. We also note, that the bulk of the CO emission under study is produced in the warm inner layers of the CSEs of our targets down to a location where $\tau \sim 1$. For very optically thick CSEs, there may be an additional amount of gas that is not fully recovered after the moderate opacity correction applied. Another reason for $\dot{M}$ discrepancies is the different number of transitions and range of E_u covered by different studies. Non-LTE excitation and radiative transfer models of the CO emission including a wide range of J- transitions is needed to obtain accurate estimates of the mass-loss rates and, in particular, to address $\dot{M}$ time modulations.

6.3. Comparison between the sample of O-rich and C-rich stars

In the Appendix we provide Fig. C.1 where we plot together the results presented here to the ones obtained for the sample of O-rich and S-type stars in Paper I.

We find that the range of T_{rot} is approximately the same among C-rich and O-rich stars, but the O-rich AGBs have less massive CSEs by typically one order of magnitude, and lower expansion velocities. This in turn reflects on lower mass-loss rates on average. The scenario is reversed in the groups of PNes with the few O-rich PNes having more warm gas than the carbon counterparts. Probably the O-rich AGB stars studied in Paper I are typically low massive stars with very large evolution times, while the O-rich post-AGBs and PNe are very massive objects that have undergone through the Hot Bottom Burning stage.

We stress that despite these trends being indicative of clear differences in the properties of the CSEs of the targets in the THROES catalogue, they may not be a general property of C-rich versus non C-rich targets, since our samples are not necessarily unbiased and they are definitely not statistically significant.

7. Summary

In this paper (Paper II), we use *Herschel*/PACS FIR spectra of a sample of 15 C-rich evolved stars, including AGBs, post-AGBs and yPNe, from the THROES catalogue (Ramos-Medina et al. 2018b). These data contain valuable information about the physical-chemical properties of evolved stars as shown, for instance, by the striking differences of spectral features (molecular, atomic/ionized and solid state) as a function of evolutionary stage. In this work, we focus on the rotational spectrum of CO (up to $J = 45 - 44$) which was used as a proxy for the molecular component of the gas in the warm regions of the CSEs. Our findings can be summarized as follows:

– Due to *Herschel's* higher sensitivity compared to ISO, the range of detected ^{12}CO transitions has been extended to high rotational levels of up to J_u=45 in low-to-intermediate mass evolved stars. Rotational diagrams using high-excitation CO (v=0) rotational emission lines, with upper-level energies $E_u \sim 580$ to 5000 K, have been plotted to estimate rotational temperatures (T_{rot}), total molecular mass in the CO-emitting layers (M_{H_2}) and average mass-loss rates during the ejection of these layers ($\dot{M}$).

- The range of temperatures found in our sample, $T_{\rm rot}$~200-700 K, is larger than what had been deduced from mm/submm observations, and even *Herschel*/HIFI and SPIRE observations, confirming that PACS CO lines probe deeper layers yet poorly studied to date (typically, $\approx 10^{15}$ cm for AGBs and $\approx 10^{16}$ cm for post-AGBs and yPNes).)
- The total gas mass of the warm envelope layers sampled by PACS data are between $M \sim 10^{-5} - 10^{-3}$ M$_\odot$, with post-AGBs and yPNe being overall more massive.
- We find clearly different temperature distributions for the different classes with AGBs having typically hotter gas (up to $T_{\rm rot} \sim 1000$ K) than post-AGBs ($T_{\rm rot} \lesssim 500$ K) and yPNes ($T_{\rm rot} \lesssim 400$ K). The yPN AFGL 618 is a clear outlier with a very high amount ($M_{\rm H_2}$~2×10^{-3} M$_\odot$) of rather hot (up to T$_{\rm h}$~900 K) gas, similar to the most massive AGBs in the sample.
- For AFGL 3116, CIT 6, AFGL 2513, V Hya, IRAS 16594-4656 and AFGL 618 a double temperature (hot and warm) component is inferred from the RDs. The mean temperatures of the warm and hot components are ~400 K and ~820 K, respectively. The mass of the warm component (~10^{-5}-8×10^{-3}M$_\odot$) is always larger than that of the hot component, by a factor ~4-10.
- The warm-to-hot $M_{\rm H_2}$ and $T_{\rm rot}$ ratios in our sample are correlated and are consistent with an average temperature radial profile of $T \propto r^{-0.4}$, that is, slightly shallower than in the outer envelope layers, in agreement with recent studies.
- The mass-loss rates estimated are in the range $\dot{M}\approx10^{-7}$-10^{-4}M$_\odot$ yr^{-1}, in agreement (within the uncertainties) with values found in the literature for our targets.
- We investigated the impact of CO line flux variability on the values of $M_{\rm H_2}$ and $T_{\rm rot}$ derived from the simple RD analysis. We studied in detail the case of the Mira-variable AGB star IRC+10216, for which multi-epoch PACS data exist. In spite of strong line flux variability we find that the total gas mass and the average temperature derived from the RDs at different epochs are minimally affected. Only the hot component does show the sign of line variability ($\delta T/T \sim 16\%$), roughly in-phase with the continuum periodicity.
- Similarly to Paper I, we find an anti-correlation between $T_{\rm rot}$ and $M_{\rm H_2}$, which may result from a combination of CO line cooling and opacity effects, and we find a correlation between $\dot{M}$ and $v_{\rm exp}$, which is consistent with the wind acceleration mechanism being more efficient the more luminous/massive the star is. These trends had been reported in previous studies using low-J CO transitions.

We show that high-J CO emission lines probed by *Herschel*/PACS are good tracers of the warm gas ($T \sim 200 - 900$ K) surrounding evolved carbon stars. Using the simple RD technique, we have provided systematic and homogeneous insight into the deepest layers of these CSEs, though it relies on several approximations. Detailed non-LTE excitation and radiative transfer calculations are needed to determine the temperature stratification of the CSEs, to infer mass-loss rates and to address their time-variability.

Acknowledgements. We thank the referee for the useful comments and remarks. PACS has been developed by a consortium of institutes led by MPE (Germany) and including UVIE (Austria); KU Leuven, CSL, IMEC (Belgium); CEA, LAM (France); MPIA (Germany); INAF-IFSI/OAA/OAP/OAT, LENS, SISSA (Italy); IAC (Spain). This development has been supported by the funding agencies BMVIT (Austria), ESA-PRODEX (Belgium), CEA/CNES (France), DLR (Germany), ASI/INAF (Italy), and CICYT/MCYT (Spain). This publication makes use of data products from the THROES catalog, which is a project of the Centro de Astrobiología (CAB-CSIC) with the collaboration of the Spanish Virtual Observatory (SVO), funded by the European Space Agency (ESA). J.M.S.S. acknowledges financial support from the ESAC Faculty and the ESA Education Office under the ESAC trainee program. The Institute for Solar Physics is supported by a grant for research infrastructures of national importance from the Swedish Research Council (registration number 2017-00625). C.S.C. acknowledges financial support by the Spanish MINECO through grants AYA2016-75066-C2-1-P and by the European Research Council through ERC grant 610256: NANOCOSMOS.

References

Akaike, H. 1974, IEEE Transactions on Automatic Control, 19, 716
Balick, B., Gomez, T., Vinković, D., et al. 2012, ApJ, 745, 188
Balm, S. P. & Jura, M. 1992, A&A, 261, L25
Bedijn, P. J. 1987, A&A, 186, 136
Bergeat, J. & Chevallier, L. 2005, A&A, 429, 235
Blommaert, J. A. D. L., de Vries, B. L., Waters, L. B. F. M., et al. 2014, A&A, 565, A109
Bocchio, M., Bianchi, S., & Abergel, A. 2016, A&A, 591, A117
Bujarrabal, V. 2006, in IAU Symposium, Vol. 234, Planetary Nebulae in our Galaxy and Beyond, ed. M. J. Barlow & R. H. Méndez, 193–202
Bujarrabal, V. & Alcolea, J. 2013, A&A, 552, A116
Bujarrabal, V., Alcolea, J., & Planesas, P. 1992, A&A, 257, 701
Bujarrabal, V., Alcolea, J., Soria-Ruiz, R., et al. 2012, A&A, 537, A8
Bujarrabal, V., Alcolea, J., Soria-Ruiz, R., et al. 2010, A&A, 521, L3
Bujarrabal, V., Castro-Carrizo, A., Alcolea, J., & Sánchez Contreras, C. 2001, A&A, 377, 868
Bujarrabal, V., Castro-Carrizo, A., Alcolea, J., et al. 2016, A&A, 593, A92
Bujarrabal, V., Gomez-Gonzalez, J., & Planesas, P. 1989, A&A, 219, 256
Camps, D. 2011, Master's thesis, Leuven University
Castro-Carrizo, A., Quintana-Lacaci, G., Neri, R., et al. 2010, A&A, 523, A59
Cernicharo, J., Liu, X.-W., González-Alfonso, E., et al. 1997, The Astrophysical Journal Letters, 483, L65
Cernicharo, J., Marcelino, N., Agúndez, M., & Guélin, M. 2015a, A&A, 575, A91
Cernicharo, J., McCarthy, M. C., Gottlieb, C. A., et al. 2015b, ApJ, 806, L3
Cernicharo, J., Teyssier, D., Quintana-Lacaci, G., et al. 2014, The Astrophysical Journal Letters, 796, L21
Cohen, M., Barlow, M. J., Liu, X.-W., & Jones, A. F. 2002, MNRAS, 332, 879
Cordiner, M. A., Boogert, A. C. A., Charnley, S. B., et al. 2016, ApJ, 828, 51
Cox, P., Lucas, R., Huggins, P. J., et al. 2000, A&A, 353, L25
da Silva Santos, J. M. 2016, Master's thesis, University of Porto
Danehkar, A. & Parker, Q. A. 2015, MNRAS, 449, L56
Danilovich, T., Bergman, P., Justtanont, K., et al. 2014, A&A, 569, A76
Danilovich, T., Teyssier, D., Justtanont, K., et al. 2015, A&A, 581, A60
De Beck, E., Decin, L., de Koter, A., et al. 2010, A&A, 523, A18
De Beck, E., Lombaert, R., Agúndez, M., et al. 2012, A&A, 539, A108
De Marco, O. & Crowther, P. A. 1998, MNRAS, 296, 419
Decin, L., Cernicharo, J., Barlow, M. J., et al. 2010, A&A, 518 [arXiv:1005.4675]
Goldsmith, P. F. & Langer, W. D. 1999, ApJ, 517, 209
Groenewegen, M. A. T., Baas, F., de Jong, T., & Loup, C. 1996, A&A, 306, 241
Groenewegen, M. A. T., Sevenster, M., Spoon, H. W. W., & Pérez, I. 2002, A&A, 390, 511
Groenewegen, M. A. T., Waelkens, C., Barlow, M. J., et al. 2011, A&A, 526, A162
Guandalini, R., Busso, M., Ciprini, S., Silvestro, G., & Persi, P. 2006, A&A, 445, 1069
Guélin, M., Patel, N. A., Bremer, M., et al. 2017, ArXiv e-prints [arXiv:1709.04738]
Guélin, M., Patel, N. A., Bremer, M., et al. 2018, A&A, 610, A4
Habing, H. 1996, The Astronomy and Astrophysics Review, 7, 97
Hasegawa, T. I. & Kwok, S. 2003, ApJ, 585, 475
He, J. H., Dinh-V-Trung, & Hasegawa, T. I. 2017, ApJ, 845, 38
Hirano, N., Shinnaga, H., Dinh-V-Trung, et al. 2004, ApJ, 616, L43
Höfner, S. & Olofsson, H. 2018, The Astronomy and Astrophysics Review, 26, 1
Hrivnak, B. J., Smith, N., Su, K. Y. L., & Sahai, R. 2008, ApJ, 688, 327
Huang, P.-S., Lee, C.-F., Moraghan, A., & Smith, M. 2016, ApJ, 820, 134
Ishigaki, M. N., Parthasarathy, M., Reddy, B. E., et al. 2012, MNRAS, 425, 997
Jorissen, A. & Knapp, G. R. 1998, A&AS, 129, 363
Justtanont, K., Barlow, M. J., Tielens, A. G. G. M., et al. 2000, A&A, 360, 1117
Khouri, T., de Koter, A., Decin, L., et al. 2014, A&A, 561, A5
Knapp, G. R. & Chang, K. M. 1985, ApJ, 293, 281
Knapp, G. R., Dobrovolsky, S. I., Ivezić, Z., et al. 1999, A&A, 351, 97
Knapp, G. R., Jorissen, A., & Young, K. 1997, A&A, 326, 318
Knapp, G. R. & Morris, M. 1985, ApJ, 292, 640
Knapp, G. R., Phillips, T. G., Leighton, R. B., et al. 1982, ApJ, 252, 616

Table 1: Results of the CO rotational diagram analysis with opacity correction and double-component fit. The assumed distance (d), expansion velocity (v_{exp}) and radius (r_{CO}), the derived rotational temperature (T_{rot}), CO column density (N_{CO}^{col}), total mass of H_2 within the CO emitting-volume (M_{H_2}), mass-loss rate ($\dot{M} = M_{H_2} \times v_{exp}/r_{CO}$) and ratio between opacity corrected and uncorrected total masses.

Target	d (pc)	v_{exp} (km s^{-1})	r_{CO} (cm)	T_{rot}(K)	N_{CO}^{col}(cm^{-2})	M_{H_2}(M$_\odot$)	$\dot{M}$ (M$_\odot$ yr^{-1})	Correction M_{H_2}
AFGL 3068	1100	13	6×10^{15}	350±20	3×10^{18}	$7(\pm1) \times 10^{-4}$	5×10^{-6}	1.6
AFGL 3116	630	14	2×10^{15}	670±30	5.4×10^{18}	$1.4(\pm0.2) \times 10^{-4}$	3×10^{-6}	1.6
				460±30	9.8×10^{18}	$2.6(\pm0.4) \times 10^{-4}$	6×10^{-6}	1.8
				790±70	2.4×10^{18}	$6(\pm3) \times 10^{-5}$	1×10^{-6}	1.3
IRAS 15194-5115	500	23	2×10^{15}	410±20	9.8×10^{18}	$2.6(\pm0.4) \times 10^{-4}$	9×10^{-6}	1.9
CIT 6	440	21	2×10^{15}	670±20	7.4×10^{18}	$2(\pm0.3) \times 10^{-4}$	7×10^{-6}	1.6
				460±30	1.3×10^{19}	$3.5(\pm0.7) \times 10^{-4}$	1×10^{-5}	1.7
				830±40	2.8×10^{18}	$7(\pm2) \times 10^{-5}$	2×10^{-6}	1.3
AFGL 2513	1760	26	3×10^{15}	530±30	7.3×10^{18}	$4.4(\pm0.8) \times 10^{-4}$	1×10^{-5}	1.6
				400±30	1.1×10^{19}	$7(\pm1) \times 10^{-4}$	2×10^{-5}	1.7
				1100±200	9.5×10^{17}	$6(\pm2) \times 10^{-5}$	2×10^{-6}	1.3
V Cyg	271	15	1×10^{15}	490±20	4.2×10^{18}	$2.7(\pm0.4) \times 10^{-5}$	1×10^{-6}	1.6
V Hya	380	24	1×10^{15}	650±20	1.6×10^{19}	$1.0(\pm0.1) \times 10^{-4}$	8×10^{-6}	1.9
				460±30	2.7×10^{19}	$1.8(\pm0.3) \times 10^{-4}$	1×10^{-5}	2.1
				780±40	6.7×10^{18}	$4.5(\pm0.9) \times 10^{-5}$	3×10^{-6}	1.4
AFGL 2688	340	20	8×10^{15}	300±20	2×10^{18}	$9(\pm2) \times 10^{-4}$	7×10^{-6}	1.2
HD 44179	710	10	4×10^{15}	440±50	3×10^{17}	$3.2(\pm0.8) \times 10^{-5}$	2×10^{-7}	1.1
IRAS 16594-4656	1800	14	1×10^{16}	460±20	2×10^{18}	$1.4(\pm0.3) \times 10^{-3}$	6×10^{-6}	1.4
				220±5	1×10^{19}	$6.5(\pm0.6) \times 10^{-3}$	3×10^{-5}	1.5
				530±20	1×10^{18}	$7.3(\pm0.9) \times 10^{-4}$	3×10^{-6}	1.3
AFGL 618	900	80	690±30	1×10^{16}	2.8×10^{18}	$1.9(\pm0.3) \times 10^{-3}$	5×10^{-5}	1.1
				415±20	6.8×10^{18}	$4.5(\pm0.6) \times 10^{-3}$	1×10^{-4}	1.1
				915±60	7.9×10^{17}	$5(\pm1) \times 10^{-4}$	1×10^{-5}	1
IRAS 21282+5050	2000	14	4×10^{16}	170±10	7.5×10^{17}	$8(\pm2) \times 10^{-3}$	1×10^{-5}	1.2
CPD-568032	1530	22.6	4×10^{16}	380±20	6.8×10^{16}	$7(\pm1) \times 10^{-4}$	1×10^{-6}	1
Hen 2-113	1230	23	4×10^{16}	390±20	4.7×10^{16}	$5.0(\pm0.6) \times 10^{-4}$	9×10^{-7}	1

Table 1: Continued.

Target	d (pc)	$v_{\rm exp}$ (km s^{-1})	$r_{\rm CO}$ (cm)	$T_{\rm rot}$(K)	$N_{\rm CO}^{\rm col}$(cm^{-2})	$M_{\rm H_2}$(M$_\odot$)	$\dot{M}$ (M$_\odot$ yr^{-1})	Correction $M_{\rm H_2}$
IRC+10216 (OD 745)	150	14.5	3×10^{15}	510±20	5.8×10^{18}	$3.5(\pm0.5)\times10^{-4}$	5×10^{-6}	1.8
				290±30	1.2×10^{19}	$7(\pm2)\times10^{-4}$	1×10^{-5}	1.9
				620±40	2.3×10^{18}	$1.3(\pm0.3)\times10^{-4}$	2×10^{-6}	1.3
(OD 894)*	150	14.5	3×10^{15}	490±20	1×10^{19}	$6(\pm1)\times10^{-4}$	9×10^{-6}	2.2
				260±30	2×10^{19}	$1(\pm1)\times10^{-3}$	2×10^{-5}	2.1
				680±150	3×10^{18}	$2(\pm2)\times10^{-4}$	3×10^{-6}	1.5
(OD 1087)	150	14.5	3×10^{15}	580±20	5.5×10^{18}	$3.3(\pm0.5)\times10^{-4}$	5×10^{-6}	1.7
				290±30	1.2×10^{19}	$7(\pm2)\times10^{-4}$	1×10^{-5}	1.7
				740±50	2.1×10^{18}	$1.2(\pm0.4)\times10^{-4}$	2×10^{-6}	1.3
(OD 1113)*	150	14.5	3×10^{15}	500±20	9×10^{18}	$6(\pm1)\times10^{-4}$	8×10^{-6}	2.1
				270±50	1.7×10^{19}	$1(\pm3)\times10^{-3}$	2×10^{-5}	2
				680±150	3×10^{18}	$2(\pm2)\times10^{-4}$	3×10^{-6}	1.5
(OD 1257)	150	14.5	3×10^{15}	500±20	6.6×10^{18}	$3.9(\pm0.6)\times10^{-4}$	6×10^{-6}	1.8
				320±60	1.2×10^{19}	$7(\pm3)\times10^{-4}$	1×10^{-5}	1.9
				620±40	2.5×10^{18}	$1.5(\pm0.4)\times10^{-4}$	2×10^{-6}	1.3
(OD 1288)*	150	14.5	3×10^{15}	440±20	1×10^{19}	$6(\pm1)\times10^{-4}$	9×10^{-6}	2.2
				260±15	1.9×10^{19}	$1.1(\pm0.3)\times10^{-3}$	2×10^{-5}	2.1
				580±120	2.9×10^{18}	$2(\pm2)\times10^{-4}$	3×10^{-6}	1.5
(OD 1296)	150	14.5	3×10^{15}	500±20	6.3×10^{18}	$3.7(\pm0.6)\times10^{-4}$	6×10^{-6}	1.8
				290±50	1.3×10^{19}	$8(\pm4)\times10^{-4}$	1×10^{-5}	1.9
				630±40	2.1×10^{18}	$1.2(\pm0.4)\times10^{-4}$	2×10^{-6}	1.3

Notes. In the case of IRC+10216 the fit was performed using 15 spectral lines except for the OBSIDS marked with an asterisk (OD 894, 1113, 1296) for which we were only able to use 9 lines which then reflects on the accuracy of the best-fit parameters.

Kwok, S. 2000, The Origin and Evolution of Planetary Nebulae
Lee, C.-F., Sahai, R., Sánchez Contreras, C., Huang, P.-S., & Hao Tay, J. J. 2013, ApJ, 777, 37
Leuenhagen, U., Hamann, W.-R., & Jeffery, C. S. 1996, A&A, 312, 167
Likkel, L., Morris, M., Forveille, T., & Omont, A. 1988, A&A, 198, L1
Lombaert, R., Decin, L., Royer, P., et al. 2016, A&A, 588, A124
Maercker, M., Danilovich, T., Olofsson, H., et al. 2016, A&A, 591, A44
Maindonald, J. & Braun, W. J. 2010, Data Analysis and Graphics Using R: An Example-Based Approach, 3rd edn. (New York, NY, USA: Cambridge University Press)
Matsuura, M., Yates, J. A., Barlow, M. J., et al. 2014, MNRAS, 437, 532
Meixner, M., Campbell, M. T., Welch, W. J., & L. 1998, The Astrophysical Journal, 509, 392
Men'shchikov, A. B., Schertl, D., Tuthill, P. G., Weigelt, G., & Yungelson, L. R. 2002, A&A, 393, 867
Milam, S. N., Woolf, N. J., & Ziurys, L. M. 2009, ApJ, 690, 837
Mishra, A., Li, A., & Jiang, B. W. 2015, ApJ, 802, 39
Neufeld, D. A., González-Alfonso, E., Melnick, G., et al. 2010, A&A, 521, L5
Nicolaes, D., Groenewegen, M. A. T., Royer, P., et al. 2018, ArXiv e-prints [arXiv:1808.03467]
Olofsson, H., Eriksson, K., & Gustafsson, B. 1987, A&A, 183, L13
Olofsson, H., Eriksson, K., & Gustafsson, B. 1988, A&A, 196, L1
Olofsson, H., Eriksson, K., Gustafsson, B., & Carlstrom, U. 1993, ApJS, 87, 267
Pilbratt, G. L., Riedinger, J. R., Passvogel, T., et al. 2010, A&A, 518, L1
Poglitsch, A., Waelkens, C., Geis, N., et al. 2010, A&A, 518, L2
Ramos-Medina, J., Sánchez Contreras, C., García-Lario, P., & da Silva Santos, J. M. 2018a, A&A, 618, A171
Ramos-Medina, J., Sánchez Contreras, C., García-Lario, P., et al. 2018b, A&A, 611, A41
Ramstedt, S. & Olofsson, H. 2014, A&A, 566, A145
Ramstedt, S., Schöier, F. L., Olofsson, H., & Lundgren, A. A. 2008, A&A, 487, 645
Ryde, N., Schöier, F. L., & Olofsson, H. 1999, A&A, 345, 841
Sahai, R., Sugerman, B. E. K., & Hinkle, K. 2009, ApJ, 699, 1015
Sanchez Contreras, C., Baez-Rubio, A., Alcolea, J., Bujarrabal, V., & Martin-Pintado, J. 2017, ArXiv e-prints [arXiv:1704.01773]
Sánchez Contreras, C., Bujarrabal, V., Castro-Carrizo, A., Alcolea, J., & Sargent, A. 2004, ApJ, 617, 1142
Sánchez Contreras, C. & Sahai, R. 2012, ApJS, 203, 16
Schöier, F. L., Maercker, M., Justtanont, K., et al. 2011, A&A, 530, A83
Schöier, F. L. & Olofsson, H. 2001, A&A, 368, 969
Schöier, F. L., Ryde, N., & Olofsson, H. 2002, A&A, 391, 577
Schwarz, G. 1978, Ann. Statist., 6, 461
Teyssier, D., Cernicharo, J., Quintana-Lacaci, G., et al. 2015, in Astronomical Society of the Pacific Conference Series, Vol. 497, Why Galaxies Care about AGB Stars III: A Closer Look in Space and Time, ed. F. Kerschbaum, R. F. Wing, & J. Hron, 43
Teyssier, D., Hernandez, R., Bujarrabal, V., Yoshida, H., & Phillips, T. G. 2006, A&A, 450, 167
Van de Sande, M., Decin, L., Lombaert, R., et al. 2018, A&A, 609, A63
van der Veen, W. E. C. J. & Habing, H. J. 1988, A&A, 194, 125
van Winckel, H. 2003, ARA&A, 41, 391
Volk, K., Kwok, S., & Langill, P. P. 1992, ApJ, 391, 285
Waters, L. B. F. M., Cami, J., de Jong, T., et al. 1998, Nature, 391, 868
Wesson, R., Cernicharo, J., Barlow, M. J., et al. 2010, A&A, 518, L144
Winters, J. M., Fleischer, A. J., Le Bertre, T., & Sedlmayr, E. 1997, A&A, 326, 305
Woods, P. M., Nyman, L.-Å., Schöier, F. L., et al. 2005, A&A, 429, 977
Zeileis, A., Leisch, F., Hornik, K., & Kleiber, C. 2002, Journal of Statistical Software, 7, 1
Zuckerman, B. & Dyck, H. M. 1986, ApJ, 311, 345

Appendix A: Methods

Appendix A.1: Opacity correction

In case of optically thick emission, an optical depth correction factor C_τ should be added to the RD to compensate for an underestimation of the mass within the CO-emitting volume. The optical depth at the line center (τ) of a given CO (J_u-J_l) transition is:

$$\tau = \frac{A_{ij}\lambda_0^3 N_u^{col}}{8\pi V} \times [e^{(h\nu/kT)} - 1] \quad (A.1)$$

where $V = v_{exp}\sqrt{\pi}/(2\sqrt{\log 2})$ [km s^{-1}] with v_{exp} being the expansion velocity of the gas, $N_u^{col} = N_u/\pi r_{CO}^2$ is the column density of the upper level, A_{ij} is the Einstein coefficient for spontaneous emission and λ_0 is the peak wavelength. It follows that the correction factor is written as:

$$C_\tau = \frac{\tau}{1 - e^{-\tau}} \quad (A.2)$$

To compute C_τ, we perform a first fit of the RD datapoints, $\ln\left(\frac{N_u}{g_u}\right)_0$, starting with null opacity correction ($\ln C_\tau = 0$) which yields initial (or opacity-uncorrected) values of T_{rot} and N_{CO}. We use these values to calculate τ and C_τ and to apply the opacity correction, that is, $\ln\left(\frac{N_u}{g_u}\right)_1 = \ln\left(\frac{N_u}{g_u}\right)_0 + \ln C_\tau$. A second fit to $\ln\left(\frac{N_u}{g_u}\right)_1$ is then performed, which renders the so-called opacity-corrected values of T_{rot} and N_{CO} (Table 1).

We want to highlight that, as explained in Goldsmith & Langer (1999), the opacity correction is only reliable for moderate values of the optical depth. For this reason, for all objects in our sample, the minimum acceptable value of r_{CO} used to compute the CO column density is always chosen so that it results in values of τ close to, but smaller than, unity (Fig. A.1). Indeed, the envelope layers where $\tau \sim 1$ are the deepest regions observationally accessible, because of the almost null escape probability ($1/C_\tau \rightarrow 0$) from deeper, optically thicker regions. As seen in Fig. A.1, for $r_{CO} \lesssim 1\times10^{15}$ cm the opacity of the CO J=14-13 line (E_u=580 K), which is the optically thickest transition in our sample, becomes larger than 1 in all our targets. The expected size of the CO-emitting volume in our sample is discussed in detail in Section. 4.

The optical depth of the line is also sensitive to the expansion velocity of the gas (Eq. A.1), which is unconstrained from PACS data and has been assumed to be the terminal expansion velocity of the AGB CSE from the literature (values and references are given in Table B.1). In the case of pAGBs and yPNe, we adopt the average expansion velocity of the bulk of the envelope from different previous works. The uncertainty of v_{exp} is normally less than 10%.

Appendix A.2: Model selection with BIC

Here we describe the method used to automatically find a break point in the linear relation in the rotational diagram using the Bayesian information criterion (BIC)[7].

Our approach concerns the minimization of the RSS (residual sum of squares) by computing the BIC for a range of possible locations of break points. The BIC can be regarded as a rough estimate of the Bayes factor (Schwarz 1978), and it is given by:

$$BIC = n\ln(RSS/n) + k\ln(n) \quad (A.3)$$

where a penalty term, $k\ln(n)$, penalizes model complexity depending on the number of parameters k and data points n (see also Maindonald & Braun 2010). We also tested the Akaike's information criterion (AIC) (Akaike 1974), but we concluded that for this particular application it tends to overfit essentially because the penalty term is smaller. In fact, due to the small number of data points, we are not interested in splitting the rotational diagram too much in order to obtain robust results. It can happen that BIC suggests more than one breakpoint due to the smaller accuracy of the higher J line fluxes, and in that case only the

[7] Implemented in R using the package *strucchange* (Zeileis et al. 2002).

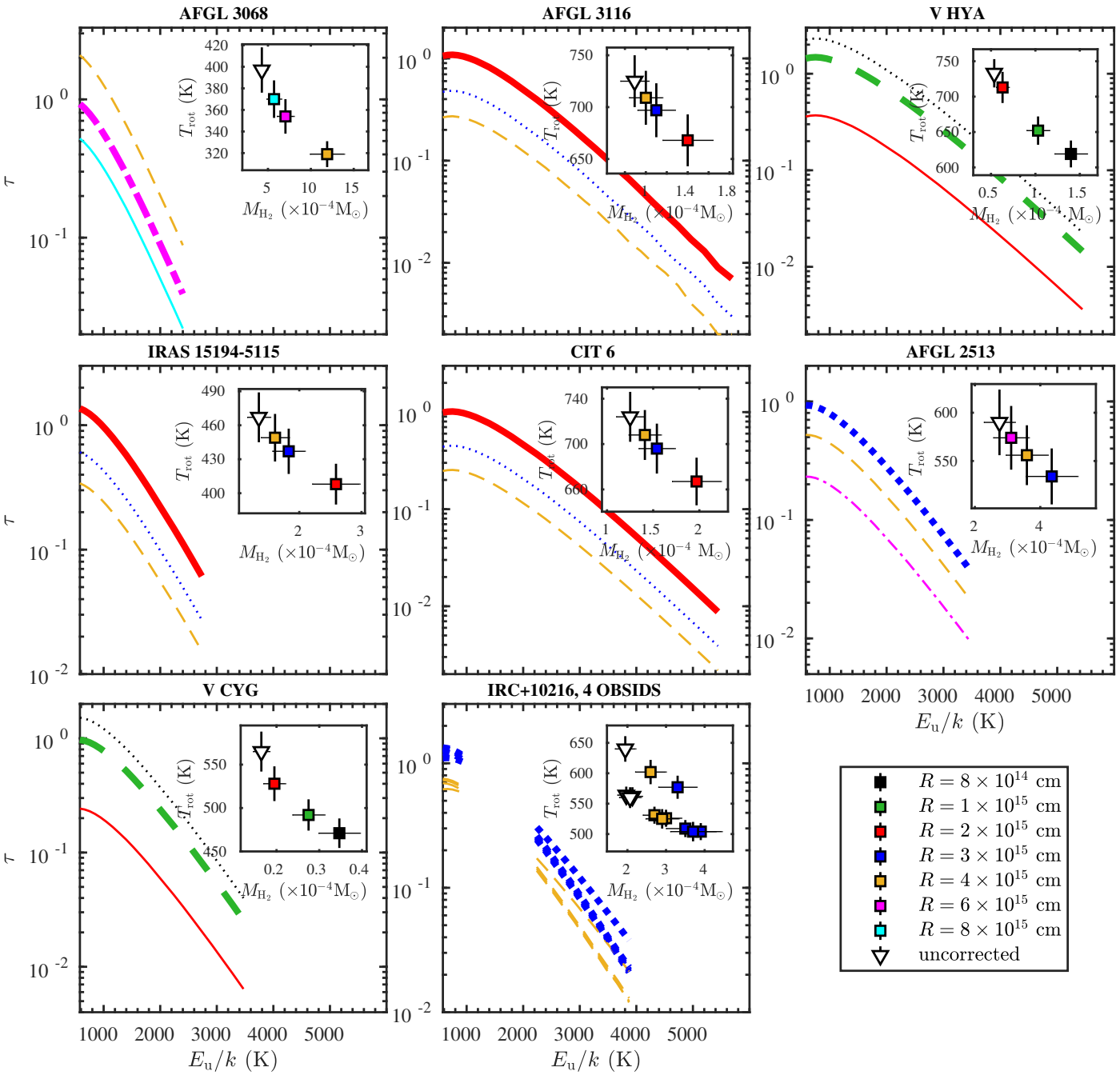

Fig. A.1: Optical depth at line center (τ) as a function of the energy of the upper level ($E_{\rm u}$). τ was computed for a range of radii; the characteristic radius adopted ($r_{\rm CO}$, Table 1) is marked with a thick line. In each panel, the inset shows the values of $T_{\rm rot}$ and $M_{\rm H_2}$ after the C_τ correction has been applied for the corresponding radii, along with the opacity-uncorrected results (open triangle).

first break point is taken into account. Obvious line blends were excluded upon the computation of both statistics.

Figure A.2 shows the BIC test in a graphical way where we see that the BIC curve is usually minimal at 0 or 1 breakpoints. For example for AFGL 2513 it is shown that the residuals of the fit keep decreasing with 2 breakpoints, although this is strongly penalized by the BIC, so a 2-component fit is favored. On the contrary, in AFGL 3068, IRAS 15194-5115 and IRC+10216 a single temperature component suffices to reproduce the data.

We note that these methods do not prove that a double temperature component is physically true, neither they provide an alternative explanation for the trends in the data. They simply highlight hidden patterns in the residuals which can be caused by many effects, being line blend the most obvious among them, or heteroscedasticity.

Appendix B: Tables

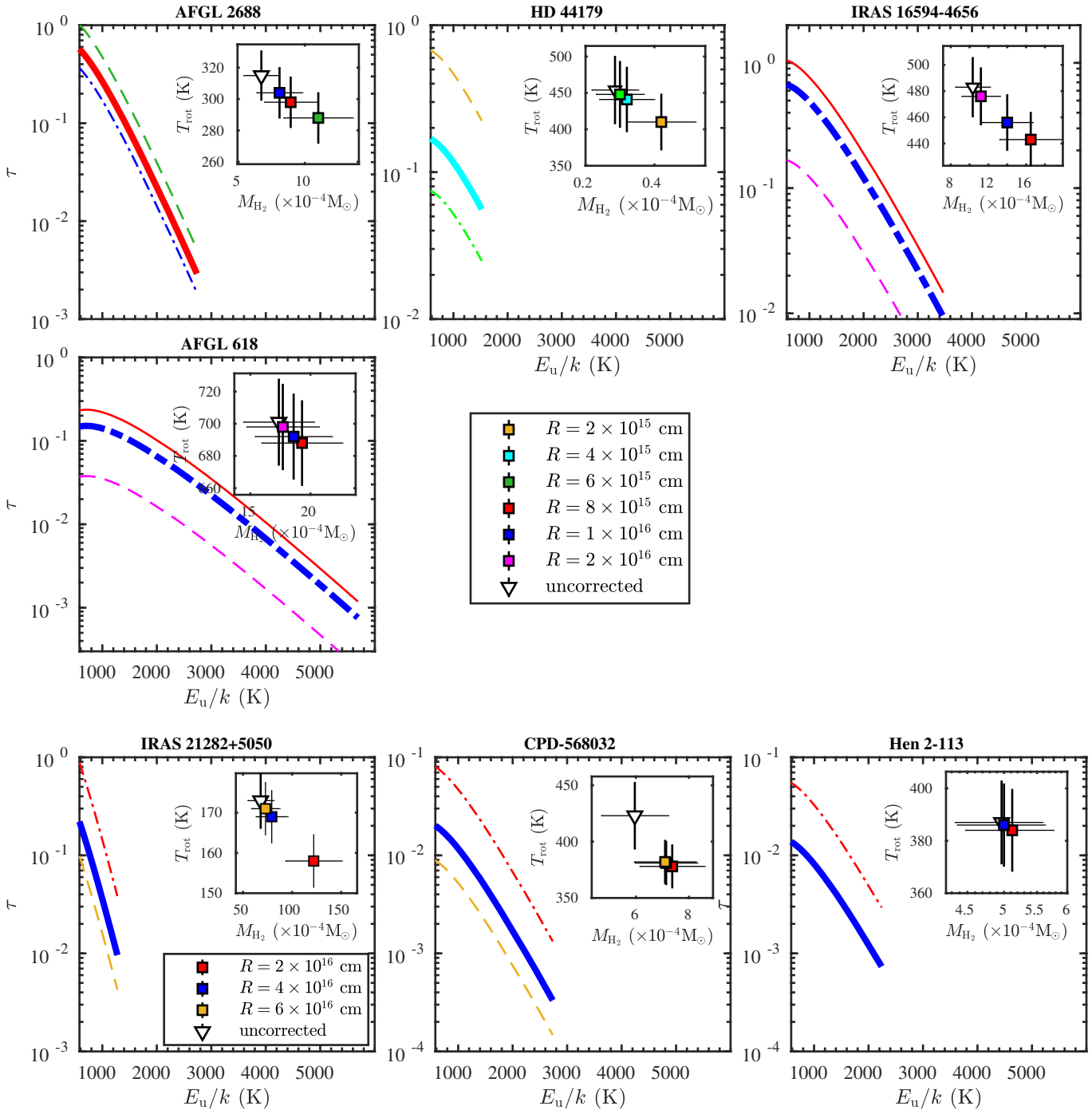

Fig. A.1: Continued.

Table B.1: Characterization of PACS observations.

Target name	Alt. name	Class	R.A. (J2000)	DEC (J2000)	OBSID	Obs. date
AFGL 3068	LL Peg	C-rich AGB	$23^h19^m12^s.39$	$17^o11'35''.4$	1342199417 1342199418	2010-06-30
AFGL 3116	LP And	C-rich AGB	$23^h34^m27^s.67$	$43^o33'2''.52$	1342212512 1342212513	2011-01-11
IRC+10216	CW Leo	C-rich AGB	$9^h47^m57^s.41$	$13^o16'43''.60$	1342221889 1342241328 1342245395 1342246381 1342253754 1342255741 1342256262	2011-05-29 2011-10-25 2012-05-05 2012-05-30 2012-10-21 2012-11-21 2012-11-30
IRAS 15194-5115	II Lup	C-rich AGB	$15^h23^m4^s.91$	$-51^o25'59''.0$	1342215685 1342215686	2010-03-10
CIT 6	RW Lmi	C-rich AGB	$10^h16^m2^s.28$	$30^o34'18''.48$	1342197799 1342197800	2010-06-05
AFGL 2513	V1969 Cyg	C-rich AGB	$20^h09^m14^s.25$	$31^o25'44''.9$	1342270010 1342269936	2013-04-14 2013-04-12
V Cyg		C-rich AGB	$20^h41^m18^s.27$	$48^o08'28''.8$	1342208939 1342208940	2010-11-15
V Hya		C-rich AGB	$10^h51^m37^s.25$	$21^o15'00''.3$	1342197790 1342197791	2010-06-05
AFGL 2688	Egg Nebula	C-rich post-AGB	$21^h2^m18^s.74$	$36^o41'37''.68$	1342199233 1342199234	2010-06-26
HD 44179	Red Rectangle	mixed post-AGB	$6^h19^m58^s.22$	$-10^o38'14''.7$	1342220928 1342220929	2011-04-30
IRAS 16594-4656	Water Lily Nebula	mixed post-AGB	$17^h03^m10^s.03$	$-47^o00'27''.7$	1342228414 1342228415	2011-09-10
AFGL 618	CRL 618	C-rich yPNe	$4^h42^m53^s.66$	$36^o6'53''.28$	1342225838 1342225839	2011-08-07
IRAS 21282+5050		C-rich yPNe	$21^h29^m58^s.42$	$51^o3'59''.76$	1342220741 1342223375	2011-05-12 2011-06-30
CPD-568032	Hen 3-1333	mixed yPNe	$17^h7^m0^s.87$	$-56^o54'48''.0$	1342228201 1342228202	2011-09-06
Hen 2-113		mixed yPNe	$14^h59^m53^s.52$	$-54^o18'07''.20$	1342225142 1342225143	2011-08-02

Notes. Target name, alternative name, evolutionary classification, coordinates given by right ascension (R.A) and declination (DEC), observation identifier (OBSID) and observation date. The spectra correspond to bands B2B and R1 in IRC+10216 and B2A, B2B and R1 for the remaining targets.

Table B.2: Properties of stars and their CSEs taken from the bibliography.

Target name	Var.	$T_{\rm eff}$ (K)	d (pc)	$v_{\rm exp}$ (km s^{-1})	$\dot{M}$ (M$_\odot$ yr^{-1})		references
AFGL 3068	Mira	2000	1100	13	(0.9, 6) $\times10^{-5}$	(0.8, 6.8) $\times10^{-5}$	2, 10, 23, 29
AFGL 3116	Mira	2000	630	14	(4.6, 12) $\times10^{-6}$	(1, 11.8) $\times10^{-6}$	2, 10, 23
IRC+10216	Mira	2330	150	14.5	(0.2, 4) $\times10^{-5}$	(0.05, 3.2) $\times10^{-5}$	2, 12, 23, 24, 31
IRAS 15194-5115	Mira	2400	500	23	(0.4, 1.5) $\times10^{-5}$	(0.08, 2.5) $\times10^{-5}$	2, 10, 13
CIT 6	SRa	2450	440	21	(5, 6) $\times10^{-6}$	(1.2, 11) $\times10^{-6}$	2, 10, 23
AFGL 2513	Mira	2500	1760	26	2 $\times10^{-5}$	(1, 4) $\times10^{-5}$	6, 14
V Cyg	Mira	2580	271	15	(0.4, 6.3) $\times10^{-6}$	(0.08, 1.7) $\times10^{-6}$	2, 10, 15
V Hya	SR/Mira	2650	380	24	(0.25, 6) $\times10^{-5}$	(0.03, 3) $\times10^{-5}$	1, 10, 17, 25
AFGL 2688		7250	340	20	(0.7, 2) $\times10^{-4}$	(0.06, 0.6) $\times10^{-4}$	3, 8, 19, 27
HD 44179		7750	710	8.3	10^{-7}-10^{-5}	10^{-7}-10^{-5}	5, 7, 10, 32
IRAS 16594-4656		10000	1800	14	1 $\times10^{-5}$	(0.4, 3.7) $\times10^{-5}$	9, 18
AFGL 618		33000	900	80	(0.3, 2) $\times10^{-4}$	(0.06, 0.7) $\times10^{-4}$	4, 16, 26, 27, 30
IRAS 21282+5050		30000	2000	14	(2, 10) $\times10^{-5}$	(1.5, 7.5) $\times10^{-5}$	11, 21, 26
CPD-568032		30000	1530	22.6	(1.2-4) $\times10^{-6}$	(1.2-4) $\times10^{-6}$	20, 28
Hen 2-113		30900	1230	23	(6.3-8) $\times10^{-7}$	(6.3-8) $\times10^{-7}$	20, 28

Notes. Type of variability, effective temperature ($T_{\rm eff}$), distance (d), expansion velocity ($v_{\rm exp}$) and range of gas mass-loss rate ($\dot{M}$) including uncertainty, with and without scaling to the same $X_{\rm CO}$, d and $v_{\rm exp}$ used in this paper on the right and left columns, respectively. In case there is only one $\dot{M}$ value in literature with no estimated uncertainty we assumed an error factor of 3 which is the typical uncertainty in mass-loss rates of AGB stars (e.g. De Beck et al. 2010; Ramstedt et al. 2008).

References. [(1)]Bergeat & Chevallier (2005), [(2)]Ramstedt & Olofsson (2014), [(3)]Balick et al. (2012), [(4)]Sánchez Contreras et al. (2004), [(5)]Bujarrabal et al. (2016) [(6)]Guandalini et al. (2006), [(7)]Men'shchikov et al. (2002), [(8)]Ishigaki et al. (2012), [(9)]Mishra et al. (2015) [(10)]De Beck et al. (2010), [(11)]Hasegawa & Kwok (2003), [(12)]Cernicharo et al. (2015a), [(13)]Ryde et al. (1999), [(14)]Groenewegen et al. (2002), [(15)]Neufeld et al. (2010), [(16)]Huang et al. (2016), [(17)]Knapp et al. (1997), [(18)]Woods et al. (2005), [(19)]Milam et al. (2009), [(20)]De Marco & Crowther (1998), [(21)]Likkel et al. (1988), [(22)]Bujarrabal et al. (2016), [(23)]Teyssier et al. (2006), [(24)]De Beck et al. (2012), [(25)]Knapp et al. (1999), [(26)]Meixner et al. (1998), [(27)]Bujarrabal et al. (2001), [(28)]Leuenhagen et al. (1996), [(29)]Sánchez Contreras & Sahai (2012), [(30)]Wesson et al. (2010), [(31)]Guélin et al. (2018), [(32)]Bujarrabal & Alcolea (2013)

Table B.3: Carriers of some of the spectral lines detected towards our sample of C-rich evolved stars.

Target Name	Molecular						Atomic/ionized				Dust
	CO	HCN	CS	OH	H_2O	CH+	[OI] 63.18μm	[NII] 121.89μm	[OI] 145.52μm	[CII] 157.74μm	forsterite 69 μm
AFGL 3068	✓	✓	✓		✓						
AFGL 3116	✓	✓	✓		✓						
IRC+10216	✓	✓	✓		✓						
IRAS 15194-5115	✓	✓	✓		✓						
CIT 6	✓	✓	✓		✓						
AFGL 2513	✓	✓	✓		✓						
V Cyg	✓	✓	✓		✓						
V Hya	✓	✓	✓		✓						
AFGL 2688	✓	✓			✓						
HD 44179	✓						✓		✓	✓	✓
IRAS 16594-4665	✓			✓		✓	✓		✓	✓	
AFGL 618	✓	✓		✓	✓		✓		✓	✓	
IRAS 21282+5050	✓					✓	✓	✓	✓	✓	
CPD-568032	✓			✓		✓	✓		✓	✓	✓
Hen 2-113	✓			✓		✓	✓	✓	✓	✓	✓

Table B.4: Line fluxes of CO rotational transitions in a sample of C-rich evolved stars.

Transition	ν_{rest} (MHz)	λ_{rest} (μm)	E_{up}/k (K)	A_{ij} (s^{-1})	F ($\times10^{-16}$ W m^{-2})				
^{12}CO (v = 0)					CIT 6	V Hya	IRAS 15194-5115	AFGL 2513	V Cyg
J = 14 → 13	1611794	185.999	580.497	0.00027	8.9±0.3	4.3±0.2	4.3±0.4	0.88±0.07	1.8±0.2
J = 15 → 14	1726603	173.631	663.361	0.00034	7.7±0.3	4.6±0.2	3.9±0.5	0.96±0.05	1.8±0.1
J = 16 → 15	1841346	162.812	751.733	0.00041	9.2±0.5	5.6±0.2	5.0±0.3	1.07±0.06	2.6±0.1
J = 17 → 16	1956018	153.267	845.608	0.00048	11.3±0.6	6.1±0.2	4.9±0.3	1.29±0.08	2.3±0.1
J = 18 → 17	2070616	144.784	944.983	0.00057	9.6±0.7	5.3±0.2	3.7±0.5	0.99±0.07	2.7±0.1
J = 19 → 18	2185135	137.196	1049.854	0.00067	8.1±0.6	5.0±0.2	4.1±0.3	0.84±0.08	2.7±0.2
J = 20 → 19	2299570	130.369	1160.217	0.00077	16.2±0.9	8.9±0.3	7.4±0.6	1.7±0.1	3.9±0.3
J = 21 → 20	2413917	124.193	1276.068	0.00088	11±1.0	6.4±0.3	4±1	1.0±0.1	2.6±0.2
J = 22 → 21	2528172	118.581	1397.402	0.00101	10.9±0.6	5.9±0.2	4.3±0.8	1.0±0.07	2.7±0.2
J = 23 → 22	2642330	113.458	1524.215	0.00114	16±2	9±1	5±2	1.5±0.2	4.1±0.4
J = 24 → 23	2756388	108.763	1656.502	0.00128	11±2	5.6±0.5	5±2*	0.9±0.1	1.9±0.3
J = 25 → 24	2870339	104.445	1794.258	0.00143	9±1	5.9±0.5	3.8±0.8	0.8±0.1	2.7±0.4*
J = 28 → 27	3211519	93.349	2240.286	0.00194	6.8±0.4	5.3±0.3	2.5±0.4*	0.7±0.1	1.2±0.2
J = 29 → 28	3325005	90.163	2399.862	0.00213	11±1.0	5.3±0.4	1.6±0.4	0.8±0.1	1.8±0.2
J = 30 → 29	3438365	87.19	2564.879	0.00232	9.7±0.9	6.4±0.5*	3.2±0.8	1.5±0.2*	2.1±0.4*
J = 31 → 30	3551592	84.411	2735.331	0.00252	9.8±0.9	4.9±0.3	1.7±0.6	0.9±0.1	1.6±0.3
J = 32 → 31	3664684	81.806	2911.209	0.00274	6.1±0.9	4.1±0.6	...	0.7±0.2	1.0±0.3
J = 33 → 32	3777636	79.359	3092.509	0.00295	5.4±0.9	5.2±0.6	...	0.7±0.2	0.96±0.3
J = 34 → 33	3890443	77.059	3279.223	0.00318	9±1	4.6±0.4	...	0.7±0.1*	1.1±0.3*
J = 35 → 34	4003101	74.89	3471.344	0.0034	8±2*	3.9±0.8	...	0.8±0.1*	1.2±0.3*
J = 36 → 35	4115606	72.843	3668.864	0.00364	4.7±0.9*	3.2±0.3	...	...	...
J = 37 → 36	4227953	70.907	3871.775	0.00388	5±1	3.0±0.6*	...	...	...
J = 38 → 37	4340138	69.074	4080.071	0.00412	3.7±0.4	2.8±0.3	...	...	...
J = 39 → 38	4452157	67.336	4293.743	0.00437	3±1*	2.5±0.5*	...	...	...
J = 40 → 39	4564006	65.686	4512.783	0.00461	3.2±1.0*	2.9±0.7	...	...	...
J = 41 → 40	4675679	64.117	4737.183	0.00486	1.1±0.6*	1.4±0.4	...	...	...
J = 42 → 41	4787174	62.624	4966.933	0.00511	2±1*	0.9±0.5*	...	...	...
J = 43 → 42	4898485	61.201	5202.026	0.00536	3.3±0.9*	1.8±0.4*	...	...	...
J = 44 → 43	5009608	59.843	5442.452	0.00561	1.7±0.6	1.9±0.5	...	...	...
J = 45 → 44	5120539	58.547	5688.201	0.00585	...	...	...	...	...

Notes. The ellipsis mark absent or noisy (SNR<3) lines, and asterisks (*) flag line blends which may have caused overestimated fluxes.

Table B.4: Continued.

AFGL 3068	AFGL 3116	AFGL 618	HD 44179	IRAS 16594-4656	AFGL 2688	Hen 2-113	CPD-568032	IRAS 21282+5050
2.1±0.2	2.7±0.2	39±1	0.4±0.1	4.1±0.1	41±1	2.24±0.09	2.4±0.1	2.96±0.06
2.1±0.2	2.9±0.2	33±1	0.39±0.09	4.1±0.1	36±1	2.16±0.07	2.3±0.1	2.92±0.05
2.3±0.1	2.8±0.1	40±1	0.4±0.1	3.9±0.3	33±1	2.3± 0.5	2.2±0.1	2.42±0.06
2.5±0.2	4.1±0.3	37±1	0.53±0.09	3.2±0.1	26±1	2.3± 0.1	2.0±0.07	1.63±0.04
2.7±0.3	3.5±0.2	38±1	0.6±0.1	2.76±0.06	25±1	2.1± 0.1	1.9±0.1	1.04±0.07
2.5±0.2	3.0±0.2	39±2	0.45±0.09	2.42±0.01	22±1	2.0± 0.1	1.6±0.1	0.9±0.1
3.9±0.2	6.1±0.4	44±1	0.4±0.1	2.5±0.1	24±1	2.2± 0.1	2±0.2	0.59±0.09
2.3±0.3	4.3±0.5	34±2	0.4±0.1	2.8±0.1	17±1	2.0± 0.1	1.7±0.2	0.50±0.08
2.7±0.2	3.6±0.2	36±2	0.7±0.1	2.2±0.2	18±1	2.4± 0.3	1.3±0.2	...
2.5±0.6	4.6±0.9	46±2	0.4±0.2	2.7±0.1	14±2	2.2±0.3	1.9±0.2	...
1.6±0.4	3.7±0.6	28±2*	...	1.9±0.1	11±2	1.2±0.2	1.0±0.2	...
1.3±0.5	3.4±0.2	31±2	...	2.1±0.2	6±2	1.6±0.2	1.2±0.3	...
1.2±0.3	3.2±0.3	21±1	...	1.6±0.1	6±1	0.7±0.2	0.9±0.1	...
1.9±0.4*	3.3±0.3	25±1	...	1±2*	11±2*	...	bad fit	...
...	4.5±0.5*	20±1	...	1.3±0.1	bad fit*	...	...	...
...	2.9±0.3	26±2	...	4.9±0.8*	4±2	...	...	...
...	2.0±0.2	17±2	...	0.9±0.1	...	...	...	...
...	2.4±0.5	15±2*	...	0.8±0.8*	...	...	...	...
...	2.4±0.7*	16±2	...	0.7±0.1	...	...	...	...
...	2.2±0.4	16±2	...	0.8±0.1*	...	...	...	...
...	2.3±0.5	11±1	...	...	...	...	...	...
...	3±1*	13±3*	...	...	...	...	...	...
...	1.3±0.2*	11±1	...	...	...	...	...	...
...	0.9±0.3	6±5	...	...	...	...	...	...
...	0.9±0.3	5±2	...	...	...	...	...	...
...	...	10±2	...	...	...	...	...	...
...	...	37±20*	...	...	...	...	...	...
...	...	9±3	...	...	...	...	...	...
...	...	6±2	...	...	...	...	...	...
...	...	3±2	...	...	...	...	...	...

Table B.5: CO line fluxes of seven observations of IRC+10216. Asterisks flag known line blends.

Transition	ν_{rest} (MHz)	λ_{rest} (μm)	E_{up}/k (K)	A_{ij} (s^{-1})	F ($\times10^{-16}$ W m^{-2})						
^{12}CO (v = 0)					OD 745	OD 894	OD 1087	OD 1113	OD 1257	OD 1288	OD 1296
$J = 14 \rightarrow 13$	1611794	185.99	580.5	0.00027	85±3	98±10	92±4	90±5	97±3	86±8	100±3
$J = 15 \rightarrow 14$	1726603	173.63	663.36	0.00034	74±5	103±13	80±6	108±30	82±5	88±8	80±5
$J = 16 \rightarrow 15$	1841346	162.81	751.73	0.00041	89±4	100±24	93±3	93±12	78±2	89±12	79±3
$J = 17 \rightarrow 16$	1956018	153.27	845.61	0.00048	92±7		99±7		92±7		89±6
$J = 18 \rightarrow 17$	2070616	144.78	944.98	0.00057	82±7		85±6		110±5		102±5
$J = 28 \rightarrow 27$	3211519	93.35	2240.29	0.00194	69±2	104±18	97±3	104±18	64±2	59±15	62±2
$J = 29 \rightarrow 28$	3325005	90.16	2399.86	0.00213	72±4	124±15	95±6	124±15	80±5	78±10	77±5
$J = 30 \rightarrow 29$	3438365	87.19	2564.88	0.00232	55±7	82±12	82±9	82±12	72±6	50±9	55±4
$J = 31 \rightarrow 30$	3551592	84.41	2735.33	0.00252	57±7	108±11	101±9	108±11	52±5	60±6	55±5
$J = 32 \rightarrow 31$	3664684	81.81	2911.21	0.00274	37±8	54±18	68±6	54±18	47±5	26±11	39±4
$J = 33 \rightarrow 32$	3777636	79.36	3092.51	0.00295	43±8	80±15	79±10	80±15	42±5	39±7	40±4
$J = 34 \rightarrow 33$	3890443	77.06	3279.22	0.00318	38±8		64±9		30±5		35±5
$J = 35 \rightarrow 34$	4003101	74.89	3471.34	0.0034	34±8*		64±9*		39±8*		38±7*
$J = 36 \rightarrow 35$	4115606	72.84	3668.86	0.00364	19±7		32±9		23±5		18±4
$J = 37 \rightarrow 36$	4227953	70.91	3871.78	0.00388	20±6		45±10		20±6		22±6

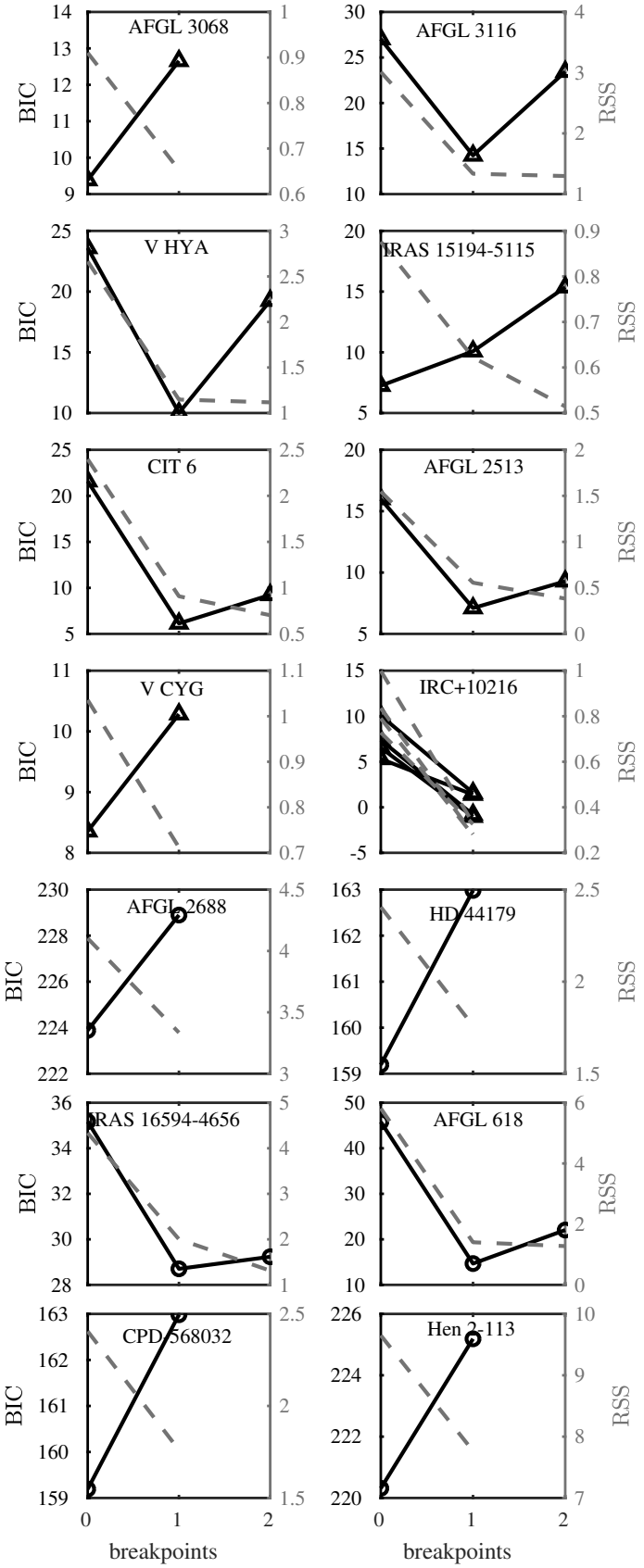

Fig. A.2: Bayesian information criterion and residual sum of squares as a function of number of breakpoints. The BIC is given by the solid line and the RSS is given by the dashed line. The statistic was not computed for IRAS 21282+5050 due to insufficient number of points.

Appendix C: Supplement figures

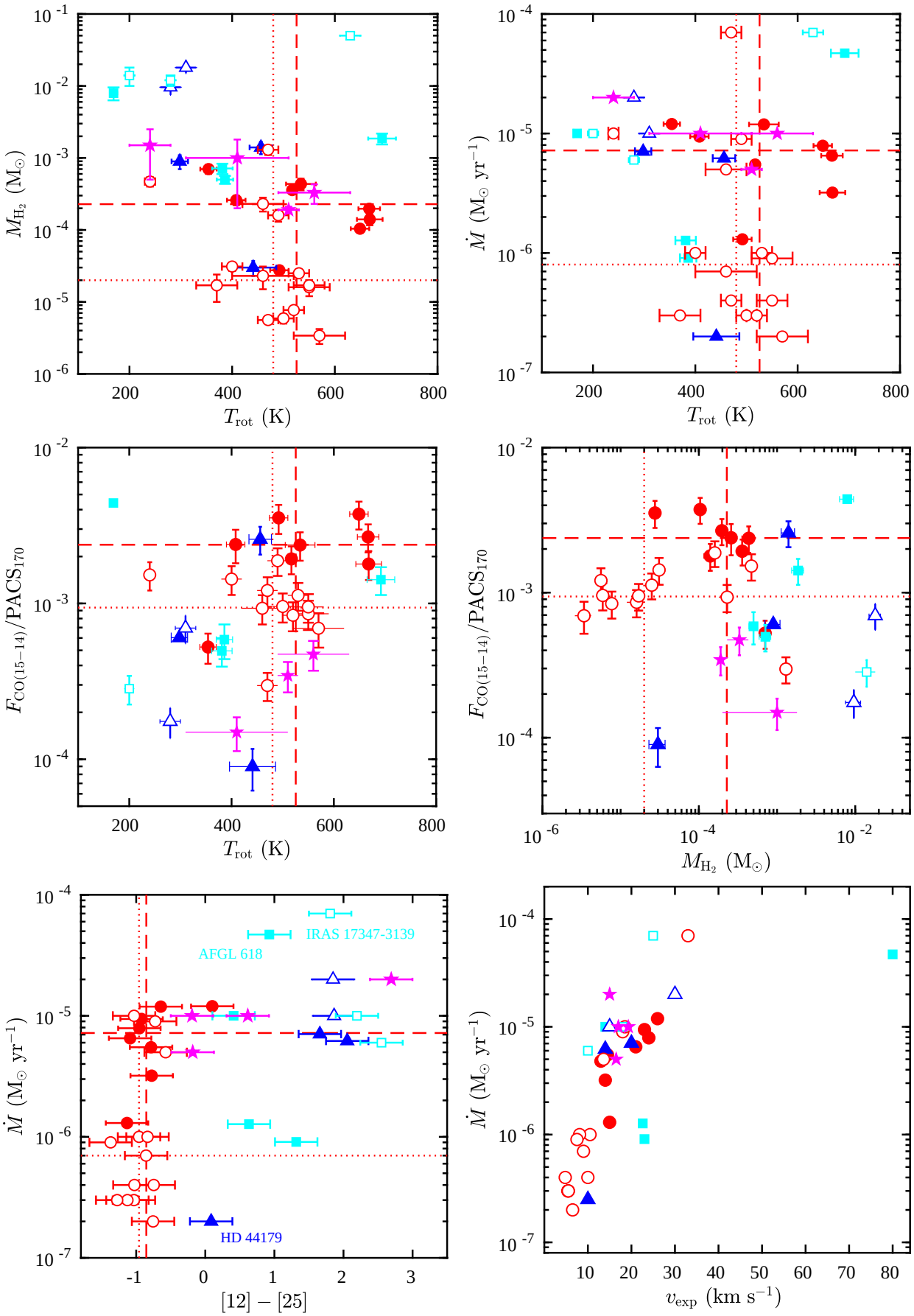

Fig. C.1: Supplementary plots. Temperature, mass, mass-loss-rate, line to continuum ratio and IRAS color of our sample of C-rich (filled symbols) and O-rich stars in Paper I (open symbols and magenta pentagrams). The color code is the same as in Fig. 1.

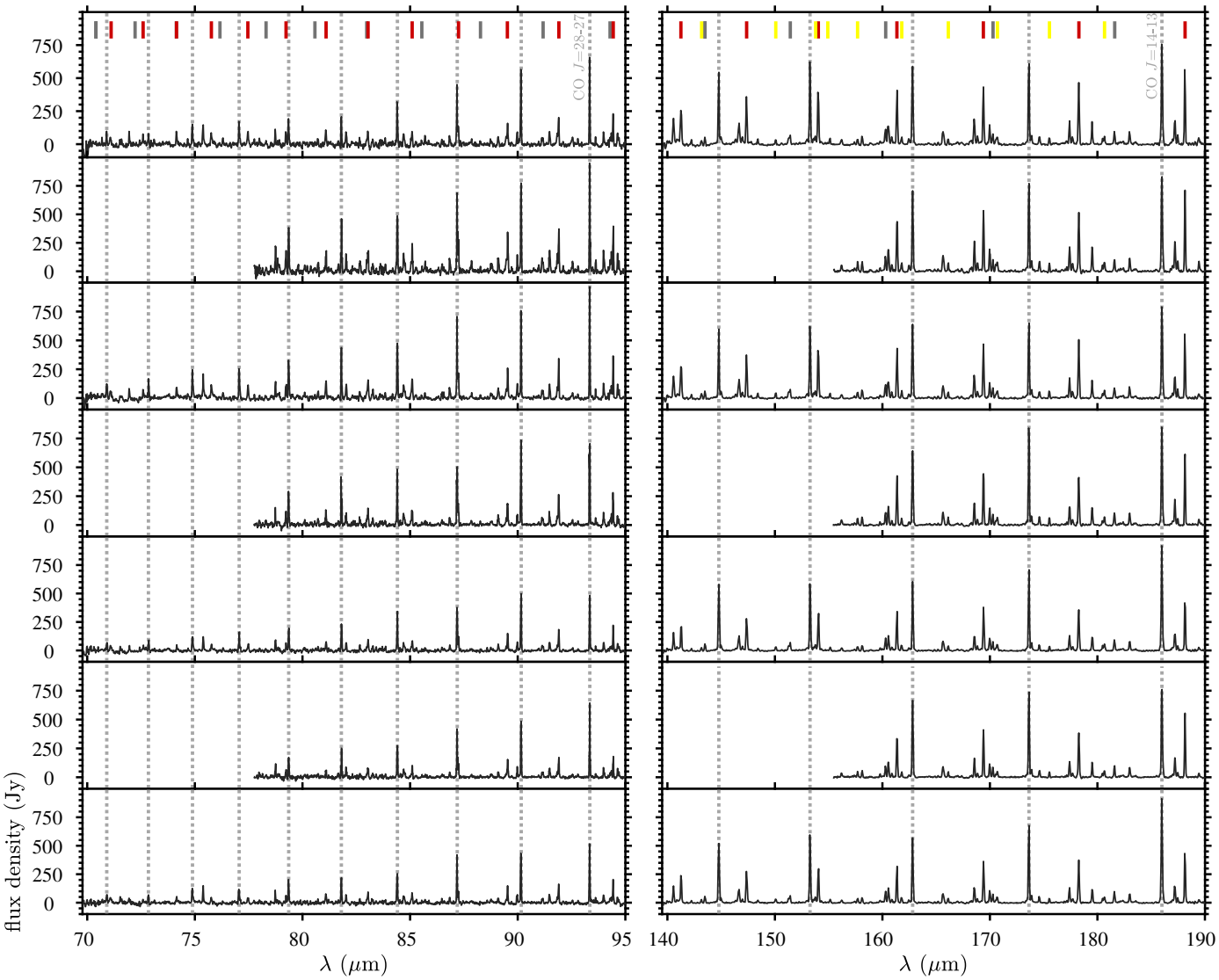

Fig. C.2: Spectra of IRC+10216 at different epochs. Each row corresponds to a different observing day (from top to bottom: OD = 745, 894, 1087, 1113, 1257, 1288, 1296). Same color code for the top tick marks as in Fig.2.

Bibliography

Akaike, H. (1974). "A New Look at the Statistical Model Identification". In: *IEEE Transactions on Automatic Control* 19, pp. 716–723.

Alcolea, J. et al. (2001). "The highly collimated bipolar outflow of OH 231.8+4.2". In: 373, pp. 932–949. DOI: 10.1051/0004-6361:20010535.

Arrieta, A. et al. (2003). "Evidence of Jets in the Bipolar Planetary Nebulae M 1-91 and M 1-92". In: *Planetary Nebulae: Their Evolution and Role in the Universe*. Ed. by Sun Kwok, Michael Dopita, and Ralph Sutherland. Vol. 209. IAU Symposium, p. 513.

Asymptotic giant branch stars (2003).

Balick, B. et al. (2012). "The Illumination and Growth of CRL 2688: An Analysis of New and Archival Hubble Space Telescope Observations". In: 745, 188, p. 188. DOI: 10.1088/0004-637X/745/2/188. arXiv: 1110.5678 [astro-ph.SR].

Balm, S. P. and M. Jura (1992). "Identification of CH(+) emission in the Red Rectangle". In: 261, pp. L25–L28.

Baud, B. and H. J. Habing (1983). "The maser strength of OH/IR stars, evolution of mass loss and the creation of a superwind". In: 127, pp. 73–83.

Bechis, K. P. (1976). "Microwave Spectral-Line Radiation from Young and Evolved Stellar Objects." PhD thesis. Massachusetts Univ., Amherst.

Bergeat, J. and L. Chevallier (2005). "The mass loss of C-rich giants". In: 429, pp. 235–246. DOI: 10.1051/0004-6361:20041280. eprint: astro-ph/0601366.

Blommaert, J. A. D. L. et al. (2014a). "Herschel/PACS observations of the 69 μm band of crystalline olivine around evolved stars". In: 565, A109, A109. DOI: 10.1051/0004-6361/201322554. arXiv: 1403.6335 [astro-ph.SR].

Blommaert, J. A. D. L. et al. (2014b). "Herschel/PACS observations of the 69 μm band of crystalline olivine around evolved stars". In: 565, A109, A109. DOI: 10.1051/0004-6361/201322554. arXiv: 1403.6335 [astro-ph.SR].

Bujarrabal, V. and J. Alcolea (2013). "Warm gas in the rotating disk of the Red Rectangle: accurate models of molecular line emission". In: 552, A116, A116. DOI: 10.1051/0004-6361/201220807. arXiv: 1303.2841 [astro-ph.GA].

Bujarrabal, V., J. Alcolea, and P. Planesas (1992). "The molecular emission of young preplanetary nebulae." In: 257, pp. 701–714.

Bujarrabal, V. and J. Cernicharo (1994). "The C/O abundance ratio in the detached circumstellar envelopes around carbon stars". In: 288, pp. 551–557.

Bujarrabal, V. et al. (2001). "Mass, linear momentum and kinetic energy of bipolar flows in protoplanetary nebulae". In: 377, pp. 868–897. DOI: 10.1051/0004-6361:20011090.

Bujarrabal, V. et al. (2010). "Herschel/HIFI observations of high-J CO transitions in the protoplanetary nebula CRL 618". In: 521, L3, p. L3. DOI: 10.1051/0004-6361/201015068. arXiv: 1007.1570 [astro-ph.SR].

Bujarrabal, V. et al. (2016). "Further ALMA observations and detailed modeling of the Red Rectangle". In: 593, A92, A92. DOI: 10.1051/0004-6361/201628546. arXiv: 1606.07238 [astro-ph.SR].

Bujarrabal, Valentín (2016). "Molecular line mapping of (young) planetary nebulae". In: *Journal of Physics Conference Series*. Vol. 728, p. 032010. DOI: 10.1088/1742-6596/728/3/032010.

Busso, M., R. Gallino, and G. J. Wasserburg (1999). "Nucleosynthesis in Asymptotic Giant Branch Stars: Relevance for Galactic Enrichment and Solar System Formation". In: 37, pp. 239–309. DOI: 10.1146/annurev.astro.37.1.239.

Camps, D. (2011). "Master thesis". In:

Castro-Carrizo, A. et al. (2010). "Mapping the ^{12}CO J = 1-0 and J = 2-1 emission in AGB and early post-AGB circumstellar envelopes. I. The COSAS program, first sample". In: 523, A59, A59. DOI: 10.1051/0004-6361/201014755.

Cernicharo, J. et al. (1997). "Discovery of Far-Infrared Pure Rotational Transitions of CH+ in NGC 7027". In: *The Astrophysical Journal Letters* 483.1, p. L65. URL: http://stacks.iop.org/1538-4357/483/i=1/a=L65.

Cernicharo, J. et al. (2014). "Discovery of Time Variation of the Intensity of Molecular Lines in IRC+10216 in the Submillimeter and Far-Infrared Domains". In: 796, L21, p. L21. DOI: 10.1088/2041-8205/796/1/L21. arXiv: 1410.5852 [astro-ph.SR].

Cernicharo, J. et al. (2014). "Discovery of Time Variation of the Intensity of Molecular Lines in IRC+10216 in the Submillimeter and Far-Infrared Domains". In: *The Astrophysical Journal Letters* 796.1, p. L21. URL: http://stacks.iop.org/2041-8205/796/i=1/a=L21.

Cernicharo, J. et al. (2015a). "Discovery of SiCSi in IRC+10216: A Missing Link between Gas and Dust Carriers of Si&ndashC Bonds". In: 806.1, L3, p. L3. DOI: 10.1088/2041-8205/806/1/L3. arXiv: 1505.01633 [astro-ph.GA].

Cernicharo, J. et al. (2015b). "Molecular shells in IRC+10216: tracing the mass loss history". In: 575, A91, A91. DOI: 10.1051/0004-6361/201424565. arXiv: 1412.1948 [astro-ph.SR].

Cherchneff, I. (2006). "A chemical study of the inner winds of asymptotic giant branch stars". In: 456, pp. 1001–1012. DOI: 10.1051/0004-6361:20064827.

— (2011). "Water in IRC+10216: a genuine formation process by shock-induced chemistry in the inner wind". In: 526, L11, p. L11. DOI: 10.1051/0004-6361/201016035. arXiv: 1012.5076 [astro-ph.SR].

— (2012). "The inner wind of IRC+10216 revisited: new exotic chemistry and diagnostic for dust condensation in carbon stars". In: 545, A12, A12. DOI: 10.1051/0004-6361/201118542. arXiv: 1111.6809 [astro-ph.SR].

Choi, Y. K. et al. (2012). "Trigonometric Parallax of the Protoplanetary Nebula OH 231.8+4.2". In: *Cosmic Masers - from OH to H0*. Ed. by Roy S. Booth, Wouter H. T. Vlemmings, and Elizabeth M. L. Humphreys. Vol. 287. IAU Symposium, pp. 407–410. DOI: 10.1017/S1743921312007387.

Cohen, M. et al. (2002). "The dual dust chemistries of planetary nebulae with [WCL] central stars". In: 332, pp. 879–890. DOI: 10.1046/j.1365-8711.2002.05350.x.

Cordiner, M. A. et al. (2016). "On the Nature of the Enigmatic Object IRAS 19312+1950: A Rare Phase of Massive Star Formation?" In: 828, 51, p. 51. DOI: 10.3847/0004-637X/828/1/51. arXiv: 1607.00432.

Cox, N. L. J. et al. (2012). "A far-infrared survey of bow shocks and detached shells around AGB stars and red supergiants (Corrigendum)". In: 543, C1, p. C1. DOI: 10.1051/0004-6361/201117910e.

Cox, P. et al. (2000). "Multiple molecular outflows in AFGL 2688". In: 353, pp. L25–L28.

da Silva Santos, J. M. (2016). "Studying evolved stars with Herschel observations". MA thesis. University of Porto.

da Silva Santos, J. M. et al. (2019). "Warm CO in evolved stars from the THROES catalogue. II. Herschel/PACS spectroscopy of C-rich envelopes". In: 622, A123, A123. DOI: 10.1051/0004-6361/201834141. arXiv: 1812.07815 [astro-ph.SR].

Danehkar, A. and Q. A. Parker (2015). "Spatially resolved kinematic observations of the planetary nebulae Hen 3-1333 and Hen 2-113". In: 449, pp. L56–L59. DOI: 10.1093/mnrasl/slv022. arXiv: 1503.01551 [astro-ph.SR].

Danilovich, T. et al. (2014). "Detailed modelling of the circumstellar molecular line emission of the S-type AGB star W Aquilae". In: 569, A76, A76. DOI: 10.1051/0004-6361/201322807. arXiv: 1408.1825 [astro-ph.SR].

Danilovich, T. et al. (2015). "New observations and models of circumstellar CO line emission of AGB stars in the Herschel SUCCESS programme". In: 581, A60, A60. DOI: 10.1051/0004-6361/201526705. arXiv: 1506.09065 [astro-ph.SR].

De Beck, E. et al. (2010a). "Probing the mass-loss history of AGB and red supergiant stars from CO rotational line profiles. II. CO line survey of evolved stars: derivation of mass-loss rate formulae". In: 523, A18, A18. DOI: 10.1051/0004-6361/200913771. arXiv: 1008.1083 [astro-ph.SR].

— (2010b). "Probing the mass-loss history of AGB and red supergiant stars from CO rotational line profiles. II. CO line survey of evolved stars: derivation of mass-loss rate formulae". In: 523, A18, A18. DOI: 10.1051/0004-6361/200913771. arXiv: 1008.1083 [astro-ph.SR].

De Beck, E. et al. (2012a). "On the physical structure of IRC +10216. Ground-based and Herschel observations of CO and C_2H". In: 539, A108, A108. DOI: 10.1051/0004-6361/201117635. arXiv: 1201.1850 [astro-ph.SR].

De Beck, E. et al. (2012b). "On the physical structure of IRC +10216. Ground-based and Herschel observations of CO and C_2H". In: 539, A108, A108. DOI: 10.1051/0004-6361/201117635. arXiv: 1201.1850 [astro-ph.SR].

de Graauw, T. et al. (2010). "The Herschel-Heterodyne Instrument for the Far-Infrared (HIFI)". In: 518, L6, p. L6. DOI: 10.1051/0004-6361/201014698.

De Marco, O. and P. A. Crowther (1998). "The WC10 central stars CPD-56 deg8032 and He2-113 - II. Model analysis and comparison with nebular properties". In: 296, pp. 419–429. DOI: 10.1046/j.1365-8711.1998.01379.x.

de Vries, B. L. et al. (2010). "Determining the forsterite abundance of the dust around asymptotic giant branch stars". In: 516, A86, A86. DOI: 10.1051/0004-6361/200913588. arXiv: 1003.3100 [astro-ph.SR].

de Vries, B. L. et al. (2015). "Micron-sized forsterite grains in the pre-planetary nebula of IRAS 17150-3224. Searching for clues to the mysterious evolution of massive AGB stars". In: 576, A98, A98. DOI: 10.1051/0004-6361/201424843. arXiv: 1502.06766 [astro-ph.SR].

Decin, L. et al. (2006). "Probing the mass-loss history of AGB and red supergiant stars from CO rotational line profiles. I. Theoretical model - Mass-loss history unravelled in

<ASTROBJ>VY CMa</ASTROBJ>". In: 456, pp. 549–563. DOI: 10.1051/0004-6361:20065230. eprint: astro-ph/0606299.

Decin, L. et al. (2007). "The variable mass loss of the AGB star <ASTROBJ>WX Piscium</ASTROBJ> as traced by the CO J = 1-0 through 7-6 lines and the dust emission". In: 475.1, pp. 233–242. DOI: 10.1051/0004-6361:20077737. arXiv: 0708.4107 [astro-ph].

Decin, L. et al. (2010). "Water content and wind acceleration in the envelope around the oxygen-rich AGB star IK Tauri as seen by Herschel/HIFI". In: 521, L4, p. L4. DOI: 10.1051/0004-6361/201015069. arXiv: 1007.1102 [astro-ph.SR].

Dinh-V-Trung et al. (2008a). "Massive Expanding Torus and Fast Outflow in Planetary Nebula NGC 6302". In: 673, 934-941, pp. 934–941. DOI: 10.1086/524373. arXiv: 0710.3803.

— (2008b). "Massive Expanding Torus and Fast Outflow in Planetary Nebula NGC 6302". In: 673, 934-941, pp. 934–941. DOI: 10.1086/524373. arXiv: 0710.3803.

Doan, L. et al. (2017). "The extended molecular envelope of the asymptotic giant branch star π^1 Gruis as seen by ALMA. I. Large-scale kinematic structure and CO excitation properties". In: 605, A28, A28. DOI: 10.1051/0004-6361/201730703. arXiv: 1709.09435 [astro-ph.SR].

Engels, D. (1997). "Masers: Probing the mass loss process in PPN". In: *Planetary Nebulae*. Ed. by H. J. Habing and H. J. G. L. M. Lamers. Vol. 180. IAU Symposium, p. 348.

Fong, D. et al. (2001). "Low-excitation atomic gas around evolved stars. I. ISO observations of C-rich nebulae". In: 367, pp. 652–673. DOI: 10.1051/0004-6361:20000434.

Fong, D. et al. (2006). "Evolution of the Circumstellar Molecular Envelope. I. A BIMA CO Survey of Evolved Stars". In: 652.2, pp. 1626–1653. DOI: 10.1086/508127.

García-Hernández, D. A. et al. (2007). "Spitzer IRS Spectroscopy of High-Mass Precursors of Planetary Nebulae". In: 666, pp. L33–L36. DOI: 10.1086/521673. arXiv: 0707.4314.

García-Hernández, D. A. et al. (2010). "Formation of Fullerenes in H-containing Planetary Nebulae". In: 724, pp. L39–L43. DOI: 10.1088/2041-8205/724/1/L39. arXiv: 1009.4357 [astro-ph.SR].

Geballe, T. R. et al. (1989). "Unusual Features of the 1–4 Micron Spectrum of HR 4049". In: 340, p. L29. DOI: 10.1086/185431.

Goldman, Steven R. et al. (2017). "The wind speeds, dust content, and mass-loss rates of evolved AGB and RSG stars at varying metallicity". In: *Monthly Notices of the Royal Astronomical Society* 465.1, pp. 403–433. DOI: 10.1093/mnras/stw2708. eprint: /oup/backfile/content_public/journal/mnras/465/1/10.1093_mnras_stw2708/3/stw2708.pdf. URL: http://dx.doi.org/10.1093/mnras/stw2708.

Goldsmith, P. F. and W. D. Langer (1999). "Population Diagram Analysis of Molecular Line Emission". In: 517, pp. 209–225. DOI: 10.1086/307195.

Gómez, J. F. et al. (2005). "Spectral index of the H_2O-maser-emitting planetary nebula IRAS 17347-3139". In: 364.2, pp. 738–742. DOI: 10.1111/j.1365-2966.2005.09592.x. arXiv: astro-ph/0509246 [astro-ph].

Griffin, M. J. et al. (2010). "The Herschel-SPIRE instrument and its in-flight performance". In: 518, L3, p. L3. DOI: 10.1051/0004-6361/201014519. arXiv: 1005.5123 [astro-ph.IM].

Groenewegen, M. A. T. (1994). "The mass loss rates of OH/IR 32.8-0.3 and OH/IR 44.8-2.3." In: 290, pp. 544–552.

Groenewegen, M. A. T. et al. (1998). "Dust shells around carbon Mira variables". In: 293.1, pp. 18–42. DOI: 10.1046/j.1365-8711.1998.01113.x.

Groenewegen, M. A. T. et al. (2002). "Millimetre observations of infrared carbon stars. II. Mass loss rates and expansion velocities". In: 390, pp. 511–522. DOI: 10.1051/0004-6361:20020728.

Guandalini, R. et al. (2006). "Infrared photometry and evolution of mass-losing AGB stars. I. Carbon stars revisited". In: 445, pp. 1069–1080. DOI: 10.1051/0004-6361:20053208. eprint: astro-ph/0509739.

Hasegawa, T. I. and S. Kwok (2003). "Neutral Carbon in Post-Asymptotic Giant Branch Stars and Planetary Nebulae". In: 585, pp. 475–481. DOI: 10.1086/345950.

He, J. H., Dinh-V-Trung, and T. I. Hasegawa (2017a). "Monitor Variability of Millimeter Lines in IRC+10216". In: 845, 38, p. 38. DOI: 10.3847/1538-4357/aa7e76. arXiv: 1707.04329 [astro-ph.SR].

— (2017b). "Monitor Variability of Millimeter Lines in IRC+10216". In: 845, p. 38. DOI: 10.3847/1538-4357/aa7e76. arXiv: 1707.04329 [astro-ph.SR].

He, J. H. et al. (2014). "Observed Relationship between CO 2-1 and Dust Emission during the Post-asymptotic-giant-branch Phase". In: 210.2, 26, p. 26. DOI: 10.1088/0067-0049/210/2/26. arXiv: 1312.6975 [astro-ph.SR].

Heras, A. M. and S. Hony (2005). "Oxygen-rich AGB stars with optically thin dust envelopes". In: 439.1, pp. 171–182. DOI: 10.1051/0004-6361:20042296.

Herwig, F. (2005). "Evolution of Asymptotic Giant Branch Stars". In: 43, pp. 435–479. DOI: 10.1146/annurev.astro.43.072103.150600.

Hirano, Naomi et al. (2004). "High-Velocity Bipolar Outflow and Disklike Envelope in the Carbon Star V Hydrae". In: 616.1, pp. L43–L46. DOI: 10.1086/424382. arXiv: astro-ph/0407337 [astro-ph].

Höfner, Susanne and Hans Olofsson (2018). "Mass loss of stars on the asymptotic giant branch". In: *The Astronomy and Astrophysics Review* 26.1, p. 1. DOI: 10.1007/s00159-017-0106-5. URL: https://doi.org/10.1007/s00159-017-0106-5.

Hrivnak, Bruce J. and John H. Bieging (2005). "CO J = 2-1 and 4-3 Observations of Protoplanetary Nebulae: Time-variable Mass Loss". In: 624.1, pp. 331–351. DOI: 10.1086/428894.

Huang, P.-S. et al. (2016a). "The Shaping of the Multipolar Pre-planetary Nebula CRL 618 by Multidirectional Bullets". In: 820, 134, p. 134. DOI: 10.3847/0004-637X/820/2/134. arXiv: 1603.00199 [astro-ph.SR].

Huang, Po-Sheng et al. (2016b). "The Shaping of the Multipolar Pre-planetary Nebula CRL 618 by Multidirectional Bullets". In: 820.2, 134, p. 134. DOI: 10.3847/0004-637X/820/2/134. arXiv: 1603.00199 [astro-ph.SR].

Huarte Espinosa, Martin et al. (2010). "From Bipolar to Elliptical: Morphological Changes in the Temporal Evolution of PN". In: *arXiv e-prints*, arXiv:1011.4312, arXiv:1011.4312. arXiv: 1011.4312 [astro-ph.SR].

Ishigaki, M. N. et al. (2012). "The chemical composition of the post-asymptotic giant branch F supergiant CRL 2688". In: 425, pp. 997–1006. DOI: 10.1111/j.1365-2966.2012.21393.x. arXiv: 1205.6101 [astro-ph.SR].

Jeong, W. S. et al. (2007). "The Far-Infrared Properties of Spatially Resolved AKARI Observations". In: 59, S429. DOI: 10.1093/pasj/59.sp2.S429. arXiv: 0708.0254 [astro-ph].

Justtanont, K. et al. (2000). "ISO-LWS observations of rotational CO lines from C-rich objects: AFGL 2688, AFGL 618 and NGC 7027". In: 360, pp. 1117–1125.

Justtanont, K. et al. (2010). "A HIFI preview of warm molecular gas around χ Cygni: first detection of H_2O emission toward an S-type AGB star". In: 521, L6, p. L6. DOI: 10.1051/0004-6361/201015092. arXiv: 1007.1536 [astro-ph.GA].

Justtanont, K. et al. (2013). "OH/IR stars and their superwinds as observed by the Herschel Space Observatory". In: 556, A101, A101. DOI: 10.1051/0004-6361/201321812. arXiv: 1306.1777 [astro-ph.SR].

Karakas, Amanda I. and John C. Lattanzio (2014). "The Dawes Review 2: Nucleosynthesis and Stellar Yields of Low- and Intermediate-Mass Single Stars". In: 31, e030, e030. DOI: 10.1017/pasa.2014.21. arXiv: 1405.0062 [astro-ph.SR].

Khouri, T. et al. (2014). "The wind of W Hydrae as seen by Herschel. II. The molecular envelope of W Hydrae". In: 570, A67, A67. DOI: 10.1051/0004-6361/201424298. arXiv: 1409.0396 [astro-ph.SR].

Knapp, G. R., A. Jorissen, and K. Young (1997). "A 200km/s molecular wind in the peculiar carbon star V Hya." In: 326, pp. 318–328.

Knapp, G. R. et al. (1982). "Mass loss from evolved stars. I. Observations of 17 stars in the CO(2-1) line." In: 252, pp. 616–634. DOI: 10.1086/159589.

Knapp, G. R. et al. (1999). "The light curve and evolutionary status of the carbon star V Hya". In: 351, pp. 97–102. eprint: astro-ph/9907234.

Kress, M. E. (1997). "The Role of Dust in the Formation of Organics in Warm Circumstellar Media". PhD thesis. RENSSELAER POLYTECHNIC INSTITUTE.

Kwok, S. (2000a). *The Origin and Evolution of Planetary Nebulae*.

Kwok, Sun (1993). "Proto-planetary nebulae." In: 31, pp. 63–92. DOI: 10.1146/annurev.aa.31.090193.000431.

— (2000b). *The Origin and Evolution of Planetary Nebulae*.

Lambert, D. L. (1992). "Observational Effects of Nucleosynthesis in Evolved Stars". In: *Elements and the Cosmos*. Ed. by Mike G. Edmunds and Roberto Terlevich, p. 92.

Latter, W. B. and S. B. Charnley (1996). "Methanol in the Circumstellar Envelope of IRC +10 degrees 216". In: 463, p. L37. DOI: 10.1086/310046.

Lee, C.-F. et al. (2013). "Multiple Fast Molecular Outflows in the Pre-planetary Nebula CRL 618". In: 777, 37, p. 37. DOI: 10.1088/0004-637X/777/1/37. arXiv: 1308.6332.

Leuenhagen, U., W.-R. Hamann, and C. S. Jeffery (1996). "Spectral analyses of late-type WC central stars of planetary nebulae." In: 312, pp. 167–185.

Likkel, L. et al. (1988). "The molecular shell surrounding the compact planetary nebula IRAS 21282+5050". In: 198, pp. L1–L4.

Lombaert, R. et al. (2016a). "Constraints on the H_2O formation mechanism in the wind of carbon-rich AGB stars". In: 588, A124, A124. DOI: 10.1051/0004-6361/201527049. arXiv: 1601.07017 [astro-ph.SR].

— (2016b). "Constraints on the H_2O formation mechanism in the wind of carbon-rich AGB stars". In: 588, A124, A124. DOI: 10.1051/0004-6361/201527049. arXiv: 1601.07017 [astro-ph.SR].

Loup, C. et al. (1993). "CO and HCN observations of circumstellar envelopes. A catalogue - mass loss rates and distributions." In: 99, pp. 291–377.

Maercker, M. et al. (2008). "Circumstellar water vapour in M-type AGB stars: radiative transfer models, abundances, and predictions for HIFI". In: 479.3, pp. 779–791. DOI: 10.1051/0004-6361:20078680. arXiv: 0801.0971 [astro-ph].

Maercker, M. et al. (2016a). "A detailed view of the gas shell around R Sculptoris with ALMA". In: 586, A5, A5. DOI: 10.1051/0004-6361/201527128. arXiv: 1512.01350 [astro-ph.SR].

Maercker, M. et al. (2016b). "A HIFI view on circumstellar H_2O in M-type AGB stars: radiative transfer, velocity profiles, and H_2O line cooling". In: 591, A44, A44. DOI: 10.1051/0004-6361/201628310. arXiv: 1605.00504 [astro-ph.SR].

Maindonald, John and W. John Braun (2010). *Data Analysis and Graphics Using R: An Example-Based Approach*. 3rd. New York, NY, USA: Cambridge University Press. ISBN: 0521762936, 9780521762939.

Matsuura, M. et al. (2005). "The symmetric dust shell and the central star of the bipolar planetary nebula NGC6537*†". In: 363.2, pp. 628–640. DOI: 10.1111/j.1365-2966.2005.09464.x. arXiv: astro-ph/0507641 [astro-ph].

Matsuura, M. et al. (2014). "Herschel SPIRE and PACS observations of the red supergiant VY CMa: analysis of the molecular line spectra". In: 437, pp. 532–546. DOI: 10.1093/mnras/stt1906. arXiv: 1310.2947.

Matsuura, Mikako et al. (2016). "The mass-loss rates of red supergiants at low metallicity: detection of rotational CO emission from two red supergiants in the Large Magellanic Cloud". In: *Monthly Notices of the Royal Astronomical Society* 462.3, pp. 2995–3005. DOI: 10.1093/mnras/stw1853. eprint: /oup/backfile/content_public/journal/mnras/462/3/10.1093_mnras_stw1853/4/stw1853.pdf. URL: http://dx.doi.org/10.1093/mnras/stw1853.

Meaburn, J. et al. (2008). "Hubble-type outflows of the high-excitation poly-polar planetary nebula NGC 6302 - from expansion proper motions". In: 385.1, pp. 269–273. DOI: 10.1111/j.1365-2966.2007.12782.x. arXiv: 0711.4359 [astro-ph].

Meixner, M. and D. Fong (2004). "BIMA CO Survey of Evolved Stars". In: *Asymmetrical Planetary Nebulae III: Winds, Structure and the Thunderbird*. Ed. by Margaret Meixner et al. Vol. 313. Astronomical Society of the Pacific Conference Series, p. 307.

Meixner, M. et al. (1998). "Mass-Loss Histories of Three Carbon-rich Evolved Stars as Revealed by 12CO Emission". In: *The Astrophysical Journal* 509.1, p. 392. URL: http://stacks.iop.org/0004-637X/509/i=1/a=392.

Men'shchikov, A. B. et al. (2002). "Properties of the close binary and circumbinary torus of the <ASTROBJ>Red Rectangle</ASTROBJ>". In: 393, pp. 867–885. DOI: 10.1051/0004-6361:20020859. eprint: astro-ph/0206189.

Milam, S. N., N. J. Woolf, and L. M. Ziurys (2009). "Circumstellar $^{12}C/^{13}C$ Isotope Ratios from Millimeter Observations of CN and CO: Mixing in Carbon- and Oxygen-Rich Stars". In: 690, pp. 837–849. DOI: 10.1088/0004-637X/690/1/837.

Mishra, A., A. Li, and B. W. Jiang (2015). "A Tale of Three Mysterious Spectral Features in Carbon-rich Evolved Stars: The 21 μm, 30 μm, and Unidentified Infrared Emission Features". In: 802, 39, p. 39. DOI: 10.1088/0004-637X/802/1/39. arXiv: 1507.06596.

Molinari, Sergio et al. (1999). "Detection of the 62 Micron Crystalline H_2O Ice Feature in Emission toward HH 7 with the Infrared Space Observatory Long-Wavelength Spectrometer". In: 521.1, pp. L71–L74. DOI: 10.1086/312178.

Molster, F. J. et al. (2002). "Crystalline silicate dust around evolved stars. I. The sample stars". In: 382, pp. 184–221. DOI: 10.1051/0004-6361:20011550. arXiv: astro-ph/0201303 [astro-ph].

Neufeld, D. A. et al. (2010). "Discovery of water vapour in the carbon star V Cygni from observations with Herschel/HIFI". In: 521, L5, p. L5. DOI: 10.1051/0004-6361/201015080. arXiv: 1007.1235 [astro-ph.SR].

Neugebauer, G. et al. (1984). "The Infrared Astronomical Satellite (IRAS) mission." In: 278, pp. L1–L6. DOI: 10.1086/184209.

Nhung, P. T. et al. (2015). "^{12}CO emission from EP Aquarii: Another example of an axi-symmetric AGB wind?" In: 583, A64, A64. DOI: 10.1051/0004-6361/201526556. arXiv: 1508.05208 [astro-ph.SR].

Olofsson, H., K. Eriksson, and B. Gustafsson (1987). "CO (J=1-0) observations of bright carbon stars." In: 183, pp. L13–L16.

— (1988). "SEST CO (J=1-0) observations of carbon-rich circumstellar envelopes." In: 196, pp. L1–L4.

Olofsson, H. et al. (1993). "A study of circumstellar envelopes around bright carbon stars. I - Structure, kinematics, and mass-loss rate." In: 87, pp. 267–304. DOI: 10.1086/191804.

Olofsson, H. et al. (2002). "Mass loss rates of a sample of irregular and semiregular M-type AGB-variables". In: 391, pp. 1053–1067. DOI: 10.1051/0004-6361:20020841. eprint: astro-ph/0206172.

Olofsson, Hans (1996). "Circumstellar Molecular Envelopes of AGB and Post-AGB Objects". In: 245.2, pp. 169–200. DOI: 10.1007/BF00642225.

Pilbratt, G. L. et al. (2010). "Herschel Space Observatory. An ESA facility for far-infrared and submillimetre astronomy". In: 518, L1, p. L1. DOI: 10.1051/0004-6361/201014759. arXiv: 1005.5331 [astro-ph.IM].

Poglitsch, A. et al. (2010). "The Photodetector Array Camera and Spectrometer (PACS) on the Herschel Space Observatory". In: 518, L2, p. L2. DOI: 10.1051/0004-6361/201014535. arXiv: 1005.1487 [astro-ph.IM].

Ramos-Medina, J. et al. (2018a). "THROES: a caTalogue of HeRschel Observations of Evolved Stars. I. PACS range spectroscopy". In: 611, A41, A41. DOI: 10.1051/0004-6361/201731940. arXiv: 1711.05992 [astro-ph.SR].

Ramos-Medina, J. et al. (2018b). "Warm CO in evolved stars from the THROES catalogue. I. Herschel-PACS spectroscopy of O-rich envelopes". In: 618, A171, A171. DOI: 10.1051/0004-6361/201833177.

— (2018c). "Warm CO in evolved stars from the THROES catalogue. I. Herschel-PACS spectroscopy of O-rich envelopes (Corrigendum)". In: 619, C2, p. C2. DOI: 10.1051/0004-6361/201833177e.

Ramstedt, S. and H. Olofsson (2014a). "The ^{12}CO/^{13}CO ratio in AGB stars of different chemical type. Connection to the ^{12}C/^{13}C ratio and the evolution along the AGB". In: 566, A145, A145. DOI: 10.1051/0004-6361/201423721. arXiv: 1405.6404 [astro-ph.SR].

— (2014b). "The ^{12}CO/^{13}CO ratio in AGB stars of different chemical type. Connection to the ^{12}C/^{13}C ratio and the evolution along the AGB". In: 566, A145, A145. DOI: 10.1051/0004-6361/201423721. arXiv: 1405.6404 [astro-ph.SR].

Ramstedt, S., F. L. Schöier, and H. Olofsson (2009). "Circumstellar molecular line emission from S-type AGB stars: mass-loss rates and SiO abundances". In: 499, pp. 515–527. DOI: 10.1051/0004-6361/200911730. arXiv: 0903.1672 [astro-ph.SR].

Ramstedt, S. et al. (2006). "Mass-loss properties of S-stars on the AGB". In: 454.2, pp. L103–L106. DOI: 10.1051/0004-6361:20065285. arXiv: astro-ph/0605664 [astro-ph].

— (2008a). "On the reliability of mass-loss-rate estimates for AGB stars". In: 487, pp. 645–657. DOI: 10.1051/0004-6361:20078876. arXiv: 0806.0517.

— (2008b). "On the reliability of mass-loss-rate estimates for AGB stars". In: 487, pp. 645–657. DOI: 10.1051/0004-6361:20078876. arXiv: 0806.0517.

Ryde, N., F. L. Schöier, and H. Olofsson (1999a). "The carbon star IRAS 15194-5115: circumstellar CO radio and FIR rotational lines". In: 345, pp. 841–846. eprint: astro-ph/9903359.

— (1999b). "The carbon star IRAS 15194-5115: circumstellar CO radio and FIR rotational lines". In: 345, pp. 841–846. arXiv: astro-ph/9903359 [astro-ph].

Sackmann, I. J. and Arnold I. Boothroyd (1992). "The Creation of Superrich Lithium Giants". In: 392, p. L71. DOI: 10.1086/186428.

Sahai, R. et al. (2017). "ALMA Observations of the Water Fountain Pre-planetary Nebula IRAS 16342-3814: High-velocity Bipolar Jets and an Expanding Torus". In: 835.1, L13, p. L13. DOI: 10.3847/2041-8213/835/1/L13. arXiv: 1612.05616 [astro-ph.SR].

Sahai, Raghvendra, Ben E. K. Sugerman, and Kenneth Hinkle (2009). "Sculpting an Asymptotic Giant Branch Mass-Loss Envelope into a Bipolar Planetary Nebula: High-Velocity Outflows in V Hydrae". In: 699.2, pp. 1015–1023. DOI: 10.1088/0004-637X/699/2/1015. arXiv: 0905.0460 [astro-ph.GA].

Sánchez Contreras, C. and R. Sahai (2012a). "OPACOS: OVRO Post-AGB CO (1-0) Emission Survey. I. Data and Derived Nebular Parameters". In: 203.1, 16, p. 16. DOI: 10.1088/0067-0049/203/1/16.

— (2012b). "OPACOS: OVRO Post-AGB CO (1-0) Emission Survey. I. Data and Derived Nebular Parameters". In: 203, 16, p. 16. DOI: 10.1088/0067-0049/203/1/16.

Sánchez Contreras, C. et al. (2002). "Submilliarcsecond-resolution mapping of the 43 GHz SiO maser emission in the bipolar post-AGB nebula OH231.8+4.2". In: 385, pp. L1–L4. DOI: 10.1051/0004-6361:20020233.

Sánchez Contreras, C. et al. (2004). "1" Resolution Mapping of the Molecular Envelope of the Protoplanetary Nebula CRL 618". In: 617, pp. 1142–1156. DOI: 10.1086/425409.

Sánchez Contreras, C. et al. (2015). "Molecular ions in the O-rich evolved star OH231.8+4.2: HCO^+, $H^{13}CO^+$ and first detection of SO^+, N_2H^+, and H_3O^+". In: 577, A52, A52. DOI: 10.1051/0004-6361/201525652. arXiv: 1503.01290 [astro-ph.SR].

Sanchez Contreras, C. et al. (2017). "A pilot search for mm-wavelength recombination lines from emerging ionized winds in pre-planetary nebulae candidates". In: *ArXiv e-prints*. arXiv: 1704.01773 [astro-ph.SR].

Santander-García, M. et al. (2015). "SHAPEMOL: a 3D code for calculating CO line emission in planetary and protoplanetary nebulae. Detailed model-fitting of the complex nebula NGC 6302". In: 573, A56, A56. DOI: 10.1051/0004-6361/201322348. arXiv: 1410.6691 [astro-ph.IM].

Schöier, F. L. and H. Olofsson (2001a). "Models of circumstellar molecular radio line emission. Mass loss rates for a sample of bright carbon stars". In: 368, pp. 969–993. DOI: 10.1051/0004-6361:20010072. eprint: astro-ph/0101477.

— (2001b). "Models of circumstellar molecular radio line emission. Mass loss rates for a sample of bright carbon stars". In: 368, pp. 969–993. DOI: 10.1051/0004-6361:20010072. eprint: astro-ph/0101477.

Schöier, F. L., N. Ryde, and H. Olofsson (2002). "Probing the mass loss history of carbon stars using CO line and dust continuum emission". In: 391, pp. 577–586. DOI: 10.1051/0004-6361:20020833. arXiv: astro-ph/0206078 [astro-ph].

Schöier, F. L. et al. (2011). "A chemical inventory of the S-type AGB star χ Cygni based on Herschel/HIFI observations of circumstellar line emission. The importance of non-LTE

chemical processes in a dynamical region". In: 530, A83, A83. DOI: 10.1051/0004-6361/201116597.

Schwarz, Gideon (1978). "Estimating the Dimension of a Model". In: *Ann. Statist.* 6.2, pp. 461–464. DOI: 10.1214/aos/1176344136. URL: http://dx.doi.org/10.1214/aos/1176344136.

Shaw, Richard A. (2012). "Shape, structure, and morphology in planetary nebulae". In: *IAU Symposium*. Vol. 283. IAU Symposium, pp. 156–163. DOI: 10.1017/S1743921312010873. arXiv: 1111.3269 [astro-ph.SR].

Tafoya, D. et al. (2009). "A Collimated, Ionized Bipolar Structure and a High Density Torus in the Planetary Nebula IRAS 17347-3139". In: 691.1, pp. 611–620. DOI: 10.1088/0004-637X/691/1/611. arXiv: 0809.3931 [astro-ph].

Teyssier, D. et al. (2006a). "CO line emission from circumstellar envelopes". In: 450, pp. 167–179. DOI: 10.1051/0004-6361:20053759.

— (2006b). "CO line emission from circumstellar envelopes". In: 450, pp. 167–179. DOI: 10.1051/0004-6361:20053759.

Teyssier, D. et al. (2012). "Herschel/HIFI observations of red supergiants and yellow hypergiants. I. Molecular inventory". In: 545, A99, A99. DOI: 10.1051/0004-6361/201219545. arXiv: 1208.3143 [astro-ph.GA].

Teyssier, D. et al. (2015a). "Time Variability of Molecular Line Emission in IRC +10216". In: *Why Galaxies Care about AGB Stars III: A Closer Look in Space and Time*. Ed. by F. Kerschbaum, R. F. Wing, and J. Hron. Vol. 497. Astronomical Society of the Pacific Conference Series, p. 43.

— (2015b). "Time Variability of Molecular Line Emission in IRC +10216". In: *Why Galaxies Care about AGB Stars III: A Closer Look in Space and Time*. Ed. by F. Kerschbaum, R. F. Wing, and J. Hron. Vol. 497. Astronomical Society of the Pacific Conference Series, p. 43.

Van de Sande, M. et al. (2018). "Chemical content of the circumstellar envelope of the oxygen-rich AGB star R Doradus. Non-LTE abundance analysis of CO, SiO, and HCN". In: 609, A63, A63. DOI: 10.1051/0004-6361/201731298. arXiv: 1708.09190 [astro-ph.SR].

van der Veen, W. E. C. J. and H. J. Habing (1988). "The IRAS two-colour diagram as a tool for studying late stages of stellar evolution". In: 194, pp. 125–134.

van Winckel, H. (2003). "Post-AGB Stars". In: 41, pp. 391–427. DOI: 10.1146/annurev.astro.41.071601.170018.

Vickers, Shane B. et al. (2015). "New light on Galactic post-asymptotic giant branch stars - I. First distance catalogue". In: 447.2, pp. 1673–1691. DOI: 10.1093/mnras/stu2383. arXiv: 1403.7230 [astro-ph.SR].

Volk, K., S. Kwok, and P. P. Langill (1992). "Candidates for extreme carbon stars". In: 391, pp. 285–294. DOI: 10.1086/171344.

Waters, L. B. F. M. (1996). "New dust features in oxygen-rich envelopes". In: *Molecules in Astrophysics: Probes & Processes*. Ed. by Ewine Fleur van Dishoeck. Vol. 178. IAU Symposium, p. 367.

Wesson, R. et al. (2010a). "Herschel-SPIRE FTS spectroscopy of the carbon-rich objects AFGL 2688, AFGL 618, and NGC 7027". In: 518, L144, p. L144. DOI: 10.1051/0004-6361/201014589. arXiv: 1005.3279 [astro-ph.SR].

— (2010b). "Herschel-SPIRE FTS spectroscopy of the carbon-rich objects AFGL 2688, AFGL 618, and NGC 7027". In: 518, L144, p. L144. DOI: 10.1051/0004-6361/201014589. arXiv: 1005.3279 [astro-ph.SR].

Winters, J. M. et al. (1997). "Circumstellar dust shells around long-period variables. V. A consistent time-dependent model for the extreme carbon star AFGL 3068." In: 326, pp. 305–317.

Woods, P. M. et al. (2005). "Molecules in bipolar proto-planetary nebulae". In: 429, pp. 977–992. DOI: 10.1051/0004-6361:20034388. eprint: astro-ph/0407390.

Woods, Paul M. and Lars-Åke Nyman (2005). "H_2CO and CS in planetary nebulae". In: *IAU Symposium*. Vol. 235, p. 326.

Yang, B. et al. (2010). "Rotational Quenching of CO due to H_2 Collisions". In: 718, pp. 1062–1069. DOI: 10.1088/0004-637X/718/2/1062. arXiv: 1004.3923 [astro-ph.SR].

Young, K. (1995). "A CO(3–2) Survey of Nearby Mira Variables". In: 445, p. 872. DOI: 10.1086/175747. arXiv: astro-ph/9501020 [astro-ph].

Zeileis, A. et al. (2002). "strucchange: An R Package for Testing for Structural Change in Linear Regression Models". In: *Journal of Statistical Software* 7.1, pp. 1–38. ISSN: 1548-7660. DOI: 10.18637/jss.v007.i02. URL: https://www.jstatsoft.org/index.php/jss/article/view/v007i02.

Zijlstra, A. A. (2015). "Planetary nebulae in 2014: A review of research". In: 51, p. 221. arXiv: 1506.05508 [astro-ph.SR].

Zuckerman, B. and H. M. Dyck (1986). "Dust grains and gas in the circumstellar envelopes around luminous red giant stars". In: 311, pp. 345–359. DOI: 10.1086/164776.